Model Uncertainties Related to Construction Phases, Restrained Deformations and Concrete Hydration in a Top-down Reinforced Concrete Cut-and-cover Tunnel: a Nonlinear Study

---

Application in Galleria Piscinale – San Donato Bypass



Supervisors:

Prof. Gabriele Bertagoli

Ing. Mario Ferrara

Candidate:

Nicolas Ballesteros

(s337599)

September 2026

Statement of Originality

I hereby declare that the content and structure of this thesis constitute my own original work, except where otherwise explicitly acknowledged. All sources, contributions, and materials produced by others have been appropriately identified and cited in accordance with accepted academic standards.

To the best of my knowledge, this thesis does not infringe upon any rights of third parties, including intellectual property rights and rights relating to privacy and the protection of personal data.

Confidentiality Notice

This thesis contains confidential and/or sensitive information and is therefore subject to restricted access. It is not intended for public dissemination, publication, or distribution.

The contents of this thesis are confidential and may not be reproduced, disclosed, distributed, quoted, published, or otherwise used, in whole or in part, by third parties without the prior written authorization of the author and, where applicable, of the parties holding rights or legitimate interests in the information concerned.

Any access to this thesis granted for academic or administrative purposes shall not be construed as permission to use, reproduce, disclose, or disseminate its contents.

Acknowledgment

I would like to express my sincere gratitude to my supervisors, Prof. Gabrielle Bertagnoli and Eng. Mario Ferrara for their continuous guidance, valuable insights, and steadfast support throughout the development of this thesis. I am also grateful to the faculty members and staff of the Politecnico di Torino for providing the resources and academic environment essential to this work.

My appreciation extends to my colleagues and all my friends for their fruitful discussions, assistance, and collaborative spirit during this research.

Finally, I want to express my deepest gratitude to my family for giving me the opportunity to study abroad and for their unwavering support, encouragement, and patience throughout my academic journey. I also thank my friends for their constant companionship along the way.

Abstract

Massive underground infrastructure, such as highway cut-and-cover tunnels, operates under complex mechanical boundary conditions where evaluating structural restraint represents a significant challenge. These structures must withstand gravitational and geotechnical actions; including lateral earth pressures, landslide thrusts, and groundwater fluctuations; while simultaneously undergoing restrained deformations. Because the structural lining interacts continuously with the surrounding ground and deep pile foundations, concrete hydration heat, drying shrinkage, viscoelastic creep, and seasonal temperature shifts generate implicit coactions governed by systemic boundary stiffness across multi-year construction sequences.

To investigate the structural impact of these implicit actions, this study presents a numerical analysis of a top-down reinforced concrete portal frame tunnel anchored by deep pile foundations as a representative case study. A time-dependent, thermo-mechanical Finite Element Analysis (FEA) framework was developed to simulate the staged construction process, encompassing chronological casting phases, maturity-based material property evolution, backfilling, internal core excavation, and long-term environmental thermal cycling. To evaluate the sensitivity of structural safety to numerical idealizations, five modelling configurations of varying fidelity, ranging from a conventional linear elastic baseline to stage non-linear continuum formulations, were systematically analysed.

Under the adopted numerical assumptions, the multi-field continuum framework captures significant stress-relief mechanisms. Incorporating concrete tensile cracking and viscoelastic strain compliance into the continuum allows localized stress concentrations to relax, reducing computed seasonal thermal load swings by up to 70% compared to uncracked elastic baselines. Furthermore, when transitioning from local cross-sectional checks to the Estimation of Coefficient of Variation (ECOV) global safety format, the non-linear assessment produces higher global resistance estimates than the conventional linear sectional verification. By accounting for plastic load redistribution across the integrated frame-pile system rather than relying on localized elastic stress peaks, the findings suggest that structural utilization estimates may vary significantly depending on the assumed level of numerical detail and safety format.

Table of Contents

Chapter 1 Problem Statement *1*

1.1 Early-Age Concrete Durability and Property Evolution **1**

1.1.1 Microstructural Durability and Cracking Risk 1

1.1.2 Mathematical Modelling of Early-Age Concrete properties 2

1.2 Thermal Dynamics of Cement Hardening **3**

1.3 Shrinkage and Rheological creep Interactions **4**

1.4 Problem of Early Age Concrete Applied to massive structural castings **6**

Chapter 2 The Artificial Tunnel: Layout and Materials *7*

2.1 Tunnel Geometric Characteristics **7**

2.2 Mechanical Properties and Structural Allocations **9**

2.2.1 Concrete Characteristics 9

2.2.2 Steel Characteristics 10

2.2.3 Reinforcement Layout 11

2.3 Project Timeline **15**

Chapter 3 Finite Element Discretization and Model Configurations in DIANA *17*

3.1 General Numerical Framework and Structural Modelling Principles **18**

3.1.1 Model Geometry 18

3.1.2 Material Non-Linearity Assumptions 18

3.1.3 Modelling of the Concrete Shrinkage 20

3.1.4 Modelling of the Concrete Creep 22

3.1.5 Modelling of Thermal Properties of Concrete 24

3.1.6 Modelling of the Geotechnical Effects 29

3.1.7 Modelling of the Reinforcements and the Soil Interaction 29

3.1.8 Modelling of the Internal Interfaces 31

3.1.9 Stress Convention 32

3.2 Model 1: Research Model and Reference Baseline **33**

3.3 Model 2: Numerical Discretization of the Hydration Effect **35**

3.4 Model 3: Standard Non-Linear Model without Cracking **38**

3.5 Model 4: Standard Non-Linear Model without Creep **38**

3.6 Model 5: Standard Linear Elastic Baseline with Aging **39**

Chapter 4 Comparison Between the Models *40*

4.1 Cover Slab Structural Sections **41**

4.1.1 Uphill Support Section 41

4.1.2 Midspan Section 46

4.1.3 Downhill Support Section 50

4.1.4 Discrepancies Between Models and Actions Combinations 55

4.2 Uphill Pile (D = 1200 mm) **57**

4.2.1 Head Section 57

4.2.2 Cover Slab Level Section 62

4.2.3 Discrepancies between Models and Actions Combinations 66

4.3 Uphill Pile (D = 2000 mm) **69**

4.3.1 Head Section 69

4.3.2 Cover Slab Level Section 74

4.3.3 Discrepancies between Models and Actions Combinations 78

4.4 Downhill Pile (D = 2000 mm) **81**

4.4.1 Head Section 81

4.4.2 Cover Slab Level Section 86

4.4.3 Discrepancies between Models and Actions Combinations 90

4.5 Foundation Slab **92**

4.5.1 Uphill Support 92

4.5.2 Midspan Section 97

4.5.3 Downhill Support Section 101

4.5.4 Discrepancies between Models and Actions Combinations 106

4.6 Uphill Wall **108**

4.6.1 Top Section 108

4.6.2 Mid-height Section 113

4.6.3 Bottom Section 117

4.6.4 Discrepancies between Models and Actions Combinations 122

4.7 Downhill Wall **123**

4.7.1 Top Section 123

4.7.2 Mid-height Section 128

4.7.3 Bottom Section 132

4.7.4 Discrepancies between Models and Actions Combinations 137

Chapter 5 Safety Evaluation *139*

5.1 Traditional Design Approach **139**

5.1.1 Theoretical Principles 139
5.1.2 Component Breakdown of Internal Actions 141
5.1.3 ULS for Bending and Axial Actions – Rectangular Section 155
5.1.4 ULS for Bending and Axial Actions – Circular Section 157
5.1.5 ULS for Shear Actions – Rectangular Section 159
5.1.6 ULS for Shear Actions – Circular Section 161
5.1.7 Bending Moment Verification Results 162
5.1.8 Shear Force Verification Results 166

5.2 ECOV Global Safety Format Approach 171
5.2.1 Conceptual Framework 171
5.2.2 Load Evolution 171
5.2.3 Dual Non-Linear Computational Strategy 172
5.2.4 Probabilistic Formulation 174
5.2.5 Model Uncertainty in Non-Linear Analyses 174
5.2.6 Design Global Resistance 177
5.2.7 Global Safety Evaluation via the ECOV Method 179

Chapter 6 Non-Linear Failure Mechanisms and Collapse Analysis 187

6.1 Methodological Framework 187

6.2 Collapse Dynamics of Model 1 189
6.2.1 Winter Casting: Peak Maximum and Peak Minimum Temperature 189
6.2.2 Summer Casting: Peak Maximum and Peak Minimum Temperature 196

6.3 Collapse Dynamics of Model 2 202
6.3.1 Winter Casting: Peak Maximum and Peak Minimum Temperatures 202
6.3.2 Summer Casting: Peak Maximum Temperatures and Peak Minimum Temperatures 209

6.4 Comparative Synthesis: Model 1 vs Model 2 Collapse Behaviour 215

Chapter 7 Final Conclusions 217

Bibliography 221

Index of Figures

Figure 2-1 - Cross-section of artificial tunnel section AA 8
Figure 2-2 - Foundation Slab Reinforcement Layout 14
Figure 2-3 - Reinforcement Layout at the Pile Head of (a) Downhill Pile (b) Uphill Piles 15
Figure 3-1 - Geometry of the FEM Model 18
Figure 3-2 - Non-Linear Behaviour of Concrete Under Tension, (a) Tensile and Tensile-Compression Failure Envelopes in the Principal Stress Plane, (b) Tension Softening 20
Figure 3-3 - Shrinkage Curves 22
Figure 3-4 - Physical Representation of a Kelvin Chain 23
Figure 3-5 - Creep Curves 23
Figure 3-6 - Evolution of Elastic Modulus over Time 24
Figure 3-7 - Adiabatic Curve for Concrete 28
Figure 3-8 - Reinforcement Arrangement 30
Figure 3-9 - Elasto-Plastic-Yielding Constitutive Relationship of the Reinforcement 30
Figure 3-10 - Constitutive Relationship of the Soil 31
Figure 3-11 - Interfaces between Structural Elements 31
Figure 3-12 - Stress Conventions (a) Bending Moment in the Main Beam and Strut (b) Bending Moment in the Piles and Shafts (c) Shear in the Main Beam and Strut (d) Shear in the Piles and Shafts 33
Figure 3-13 - Linear Tension Softening Stress-Strain Diagram 36
Figure 3-14 - Overview of the 5 Models 39
Figure 4-1 - Moment – Geotechnical Actions and Coactions - Cover Slab Uphill Support 41
Figure 4-2 - Moment - Geotechnical and Creep Actions – Cover Slab Uphill Support 42
Figure 4-3 - Moment - Complete Coactions - Cover Slab Uphill Support 42
Figure 4-4 - Axial Force - Geotechnical Actions and Coactions - Cover Slab Uphill Support 43
Figure 4-5 - Axial Force - Geotechnical and Creep Actions - Cover Slab Uphill Support 43
Figure 4-6 - Axial Force - Complete Coactions - Cover Slab Uphill Support 44
Figure 4-7 – Shear Force - Geotechnical Actions and Coactions - Cover Slab Uphill Support 44
Figure 4-8 – Shear Force - Geotechnical and Creep Actions - Cover Slab Uphill Support 45
Figure 4-9 – Shear Force - Complete Coactions - Cover Slab Uphill Support 45
Figure 4-10 - Moment - Geotechnical Actions and Coactions - Cover Slab Midspan 46
Figure 4-11 - Moment - Geotechnical and Creep Actions - Cover Slab Midspan 46
Figure 4-12 - Moment - Complete Coactions - Cover Slab Midspan 47
Figure 4-13 - Axial Force - Geotechnical Actions and Coactions - Cover Slab Midspan 47
Figure 4-14 - Axial Force - Geotechnical and Creep Actions - Cover Slab Midspan 48
Figure 4-15 - Axial Force - Complete Coactions - Cover Slab Midspan 48
Figure 4-16 – Shear Force - Geotechnical Actions and Coactions - Cover Slab Midspan 49
Figure 4-17 – Shear Force - Geotechnical and Creep Actions - Cover Slab Midspan 49
Figure 4-18 – Shear Force - Complete Coactions - Cover Slab Midspan 50
Figure 4-19 - Moment - Geotechnical Actions and Coactions - Cover Slab Downhill Support 50
Figure 4-20 - Moment - Geotechnical and Creep Actions - Cover Slab Downhill Support 51
Figure 4-21 - Moment - Complete Coactions - Cover Slab Downhill Support 51
Figure 4-22 - Axial Force - Geotechnical Actions and Coactions - Cover Slab Downhill Support 52
Figure 4-23 - Axial Force - Geotechnical and Fluage Actions - Cover Slab Downhill Support 52
Figure 4-24 - Axial Force - Complete Coactions - Cover Slab Downhill Support 53
Figure 4-25 – Shear Force - Geotechnical Actions and Coactions- Cover Slab Downhill Support 53
Figure 4-26 – Shear Force - Geotechnical and Creep Actions - Cover Slab Downhill Support 54
Figure 4-27 – Shear Force - Complete Coactions - Cover Slab Downhill Support 54
Figure 4-28 - Moment - Geotechnical Actions and Coactions - Head Pile 1200 57
Figure 4-29 - Moment - Geotechnical and Creep Actions - Head Pile 1200 58
Figure 4-30 - Moment - Complete Coactions – Head Pile 1200 58
Figure 4-31 - Axial Force - Geotechnical Actions and Coactions - Head Pile 1200 59
Figure 4-32 - Axial Force - Geotechnical and Creep Actions - Head Pile 1200 59
Figure 4-33 - Axial Force - Complete Coactions - Head Pile 1200 60
Figure 4-34 – Shear Force- Geotechnical Actions and Coactions - Head Pile 1200 60
Figure 4-35 – Shear Force- Geotechnical and Creep Actions – Head Pile 1200 61
Figure 4-36 – Shear Force- Complete Coactions – Head Pile 1200 61
Figure 4-37 - Moment - Geotechnical Actions and Coactions - Pile 1200 Cover Slab Level 62
Figure 4-38 - Moment - Geotechnical and Creep Actions - Pile 1200 Cover Slab Level 62
Figure 4-39 - Moment - Complete Actions - Pile 1200 Cover Slab Level 63

Figure 4-40 - Axial Force - Geotechnical Actions and Coactions - Pile 1200 Cover Slab Level 63
Figure 4-41 - Axial Force - Geotechnical and Creep Actions - Pile 1200 Cover Slab Level 64
Figure 4-42 - Axial Force - Complete Coactions - Pile 1200 Cover Slab Level 64
Figure 4-43 – Shear Force - Geotechnical Actions and Coactions - Pile 1200 Cover Slab Level 65
Figure 4-44 – Shear Force - Geotechnical and Creep Actions - Pile 1200 Cover Slab Level 65
Figure 4-45 – Shear Force - Complete Coactions- Pile 1200 Cover Slab Level 66
Figure 4-46 - Moment - Geotechnical Actions and Coactions - Head Pile 2000 Uphill 69
Figure 4-47 - Moment - Geotechnical and Creep Actions - Head Pile 2000 Uphill 70
Figure 4-48 - Moment - Complete Coactions - Head Pile 2000 Uphill 70
Figure 4-49 - Axial Force - Geotechnical Actions and Coactions - Head Pile 2000 Uphill 71
Figure 4-50 - Axial Force - Geotechnical and Creep Actions - Head Pile 2000 Uphill 71
Figure 4-51 - Axial Force - Complete Coactions - Head Pile 2000 Uphill 72
Figure 4-52 – Shear Force - Geotechnical Actions and Coactions - Head Pile 2000 Uphill 72
Figure 4-53 – Shear Force - Geotechnical and Creep Actions - Head Pile 2000 Uphill 73
Figure 4-54 – Shear Force - Complete Coactions - Head Pile 2000 Uphill 73
Figure 4-55 - Moment - Geotechnical Actions - Pile 2000 Uphill Cover Slab Level 74
Figure 4-56 - Moment - Geotechnical and Creep Actions - Pile 2000 Uphill Cover Slab Level 74
Figure 4-57 - Moment - Complete Coactions - Pile 2000 Uphill Cover Slab Level 75
Figure 4-58 - Axial Force - Geotechnical Actions and Coactions - Pile 2000 Uphill Cover Slab Level 75
Figure 4-59 - Axial Force - Geotechnical and Creep Actions - Pile 2000 Uphill Cover Slab Level 76
Figure 4-60 - Axial Force - Complete Coactions - Pile 2000 Uphill Cover Slab Level 76
Figure 4-61 – Shear Force - Geotechnical Actions and Coactions - Pile 2000 Uphill Cover Slab Level 77
Figure 4-62– Shear Force - Geotechnical and Creep Actions - Pile 2000 Uphill Cover Slab Level 77
Figure 4-63 – Shear Force - Complete Coactions - Pile 2000 Uphill Cover Slab Level 78
Figure 4-64 - Moment - Geotechnical Actions and Coactions - Head Pile 2000 Downhill 81
Figure 4-65 - Moment - Geotechnical and Creep Actions - Head Pile 2000 Downhill 82
Figure 4-66 - Moment - Complete Coactions - Head Pile 2000 Downhill 82
Figure 4-67 - Axial Force - Geotechnical Actions and Coactions- Head Pile 2000 Downhill 83
Figure 4-68 - Axial Force - Geotechnical and Creep Actions - Head Pile 2000 Downhill 83
Figure 4-69 - Axial Force - Geotechnical and Creep Actions - Head Pile 2000 Downhill 84
Figure 4-70 – Shear Force - Geotechnical Actions and Coactions - Head Pile 2000 Downhill 84
Figure 4-71 – Shear Force - Geotechnical and Creep Actions - Head Pile 2000 Downhill 85
Figure 4-72 - Shear Force - Complete Coactions - Head Pile 2000 Downhill 85
Figure 4-73 - Moment - Geotechnical Actions and Coactions - Pile 2000 Downhill Cover Slab Level 86
Figure 4-74 - Moment - Geotechnical and Creep Actions - Pile 2000 Downhill Cover Slab Level 86
Figure 4-75 - Moment - Complete Coactions - Pile 2000 Downhill Cover Slab Level 87
Figure 4-76 - Axial Force - Geotechnical Actions - Pile 2000 Downhill Cover Slab Level 87
Figure 4-77 - Axial Force - Geotechnical and Creep Actions - Pile 2000 Downhill Cover Slab Level 88
Figure 4-78 - Axial Force - Complete Coactions - Pile 2000 Downhill Cover Slab Level 88
Figure 4-79 – Shear Force - Geotechnical Actions and Coactions - Pile 2000 Downhill Cover Slab Level 89
Figure 4-80 – Shear Force - Geotechnical and Creep Actions - Pile 2000 Downhill Cover Slab Level 89
Figure 4-81 – Shear Force - Complete Coactions - Pile 2000 Downhill Cover Slab Level 90
Figure 4-82 - Moment - Geotechnical Actions and Coactions - Foundation Slab Uphill Support 92
Figure 4-83 - Moment - Geotechnical and Creep Actions - Foundation Slab Uphill Support 93
Figure 4-84 - Moment - Complete Coactions - Foundation Slab Uphill Support 93
Figure 4-85 - Axial Force - Geotechnical Actions and Coactions - Foundation Slab Uphill Support 94
Figure 4-86 - Axial Force - Geotechnical and Creep Actions - Foundation Slab Uphill Support 94
Figure 4-87 - Axial Force - Complete Coactions - Foundation Slab Uphill Support 95
Figure 4-88 – Shear Force - Geotechnical Actions and Coactions - Foundation Slab Uphill Support 95
Figure 4-89 – Shear Force - Geotechnical and Creep Actions - Foundation Slab Uphill Support 96
Figure 4-90 – Shear Force - Complete Coactions - Foundation Slab Uphill Support 96
Figure 4-91 - Moment - Geotechnical Actions and Coactions - Foundation Slab Midspan 97
Figure 4-92 - Moment - Geotechnical and Creep Actions - Foundation Slab Midspan 97
Figure 4-93 - Moment - Complete Coactions - Foundation Slab Midspan 98
Figure 4-94 - Axial Force - Geotechnical Actions and Coactions - Foundation Slab Midspan 98
Figure 4-95 - Axial Force - Geotechnical and Creep Actions - Foundation Slab Midspan 99
Figure 4-96 - Axial Force - Complete Coactions - Foundation Slab Midspan 99
Figure 4-97 – Shear Force - Geotechnical Actions and Coactions - Foundation Slab Midspan 100
Figure 4-98 – Shear Force - Geotechnical and Creep Actions - Foundation Slab Midspan 100
Figure 4-99 – Shear Force - Complete Coactions - Foundation Slab Midspan 101

Figure 4-100 - Moment - Geotechnical Actions and Coactions - Foundation Slab Downhill Support 101
Figure 4-101 - Moment - Geotechnical and Creep Actions - Foundation Slab Downhill Support 102
Figure 4-102 - Moment - Complete Coactions - Foundation Slab Downhill Support 102
Figure 4-103 - Axial Force - Geotechnical Actions and Coactions - Foundation Slab Downhill Support 103
Figure 4-104 - Axial Force - Geotechnical and Creep Actions - Foundation Slab Downhill Support 103
Figure 4-105 - Axial Force - Complete Coactions - Foundation Slab Downhill Support 104
Figure 4-106 – Shear Force - Geotechnical Actions and Coactions - Foundation Slab Downhill Support 104
Figure 4-107 – Shear Force - Geotechnical and Creep Actions - Foundation Slab Downhill Support 105
Figure 4-108 – Shear Force - Complete Coactions - Foundation Slab Downhill Support 105
Figure 4-109 - Moment - Geotechnical Actions and Coactions - Top Uphill Wall 108
Figure 4-110 - Moment - Geotechnical and Creep Actions - Top Uphill Wall 109
Figure 4-111 - Moment - Complete Coactions - Top Uphill Wall 109
Figure 4-112 - Axial Force - Geotechnical Actions and Coactions - Top Uphill Wall 110
Figure 4-113 - Axial Force - Geotechnical and Creep Actions - Top Uphill Wall 110
Figure 4-114 - Axial Force - Complete Coactions - Top Uphill Wall 111
Figure 4-115 – Shear Force - Geotechnical Actions and Coactions - Top Uphill Wall 111
Figure 4-116 – Shear Force - Geotechnical and Creep Actions - Top Uphill Wall 112
Figure 4-117 – Shear Force - Complete Coactions - Top Uphill Wall 112
Figure 4-118 - Moment - Geotechnical Actions and Coactions – Mid-height Uphill Wall 113
Figure 4-119 - Moment - Geotechnical and Creep Actions – Mid-height Uphill Wall 113
Figure 4-120 - Moment - Complete Coactions – Mid-height Uphill Wall 114
Figure 4-121 - Axial Force - Geotechnical Actions – Mid-height Uphill Wall 114
Figure 4-122 - Axial Force - Geotechnical and Creep Actions – Mid-height Uphill Wall 115
Figure 4-123 - Axial Force - Complete Coactions – Mid-height Uphill Wall 115
Figure 4-124 – Shear Force - Geotechnical Actions and Coc-actions – Mid-height Uphill Wall 116
Figure 4-125 – Shear Force - Geotechnical and Creep Actions – Mid-height Uphill Wall 116
Figure 4-126 – Shear Force - Complete Coactions – Mid-height Uphill Wall 117
Figure 4-127 - Moment - Geotechnical Actions and Coactions - Bottom Uphill Wall 117
Figure 4-128 - Moment - Geotechnical and Creep Actions - Bottom Uphill Wall 118
Figure 4-129 - Moment - Complete Coactions - Bottom Uphill Wall 118
Figure 4-130 - Axial Force - Geotechnical Actions and Coactions - Bottom Uphill Wall 119
Figure 4-131 - Axial Force - Geotechnical and Creep Actions - Bottom Uphill Wall 119
Figure 4-132 - Axial Force - Complete Coactions - Bottom Uphill Wall 120
Figure 4-133 – Shear Force - Geotechnical Actions and Coactions- Bottom Uphill Wall 120
Figure 4-134 – Shear Force - Geotechnical and Creep Actions - Bottom Uphill Wall 121
Figure 4-135 – Shear Force - Complete Coactions - Bottom Uphill Wall 121
Figure 4-136 - Moment - Geotechnical Actions and Coactions - Top Downhill Wall 123
Figure 4-137 - Moment - Geotechnical and Creep Actions - Top Downhill Wall 124
Figure 4-138 - Moment - Complete Coactions - Top Downhill Wall 124
Figure 4-139 - Axial Force - Geotechnical Actions and Coactions - Top Downhill Wall 125
Figure 4-140 - Axial Force - Geotechnical and Creep Actions - Top Downhill Wall 125
Figure 4-141 - Axial Force - Complete Coactions - Top Downhill Wall 126
Figure 4-142 – Shear Force - Geotechnical Actions and Coactions - Top Downhill Wall 126
Figure 4-143 – Shear Force - Geotechnical and Creep Actions - Top Downhill Wall 127
Figure 4-144 – Shear Force - Complete Coactions - Top Downhill Wall 127
Figure 4-145 - Moment - Geotechnical Actions and Coactions – Mid-height Downhill Wall 128
Figure 4-146 - Moment - Geotechnical and Creep Actions – Mid-height Downhill Wall 128
Figure 4-147 - Moment - Complete Coactions – Mid-height Downhill Wall 129
Figure 4-148 - Axial Force - Geotechnical Actions and Coactions – Mid-height Downhill Wall 129
Figure 4-149 - Axial Force - Geotechnical and Fluage Actions – Mid-height Downhill Wall 130
Figure 4-150 - Axial Force - Complete Coactions – Mid-height Downhill Wall 130
Figure 4-151 – Shear Force - Geotechnical Actions and Coactions – Mid-height Downhill Wall 131
Figure 4-152 – Shear Force - Geotechnical and Creep Actions – Mid-height Downhill Wall 131
Figure 4-153 – Shear Force - Complete Coactions – Mid-height Downhill Wall 132
Figure 4-154 - Moment - Geotechnical Actions and Coactions - Bottom Downhill Wall 132
Figure 4-155 - Moment - Geotechnical and Creep Actions - Bottom Downhill Wall 133
Figure 4-156 - Moment - Complete Coactions - Bottom Downhill Wall 133
Figure 4-157 - Axial Force - Geotechnical Actions and Coactions- Bottom Downhill Wall 134
Figure 4-158 - Axial Force - Geotechnical and Creep Actions - Bottom Downhill Wall 134
Figure 4-159 - Axial Force - Complete Coactions - Bottom Downhill Wall 135

Figure 4-160 – Shear Force - Geotechnical Actions and Coactions - Bottom Downhill Wall 135
Figure 4-161 – Shear Force - Geotechnical and Creep Actions - Bottom Downhill Wall 136
Figure 4-162 – Shear Force - Complete Coactions - Bottom Downhill Wall 136
Figure 5-1 - Component Disaggregation of Bending Moment – Cover Slab Midspan 141
Figure 5-2 - Component Disaggregation of Axial Force – Cover Slab Midspan 142
Figure 5-3 - Component Disaggregation of Shear Force – Cover Slab Midspan 142
Figure 5-4 - Component Disaggregation of Bending Moment - Head of Pile 1200 Uphill 143
Figure 5-5 - Component Disaggregation of Axial Force - Head of Pile 1200 Uphill 144
Figure 5-6 - Component Disaggregation of Shear Force - Head of Pile 1200 Uphill 144
Figure 5-7 - Component Disaggregation of Bending Moment - Pile 2000 Uphill Cover Slab level 145
Figure 5-8 - Component Disaggregation of Axial Force - Pile 2000 Uphill Cover Slab level 146
Figure 5-9 - Component Disaggregation of Shear Force - Pile 2000 Uphill Cover Slab level 146
Figure 5-10 - Component Disaggregation of Bending Moment - Head of Pile 2000 Downhill 147
Figure 5-11 - Component Disaggregation of Axial Force - Head of Pile 2000 Downhill 148
Figure 5-12 - Component Disaggregation of Shear Force - Head of Pile 2000 Downhill 148
Figure 5-13 - Component Disaggregation of Bending Moment - Top Uphill Wall 149
Figure 5-14 - Component Disaggregation of Axial Force - Top Uphill Wall 150
Figure 5-15 - Component Disaggregation of Shear Force - Top Uphill Wall 150
Figure 5-16 -Component Disaggregation of Bending Moment – Top Downhill Wall 151
Figure 5-17 - Component Disaggregation of Axial Force - Top Downhill Wall 152
Figure 5-18 - Component Disaggregation of Shear Force - Top Downhill Wall 152
Figure 5-19 - Component Disaggregation of Bending Moment - Uphill Section Foundation Slab 153
Figure 5-20 - Component Disaggregation of Axial Force - Uphill Section Foundation Slab 154
Figure 5-21 - Component Disaggregation of Shear Force - Uphill Section Foundation Slab 154
Figure 5-22 - Variable Angle Truss Model 160
Figure 5-23 - Probability Density Function of Load Multipliers 178
Figure 5-24 - Cumulative Density Function of Load Multipliers 179
Figure 5-25 - Safety Coefficients Comparison 184
Figure 6-1 - Model 1: Winter Casting Max Temperatures - εkn 189
Figure 6-2 - Model 1: Winter Casting Max Temperatures - $S1$ 190
Figure 6-3 - Model 1: Winter Casting Max Temperatures - $S2$ 190
Figure 6-4 - Model 1: Winter Casting Max Temperatures - Sxx 191
Figure 6-5 - Figure 6 2 - Model 1: Winter Casting Max Temperatures - Syy 191
Figure 6-6 - Model 1: Winter Casting Min Temperatures - εkn 192
Figure 6-7 - Model 1: Winter Casting Min Temperatures - $S1$ 193
Figure 6-8 - Model 1: Winter Casting Min Temperatures - $S2$ 193
Figure 6-9 - Model 1: Winter Casting Min Temperatures - Sxx 194
Figure 6-10 - Model 1: Winter Casting Min Temperatures - Syy 194
Figure 6-11 - Model 1: Summer Casting Max Temperatures - εkn 196
Figure 6-12 - Model 1: Summer Casting Max Temperatures - $S1$ 196
Figure 6-13 - Model 1: Summer Casting Max Temperatures - $S2$ 197
Figure 6-14 - Model 1: Summer Casting Max Temperatures – SXX 197
Figure 6-15 - Model 1: Summer Casting Max Temperatures - Syy 198
Figure 6-16 - Model 1: Summer Casting Min Temperatures - εkn 199
Figure 6-17 - Model 1: Summer Casting Min Temperatures - $S1$ 199
Figure 6-18- Model 1: Summer Casting Min Temperatures - $S2$ 200
Figure 6-19- Model 1: Summer Casting Min Temperatures - Sxx 200
Figure 6-20 - Model 1: Summer Casting Min Temperatures - Syy 201
Figure 6-21 - Model 2: Winter Casting Max Temperatures - εkn 202
Figure 6-22- Model 2: Winter Casting Max Temperatures -$S1$ 203
Figure 6-23- Model 2: Winter Casting Max Temperatures - $S2$ 203
Figure 6-24 - Model 2: Winter Casting Max Temperatures -Sxx 204
Figure 6-25 - Model 2: Winter Casting Max Temperatures - Syy 204
Figure 6-26 - Model 2: Winter Casting Min Temperatures - εkn 205
Figure 6-27- Model 2: Winter Casting Min Temperatures - $S1$ 206
Figure 6-28- Model 2: Winter Casting Min Temperatures - $S2$ 206
Figure 6-29- Model 2: Winter Casting Min Temperatures - Sxx 207
Figure 6-30- Model 2: Winter Casting Min Temperatures - Syy 207
Figure 6-31- Model 2: Summer Casting Max Temperatures - εkn 209
Figure 6-32- Model 2: Summer Casting Max Temperatures - $S1$ 209

Figure 6-33- Model 2: Summer Casting Max Temperatures - $S2$ 210
Figure 6-34- Model 2: Summer Casting Max Temperatures - Sxx 210
Figure 6-35- Model 2: Summer Casting Max Temperatures – Syy 211
Figure 6-36 - Model 2: Summer Casting Min Temperatures - εkn 212
Figure 6-37- Model 2: Summer Casting Min Temperatures - $S1$ 212
Figure 6-38- Model 2: Summer Casting Min Temperatures -$S2$ 213
Figure 6-39- Model 2: Summer Casting Min Temperatures - Sxx 213
Figure 6-40- Model 2: Summer Casting Min Temperatures - Syy 214

Index of Tables

Table 2-1 - Timeline of the Project 16
Table 5-1- Safety Factor Combination 140
Table 5-2 - Bending Moment Cover Slab Linear Verification 162
Table 5-3 - Bending Moment Foundation Slab Linear Verification 163
Table 5-4 - Bending Moment Uphill Wall Linear Verification 163
Table 5-5 - Bending Moment Downhill Wall Linear Verification 164
Table 5-6 - Bending Moment Pile 2000 Uphill Linear Verification 164
Table 5-7 - Bending Moment Pile 1200 Uphill Linear Verification 165
Table 5-8 - Bending Moment Pile 2000 Downhill Linear Verification 165
Table 5-9 – Shear Force Cover Slab Linear Verification 167
Table 5-10 – Shear Force Foundation Slab Linear Verification 167
Table 5-11 – Shear Force Uphill Wall Linear Verification 168
Table 5-12 – Shear Force Downhill Wall Linear Verification 168
Table 5-13 – Shear Force Pile 2000 Uphill Linear Verification 169
Table 5-14 – Shear Force Pile 1200 Uphill Linear Verification 169
Table 5-15 – Shear Force Pile 2000 Downhill Linear Verification 170
Table 5-16 - Calculation of γRd Depending on Various Cases 176
Table 5-17 - Standard Load Multipliers 177
Table 5-18 - Model 1 Winter Start LMU 180
Table 5-19 - Model 1 Winter Start HMU 181
Table 5-20 - Model 1 Summer Start LMU 181
Table 5-21 - Model 1 Summer Start HMU 182
Table 5-22 - Model 2 Winter Start LMU 182
Table 5-23 - Model 2 Winter Start HMU 183
Table 5-24 - Model 2 Summer Start LMU 183
Table 5-25 - Model 2 Summer Start HMU 184

Chapter 1 Problem Statement

The design and maintenance of modern concrete infrastructure require a fundamental understanding of long-term material durability and structural integrity. Historically, structural engineering methodologies focused primarily on checking structural members against ultimate limit states driven by external live and dead gravity loads. However, experience with large-scale civil infrastructure highlights that long-term performance and service life depend heavily on physical and chemical degradation mechanisms that initiate immediately after casting. The discussion establishes why the initial hours and days of a concrete mixture's lifecycle represent its most critical phase. During this transient period, the material undergoes rapid microstructural transformations that dictate its resistance to environmental aggression and determine its vulnerability to early-age cracking.

1.1 Early-Age Concrete Durability and Property Evolution

1.1.1 Microstructural Durability and Cracking Risk

The paradigm of modern structural engineering places concrete durability at the forefront of infrastructure asset management. Historically, structural design frameworks optimized material cross-sections almost exclusively against ultimate limit states driven by external live and dead gravity actions. However, long-term performance and service life maximization are profoundly governed by chemical and physical mechanisms that initiate immediately during casting and progress through the first hours and days of the mixture’s lifecycle (Tuutti 1982)

The primary physical parameter controlling concrete durability is the openness and connectivity of its internal microstructure (Mehta and Monteiro 2006). An open, interconnected

porous matrix provides a direct transport path for external aggressive agents, such as chloride ions, sulfates, and carbon dioxide, to penetrate the concrete cover shell. Once these agents reach the embedded steel reinforcement, they destroy the passive alkaline protective layer of the concrete, triggering localized pitting and generalized corrosion that compromises structural integrity (Tuutti 1982). Consequently, maintaining the durability of reinforced or composite structures depends on preventing the formation of early-age micro- and macro-cracks. Early-age cracking typically occurs before the structural asset is subjected to any external dead or service actions. It represents a complex engineering problem because it occurs concurrently with the stage where the mechanical properties of concrete are developing rapidly (Mihashi and Leite 2004). During this transient phase, the material transitions from a fluid suspension into a solid viscoelastic matrix, with its compressive strength, tensile capacity, and Young's modulus changing by orders of magnitude in a matter of hours (Saffiudin et al. 2018).

Current standard structural design guidelines offer simplistic and sometimes ambiguous provisions for early-age actions. For example, design standard EN 1994-2 (CEN 2005; Hendy and Johnson 2006) dictates applying a short-term elastic modulus combined with a fixed 20 K temperature difference between components to evaluate early thermal behaviour. Conversely, alternative guidelines such as the SETRA Guidance Book for Eurocode 3 and 4 (SESTRA 2010), reduce this thermal differential to 10 K, while remaining ambiguous about the specific elastic modulus evolution path that should be considered. More importantly, standard design recommendations assume complete, rigid shear interaction between contiguous layers or steel-concrete boundaries from the inception of hardening. This assumption contradicts physical reality and experimental push-out data, which reveal that connection stiffness is highly flexible and cures dynamically alongside the adjacent concrete matrix. Traditional, non-incremental code equations are therefore unable to simulate structural behaviour when changing stiffness metrics, creep relaxation, and thermal fields overlap. This limitation highlights the need for advanced coupled non-linear thermo-mechanical frameworks.

1.1.2 Mathematical Modelling of Early-Age Concrete properties

To track the development of early-age stresses and cracking, the structural engineer must deploy rigorous mathematical models that capture the rapid maturation of concrete's mechanical performance. In structural design practice, the chronological evolution of these properties is conventionally modelled using macroscopic time-dependent frameworks, as codified in international design standards (CEN 2004; fib 2013). According to the standard

formulations found in fib Model Code 2010, the progressive development of the mean compressive strength $f_{cm}(t)$, the progressive development of the mean tensile strength $f_{cmt}(t)$ and the mean modulus of elasticity $E_{cm}(t)$ at an age t (expressed in days) is governed by an exponential curing function:

$$f_{cm}(t) = \beta_{cc}(t) * f_{cm}(28) \quad (1)$$

$$f_{ctm}(t) = \beta_{cc}(t) * f_{ctm}(28) \quad (2)$$

$$E_{cm}(t) = [\beta_{cc}(t)]^{0,5} * E_{cm}(28) \quad (3)$$

Where $f_{cm}(28)$ and $E_{cm}(28)$ represent the reference compressive strength and Young's modulus developed at the standard maturity threshold of 28 days. The time-dependent hardening kinetics are driven by the function $\beta_{cc}(t)$, which is mathematically defined as:

$$\beta_{cc}(t) = \exp\left[s\left(1 - \sqrt{\frac{28}{t}}\right)\right] \quad (4)$$

s is defined as 0,38 in the models presented because the cement type is of Class S (Slow hardening). While these classical time-dependent code models provide a convenient baseline for standard situations, they are highly unreliable during the first 48 hours following casting.

1.2 Thermal Dynamics of Cement Hardening

The fundamental driving force behind early-age structural deformation is the exothermic (Bertagnoli et al. 2011; Neville 2011) nature of cement hydration. The chemical recombination of clinker phases with water releases considerable heat, ranging from 250 to 450 kJ per kilogram of cement. The quantity of hydration heat produced is used to define the internal degree of reaction (r):

$$r = \frac{Q(t,r)}{Q_{max}} \quad (5)$$

Where Q_{max} $[J/m^3]$ is the total hydration heat produced until the end of the hydration process and $Q(t,r)$ is the hydration heat produced from the beginning of the reaction time t, that can be written as:

$$Q\ (t,r) = \int_0^t q(\tau,r)d\tau \tag{6}$$

Where $q(\tau,r)$ is the gradient of heat production per unit of time, that can be described by decoupling time and degree of reaction as follows (Bertagnoli et al. 2009):

$$q(\tau,r) = q_r(r) * q_T(T) \tag{7}$$

Where $q_r(r)$ is the heat power as a function of the degree of reaction, $q_T(T)$ is the heat power as a function of the temperature and with a further substitution:

$$q(\tau,r) = q_{max} * q_{r,norm}(r) * q_T(T) \tag{8}$$

Where q_{max} is the maximum value of $q_r(r)$, and $q_T(T)$ is $q_r(r)$ normalized to 1.

$$q_T(T) = \exp\left(-\frac{c_a(T,r)}{T+273}\right) \tag{9}$$

Where $c_a(T,r)$ is the Arrhenius constant. Simultaneously, the specific heat of thermal capacity per unit of volume of concrete ($C_s(r)$) is a function of the density, the w/c ratio, the degree of hydration and the temperature of the paste. changes significantly as a linear function of reaction progress, according to De Schutter:

$$C_s(r) = C_{s_{r=1}}(1{,}15 - 0{,}15 * r) \tag{10}$$

Where $C_{s_{r=1}}$ is the specific heat at the end of the hydration process.

1.3 Shrinkage and Rheological creep Interactions

Tracking early-age stresses requires isolating the combined, often conflicting effects of volumetric shrinkage and viscoelastic creep relaxation. Total load-independent strain

increments ($\Delta\varepsilon_{imp}$) are generated by the summation of drying shrinkage, autogenous chemical volume loss, and temperature variation:

$$\Delta\varepsilon_{imp,i} = \Delta\varepsilon_{TS}, i + \Delta\varepsilon_{C,i} = [\varepsilon_{TS}(t_i) - \varepsilon_{TS}(t_{i-1})] + \Delta\varepsilon_{C,i} \tag{11}$$

Where $\varepsilon_{TS}(t)$is the imposed deformation in concrete due to both shrinkage and endogenous thermal effects and $\Delta\varepsilon_{C,i}$ isolates delayed creep increments. Drying shrinkage is driven by moisture migration from the internal pore matrix to the external environment. This process is highly sensitive to the hydraulic radius ($R_h = \frac{V}{A_{exp}}$) of the structural element, which measures the ratio of concrete volume to the surface area exposed to drying. In thick or massive elements, a single hydraulic radius cannot describe the cross-sectional moisture distribution. The outer layers dry out rapidly, while the deep internal core remains permanently humid. To prevent artificial stress steps in numerical simulations, the cross-section must be discretized into concentric drying zones or micro-regions with unique, spatially smoothed shrinkage functions. Simultaneously, viscoelastic creep acts as a key stress-modifying mechanism during structural hardening. Under the classical incremental convolution framework, delayed creep strains are calculated by tracking all historical elastic strain increments ($\Delta\varepsilon_{el}(t_k)$) modified by an aging viscoelastic creep function $\varphi(t_i, t_k)$:

$$\Delta\varepsilon_{C,i} = \sum_{k=1}^{i} \Delta\varepsilon_{el}(t_k) * \varphi(t_i, t_k) - \sum_{k=1}^{i-1} \Delta\varepsilon_{el}(t_k) * \varphi(t_{i-1}, t_k) \tag{12}$$

To model this within non-linear finite element frameworks, the creep compliance function ($J(t,\tau)$)is representing using a Dirichlet series, which can be physically interpreted as an aging multi-element Kelvin chain:

$$J(t,\tau) = \sum_{a} \frac{1}{E_a(\tau)} [1 - \exp(-\frac{t-\tau}{\hat{\lambda_a}(\tau)})] \tag{13}$$

$$\hat{\lambda_a} = \frac{\eta_a}{E_a(\tau, r)} \tag{14}$$

Where $\hat{\lambda_a}$ defines the independent delay times obtained as ratios between the damping coefficients $\eta_a$and the aging moduli of elasticity E_a for each element in the chain.

1.4 Problem of Early Age Concrete Applied to massive structural castings

The technical challenges of early-age deformations are most acute in massive structural castings (ACI Committee 207 2007). In large structural elements, the immense physical volume isolates the core from the exterior environment. This lack of thermal dissipation causes core temperatures to peak (Bamforth 2007; Bertagnoli et al. 2011). Furthermore, casting logistics create complex internal thermal profiles. When massive sections are poured in successive horizontal layers, upper layers are placed against lower zones that are already generating hydration heat. This shifts the absolute peak temperature zone slightly above mid-depth (Klemczak and Knoppik-Wróbel 2015). The high thermal inertia of these massive elements traps this heat, requiring 90 to 110 days for core regions to return to ambient conditions. Conversely, lower zones lose heat to the ground, which reduces early peak temperatures but stores thermal energy that keeps the base slab warmer during winter months.

This severe thermal variation creates an internal structural restraint. The cross-section divides into two macro-regions: an inner core comprising roughly 60% of the radius, and an outer cortex shell (Bertagnoli et al. 2011). The hot core expands early and acts as a rigid internal anchor, while the outer shell cools rapidly in contact with the air and undergoes drying shrinkage. This restraint subjects the inner core to compression, while the outer cortex shell develops high vertical and circumferential tensile stresses that exceed the concrete's early age tensile capacity, causing deep surface cracks within the first 5 days (Bamforth 2007). External boundary conditions introduce additional self-restrained cracking risks. Heavy friction along ground boundaries or rigid contact with perimeter diaphragms prevents free volumetric contraction during cooling (ACI committee 207 2007; Bertagnoli et al. 2011). This restraint can trigger vertical cracks on the exposed transverse faces of a casting, which can penetrate up to 1 meter deep into the foundation block.

Chapter 2 The Artificial Tunnel: Layout and Materials

Before executing advanced non-linear finite element simulations, it is necessary to establish a comprehensive physical and mechanical definition of the structural asset under investigation. The translation of a real-world infrastructure system into a series of numerical models requires an exact characterization of its macro-geometry, boundary constraint mechanics, and localized material properties. To provide this foundational framework, this chapter presents the detailed design configuration and engineering specifications of the target structure. Focusing first on the structural and geotechnical characteristics of the tunnel and then detailing the material properties constituting the main structural elements.

2.1 Tunnel Geometric Characteristics

The structural system under investigation is the Galleria Piscinale, an artificial cut-and-cover tunnel designed within the framework of the San Donato bypass project along the A1 Motorway. This protective structural gallery is engineered to stabilize a highly complex transit route characterized by significant geotechnical vulnerabilities and acute landslide risks. To accommodate localized topographic variations and effectively manage structural construction joints, the tunnel extends for a total longitudinal length of 210 meters, which is systematically subdivided into 15 independent longitudinal segments measuring approximately 14 meters each. This segmented configuration allows the infrastructure to adapt to the varying lateral soil pressures exerted by the moving slope along the main alignment of the motorway axis.

The non-linear numerical simulations conducted in this research focus specifically on Section A-A, see below, that is characterized by an asymmetric structural configuration designed to manage complex slope instabilities:

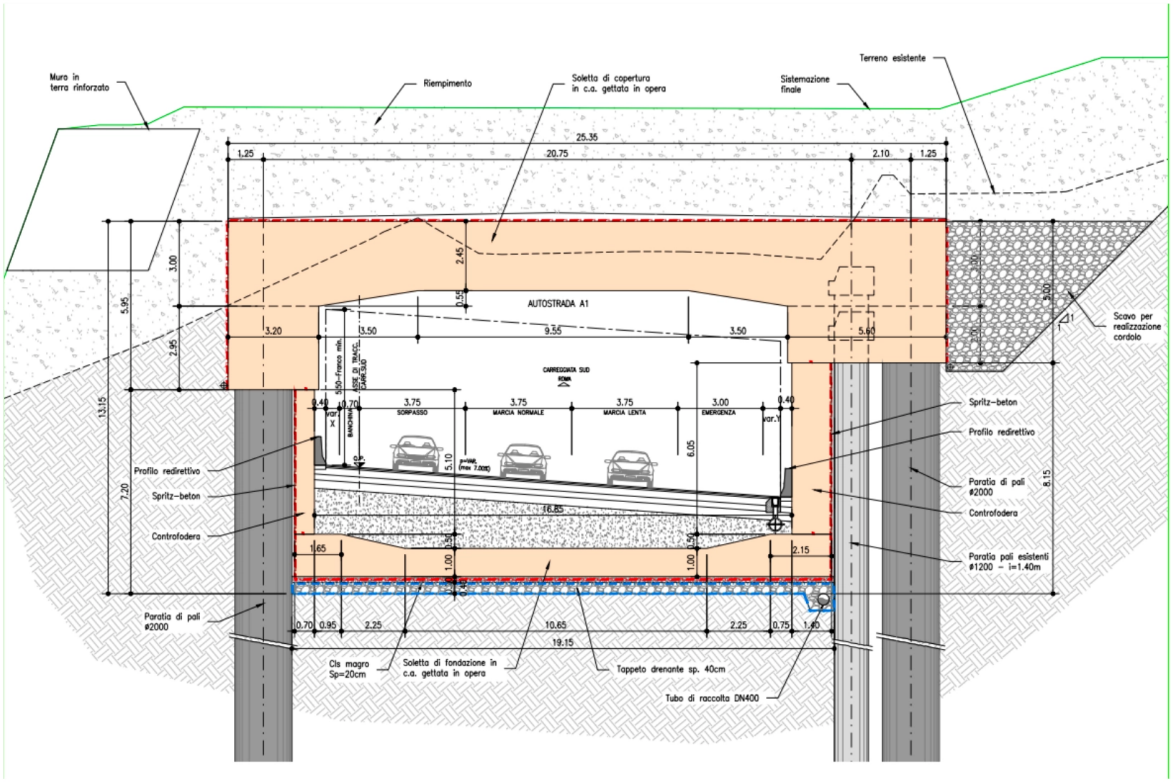


Figure 2-1 - Cross-section of artificial tunnel section AA

The uphill bulkhead consists of a robust double-row pile system intended to intercept the primary thrust of the landslide. This system is composed of a primary structural row of large-diameter 2000 mm reinforced concrete piles and a secondary auxiliary row of 1200 mm piles positioned further uphill. These secondary piles feature a tighter spacing of 1.3 m, and the two rows are separated by a centre-to-centre distance of 2.4 m. In contrast, the downhill side of the section is subjected to significantly lower lateral earth pressure and is configured as a single-row system. It consists of a single line of 2000 mm piles, mirroring the diameter of the primary uphill row, with a consistent longitudinal spacing of 2.3 m. While this downhill bulkhead provides essential lateral resistance against the lower slope, its primary structural function is to provide vertical support for the cover slab, thereby completing the hyperstatic frame of the artificial tunnel.

The upper cover slab consists of a massive, cast-in-place reinforced concrete member whose depth varies continuously across the transverse span. At the rigid lateral column and pile supports, where the negative support bending moments and structural shear demands reach their absolute peak, the slab features a maximum thickness of 300 cm. Moving toward the longitudinal centre line of the tunnel clearances, where structural efficiency allows for a reduction in dead weight, the slab tapers down to a minimum nominal thickness of 245 cm. The

lower perimeter of the structural frame is finalized by a variable-thickness foundation slab similarly to the cover slab structure. The depth of this invert slab is hunched, expanding from a minimum thickness of 100 cm at the centre line to a maximum depth of 150 cm at the lateral pile connection zones. To stiffen the tunnel in its final configuration, reinforced concrete counter-linings with a thickness of 1.4m on the uphill side and 0.7 m on the downhill side are provided, connected to the curb of the upper slab by shear connectors.

2.2 Mechanical Properties and Structural Allocations

2.2.1 Concrete Characteristics

The structural framework of the Galleria Piscinale utilizes two distinct classes of concrete, selected to balance localized mechanical demands with long-term environmental durability. Class C35/45 concrete is specified for the primary portal frame members, including the vertical sidewalls and the variable-thickness upper cover slab.

At the standard 28-day mature curing threshold, this mix exhibits:

- Characteristic cylinder compressive strength: $f_{ck} = 35\ MPa$
- Characteristic cube compressive strength: $R_{ck} = 45\ MPa$
- Mean compressive strength: $f_{cm} = 43\ MPa$
- Mean tensile capacity: $f_{ctm} = 3{,}2\ MPa$
- Mean modulus of elasticity: $E_{cm} = 34\ GPa$

Furthermore, the compressive strength at 50 years is required for posterior computations regarding the safety factors in the linear analysis:

- Characteristic cylinder compressive strength at 50 years:

$$f_{ck,50\,y} = \alpha_{cc} * f_{ck} = 1{,}3 * 35 = 45{,}5\ MPa \tag{13}$$

Conversely, Class C30/37 concrete is allocated exclusively to the deep foundation pile system, that include the piles and the foundation slab.

At the standard 28-day mature curing threshold, this mix exhibits:

- Characteristic cylinder compressive strength: $f_{ck} = 30\ MPa$
- Characteristic cube compressive strength: $R_{ck} = 37\ MPa$

- Mean compressive strength: $f_{cm} = 38\ MPa$
- Mean tensile capacity: $f_{ctm} = 2{,}9\ MPa$
- Mean modulus of elasticity: $E_{cm} = 33\ GPa$

The compressive strength at 50 years is required for posterior computations regarding the safety factors in the linear analysis:

- Characteristic cylinder compressive strength at 50 years:

$$f_{ck,50\,y} = \alpha_{cc} * f_{ck} = 1{,}3 * 30 = 39\ MPa \quad (14)$$

2.2.2 Steel Characteristics

The reinforcement network of the Galleria Piscinale structural continuum is composed entirely of high-ductility, hot-rolled ribbed steel bars designated as grade B450C, complying with standard Eurocode 2 and Italian national regulatory frameworks (NTC 2018). The standard mechanical parameters and design baselines governing the reinforcement bars are detailed below:

- Characteristic yield strength: $f_{yk} \geq 450\ MPa$
- Characteristic tensile strength: $f_{tk} \geq 540\ MPa$
- Mean modulus of elasticity: $E_s = 200\ GPa$

To accurately represent these properties within the numerical models, the constitutive behaviour of the B450C steel is governed by a linear elastic isotropic material law. Under serviceability conditions and early-age thermal loading stages, the mechanical response of the reinforcement bars is assumed to follow Hooke's Law perfectly:

$$\sigma_s = E_s * \epsilon_s \quad (15)$$

This linear relation implies a constant, unreduced structural stiffness where stress increments scale proportionally with axial strain up to the explicit characteristic yield threshold, $f_{yk} = 450\ MPa$. By maintaining a strict linear elastic envelope for the steel, the numerical model can isolate how the localized stiffness of the internal bars restrains early-age thermal cooling and autogenous shrinkage deformations within the concrete matrix, directly controlling the computed crack spacing and development fields.

2.2.3 Reinforcement Layout

To account for the high hyperstatic restraints and asymmetric earth pressures acting on the Galleria Piscinale, the reinforcement layouts are meticulously varied along the cross-section of each structural element.

1. Cover slab

The upper cover slab functions as a variable-depth portal frame roof, its section features a hunched geometry, decreasing continuously from a maximum thickness of 300 cm at the rigid lateral supports down to a minimum nominal thickness of 245 cm at the longitudinal midspan centreline. The longitudinal and transversal reinforcements are described below:

- Longitudinal reinforcement:
    - At the support sections, the extrados is reinforced with 4 layers of 5ϕ32 (40,2 cm^2 per layer) and the intrados contains 4 layers of 5ϕ32 (40,2 cm^2 per layer) supplemented by an auxiliary steel layer of 5ϕ18 providing an additional 14 cm^2.
    - At midspan, the extrados reduces to 2 layers of 5ϕ32 (40,2 cm^2 per layer) and the intrados preserve a dense arrangement of 4 layers of 5ϕ32 (40,2 cm^2 per layer).
- Transversal shear reinforcement:
    - The symmetrical shear transfer is maintained constant across the entire span using a single vertical leg of 1ϕ24 spaced every 60 cm, working in parallel with a multi-leg stirrup matrix containing 12 vertical legs of 1ϕ20 at a 60 cm interval.

The heavy reinforcement concentration at the extremities compared to the midspan is directly dictated by the frame's structural mechanics under high gravity loads and lateral landslide thrusts. The intersection between the cover slab, vertical sidewalls, and the stiff uphill pile bulkhead acts as a rigid corner joint. This configuration generates peak negative bending moments and severe localized shear forces at the supports. To accommodate these extreme support stresses, the section is packed with multi-layered ϕ32 bars at both the extrados and intrados. Moving toward the midspan, the structural behaviour transitions into a positive bending moment regime where the bottom fibres experience tension and the top fibres experience compression. Consequently, the top extrados reinforcement can be safely reduced by half, and the total thickness tapers down to 245 cm to optimize the structural dead weight without compromising flexural capacity.

2. Pile system

The deep foundation system comprises a robust, double-row retaining bulkhead layout embedded along the perimeter of the tunnel cell. The cross-sectional layout consists of primary uphill and downhill piles featuring a circular diameter of 2000 mm, supplemented by a secondary row of uphill stabilizing piles with a diameter of 1200 mm.

- Longitudinal reinforcement:
    - The primary piles (ϕ2000 mm) critical upper termination zone connecting directly to the portal frame struts contain a high-density configuration of 80ϕ32 bars. Further down the embedment shaft the reinforcement optimizes down to 40ϕ32 bars.
    - In the secondary pile (ϕ1200 mm), a uniform reinforcement profile consisting of 48ϕ26 longitudinal bars are sustained continuously along the full length of the pile shaft
- Transversal shear reinforcement:
    - Transversal confinement and shear transfer for both the 2000 mm and 1200 mm elements are governed by a continuous spiral or hoop network consisting of 1ϕ14 loops spaced tightly at a pitch of 10 cm, these loops will be considered as providing 1,7 legs in the calculations.

The localized doubling of the longitudinal steel bars at the pile heads, 80ϕ32 versus 40ϕ32, is required to handle the massive moment transfers at the structural foundation interface. The longitudinal steel distribution mirrors this structural demand curve, optimizing material efficiency while providing a high safety margin at the zone of maximum stress. Additionally, the exceptionally tight 10 cm pitch of the ϕ14 mm transversal stirrups ensure robust concrete confinement and shear integrity against the sudden lateral force variations inherent to moving landslide masses.

3. Walls

The vertical sidewalls function as the main vertical compression and shear-retaining panels of the portal vault. Reflecting the geometric asymmetry of the terrain, the cross-section transitions from a massive uphill wall featuring a constant thickness of 140 cm down to a highly slender downhill wall with a nominal thickness of 70 cm.

- Longitudinal reinforcement:
    - The uphill sidewall is reinforced with 3 layers of 5ϕ32 (40,2 cm^2 per layer) working in parallel with an auxiliary flexural layer of 5ϕ14 (7,70 cm^2 per layer)
    - The downhill sidewall incorporates an arrangement composed of 3 regular layers of 5ϕ32 (40,2 cm^2 per layer).
- Transversal shear reinforcement:
    - Both the uphill and downhill concrete sidewalls are reinforced with stirrups providing 2,5 legs of 1ϕ16 bars spaced every 40 cm.

The structural asymmetry of the cross-section directly explains why the uphill wall requires significantly higher reinforcement and thickness than its downhill counterpart. The uphill sidewall directly interfaces with the massive deep foundation pile bulkhead, bearing the primary brunt of the lateral earth pressures and out-of-plane bending moments triggered by the slope instability. This severe structural loading requires an expanded section thickness of 140 cm and a supplementary layer of 5ϕ14 steel bars to control tensile cracking. Conversely, the downhill sidewall is shielded from the main landslide path and experiences a significantly lower structural demand curve. It functions primarily as a closing vertical member of the structural portal frame, allowing the layout to be downsized to a thickness of 70 cm while maintaining standard baseline layers of ϕ32 bars.

4. Foundation slab

The foundation invert slab seals the bottom perimeter of the tunnel cell, closing the portal frame mechanism. The cross-section features a haunched depth profile optimized for subgrade interactions, expanding from a minimum thickness of 100 cm along the span centreline up to a maximum thickness of 150 cm at the pile support connections.

- Longitudinal reinforcement:
    - At the extremities, the slab features 2 layers of 5ϕ26 (26,5 cm^2 per layer) at the top, working alongside a primary layer of 5ϕ32 (40,2 cm^2 per layer) at the bottom.
    - In the thinner central section, the foundation slab only uses a single layer 5ϕ26 working with one layer of 5ϕ32.

- Transversal shear reinforcement:
    - Globally along the foundation slab shear resistance is provided by a uniform grid supplying 2,5 vertical legs of 1ϕ16 bars spaced at a rectangular 40 cm pitch.

The reinforcement and thickness discrepancies across the foundation invert slab are driven by the localized reactions of the deep foundation pile supports. Because the connection between the invert slab and the underlying piles is explicitly engineered as a compression-only contact interface, the global vertical loads of the tunnel portal frame become highly concentrated at these lateral boundaries. This concentrated reaction creates severe upward shear stress gradients and high localized bending moments at the corners. Thickening the slab extremities to 150 cm and adding an extra 26,5 cm^2 reinforcement layer ensures adequate structural capacity against punching shear failure and localized bending stress concentrations. At the midspan zone, the upward subgrade pressure field becomes relatively uniform and less severe. This reduction in structural demand allows the section depth to taper down to 100 cm and permits a more economical reinforcement arrangement without risking structural failure.

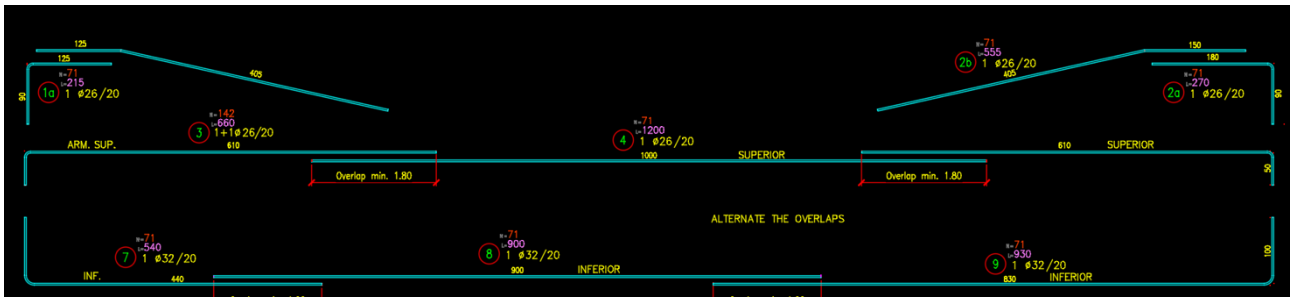


Figure 2-2 - Foundation Slab Reinforcement Layout

(a) (b)

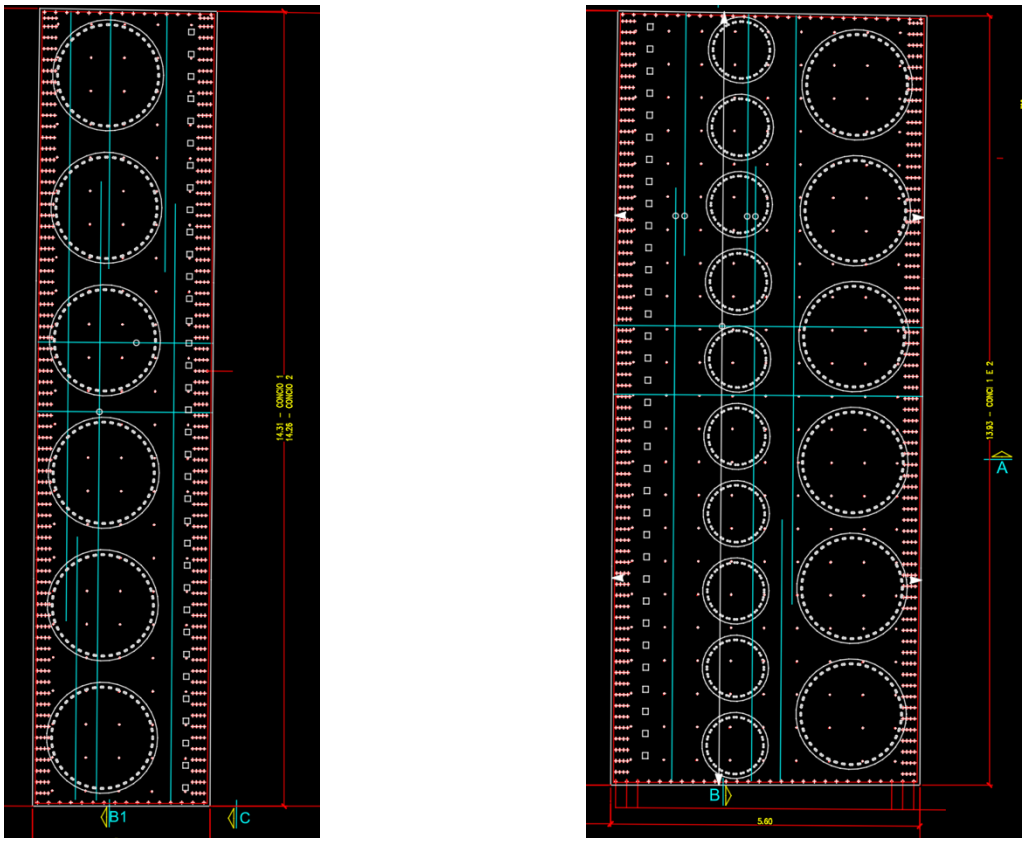


Figure 2-3 - Reinforcement Layout at the Pile Head of (a) Downhill Pile (b) Uphill Piles

2.3 Project Timeline

The numerical simulation of an artificial cut-and-cover tunnel requires an exact chronological mapping of its staging sequence. Because concrete undergoes time-dependent aging, stiffness hardening, and visco-elastic relaxation, the precise timing of mechanical and thermal load applications fundamentally changes the structural stress evolution. The exact chronology of the project is described in the table below:

Table 2-1 - Timeline of the Project

Phases	Duration [days]	Description	Timeline [days]
Phase 1	3	Construction of upper slab kerbs	0 to 3
Phase 2	5	Completion of kerb curing and preparation of the internal ground for the slab pour	3 to 8
Phase 3	26 + 75 (waiting period before starting the next phase)	Pouring of the slab and associated curing	16 to 42
Phase 4	8 + 384 (waiting period before starting the next phase)	Partial backfilling	117 to 125
Phase 5	180	Groundwater level reduction	509 to 689
Phase 6	5	Internal tunnel excavation and installation of foundation slab reinforcement	689 to 694
Phase 7	14 + 133 (waiting period before starting the next phase)	Casting of the foundation slab and associated curing	694 to 708
Phase 8	12 + 212 (waiting period before starting the next phase)	Pouring of the walls and associated curing	841 to 853
Phase 9	57	Complete backfilling	1065 to 1122

Chapter 3 Finite Element Discretization and Model Configurations in DIANA

The predictive assessment of early-age thermomechanical phenomena and long-term durability metrics within the Galleria Piscinale structural continuum requires a robust numerical computation platform capable of handling coupled multi-field problems. To achieve this, the global finite element simulations within this investigation are executed using the advanced multi-purpose environment DIANA FEA. This software environment is chosen specifically for its comprehensive suite of non-linear concrete material models, transient heat flow integration solvers, and specialized capabilities in parsing visco-elastic relaxation chains. The primary objective of this chapter is to detail the distinct mathematical architectures and behavioural hypotheses applied across the simulation matrix. Rather than relying on a singular modelling formulation, the analysis utilizes five separate numerical configurations, which range from a fully coupled thermo-chemo-mechanical multiphysics framework down to idealized conventional design-office baselines. The overview of the 5 different models is explained in the next figures, and each model will be fully explained in the next sub-chapters.

3.1 General Numerical Framework and Structural Modelling Principles

3.1.1 Model Geometry

The geometry of the numerical model is shown in Figure 3-1. The landslide plane is highlighted in red, and the soil modelling extends 17 metres below the landslide plane and 40 metres upstream and downstream of the tunnel. The concrete parts were modelled with eight-node quadrangular isoparametric elements. The maximum size of the elements constituting the concrete parts is 0.25 m.

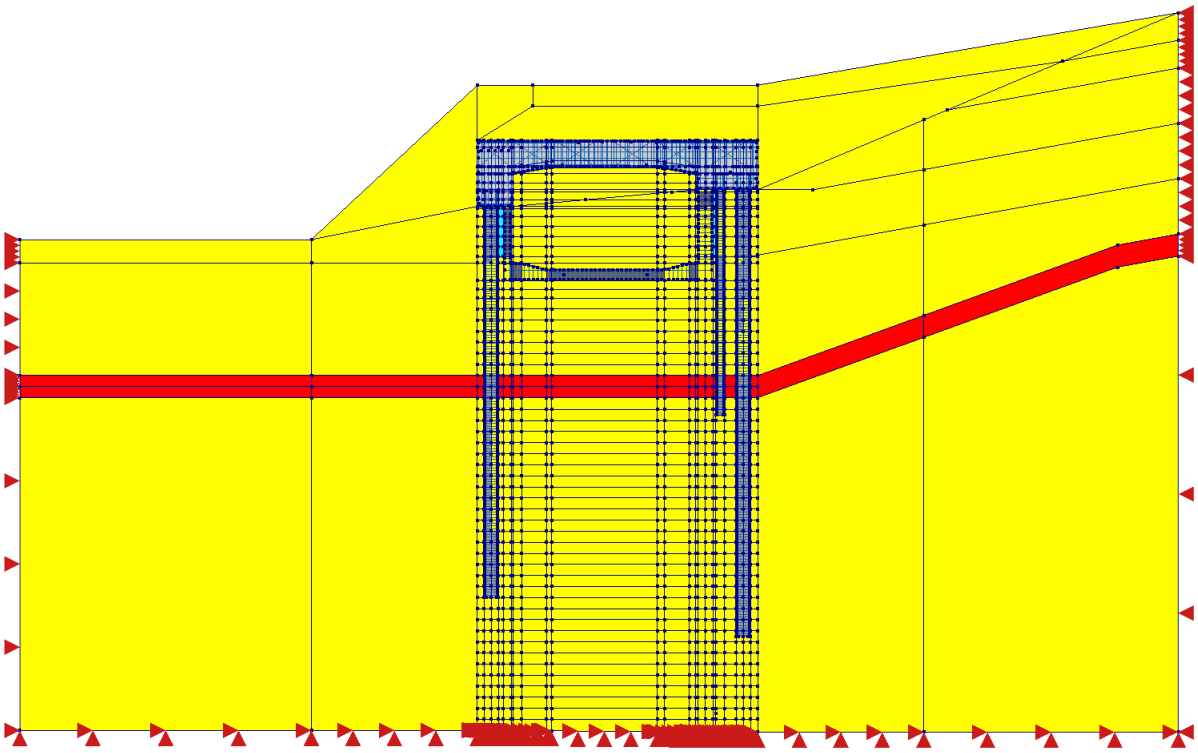


Figure 3-1 - Geometry of the FEM Model

3.1.2 Material Non-Linearity Assumptions

During construction and operational phases, the tunnel lining is subjected to permanent self-weight, geotechnical earth thrusts, including active landslide actions and groundwater table drawdown, and passive ground confinement. Because compressive stress levels throughout the reinforced concrete cross-sections remain strictly within linear elastic serviceability limits, non-linear compressive plasticity formulations are omitted.

To describe the behaviour of concrete under tension, a model with diffuse cracking, a fixed cracking direction, and possible rotation of the stress fields in the cracked state has been

adopted. Diffuse or 'smeared' cracking is an approach to analysing the tensile behaviour of reinforced concrete which involves a reduction in the material's tensile strength and stiffness once the tensile strength in the principal direction has been exceeded. The material's behaviour thus changes from isotropic to orthotropic in the principal stress reference system. Rather than explicitly tracking discrete individual crack openings, the smeared crack formulation homogenizes localized cracking strain across element integration points, capturing the global increase in structural compliance.

For complex underground portal frame structures characterized by dense, distributed cracking networks, this continuum approach provides the most computationally robust and versatile framework for capturing non-linear stress redistribution. Diffuse cracking theories fall into two main categories: models with a fixed crack direction and those with a rotating crack direction. The former assume that the crack direction remains constant at the individual finite element integration point from the moment the crack forms and throughout all subsequent load increments. The latter update the crack direction at each load step following crack formation.

In fixed-crack models, the orientation of principal stresses can shift relative to established crack planes as loading conditions evolve. Prior to cracking, the principal tensile stress acts normal to the crack plane. Upon crack initiation, reinforcement anisotropy breaks this coaxial alignment, forcing an immediate rotation of the principal stress field to maintain internal equilibrium. Under continued loading, shear transfer across the crack interface generates tangential stresses, driving further rotation of the principal stress coordinate system.

The failure envelope for tension and tension-compression in the principal stress plane is shown in Figure 3-2 (a) the residual tensile strength after cracking has occurred (tension softening) is modelled as linear and is presented in Figure 3-2 (b). The value of the ultimate strain at which residual tensile strength is present, ε_u, has been assumed to be: $2 * \varepsilon_{cr}$. Consequently, a quasi-brittle behaviour of concrete under tension has been assumed. This assumption is conservative, as, according to recognised scientific literature, this value could be considerably higher depending on the reinforcement in the cracked zone. The cracking strain is calculated as follows:

$$\varepsilon_{cr} = \frac{ft}{E} \tag{16}$$

Since both the tensile strength ft and the modulus of elasticity E are quantities that vary with the degree of reaction, it follows that ε_{cr} also varies over time depending on the setting reaction of the concrete.

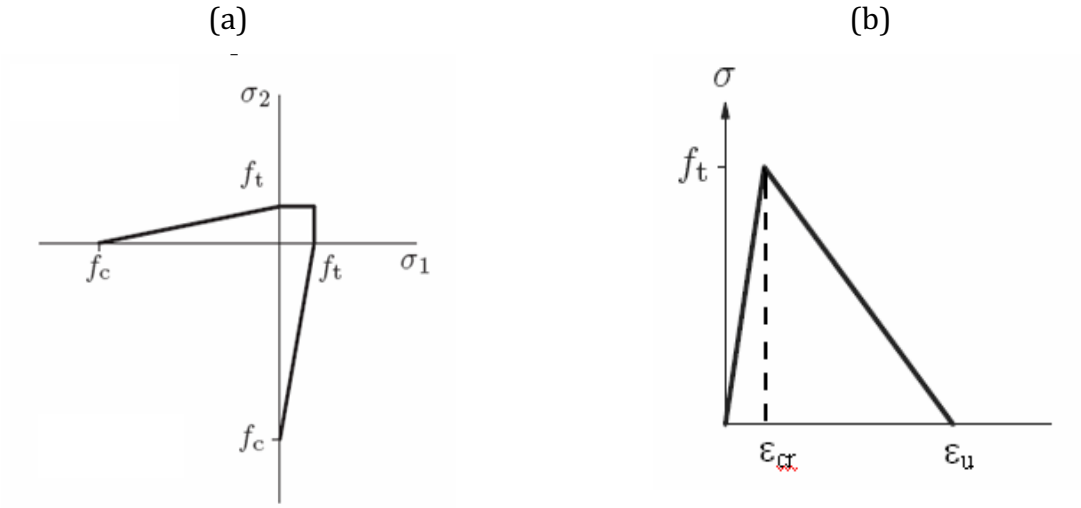


Figure 3-2 - Non-Linear Behaviour of Concrete Under Tension, (a) Tensile and Tensile-Compression Failure Envelopes in the Principal Stress Plane, (b) Tension Softening

The shear modulus reduction coefficient G, known as the 'shear retention factor', has been set at 0.2.

3.1.3 Modelling of the Concrete Shrinkage

The hygrometric shrinkage of the mixture, measured in accordance with ASTM C 157/C157M-08 on 10 * 10 * 50 cm prisms ensures that shrinkage deformations in the actual structure are kept to a minimum. The modelling of shrinkage was carried out in accordance with MC2010, thus adopting the expressions from (19) to (26).

$$\varepsilon_{cs}(t, t_s) = \varepsilon_{cas}(t) + \varepsilon_{cds}(t, t_s) \tag{17}$$

Where:

$\varepsilon_{cas}(t)$ represents autogenous shrinkage and $\varepsilon_{cds}(t, t_s)$ represents drying shrinkage and $\varepsilon_{cas}(t)$ and $\varepsilon_{cds}(t, t_s)$ are expressed below:

$$\varepsilon_{cas}(t) = \varepsilon_{cas0}(f_{cm}) * \beta_{as}(t) \tag{18}$$

$$\varepsilon_{cds}(t, t_s) = \varepsilon_{cds0}(f_{cm}) * \beta_{HR}(HR) * \beta_{ds}(t - t_s) \tag{19}$$

Where, t is the age, in days, since casting; t_s is the time, in days, to the end of curing. And:

$$\varepsilon_{cas0}(f_{cm}) = -\alpha_{as} * \left(\frac{\frac{f_{cm}}{10}}{6 + \frac{f_{cm}}{10}} \right)^{2.5} * 10^{-6} \tag{20}$$

$$\beta_{as}(t) = 1 - exp\left(-0{,}2 * \sqrt{t}\right) \quad (21)$$

Where, f_{cm} is the average cylindrical compressive strength at 28 days; α_{as} is a coefficient that depends on the type of cement used.

$$\varepsilon_{cds0}(f_{cm}) = [(220 + 110 * \alpha_{ds1}) * exp(-\alpha_{ds2} * f_{cm})] * 10^{-6} \quad (22)$$

$$\beta_{HR}(HR) = -1.55 * \left[1 - \left(\frac{RH}{100}\right)^3\right] \; per \; 40 \leq RH \leq 99 \quad (23)$$

$$\beta_{ds}(t - t_s) = \left(\frac{(t - t_s)}{0.035 * h^2 + (t - t_s)}\right)^{0,5} \quad (24)$$

Where, HR is the relative humidity; α_{ds1} and α_{ds2} are coefficients that depend on the type of cement used; h is the hydraulic radius of the cross-section, calculated as $2A_c/p$ (A_c is the area of the concrete cross-section and p is the perimeter of the cross-section exposed to the atmosphere). The shrinkage of the concrete is shown in Figure 3-3. The tunnel slab exhibits four distinct shrinkage zones:

- R 600 mm external. This is the shrinkage assigned to the first 600 mm of concrete from the extrados of the slab; these elements begin their life in contact with the atmosphere and therefore undergo rapid shrinkage at this stage; following backfilling, their shrinkage is slower.
- R 600 mm internal. This is the shrinkage assigned to the first 600 mm of concrete from the underside of the slab. These elements are initially in contact with the ground and therefore undergo slow initial shrinkage; following the excavation of the tunnel, the concrete encounters the air and thus shrinks more rapidly.
- R 4800 mm. This is the shrinkage assigned to the internal elements of the slab in the central section.
- R 8800 mm. This is the shrinkage assigned to the internal elements of the slab at the edges (the thickest part of the slab).

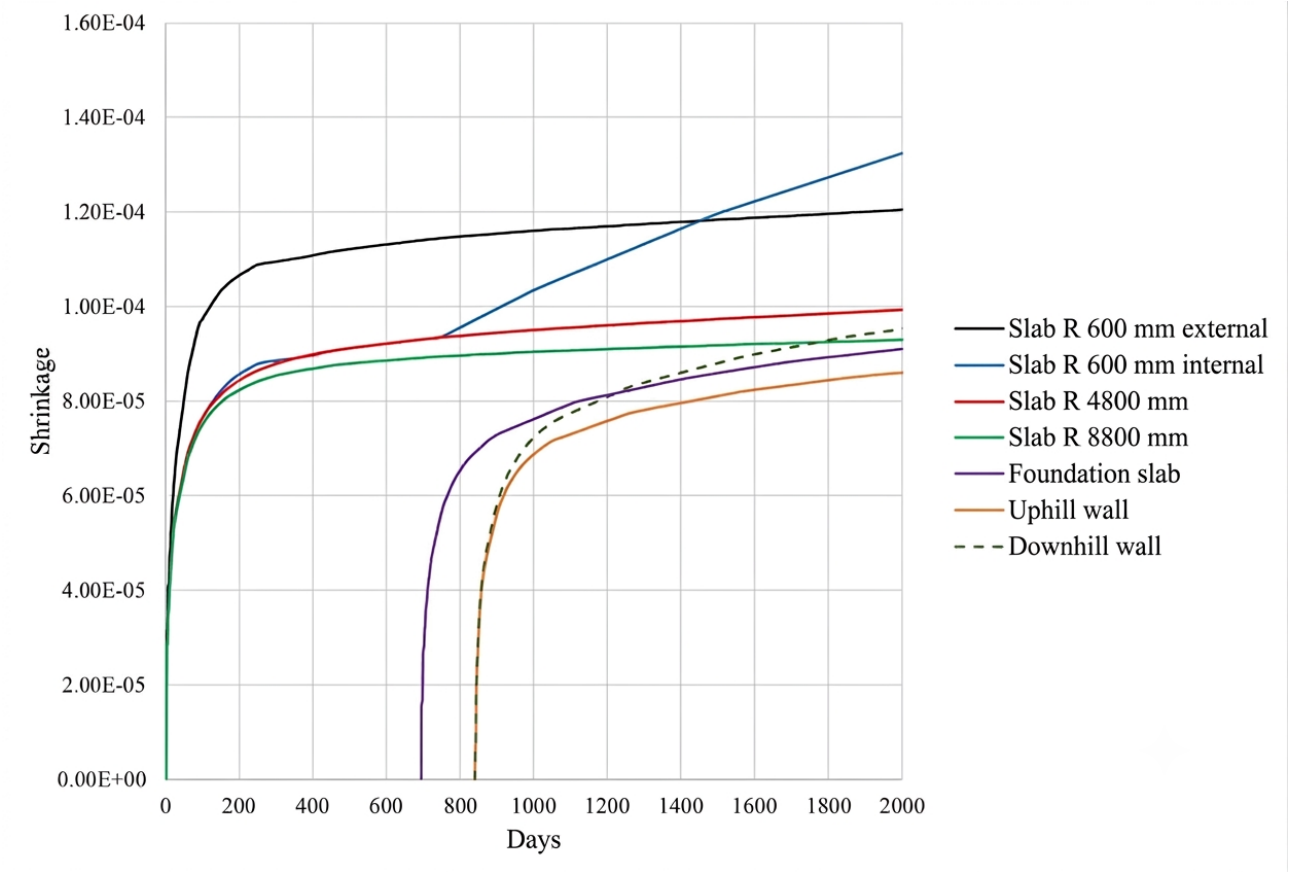


Figure 3-3 - Shrinkage Curves

3.1.4 Modelling of the Concrete Creep

The creep modelling was carried out in accordance with MC2010. The viscous behaviour of the concrete is described according to the classical formulation using equation (27) for a single stress increment at time t_0 or equation (28) for continuous stress variations.

$$\varepsilon_{c\sigma}(t,t_0) = \sigma_c(t_0) * \left[\frac{1}{E_c(t_0)} + \frac{\varphi(t,t_0)}{E_c(28)}\right] = \sigma_c(t_0) * J(t,t_0) \tag{25}$$

$$\varepsilon_{c\sigma}(t,t_0) = \sigma_c(t_0) * J(t,t_0) + \int_{t_0}^{t} J(t,\tau) * \frac{\partial \sigma_c(\tau)}{\partial \tau} d\tau \tag{26}$$

The creep function $J(t,\tau)$ can be implemented in the DIANA code as a Dirichlet series using equation (29), which can be physically interpreted as a Kelvin chain:

$$J(t,\tau) = \sum_{\alpha} \frac{1}{E_\alpha(\tau)}\left(1 - exp\left(-\frac{t-\tau}{\lambda_\alpha}\right)\right) \tag{27}$$

Where: $\lambda_\alpha = \frac{\eta_\alpha}{E_\alpha}$. The model stiffness, elastic modulus,$E_\alpha(\tau)$, is time dependent as it is linked to the material's aging. The spring stiffnesses and damping coefficients of each element in the Kelvin chain determine the delay days λ_α.The number of chain elements to be considered and the values of the parameters λ_α are chosen to fit the curves proposed by MC2010.

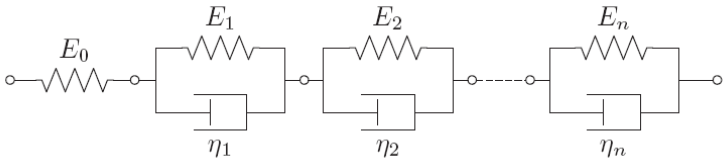


Figure 3-4 - Physical Representation of a Kelvin Chain

Creep for all types of concrete used is modelled using 4-link Kelvin chains. The first link represents the evolution of the concrete's elastic modulus over time. The remaining links model the evolution of creep. For the slab concrete, the creep curves as a function of loading time are shown in Figure 3-5. The evolution of the elastic modulus over time is shown in Figure 3-6.

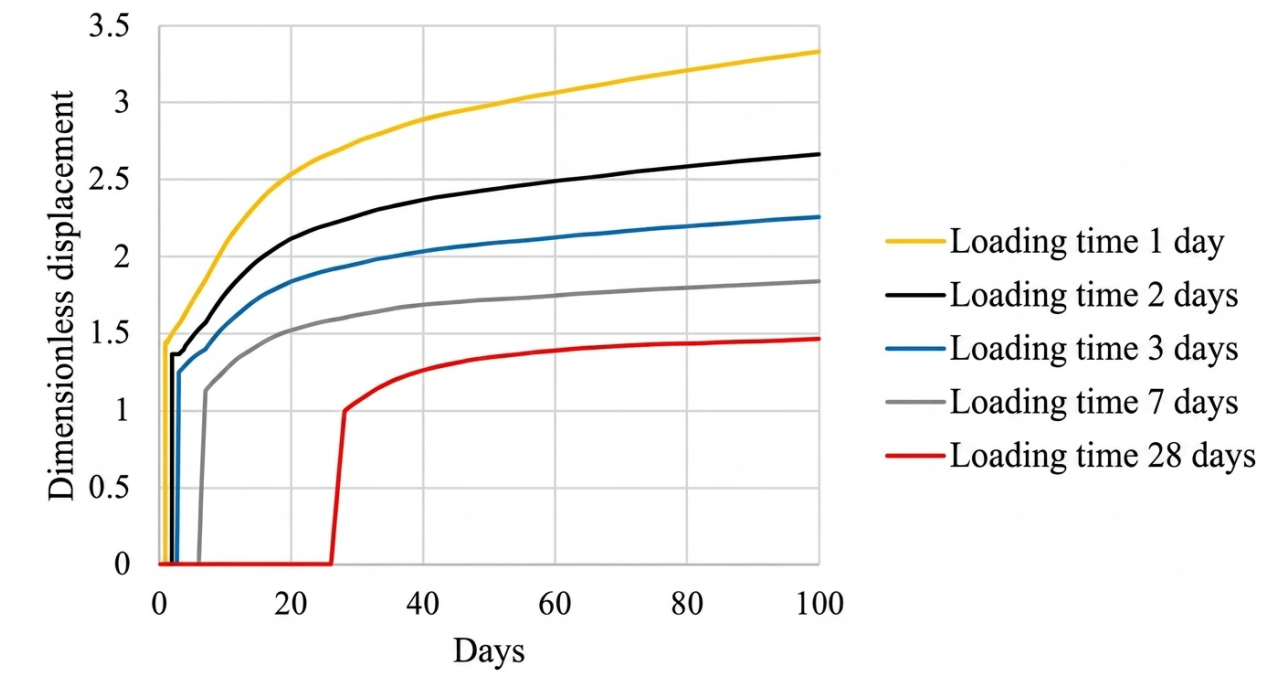


Figure 3-5 - Creep Curves

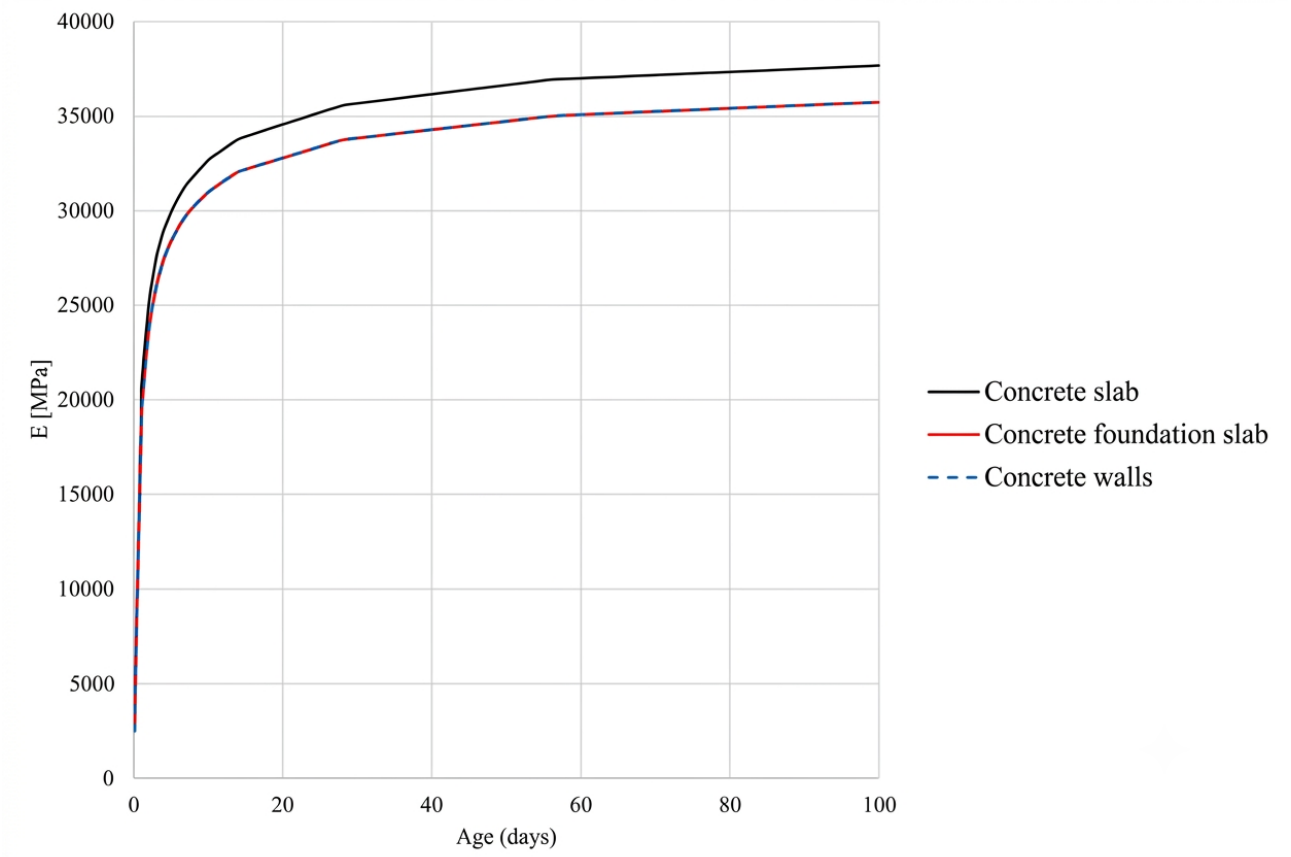


Figure 3-6 - Evolution of Elastic Modulus over Time

3.1.5 Modelling of Thermal Properties of Concrete

During the setting and hardening of concrete, the chemical reactions involved in cement hydration generate heat as they are exothermic. This heat spreads through the concrete, raises the temperature and is dissipated into the environment. The rise in temperature can give rise to induced deformations that are detrimental to the quality of the concrete and therefore needs to be studied carefully. For the analysis of heat diffusion, the classical Fourier equation model found in the literature was chosen. The Fourier differential equation per unit volume is presented below:

$$q + \frac{dg}{dt} = q_v \tag{28}$$

With:

$$q = -k(T,t)\nabla T \tag{29}$$

Where q is the heat flux; $-k(T,t)$ is the thermal conductivity, which may be a function of temperature T, time t or, as in the following case, the degree of hydration reaction r; ∇T is the

temperature gradient; $\frac{dg}{dt}$ is the energy produced per unit of time in the unit of volume under consideration

$$q_v = -c(T,t)\frac{dT}{dt} \tag{30}$$

Where q_v is the heat stored; $-c(T,t)$ is the heat capacity which may depend on temperature T, time t or, as in the following case, the degree of reaction r; $\frac{dT}{dt}$ is the change in temperature of the concrete over time.

The heat capacity of concrete [J/(m^3°K)] varies mainly as a function of its density, the water-to-cement ratio, the temperature and the degree of hydration (or reaction). The degree of reaction is identified by a variable r ranging from 0 to 1, which indicates the progress of the concrete's setting reaction (r = 0: start of setting; r = 1: reaction fully complete). For concrete with a density of 2400 kg/m^3, this value once hydration is complete is, according to Neville:

$$Cs = 840\ J/(kg\ °K) * 2400\ kg/m^3 = 2{,}02 * 10^6 J/(m^3\ °K) \tag{33}$$

If we consider an average cement content of 350 kg/m^3 and a water-to-cement ratio of 0,5, there are 175 litres of water in the mix when the reaction begins, which means 2,225 kg of aggregates and cement. If we assume that the heat capacity of the finished product is similar to that of its solid components, at the start of the reaction the heat capacity of the paste is higher due to the presence of water, as shown below:

$$Cs = 840\ J/(kg * °K) * 2225\ kg/m^3 + 4{,}190\ J/(kg * °K) * 175 KG/m^3 = 2{,}60 * 10^6 J/(m^3 * °K) \tag{34}$$

Different dosages lead to different results. De Schutter provides the variation in specific heat as a function of the degree of reaction r:

$$Cs(r) = Cs_{r=1}(1{,}15 - 0{,}15r) \tag{35}$$

Where $Cs_{r=1}$ is the specific heat of hardened concrete, after complete hydration. It follows that fresh cement paste has a specific heat 15 per cent higher than that of hardened concrete, and this property decreases linearly with the degree of reaction. In the absence of experimental data regarding this mixture parameter, the values 2,5E6 [J/(m^3 °K)] for fresh concrete and 2,0E6 [J/(m^3 °K)] for hardened concrete were chosen, assuming a linear variation with the degree of reaction r between the two extremes.

The thermal conductivity of concrete is the amount of heat transmitted through a unit area over a unit distance in a unit of time for a unit temperature gradient [J/ (m^2 °K/m)].

A second parameter, also used in describing the phenomenon of thermal diffusion, is called thermal diffusivity and is expressed as follows:

$$\alpha = \frac{k}{Cs} \tag{36}$$

Where: k is the thermal conductivity [J/ (s * m² °K/m)], Cs is the specific heat per unit volume [J/(m^3·°K)], De Schutter provides the variation in thermal diffusivity as a function of the reaction degree r:

$$\alpha(r) = \alpha_{r=1}(1{,}10 - 0{,}10r) \tag{37}$$

Where $\alpha_{r=1}$ is the specific heat of the thermal diffusivity of hardened concrete. It follows that fresh cement paste has a specific heat 10 per cent higher than that of hardened concrete, and this property decreases linearly with the degree of reaction. Substituting (34) into (35), the change in thermal conductivity can be expressed as follows.

$$k(r) = k_{r=1}(1{,}27 - 0{,}27r) \tag{38}$$

In the absence of experimental data regarding this mixture parameter, the values 2,0 [J/(sm^2°K/m)] for fresh concrete and 1,0 [J/ (s * m^2 * °K /m)] for hardened concrete were chosen, assuming a linear variation with the degree of reaction *r* between the two extremes.

Heat transfer between solid bodies, for example, between the structure, the formwork and the atmosphere, involves the three phenomena of conduction, convection and radiation. Conventionally, and for the sake of simplicity, this combination of mechanisms in which convection is the predominant phenomenon is modelled using an equivalent thermal conductivity Ki [J/ (s * m^2 * °K)]. The values of this thermal conductivity, for various environmental conditions, are provided by the UNI 7357-74 standard and are set out below.

In still air (inside enclosed spaces):

- Horizontal surface upward heat flux, Ki = 8
- Vertical surface, parallel heat flow: Ki = 7
- Horizontal surface, downward heat flow: Ki = 5

Outdoors (wind up to 4 m/s):

- Horizontal surface, upward heat flow: Ki = 20
- Vertical surface, parallel heat flow: Ki = 20
- Horizontal surface, downward heat flow: Ki = 14

The setting reaction normally begins between 45 and 60 minutes after placement and is completed within 12 hours. During this phase, the concrete mixture transitions from a fluid to a solid state. Hardening begins immediately after setting and continues indefinitely over time. The way in which concrete hydration takes place depends on the type of cement used and the water-to-cement ratio, the temperature, the degree of hydration itself, and the extent of the contact surface between the reacting phases. The higher the temperature, the faster the reaction, the further along the hydration process is, the less heat is produced. For different types of cement, however, the reaction characteristics depend on the mix design (content of clinker, slag, pozzolans, fly ash, etc.) and on the grinding or fineness. Cements with a high clinker content and/or finer grinding will tend to react more rapidly and generate more heat. The amount of heat produced and its evolution over time is determined for different cements by analysing adiabatic tests carried out on specially prepared mortars, in which, for a given mass with a known heat capacity, the temperature evolution and, consequently, the heat produced are measured over time.

Heat production per unit volume is described in terms of two variables: temperature and the degree of reaction.

$$r = \frac{Q(t,r)}{Q_{max}} \tag{39}$$

Where Q_{max} $[J/m^3]$ is the total heat of hydration upon completion of the reaction and *Q(t,r)* is the heat produced up to time t, which can be expressed as follows:

$$Q(t,r) = \int_0^t q(\tau,r)d\tau \tag{40}$$

Where $q(\tau,r)$ is the heat production per unit of time, which can be described by decoupling the two variables: degree of reaction and time, as follows:

$$q(\tau,r) = q_r(r) * (T) \tag{41}$$

Where $q_r(r)$ is the power generated as a function of the degree of reaction, $q_T(T)$ is the power generated as a function of temperature. That is:

$$q(\tau,r) = q_{max} * q_{r,norm}(t) * q_T(T) \tag{42}$$

Where q_{max} is the maximum value of $q(r)$; $q_{r,norm}(r)$ is the power generated as a function of the degree of reaction, normalised to 1 and $q_T(T)$ is the fraction of power

generated as a function of temperature. The fraction $q_T(T)$ can be expressed as follows:

$$q_T(T) = e^{\frac{c_a(T,r)}{T+273}} \tag{43}$$

Where $c_a(T,r)$ is the Arrhenius constant, which can also be defined as a function of temperature and the degree of reaction. In this analysis, a constant value of 6000°K has been chosen for concrete, in accordance with the literature. is the temperature in degrees Celsius. The fraction $q_r(r)$ depends on the type of mix design used and must be derived for different concretes from the analysis of adiabatic tests, in which, for a given mass of reacting concrete whose heat capacity is known, the evolution of temperature over time, and consequently the heat produced, is measured.

During the procedures for defining the thermal behaviour of a mixture, the function $Q(t,r)$ is known from laboratory adiabatic analyses, whilst $q_r(r)$ is the unknown function that we wish to determine. As no adiabatic tests were available for the mixture to be used in the construction of the tunnel, the authors, drawing on their experience, hypothesised the adiabatic temperature evolution of the mixture shown in Figure 3-7.

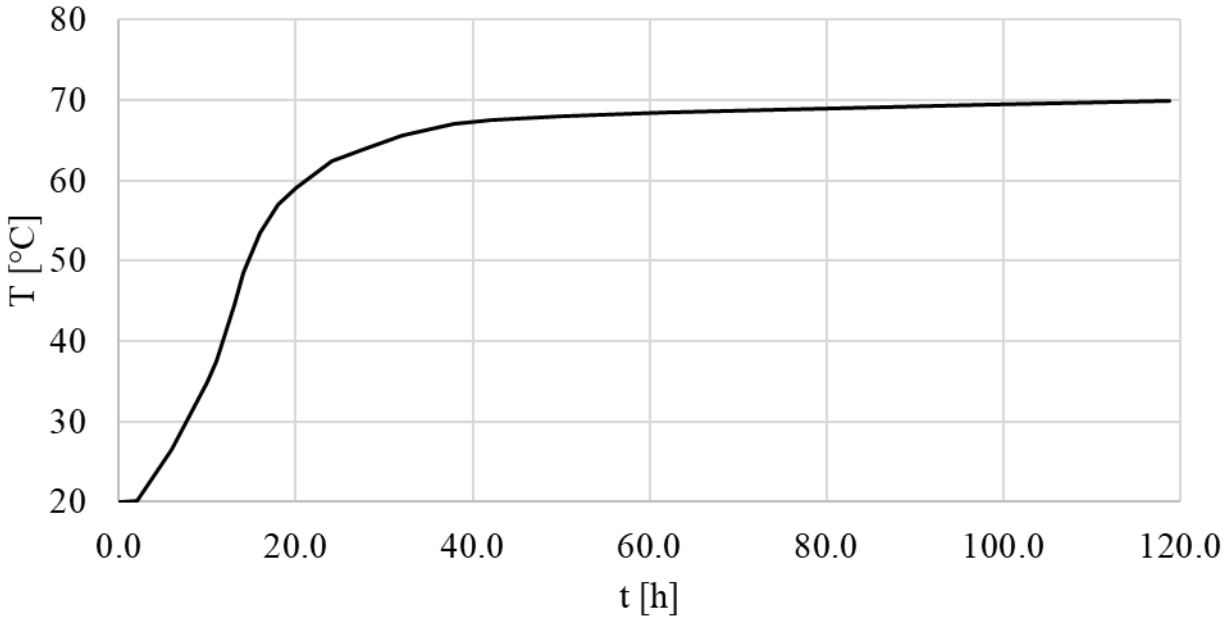


Figure 3-7 - Adiabatic Curve for Concrete

3.1.6 Modelling of the Geotechnical Effects

The modelling of geotechnical effects, in particular the landslide and the groundwater level drawdown, was carried out using an iterative procedure to align the deformations of the thermo-mechanical model with those of the linear elastic geotechnical design model. Specifically:

- The landslide is modelled by applying a horizontal constraint failure to the upstream horizontal constraints above the landslide plane. The value of the constraint failure imposed upstream is such that the horizontal displacement of the piles in the thermo-mechanical model is, to a good approximation, comparable to the horizontal displacement of the geotechnical design model.
- Groundwater drawdown is modelled by applying a vertical deformation to the soil elements below the water table. The applied vertical deformation is greater upstream of the tunnel than downstream of the tunnel to account for the non-uniform effect of the drawdown between the upstream and downstream sections (as per the geotechnical design model). The magnitude of the vertical deformation applied to the soil elements is such that the vertical displacement of the base slab in the thermo-mechanical model, resulting from the lowering of the water table, is equal to that obtained in the design geotechnical model.

3.1.7 Modelling of the Reinforcements and the Soil Interaction

The modelling of the reinforcement is shown in Figure 3-8, following the detailed description presented in the Chapter 2.2.3. The constitutive relationship of the reinforcement is of the elastoplastic-yielding type, as shown in Figure 3-9. The soil sections have been modelled using eight-node quadrangular isoparametric elements. The maximum element size adjacent to the tunnel coincides with that of the concrete elements (0.15 m); as the distance from the tunnel increases, the maximum element size increases to 1 m. A Mohr–Coulomb constitutive model is used for the soil elements, as shown in Figure 3-10. The external constraints are shown in Figure 3-1. Specifically, rigid constraints are applied at the base of the model in the vertical direction only, and rigid constraints are applied at the edges of the model in the horizontal direction only.

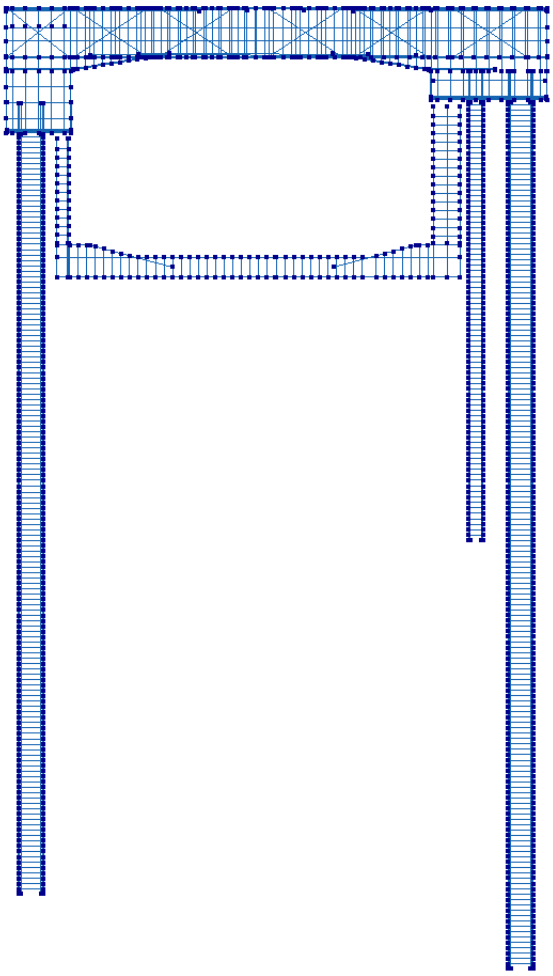


Figure 3-8 - Reinforcement Arrangement

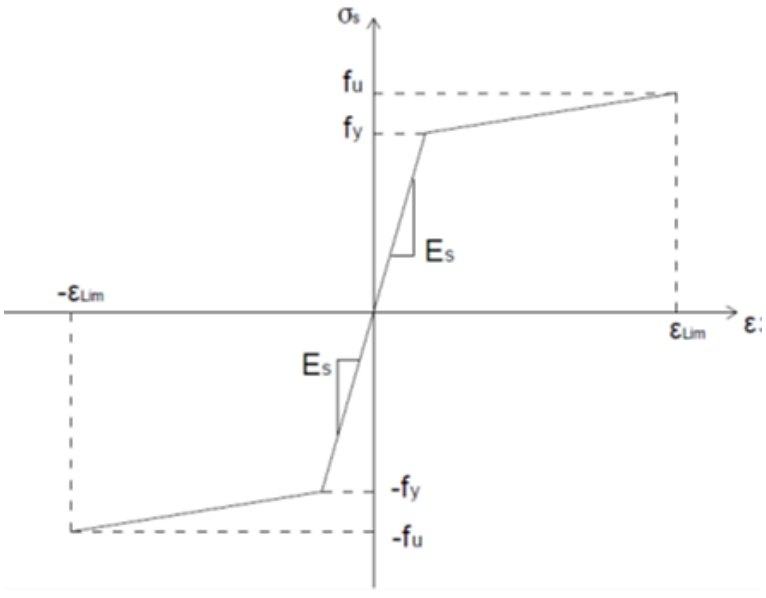


Figure 3-9 - Elasto-Plastic-Yielding Constitutive Relationship of the Reinforcement

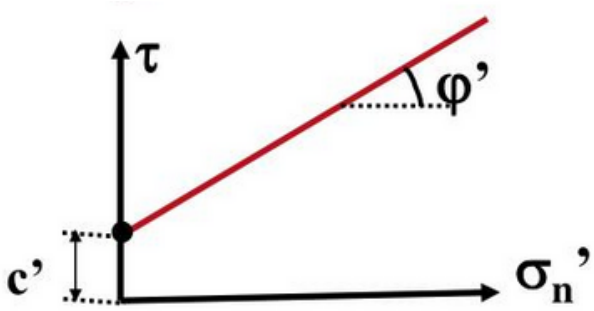


Figure 3-10 - Constitutive Relationship of the Soil

3.1.8 Modelling of the Internal Interfaces

For the connections between the various structural components, called 'internal constraints' the following assumptions were adopted:

- Fully effective connection between piles and slab: interlocking behaviour;
- Connection between liners and slab (green layer in Figure 3-11). The theoretical behaviour allows only the transfer of normal compressive and shear forces; it does not allow the transfer of tensile forces. This behaviour was modelled by inserting a layer of concrete-type material with a tensile strength of 0,1 MPa
- Connection between liners and piles (blue layer in Figure 3-11): they were modelled using a concrete-type material with virtually zero tensile strength (0,1 MPa), low shear retention capacity of the cracked material (shear retention factor 0,02) and a compressive strength of 20 MPa.

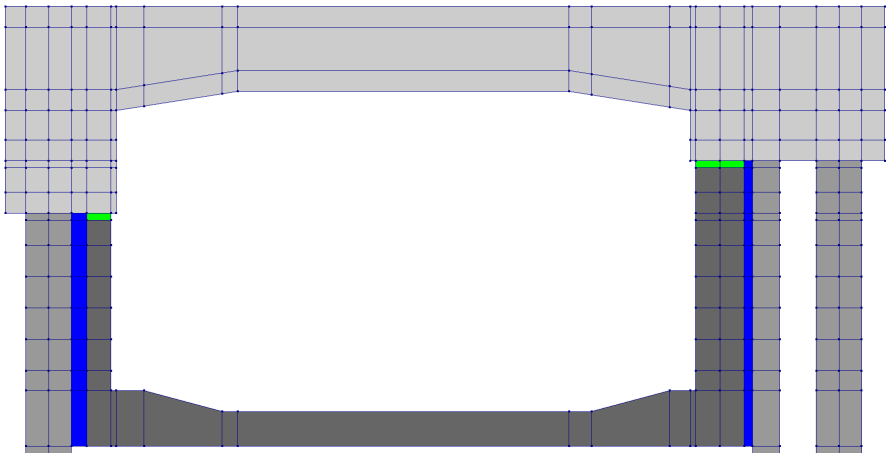


Figure 3-11 - Interfaces between Structural Elements

3.1.9 Stress Convention

The purpose of the analyses carried out is to provide stresses (N, M and T) in certain characteristic sections resulting solely from the constraints, detailed in the chapter 3.1.6, to be added to the stresses from the geotechnical design model. The thermo-mechanical model is a 2D model from which a stress state is derived. To convert the stress state into stresses (N, M and T), an integration is performed on the sections of interest. Specifically:

- The normal force acting on the sections of interest is given by the integration of the normal stresses at the sections, on both the concrete and the reinforcement.
- The bending moment acting on the sections of interest is given by the integration of the normal stresses at the section, in both the concrete and the reinforcement, multiplied by the distance from the section's centre of gravity
- The shear stress acting on the sections of interest is given by the integration of the shear stresses in the concrete only acting on the section.

It should be noted that, in the integration process, normal stresses in the concrete under tension are also taken into account. In non-linear models, it is in fact common to observe small tensile stresses in the concrete, even as a result of cracking. This is due to the phenomenon of tension softening shown in Figure 3-2 (b). Although these stresses are low, when integrated over large areas they give rise to non-negligible forces. It is wished to emphasise that the stresses provided are significantly influenced by these stresses. When the stresses (M, N, T) calculated in this way are used to check reinforced concrete sections in which the tensile strength of the concrete is completely disregarded this results in a conservative assessment. The greater the residual tensile stresses in the non-linear model, the greater the overestimation.

The stress conventions are shown in Figure 3-12:

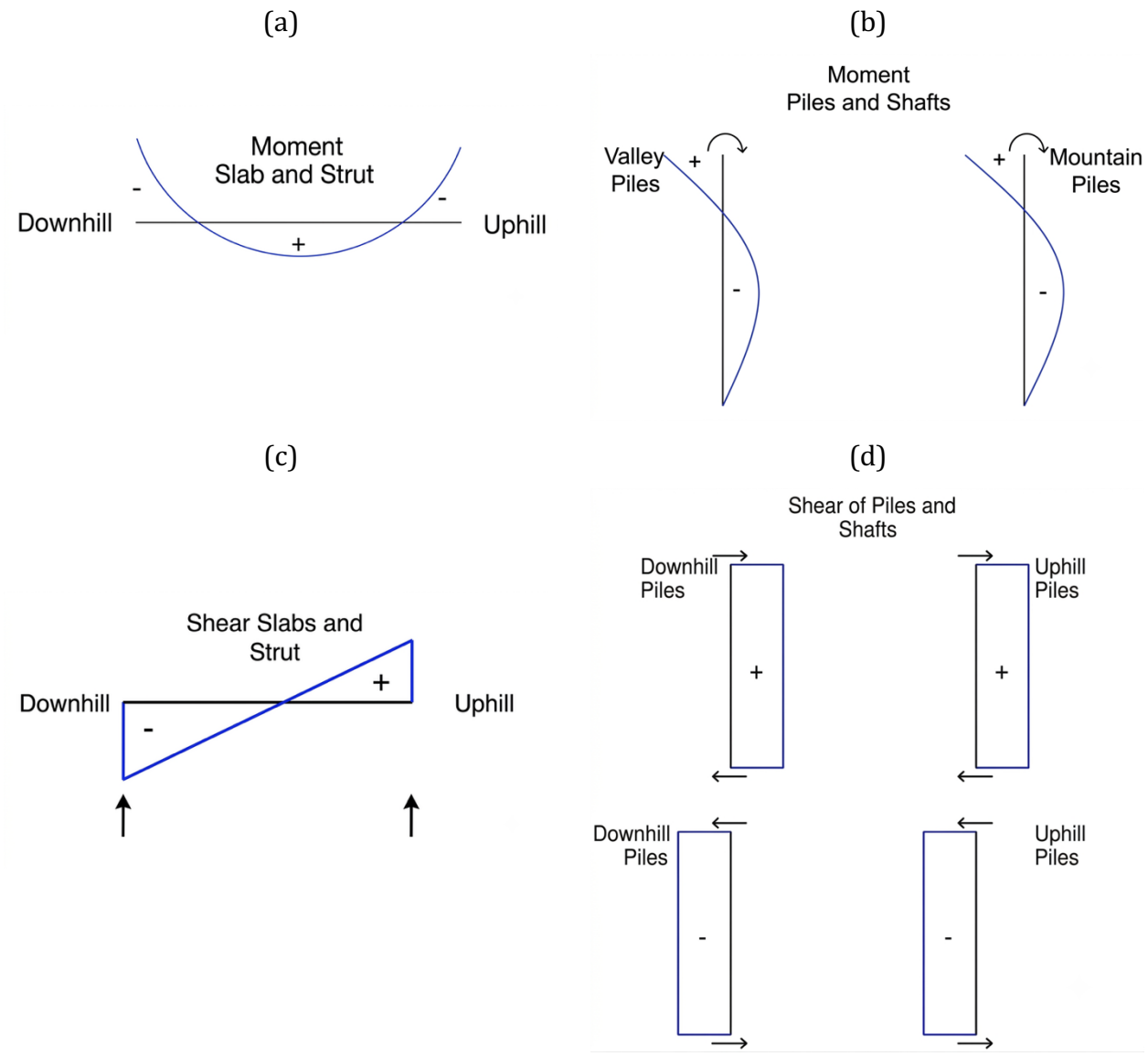


Figure 3-12 - Stress Conventions (a) Bending Moment in the Main Beam and Strut (b) Bending Moment in the Piles and Shafts (c) Shear in the Main Beam and Strut (d) Shear in the Piles and Shafts

3.2 Model 1: Research Model and Reference Baseline

Model 1 represents the highest level of detail (LoD) and mathematical resolution implemented within the DIANA FEA environment for the simulation of the tunnel structure. Within this high-fidelity framework, all concrete structural components of the tunnel, are modelled uniformly with the full suite of coupled thermo-chemo-mechanical properties.

The precision of model 1 as a research model is anchored in its fully coupled multiphysics hydration engine. Rather than prescribing static thermal variations, the transient temperature fields across the tunnel elements are driven by the exothermic kinetics of cement hydration.

The model implements an Arrhenius equivalent age framework with a verified activation constant (ARRHEN = 6.00000E+03) operating under a standard reference testing temperature (TEMREF = 2.00000E+01). This core engine dynamically governs the conversion of chronological time into chemical maturity based on the localized nodal temperature history. The chemical heat generation profile is mapped directly from empirical laboratory testing data, tracking the rise from an initial placement state of 20,0°C up to an absolute semi-adiabatic peak threshold of 70,0°C. Crucially, model 1 updates the underlying thermal material parameters as a continuous function of the calculated Degree of Reaction. The model incorporates separate multi-column scaling matrices to simulate the physical degradation of conductivity and volumetric specific heat capacity as fluid cement paste solidifies into a rigid matrix, ensuring that thermal profiles, spatial gradients, and heat retention characteristics are captured with high accuracy.

To simulate structural degradation and cracking under restrained early-age deformations, model 1 utilizes a multi-directional fixed smeared crack formulation. Upon exceeding the tensile capacity of the concrete, the model registers cracking as a distributed continuum strain within the integration points. This approach involves a reduction in the strength and stiffness of the material under tension once the tensile strength in the main direction has been exceeded. The behaviour of the material thus changes from isotropic to orthotropic in the main stress reference system. Post-cracking performance is governed by a linear tension softening law where residual tensile capacity drops linearly to zero at an ultimate cracking strain threshold of $1{,}94 * 10^{-4}$. The model accounts for changes in the structural properties of early-age concrete through time-dependent mechanical hardening tables expressed in seconds. These matrices govern the evolution of structural parameters from casting up to mature long-term service phases. Using the example of the internal part of the cover slab the values are described below:

- Stiffness matrix stabilization (t = 0 to 21 600s), provides an initial stiffness baseline that prevents numerical singular matrix failures before initial set:
    - Compressive capacity is fixed at 4,35 MPa
    - Tensile capacity is fixed at 0,335 MPa

- Hydration expansion phase ($t = 8{,}64 * 10^4$ to $2{,}59 * 10^5$s):
    - At 24h: tensile strength rises to 1,15 MPa and compressive strength is 15,51 MPa
    - At 3 days: tensile strength reaches 2,14 MPa and compressive strength is 27,13 MPa

Furthermore, post-failure shear stiffness across rough, open crack faces is managed using a constant shear retention configuration with an assigned factor of 0,20. This factor preserves exactly 20% of the uncracked elastic shear modulus, ensuring the model accurately captures aggregate interlock, multi-directional stress rotation, and shear redistribution across the tunnel lining without causing numerical instability.

Finally, to calculate early-age stresses accurately, model 1 incorporates autonomous chemical shrinkage and visco-elastic basic creep relaxation, which prevent the model from overestimating tensile stress peaks during cooling. Load-independent volumetric deformations are managed via the uniaxial shrinkage strains matrix, which supplies an empirical autogenous and drying shrinkage strain curve that progresses from 0,0 at casting up to a long-term asymptotic ceiling of $2{,}68 * 10^{-4} = 268\ \mu\varepsilon$. Concurrently, basic creep strains are computed using an aging 4-element Kelvin-Voigt chain model arranged in series. The first evolution of the creep is responsible for the evolution of the Young's Modulus, and the three other elements are responsible for the creep's evolution.

3.3 Model 2: Numerical Discretization of the Hydration Effect

Model 2 represents an intermediate level of detail (LoD) designed to optimize global processing efficiency. This model shifts away from the fully non-linear approach used across the entire structure in model 1.

A major difference between model 1 and model 2 lies in the modelling of material thermal properties. Model 1 captures transient, variable parameters by updating thermal conductivity and specific heat capacity as a continuous function of the calculated degree of reaction. Conversely, model 2 simplifies these thermal calculations by implementing steady-state, constant thermal material parameters. Moreover, model 2 alters the mathematical method used

to simulate concrete cracking. Model 1 utilizes a multi-directional fixed smeared crack formulation. In contrast, model 2 implements a Total Strain Fixed Crack Model configuration, following a strain stress curve shown in Figure 3-13:

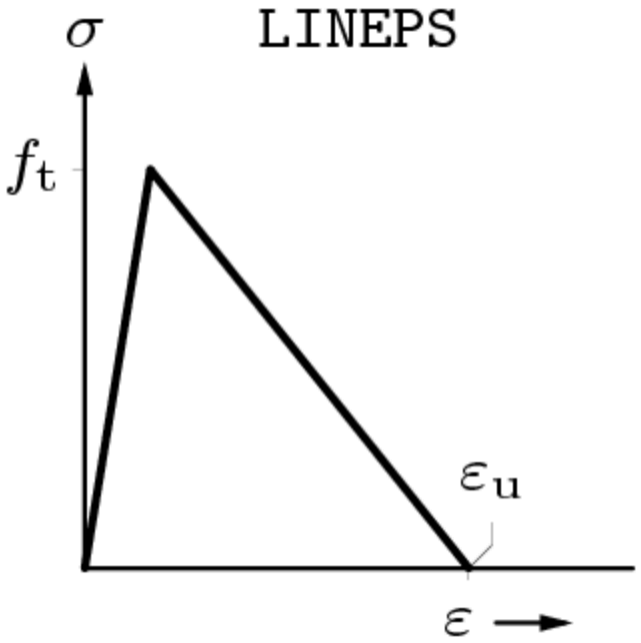


Figure 3-13 - Linear Tension Softening Stress-Strain Diagram

This architecture evaluates structural damage directly from total strain vectors along fixed principal stress axes. Post-failure tensile performance is governed by a linear strain softening law which modifies the tension softening approach of the research model. The concrete behaviour in compression is simplified into a linear elastic response, and its properties over time are controlled and computed using the Model Code of 2010, as stated in the section 1.1.2:

$$f_{cm}(t) = \beta_{cc}(t) * f_{cm}(28) \quad (44)$$

$$f_{ctm}(t) = \beta_{cc}(t) * f_{ctm}(28) \quad (45)$$

$$E_{cm}(t) = [\beta_{cc}(t)]^{0,5} * E_{cm}(28) \quad (46)$$

Where $f_{cm}(28)$ and $E_{cm}(28)$ represent the reference compressive strength and Young's modulus developed at the standard maturity threshold of 28 days. The time-dependent hardening kinetics are driven by the function $\beta_{cc}(t)$, which is mathematically defined as:

$$\beta_{cc}(t) = \exp\left\{s * \left[1 - \left(\frac{28}{t}\right)^{0,5}\right]\right\} \quad (47)$$

A fundamental difference between model 1 and model 2 lies in the mathematical tracking of viscoelastic basic creep. In model 1, basic creep is a dynamic, temperature-dependent microstructural process. Time is not an explicit parameter; instead, the Kelvin chain elements scale automatically at each integration point based on the localized Degree of Reaction (r) and thermal evolution. In contrast, model 2 completely uncouples compliance calculations from local thermal gradients or hydration speeds. It implements a pre-calculated, fixed chronological aging look-up matrix where the visco-elastic chain is discretized. According to the Model Code 2010, the creep coefficients can be calculated from:

$$\varphi\ (t, t_0) = \varphi_0 * \beta_c(t, t_0) \quad (48)$$

Where t is the age of concrete in days at the moment considered, and t_0 is the age of concrete at loading in days and is equal to 3 days in this model. Additionally, φ_0 is the notional creep coefficient that is computed as follows:

$$\varphi_0 = \varphi_{RH} * \beta(f_{cm}) * \beta(t_0) \quad (49)$$

Where:

$$\varphi_{RH} = \left[1 + \frac{1 - \frac{RH}{100}}{0,1 * \sqrt[3]{h}} * \alpha_1\right] * \alpha_2 \quad (50)$$

$$\beta(f_{cm}) = \frac{16,8}{\sqrt{f_{cm}}} \quad (51)$$

$$\beta(t_0) = \frac{1}{0,1 + (t_0)^{0,2}} \quad (52)$$

$$\alpha_1 = \left[\frac{35}{f_{cm}}\right]^{0,7} \quad (53)$$

$$\alpha_2 = \left[\frac{35}{f_{cm}}\right]^{0,2} \quad (54)$$

Where RH is the relative humidity of the environment and is set as 80%: humid atmospheric conditions., f_{cm} is the mean compressive strength at 28 days and h is the notional size of the member in mm. The development of creep with time is described by:

$$\beta_c(t,t_0) = \left[\frac{t-t_0}{\beta_H + (t-t_0)}\right]^{0,3} \quad (55)$$

$$\beta_H = 1{,}5 * h\left[1 + \left(1{,}2 * \frac{RH}{100}\right)^{18}\right] + 250 * \alpha_3 \quad (56)$$

$$\alpha_3 = \left[\frac{35}{f_{cm}}\right]^{0,5} \quad (57)$$

The resulting coefficients were combined to construct the continuous viscoelastic compliance reference curve:

$$J(t,t_0) = \frac{1}{E_c(t_0)} + \frac{\varphi(t,t_0)}{E_{c,28}} \quad (58)$$

3.4 Model 3: Standard Non-Linear Model without Cracking

Model 3 is formulated directly from model 2 to isolate the specific structural contribution of concrete cracking. Under this configuration, the concrete continuum incorporates standard regulatory property evolution, accounting for mechanical strength and stiffness ageing over time, alongside long-term viscoelastic creep compliance. However, the material is defined as strictly uncrackable, while omitting hydration heat generation, degree-of-reaction kinetics, and coupled thermo-hydration fields. By maintaining identical geotechnical boundary conditions, construction phasing, and creep laws while suppressing crack initiation, model 3 serves to isolate and quantify the exact role of concrete micro-cracking in relieving self-equilibrating thermal and shrinkage coactions.

3.5 Model 4: Standard Non-Linear Model without Creep

Model 4 represents a standard regulatory non-linear formulation configured without viscoelastic creep relaxation. In this setup, concrete tensile cracking and fracture softening are fully active alongside standard time-dependent property ageing. Conversely, viscoelastic creep deformations, hydration heat evolution, degree-of-reaction kinetics, and thermo-hydration couplings are completely excluded in opposition to the three first models. Consequently, the viscoelastic creep compliance function $J\ (t,\tau)$ reduces to a purely elastic time-dependent line.

By comparing the results of model 4 against the creep-inclusive formulations of model 1, 2 and 3 the researcher can isolate and quantify the exact stress-relieving benefit of viscoelastic creep. This comparison isolates the role of creep in preventing early-age durability failures, providing a clear demonstration of how stress relaxation prevents premature cracking in concrete infrastructure.

3.6 Model 5: Standard Linear Elastic Baseline with Aging

Model 5 corresponds to the conventional design-office approach, configured as a standard linear elastic continuum with material property ageing. Derived as the linear counterpart to model 4, it incorporates standard time-dependent maturation of the elastic modulus and compressive strength over time but treats the concrete as a purely linear elastic material in both tension and compression, without cracking or viscoelastic creep. Furthermore, all early-age hydration heat, reaction kinetics, and thermo-hydration fields are deactivated. Model 5 serves as the deterministic benchmark for traditional cross-sectional Ultimate Limit State verifications, illustrating the degree to which neglecting non-linear stress relief through cracking and creep artificially inflates restraint coactions and imposes excessive conservatism on structural safety checks.

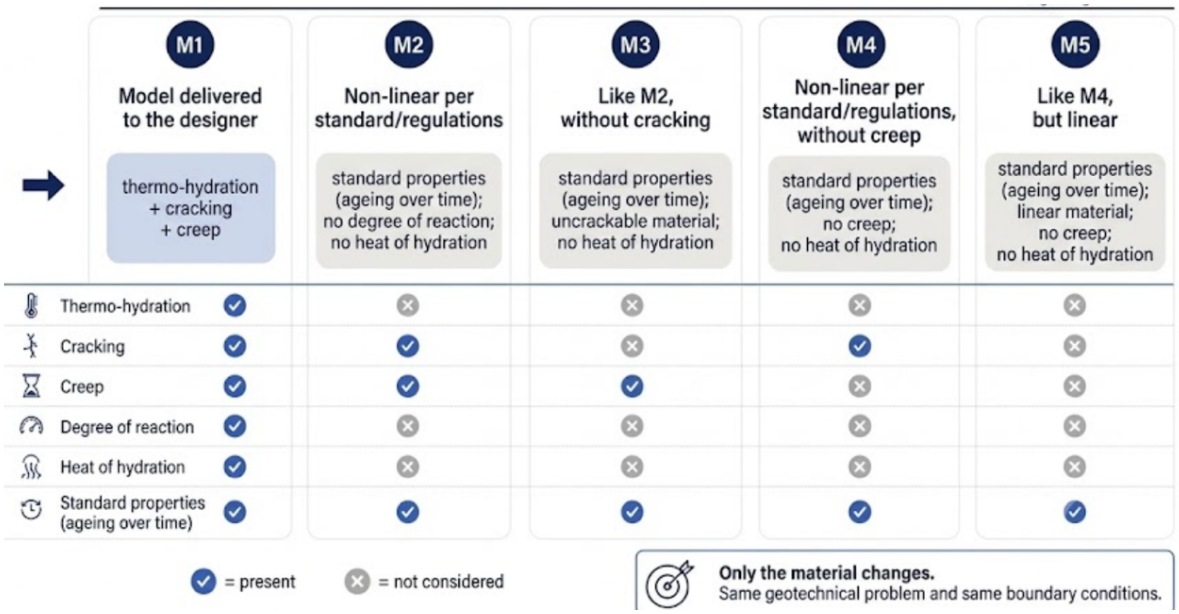


Figure 3-14 - Overview of the 5 Models

Chapter 4 Comparison Between the Models

Following the definition of the numerical approaches in Chapter 3, this chapter presents a comprehensive comparative analysis of the five finite element model configurations. The central objective is to track, isolate, and quantify how different levels of modelling detail (LoD) and material non-linearities affect the calculated internal actions within the Galleria Piscinale structural continuum. This evaluation maps the continuous time-history evolution of internal bending moments, M, axial normal force, N, and transverse shear stresses, T, over a timeline of 1825 days. This timeline reflects the real-world construction phasing schedule of the project, spanning from the initial casting of the upper cover slab (t = 0 days) through intermediate backfilling, internal core excavation, groundwater table lowering, and final long-term soil stabilization phases. To achieve a rigorous breakdown of structural behaviour, the comparative evaluation for each structural element and internal force (M, N, T) is systematically structured across three distinct actions combination cases:

- Geotechnical actions and coactions: Non-linear analysis where all phenomena are considered: self-weight; landslide, groundwater level drop and constraints due to thermal effects of hydration, seasonal thermal effects and shrinkage.
- Geotechnical actions and creep (fluage): Analysis where only effects analogous to the geotechnical model (self-weight; construction phases, landslide and groundwater level drawdown) and the concrete creep are taken into account.
- Complete combined coactions: Analysis considering the effect of the constraints solely and it is obtained by the difference between the analysis of the geotechnical actions and coactions and the analysis of the geotechnical actions and creep.

4.1 Cover Slab Structural Sections

The analysis focuses on three critical sections: the rigid connection to the uphill bulkhead layout, the central midspan node, and the rigid connection to the downhill wall.

4.1.1 Uphill Support Section

Moment diagrams:

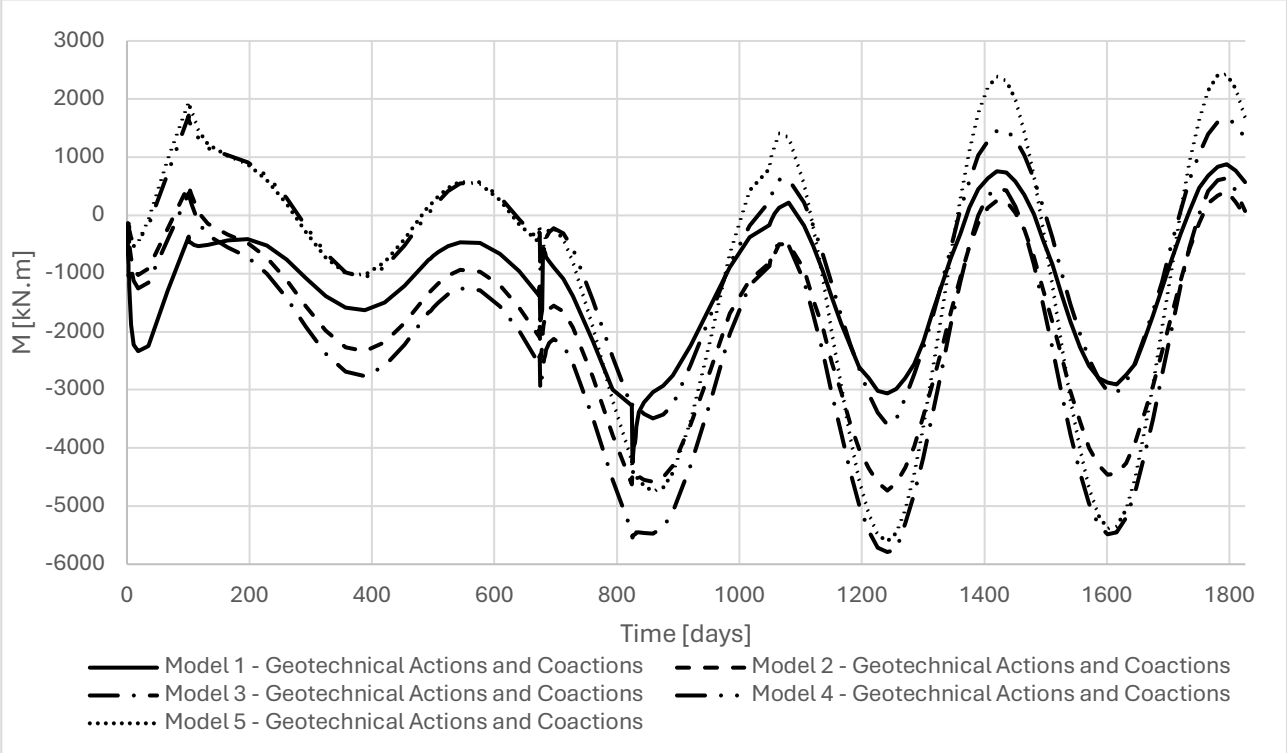


Figure 4-1 - Moment – Geotechnical Actions and Coactions - Cover Slab Uphill Support

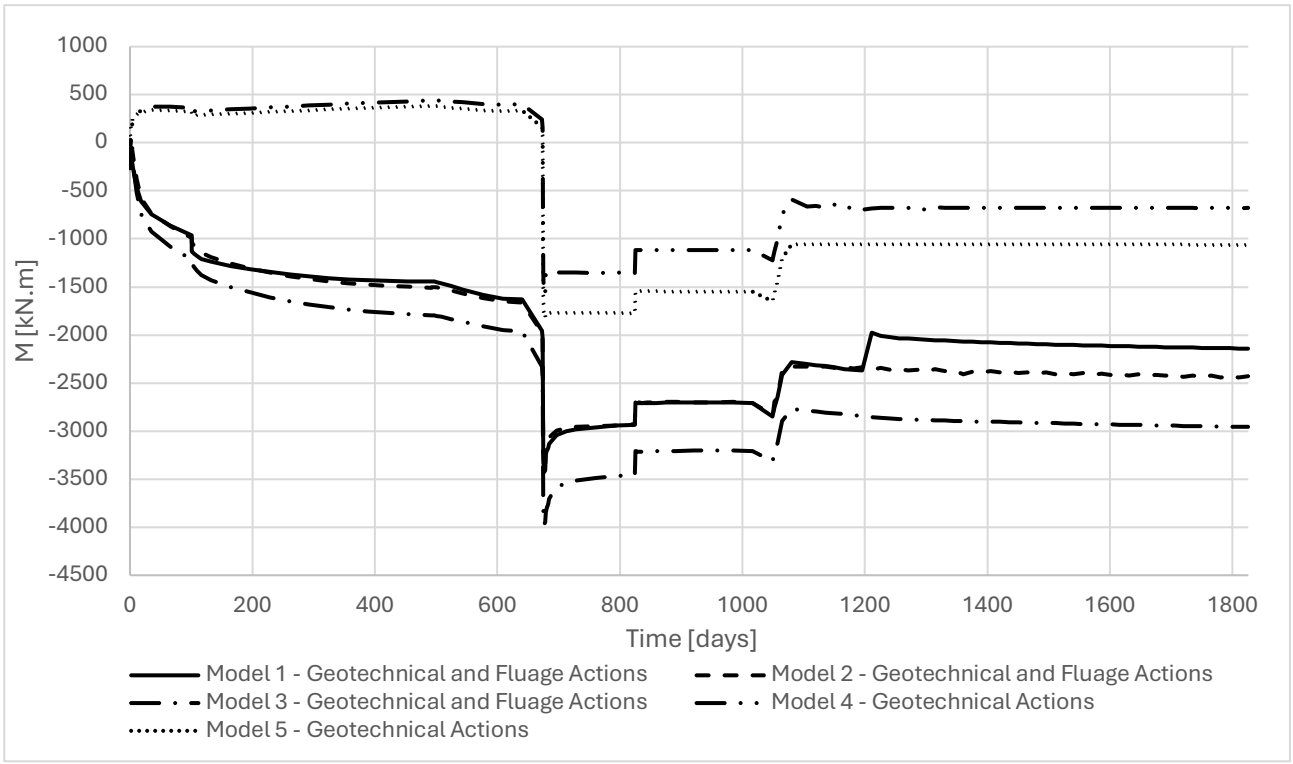


Figure 4-2 - Moment - Geotechnical and Creep Actions – Cover Slab Uphill Support

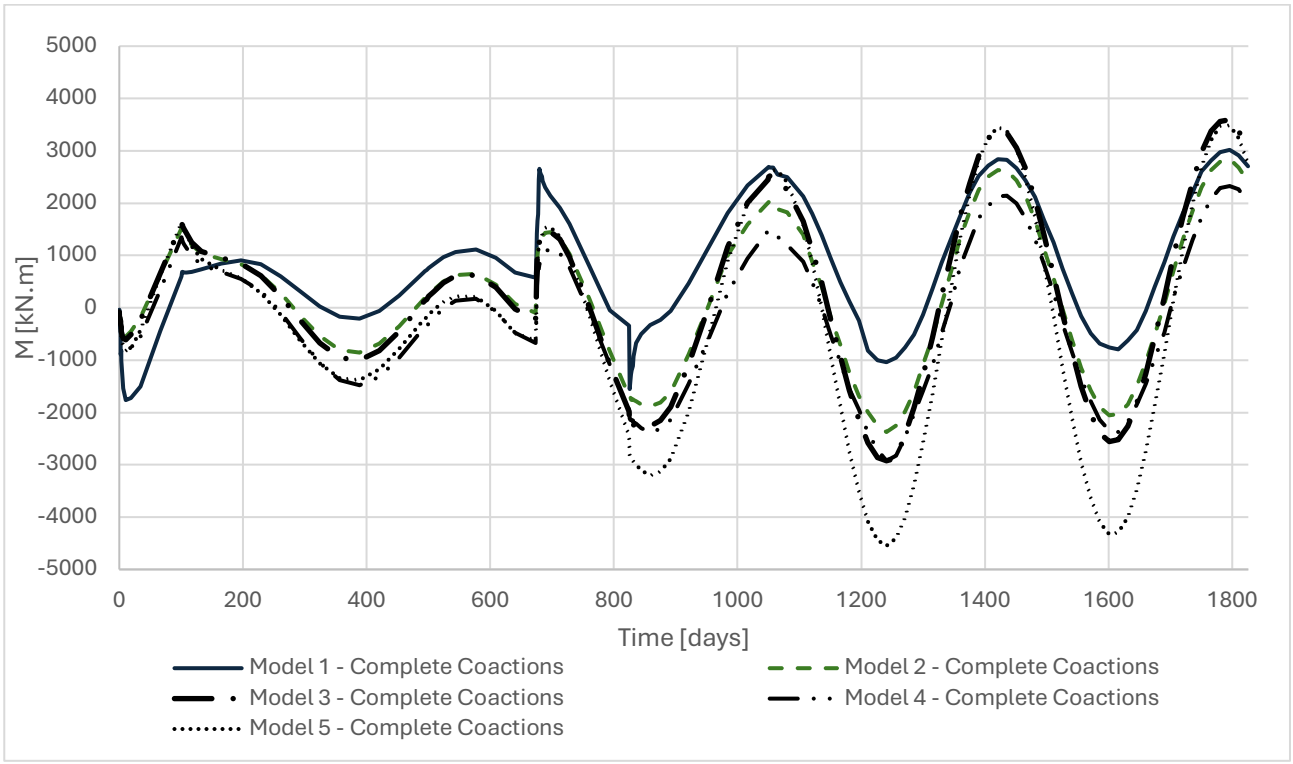


Figure 4-3 - Moment - Complete Coactions - Cover Slab Uphill Support

Axial force diagrams:

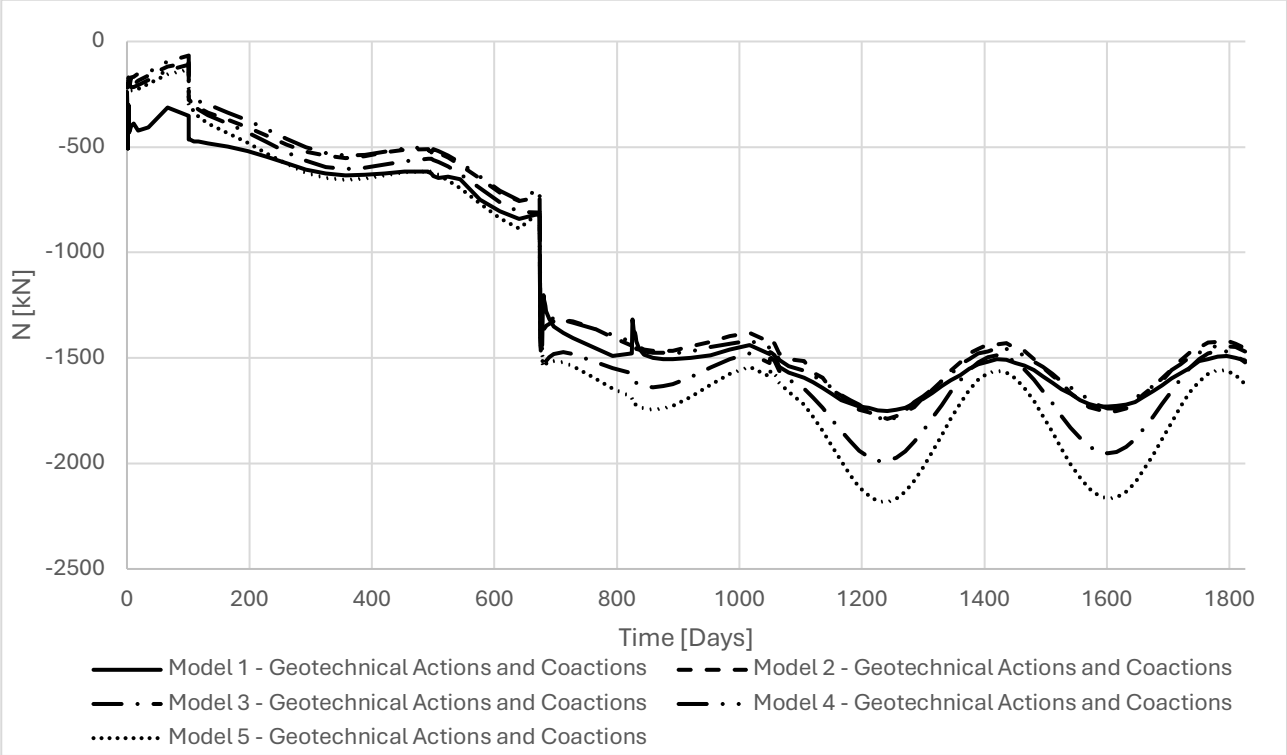


Figure 4-4 - Axial Force - Geotechnical Actions and Coactions - Cover Slab Uphill Support

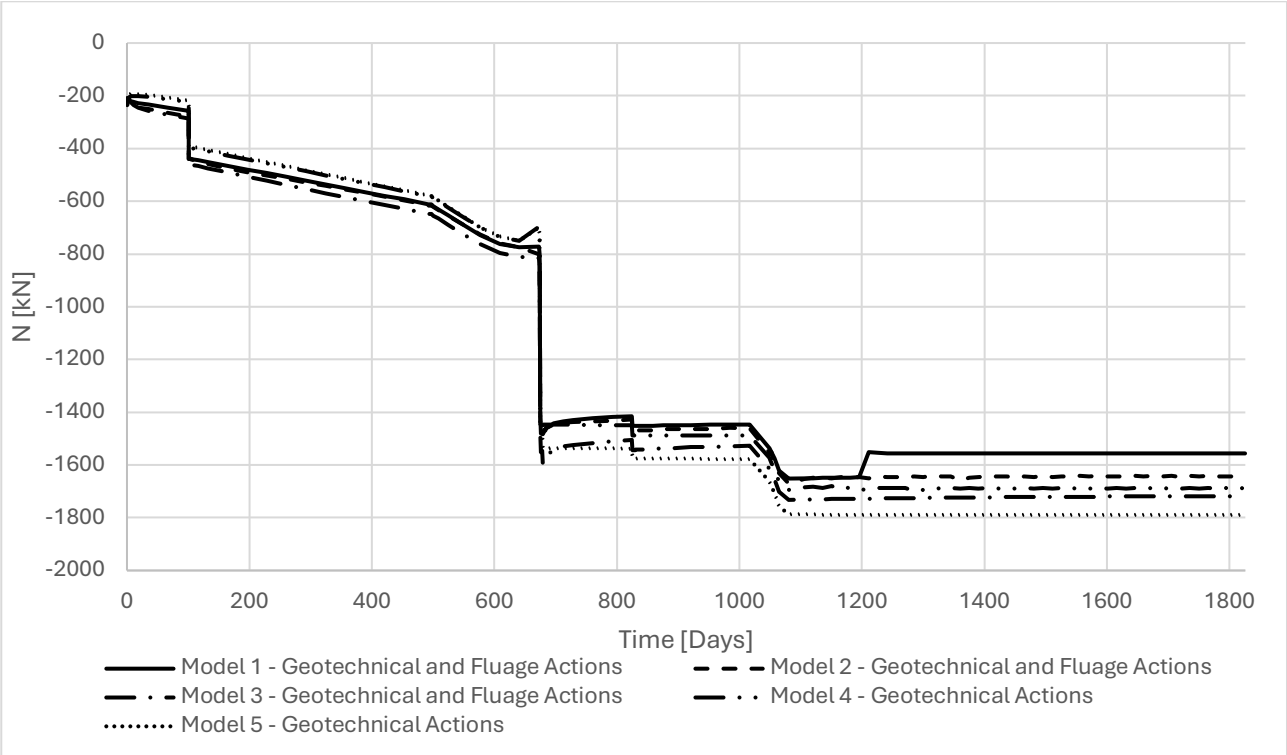


Figure 4-5 - Axial Force - Geotechnical and Creep Actions - Cover Slab Uphill Support

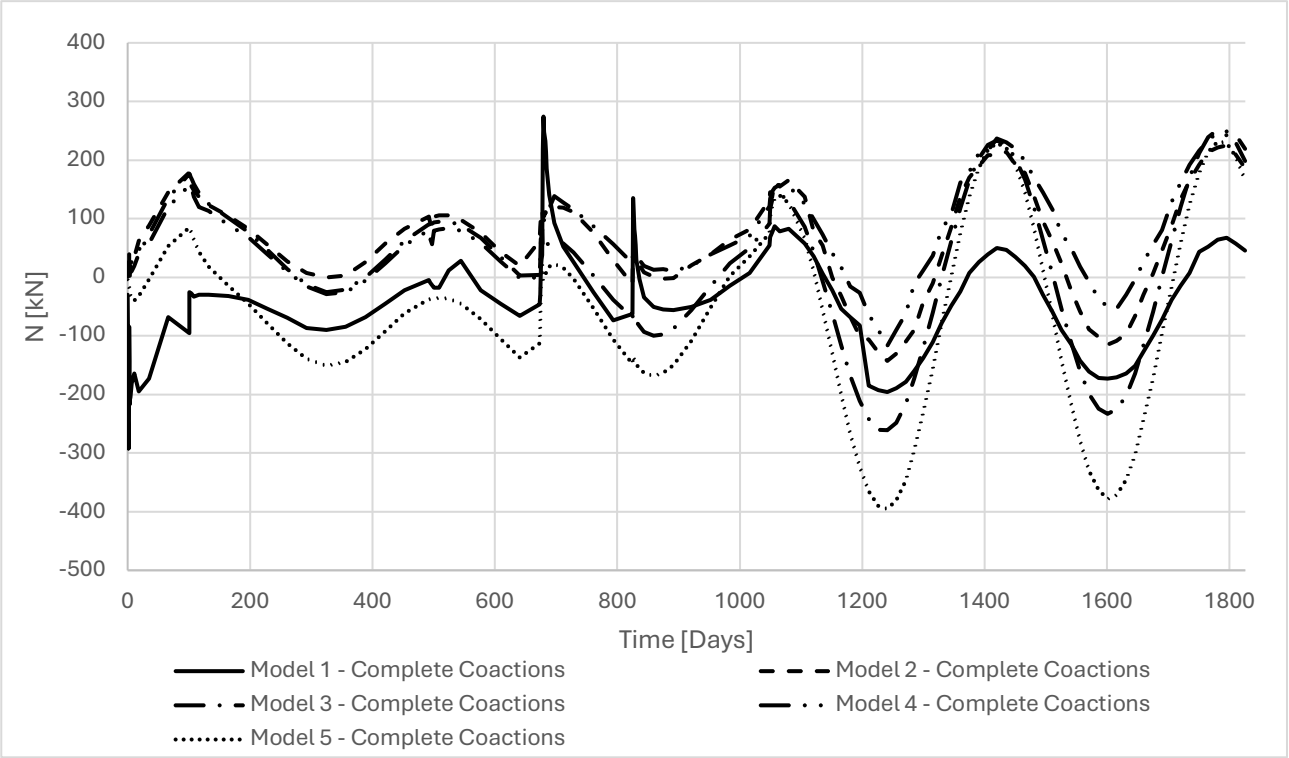


Figure 4-6 - Axial Force - Complete Coactions - Cover Slab Uphill Support

Shear force diagrams:

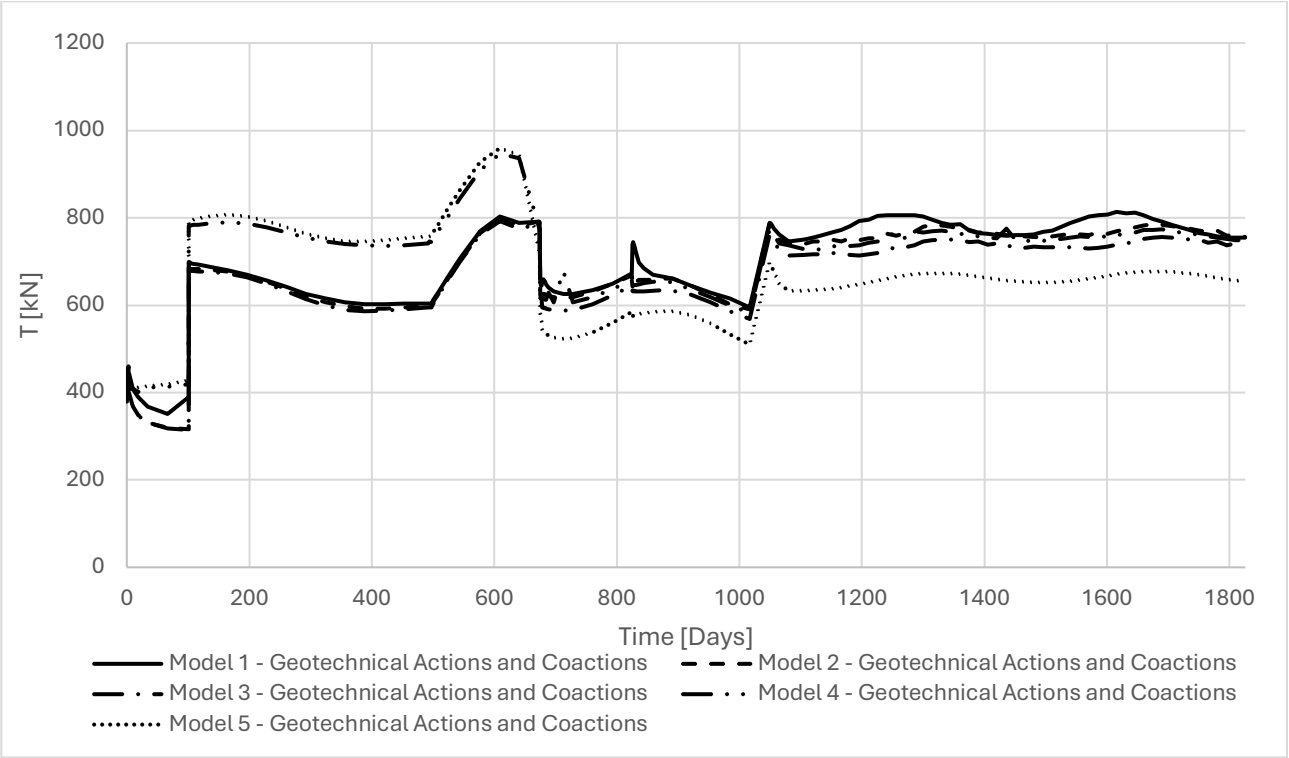


Figure 4-7 – Shear Force - Geotechnical Actions and Coactions - Cover Slab Uphill Support

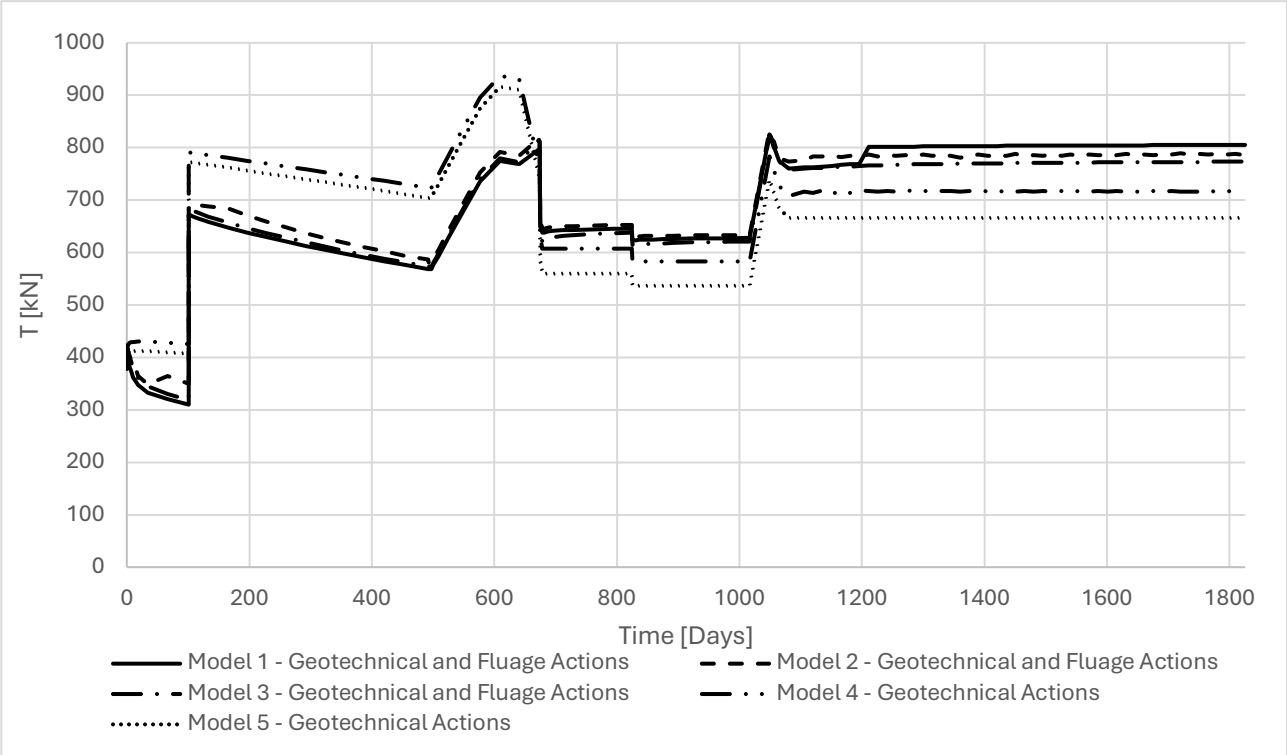


Figure 4-8 – Shear Force - Geotechnical and Creep Actions - Cover Slab Uphill Support

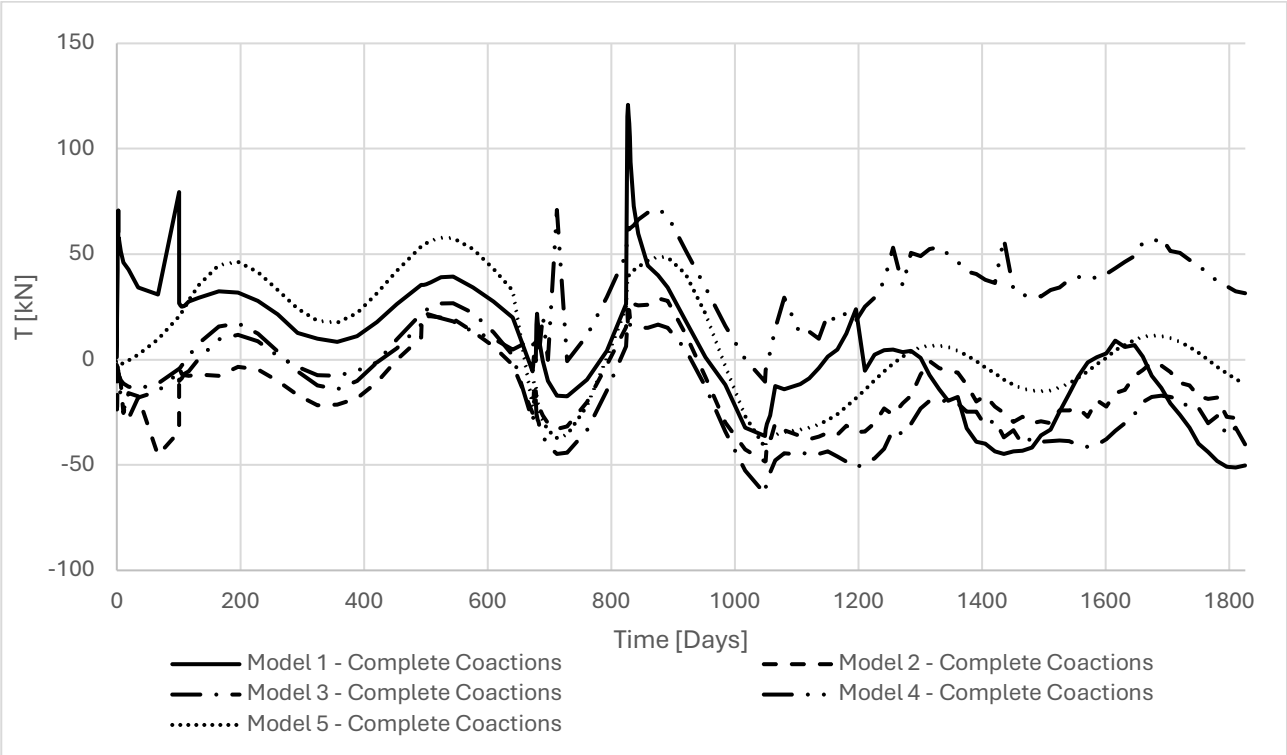


Figure 4-9 – Shear Force - Complete Coactions - Cover Slab Uphill Support

4.1.2 Midspan Section

Moment diagrams:

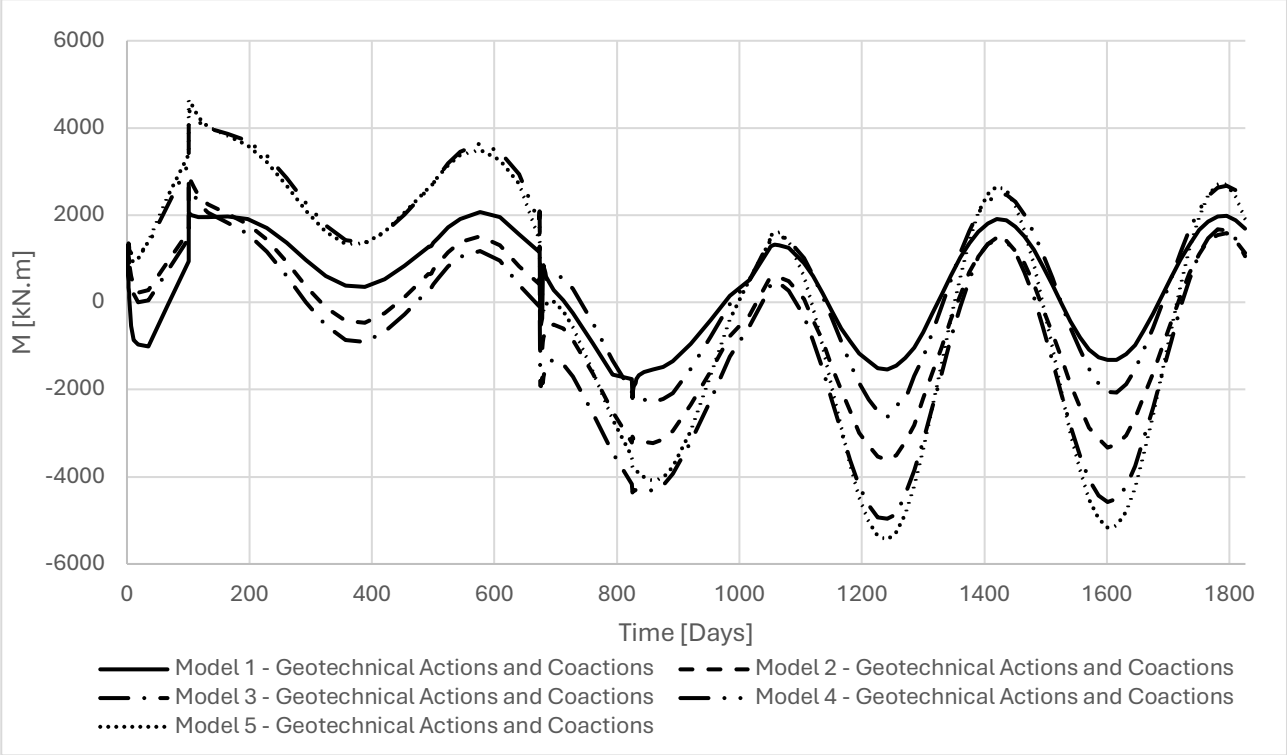


Figure 4-10 - Moment - Geotechnical Actions and Coactions - Cover Slab Midspan

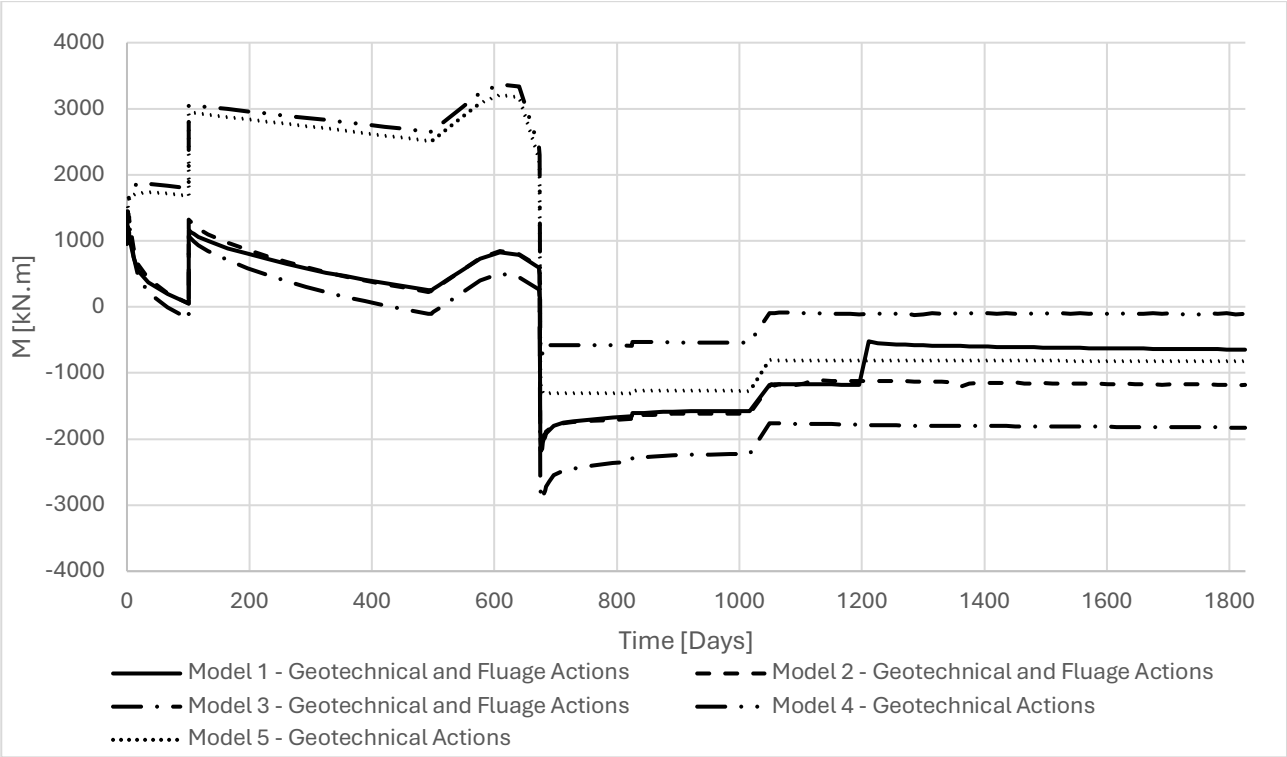


Figure 4-11 - Moment - Geotechnical and Creep Actions - Cover Slab Midspan

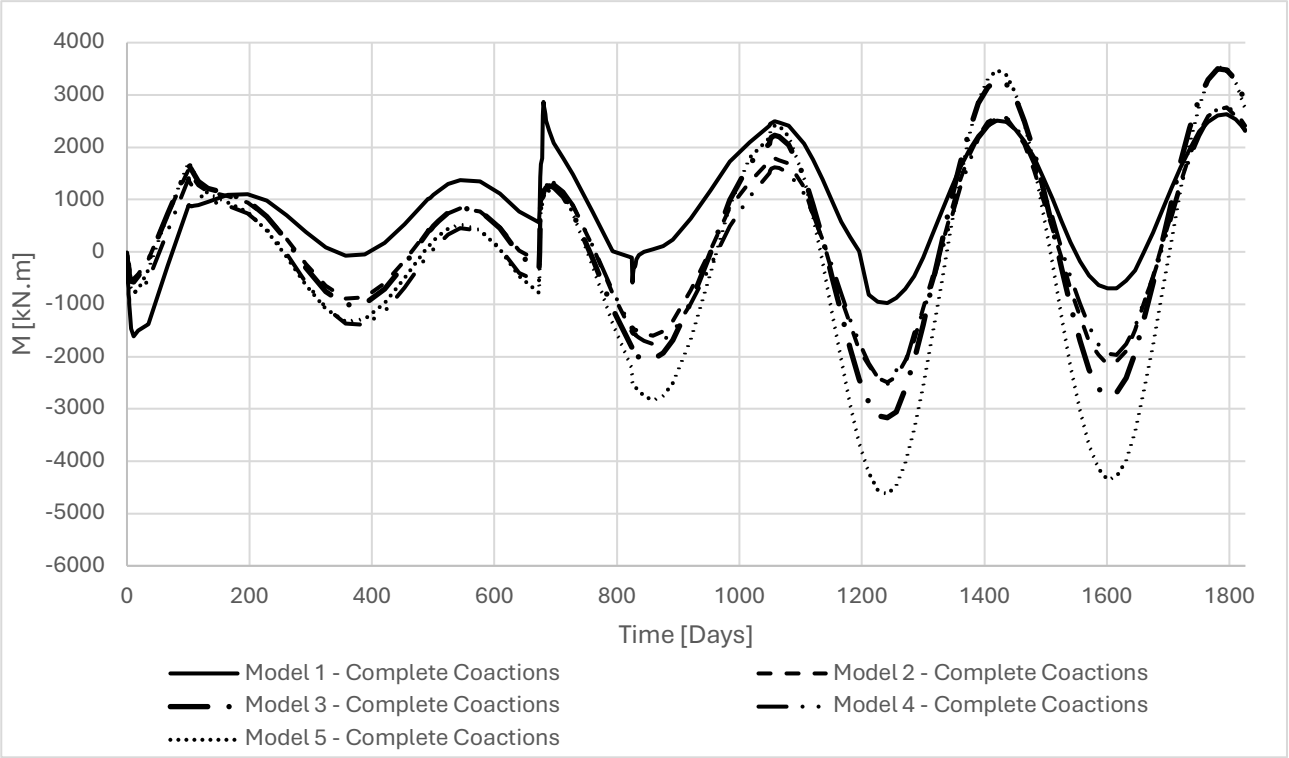


Figure 4-12 - Moment - Complete Coactions - Cover Slab Midspan

Axial force diagrams:

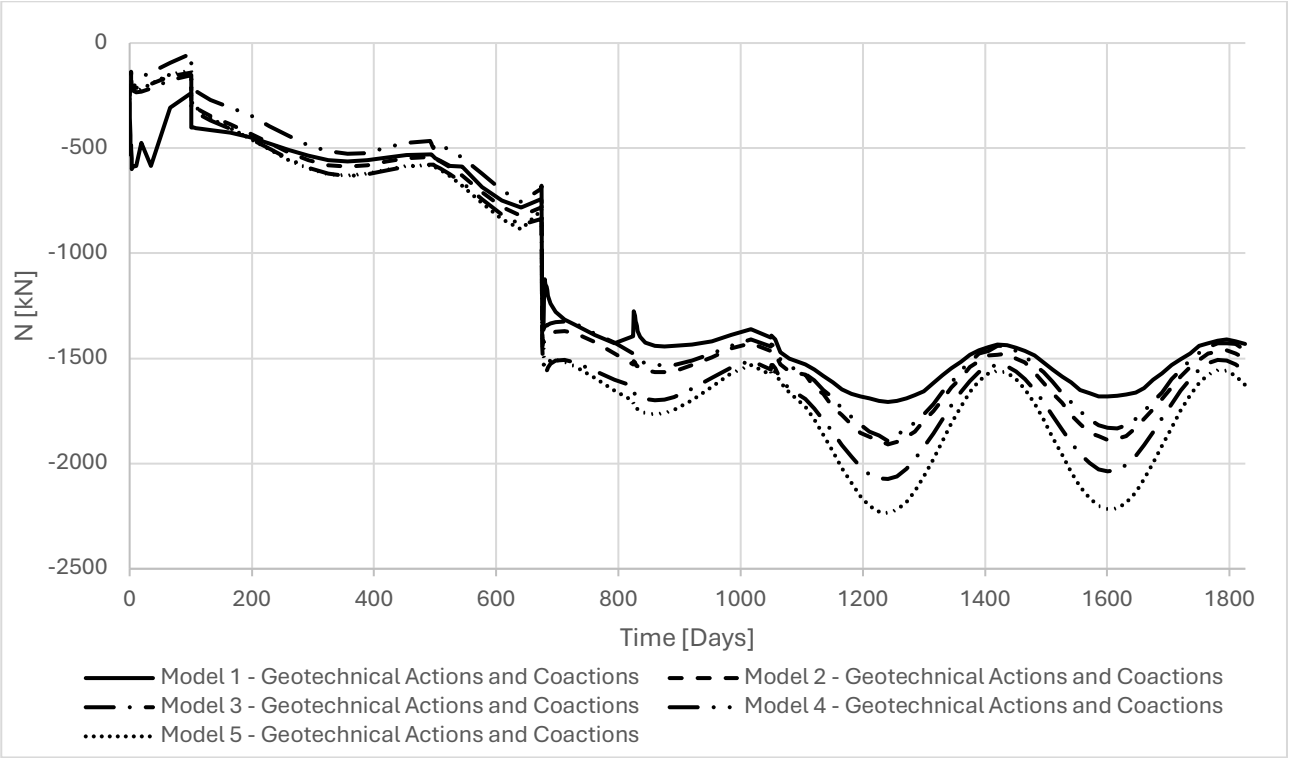


Figure 4-13 - Axial Force - Geotechnical Actions and Coactions - Cover Slab Midspan

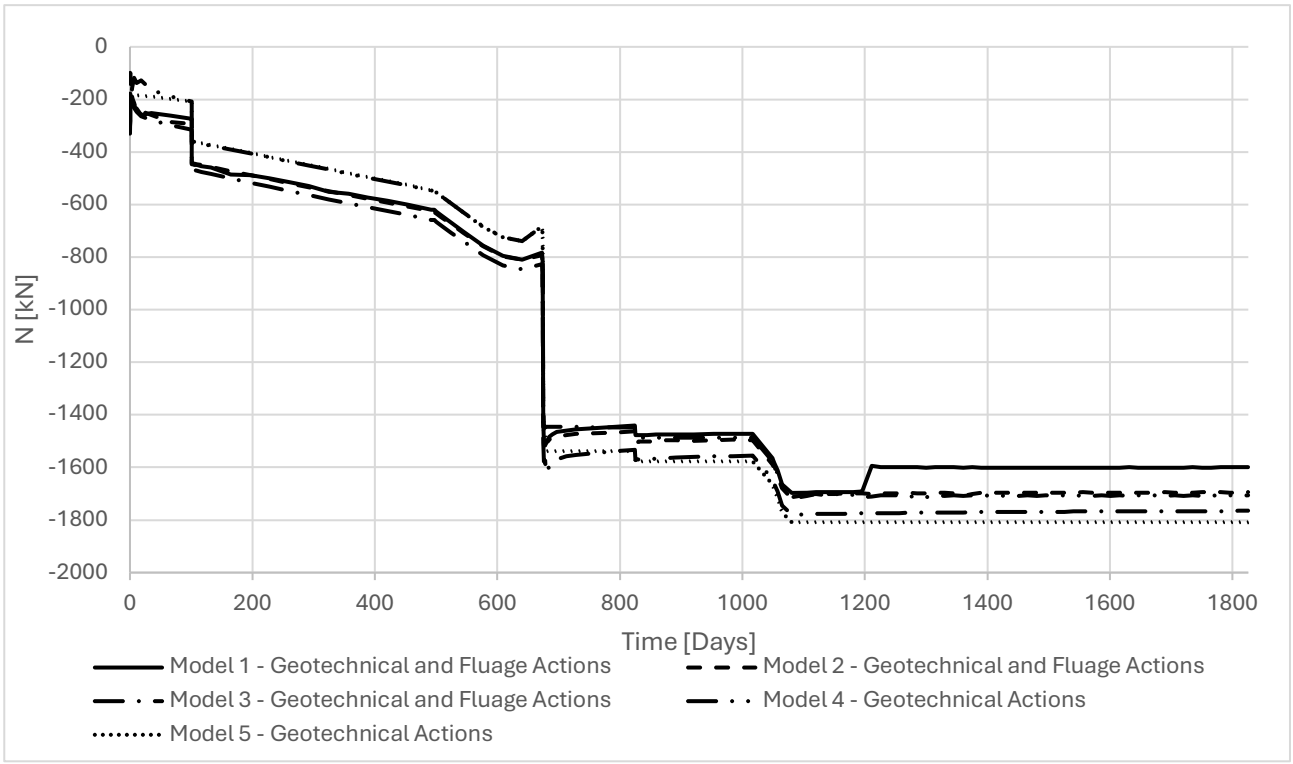


Figure 4-14 - Axial Force - Geotechnical and Creep Actions - Cover Slab Midspan

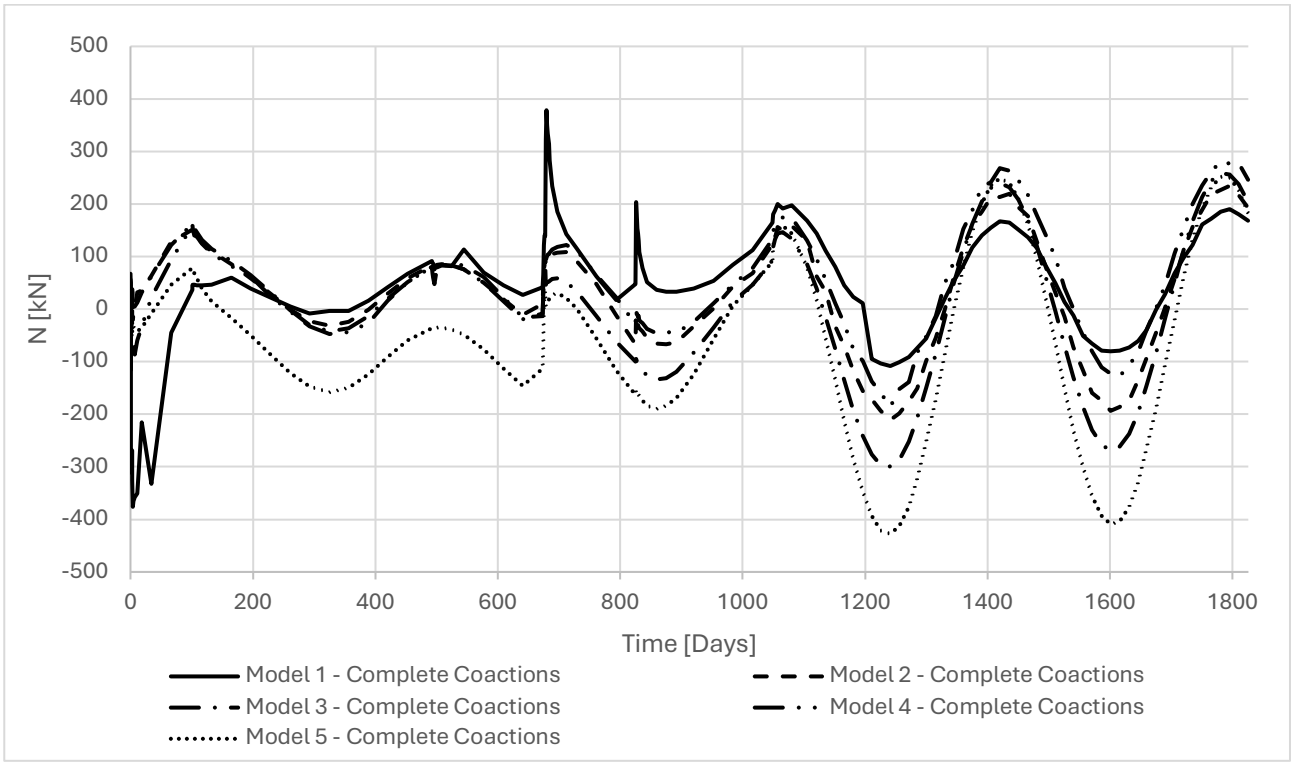


Figure 4-15 - Axial Force - Complete Coactions - Cover Slab Midspan

Shear force diagrams:

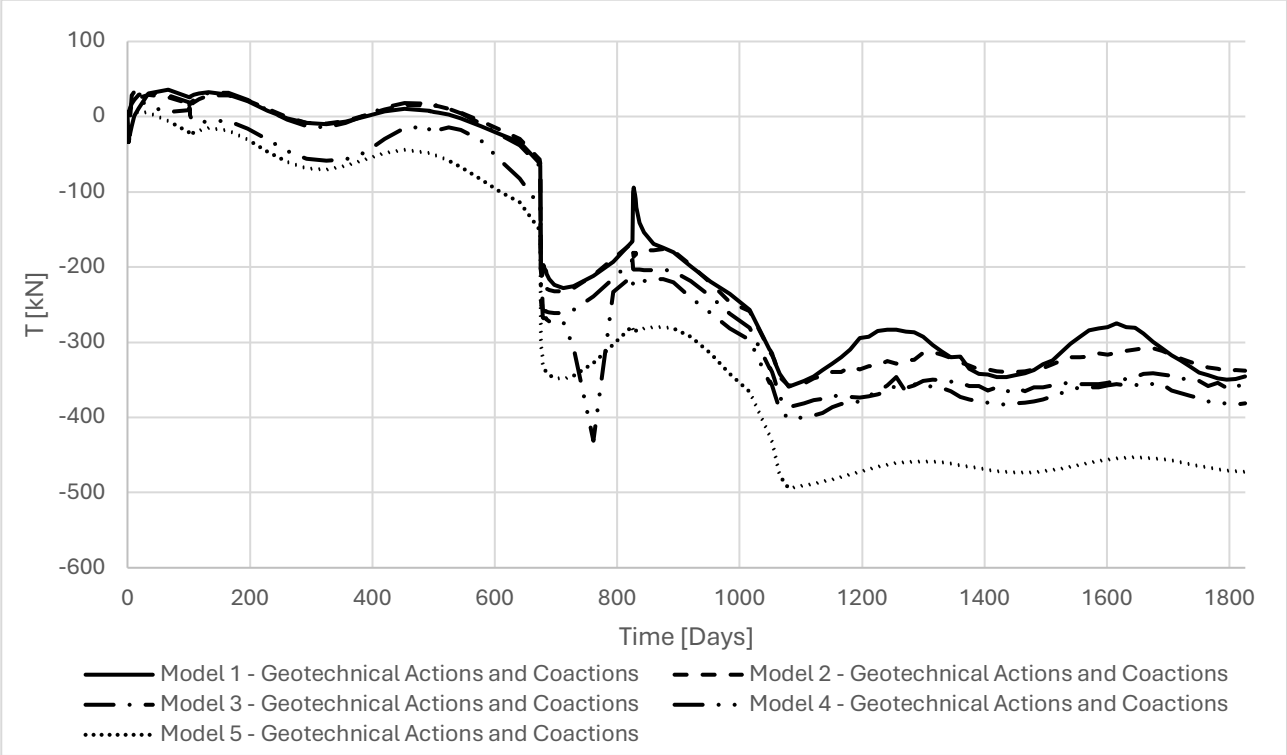


Figure 4-16 – Shear Force - Geotechnical Actions and Coactions - Cover Slab Midspan

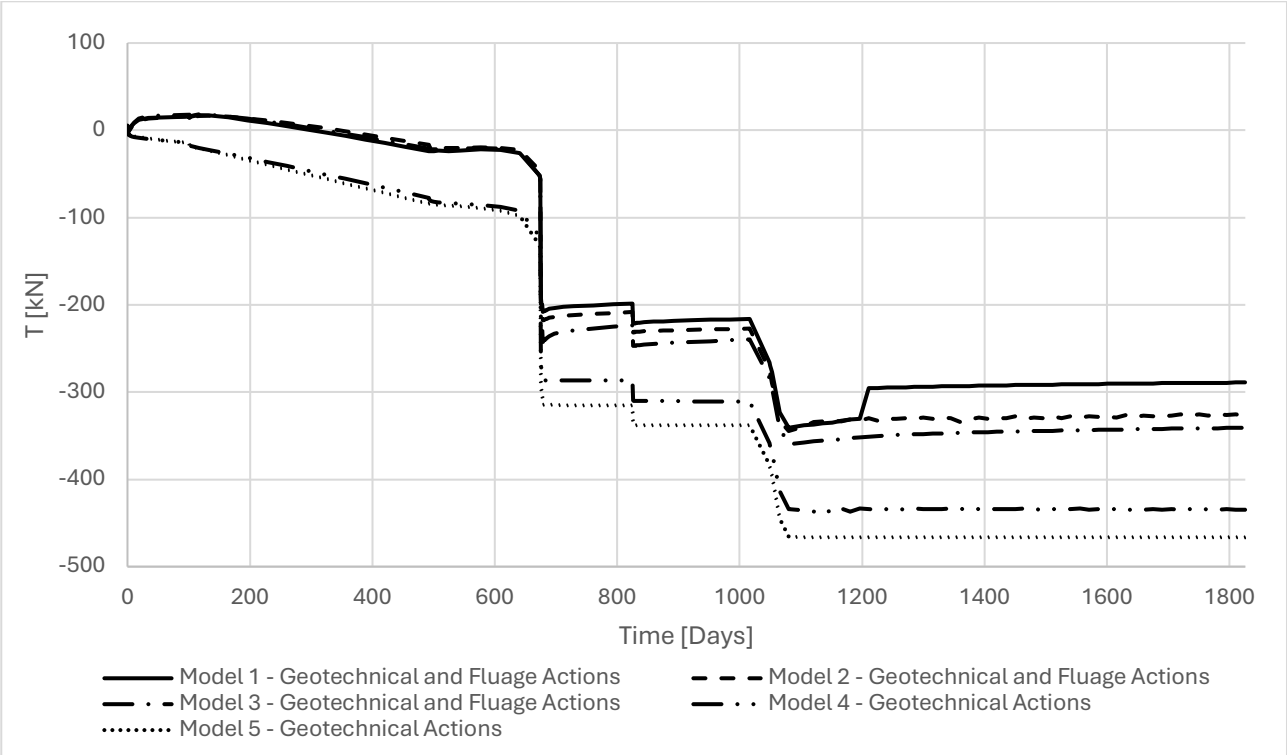


Figure 4-17 – Shear Force - Geotechnical and Creep Actions - Cover Slab Midspan

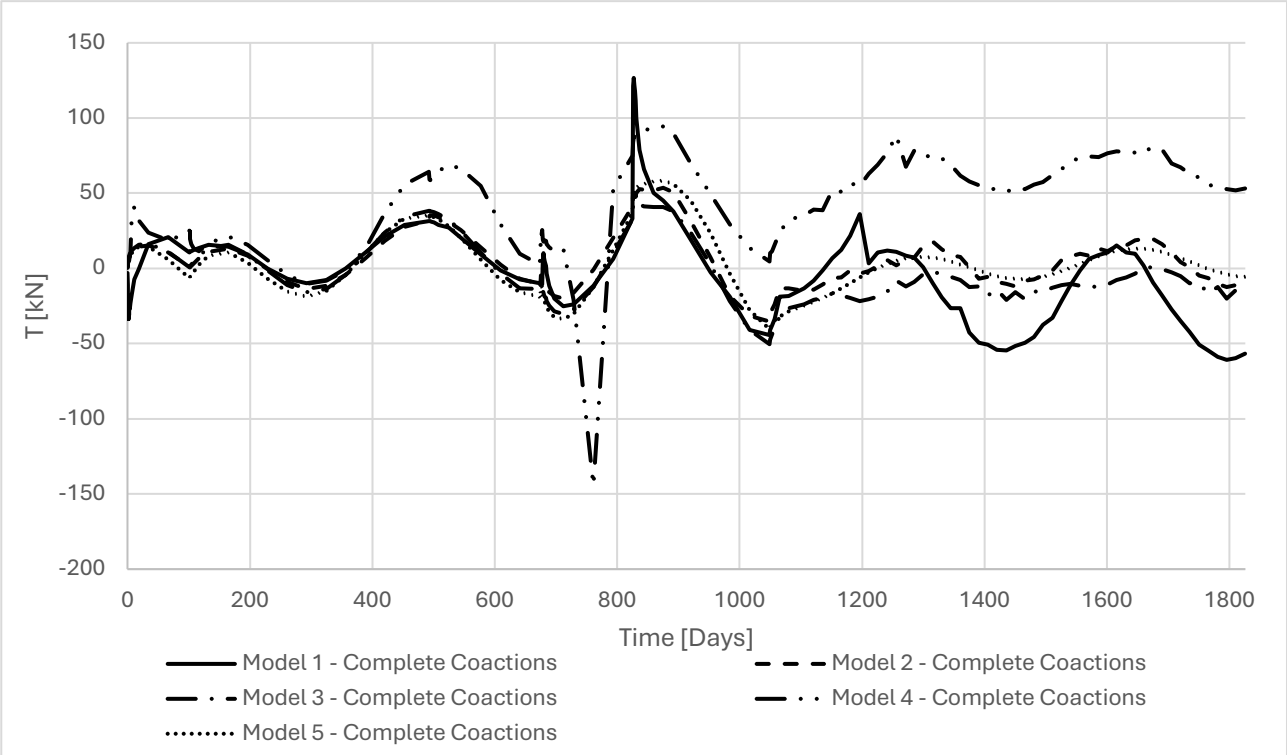


Figure 4-18 – Shear Force - Complete Coactions - Cover Slab Midspan

4.1.3 Downhill Support Section

Moment diagrams:

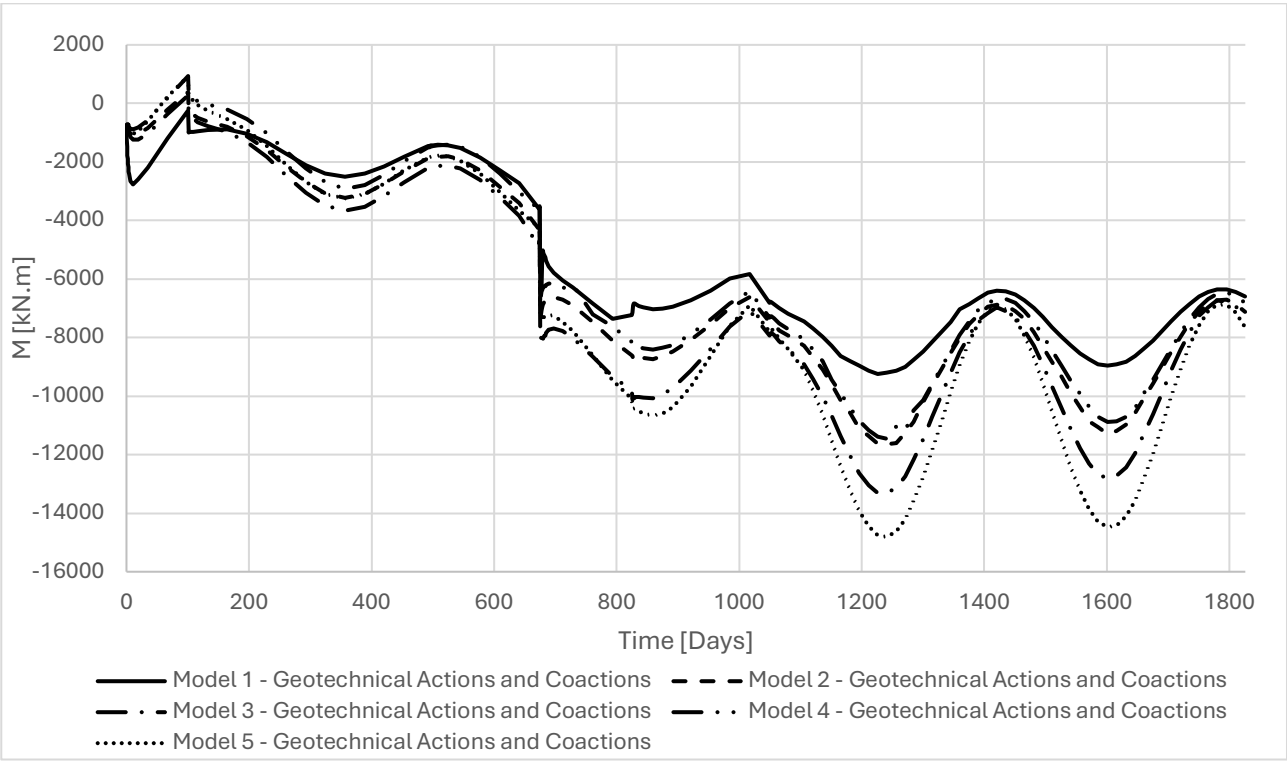


Figure 4-19 - Moment - Geotechnical Actions and Coactions - Cover Slab Downhill Support

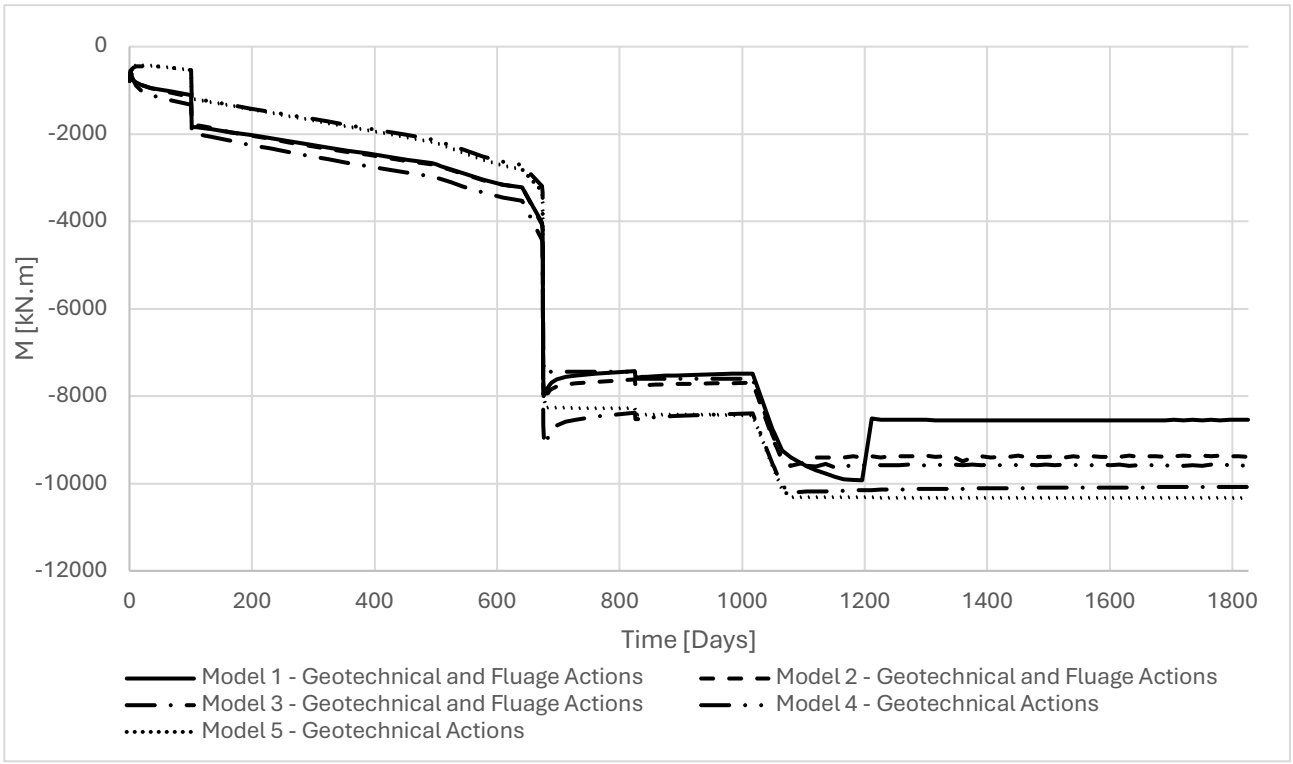


Figure 4-20 - Moment - Geotechnical and Creep Actions - Cover Slab Downhill Support

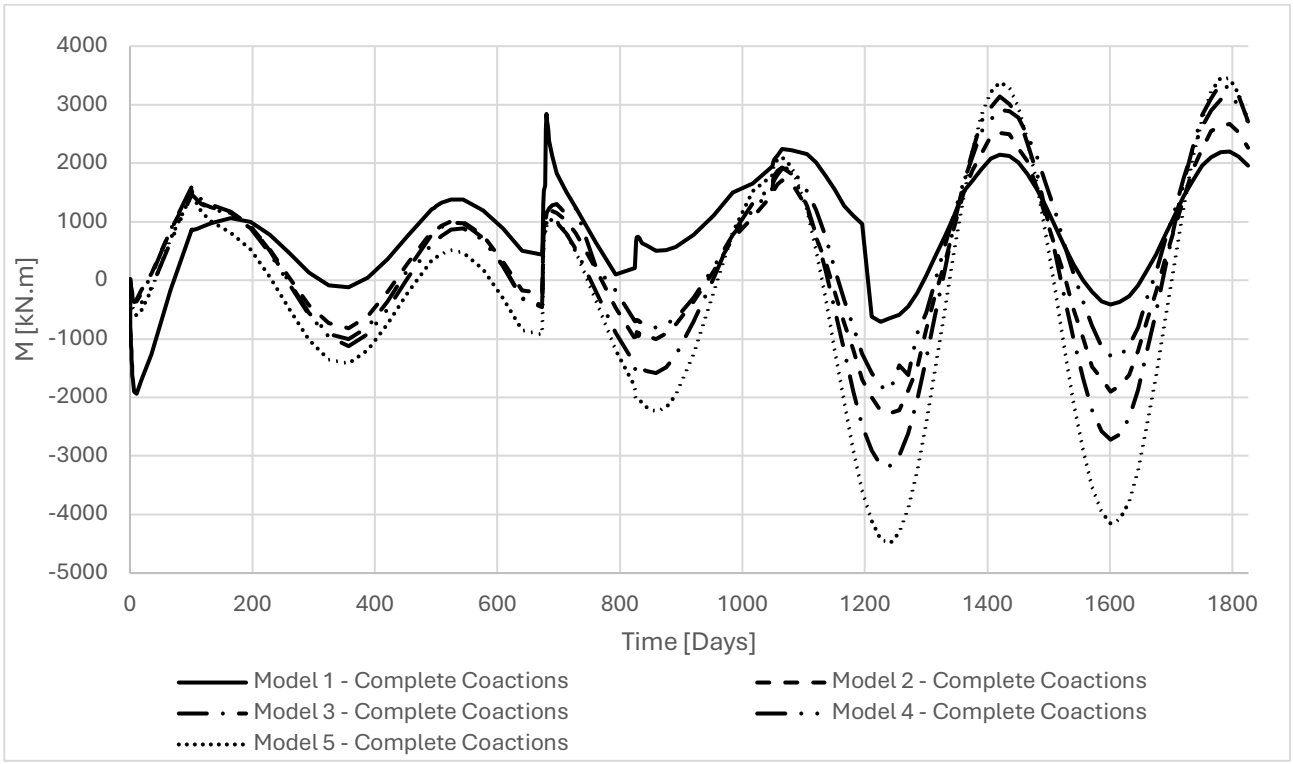


Figure 4-21 - Moment - Complete Coactions - Cover Slab Downhill Support

Axial force diagrams:

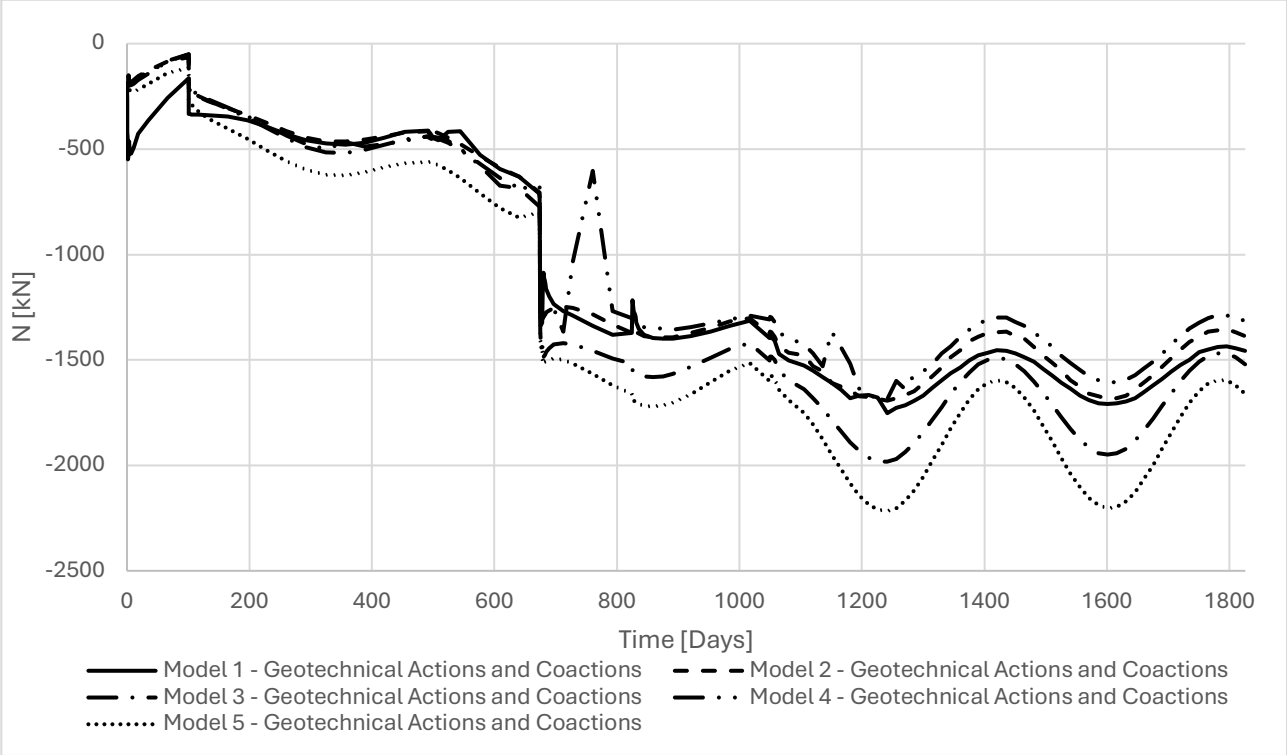


Figure 4-22 - Axial Force - Geotechnical Actions and Coactions - Cover Slab Downhill Support

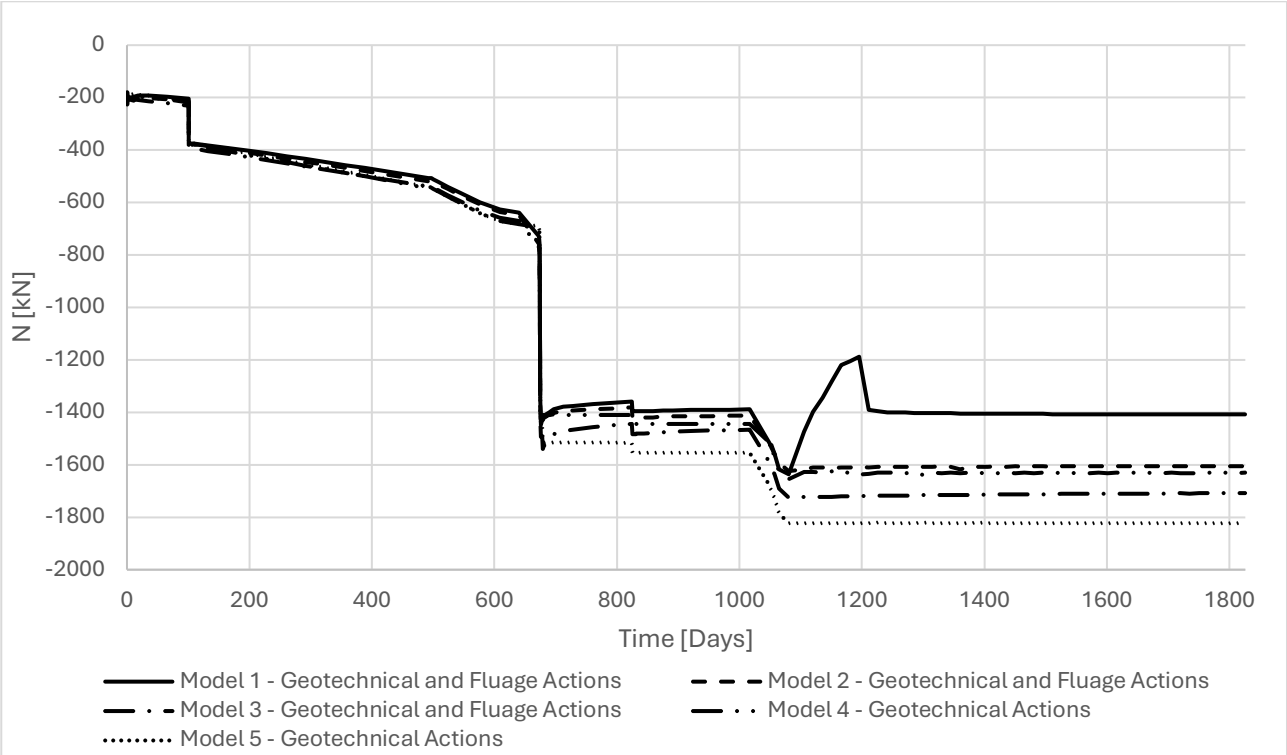


Figure 4-23 - Axial Force - Geotechnical and Fluage Actions - Cover Slab Downhill Support

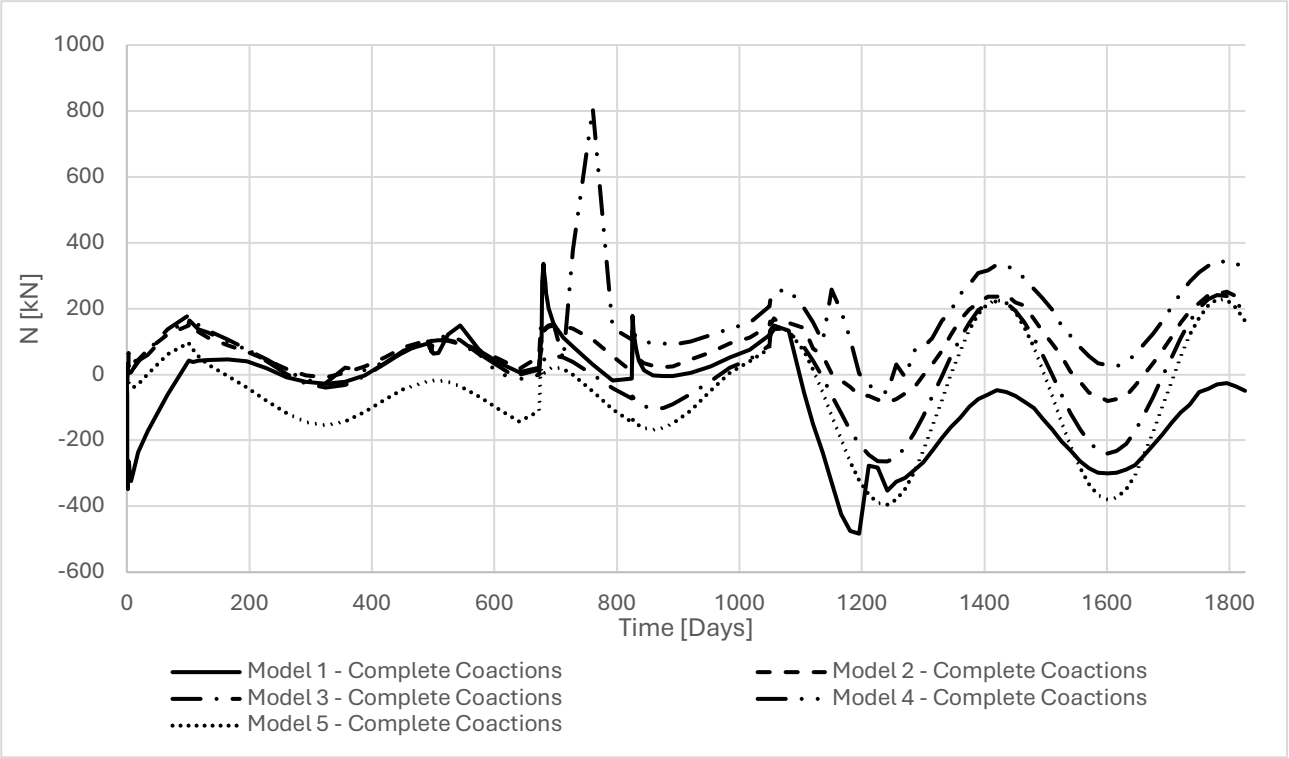


Figure 4-24 - Axial Force - Complete Coactions - Cover Slab Downhill Support

Shear Force diagrams:

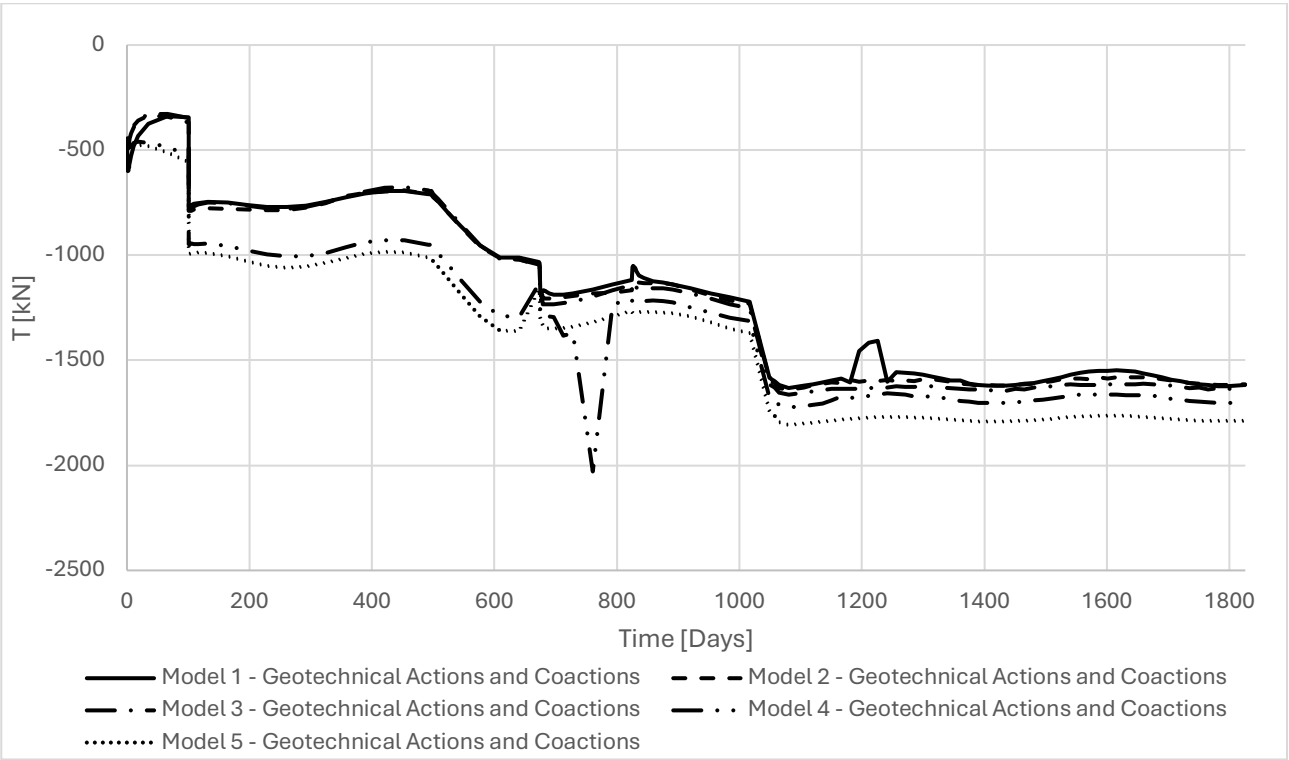


Figure 4-25 – Shear Force - Geotechnical Actions and Coactions- Cover Slab Downhill Support

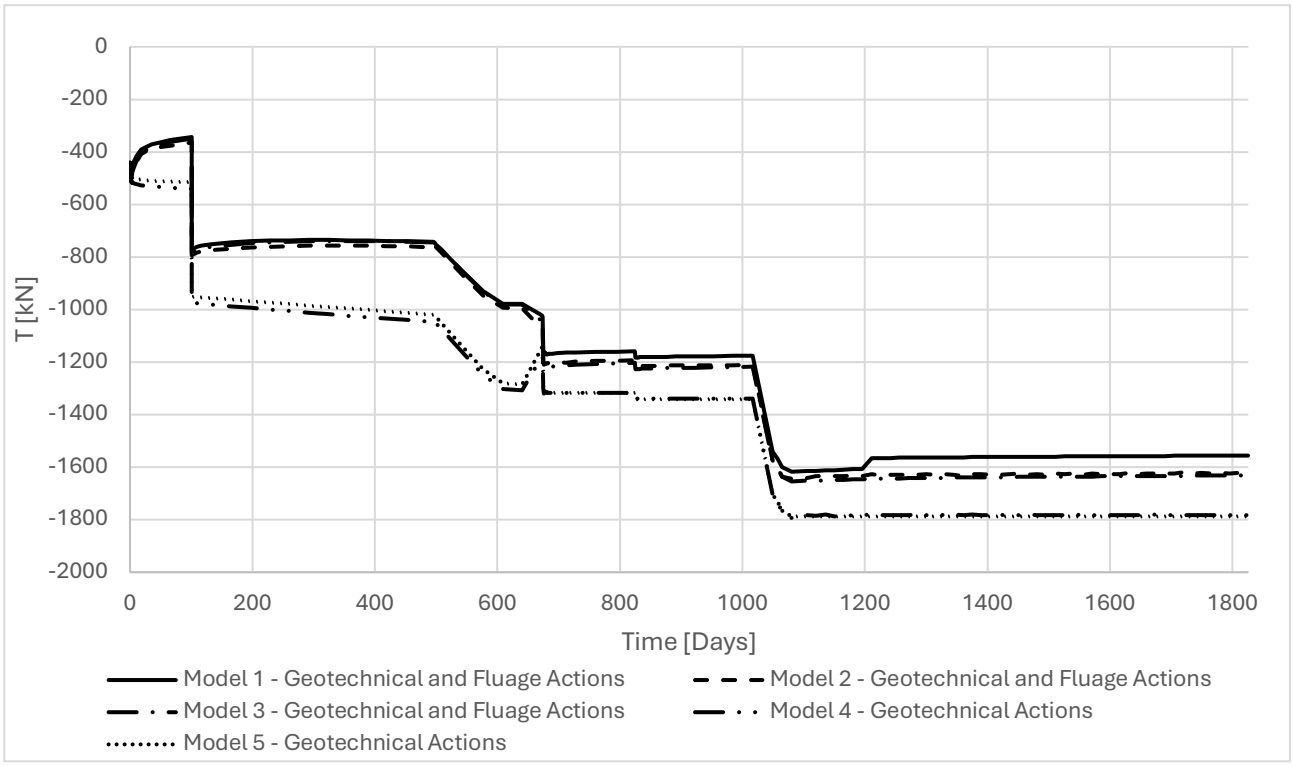


Figure 4-26 – Shear Force - Geotechnical and Creep Actions - Cover Slab Downhill Support

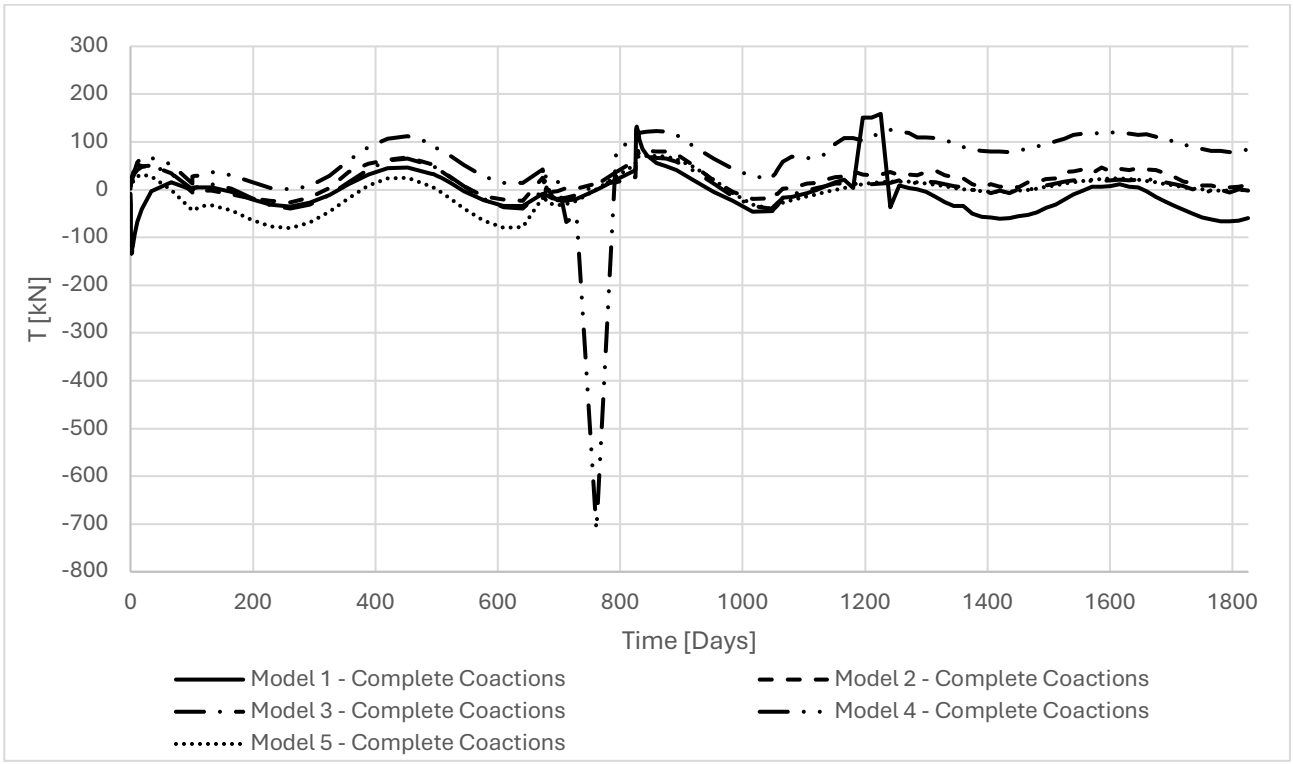


Figure 4-27 – Shear Force - Complete Coactions - Cover Slab Downhill Support

4.1.4 Discrepancies Between Models and Actions Combinations

Because the top cover slab is constructed at the beginning of the project staging (phases 1 to 3, $t = 0$ to 117 days), its finite elements are active from Day 0, causing internal forces to develop immediately under concrete maturation, boundary restraint, and sequential geotechnical operations. As the primary horizontal structural diaphragm spanning between the stiff uphill pile foundation group ($D = 2000$ mm and $D = 1200$ mm) and the downhill wall, the cover slab acts as a continuous frame member that transfers lateral landslide thrust, supports heavy earth backfill overburden, and undergoes significant seasonal thermal cycling.

During the early-age hydration and construction stages ($t = 0$ to 689 days), the degree-of-reaction thermo-mechanical coupling in model 1 captures pronounced transient coactions that standard models completely overlook. In the first 20 days, exothermic cooling and self-desiccation contractions against the perimeter kerbs induce deep negative bending drops across the entire member ($M \approx -2300\ kN * m$ at the uphill support in Figure 4-1 and Figure 4-3; $M \approx -1000$ kN · m at midspan in Figure 4-10 and Figure 4-12; $M \approx -2800\ kN * m$ at the downhill support in Figure 4-19 and Figure 4-21) together with early longitudinal compressive thrusts ($N \approx -550$ to $-600\ kN$; Figure 4-4, Figure 4-13 and Figure 4-22). Upon partial backfilling at $t = 117$ days (phase 4), the unrelaxed models (models 4 and 5) predict an exaggerated positive midspan sagging peak ($M \approx +4500\ kN * m$; Figure 4-10 and Figure 4-11) and premature positive support surges. Conversely, models 1 and 2 capture early tensile micro-cracking and viscoelastic relaxation, capping this initial flexural peak to $M \approx +2000$ kN · m and dissipating it over the 384-day waiting period. Subsequently, the execution of bulk excavation beneath the slab at $t = 689$ days (phase 6) removes bottom ground support, forcing the roof into a compressive strut mechanism that abruptly increases axial compression across all sections from $N \approx -800\ kN$ to $N \approx -1450\ kN$ (Figure 4-5, Figure 4-14 and Figure 4-23) while plunging flexural profiles into severe negative hogging (Figure 4-2, Figure 4-11 and Figure 4-20).

Following complete backfilling at $t = 1065$ days (phase 9) and the transition into sustained geotechnical equilibrium, viscoelastic creep becomes the governing mechanism for internal load redistribution. In the linear baseline (model 5) and the non-linear model without creep (model 4), the application of the full earth cover locks in severe, unrelaxed elastic force concentrations, particularly at the downhill support where sustained hogging reaches $M = -10300\ kN * m$ (Figure 4-20), sustained compression peaks at $N = -1830\ kN$ (Figure 4-23),

and sustained shear demand attains $T = -1790\ kN$ (Figure 4-26). In models 1 and 2, continuous viscous flow mitigates these stress concentrations, relaxing sustained downhill hogging to $M \approx -8600\ kN * m$, shedding axial load into the surrounding soil mass ($N \approx -1420\ kN$), and substantially attenuating sustained shear demands across both the midspan ($T \approx -290\ kN$ compared to $-480\ kN$ in model 5; Figure 4-17) and downhill joints ($T \approx -1560\ kN$; Figure 4-26). Furthermore, models 1 and 2 accurately track the historical accumulation of creep-induced rotation at the uphill support, establishing a realistic sustained hogging moment ($M \approx -2100$ to $-2450\ kN * m$; Figure 4-2) that is severely underestimated by linear models ($M = -1100\ kN * m$ in model 5) due to their lack of integration of time-dependent deformation histories.

In the long-term cyclic service regime ($t > 1122$ days), the linear elastic formulation in model 5 treats seasonal temperature fluctuations as rigid external restraints, resulting in extreme cyclic flexural amplitudes ($\Delta M \approx 7900\ kN * m$ at uphill support and midspan in Figure 4-1 and Figure 4-10; $\Delta M \approx 8300\ kN * m$ at downhill support in Figure 4-19) with winter negative moments plunging to an unrealistic $M \approx -14800\ kN * m$. Model 5 similarly overpredicts cyclic axial coactions ($\Delta N \approx 650$ to $900\ kN$; Figure 4-6, Figure 4-15 and Figure 4-24). In models 1 and 2, localized tensile cracking at re-entrant corners combined with continuous viscoelastic relaxation relieves thermal restraint stresses, reducing total cyclic moment ranges by 50% to 67% ($\Delta M \approx 2700$ to $3900\ kN * m$; bounded to $M \approx -9200\ kN * m$ downhill in Figure 4-19 and $+1800/-1600\ kN * m$ at midspan in Figure 4-10) and damping cyclic axial coactions by over 60% ($\Delta N \approx 230$ to $350\ kN$; Figure 4-6, Figure 4-15 and Figure 4-24). This comparative synthesis demonstrates that conventional linear elastic methods introduce severe, artificial conservatism into the cover slab design by neglecting concrete's intrinsic early-age relief and long-term viscous relaxation under soil-structure interaction.

4.2 Uphill Pile (D = 1200 mm)

The analysis focuses on two critical elevations: head pile elevation, the top connection to the upper foundation strut and cover slab level, the interface connection with the portal frame roof.

4.2.1 Head Section

Moment diagrams:

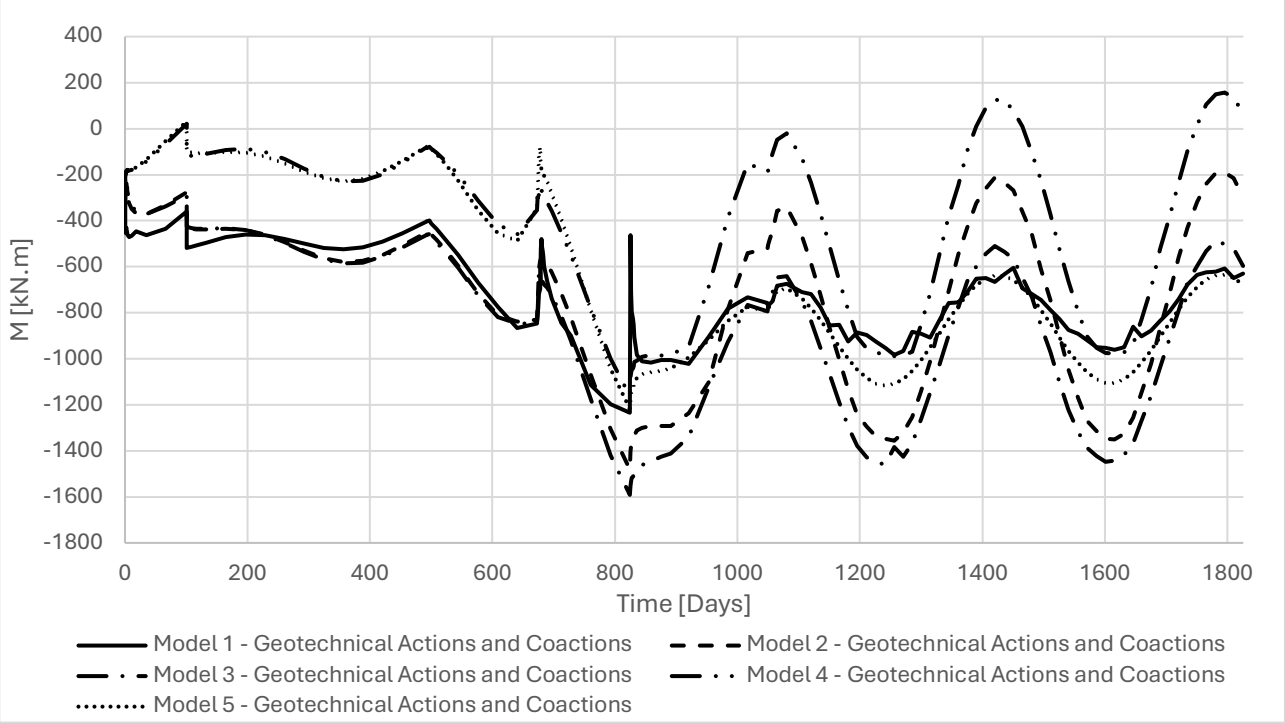


Figure 4-28 - Moment - Geotechnical Actions and Coactions - Head Pile 1200

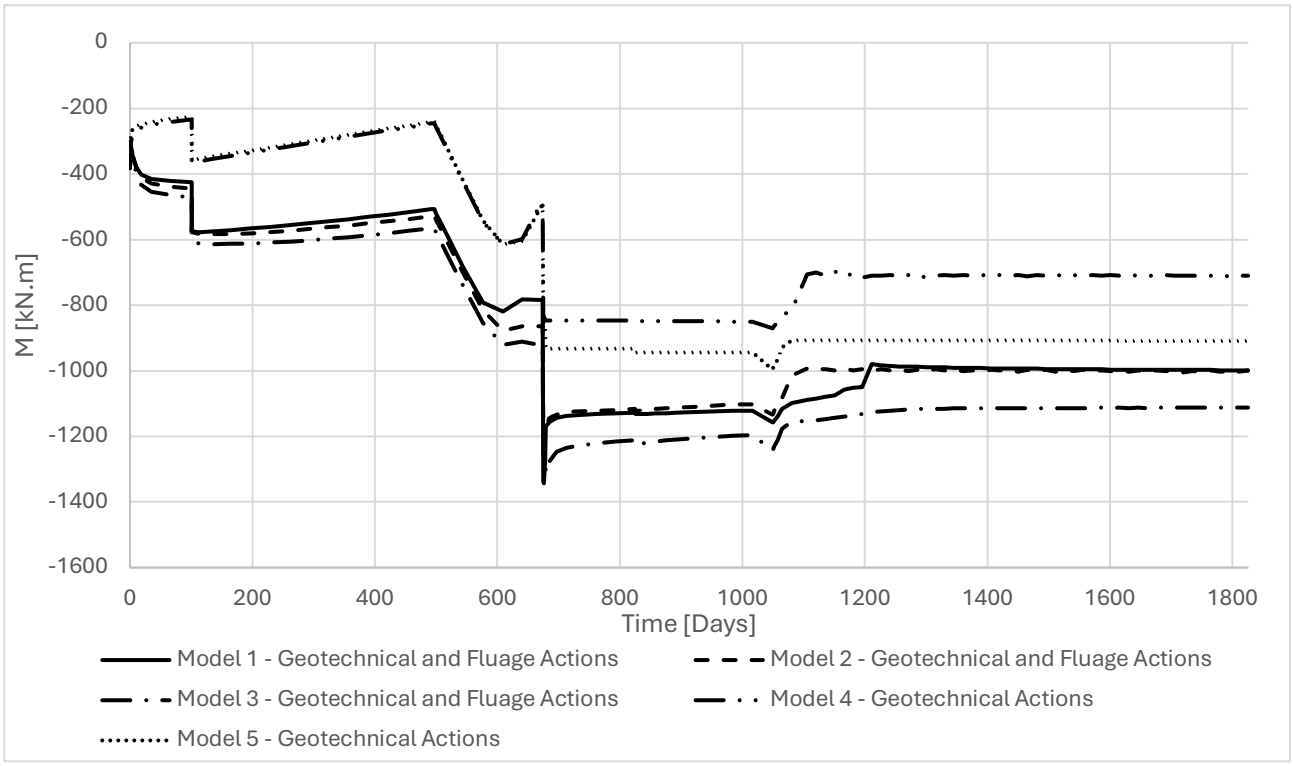


Figure 4-29 - Moment - Geotechnical and Creep Actions - Head Pile 1200

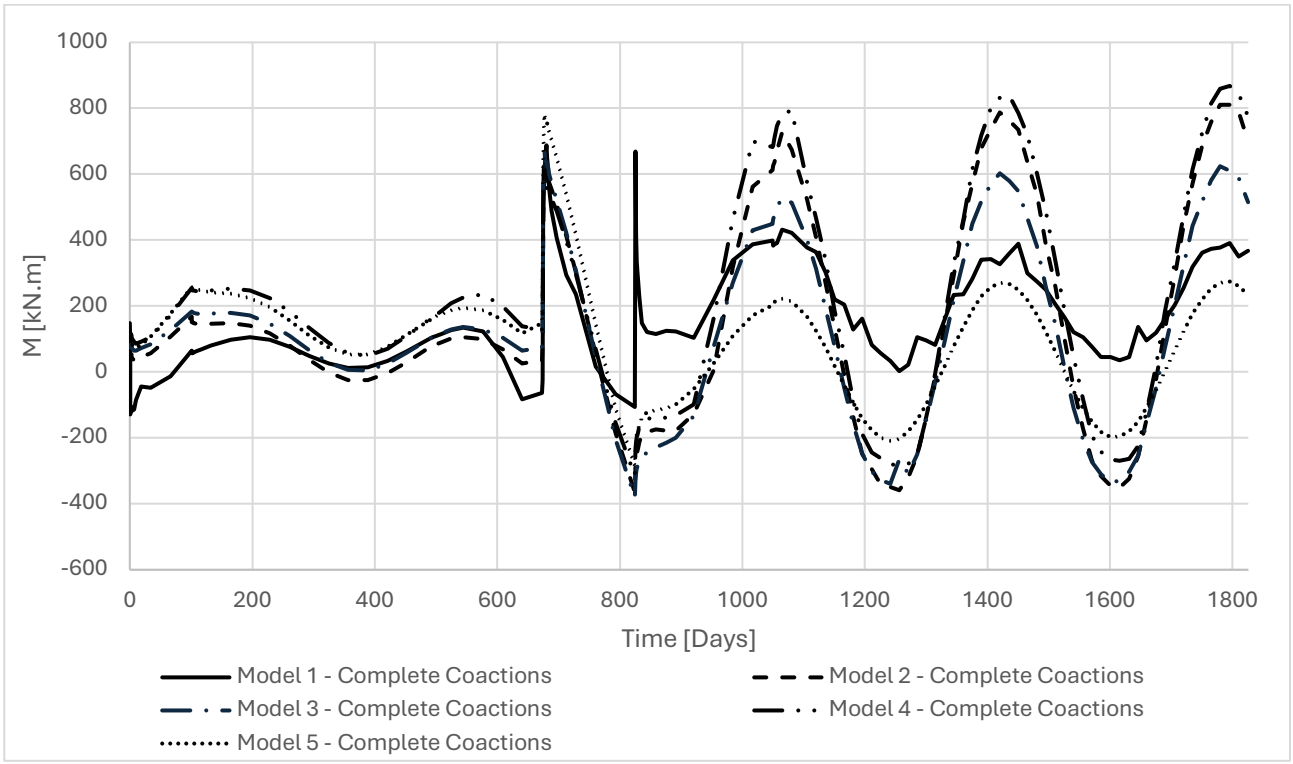


Figure 4-30 - Moment - Complete Coactions – Head Pile 1200

Axial force diagrams:

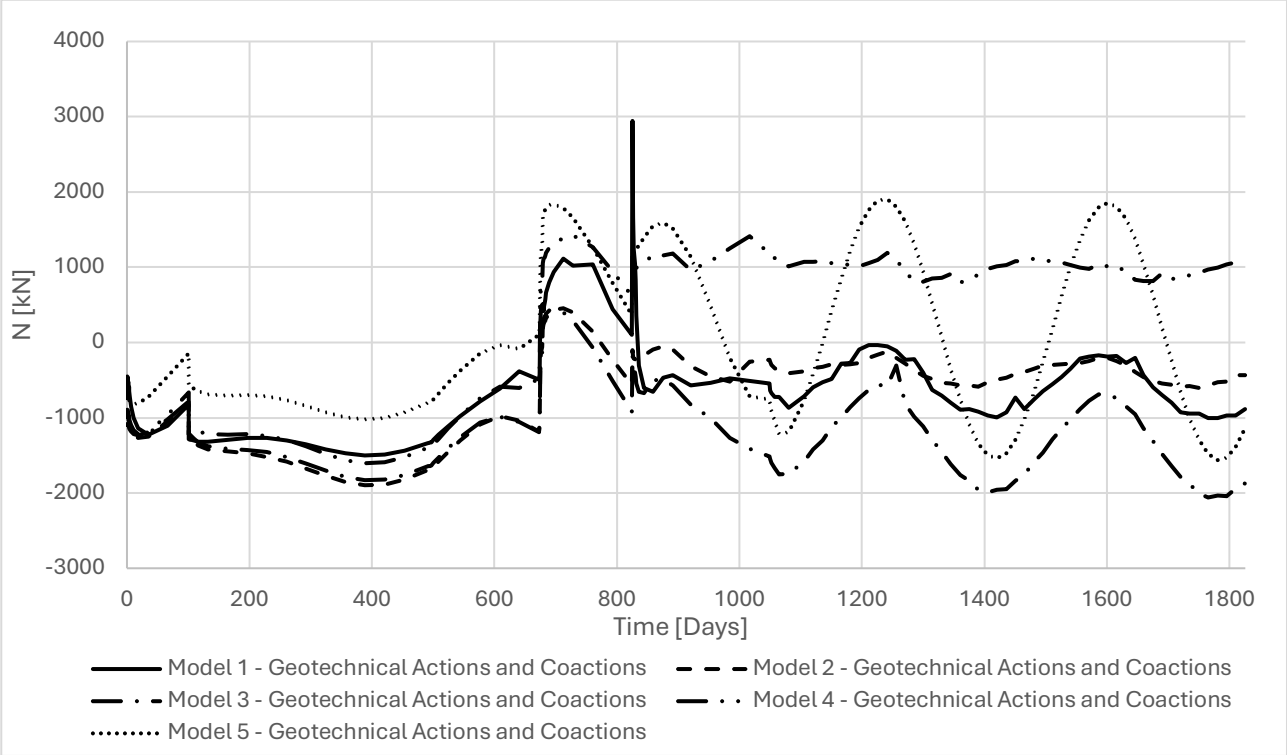


Figure 4-31 - Axial Force - Geotechnical Actions and Coactions - Head Pile 1200

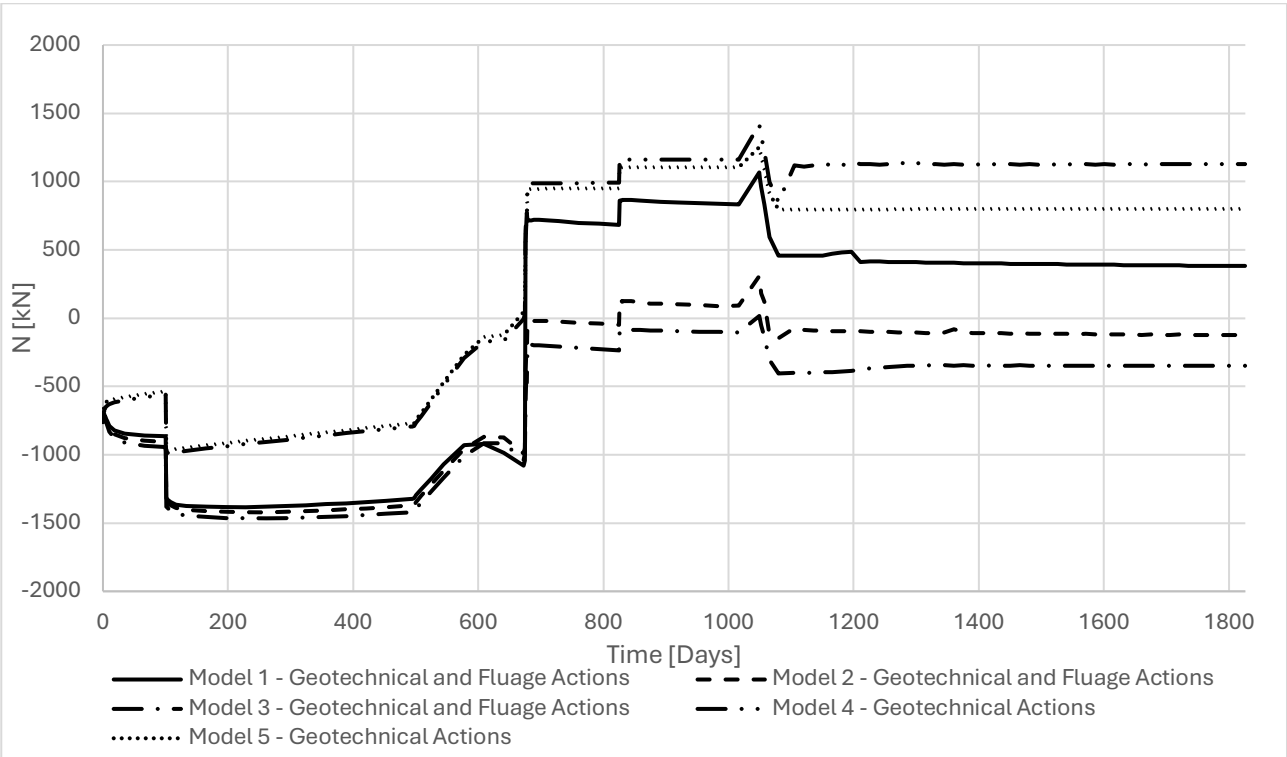


Figure 4-32 - Axial Force - Geotechnical and Creep Actions - Head Pile 1200

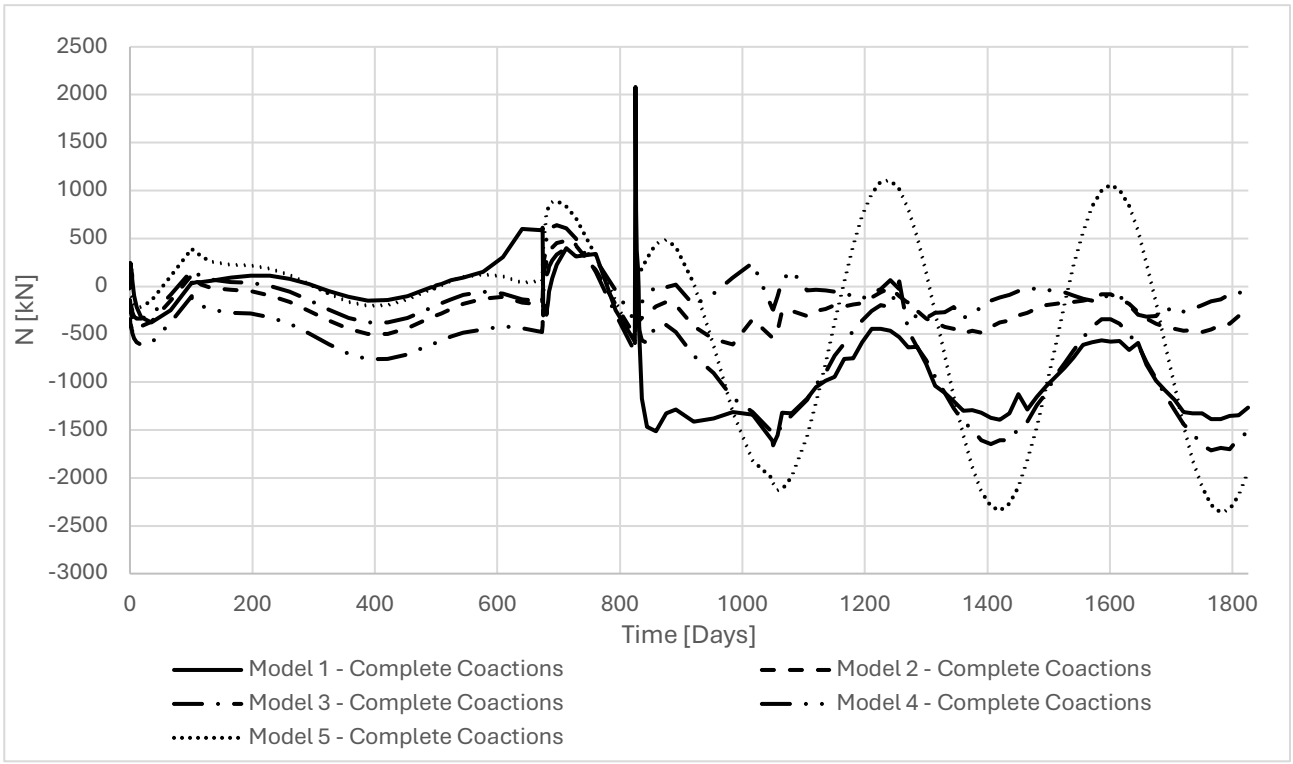


Figure 4-33 - Axial Force - Complete Coactions - Head Pile 1200

Shear force diagrams:

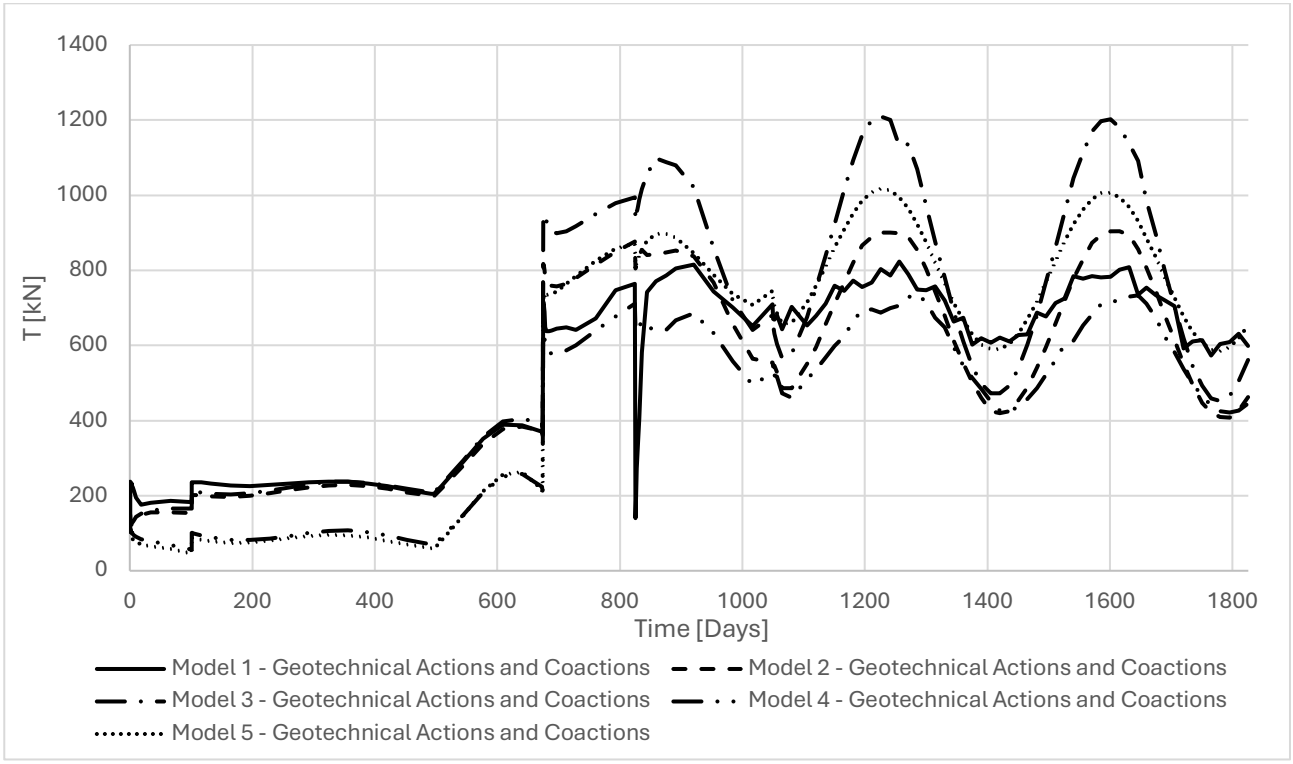


Figure 4-34 – Shear Force- Geotechnical Actions and Coactions - Head Pile 1200

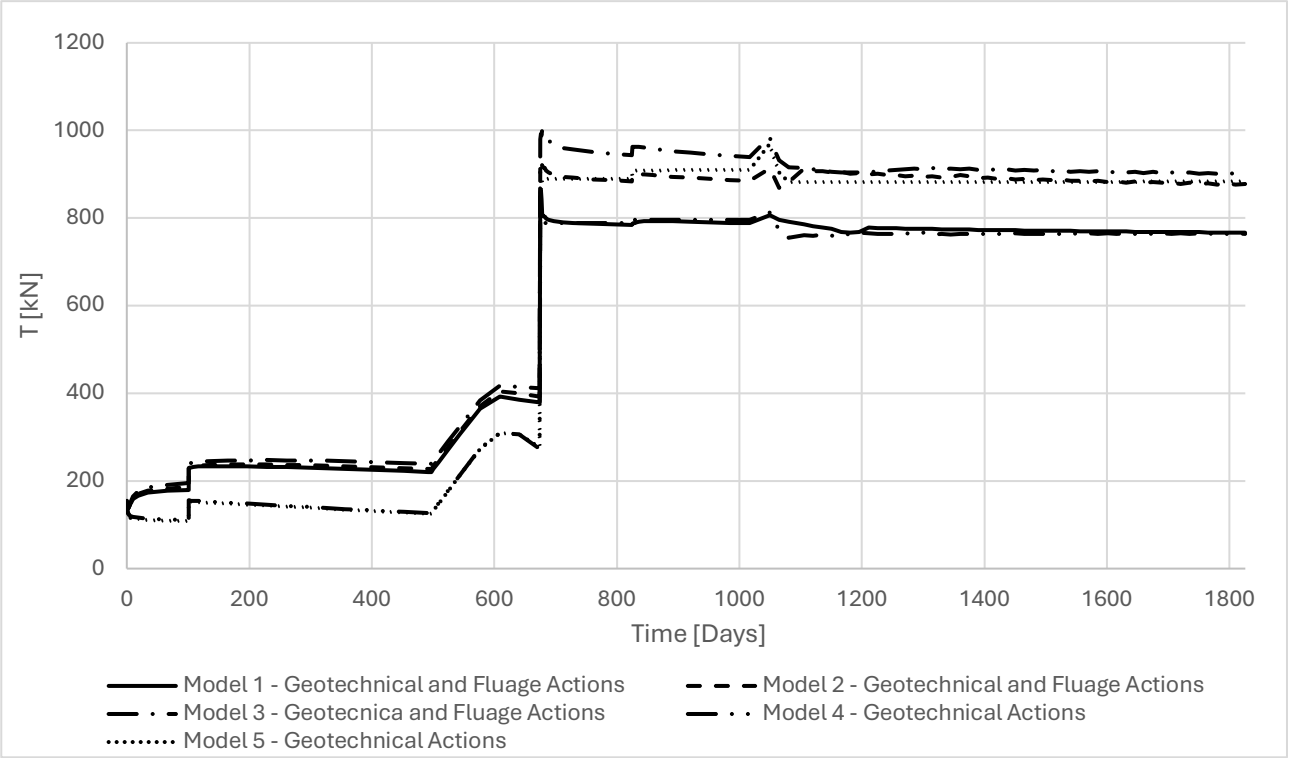


Figure 4-35 – Shear Force- Geotechnical and Creep Actions – Head Pile 1200

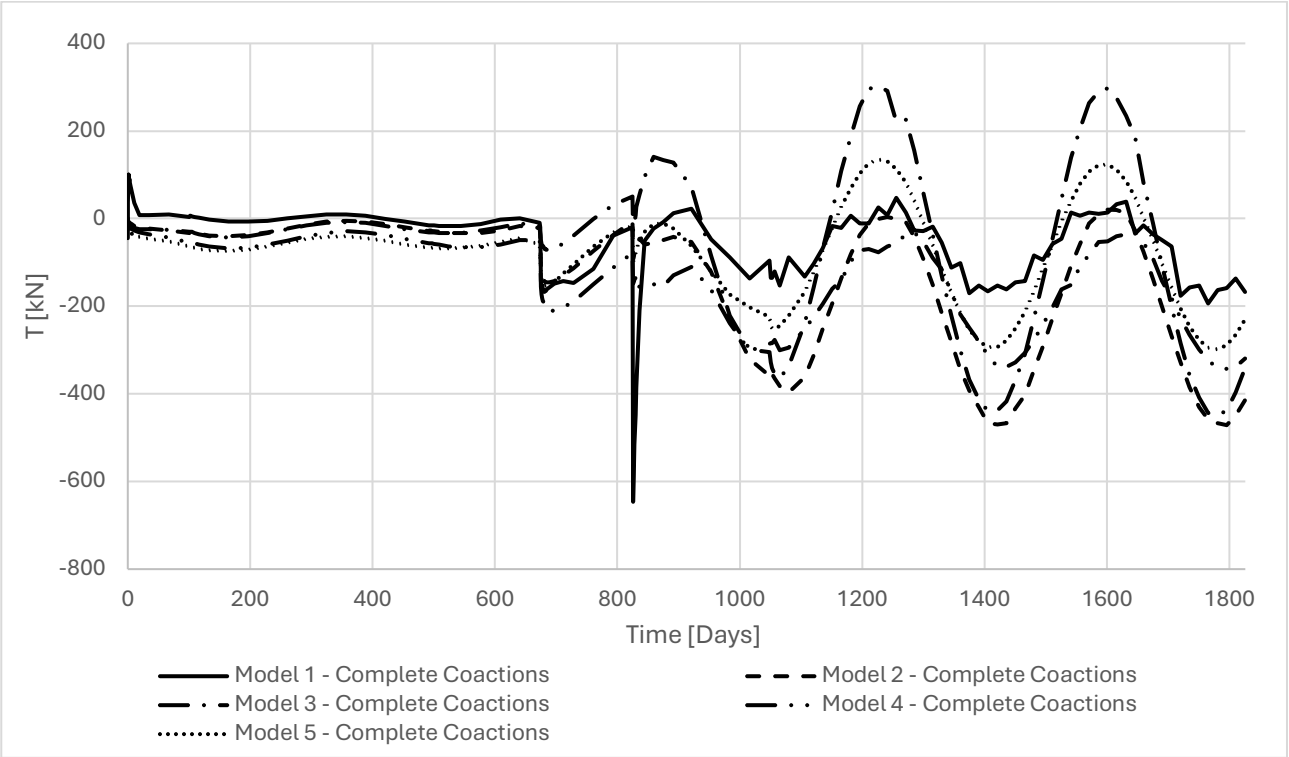


Figure 4-36 – Shear Force- Complete Coactions – Head Pile 1200

4.2.2 Cover Slab Level Section

Moment diagrams:

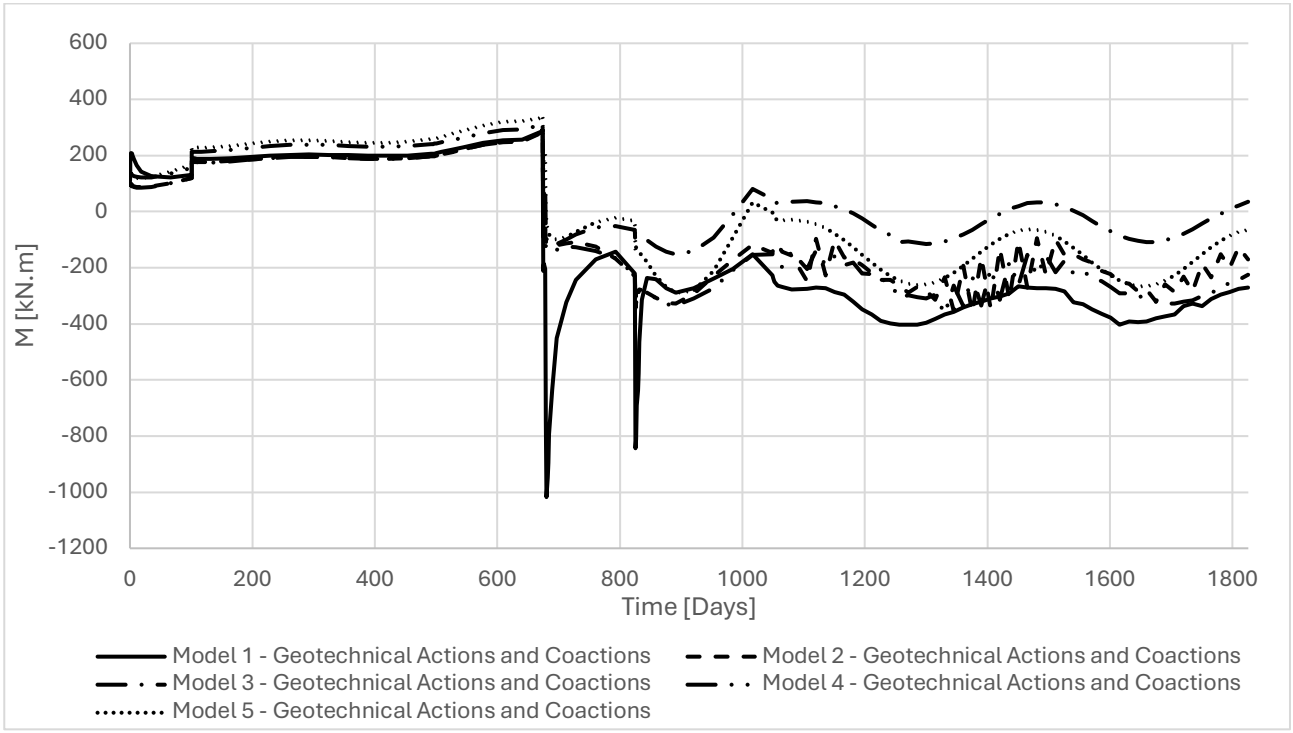


Figure 4-37 - Moment - Geotechnical Actions and Coactions - Pile 1200 Cover Slab Level

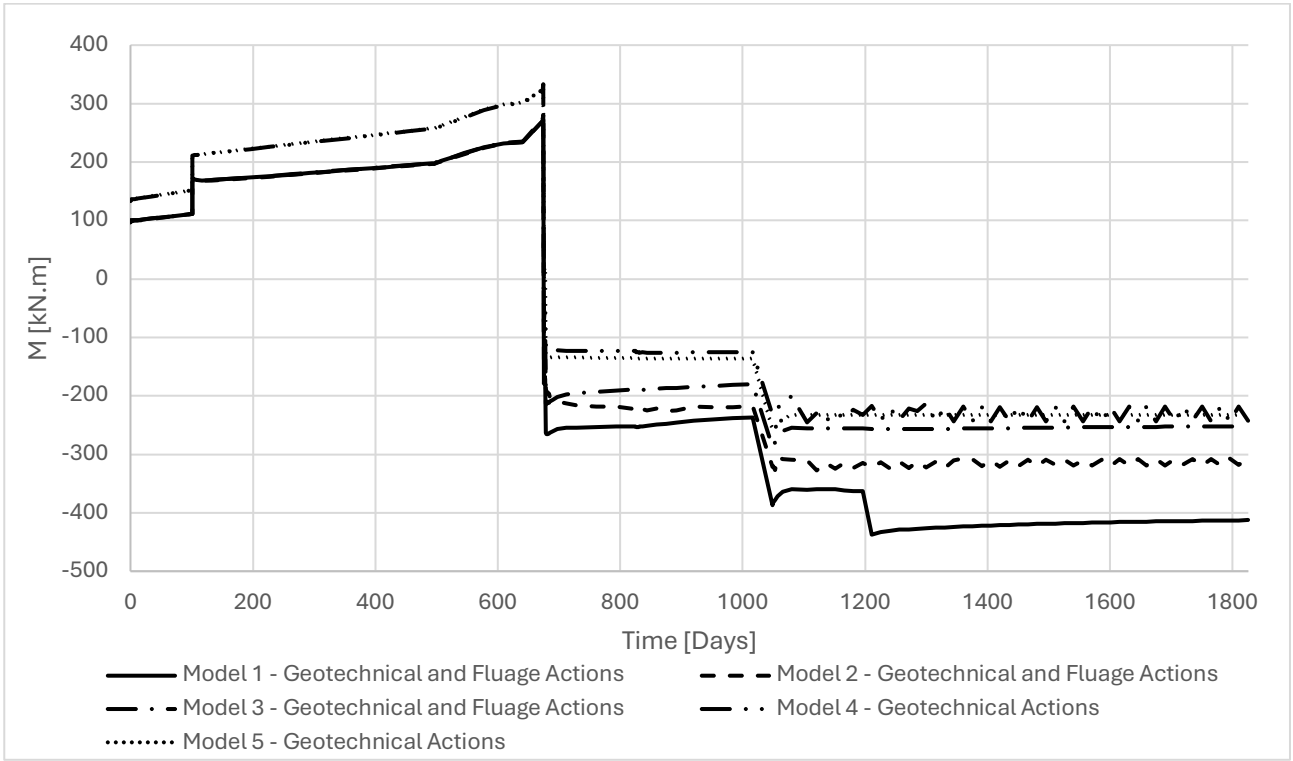


Figure 4-38 - Moment - Geotechnical and Creep Actions - Pile 1200 Cover Slab Level

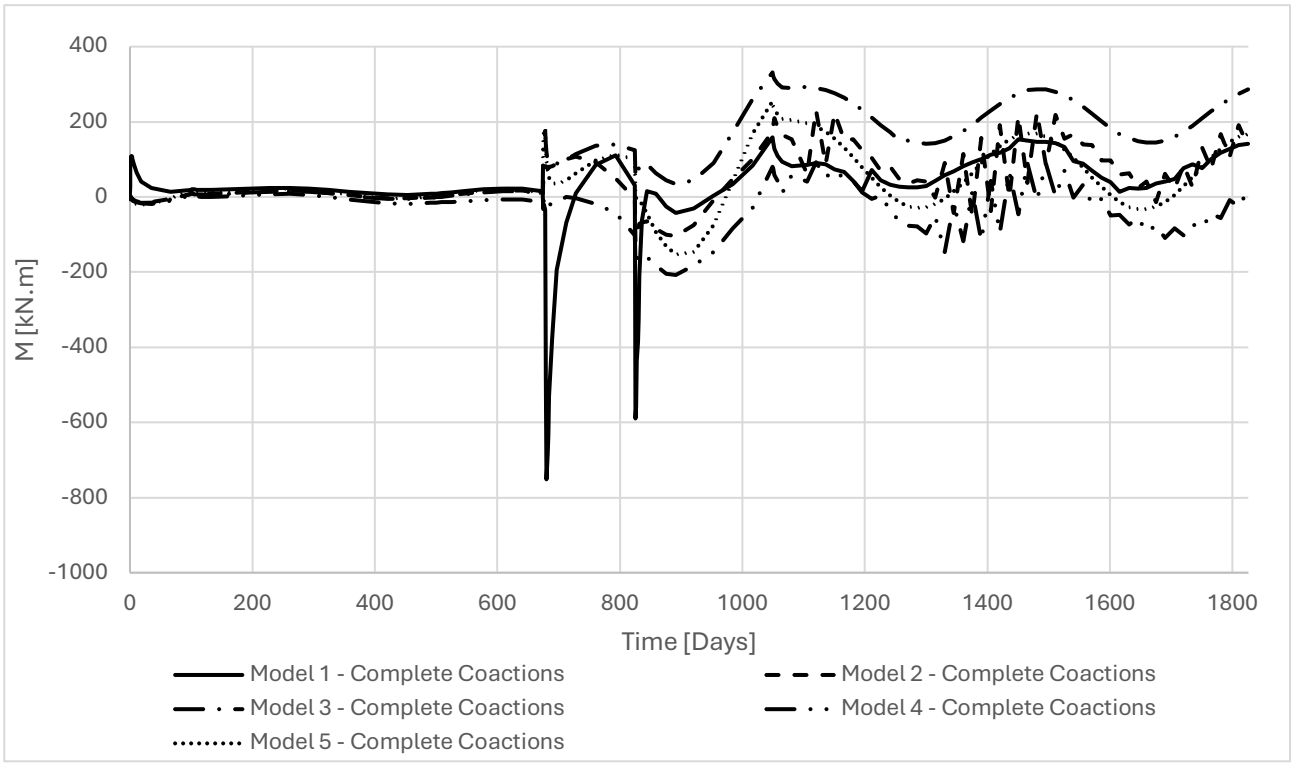


Figure 4-39 - Moment - Complete Actions - Pile 1200 Cover Slab Level

Axial force diagrams:

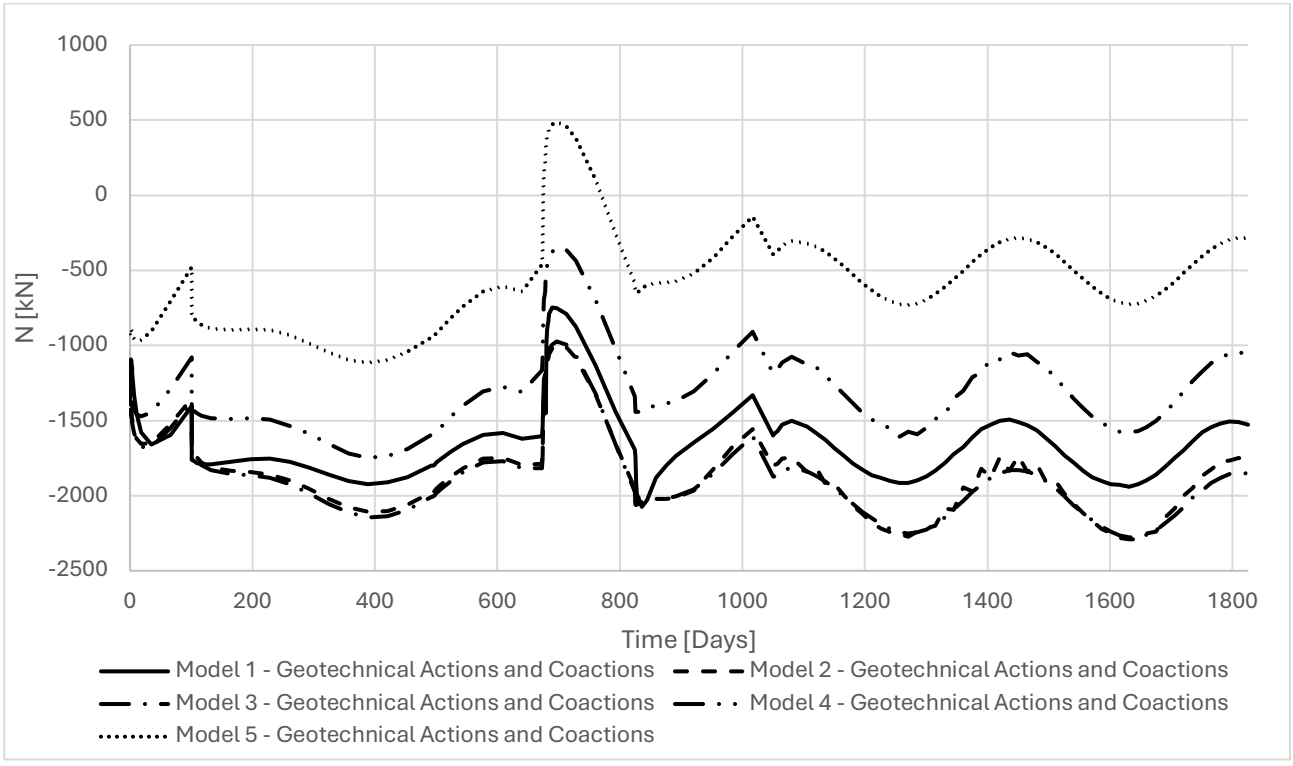


Figure 4-40 - Axial Force - Geotechnical Actions and Coactions - Pile 1200 Cover Slab Level

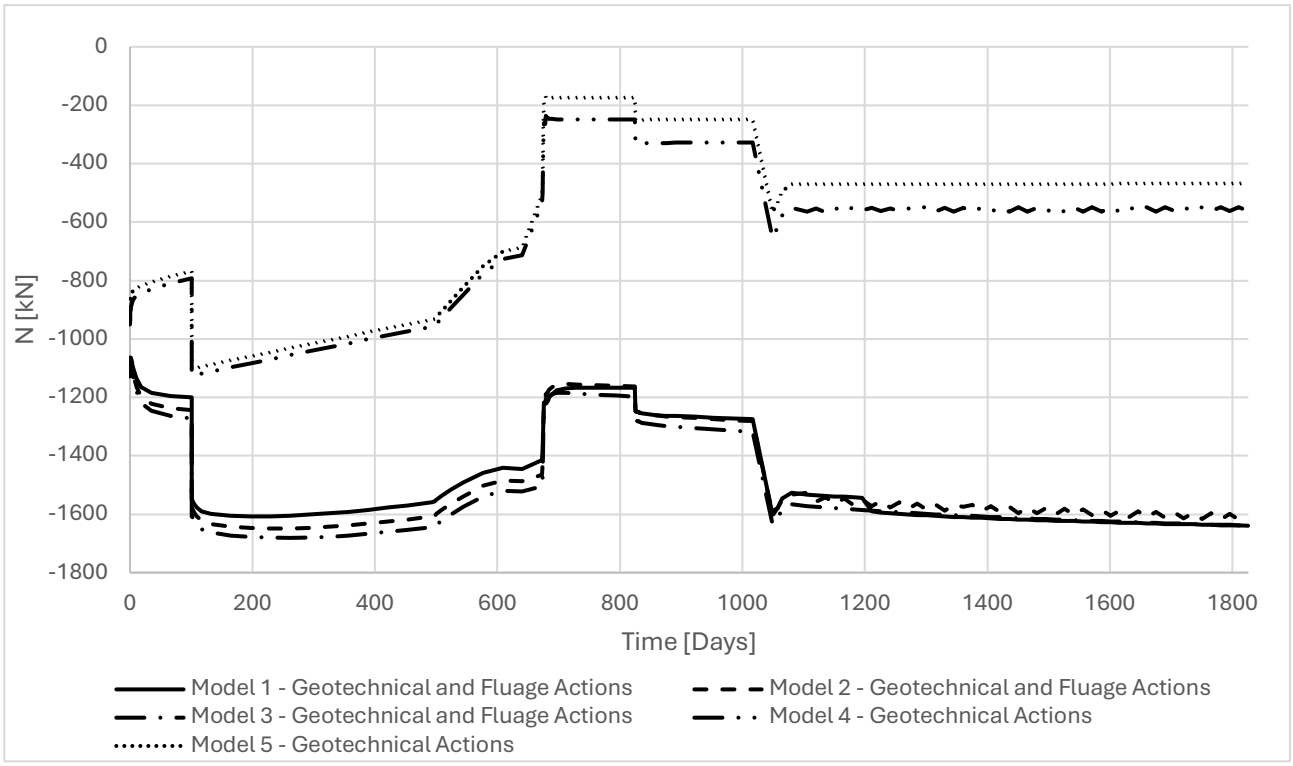


Figure 4-41 - Axial Force - Geotechnical and Creep Actions - Pile 1200 Cover Slab Level

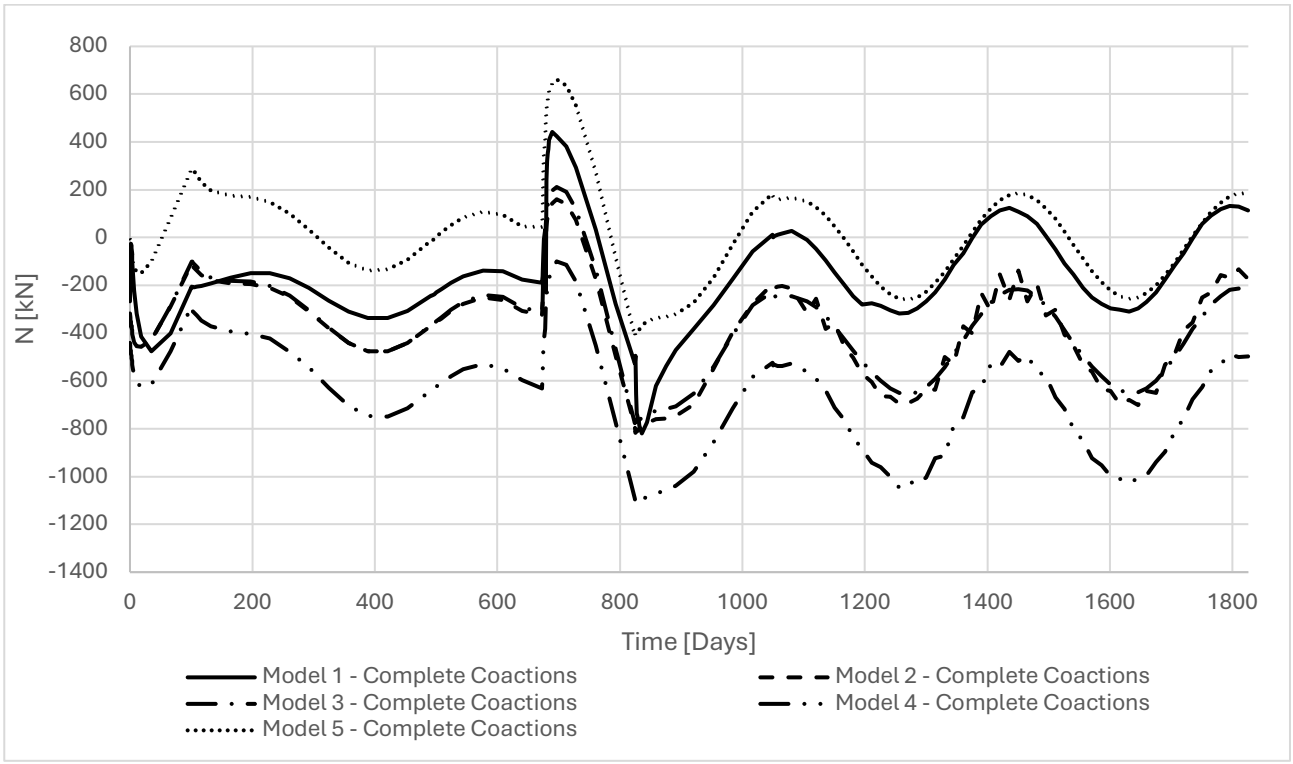


Figure 4-42 - Axial Force - Complete Coactions - Pile 1200 Cover Slab Level

Shear force diagrams:

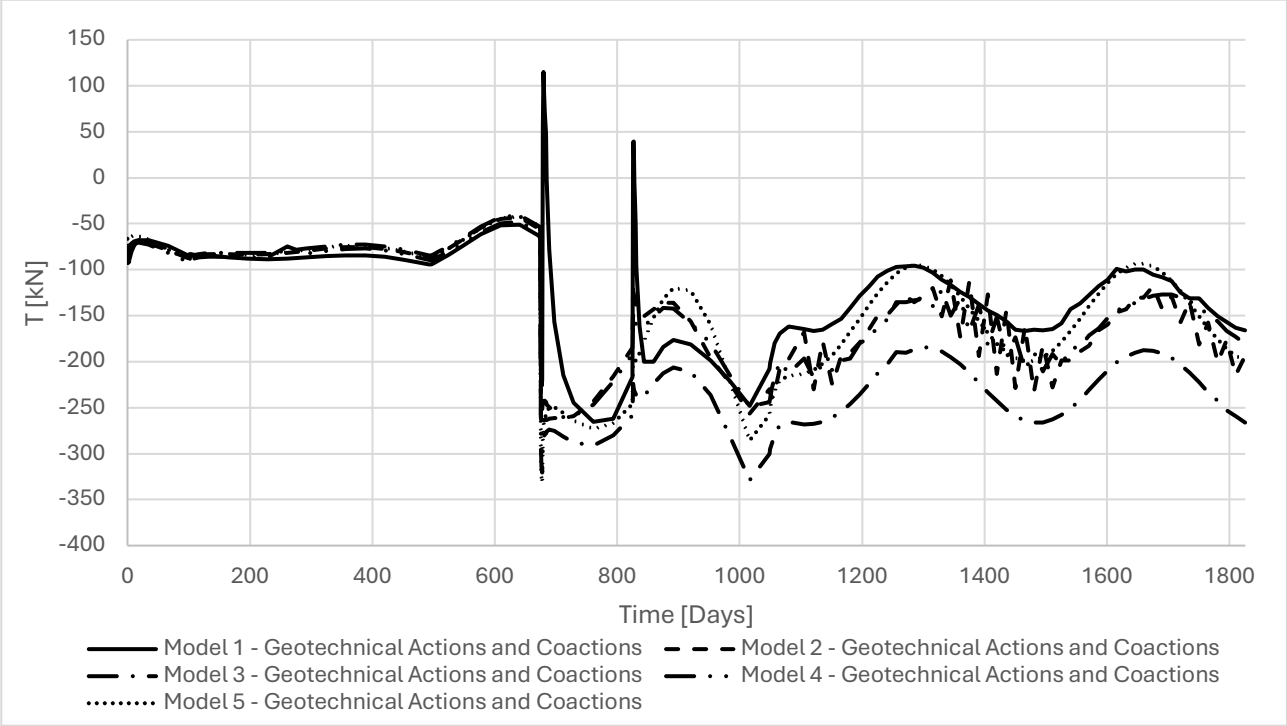


Figure 4-43 – Shear Force - Geotechnical Actions and Coactions - Pile 1200 Cover Slab Level

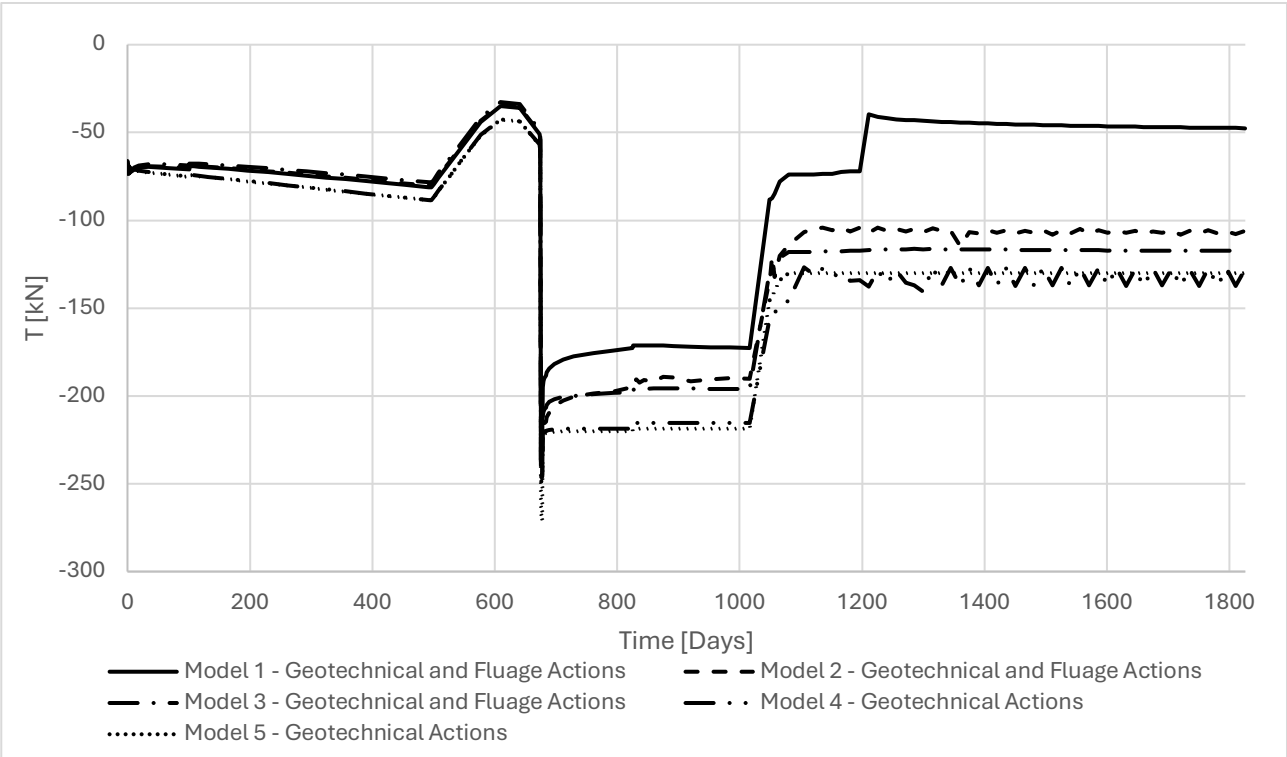


Figure 4-44 – Shear Force - Geotechnical and Creep Actions - Pile 1200 Cover Slab Level

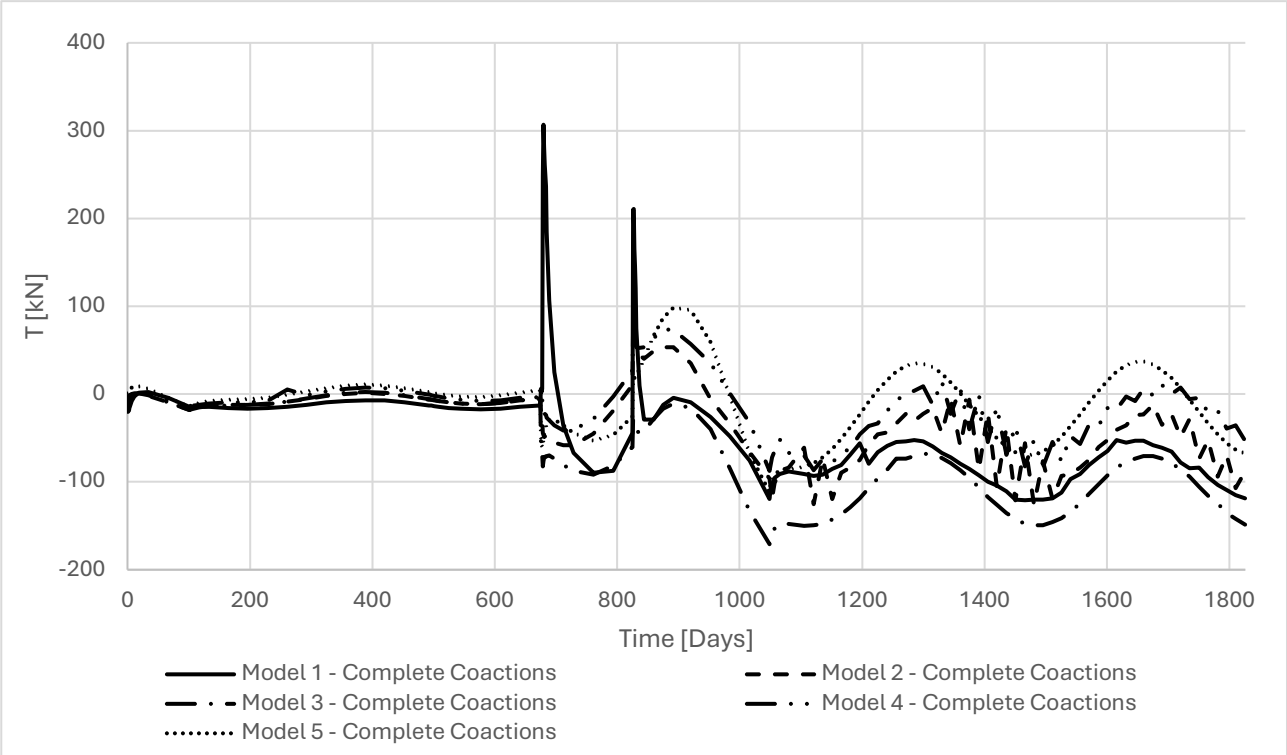


Figure 4-45 – Shear Force - Complete Coactions- Pile 1200 Cover Slab Level

4.2.3 Discrepancies between Models and Actions Combinations

Because the uphill foundation piles, including the pile $D = 1200$ mm constitute the primary vertical retaining elements of the cut-and-cover structure, their finite elements are active from day 0 ($t = 0$ days), immediately developing internal forces as the surrounding soil interacts with the curing concrete and staged site operations. During the initial construction phases ($t = 0$ to 689 days), the pile functions primarily as a cantilever retaining wall resisting outer earth pressures while supporting vertical kerb and cover slab dead loads. This cantilever action generates moderate positive bending at the cover slab level ($M \approx +100$ to $+320\ kN*m$, Figure 4-37 and Figure 4-38) alongside significant axial compression ($N \approx -1000$ to $-1800\ kN$; Figure 4-31, Figure 4-32, Figure 4-40 and Figure 4-41). The subsequent execution of internal bulk excavation at $t = 689$ days (phase 6) removes lateral earth support along the front face of the shaft, triggering a rapid transition into a framed structural mechanism where shear forces at the pile head jump to $T \approx 800$ to $950\ kN$ (Figure 4-34 and Figure 4-35) as lateral landslide thrust is transferred directly into the horizontal cover slab diaphragm.

During the execution of internal excavation and subsequent concrete casting phases ($t =$ 689 to 841 days), the degree-of-reaction thermo-mechanical coupling in model 1 captures

pronounced transient coactions that are absent in standard models. At $t = 689$ days, the combined effect of excavation unloading and early-age thermal cooling induces an acute negative flexural drop at the cover slab level ($M \approx -1050\ kN * m$ in Figure 4-37), with coactions contributing $-750\ kN * m$ in Figure 4-39) accompanied by a transient shear reversal spiking into positive shear ($T \approx +115\ kN$ in Figure 4-43 and $+310\ kN$ in Figure 4-45). Furthermore, the exothermic hydration of the newly cast side walls at $t = 841$ days (phase 8) generates an upward thermal dilation that pulls on the rigid pile connection, triggering an intense transient tensile surge at the pile head reaching $N \approx +2900\ kN$ ($N \approx +2100\ kN$ in coactions) and an acute flexural jump of $\Delta M \approx +750\ kN * m$ (Figure 4-28 and Figure 4-30). Concurrently, this wall pour induces a secondary compressive thrust at the cover slab level ($N \approx -2100\ kN$; Figure 4-40) and an additional flexural drop to $M \approx -850\ kN * m$ (Figure 4-37). Standard models (models 2 through 5), by omitting hydration thermal kinetics on subsequent pours, display smooth transitions during these stages, thereby not capturing these early-age transient damage peaks.

Following complete backfilling at $t = 1065$ days (phase 9) and the establishment of sustained geotechnical equilibrium, viscoelastic creep becomes the governing mechanism controlling permanent internal force distributions. In models that doesn't consider creep, the absence of time-dependent viscous tracking leads to significant distortions: model 5 and model 4 lock in severe, unrelaxed axial tension at the pile head ($N = +800\ kN$ and $+1150\ kN$, respectively; Figure 4-32) while substantially underestimating sustained axial compression at the cover slab level ($N = -500\ kN$ in model 5 compared to $-1650\ kN$ in Model 1, representing a nearly 70% underestimation of beneficial confinement; Figure 4-41). In models 1 and 2, continuous viscoelastic relaxation across the soil-structure interface enables the pile head to shed tensile stresses ($N \approx +380\ kN$ in model 1, representing a 65% tension relief relative to model 4; Figure 4-32) while recovering stable compressive states in model 2 ($N \approx -150\ kN$). Similarly, viscous flow dissipates sustained shear force concentrations at the cover slab joint, reducing sustained shear demand in model 1 to $T \approx -45\ kN$ a 67% reduction relative to the linear baseline of $T = -135\ kN$ in model 5 ($T \approx -110\ kN$ in model 2, an 18,5% reduction; Figure 4-44). These stresses are low whatsoever and don't represent a big decrease in internal stresses in the models. Furthermore, models 1 and 2 accurately integrate the historical accumulation of creep-induced frame rotation, capturing a sustained negative hogging moment at the cover slab level ($M \approx -450\ kN * m$ in model 1; Figure 4-38) that is cut to half in linear elastic checks ($M = -240\ kN * m$ in model 5).

In the long-term cyclic service regime ($t > 1122$ days), the models not accounting for creep: the linear elastic baseline (model 5) and the unrelaxed cracked model (model 4) treat seasonal thermal expansions as rigid external actions, generating excessively wide cyclic response envelopes. At the pile head, model 5 undergoes extreme cyclic axial swings between summer tension ($N \approx +1800\ kN$) and winter compression ($N \approx -1600\ kN$) across a total range of $\Delta N \approx 3400\ kN$ (Figure 4-31), while model 4 undergoes cyclic flexural swings of $\Delta M \approx 1600\ kN * m$ (Figure 4-28) and shear oscillations of $\Delta T \approx 750\ kN$ (Figure 4-34). In model 1, continuous viscoelastic relaxation and localized joint cracking attenuate cyclic extremes: cyclic axial excursions at the head are restricted to $\Delta N \approx 900\ kN$ (a 73.5% reduction relative to model 5), cyclic flexural amplitudes are damped to $\Delta M \approx 350\ kN * m$ (a 78% reduction in comparison to model 4 and 30,0% to model 5), and cyclic shear fluctuations are bounded to $\Delta T \approx 200\ kN$, also a 73% reduction relative to model 4 and 55% relative to model 5. At the cover slab level, model 1 similarly reduces the cyclic moment range by 50,0%: $\Delta M \approx 150\ kN * m$ versus $300\ kN * m$ in model 5 (Figure 4-37); and cyclic shear amplitude by 40.0%: $\Delta T \approx 60\ kN$ versus. $100\ kN$ in model 5 (Figure 4-43), while maintaining uninterrupted compressive confinement ($N \approx -1450$ to $-1950\ kN$, Figure 4-40) compared to model 5, which fluctuates near net tension. This comprehensive synthesis shows that in this precise application and under the modal assumptions detailed in the chapters above that deterministic linear elastic models tend to overestimate cyclic force amplitudes and mischaracterize sustained axial states by omitting concrete creep and localized cracking relief.

4.3 Uphill Pile (D = 2000 mm)

The analysis focuses on two critical elevations: head pile elevation, the top connection to the upper foundation strut and cover slab level, the interface connection with the portal frame roof.

4.3.1 Head Section

Moment diagrams:

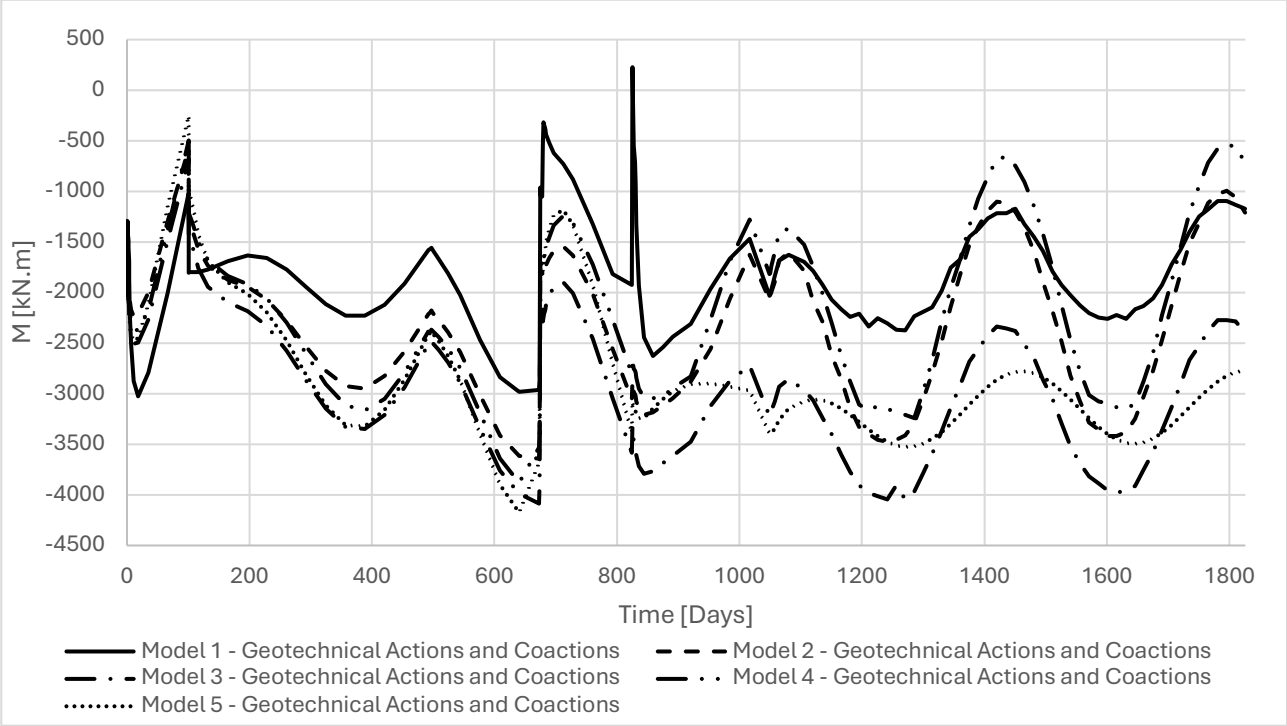


Figure 4-46 - Moment - Geotechnical Actions and Coactions - Head Pile 2000 Uphill

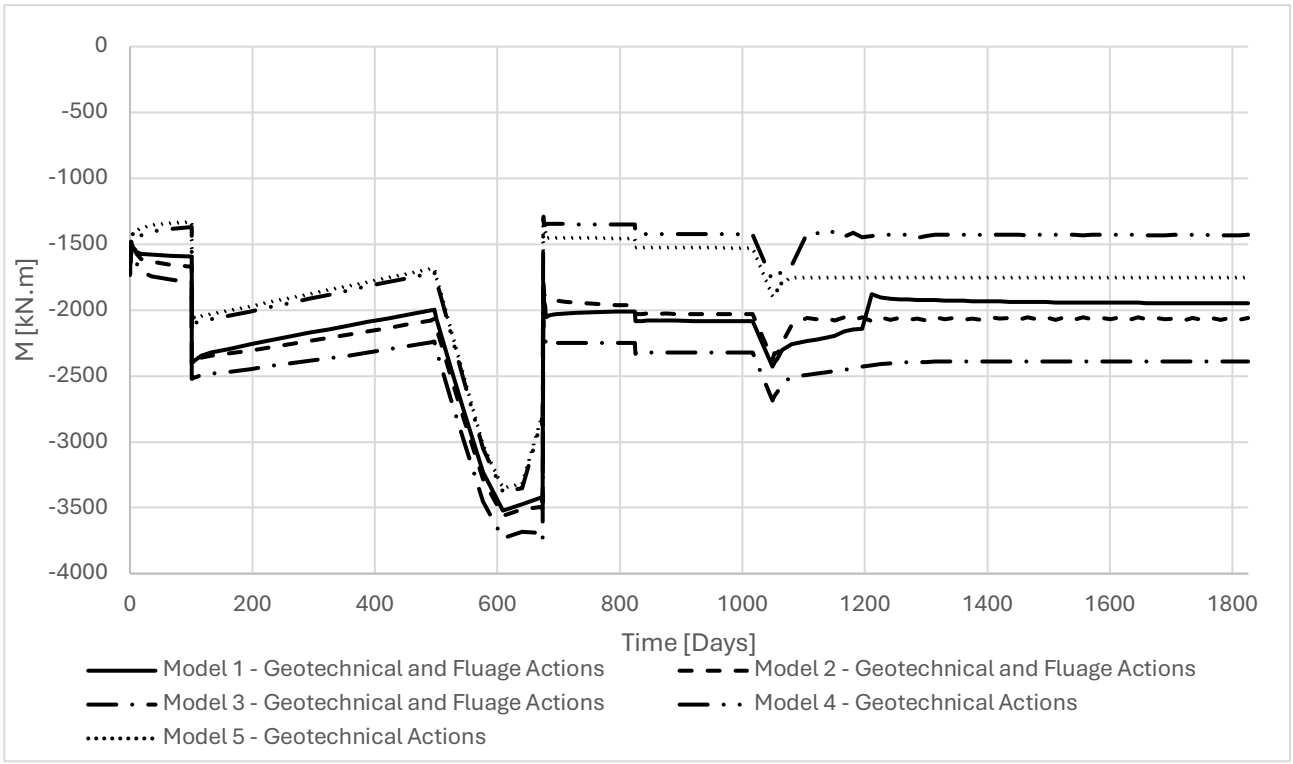


Figure 4-47 - Moment - Geotechnical and Creep Actions - Head Pile 2000 Uphill

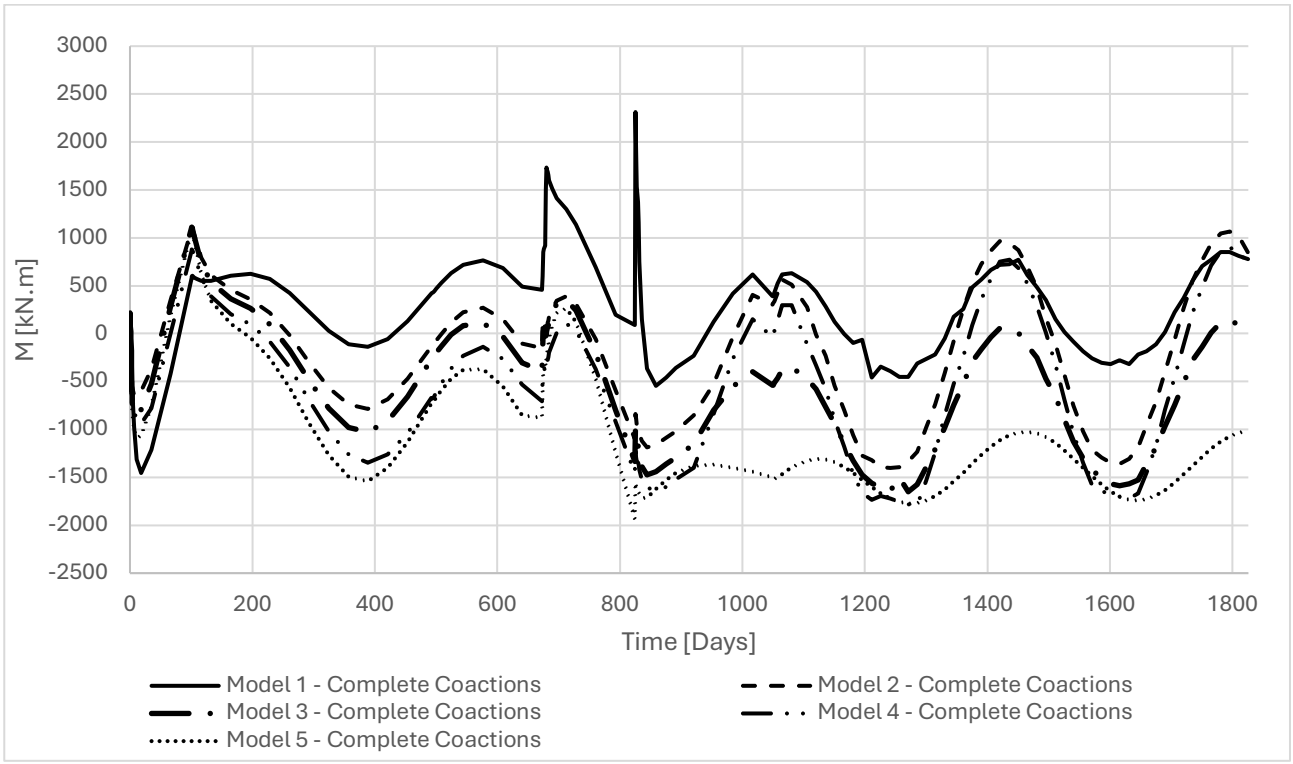


Figure 4-48 - Moment - Complete Coactions - Head Pile 2000 Uphill

Axial force diagrams:

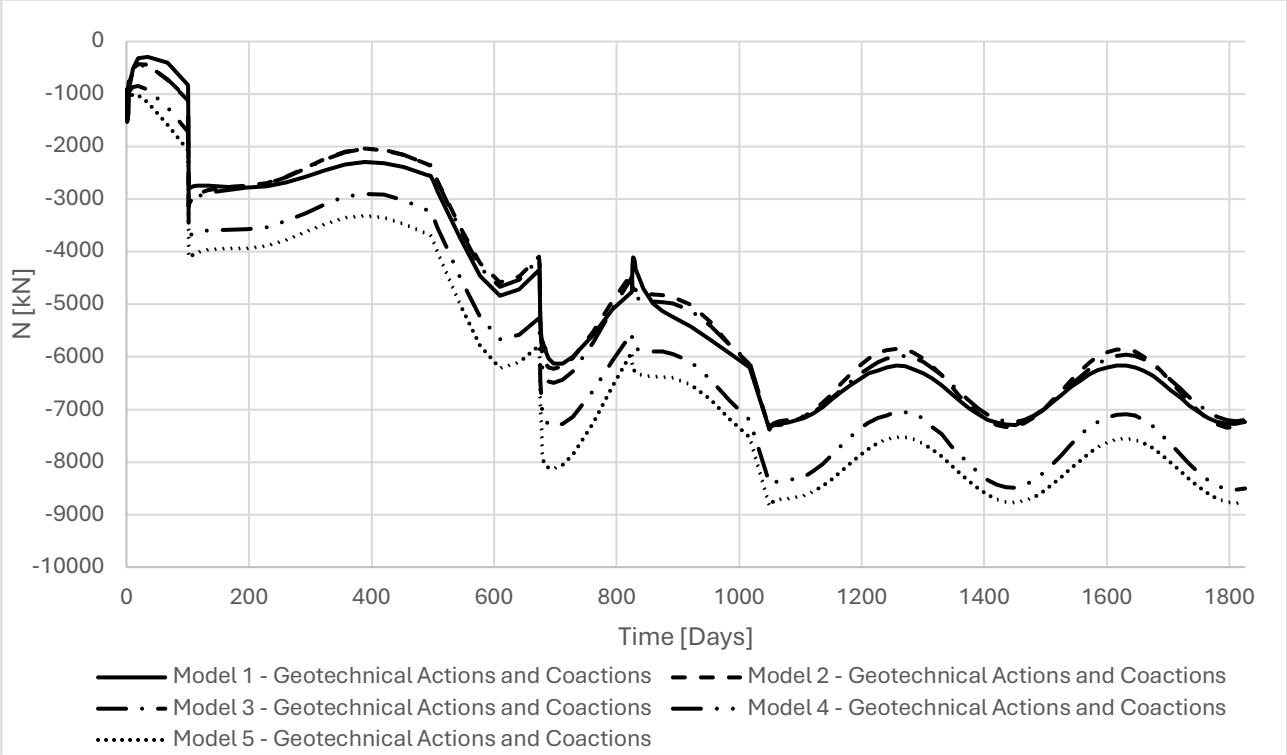


Figure 4-49 - Axial Force - Geotechnical Actions and Coactions - Head Pile 2000 Uphill

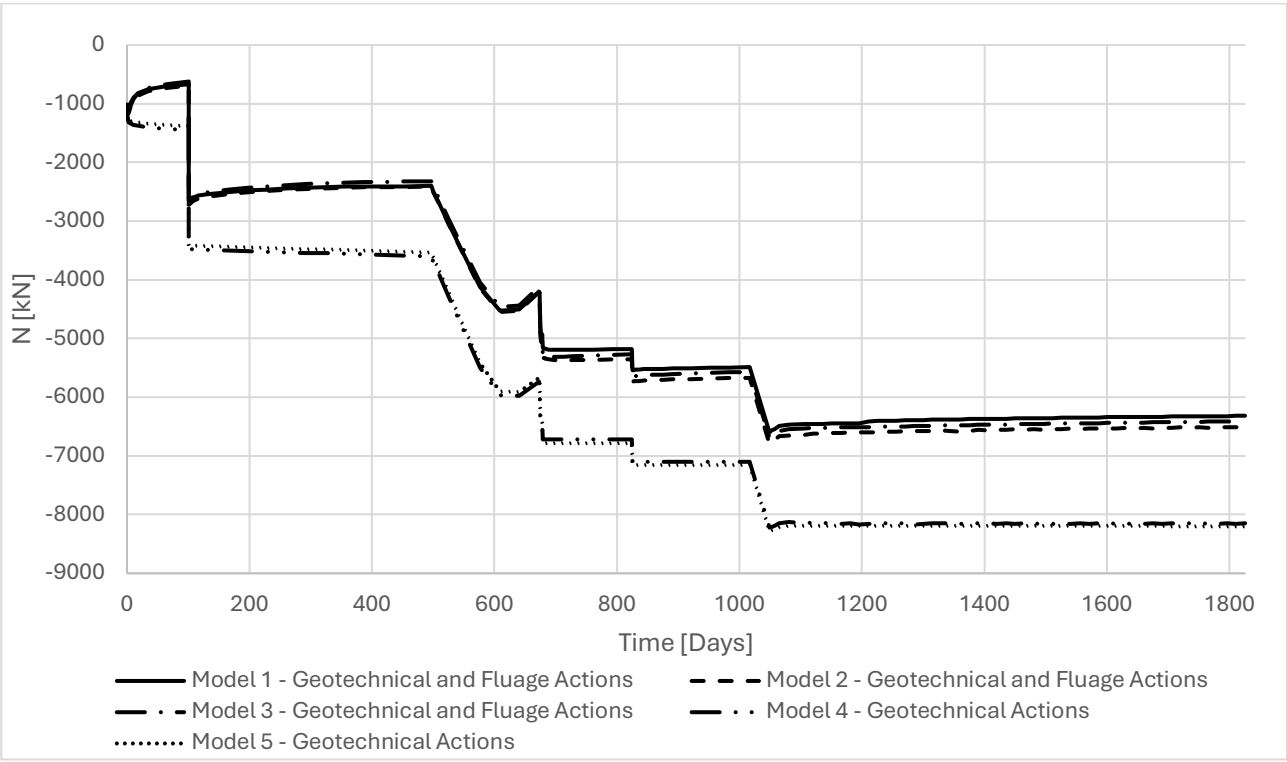


Figure 4-50 - Axial Force - Geotechnical and Creep Actions - Head Pile 2000 Uphill

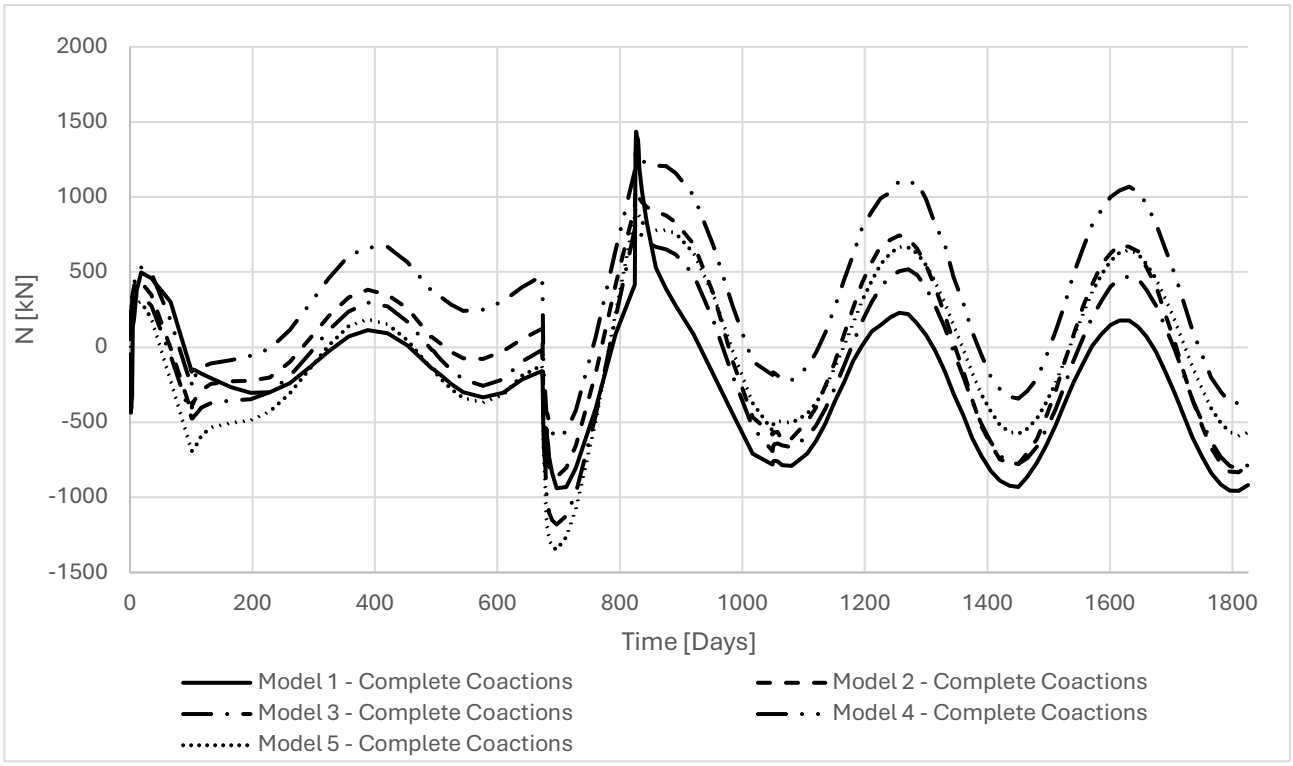


Figure 4-51 - Axial Force - Complete Coactions - Head Pile 2000 Uphill

Shear force diagrams:

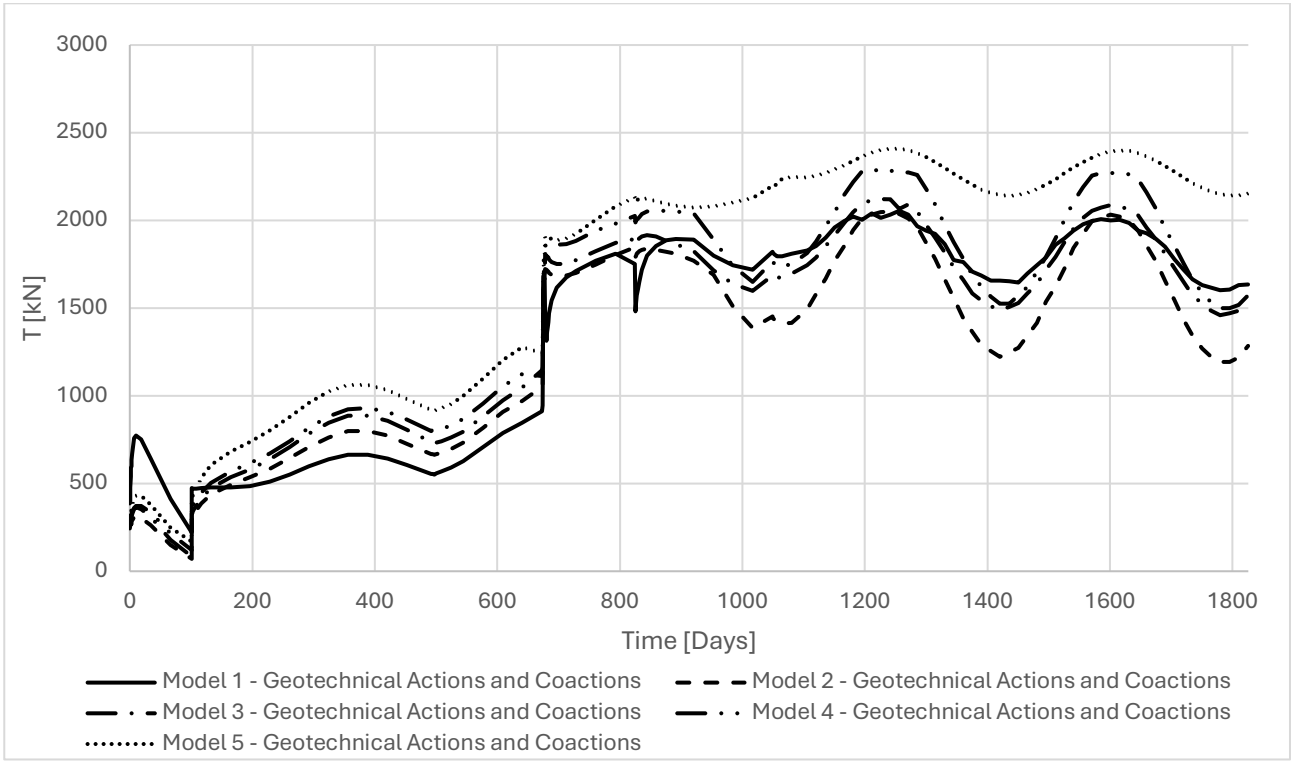


Figure 4-52 – Shear Force - Geotechnical Actions and Coactions - Head Pile 2000 Uphill

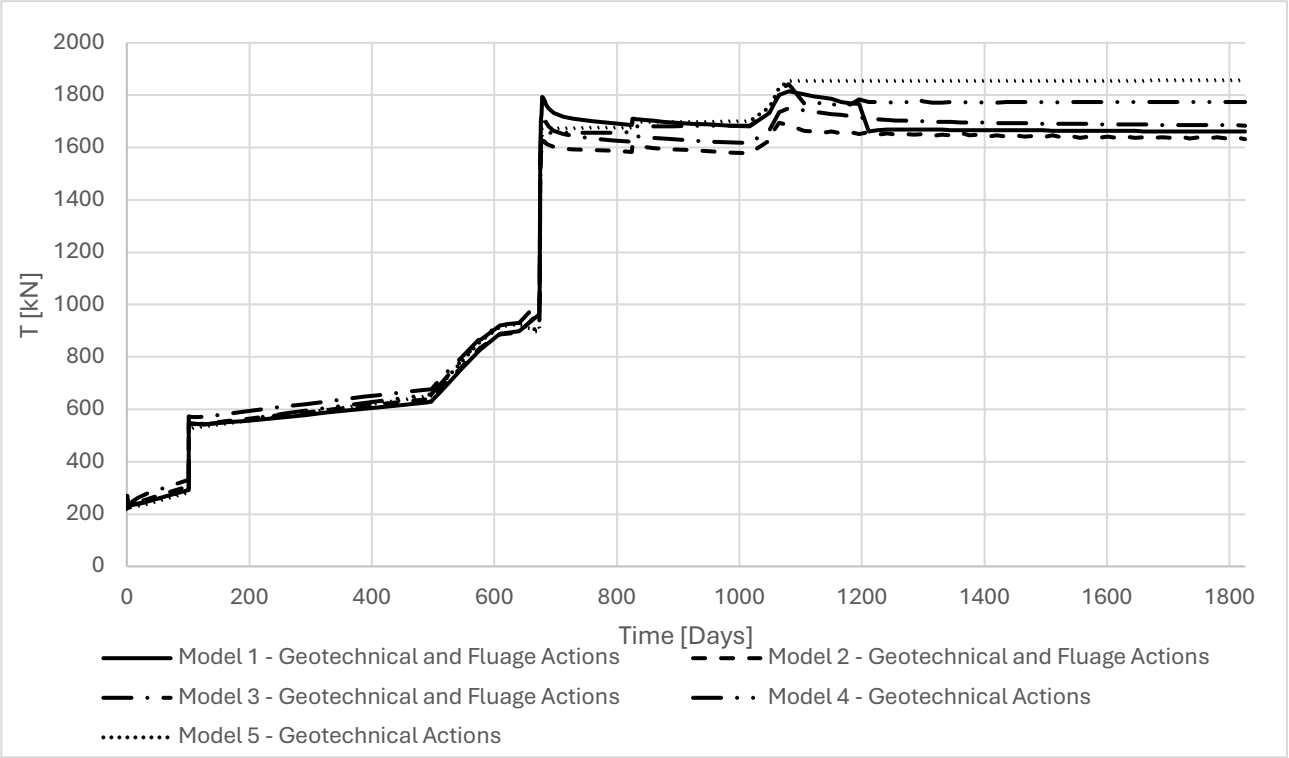


Figure 4-53 – Shear Force - Geotechnical and Creep Actions - Head Pile 2000 Uphill

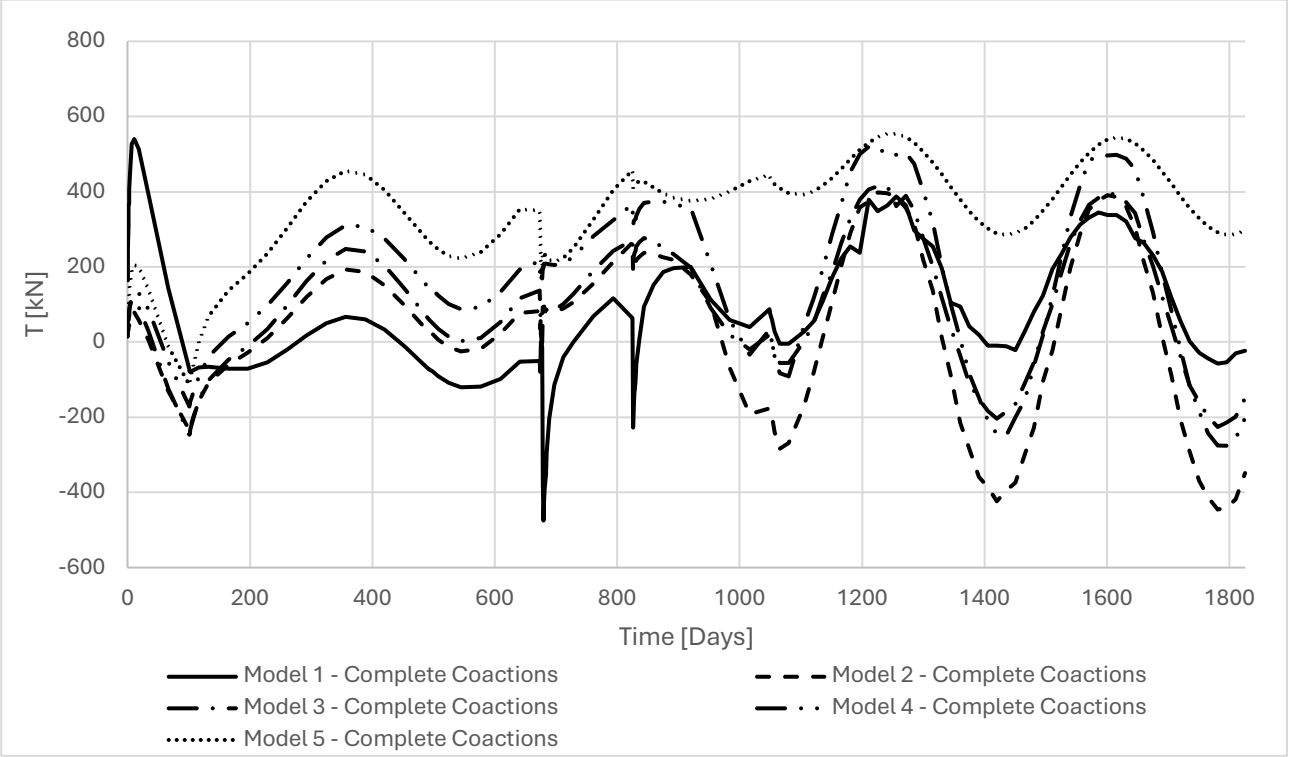


Figure 4-54 – Shear Force - Complete Coactions - Head Pile 2000 Uphill

4.3.2 Cover Slab Level Section

Moment diagrams:

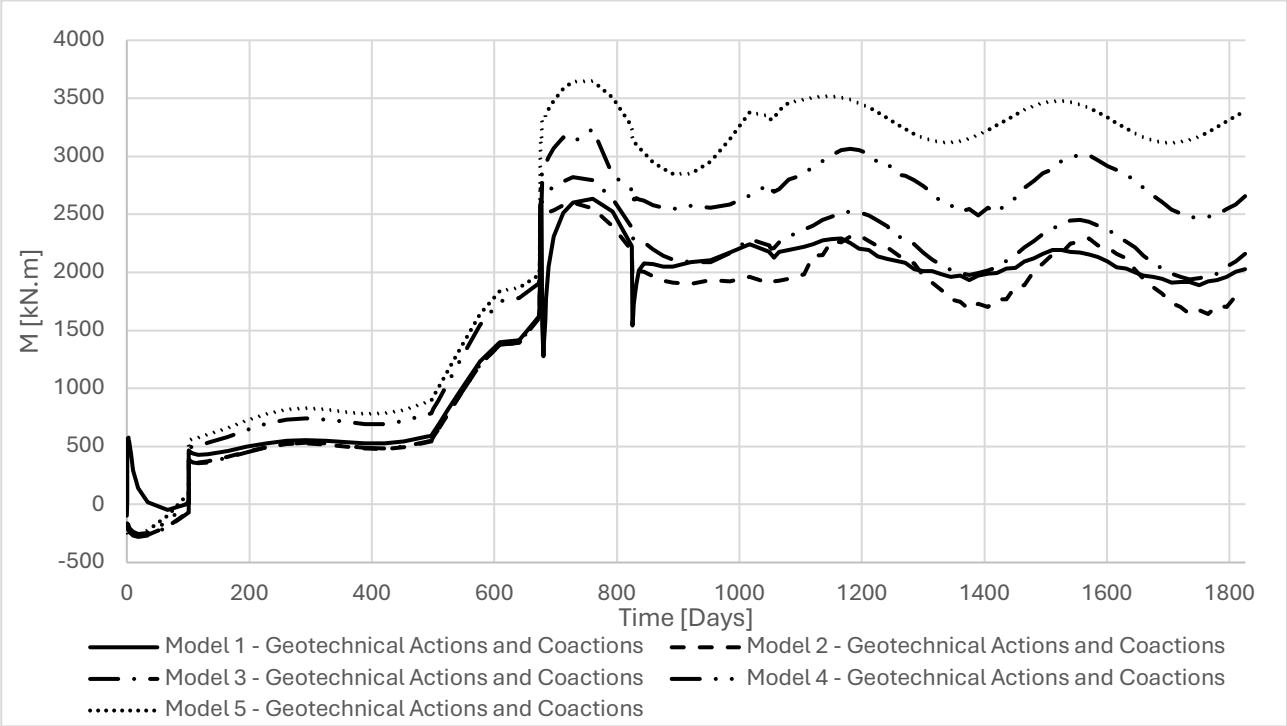


Figure 4-55 - Moment - Geotechnical Actions - Pile 2000 Uphill Cover Slab Level

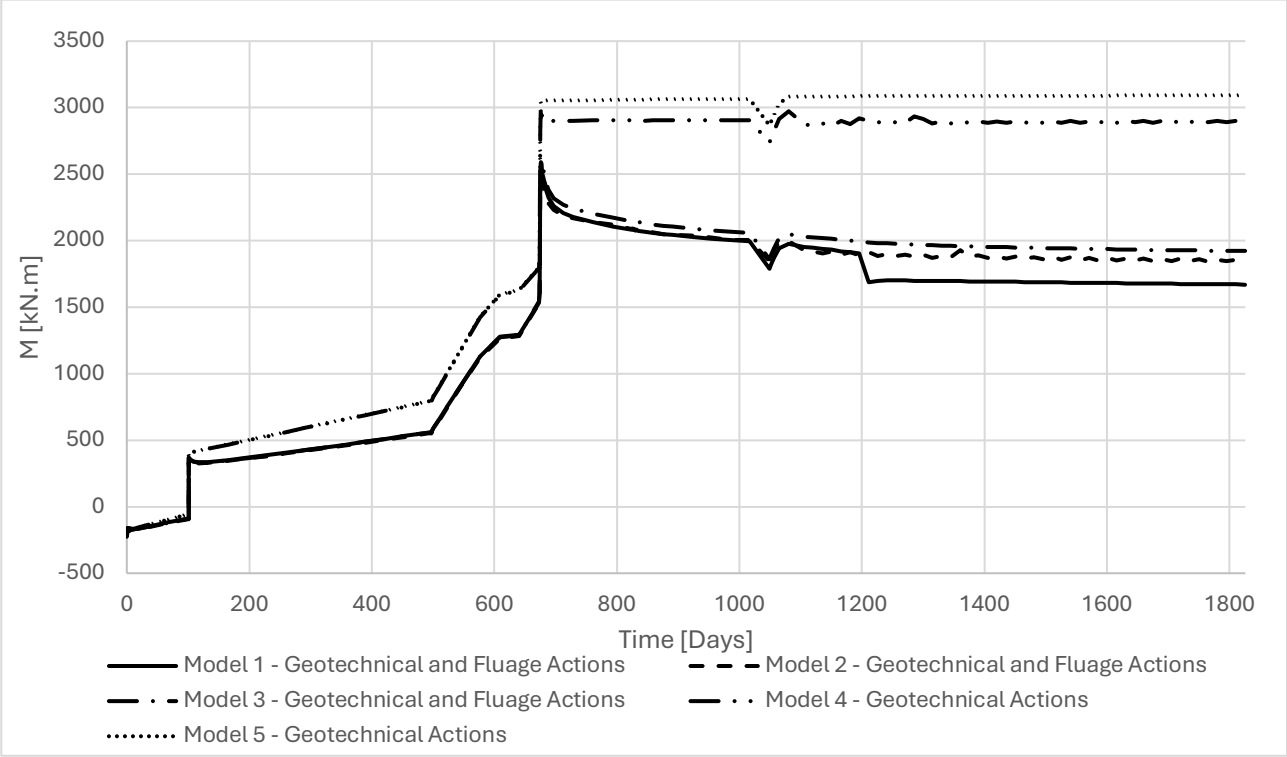


Figure 4-56 - Moment - Geotechnical and Creep Actions - Pile 2000 Uphill Cover Slab Level

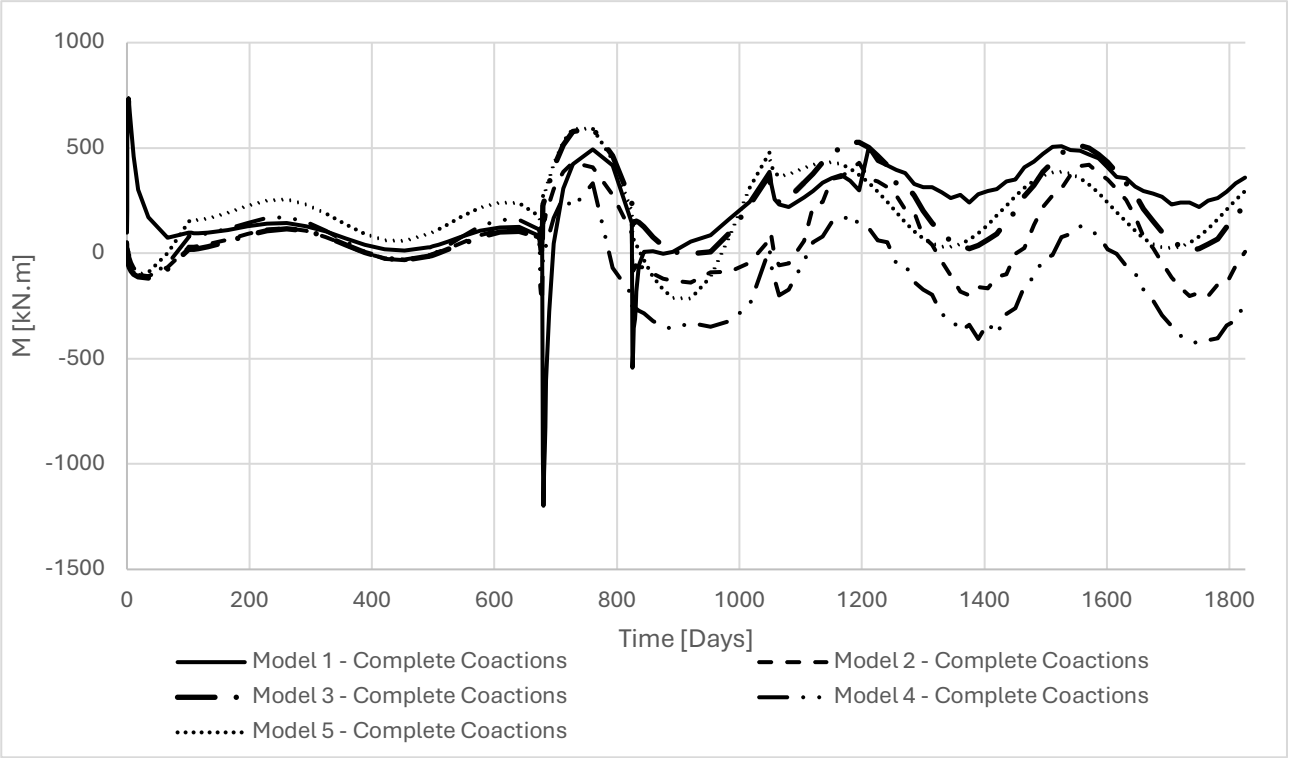


Figure 4-57 - Moment - Complete Coactions - Pile 2000 Uphill Cover Slab Level

Axial force diagrams:

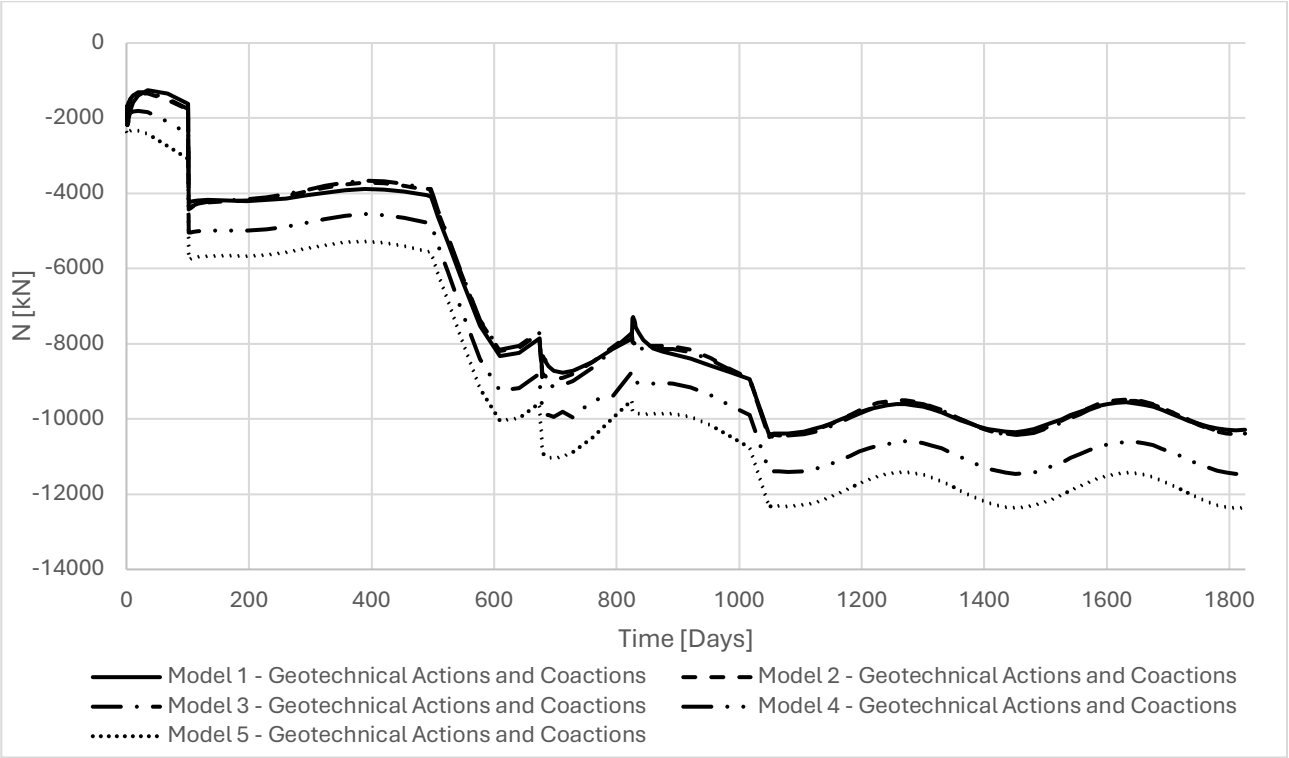


Figure 4-58 - Axial Force - Geotechnical Actions and Coactions - Pile 2000 Uphill Cover Slab Level

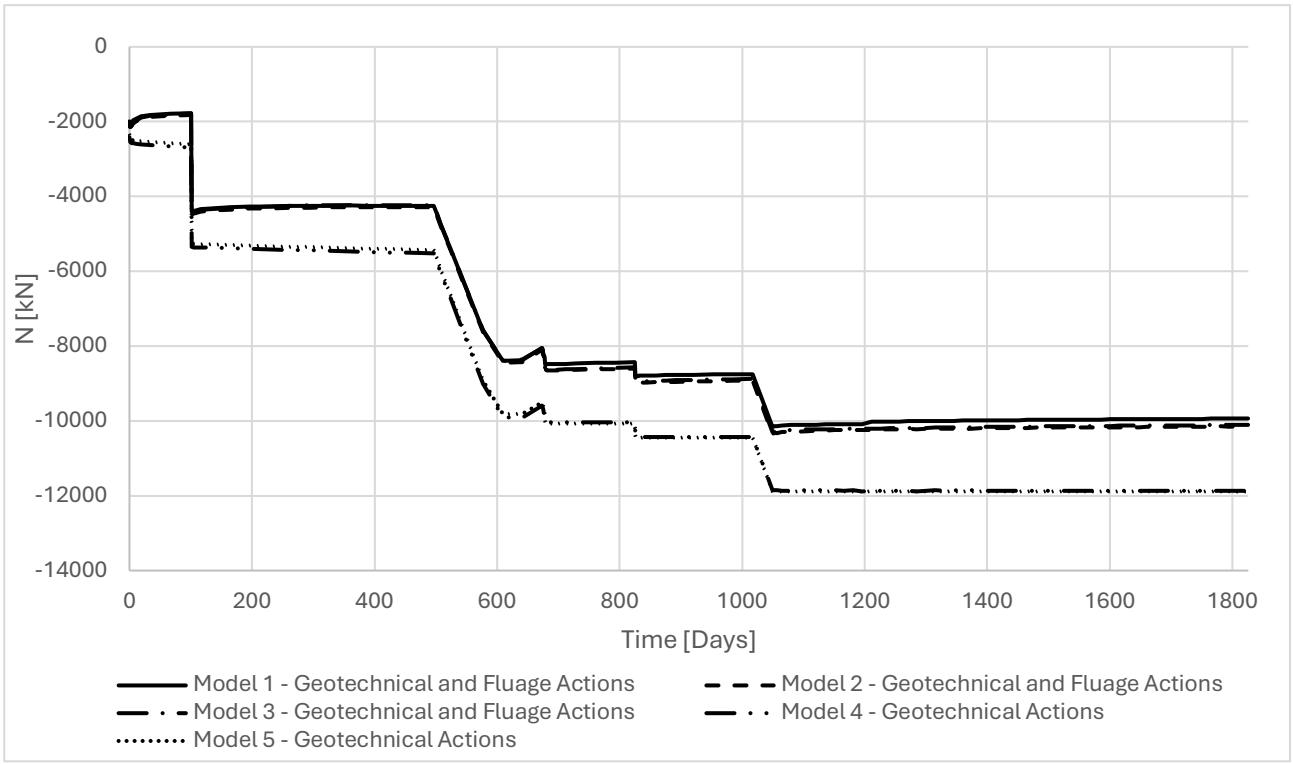


Figure 4-59 - Axial Force - Geotechnical and Creep Actions - Pile 2000 Uphill Cover Slab Level

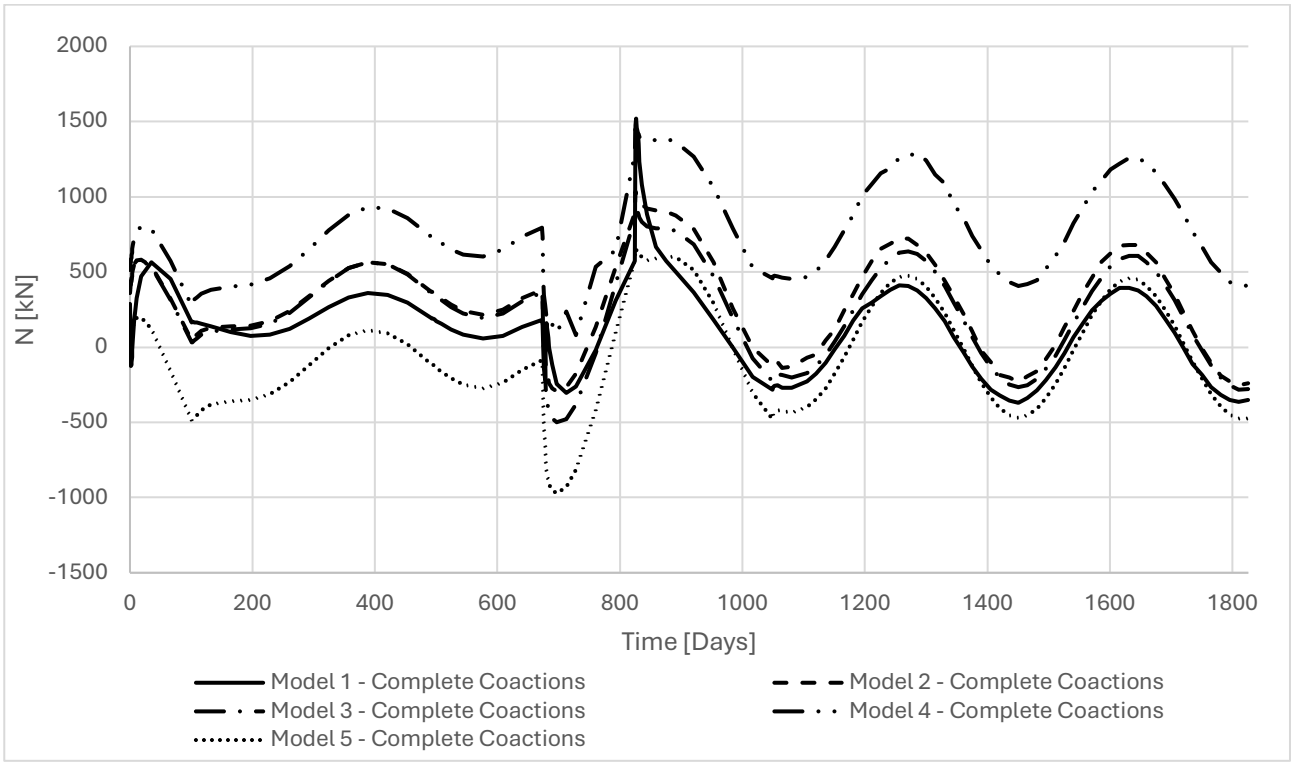


Figure 4-60 - Axial Force - Complete Coactions - Pile 2000 Uphill Cover Slab Level

Shear force diagrams:

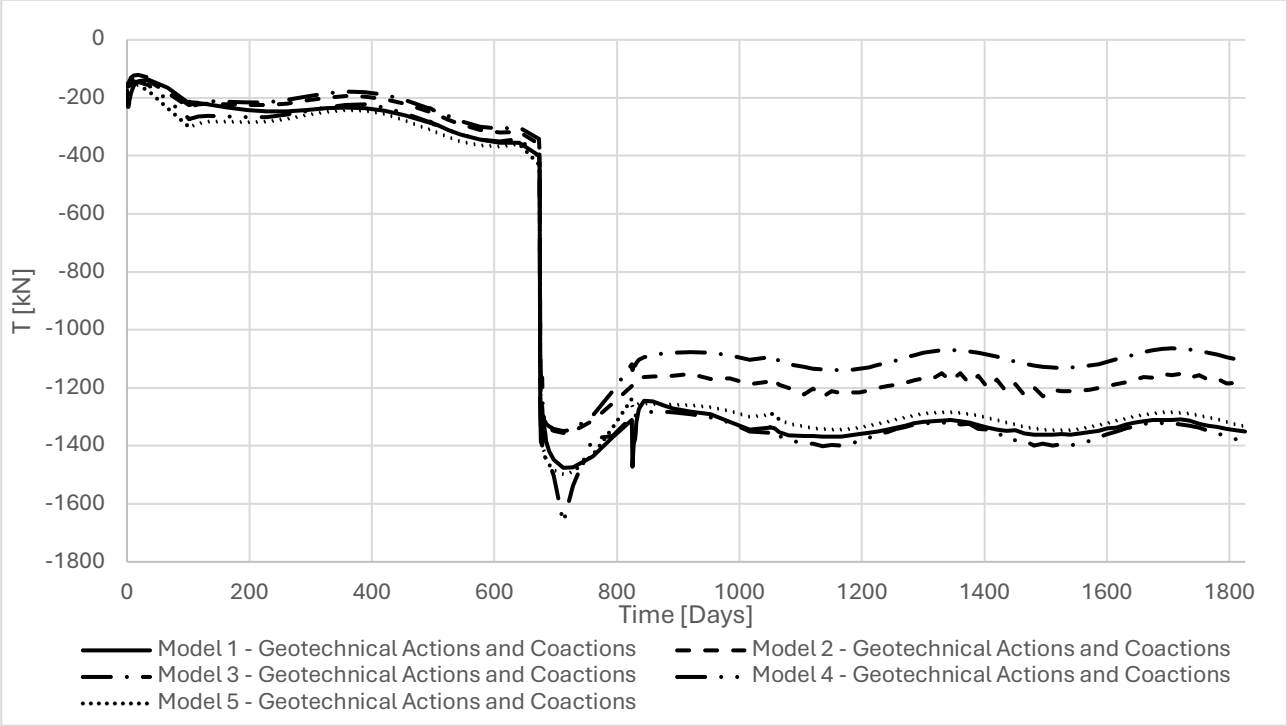


Figure 4-61 – Shear Force - Geotechnical Actions and Coactions - Pile 2000 Uphill Cover Slab Level

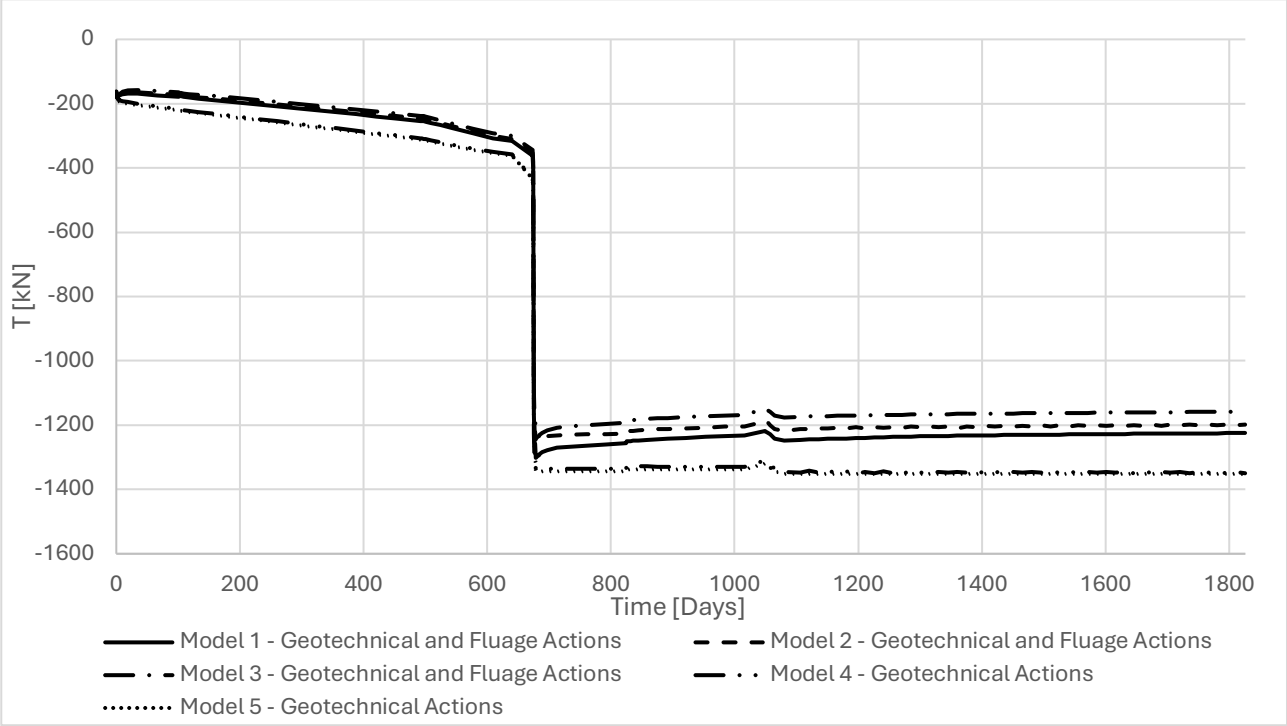


Figure 4-62– Shear Force - Geotechnical and Creep Actions - Pile 2000 Uphill Cover Slab Level

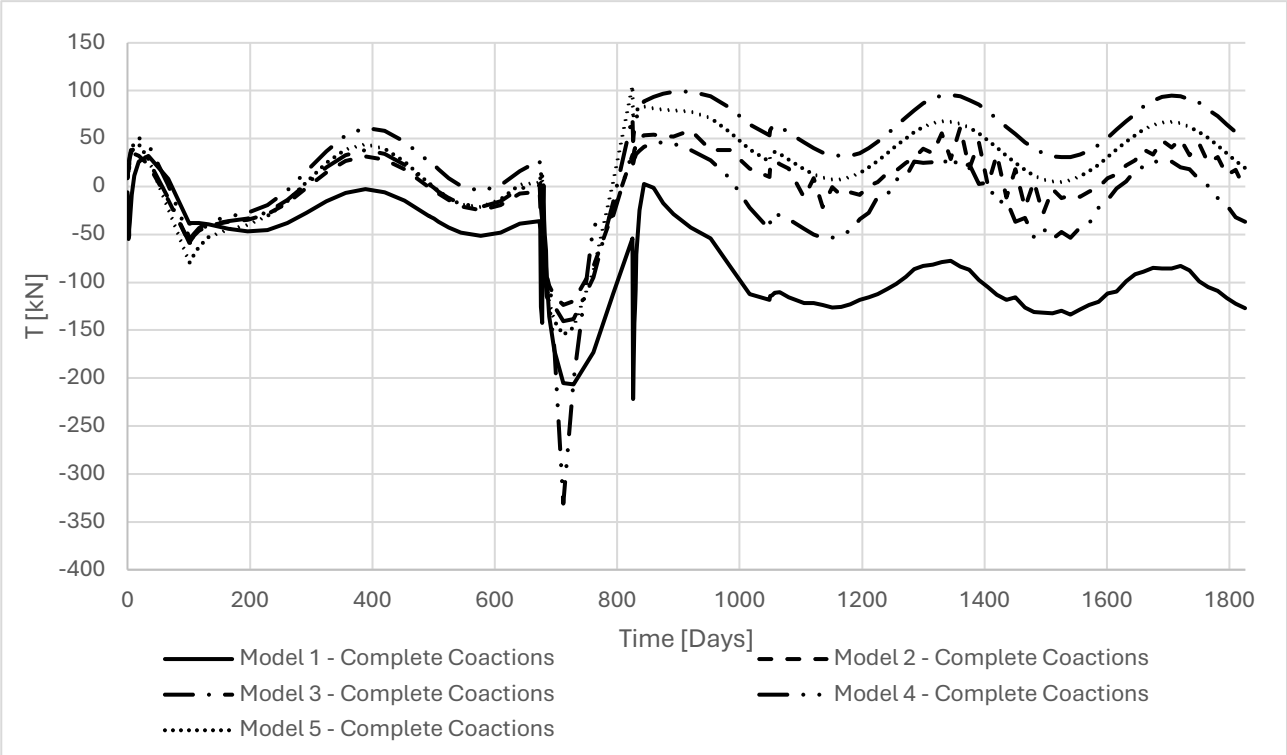


Figure 4-63 – Shear Force - Complete Coactions - Pile 2000 Uphill Cover Slab Level

4.3.3 Discrepancies between Models and Actions Combinations

Because the large-diameter uphill pile shafts ($D = 2000$ mm) provide the primary lateral bending stiffness of the retaining system, their finite elements are activated on day 0 ($t = 0$ days) and immediately begin interacting with the surrounding soil mass. During the initial construction sequence ($t = 0$ to 689 days), the pile functions as a vertical cantilever retaining wall while supporting vertical dead loads from the upper kerbs, top cover slab casting, and partial backfilling. This preliminary stage induces modest positive moments at the cover slab level ($M \approx +500$ to $+800\ kN*m$, Figure 4-55 and Figure 4-56) and accumulates significant shaft compression ($N \approx -4200$ to $-5500\ kN$, Figure 4-59). The structural mechanics shift dramatically at $t = 689$ days (phase 6), when bulk excavation removes lateral ground support in front of the shaft. Suddenly deprived of passive earth resistance, the pile is forced into a stiff framed mechanism that transfers the primary landslide thrust directly into the cover slab, causing head shear forces to jump abruptly from $T \approx 900\ kN$ to $1750\ kN$ (Figure 4-53) and driving flexural demands at the cover slab level to extreme levels.

Capturing this staged transition with full degree-of-reaction thermo-mechanical coupling reveals critical early-age coactions that are invisible in standard models. During the initial cooling of the pile cap ($t < 117$ days), model 1 records an early negative flexural dip at the pile head reaching $M \approx -3050\ kN * m$, in Figure 4-46, with coactions contributing $-1400\ kN * m$ in Figure 4-48), whereas unrelaxed models (models 4 and 5) track only a smooth transition near zero. When bulk excavation occurs at $t = 689$ days, model 5 predicts an unmitigated flexural spike at the cover slab level of $M \approx +3700\ kN * m$; in contrast, localized tensile micro-cracking and early creep in models 1 and 2 cap this peak at $M \approx +2600\ kN * m$, achieving an immediate 30% reduction in peak excavation moment. Shortly thereafter, the exothermic hydration of adjacent tunnel walls at $t = 841$ days (phase 8) generates an intense thermal shock. As the freshly poured walls expand upward and push outward against the pile cap, model 1 records a sharp positive flexural surge at the pile head of $\Delta M \approx +2100\ kN * m$ peaking at $M \approx +200\ kN * m$ (Figure 4-46 and Figure 4-48) alongside a transient tension jump of $\Delta N \approx +1900\ kN$: coactions spike to $+1400\ kN$, Figure 4-49 and Figure 4-51). Simultaneously, this wall dilation induces a steep flexural drop down to $M \approx +1500\ kN * m$ at the cover slab level (Figure 4-55 and Figure 4-57). Models 2 through 5 doesn't consider concrete hydration heat on subsequent pours and therefore bypass these transient damage-inducing coactions.

Once complete backfilling is placed at $t = 1065$ days (phase 9) and the system settles into sustained geotechnical equilibrium, viscoelastic creep becomes the dominant driver of stress redistribution. In the linear baseline (model 5) and the unrelaxed model (model 4), the absence of viscous flow locks in massive, permanent stress concentrations. Model 5 locks in an unrelaxed sustained hogging moment of $M = +3100\ kN * m$ at the cover slab level (Figure 4-56) an extreme sustained compressive thrust of $N = -12000\ kN$, and an unrelaxed sustained shear force of $T = -1350\ kN$ (Figure 4-62). In models 1 and 2, continuous creep relaxation allows the shaft to deform viscously and shed load into the surrounding soil mass. Sustained positive flexure at the cover slab level relaxes in model 1 to $M \approx +1700\ kN * m$, delivering a 45% flexural relief, $1400\ kN * m$ relative to model 5. While sustained shear relaxes to $T \approx -1150\ kN$: 14.8% relief versus model 5, Figure 4-62). At the pile head, creep similarly mitigates sustained geotechnical shear by 10% to 12% ($T \approx$ 1630-1660 kN in models 1 and 2 compared to 1850 kN in model 5; Figure 4-53) and relieves sustained vertical compression by 22%: $N \approx -6450\ kN$ versus $-825O\ kN$ in model 5 in Figure 4-50.

In the long-term cyclic service regime ($t > 1122$ days), the linear elastic framework of model 5 severely penalizes the structural assessment by treating seasonal thermal expansion as rigid

external loads. Unrelaxed models swing across vast cyclic envelopes: model 4 undergoes cyclic flexural swings of $\Delta M \approx 2850\ kN*m$ at the head (Figure 4-46) and cyclic shear oscillations of $\Delta T \approx 850\ kN$ (Figure 4-52), while model 5 forces axial compression at the cover slab level into an extreme winter peak of $N \approx -12500\ kN$ across a range of $\Delta N \approx 1500\ kN$. In model 1, continuous viscoelastic flow and joint cracking attenuate these cyclic demands. At the pile head, the cyclic moment range is restricted to $\Delta M \approx 1200\ kN*m$, a nearly 58% reduction in comparison to model 4 as shown in the Figure 4-46, while cyclic shear fluctuations are damped to $\Delta T \approx 450\ kN$ (47% reduction versus model 4; Figure 4-52). At the cover slab level, model 1 bounds the peak design operating moment to $M \approx +2250\ kN*m$, 36% lower than model 5's $+3550\ kN*m$, Figure 4-55 and dampens the cyclic axial range by approximately 47%: $\Delta N \approx 800\ kN$, keeping winter thrust capped at $-10400\ kN$).

4.4 Downhill Pile (D = 2000 mm)

The analysis focuses on two critical elevations: head pile elevation, the top connection to the upper foundation strut and cover slab level, the interface connection with the portal frame roof.

4.4.1 Head Section

Moment diagrams:

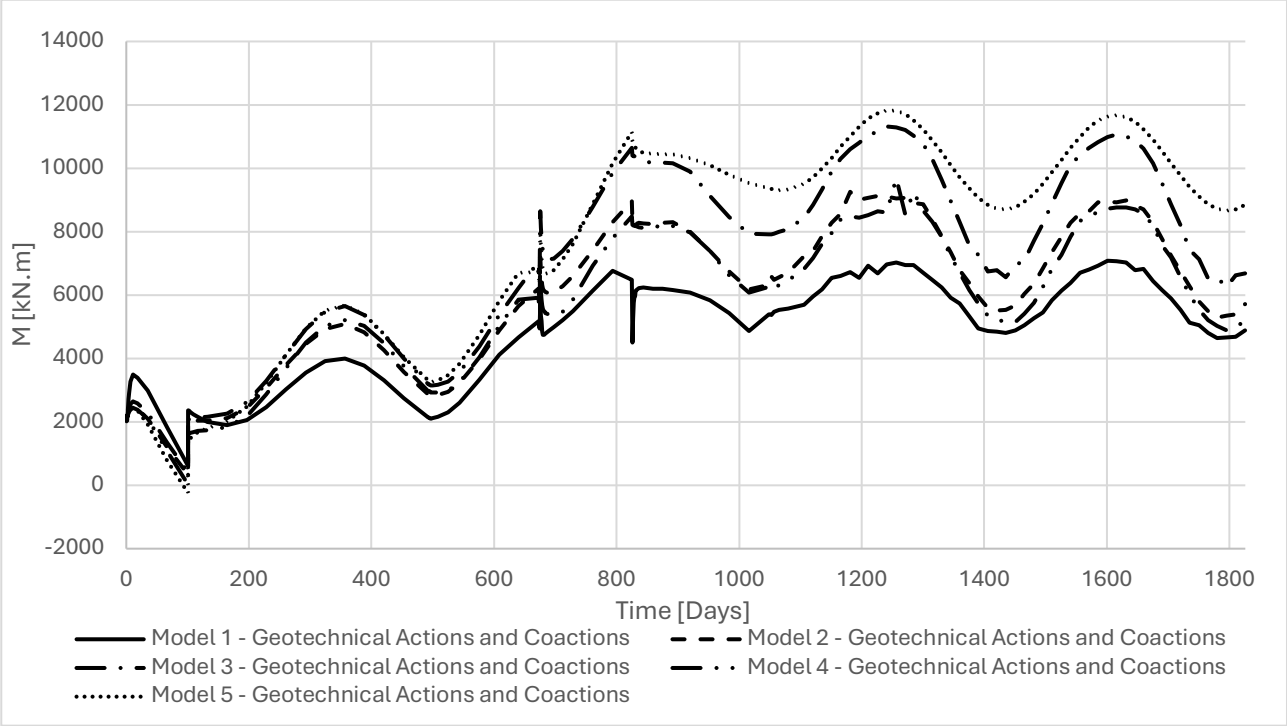


Figure 4-64 - Moment - Geotechnical Actions and Coactions - Head Pile 2000 Downhill

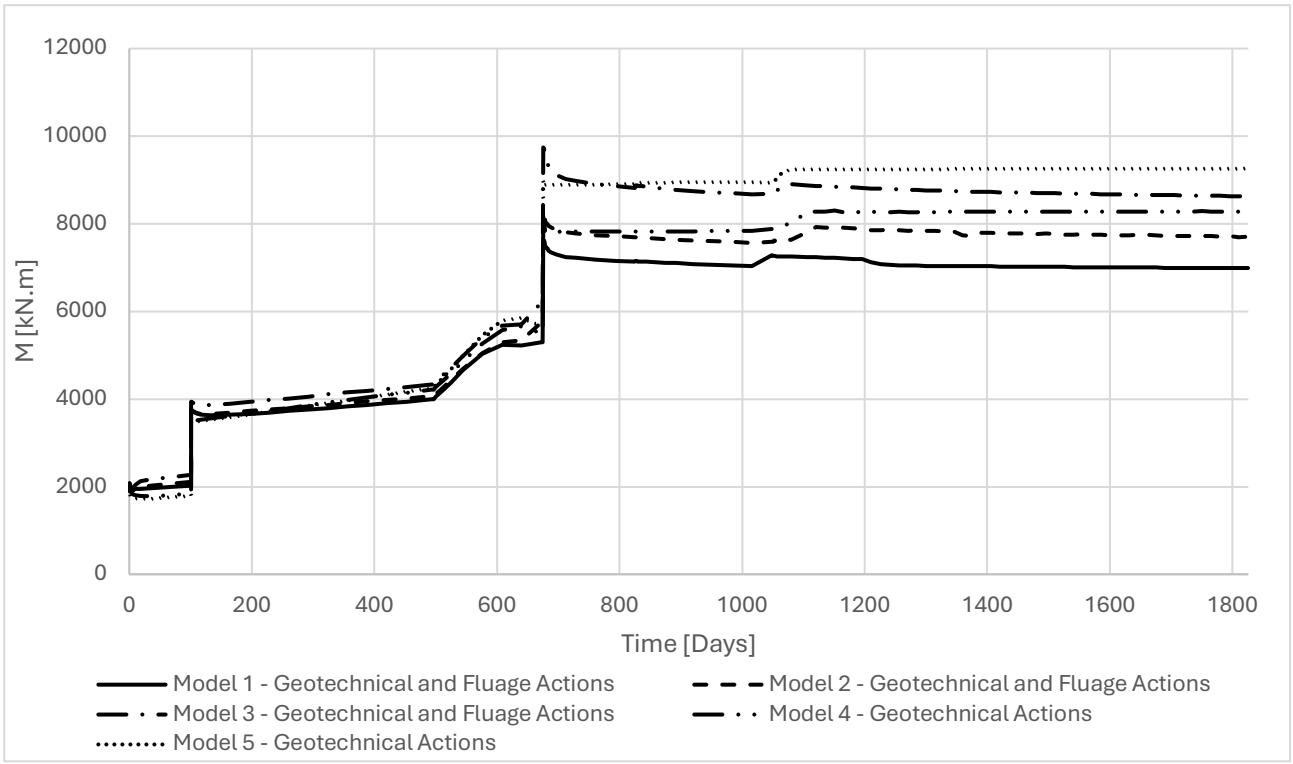


Figure 4-65 - Moment - Geotechnical and Creep Actions - Head Pile 2000 Downhill

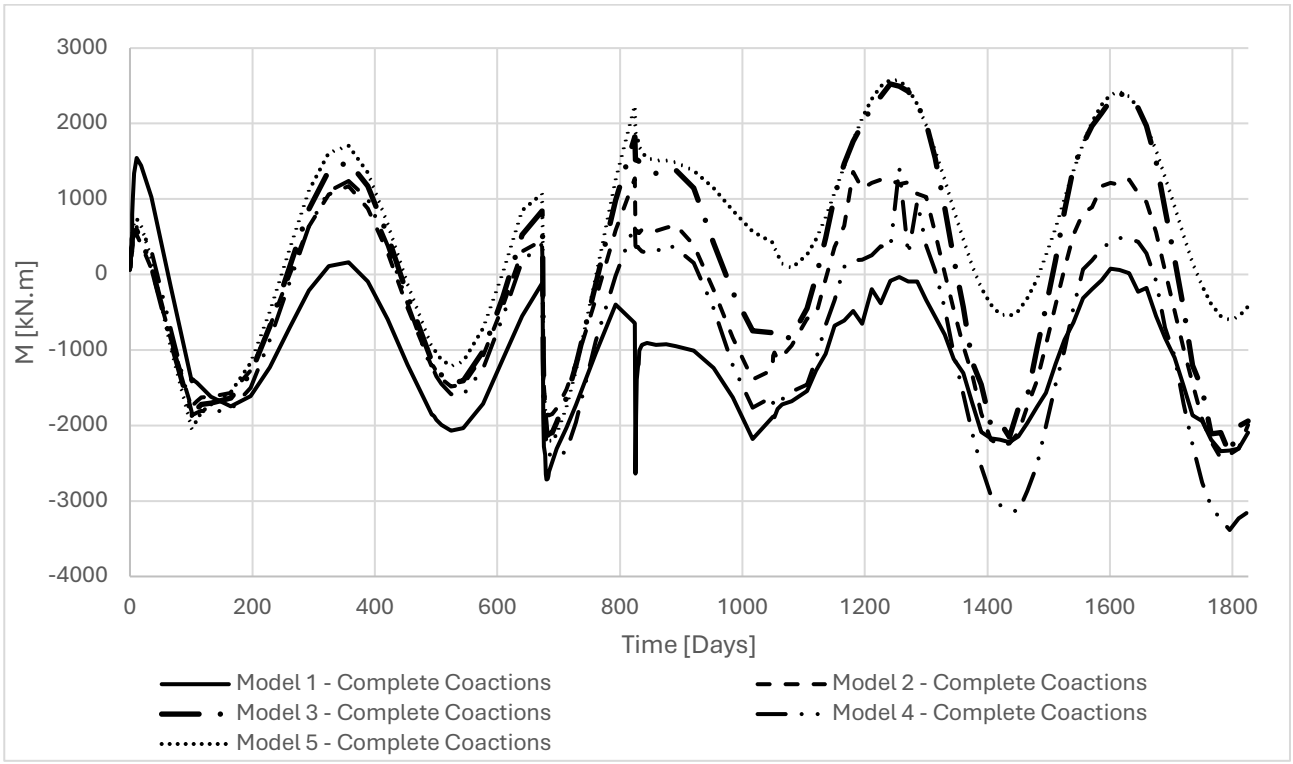


Figure 4-66 - Moment - Complete Coactions - Head Pile 2000 Downhill

Axial force diagrams:

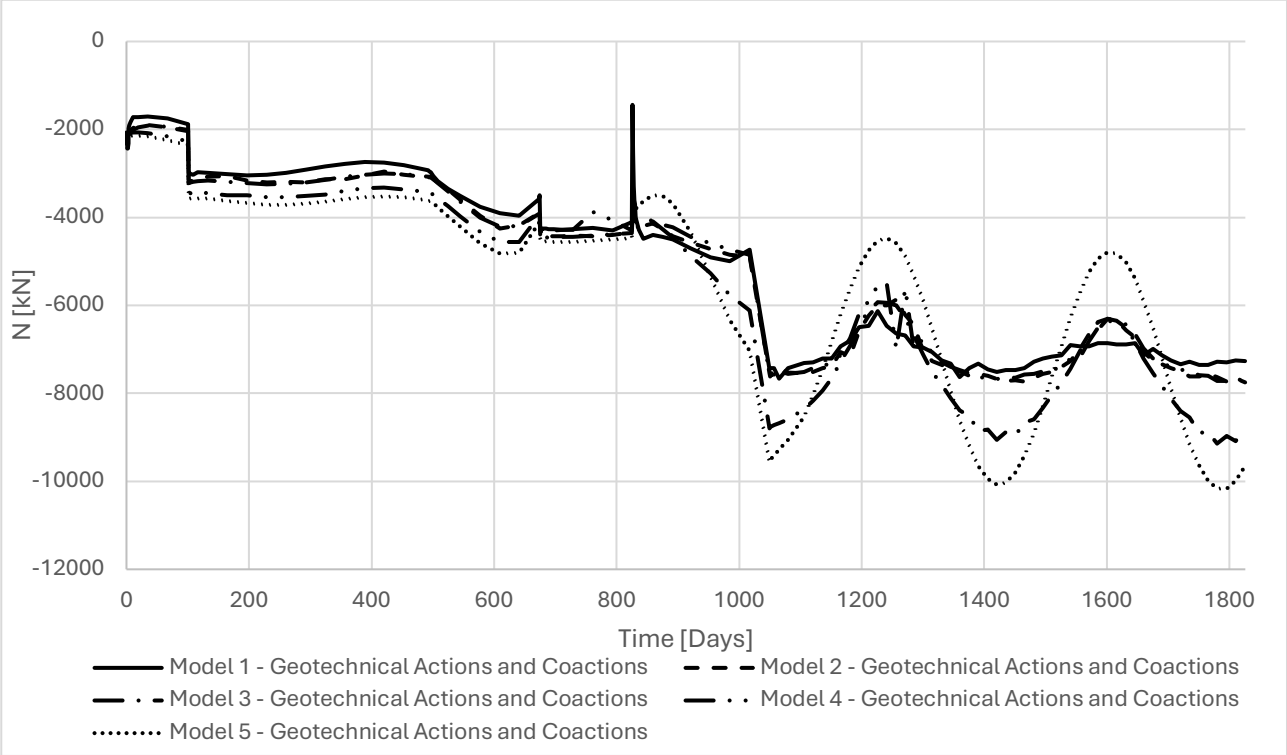


Figure 4-67 - Axial Force - Geotechnical Actions and Coactions- Head Pile 2000 Downhill

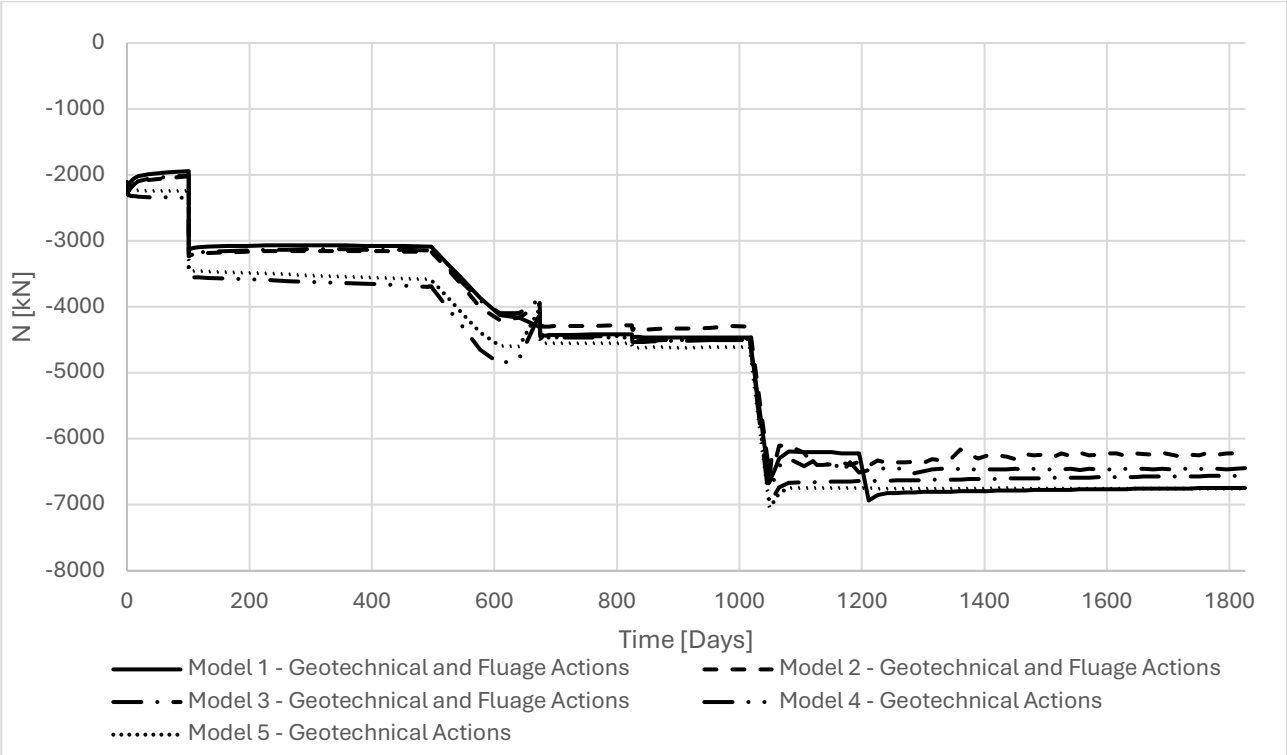


Figure 4-68 - Axial Force - Geotechnical and Creep Actions - Head Pile 2000 Downhill

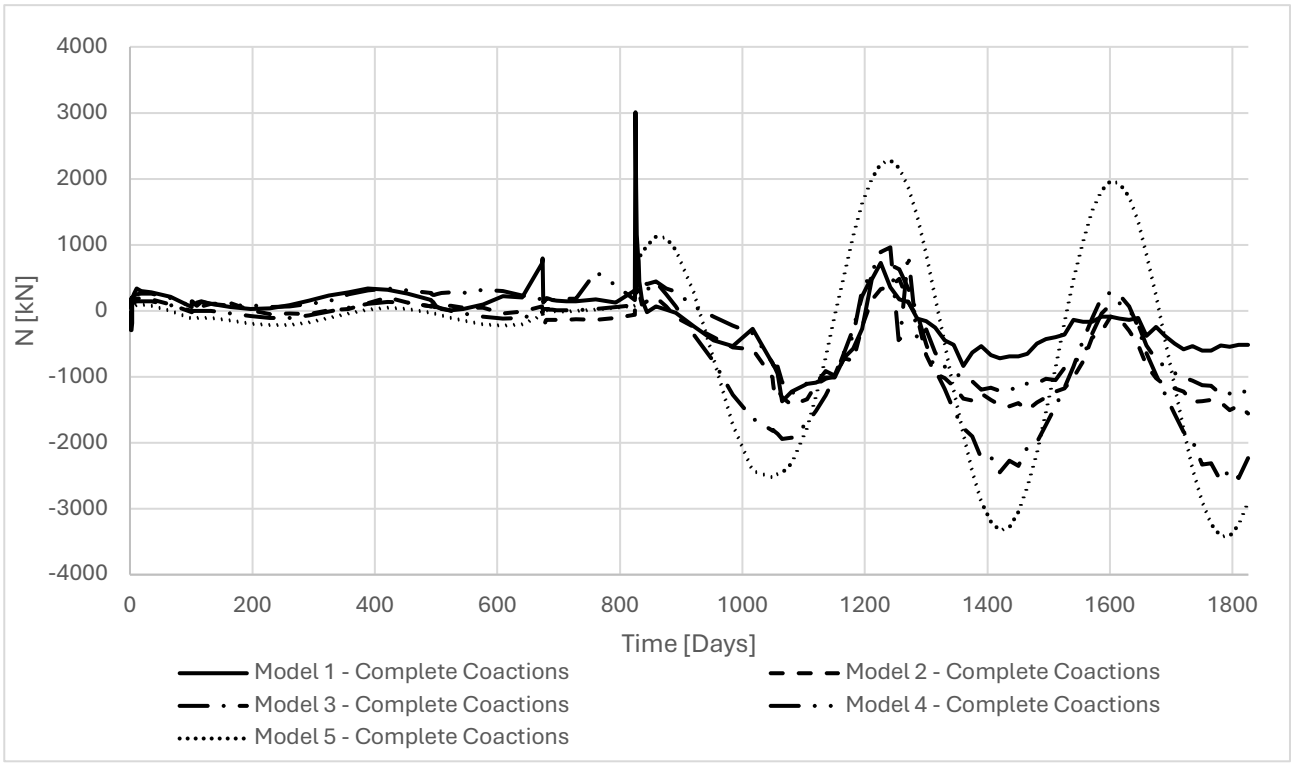


Figure 4-69 - Axial Force - Geotechnical and Creep Actions - Head Pile 2000 Downhill

Shear force diagrams:

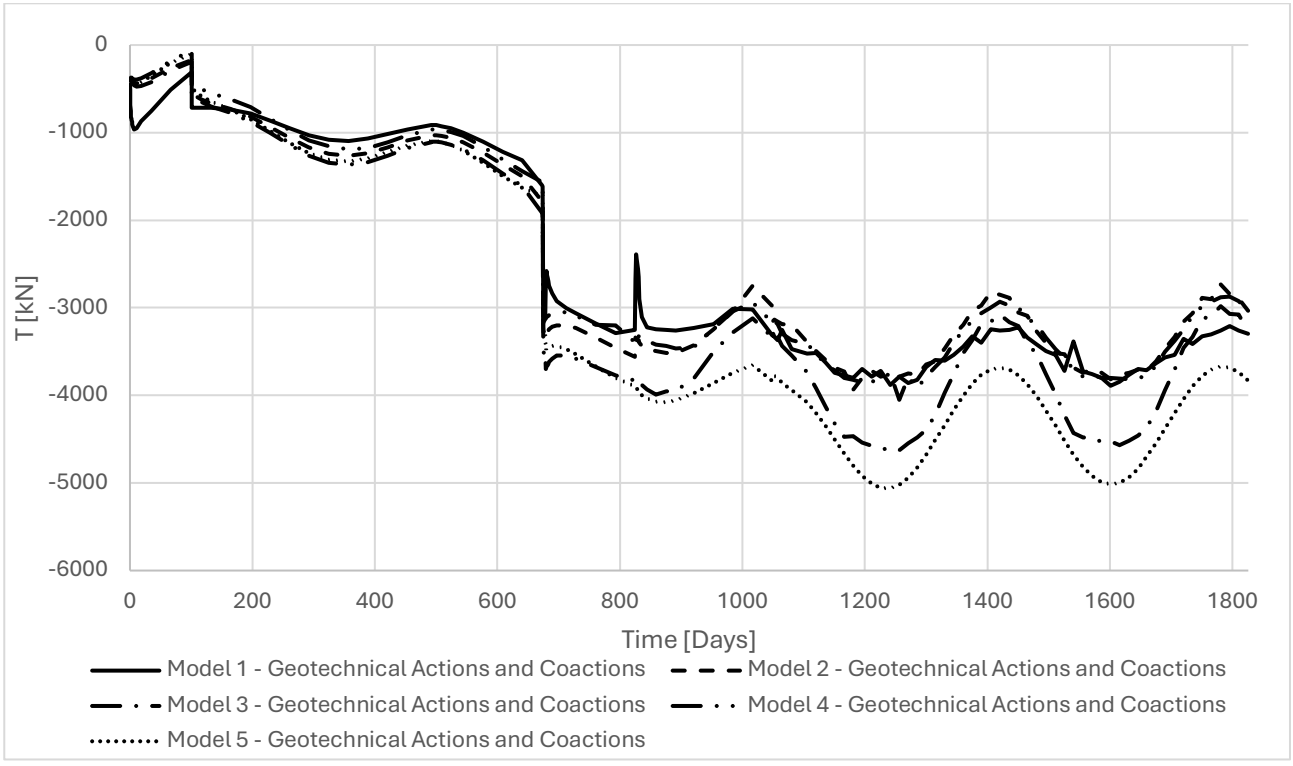


Figure 4-70 – Shear Force - Geotechnical Actions and Coactions - Head Pile 2000 Downhill

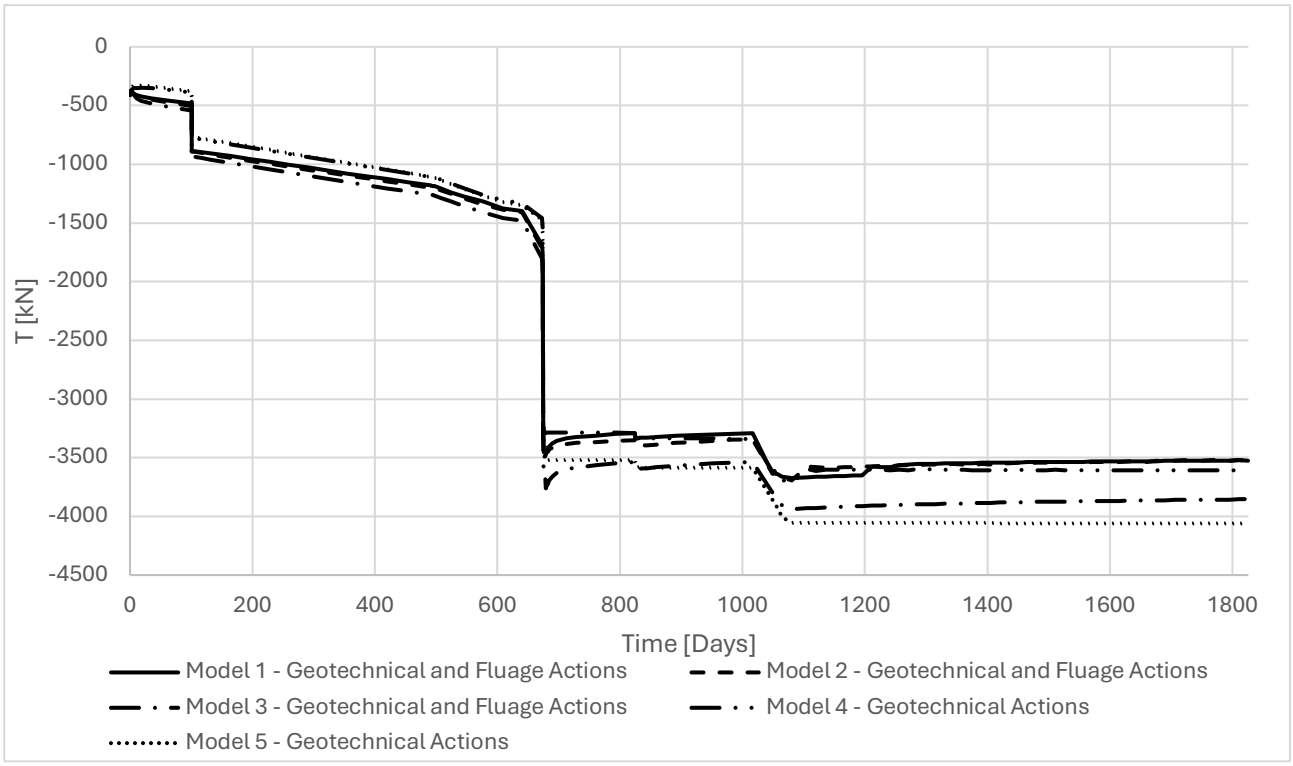


Figure 4-71 – Shear Force - Geotechnical and Creep Actions - Head Pile 2000 Downhill

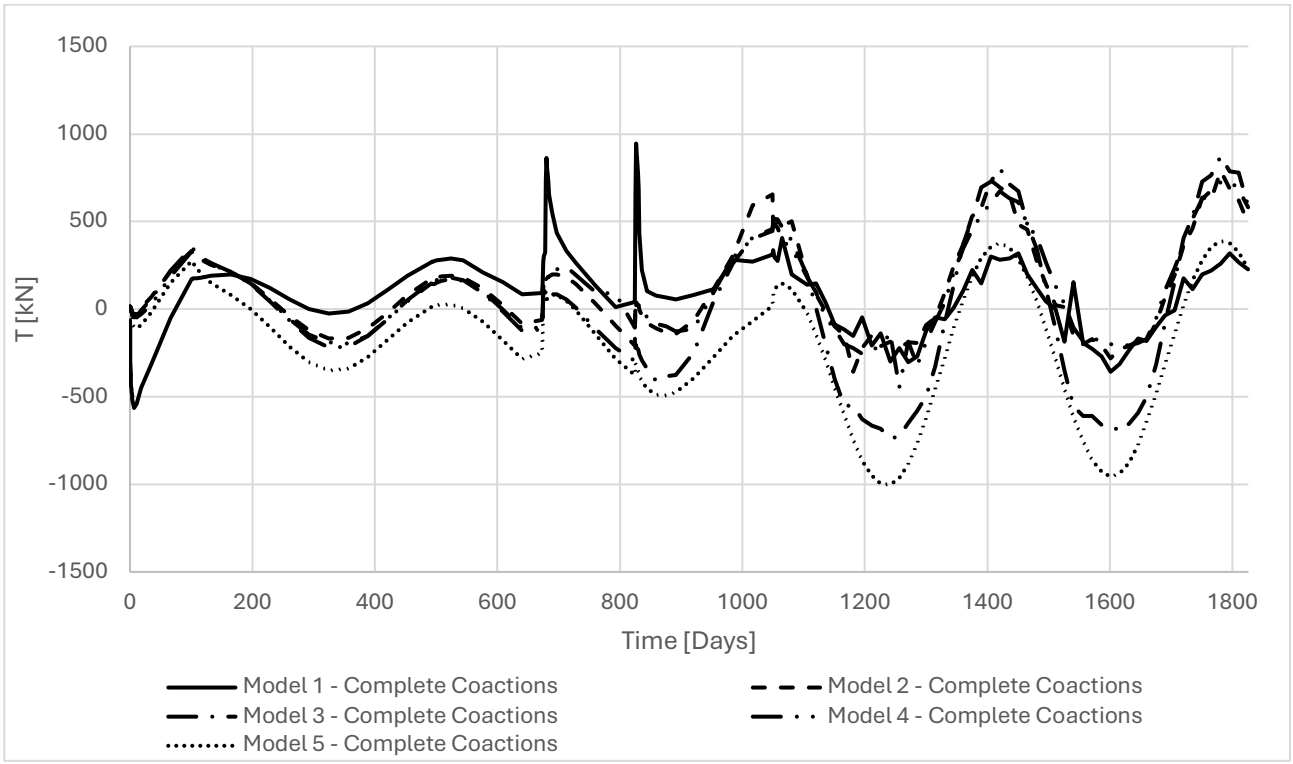


Figure 4-72 - Shear Force - Complete Coactions - Head Pile 2000 Downhill

4.4.2 Cover Slab Level Section

Moment diagrams:

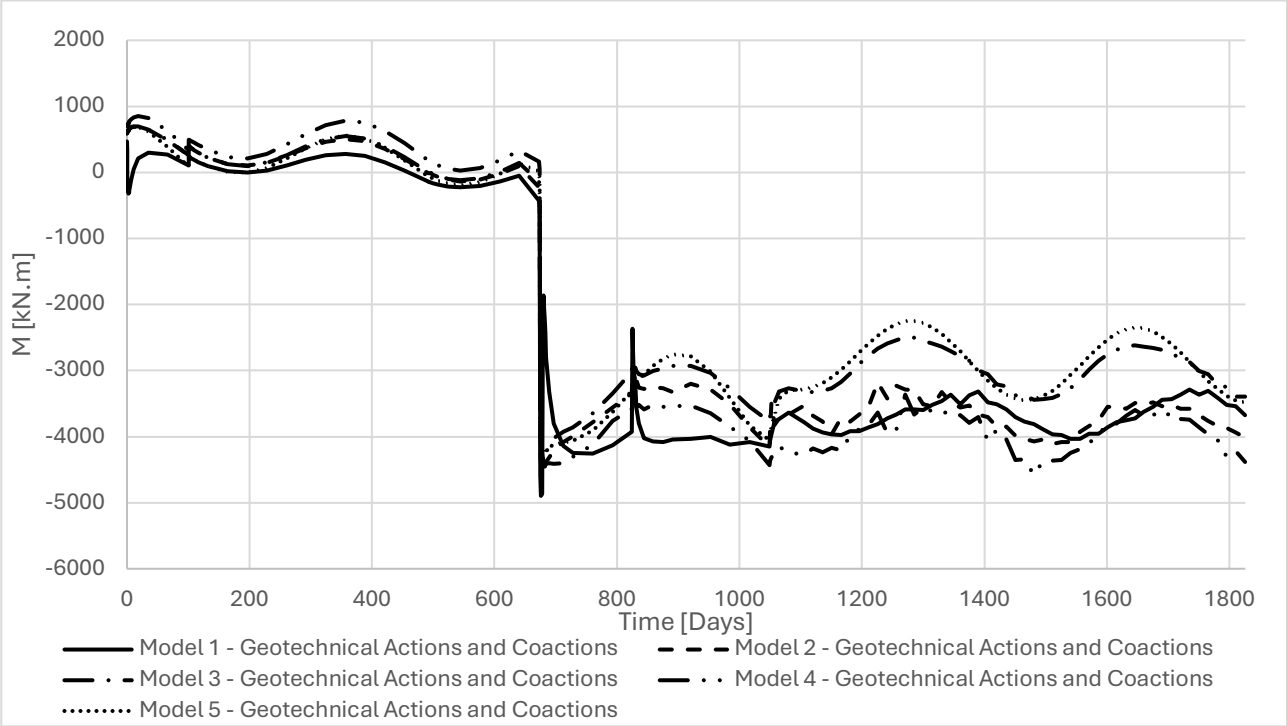


Figure 4-73 - Moment - Geotechnical Actions and Coactions - Pile 2000 Downhill Cover Slab Level

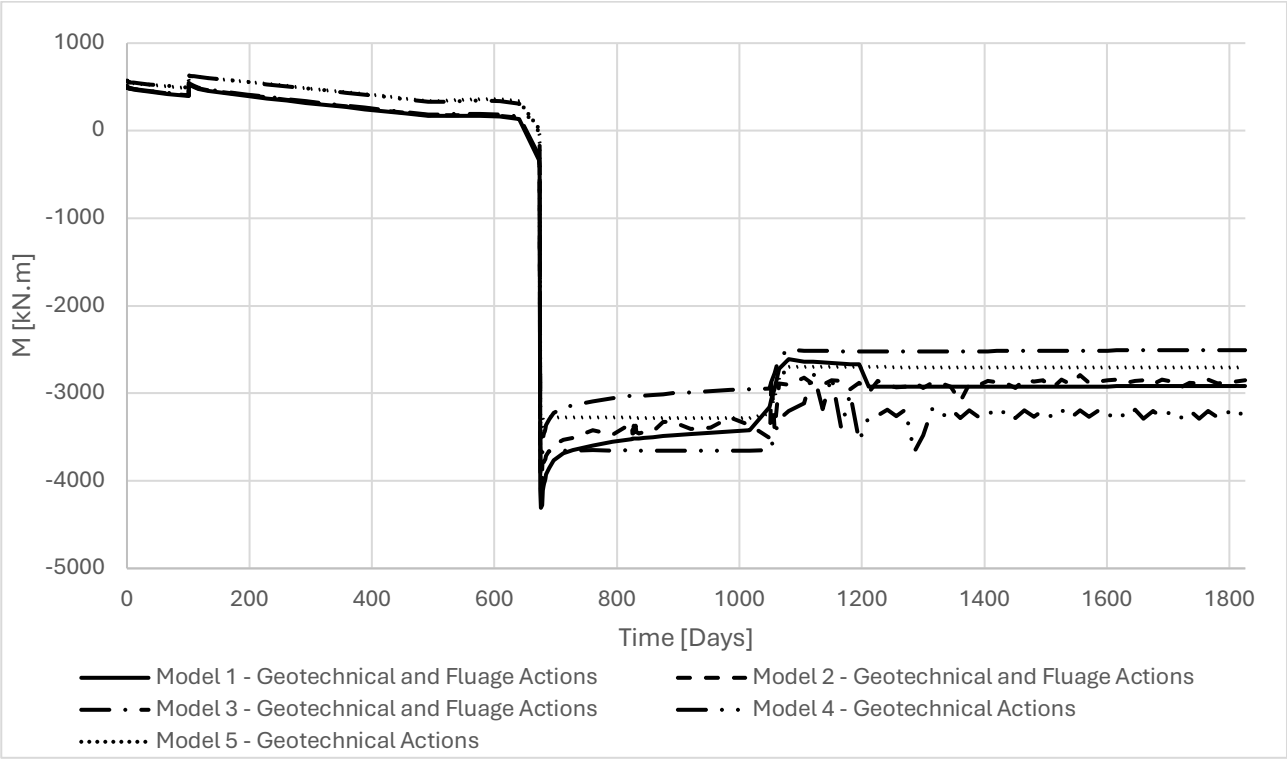


Figure 4-74 - Moment - Geotechnical and Creep Actions - Pile 2000 Downhill Cover Slab Level

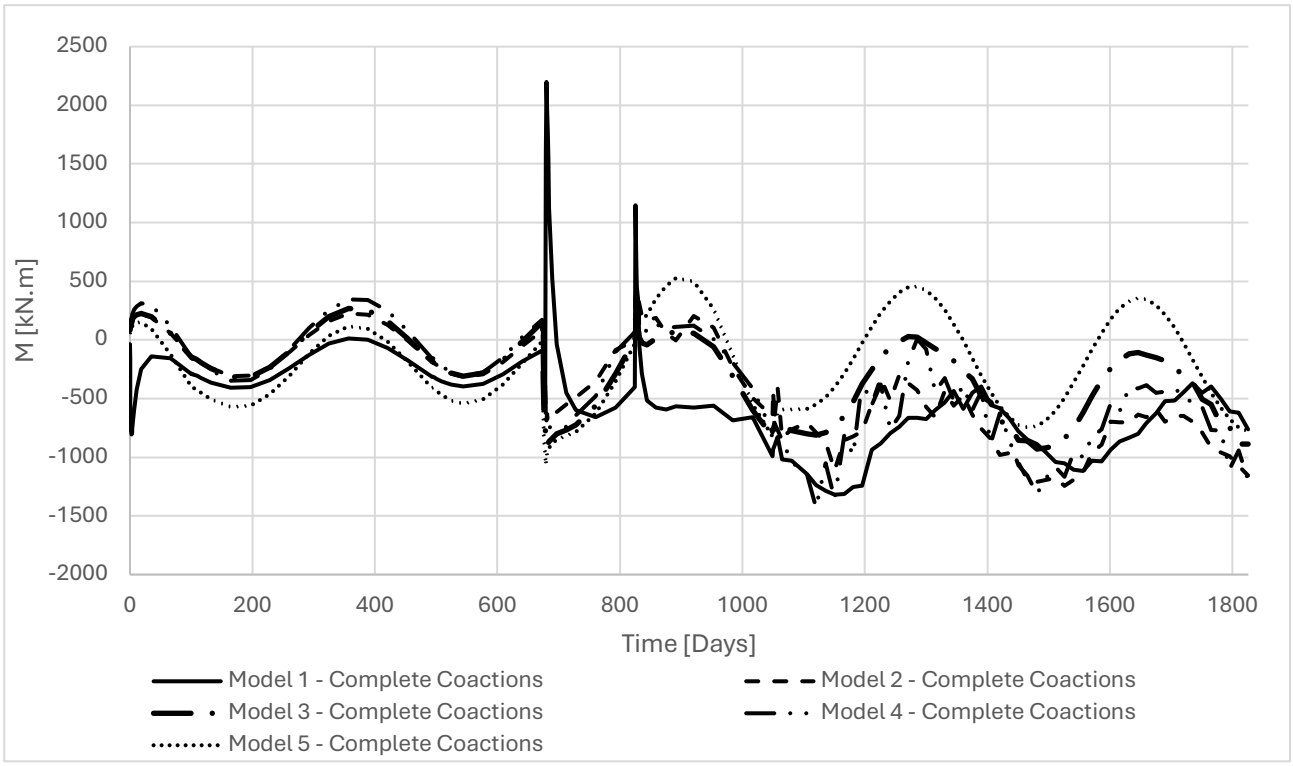


Figure 4-75 - Moment - Complete Coactions - Pile 2000 Downhill Cover Slab Level

Axial force diagrams:

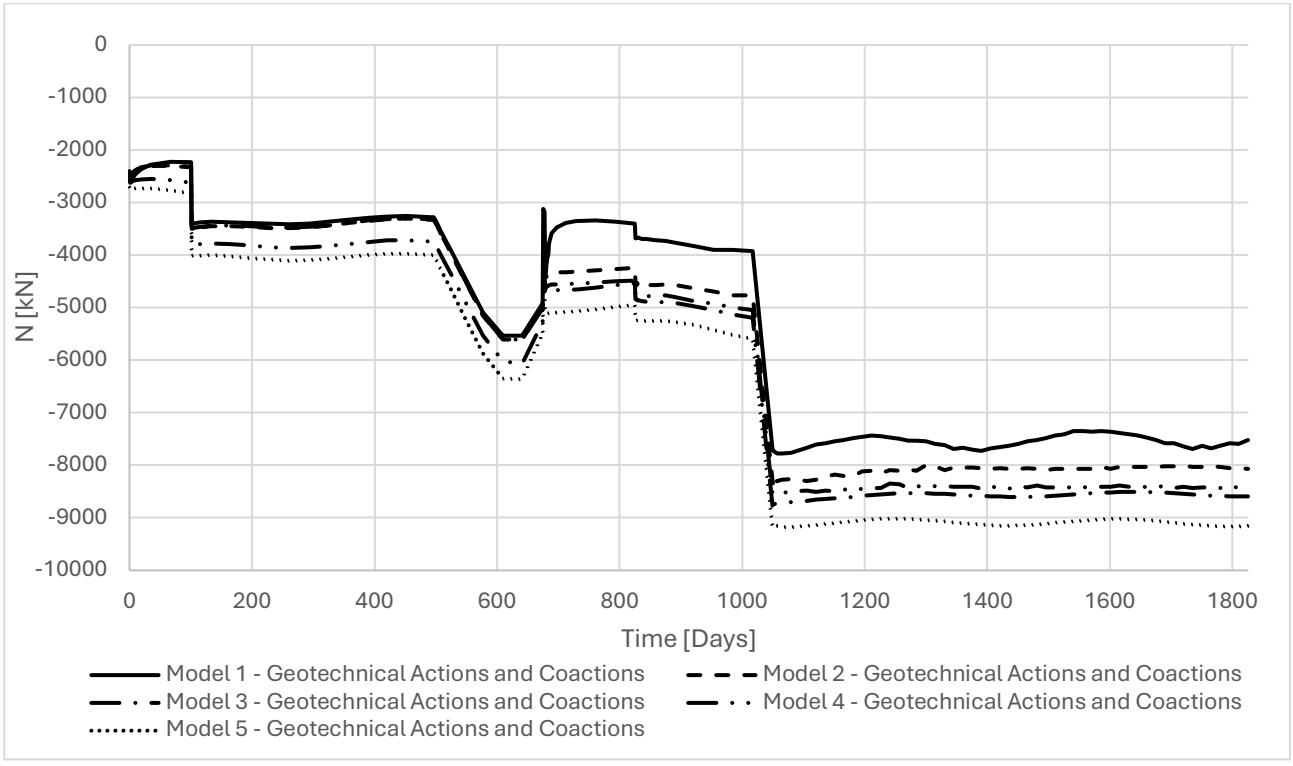


Figure 4-76 - Axial Force - Geotechnical Actions - Pile 2000 Downhill Cover Slab Level

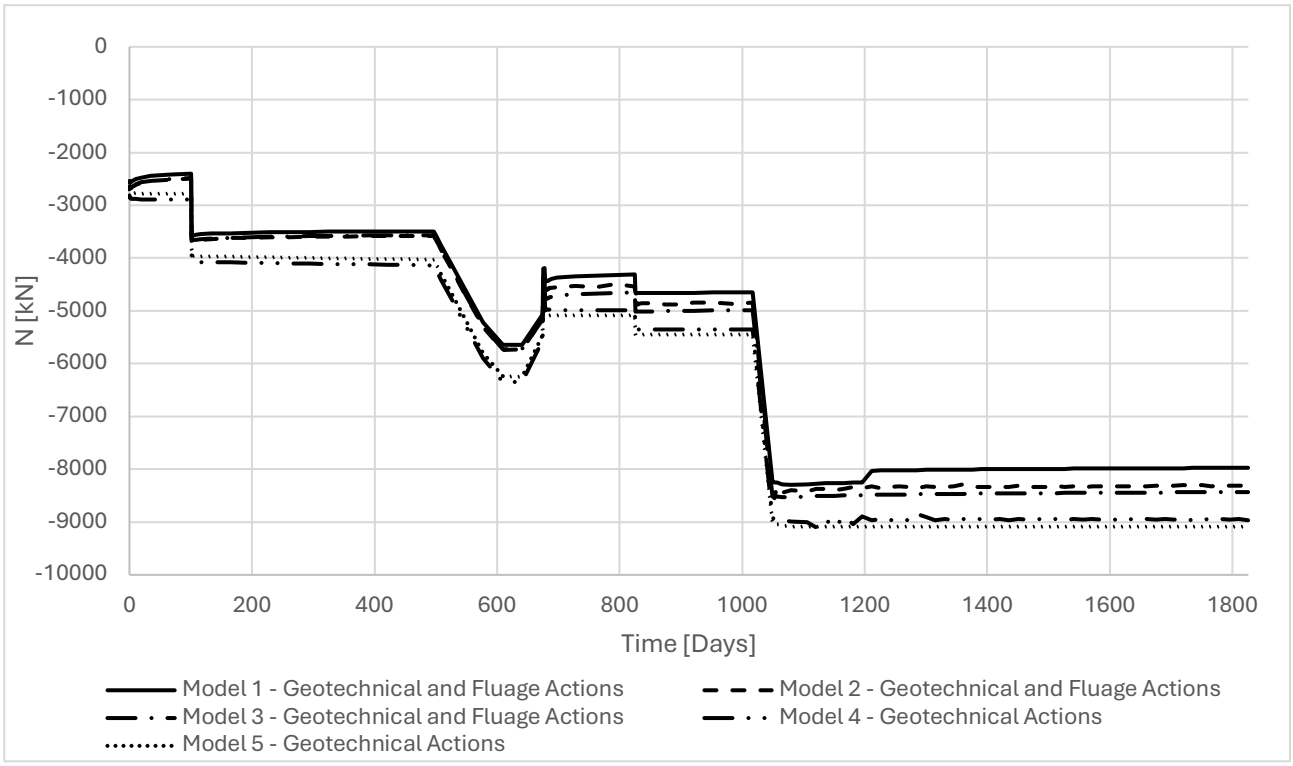


Figure 4-77 - Axial Force - Geotechnical and Creep Actions - Pile 2000 Downhill Cover Slab Level

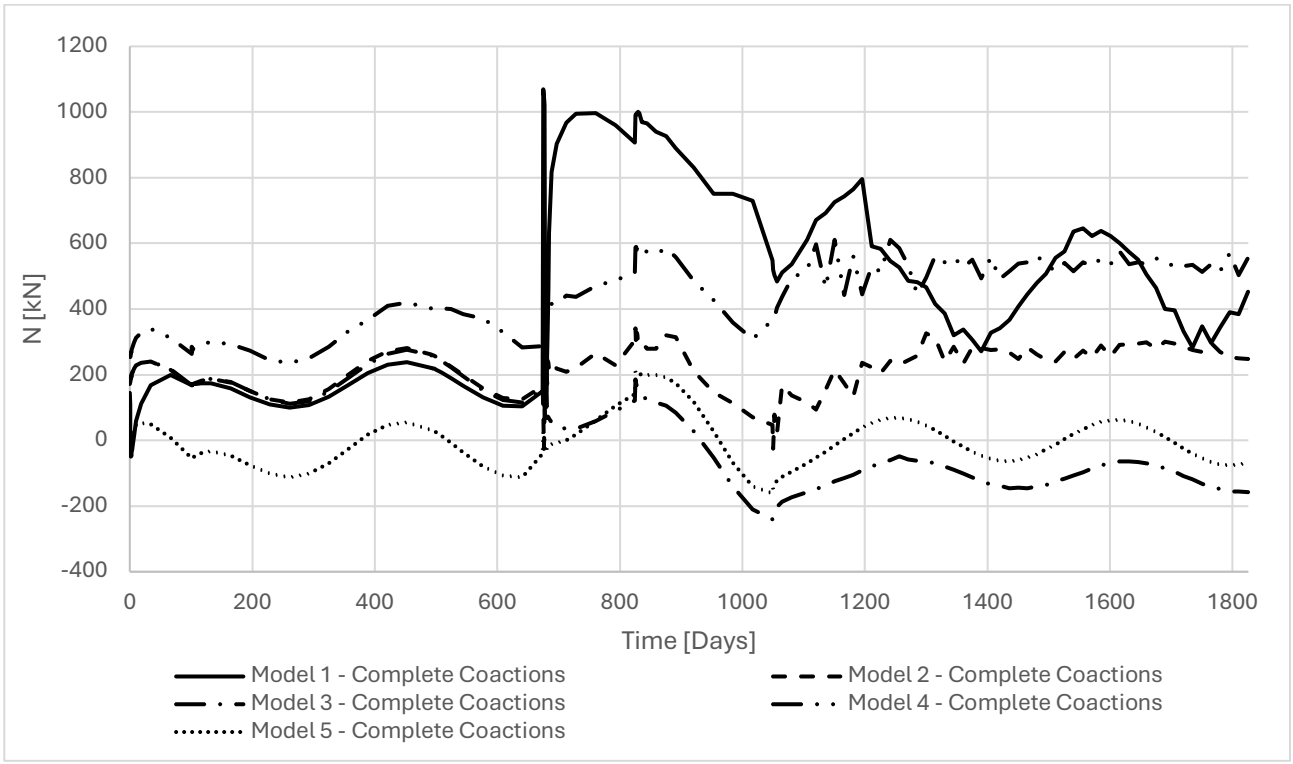


Figure 4-78 - Axial Force - Complete Coactions - Pile 2000 Downhill Cover Slab Level

Shear force diagrams:

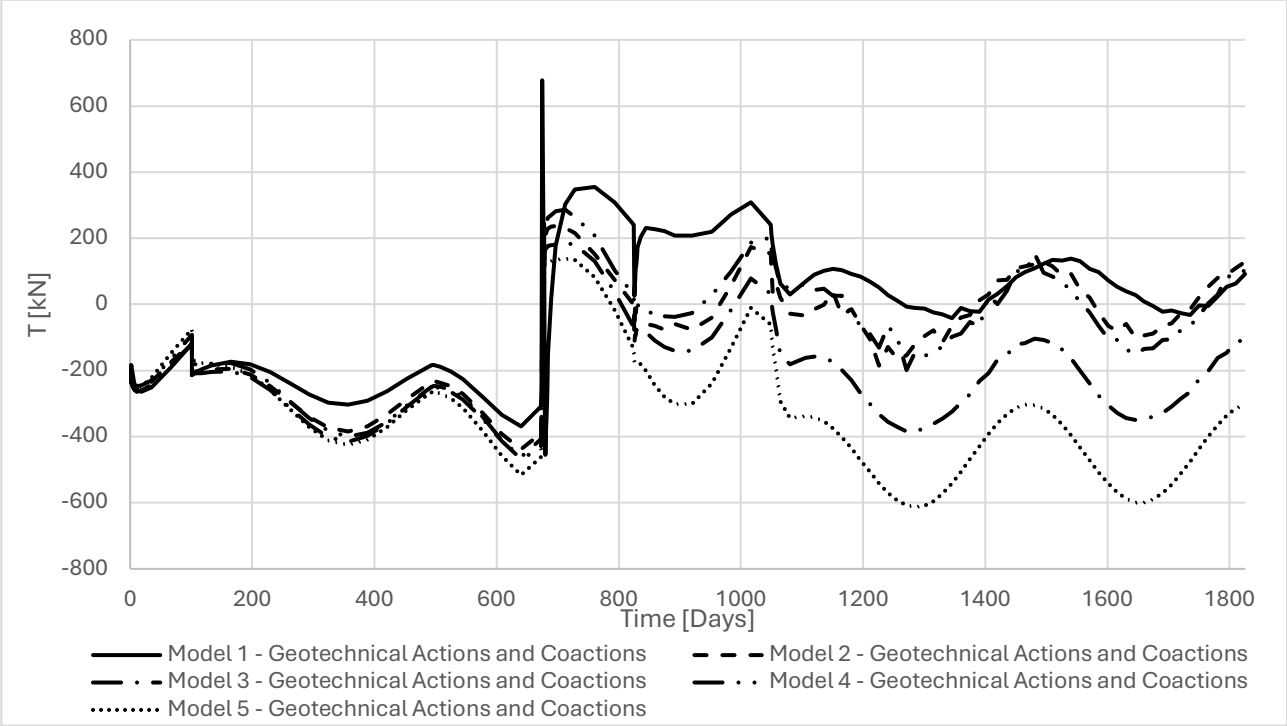


Figure 4-79 – Shear Force - Geotechnical Actions and Coactions - Pile 2000 Downhill Cover Slab Level

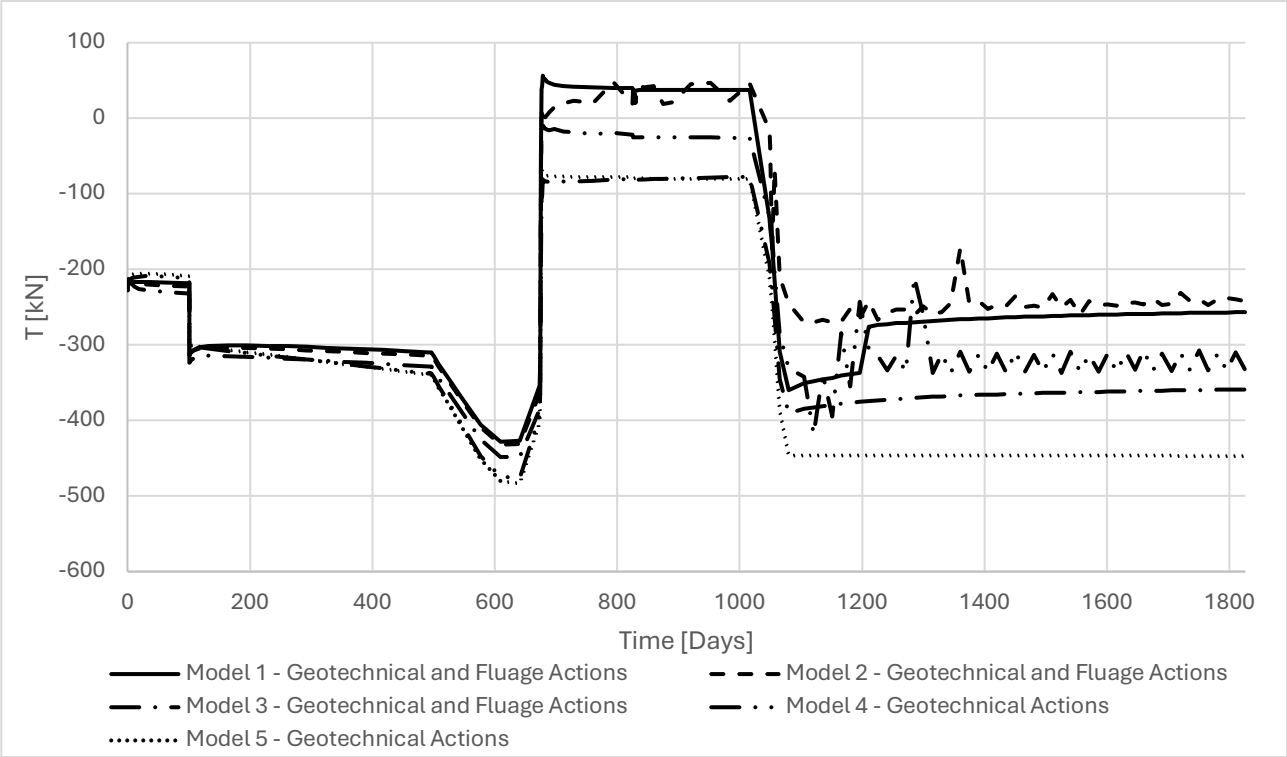


Figure 4-80 – Shear Force - Geotechnical and Creep Actions - Pile 2000 Downhill Cover Slab Level

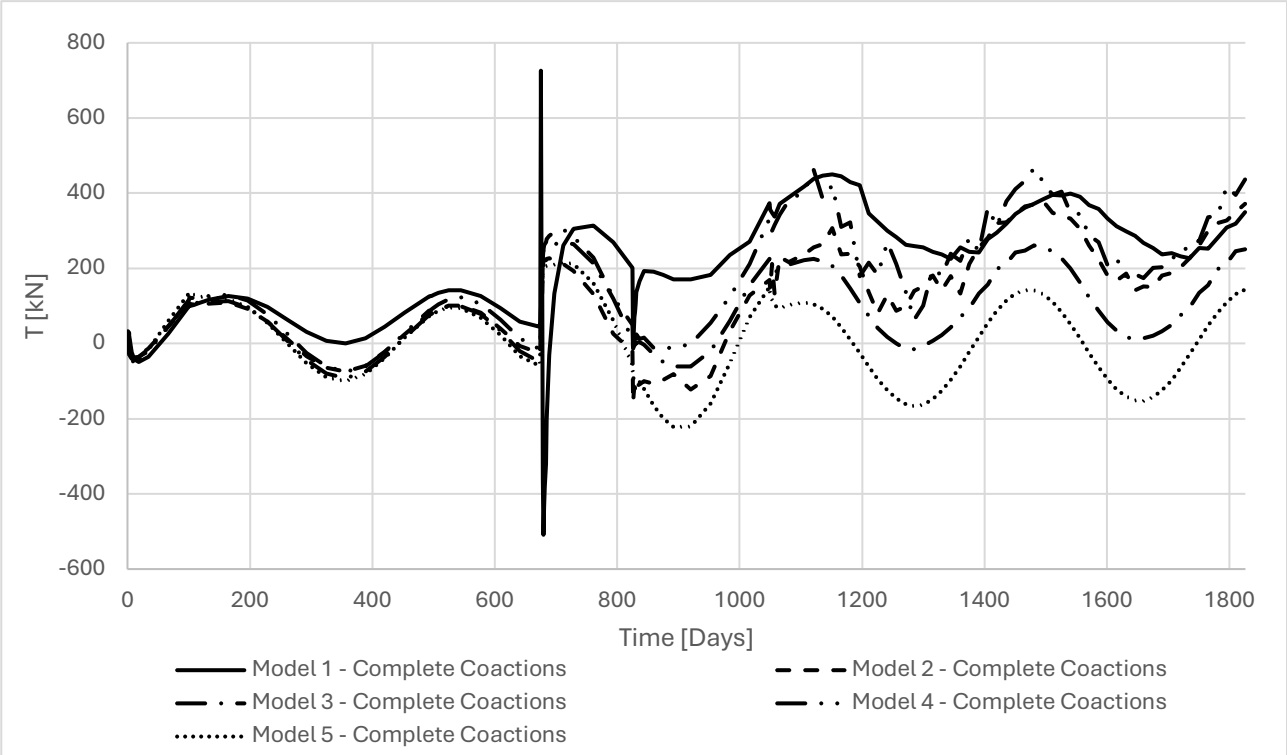


Figure 4-81 – Shear Force - Complete Coactions - Pile 2000 Downhill Cover Slab Level

4.4.3 Discrepancies between Models and Actions Combinations

Activated on Day 0 ($t = 0$ days), the large-diameter downhill piles ($D = 2000$ mm) carry the structural burden of the valley side. Throughout early site staging ($t = 0$ to 689 days), the pile functions as a vertical cantilever. It retains the outer ground while carrying the growing dead weight of the upper kerbs, top cover slab, and partial backfill. This builds up vertical shaft compression ($N \approx -3000$ to $-3500\ kN$ at the head, Figure 4-67 and Figure 4-68) $N \approx -2500$ to $-4000\ kN$ at the cover slab level; Figure 4-76 and Figure 4-77) along with moderate cantilever bending. Then comes day 689: bulk excavation in phase 6 suddenly strips away passive earth resistance in front of the shaft. The structural response shifts instantly. Lateral earth pressures force the pile into a framed mechanism, driving positive flexure at the head up to $M \approx +6000$ to $+8500\ kN*m$ (Figure 4-64) and plunging head shear to $T \approx -3300$ to $-3800\ kN$(Figure 4-71). At the cover slab connection, this excavation shock triggers an abrupt plunge into negative hogging: $M \approx -4000$ to $-4900\ kN*m$, alongside a positive shear surge in Model 1, $T \approx +680\ kN$ in the Figure 4-79 and the Figure 4-81.

Tracking these early stages with degree-of-reaction thermo-mechanical coupling reveals sharp transient coactions that standard formulations does not catch due to the omission of the creep phenomena. Concrete hydration cooling in the first 20 days drops the head moment from $+3500\ kN*m$ down to $+1000\ kN*m$ (Figure 4-64), while inducing negative bending at the cover slab level ($M \approx -300\ kN*m$). The true thermal shock arrives at $t = 841$ days during wall casting. As the freshly poured walls heat up and expand upward against the rigid top node, model 1 records a massive transient tension jump of $\Delta N \approx +2800\ kN$ at the pile head (Figure 4-67 and Figure 4-69) and $\Delta N \approx +2400\ kN$ at the cover slab level (Figure 4-76 and Figure 4-78). Concurrently, this upward thermal thrust sparks an acute flexural rebound at the cover slab connection ($\Delta M \approx +1800\ kN*m$) and a localized shear surge of $\Delta T \approx +1100\ kN$at the head. Standard models bypass these exothermic transients entirely, plotting smooth, artificial curves that overlook potential early cracking damage.

Once complete backfilling is applied at $t = 1065$ days (phase 9), long-term viscoelastic creep takes over as the primary stress-relief engine. Purely elastic or unrelaxed models lock in severe, unyielding force concentrations. Model 5 retains an unrelaxed sustained moment of $M = +9250\ kN*m$ at the head (Figure 4-65), an extreme sustained head shear of $T = -4080\ kN$ (Figure 4-71), and a sustained compressive thrust of $N = -9100\ kN$ at the cover slab level (Figure 4-77). Non-linear models with creep tell a completely different story. Viscous flow allows the pile shaft to adapt to subgrade deformation and shed stress into the surrounding soil mass. Sustained head flexure in model 1 relaxes to $M \approx +7000\ kN*m$, a 24% reduction or $2250\ kN*m$ of flexural relief relative to model 5 as shown in Figure 4-65. Sustained head shear drops to $T \approx -3550\ kN$: 13.0% relief illustrated in Figure 4-71. At the cover slab level, viscous redistribution relaxes sustained shear from $-450\ kN$ in model 5 down to $T \approx -260\ kN$ in model 1: a 42% shear relief (Figure 4-80).

In the long-term cyclic regime ($t > 1122$ days), the linear elastic baseline tends to overestimate the seasonal thermal swings. Model 5 treats thermal expansion as an unyielding external force, driving head moments to an extreme summer peak of $M \approx +11900\ kN*m$ (Figure 4-64) and forcing cyclic axial excursions across a massive range of $\Delta N \approx 5700\ kN$ (Figure 4-67). It similarly overpredicts cyclic shear demands, pushing winter shear to $-5100\ kN$ at the head and -620 kN at the cover slab level. Non-linear cracking and creep relaxation drastically compress these cyclic envelopes. In model 1, peak summer head moment is capped at $M \approx +7100\ kN*m$, 40% lower than model 5. Head axial fluctuations are damped to $\Delta N \approx 1300\ kN$, a 77% reduction versus model 5 (Figure 4-67). At the cover slab level, cyclic shear is held near

neutral equilibrium ($T \approx -50$ to $+100\ kN$, Figure 4-79), cutting peak winter shear demand by 92% compared to Model 5.

4.5 Foundation Slab

The analysis focuses on three critical sections: the rigid connection to the uphill bulkhead layout, the central midspan node, and the rigid connection to the downhill wall.

4.5.1 Uphill Support

Moment diagrams:

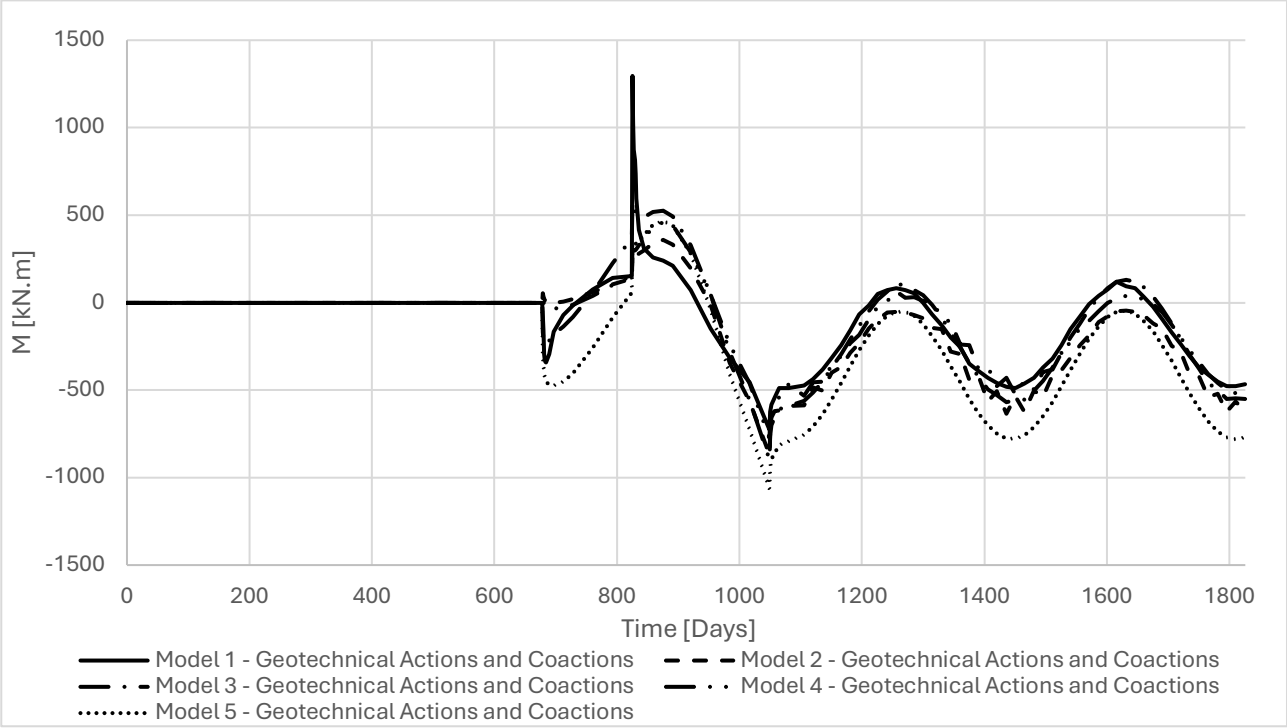


Figure 4-82 - Moment - Geotechnical Actions and Coactions - Foundation Slab Uphill Support

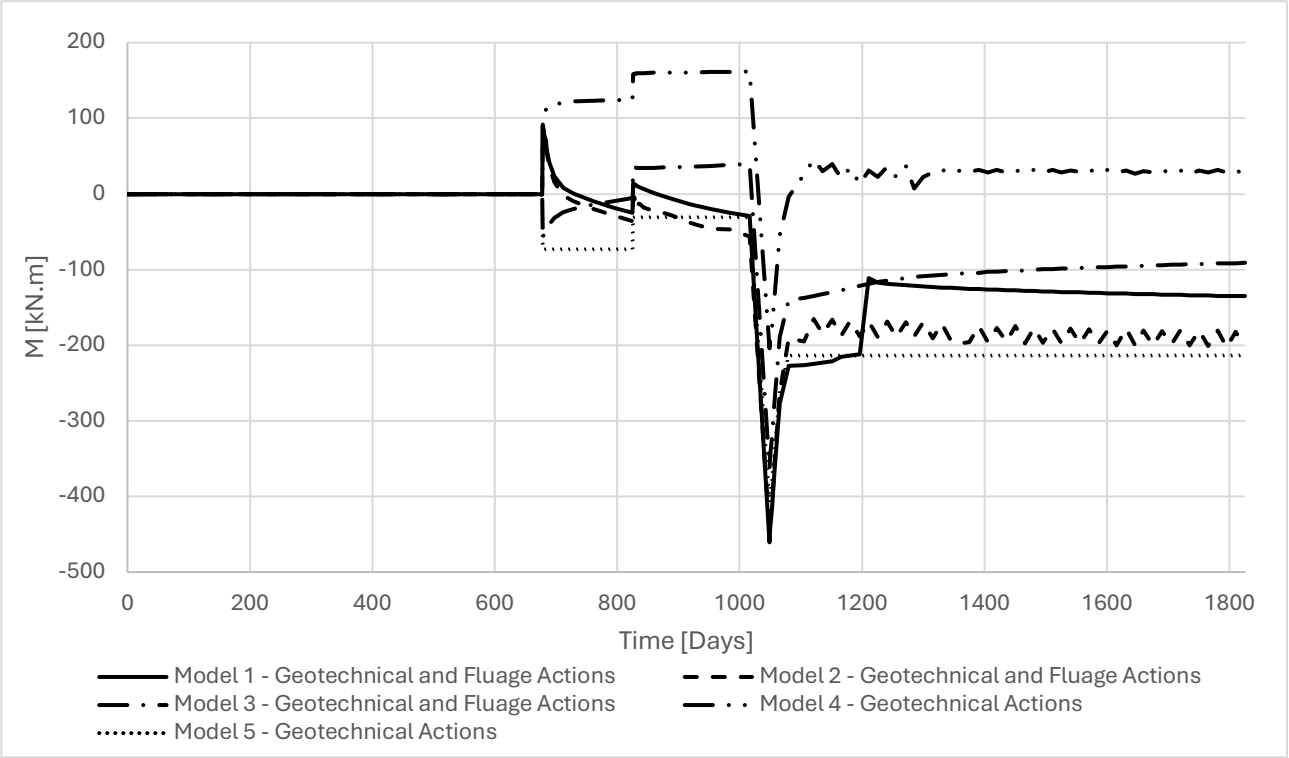


Figure 4-83 - Moment - Geotechnical and Creep Actions - Foundation Slab Uphill Support

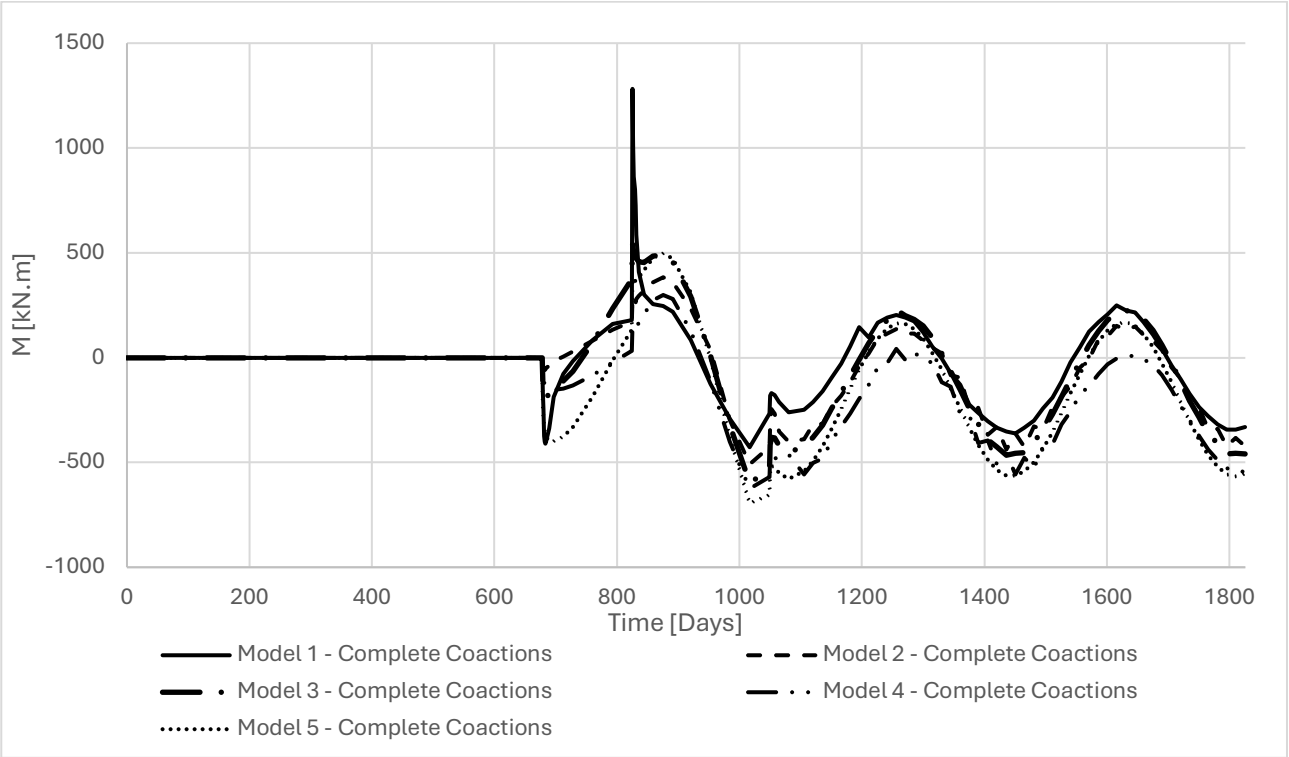


Figure 4-84 - Moment - Complete Coactions - Foundation Slab Uphill Support

Axial force diagrams:

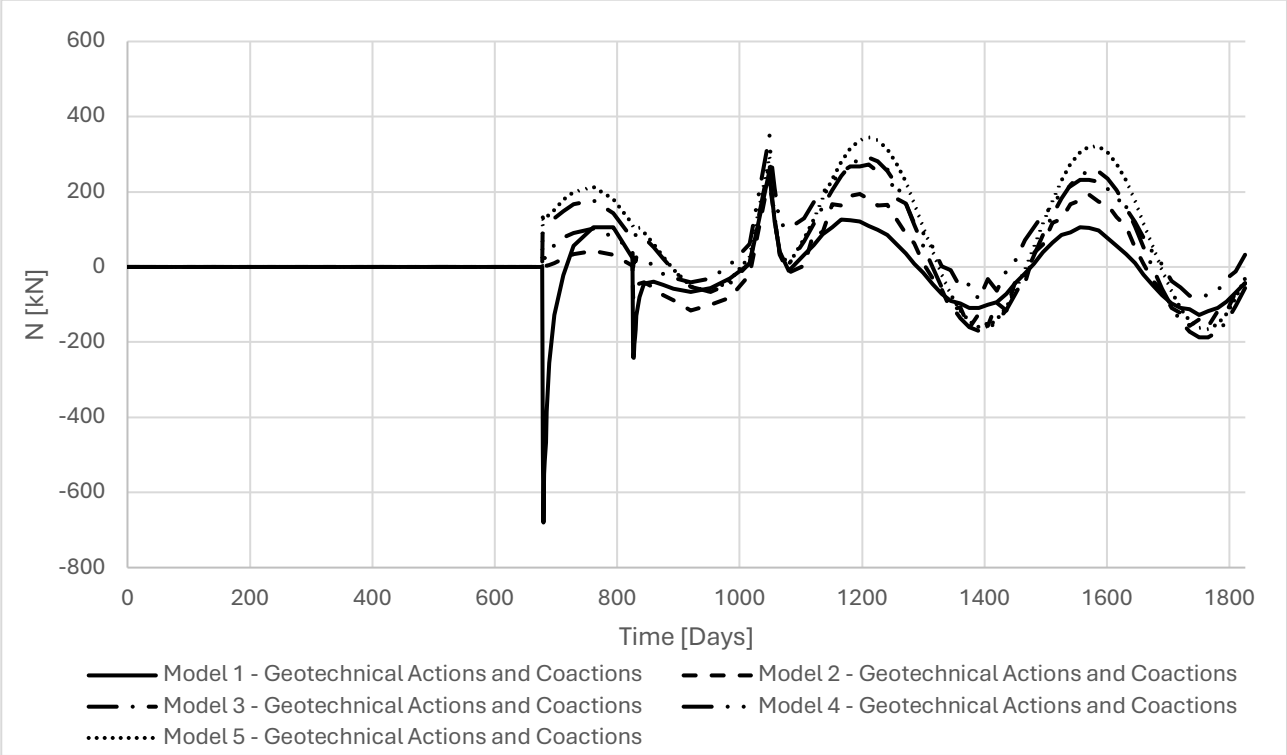


Figure 4-85 - Axial Force - Geotechnical Actions and Coactions - Foundation Slab Uphill Support

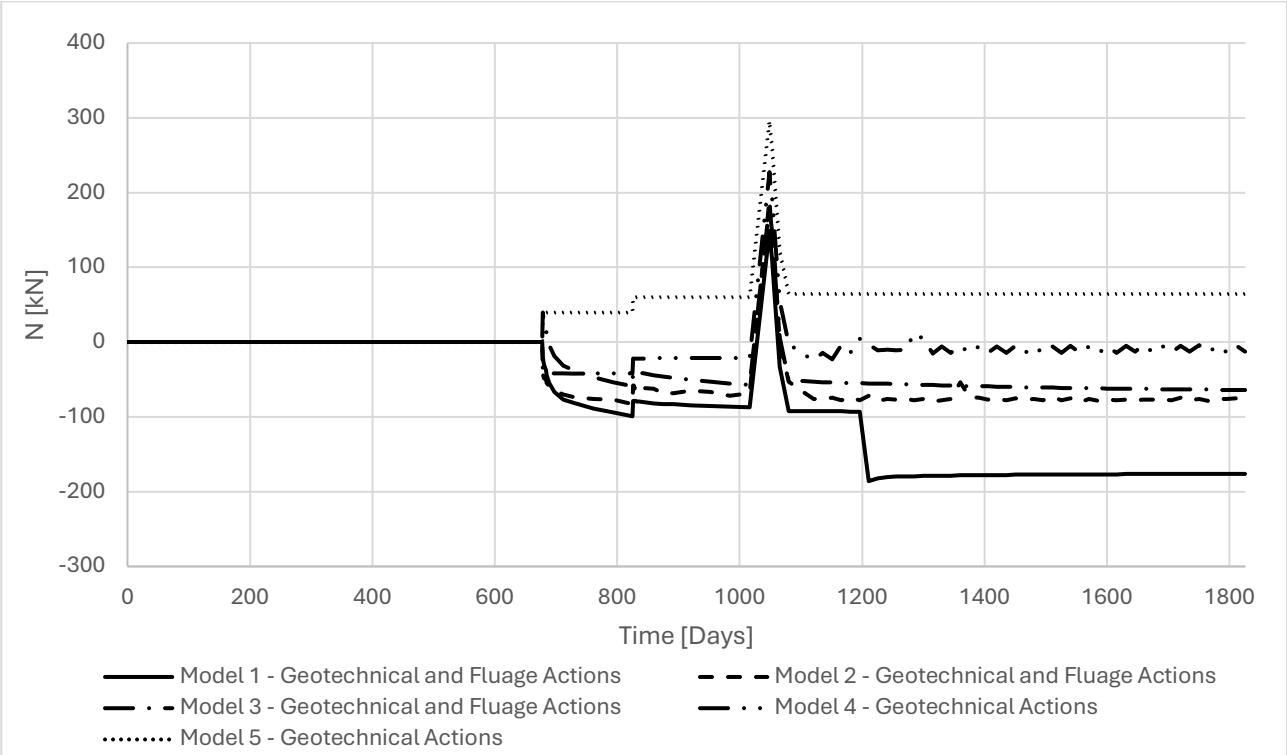


Figure 4-86 - Axial Force - Geotechnical and Creep Actions - Foundation Slab Uphill Support

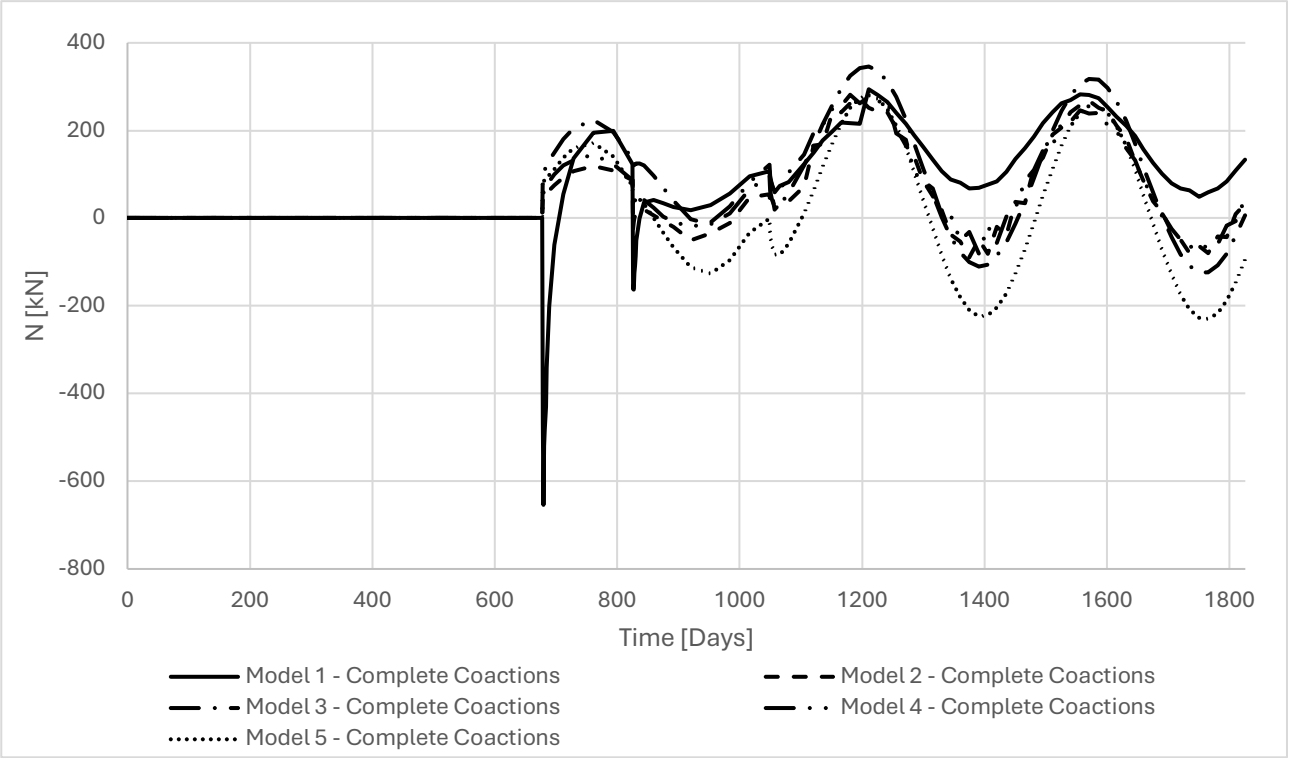


Figure 4-87 - Axial Force - Complete Coactions - Foundation Slab Uphill Support

Shear force diagrams:

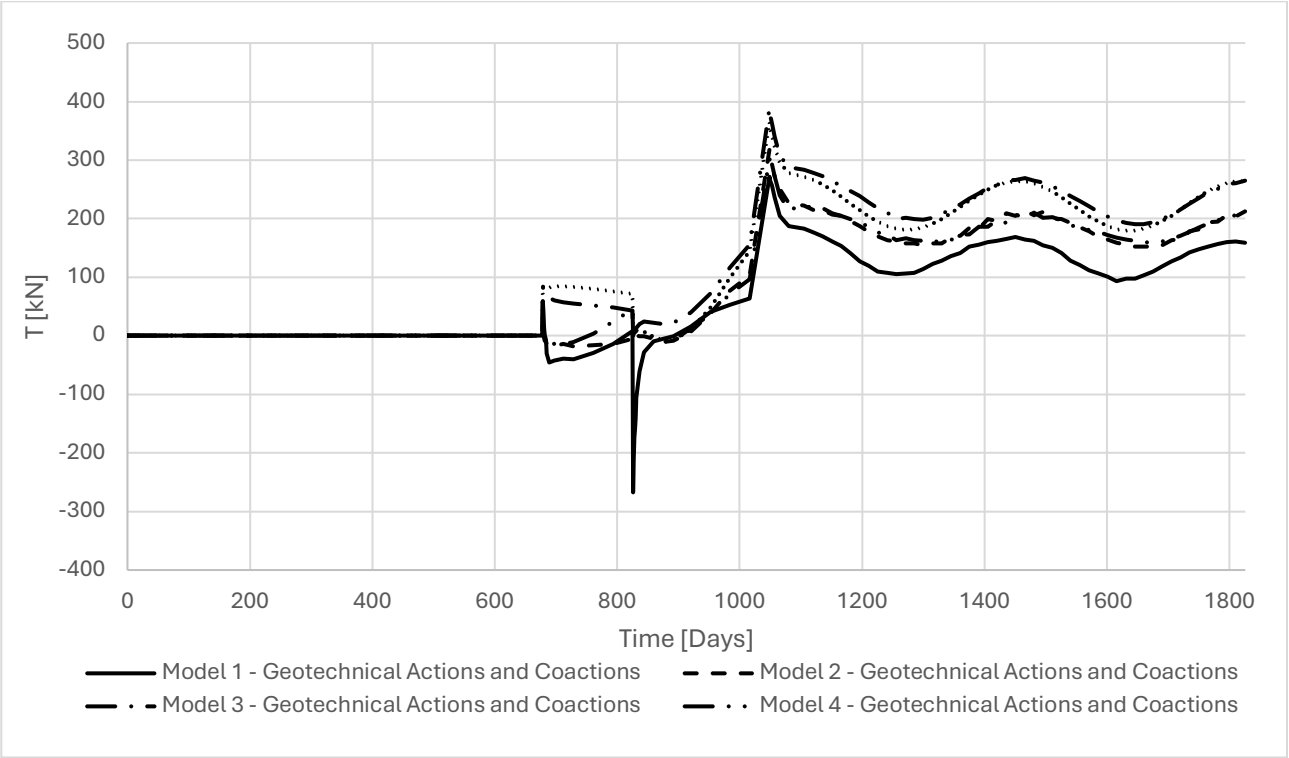


Figure 4-88 – Shear Force - Geotechnical Actions and Coactions - Foundation Slab Uphill Support

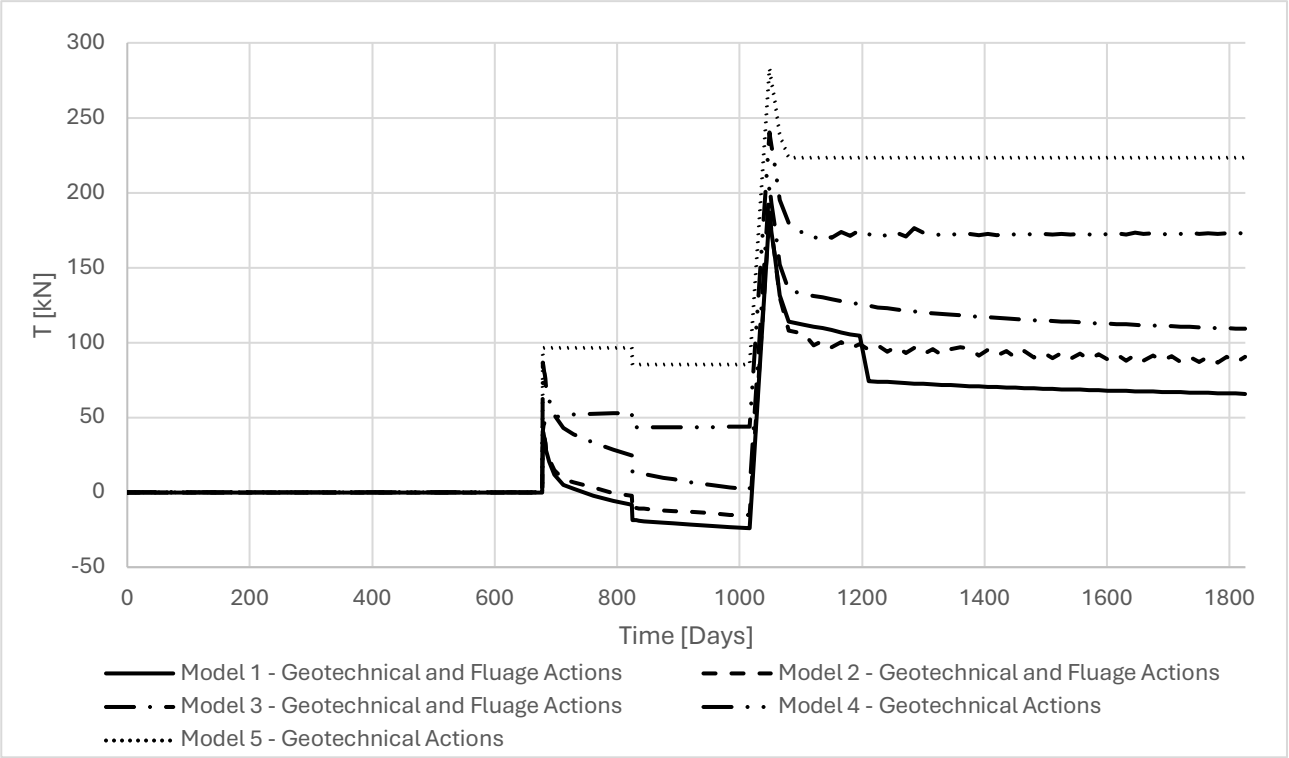


Figure 4-89 – Shear Force - Geotechnical and Creep Actions - Foundation Slab Uphill Support

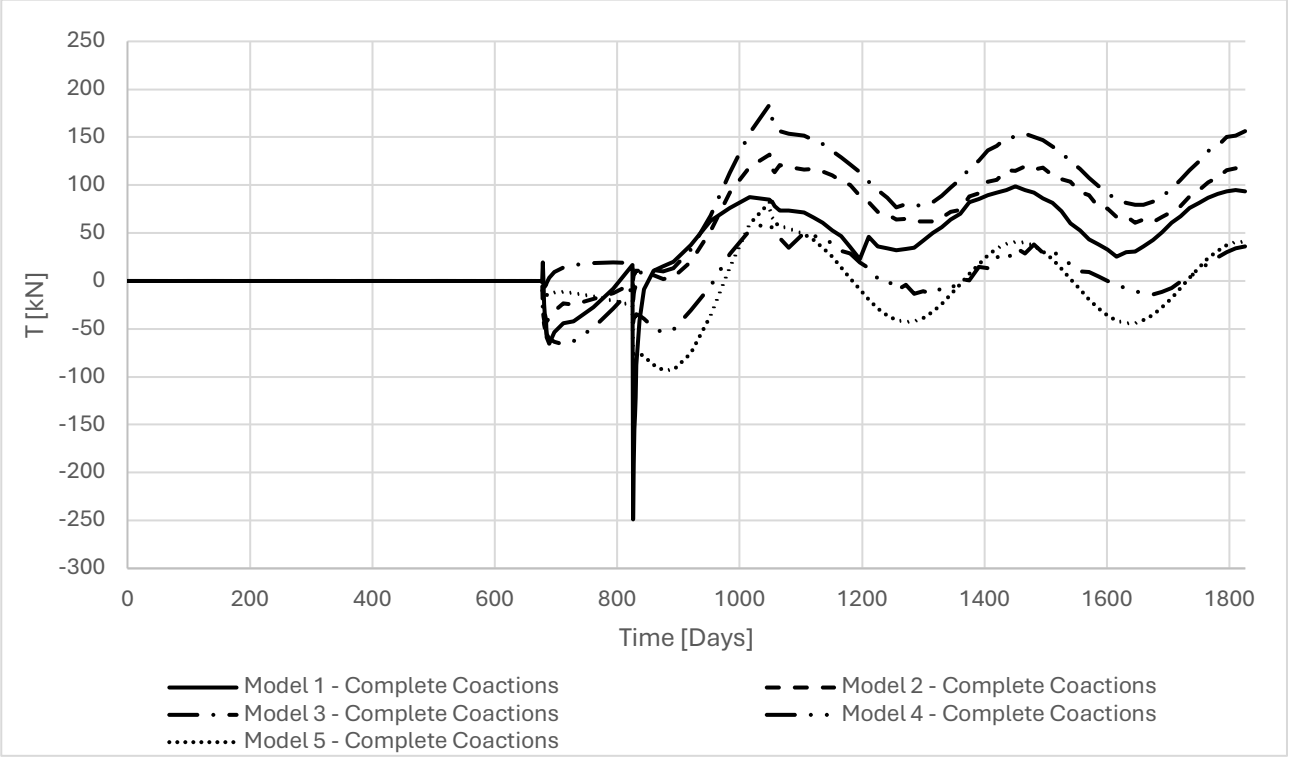


Figure 4-90 – Shear Force - Complete Coactions - Foundation Slab Uphill Support

4.5.2 Midspan Section

Moment diagrams:

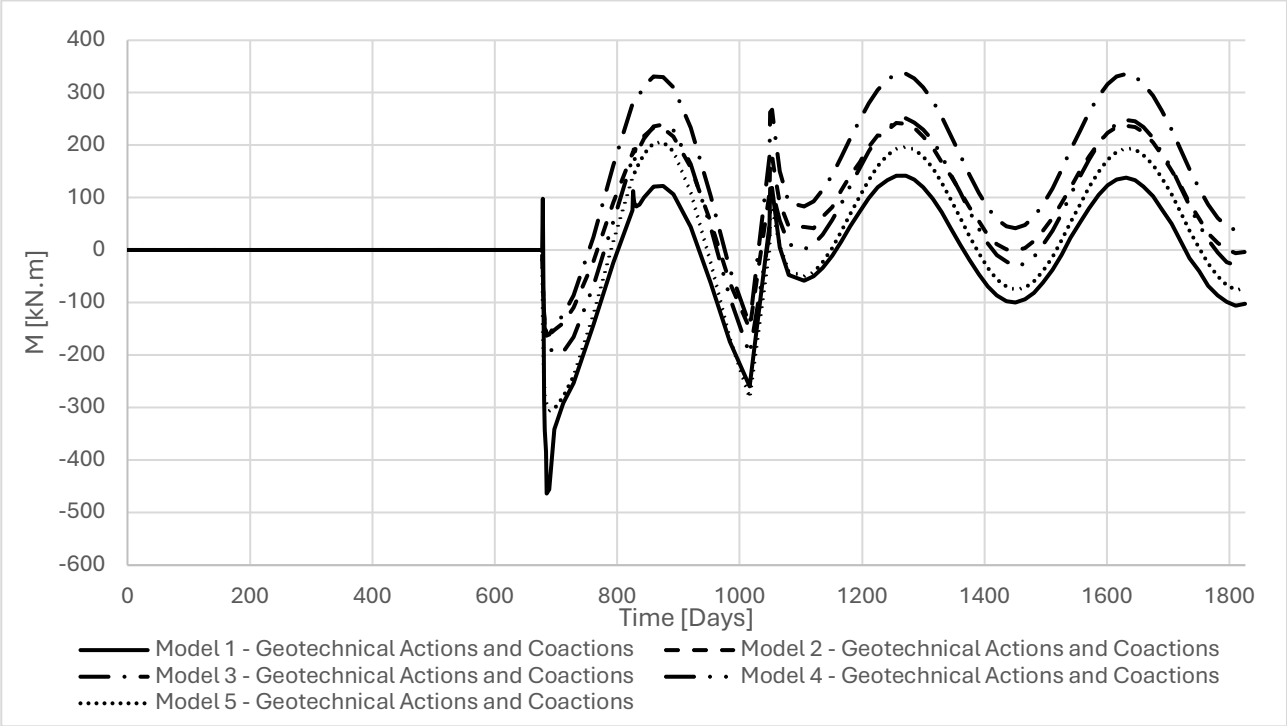


Figure 4-91 - Moment - Geotechnical Actions and Coactions - Foundation Slab Midspan

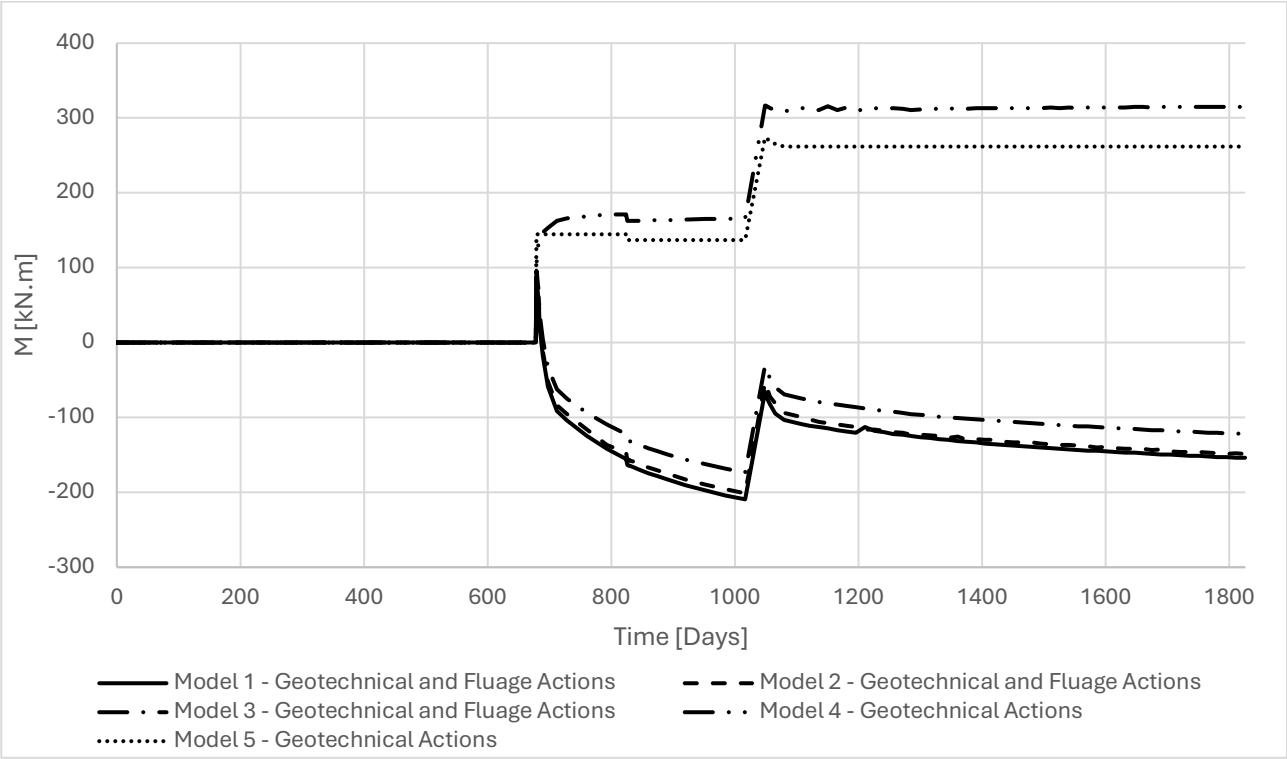


Figure 4-92 - Moment - Geotechnical and Creep Actions - Foundation Slab Midspan

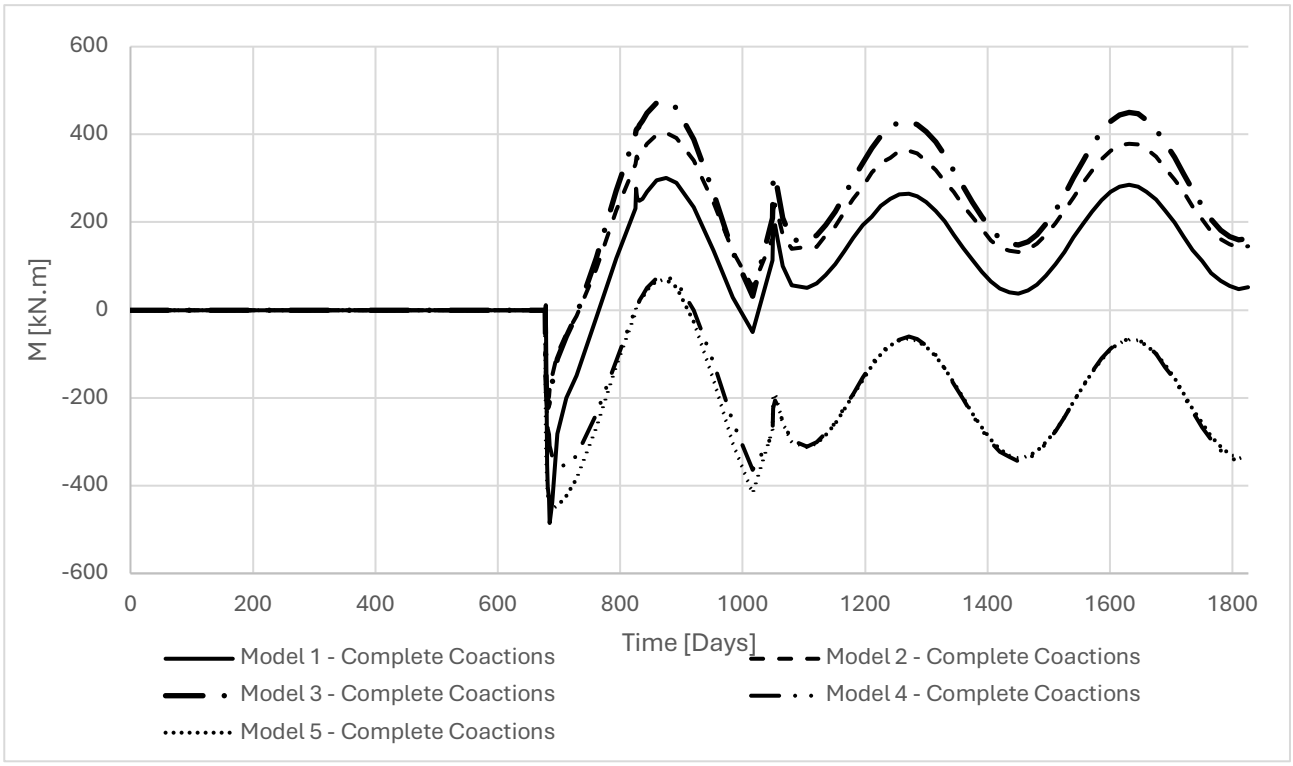


Figure 4-93 - Moment - Complete Coactions - Foundation Slab Midspan

Axial force diagrams:

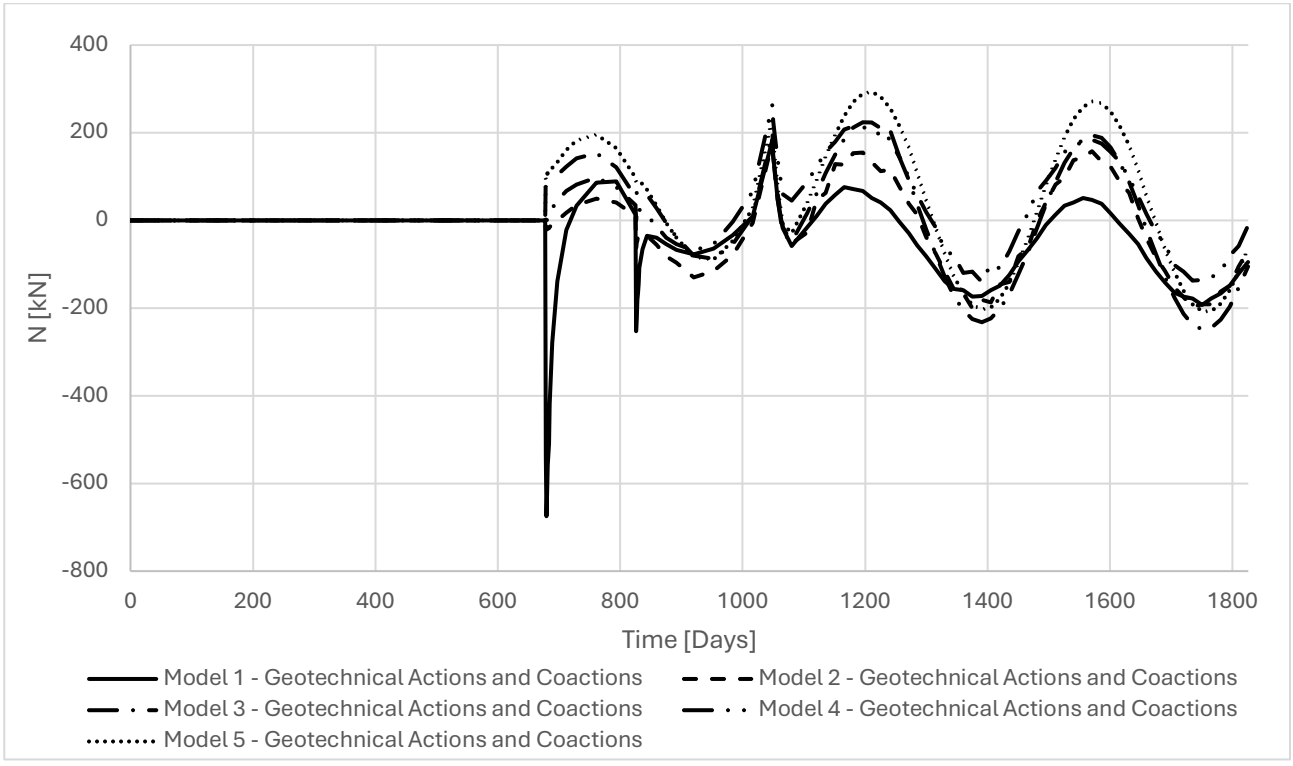


Figure 4-94 - Axial Force - Geotechnical Actions and Coactions - Foundation Slab Midspan

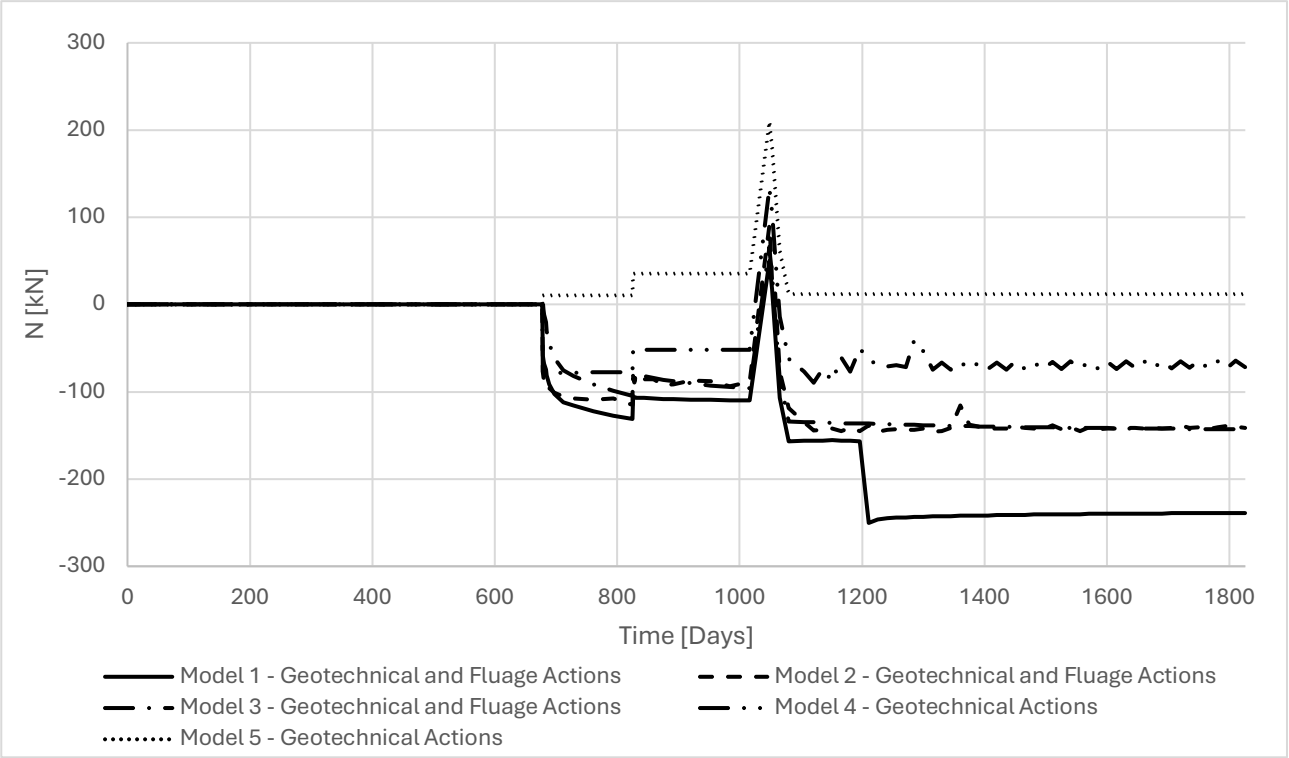


Figure 4-95 - Axial Force - Geotechnical and Creep Actions - Foundation Slab Midspan

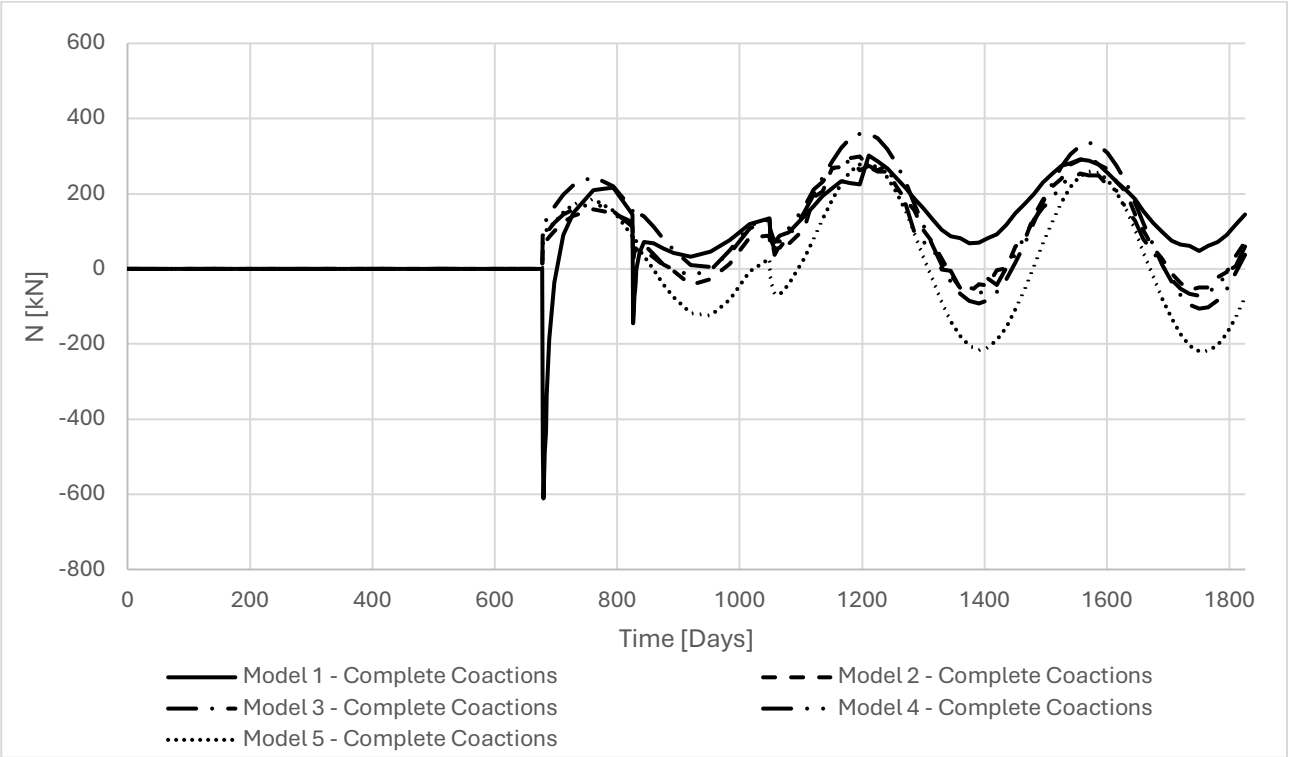


Figure 4-96 - Axial Force - Complete Coactions - Foundation Slab Midspan

Shear force diagrams:

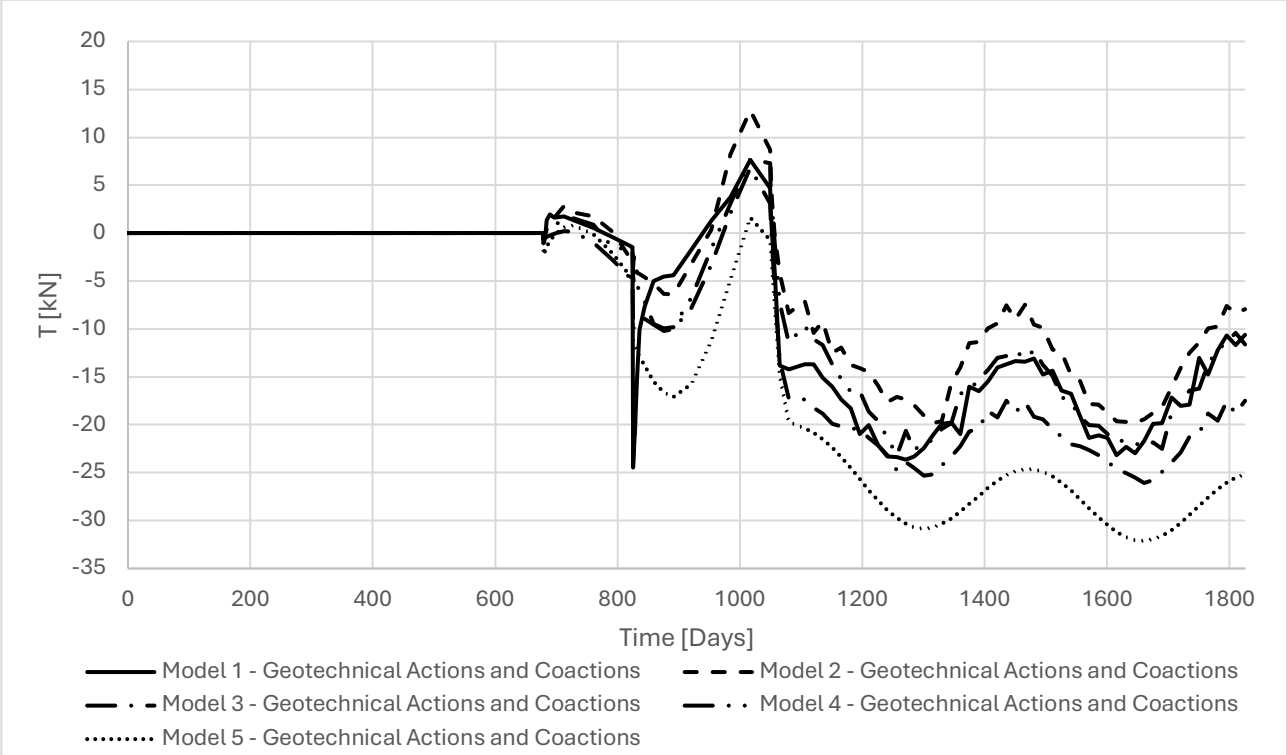


Figure 4-97 – Shear Force - Geotechnical Actions and Coactions - Foundation Slab Midspan

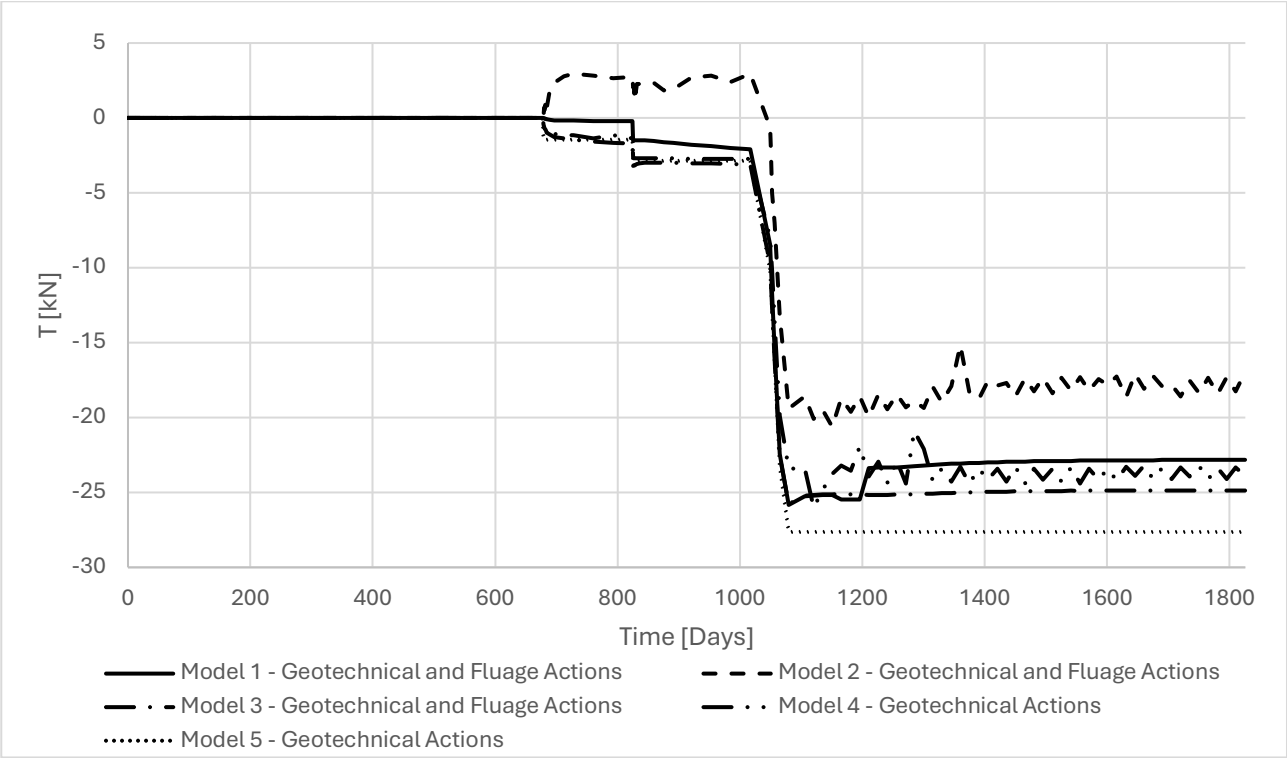


Figure 4-98 – Shear Force - Geotechnical and Creep Actions - Foundation Slab Midspan

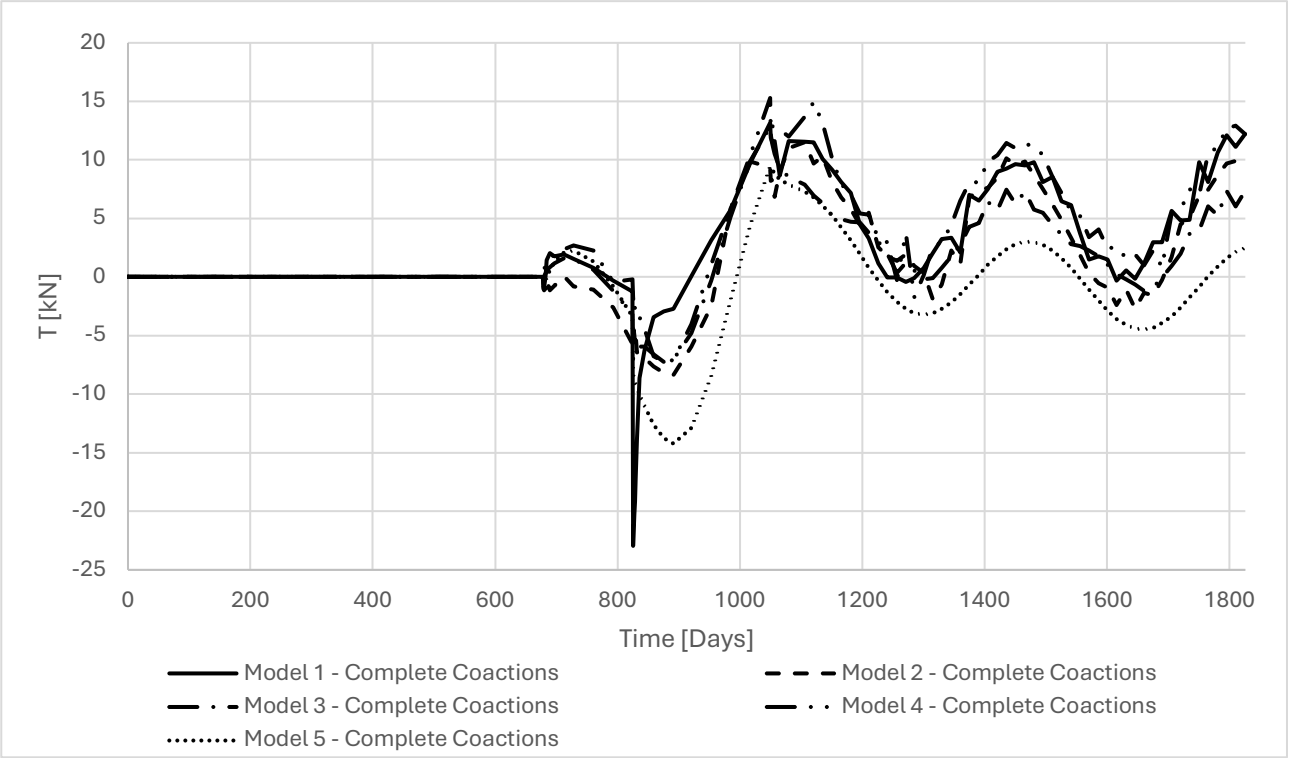


Figure 4-99 – Shear Force - Complete Coactions - Foundation Slab Midspan

4.5.3 Downhill Support Section

Moment diagrams:

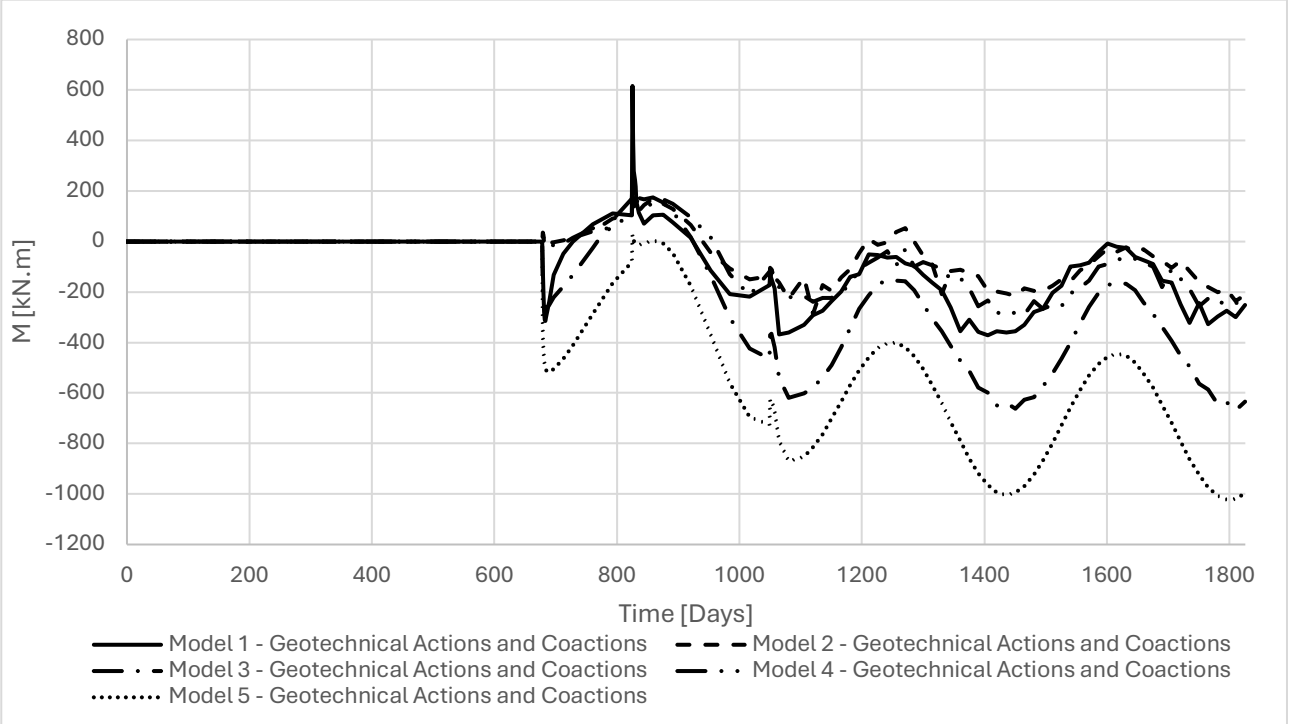


Figure 4-100 - Moment - Geotechnical Actions and Coactions - Foundation Slab Downhill Support

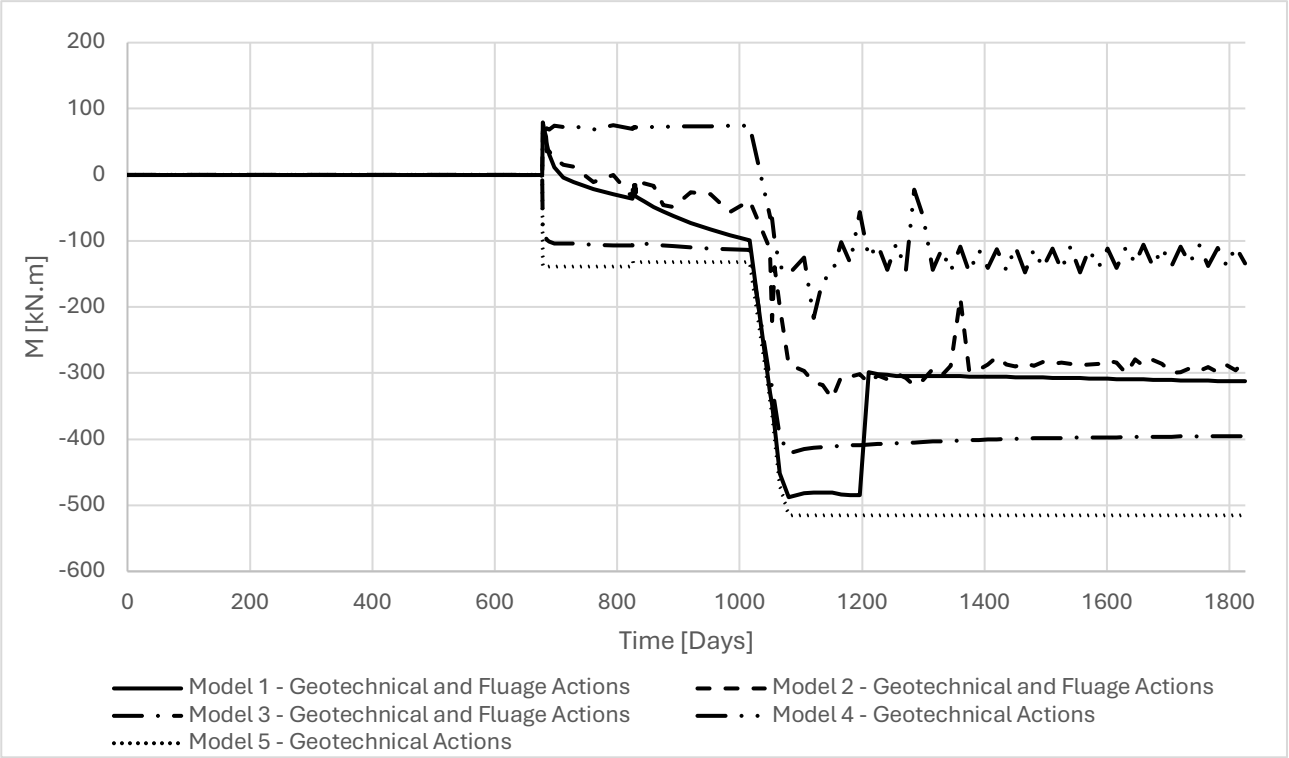


Figure 4-101 - Moment - Geotechnical and Creep Actions - Foundation Slab Downhill Support

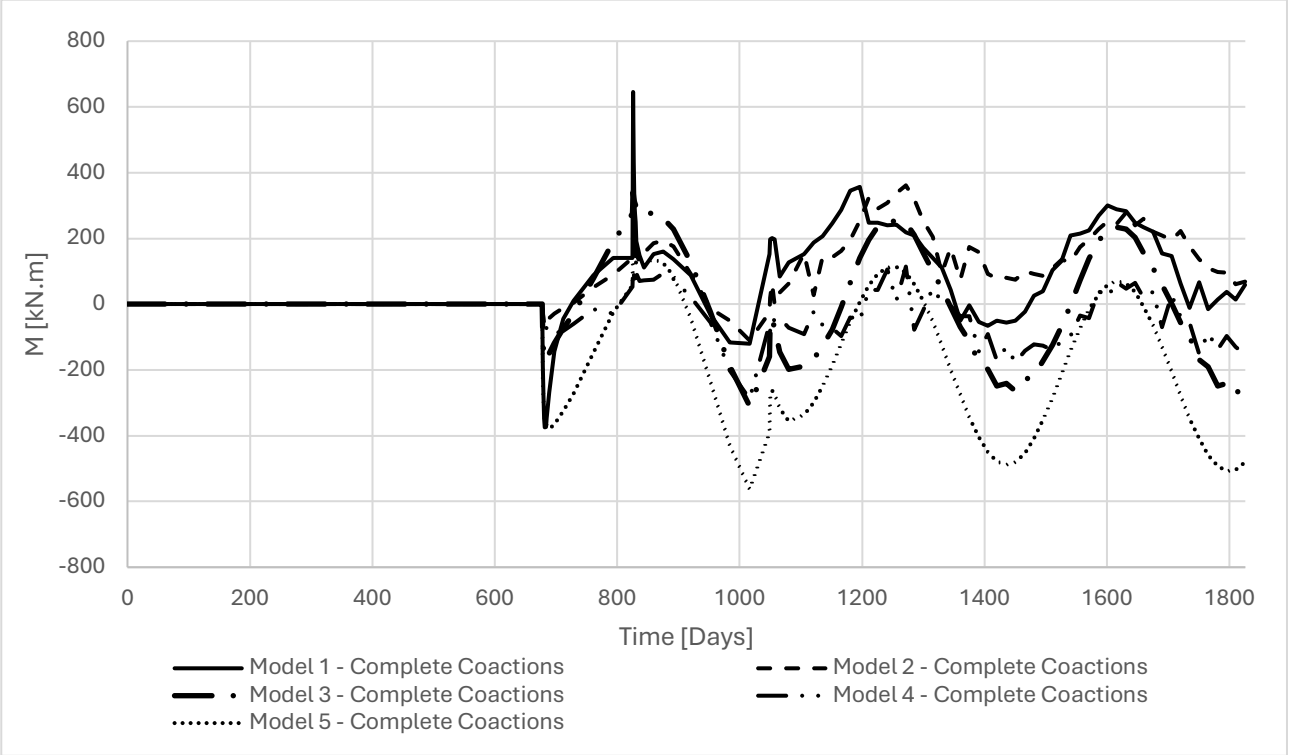


Figure 4-102 - Moment - Complete Coactions - Foundation Slab Downhill Support

Axial force diagrams:

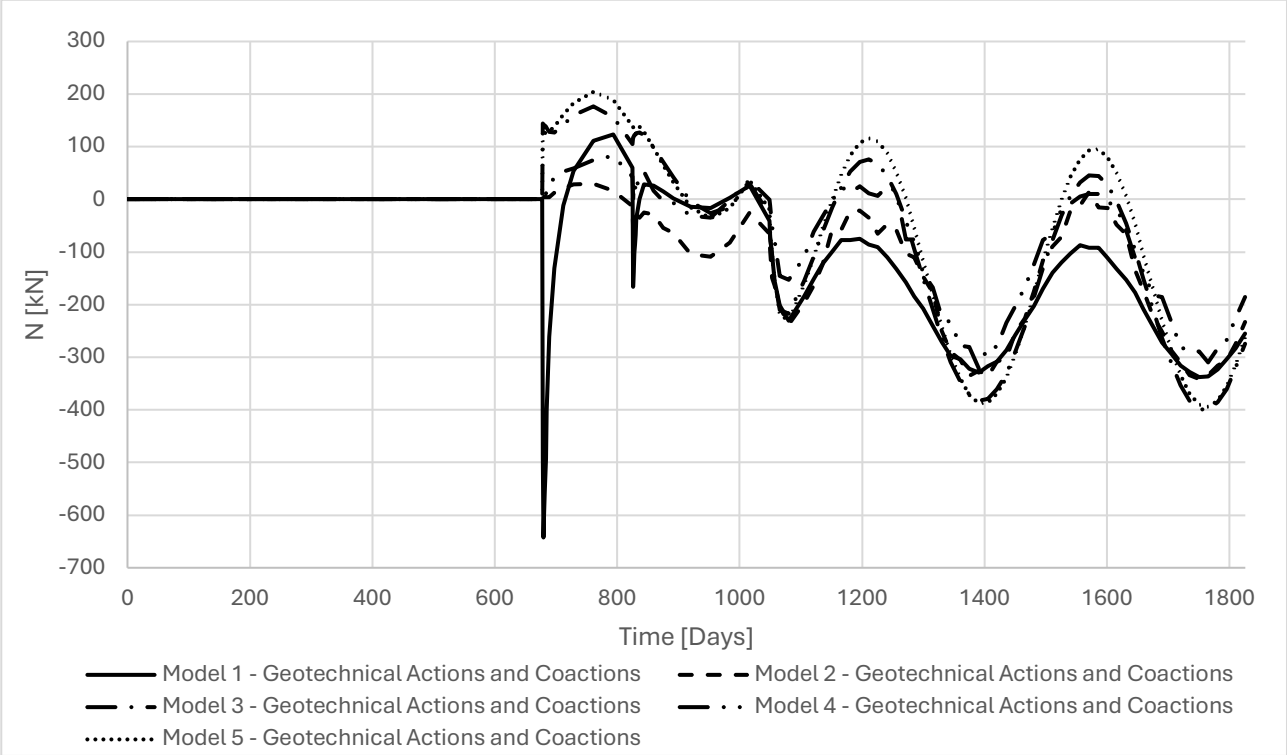


Figure 4-103 - Axial Force - Geotechnical Actions and Coactions - Foundation Slab Downhill Support

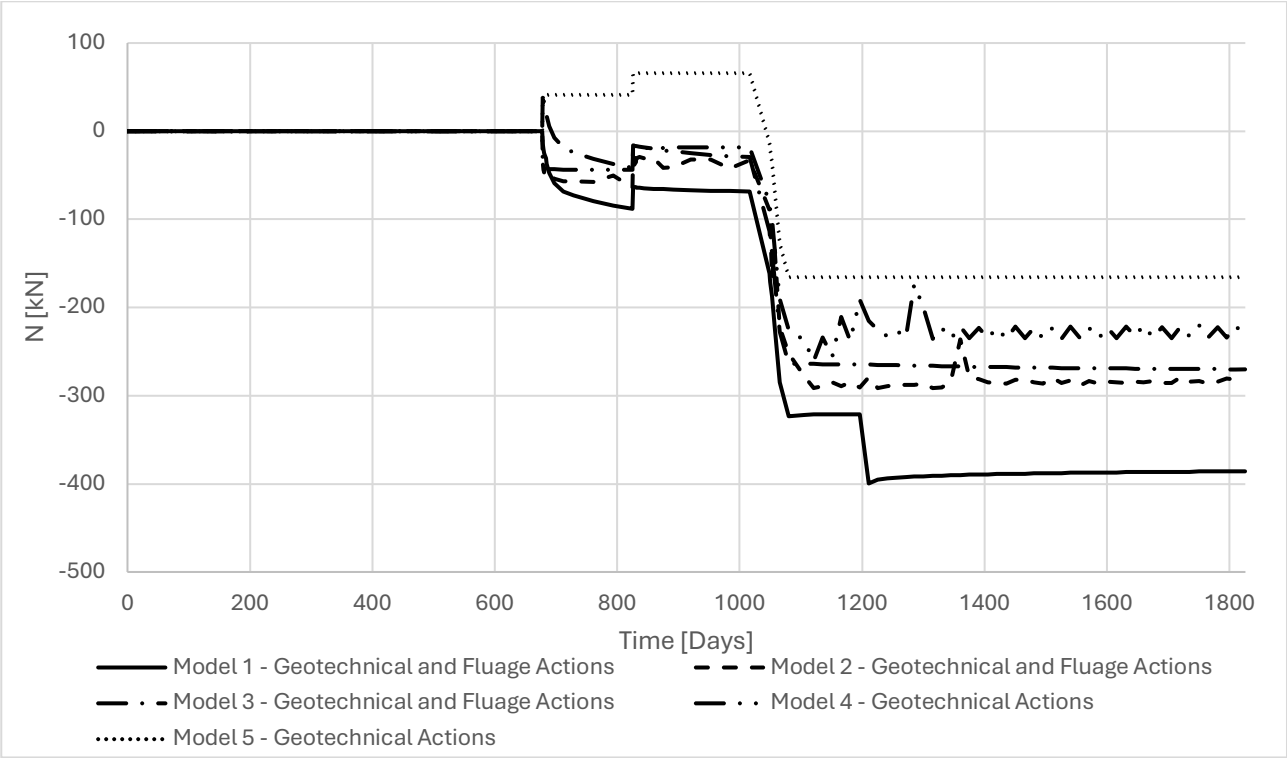


Figure 4-104 - Axial Force - Geotechnical and Creep Actions - Foundation Slab Downhill Support

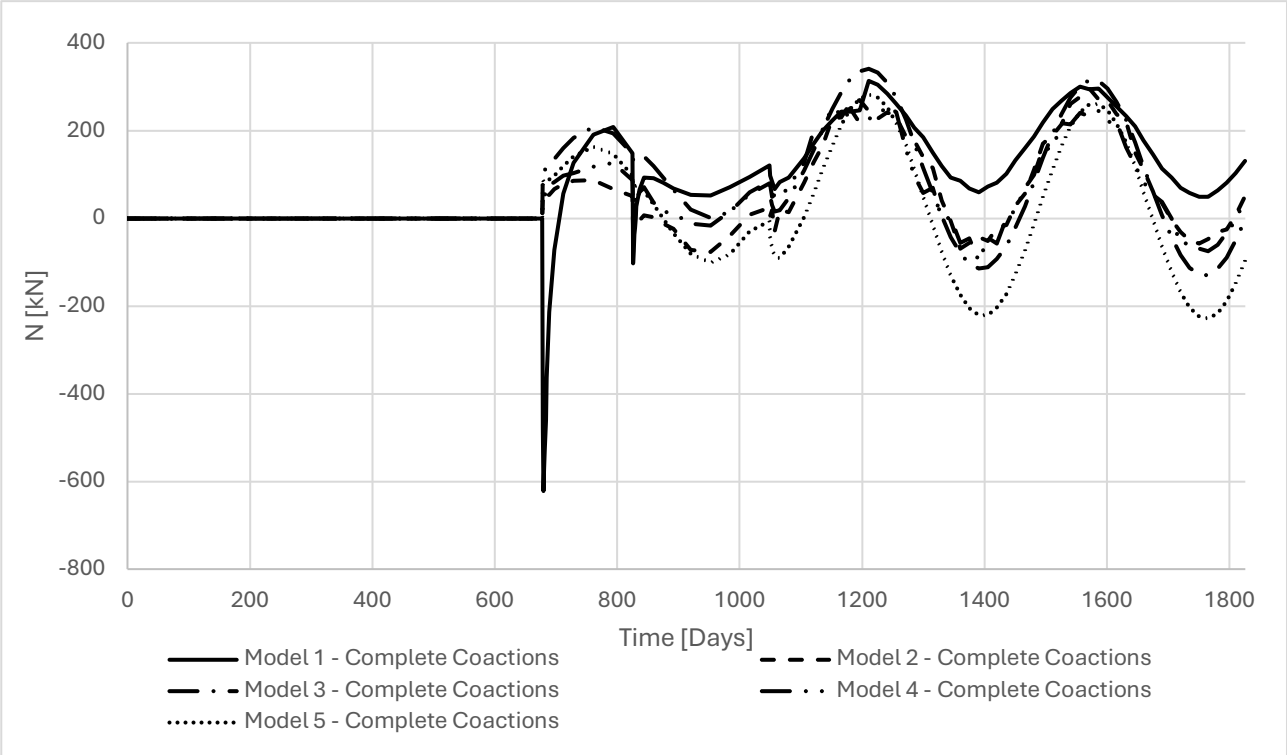


Figure 4-105 - Axial Force - Complete Coactions - Foundation Slab Downhill Support

Shear force diagrams:

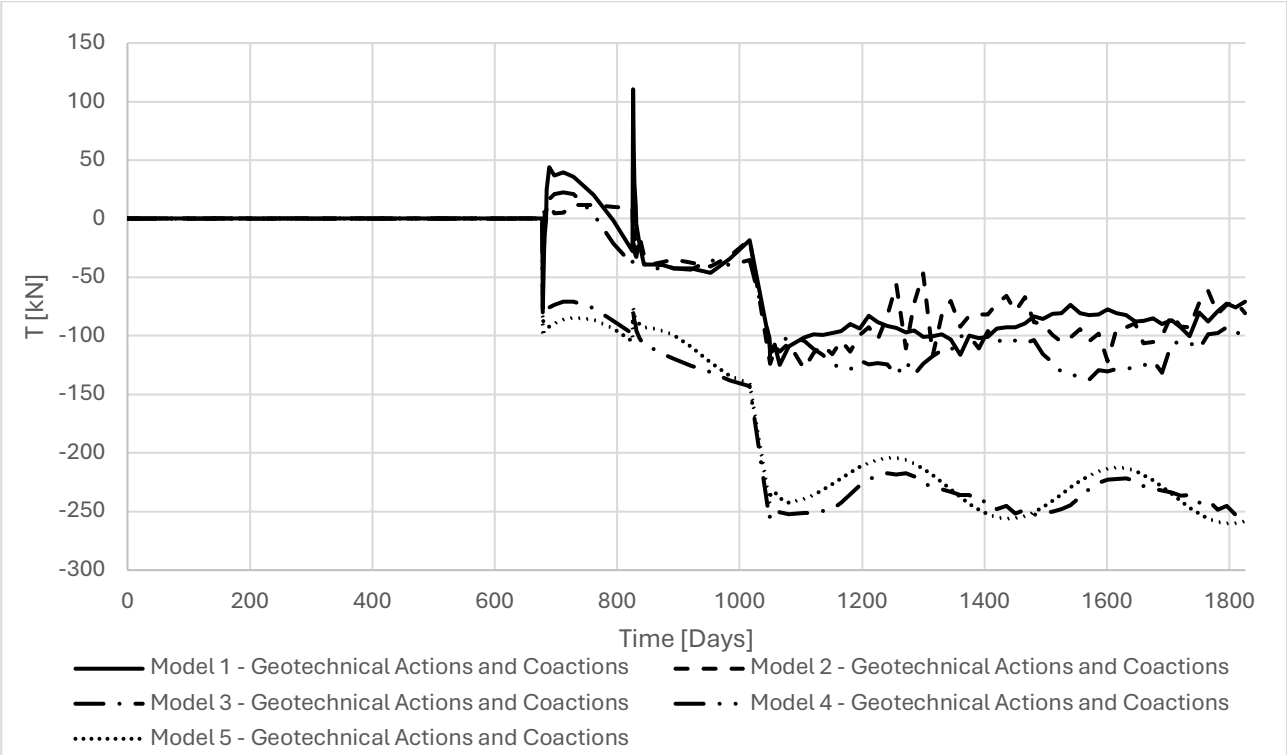


Figure 4-106 – Shear Force - Geotechnical Actions and Coactions - Foundation Slab Downhill Support

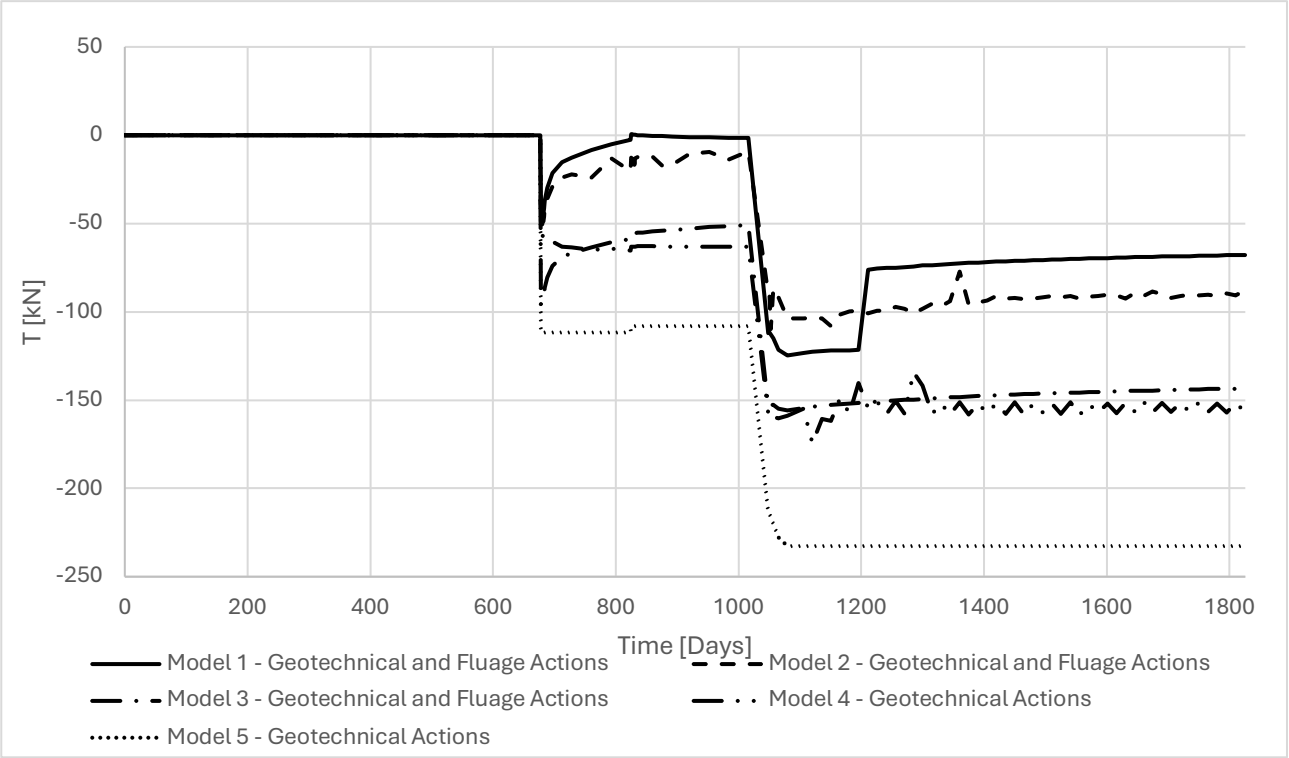


Figure 4-107 – Shear Force - Geotechnical and Creep Actions - Foundation Slab Downhill Support

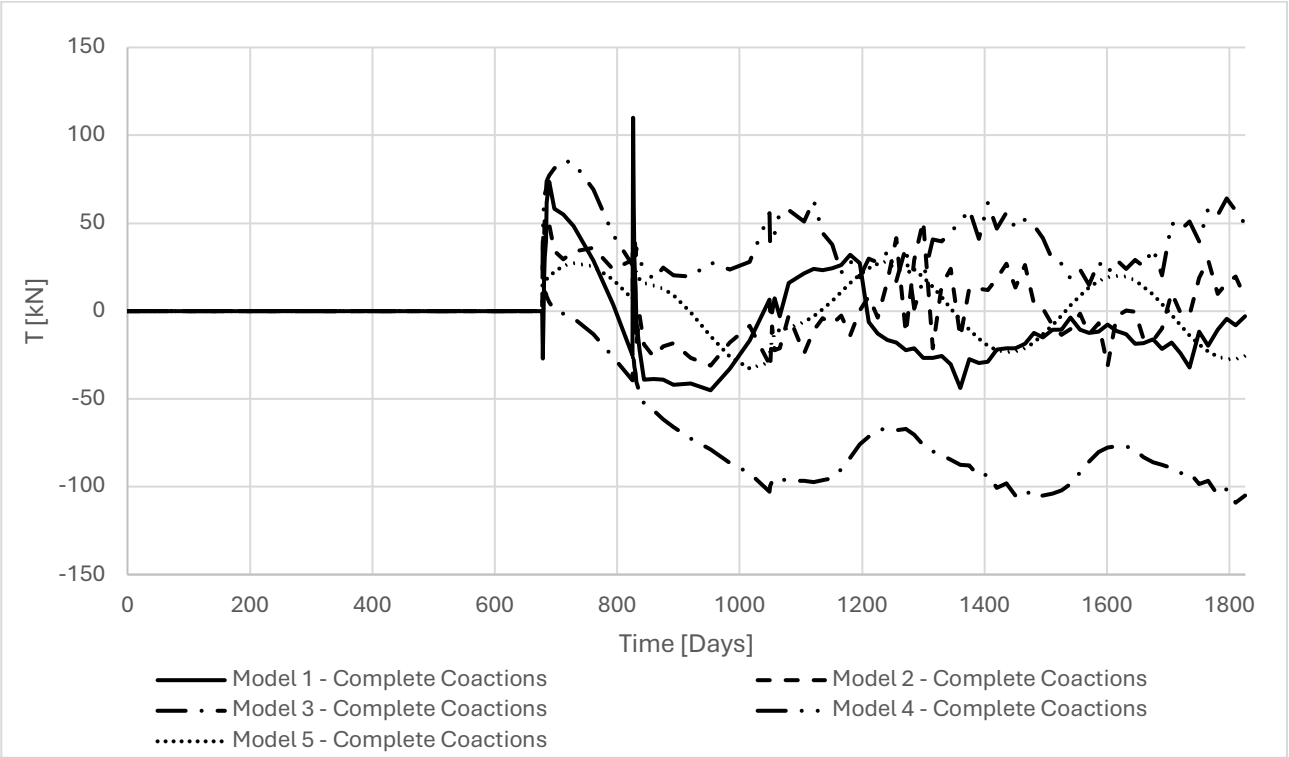


Figure 4-108 – Shear Force - Complete Coactions - Foundation Slab Downhill Support

4.5.4 Discrepancies between Models and Actions Combinations

Prior to day 694 (phases 1 to 6), all internal actions across the foundation slab are identically zero ($M = 0, N = 0, T = 0$) because the corresponding continuum finite elements remain deactivated in the numerical staging until the physical casting of phase 7. Once the member is activated at $t = 694$ days, the comparative evaluation of internal forces across the uphill support, midspan, and downhill support illustrates the decisive role of multi-field thermo-mechanical coupling, non-linear cracking, and viscoelastic relaxation in governing underground structural behaviour under asymmetric boundary conditions.

During the early-age construction stages, the degree-of-reaction thermo-mechanical coupling in model 1 exposes significant transient coactions that are entirely omitted in standard models. Casting the base slab generates an immediate compressive thrust across all three sections in the geotechnical and coactions and complete coactions combinations ($N \approx -650$ to $-680\ kN$; Figure 4-85, Figure 4-87, Figure 4-94, Figure 4-96, Figure 4-103 and Figure 4-105) due to lateral restraint, accompanied by a steep through-thickness thermal gradient that induces an acute early negative bending trough at midspan ($M \approx -465\ kN * m$; Figure 4-91 and Figure 4-93). Subsequently, the exothermic hydration of the side walls at $t = 841$ days triggers sharp localized positive bending peaks at both frame corners ($M \approx +1300\ kN * m$ uphill in Figure 4-82 and Figure 4-84; $M \approx +620\ kN * m$ downhill in Figure 4-100 and Figure 4-102) along with corresponding shear discontinuities ($T \approx -270\ kN$ in Figure 4-88 and Figure 4-90; $T \approx +115\ kN$ in Figure 4-106 and Figure 4-108). Standard formulations (Models 2 to 5), which omit hydration thermal kinetics on subsequent pours, show a smooth, monotonic transition, failing to capture these initial early-age damage-inducing peaks.

As the structure transitions from the backfilling stage ($t = 1065$ days) into sustained long-term geotechnical equilibrium, viscoelastic creep acts as the primary mechanism for stress relief. In the linear baseline (model 5) and the unrelaxed non-linear model (model 4), the application of the full earth cover locks in severe, permanent elastic force concentrations (Figure 4-83, Figure 4-89, Figure 4-101 and Figure 4-107). Conversely, in models 1 and 2, continuous viscous flow dissipates the backfilling shocks, reducing sustained support shear forces by 60% to 70% ($T \approx$ 65-90 kN compared to 225-230 kN in model 5; Figure 4-89 and Figure 4-107). At the midspan section, viscoelastic compliance under continuous ground contact pressures causes a sign inversion: while models 4 and 5 lock in high positive sagging moments ($M = +265$ to $+310\ kN * m$), models 1, 2, and 3 relax into a stable negative hogging regime ($M \approx -135$ to $-$

155 $kN.m$; Figure 4-92). This sign reversal can be attributed to the nonlinear ground compliance, and it cannot be attributed to model discrepancies, or it would need to be demonstrated.

Furthermore, time-dependent soil-structure interaction allows the slab to absorb the lateral landslide thrust, converting external earth pressures into a beneficial sustained compressive pre-stress along the entire member ($N \approx -175\ kN$ uphill, $-240\ kN$ midspan, and -390 kN downhill in model 1; Figure 4-86, Figure 4-95 and Figure 4-104). Model 5 underestimates this confinement ($N = -170$ kN downhill) and even predicts net permanent tension at the uphill support and midspan ($N > 0$). In the long-term cyclic regime, this lack of relaxation causes model 5 to treat seasonal thermal expansions as rigid external loads, producing wide cyclic envelopes and extreme peak negative moments ($M \approx -800$ to $-1020\ kN * m$, Figure 4-82 and Figure 4-100) during winter troughs. In contrast, models 1 and 2 bound peak negative moments within a relaxed range of $M \approx -300$ to $-500\ kN * m$ through localized joint softening and creep adaptation, illustrating that traditional linear elastic cross-sectional assessments tend to overestimate internal force demands by neglecting concrete's intrinsic stress-relieving mechanisms.

4.6 Uphill Wall

The analysis focuses on three critical elevations: the top section of the wall, the bottom section of the wall and the mid-height section.

4.6.1 Top Section

Moment diagrams:

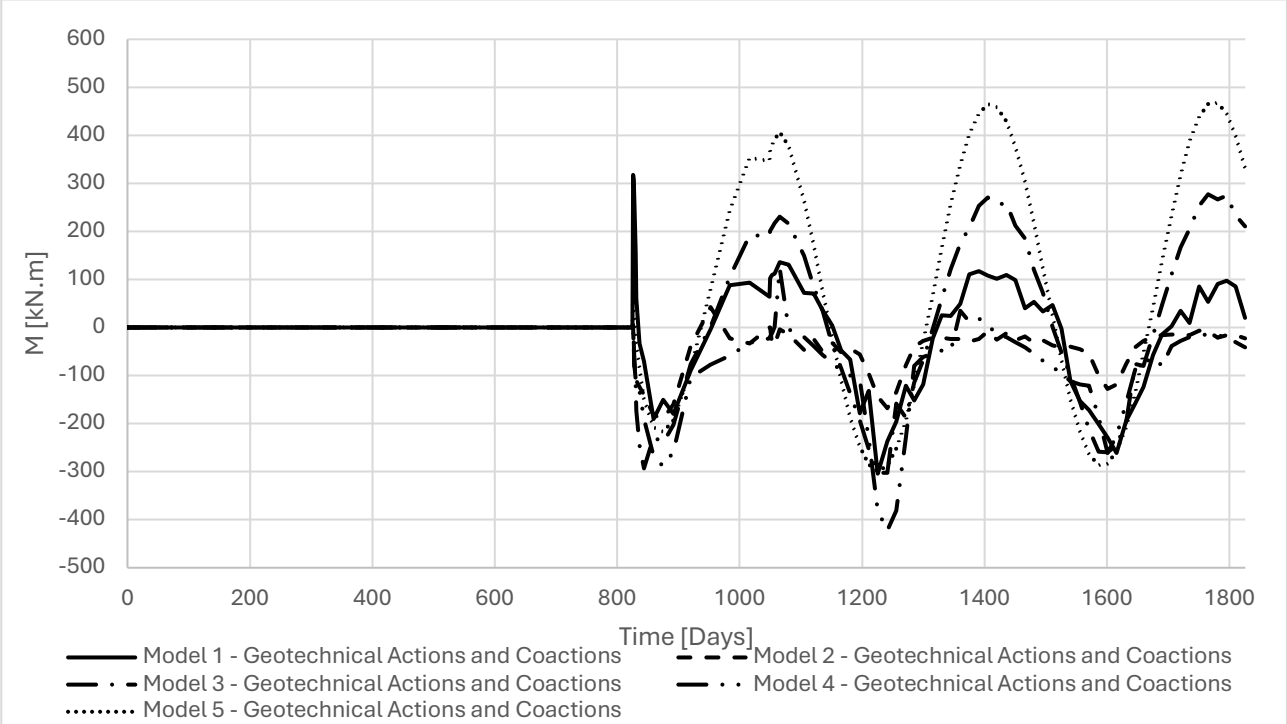


Figure 4-109 - Moment - Geotechnical Actions and Coactions - Top Uphill Wall

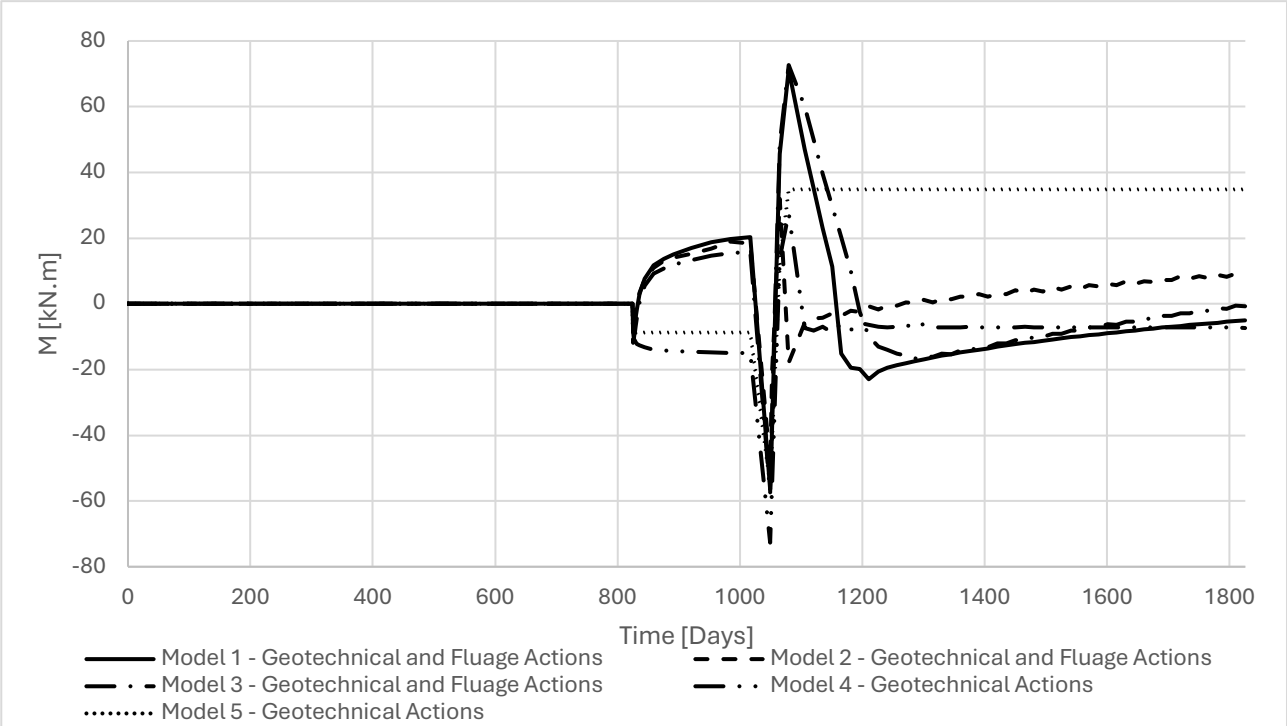


Figure 4-110 - Moment - Geotechnical and Creep Actions - Top Uphill Wall

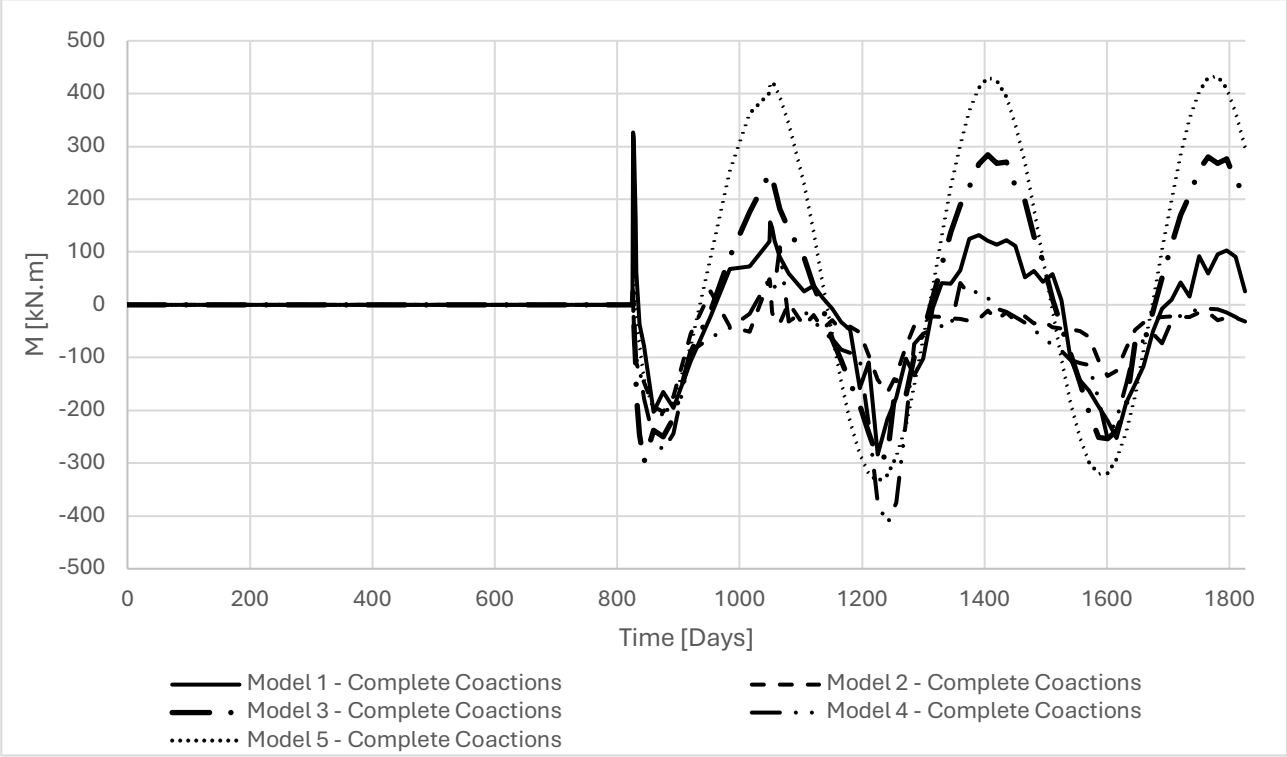


Figure 4-111 - Moment - Complete Coactions - Top Uphill Wall

Axial force diagrams:

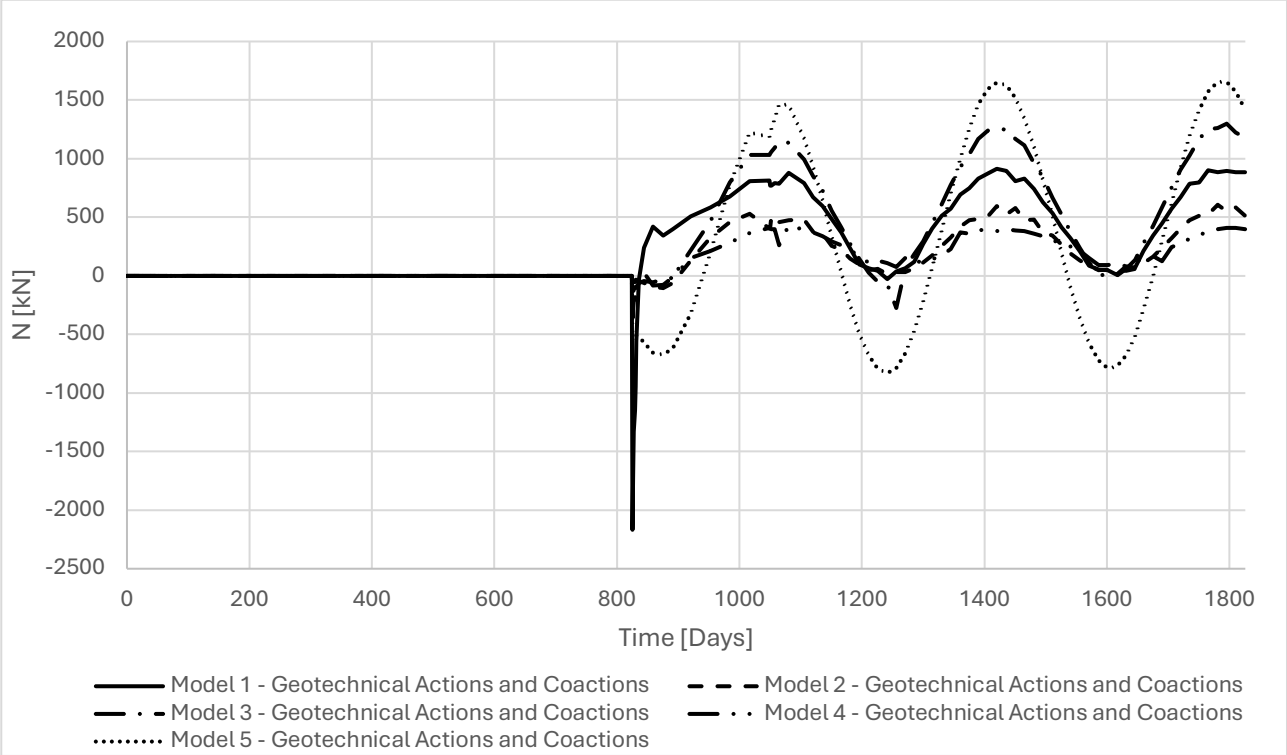


Figure 4-112 - Axial Force - Geotechnical Actions and Coactions - Top Uphill Wall

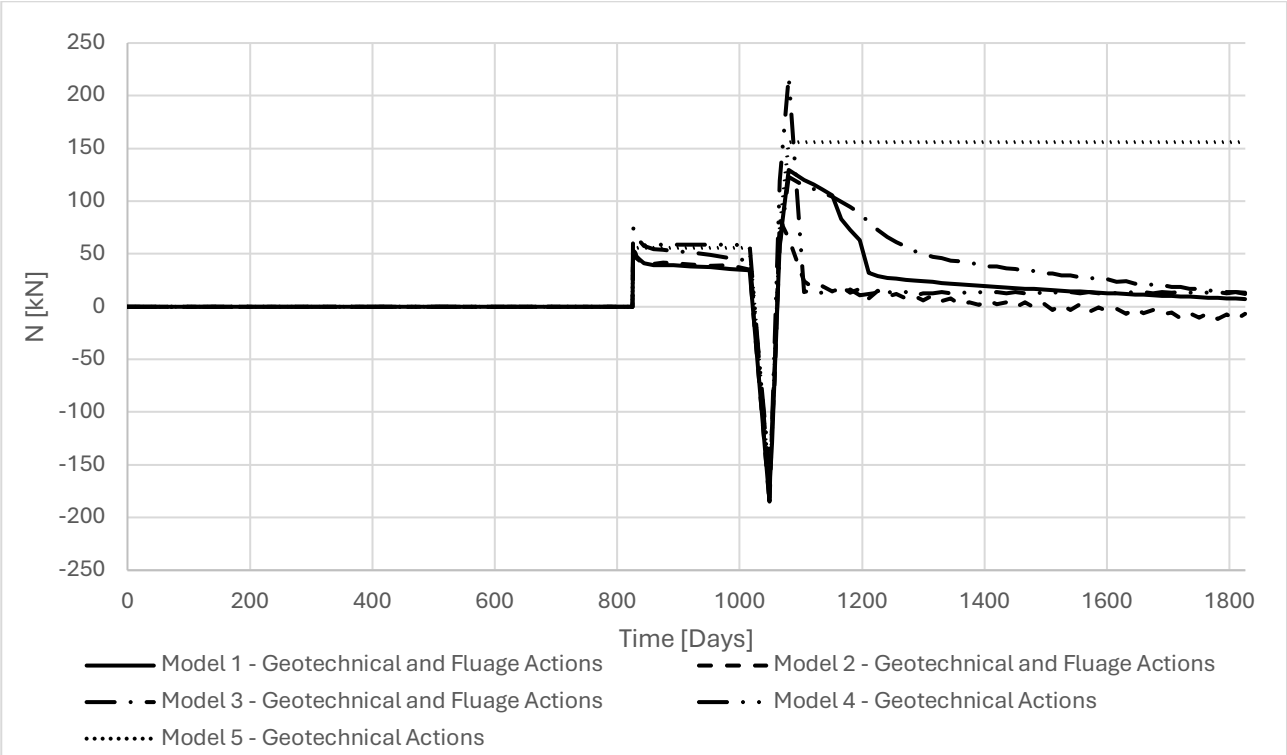


Figure 4-113 - Axial Force - Geotechnical and Creep Actions - Top Uphill Wall

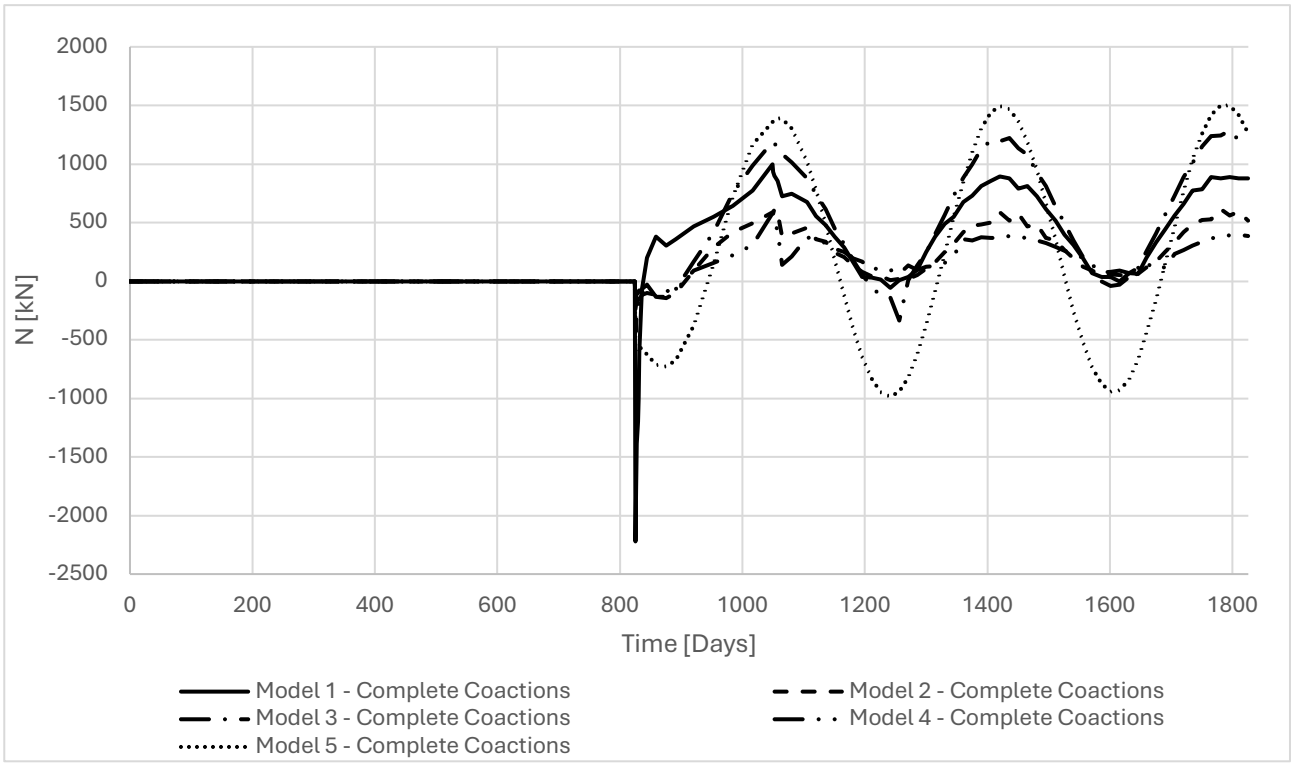


Figure 4-114 - Axial Force - Complete Coactions - Top Uphill Wall

Shear force diagrams:

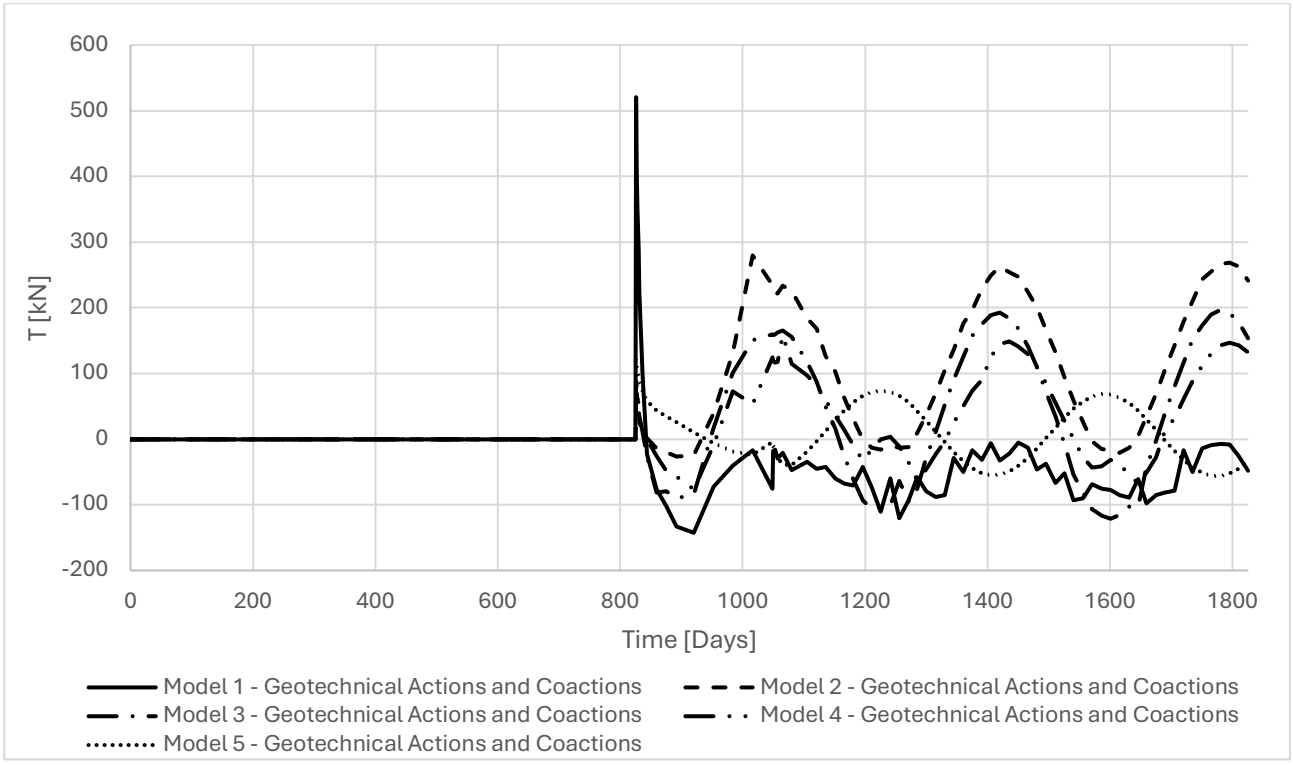


Figure 4-115 – Shear Force - Geotechnical Actions and Coactions - Top Uphill Wall

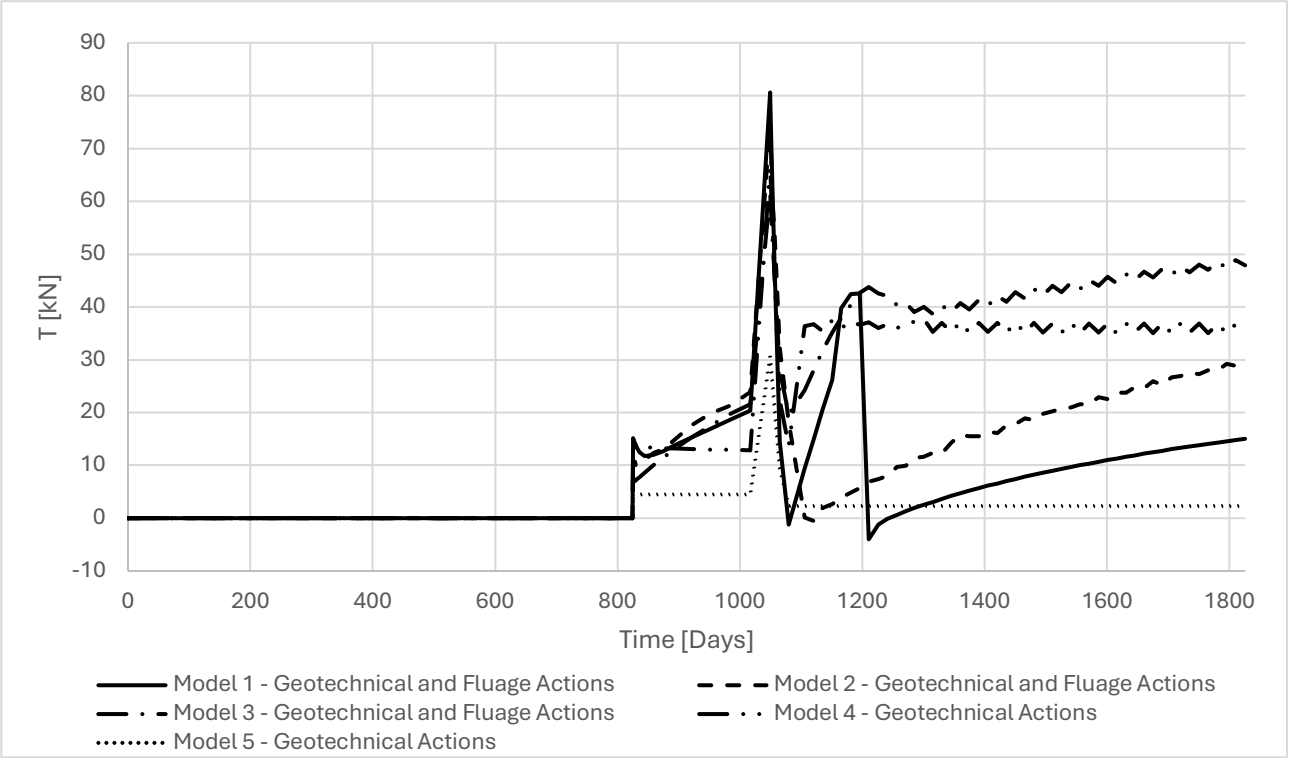


Figure 4-116 – Shear Force - Geotechnical and Creep Actions - Top Uphill Wall

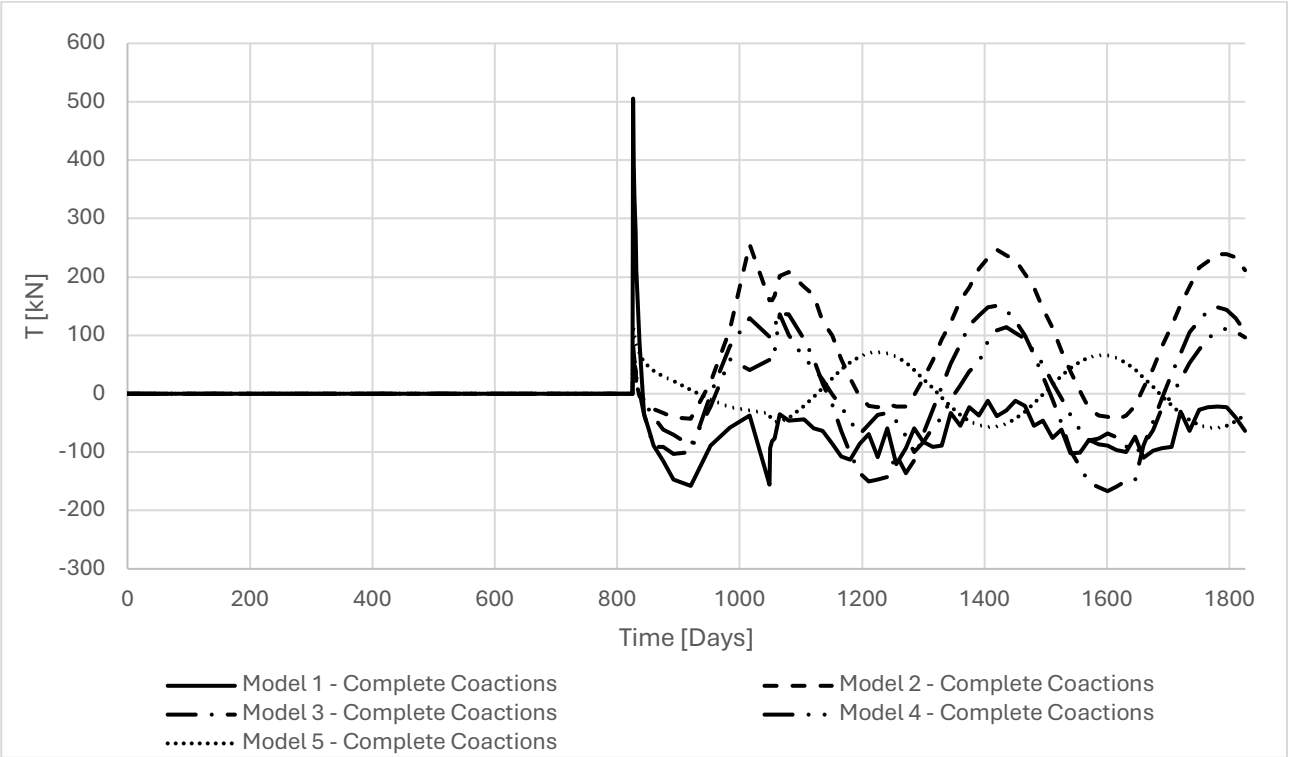


Figure 4-117 – Shear Force - Complete Coactions - Top Uphill Wall

4.6.2 Mid-height Section

Moment diagrams:

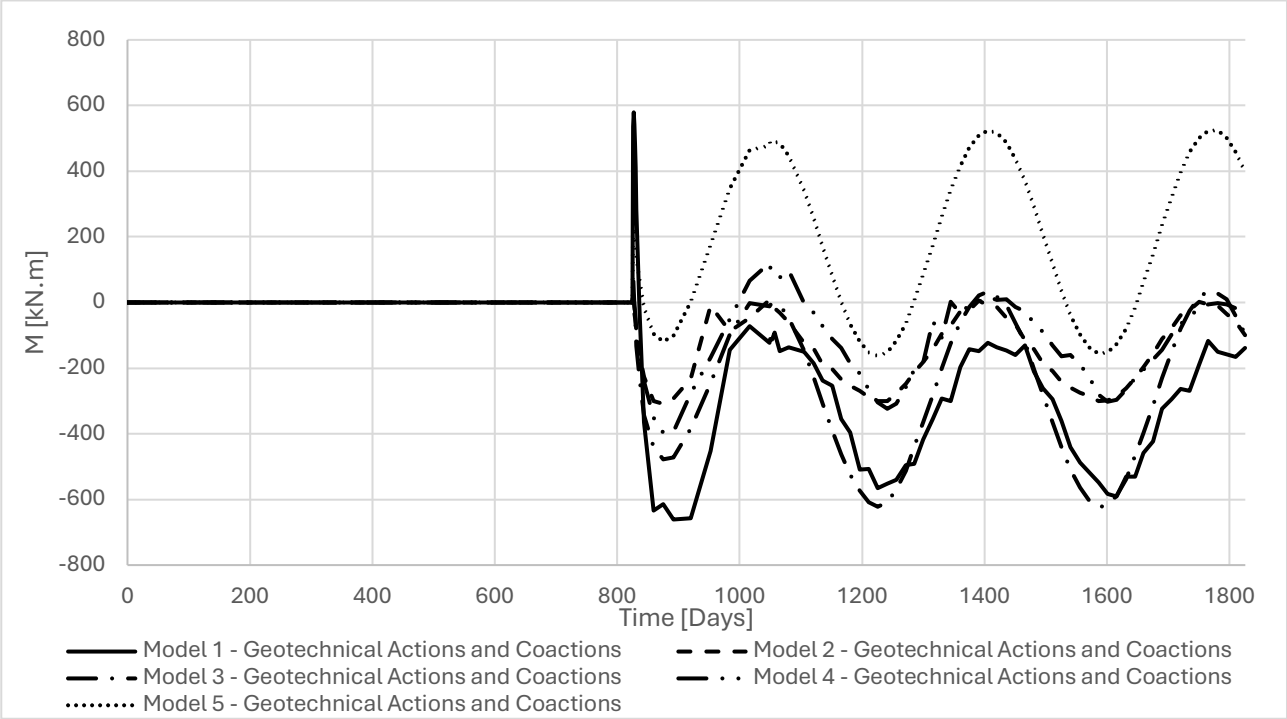


Figure 4-118 - Moment - Geotechnical Actions and Coactions – Mid-height Uphill Wall

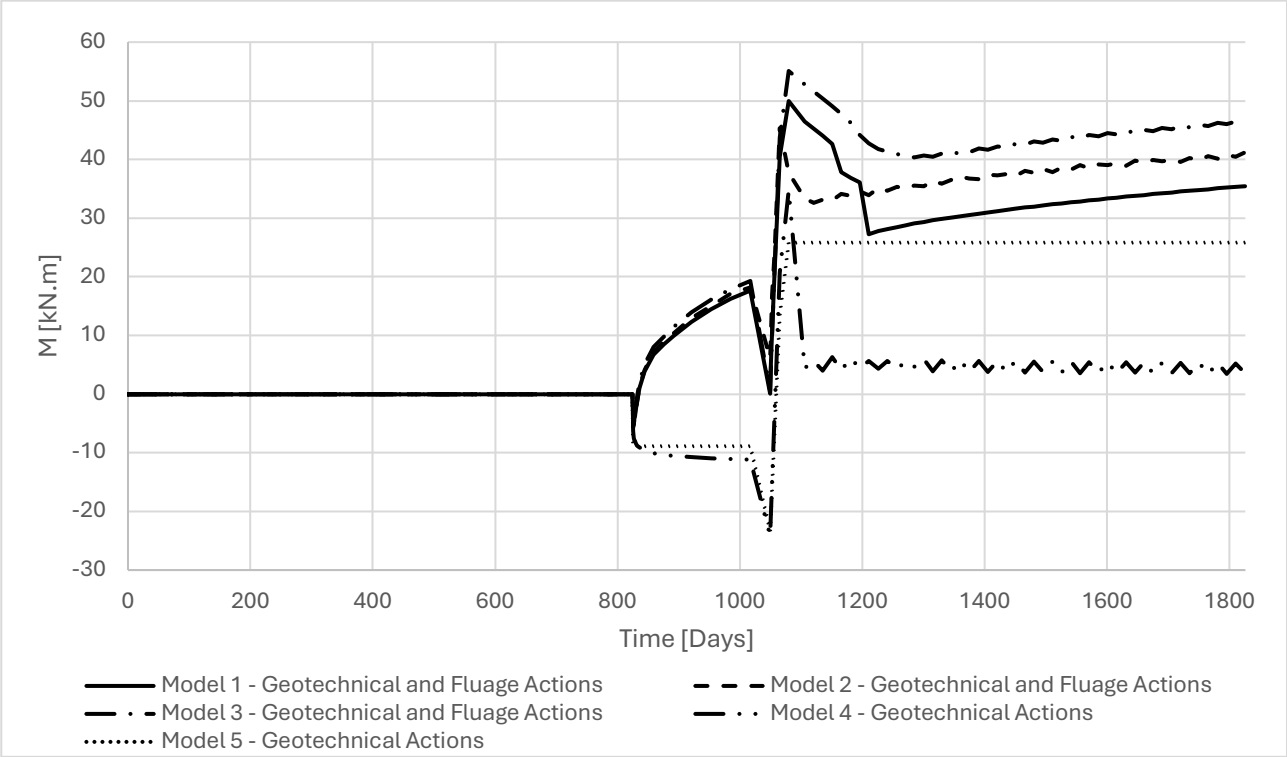


Figure 4-119 - Moment - Geotechnical and Creep Actions – Mid-height Uphill Wall

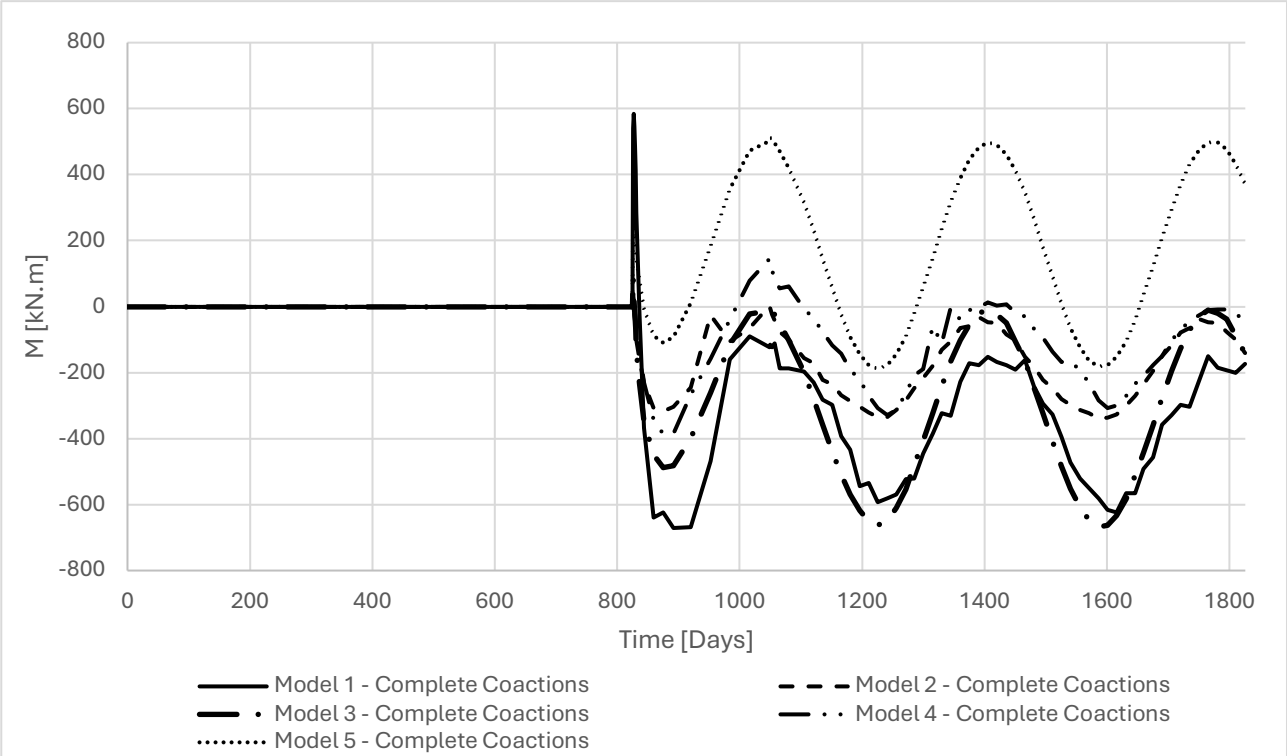


Figure 4-120 - Moment - Complete Coactions – Mid-height Uphill Wall

Axial force diagrams:

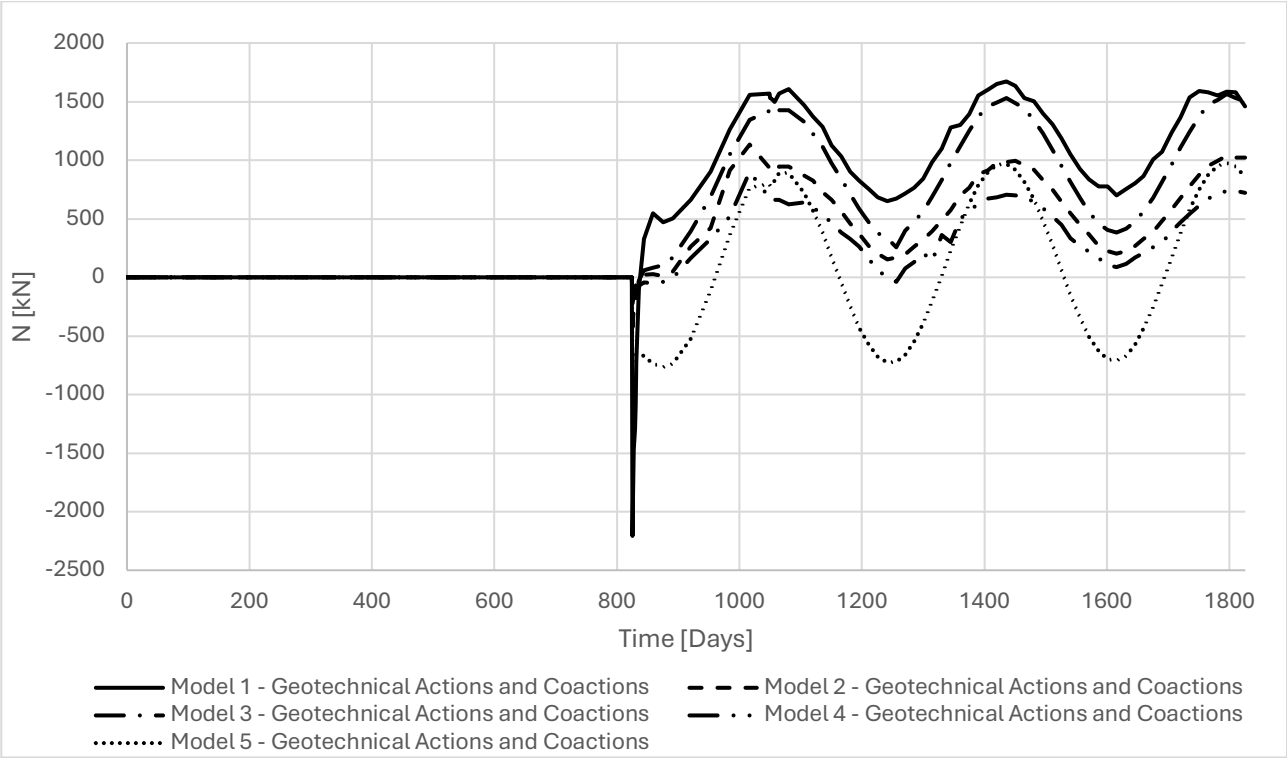


Figure 4-121 - Axial Force - Geotechnical Actions – Mid-height Uphill Wall

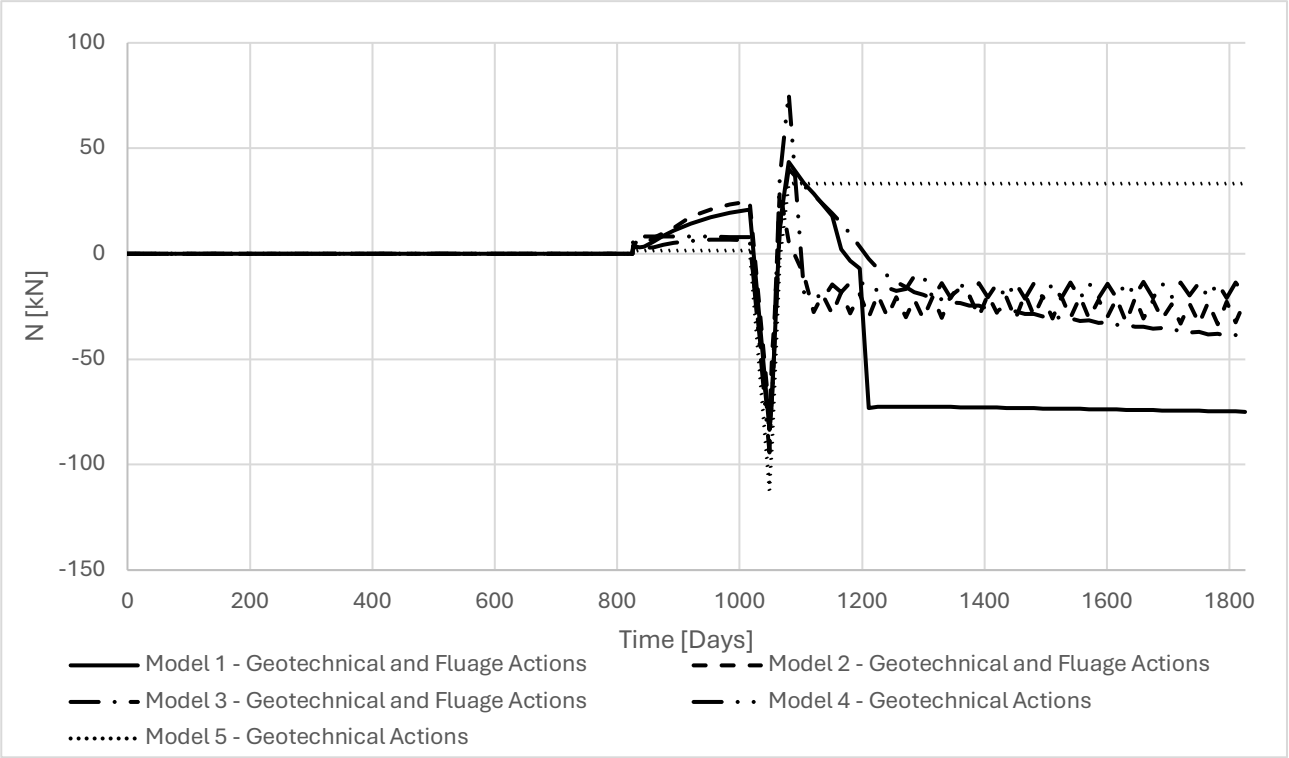


Figure 4-122 - Axial Force - Geotechnical and Creep Actions – Mid-height Uphill Wall

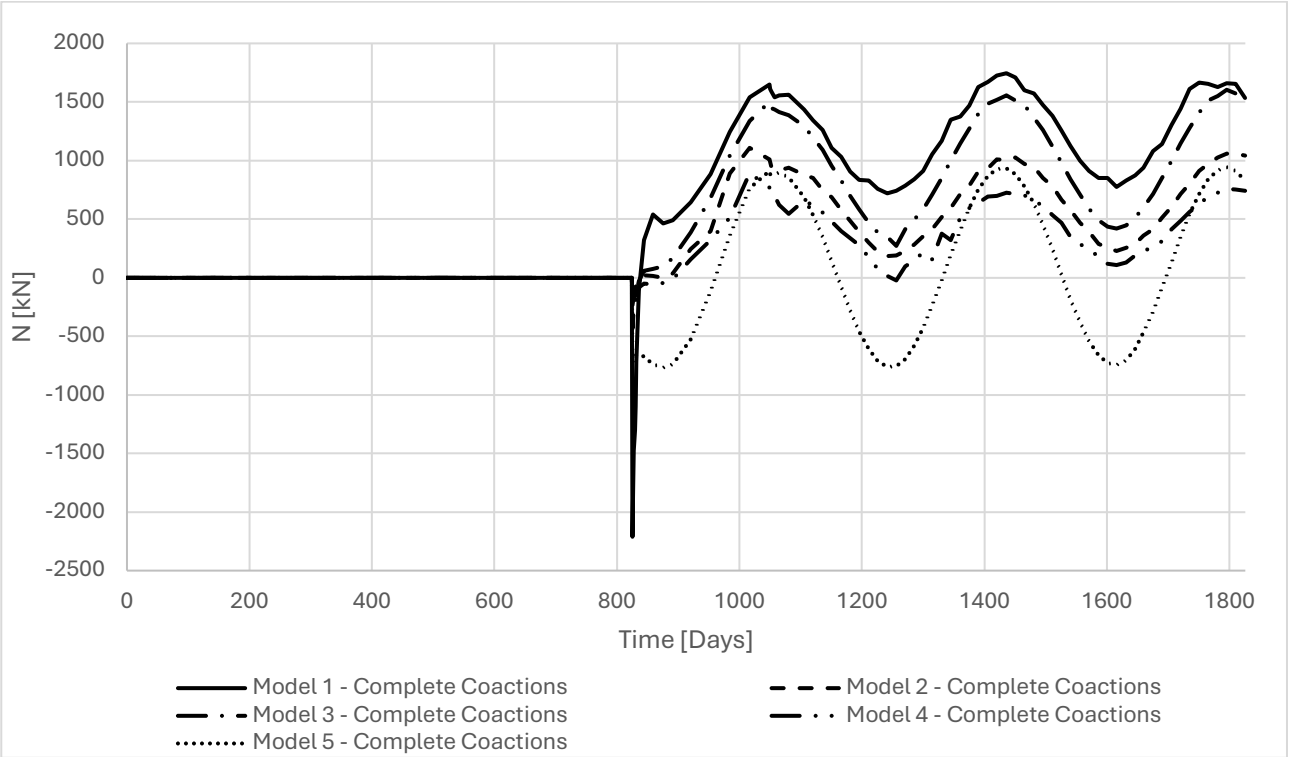


Figure 4-123 - Axial Force - Complete Coactions – Mid-height Uphill Wall

Shear force diagrams:

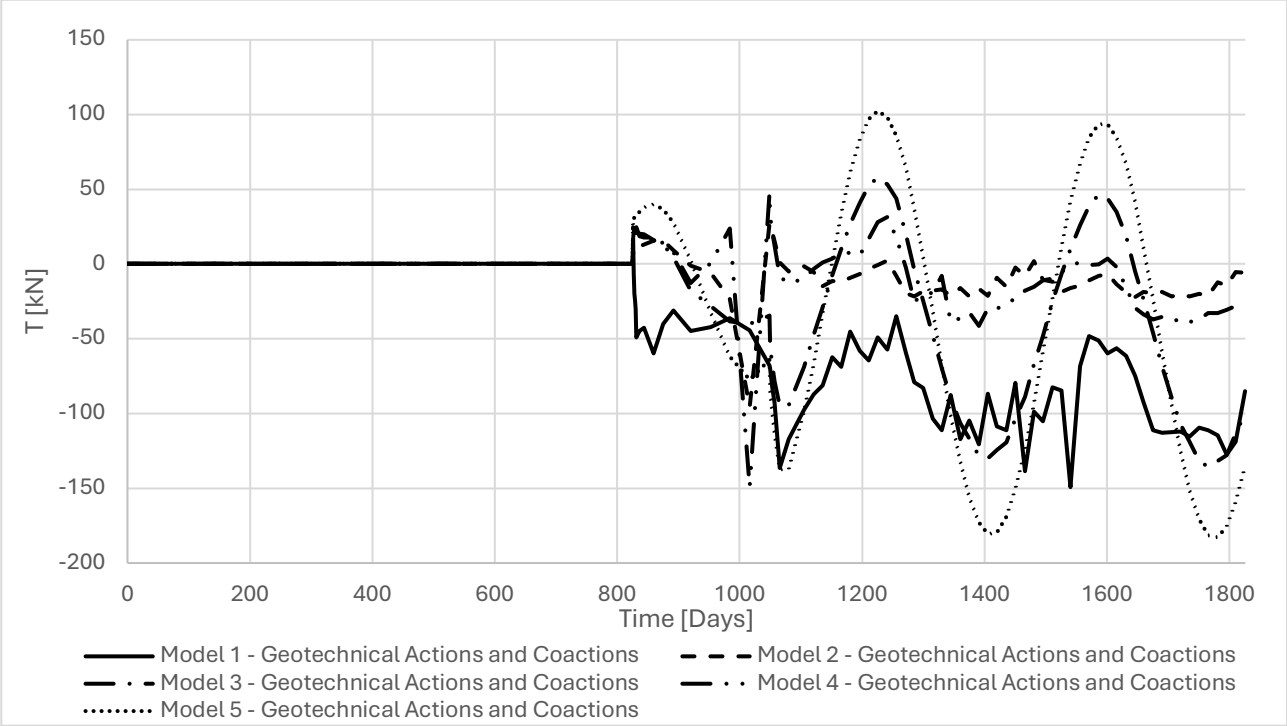


Figure 4-124 – Shear Force - Geotechnical Actions and Coc-actions – Mid-height Uphill Wall

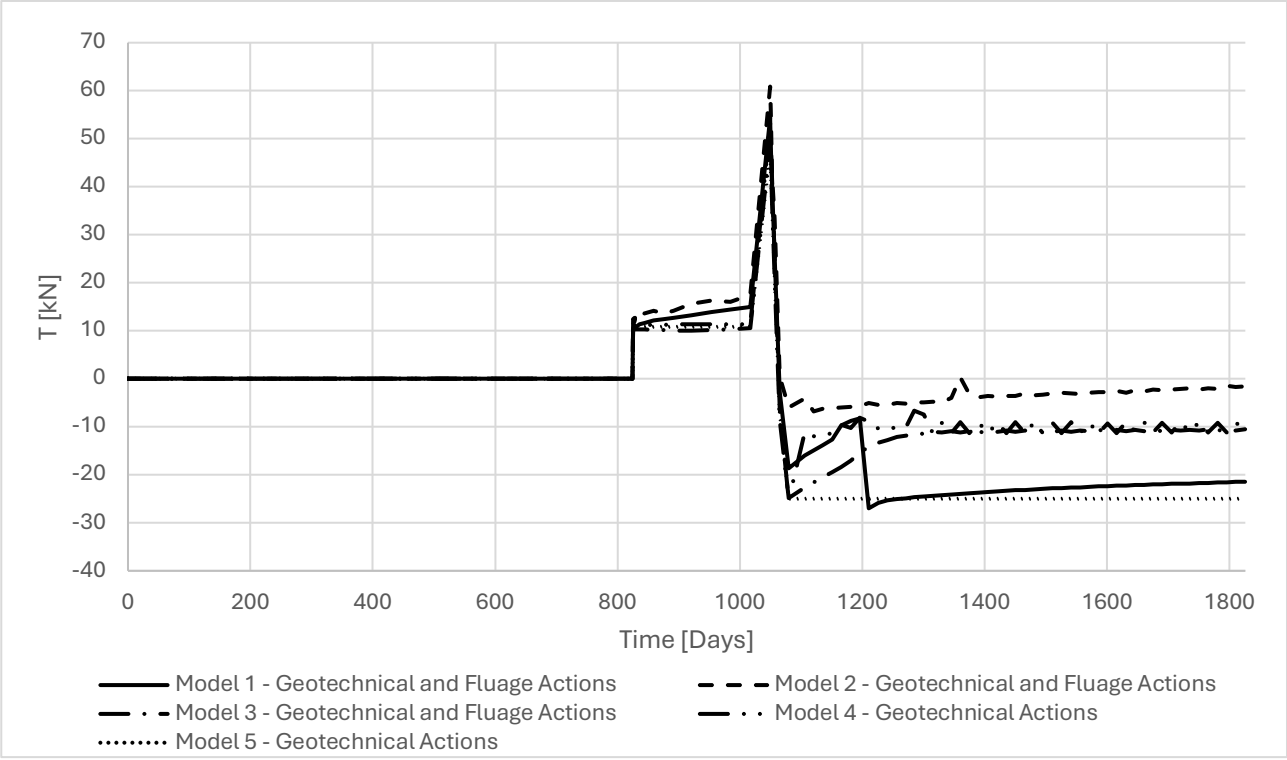


Figure 4-125 – Shear Force - Geotechnical and Creep Actions – Mid-height Uphill Wall

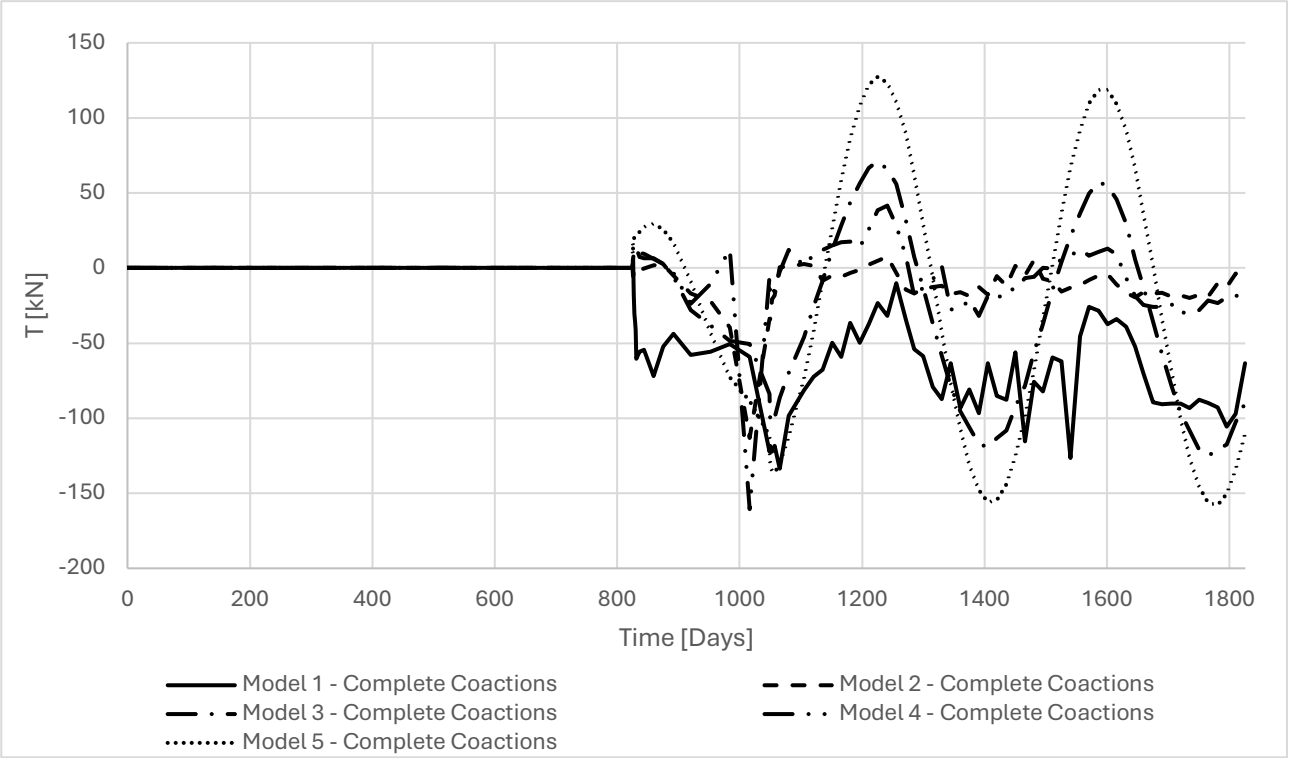


Figure 4-126 – Shear Force - Complete Coactions – Mid-height Uphill Wall

4.6.3 Bottom Section

Moment diagrams:

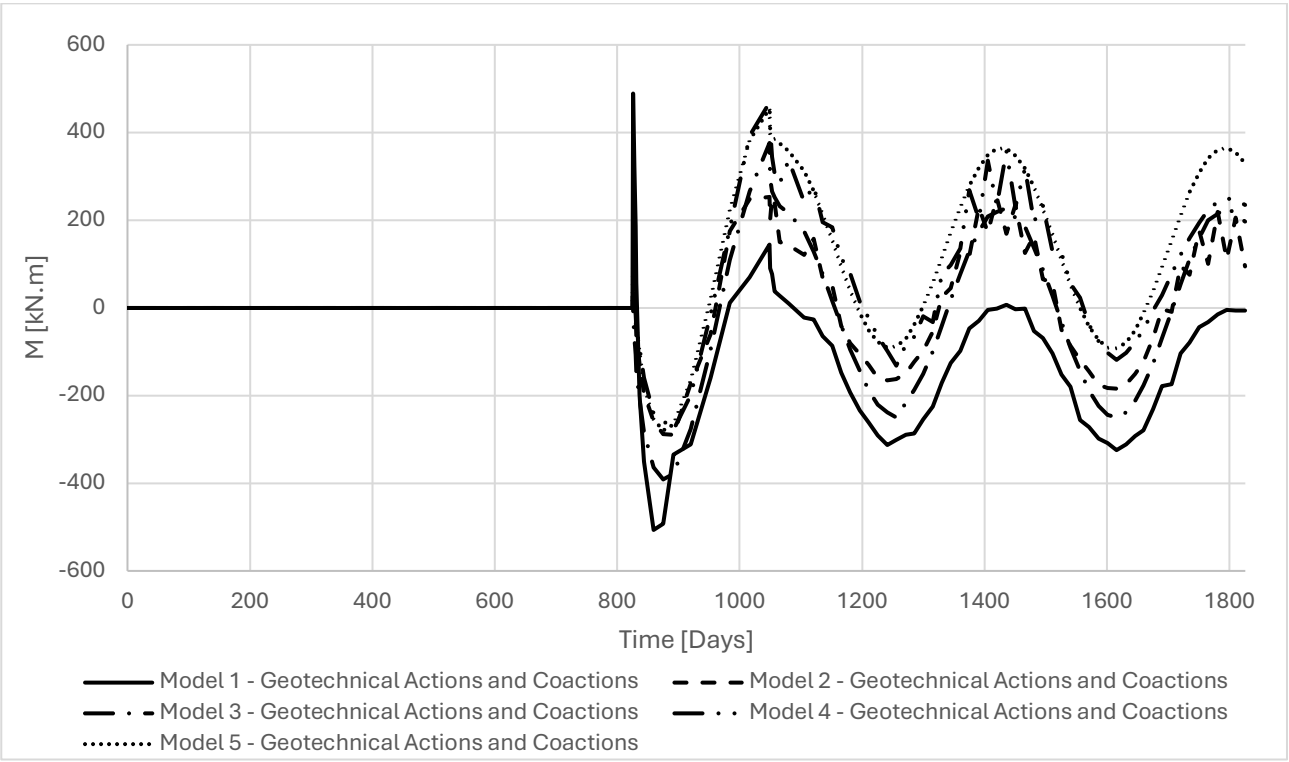


Figure 4-127 - Moment - Geotechnical Actions and Coactions - Bottom Uphill Wall

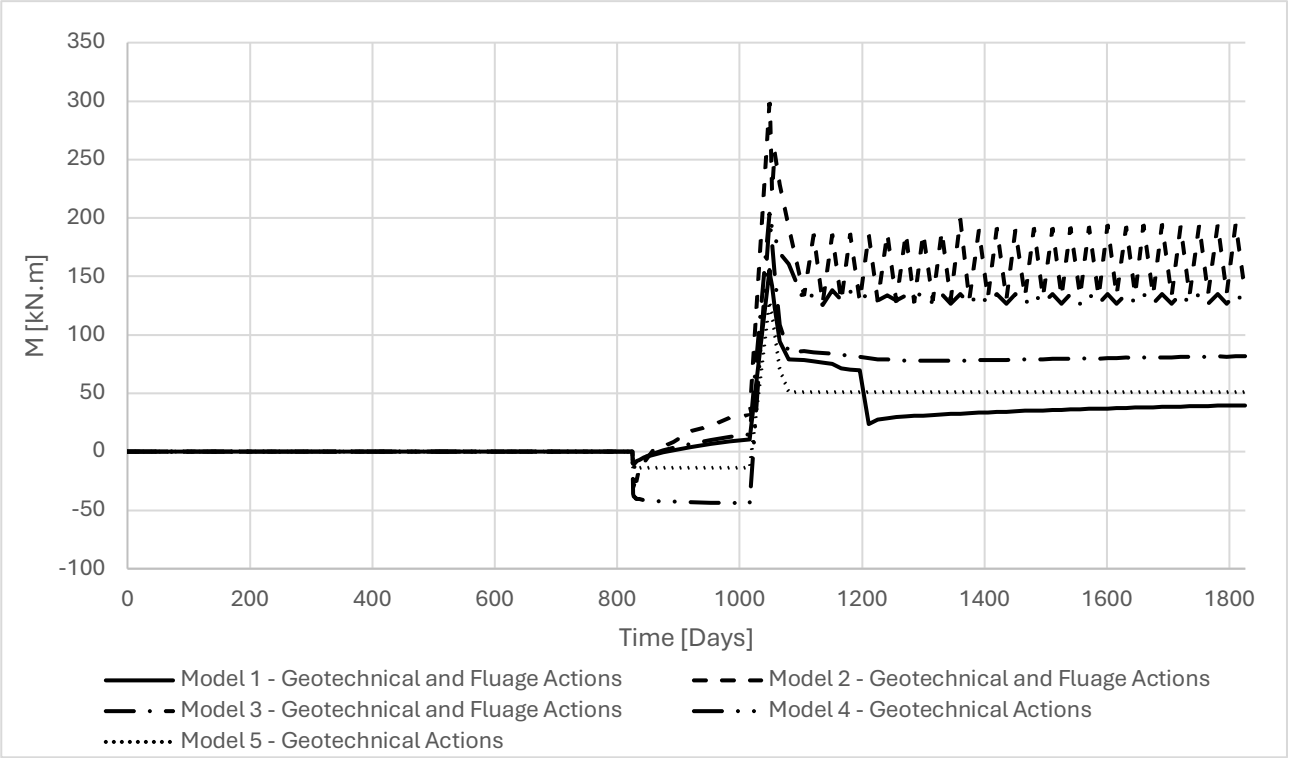


Figure 4-128 - Moment - Geotechnical and Creep Actions - Bottom Uphill Wall

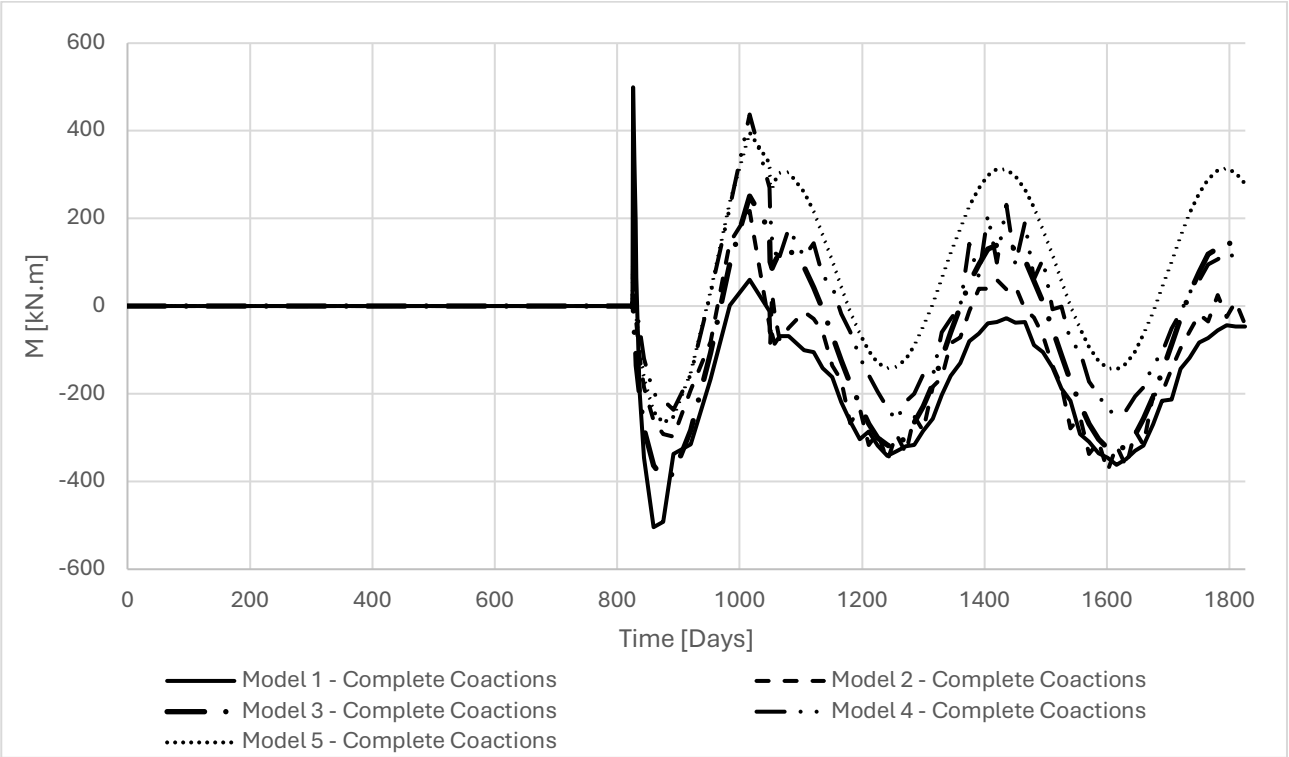


Figure 4-129 - Moment - Complete Coactions - Bottom Uphill Wall

Axial force diagrams:

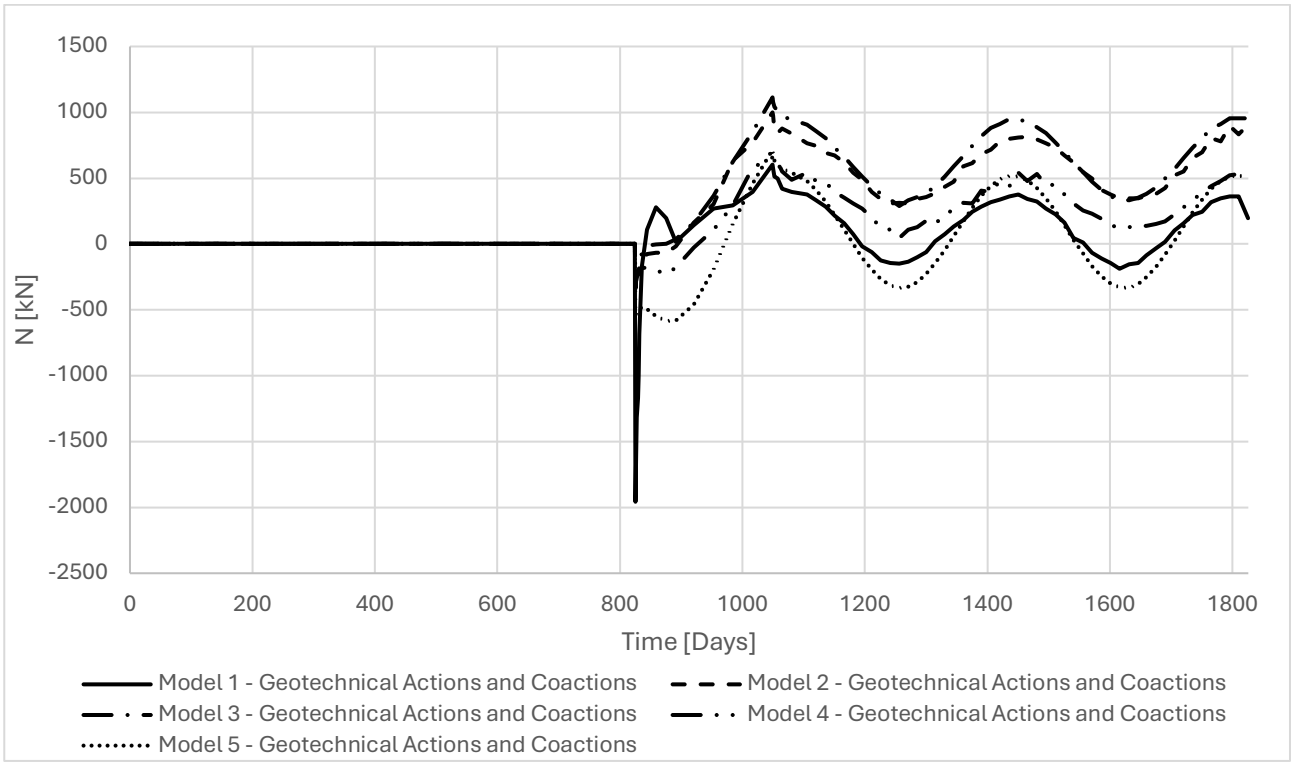


Figure 4-130 - Axial Force - Geotechnical Actions and Coactions - Bottom Uphill Wall

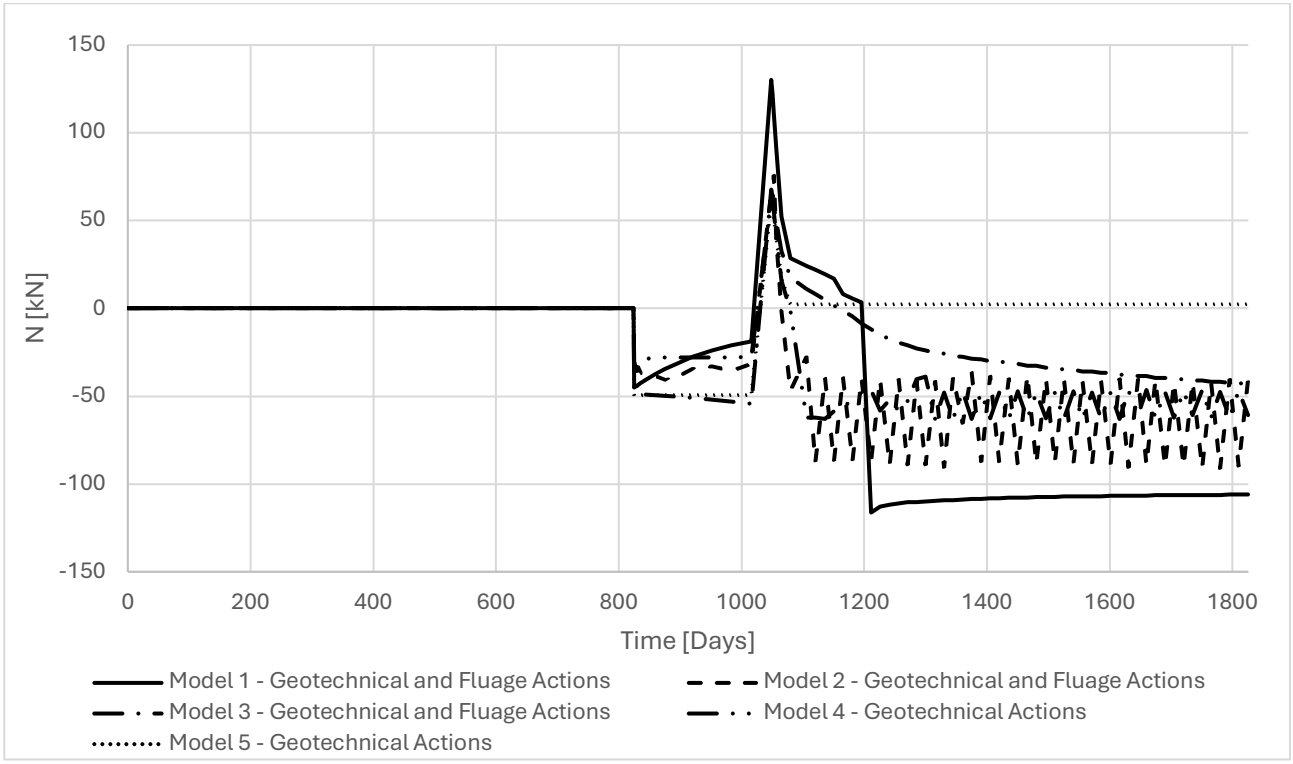


Figure 4-131 - Axial Force - Geotechnical and Creep Actions - Bottom Uphill Wall

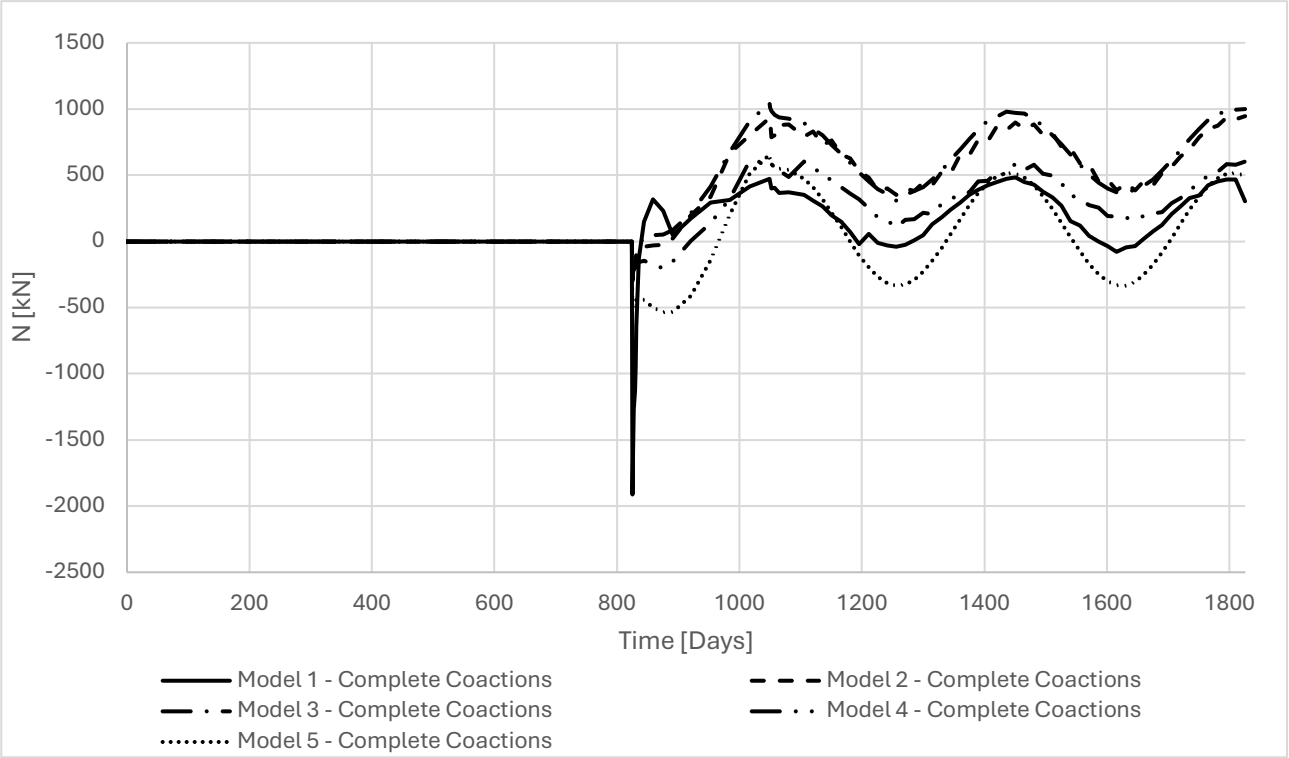


Figure 4-132 - Axial Force - Complete Coactions - Bottom Uphill Wall

Shear force diagrams:

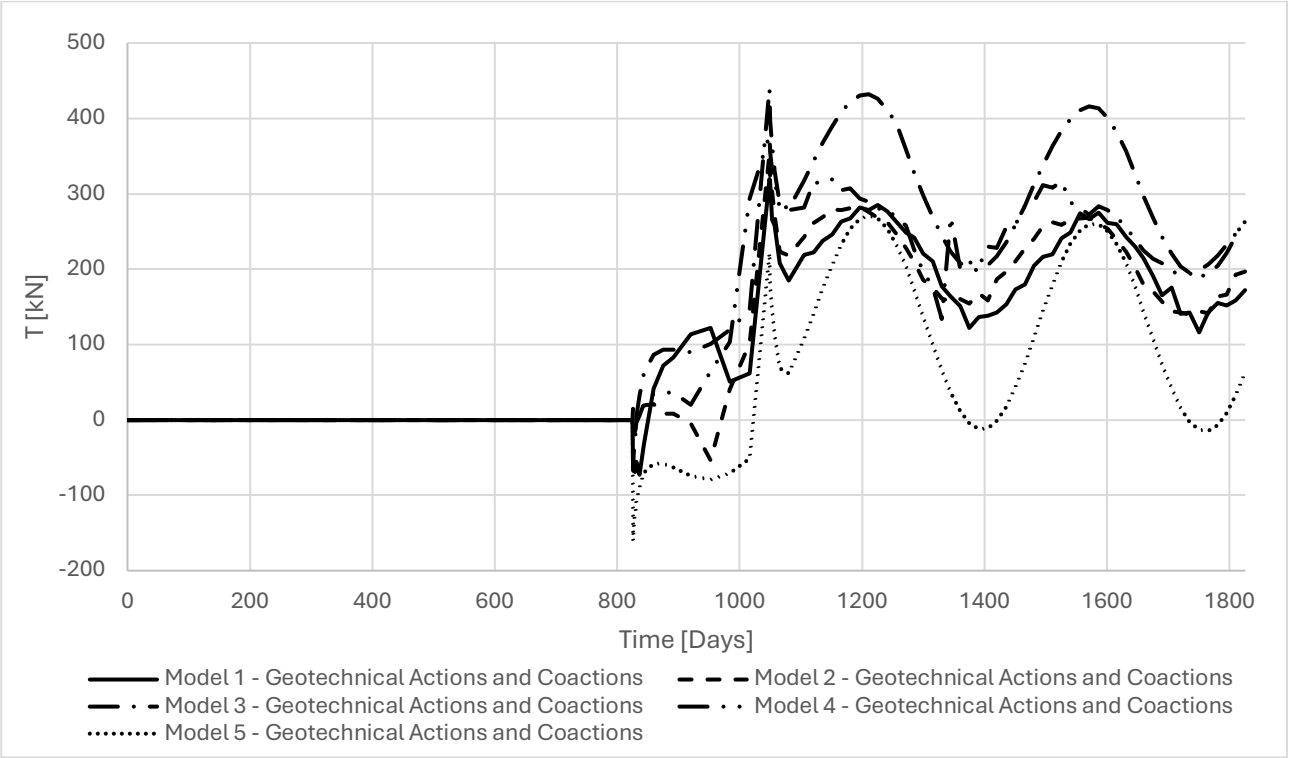


Figure 4-133 – Shear Force - Geotechnical Actions and Coactions- Bottom Uphill Wall

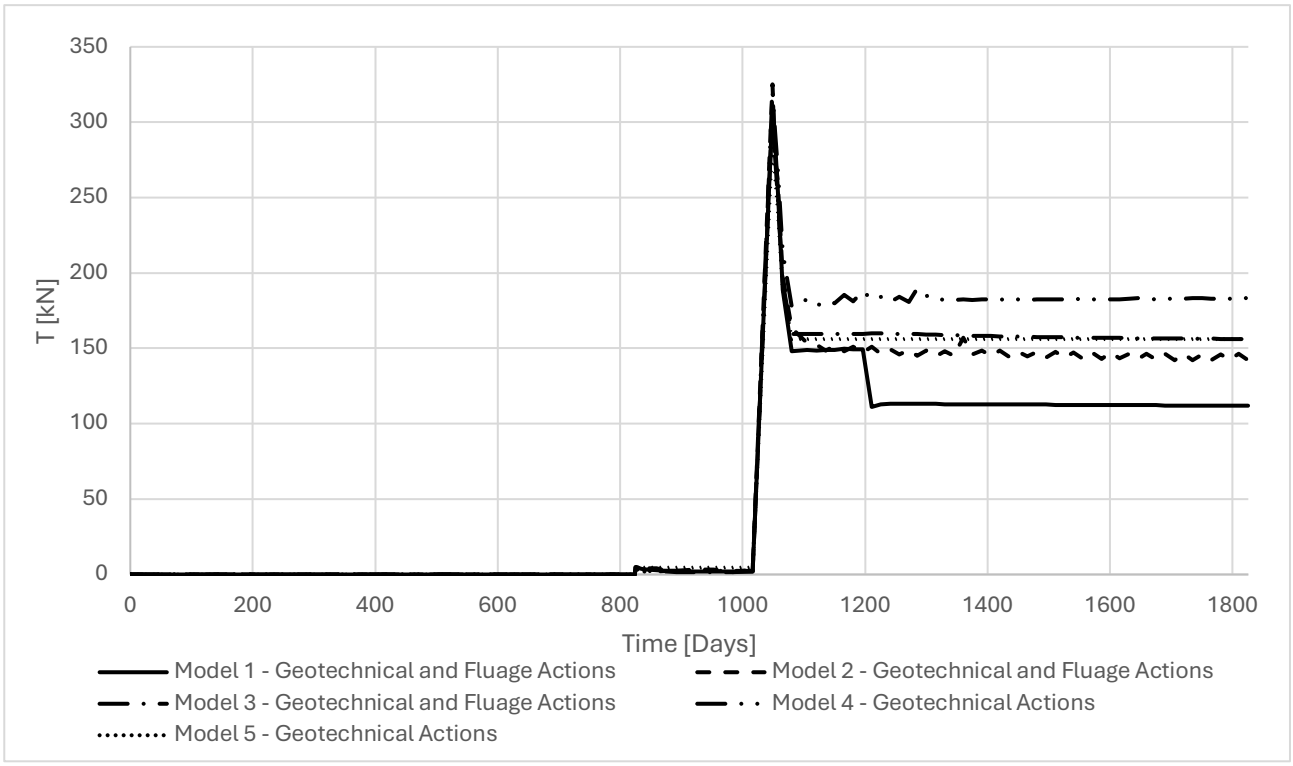


Figure 4-134 – Shear Force - Geotechnical and Creep Actions - Bottom Uphill Wall

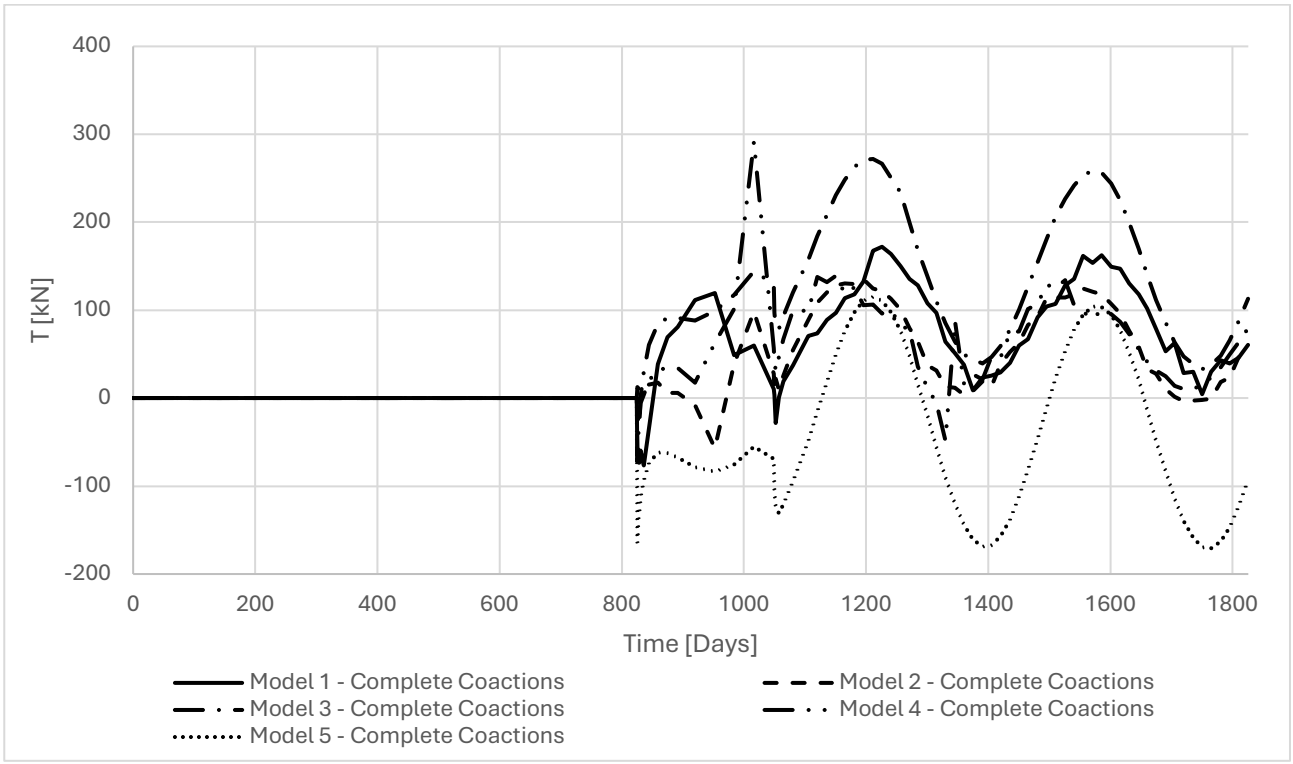


Figure 4-135 – Shear Force - Complete Coactions - Bottom Uphill Wall

4.6.4 Discrepancies between Models and Actions Combinations

The uphill lining wall remains inactive throughout the first 841 days of the staging, carrying zero internal forces while earlier excavation, slab construction, and initial resting phases unfold. Its structural role begins abruptly at day 841 when it is cast between the previously hardened foundation slab ($t = 694$ days) and the top cover slab. In model 1, tracking degree-of-reaction hydration kinetics reveals a distinct early-age thermal response. Exothermic dilation against the rigid top and bottom slab boundaries induces immediate positive flexural spikes across the height: $+320\ kN*m$ at the top (Figure 4-109 and Figure 4-111), $+580\ kN*m$ at mid-height (Figure 4-118 and Figure 4-120), and $+490\ kN*m$ at the base (Figure 4-127 and Figure 4-129). This thermal expansion generates high vertical compressive spikes between $-1980\ kN$ and $-2180\ kN$ (Figure 4-112, Figure 4-121 and Figure 4-130) as well as an initial shear surge of $+520\ kN$ at the upper framing connection. Models not accounting for hydration heat (models 2 through 5) drop directly into negative bending under basic shrinkage coactions.

As hydration heat dissipates and the sequence moves to complete backfilling at day 1065, internal stresses redistribute. Earth placement triggers temporary flexural and shear spikes across all sections, seen in the base shear step rising to roughly $+320\ kN$ in Figure 4-134. Under sustained geotechnical conditions, the inclusion of viscoelastic creep in Models 1 and 2 appears to facilitate stress relaxation. Where linear elastic model 5 locks in permanent positive moments of $M = +35\ kN*m$ at the top (Figure 4-110) and $+52\ kN*m$ at the bottom (Figure 4-128), model 1 settles into relaxed values closer to $-4\ kN*m$ and $+38\ kN*m$. A comparable trend emerges in sustained base shear, where model 1 stabilizes around $+112\ kN$, compared to $+160\ kN$ in model 5 and $+182\ kN$ in unrelaxed model 4 (Figure 4-134). At the top connection, model 1 reduces sustained tension to $+10\ kN$, whereas model 5 retains $+155\ kN$ (Figure 4-113).

In the long-term cyclic regime ($t > 1122$ days), the non-linear calculations indicate a consistent damping of seasonal thermal coactions across the entire wall. The linear elastic baseline in model 5 predicts wide cyclic flexural swings, with moment ranges reaching $\Delta M \approx 760\ kN*m$ at the top (Figure 4-109), $\Delta M \approx 680\ kN*m$ at mid-height (Figure 4-118), and $\Delta M \approx 490\ kN*m$ at the base (Figure 4-127), alongside cyclic axial excursions of $\Delta N \approx 2450\ kN$ at the roof joint (Figure 4-112). Incorporating localized cracking and continuous viscous flow in model 1 narrows these cyclic bands to $\Delta M \approx 395\ kN*m$ at the top, $\Delta M \approx 480\ kN*m$ at mid-

height, and $\Delta M \approx 310\ kN * m$ at the base, while reducing top cyclic axial fluctuations to $\Delta N \approx 950\ kN$. Cyclic shear amplitudes also contract, dropping from $\Delta T \approx 280\ kN$ in model 5 to $\Delta T \approx 105\ kN$in model 1 at mid-height (Figure 4-124) and from $\Delta T \approx 285\ kN$ to $\Delta T \approx 165\ kN$ at the base (Figure 4-133). Under the scope of this numerical setup, these results suggest that accounting for creep and softening mechanisms reduces artificial elastic force peaks, reflecting a more moderate service envelope for the lining wall.

4.7 Downhill Wall

The analysis focuses on three critical elevations: the top section of the wall, the bottom section of the wall and the mid-height section.

4.7.1 Top Section

Moment diagrams:

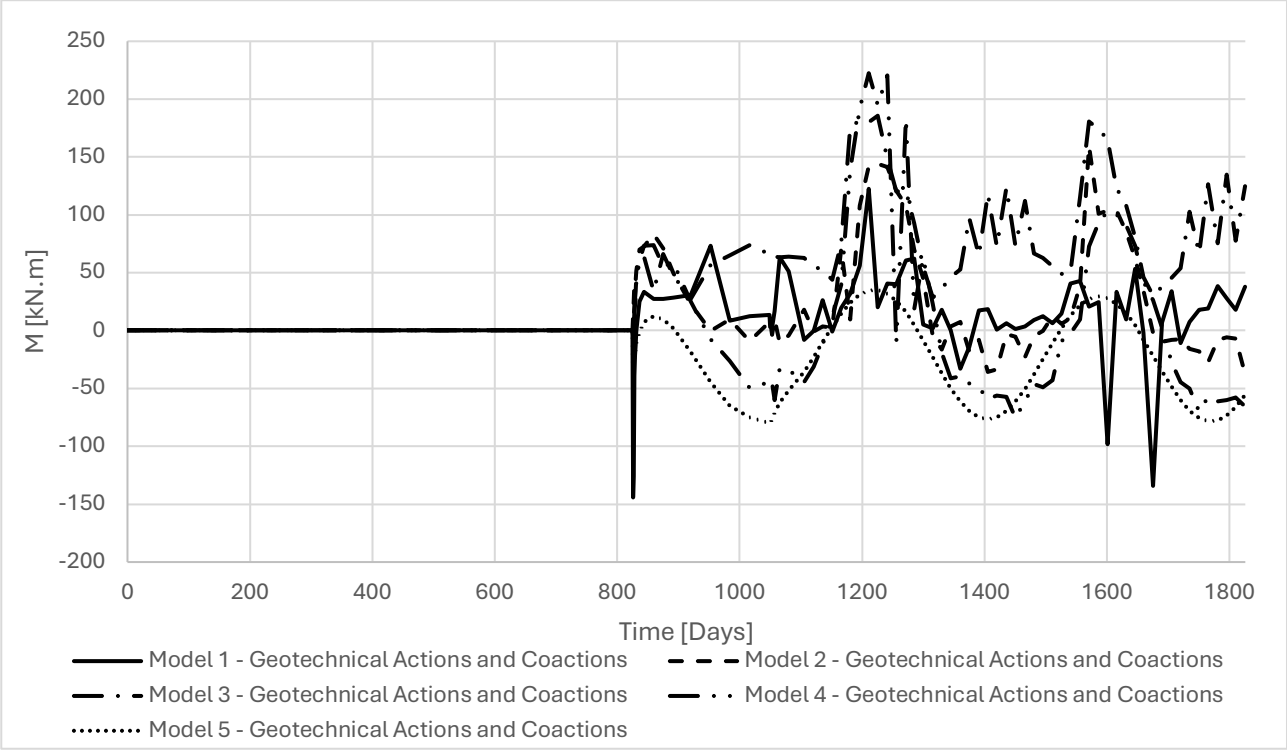


Figure 4-136 - Moment - Geotechnical Actions and Coactions - Top Downhill Wall

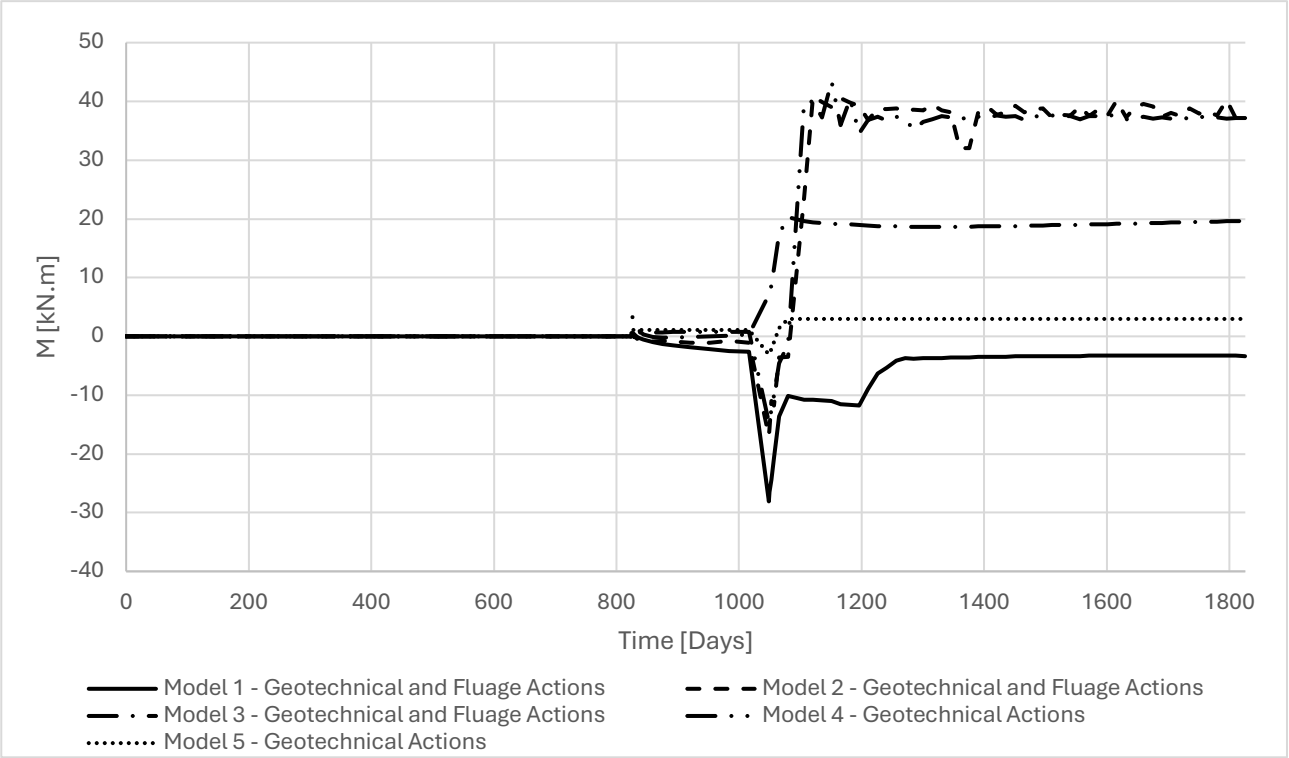


Figure 4-137 - Moment - Geotechnical and Creep Actions - Top Downhill Wall

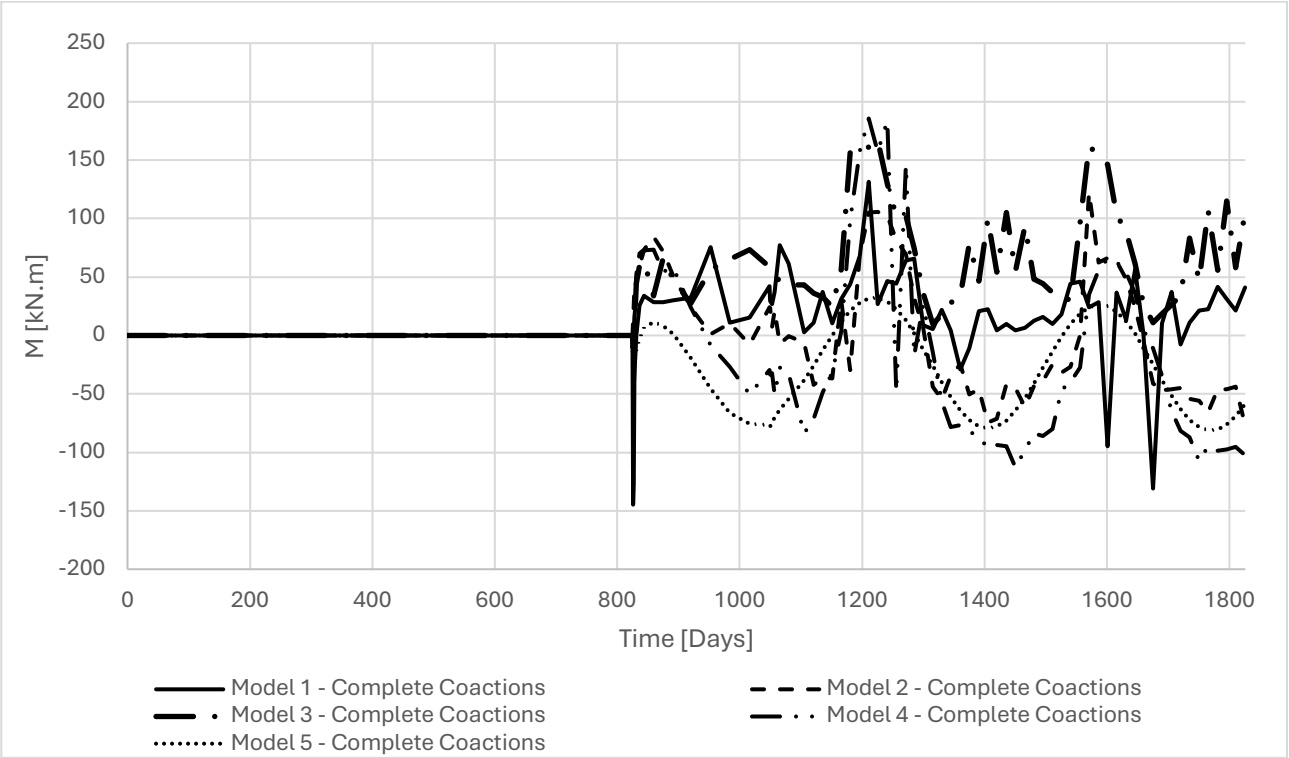


Figure 4-138 - Moment - Complete Coactions - Top Downhill Wall

Axial force diagrams:

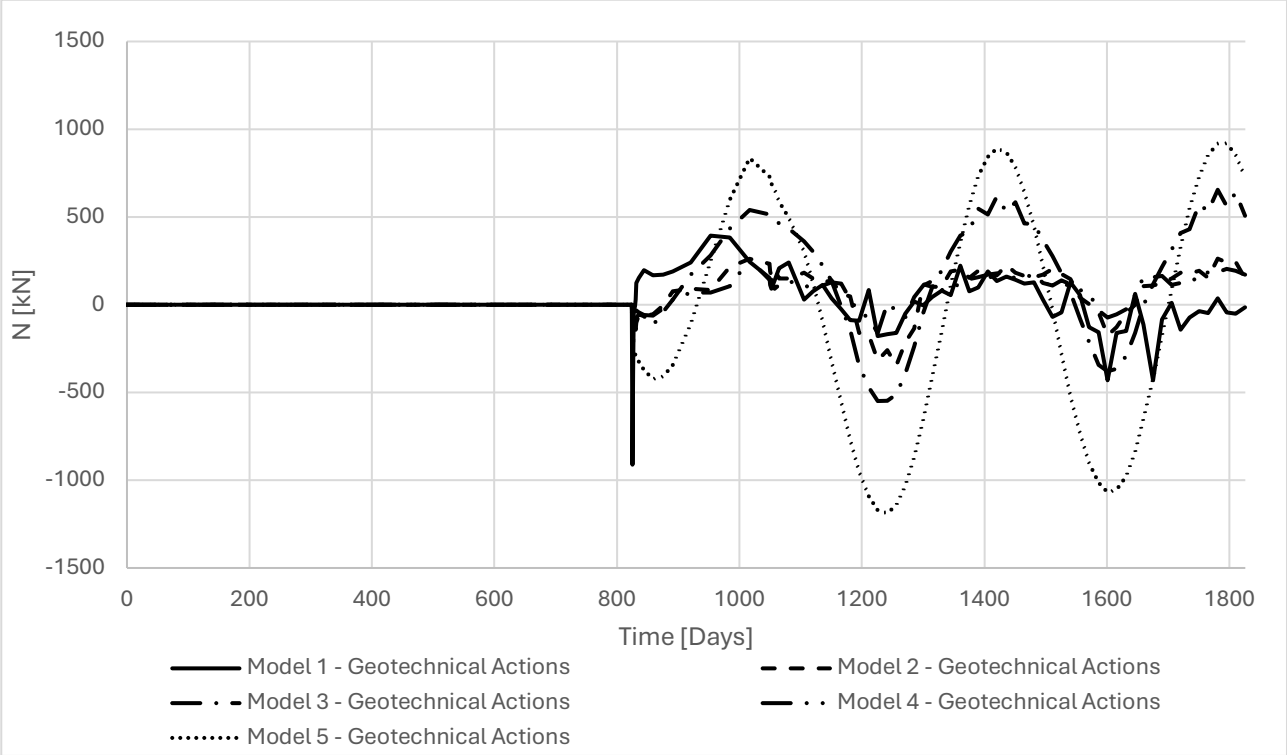


Figure 4-139 - Axial Force - Geotechnical Actions and Coactions - Top Downhill Wall

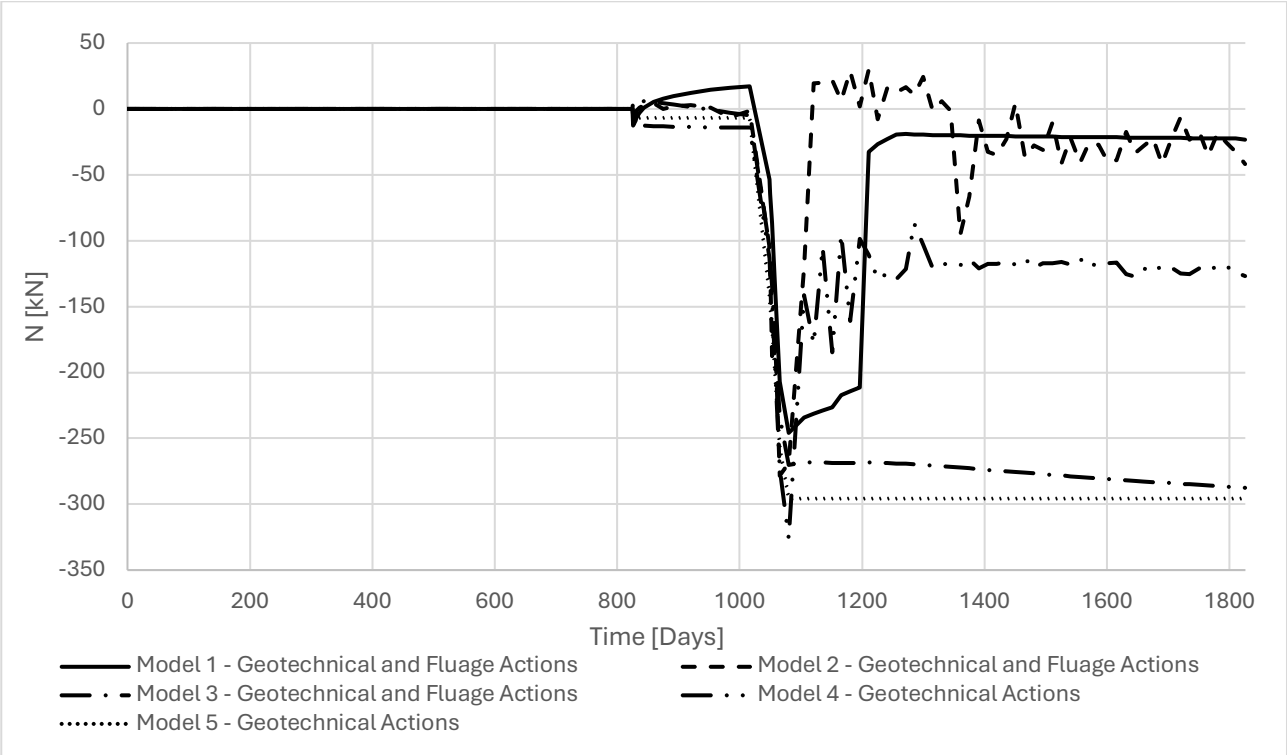


Figure 4-140 - Axial Force - Geotechnical and Creep Actions - Top Downhill Wall

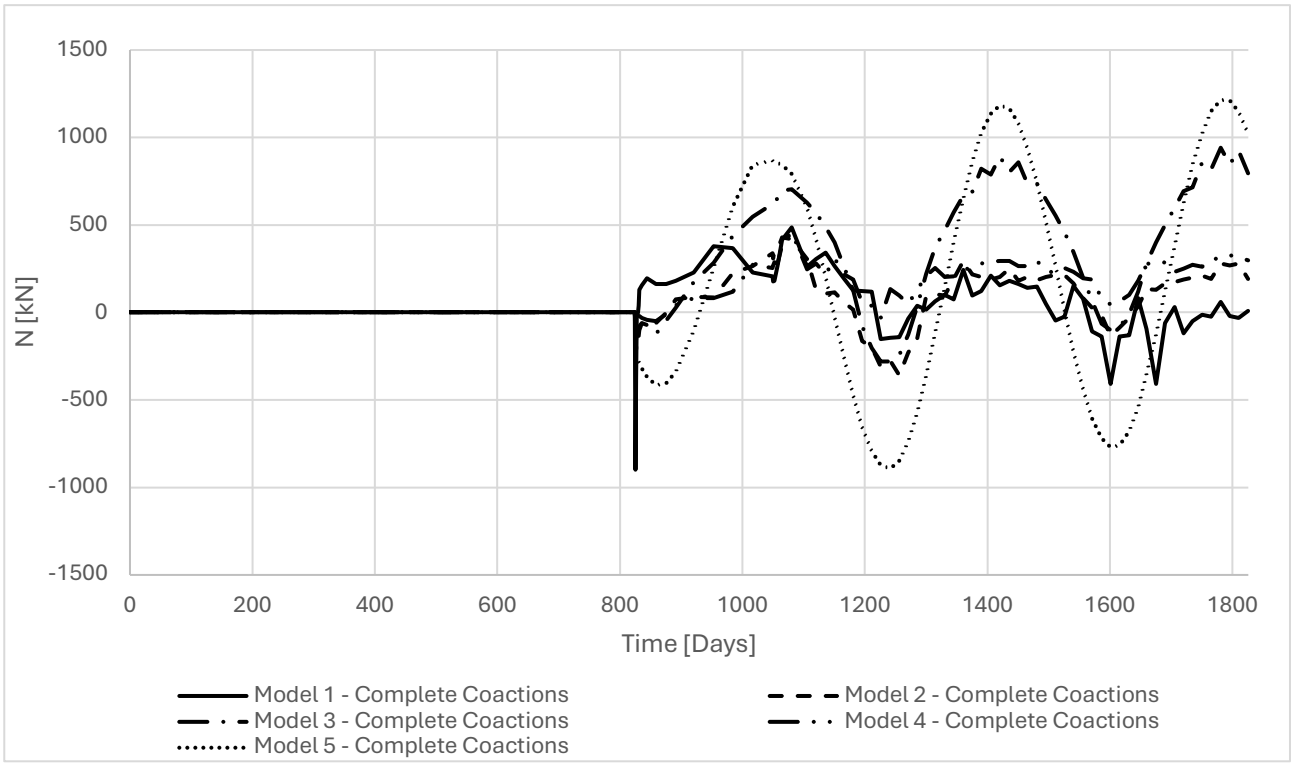


Figure 4-141 - Axial Force - Complete Coactions - Top Downhill Wall

Shear force diagrams:

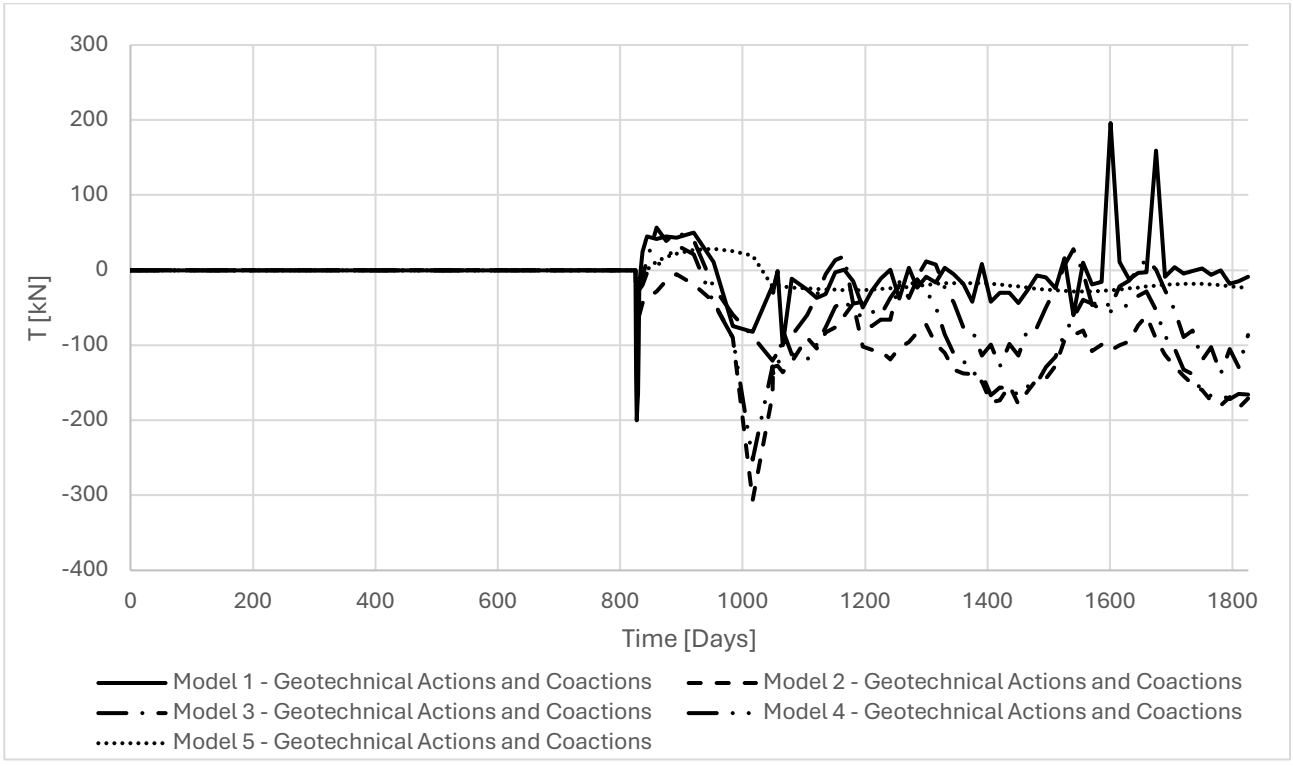


Figure 4-142 – Shear Force - Geotechnical Actions and Coactions - Top Downhill Wall

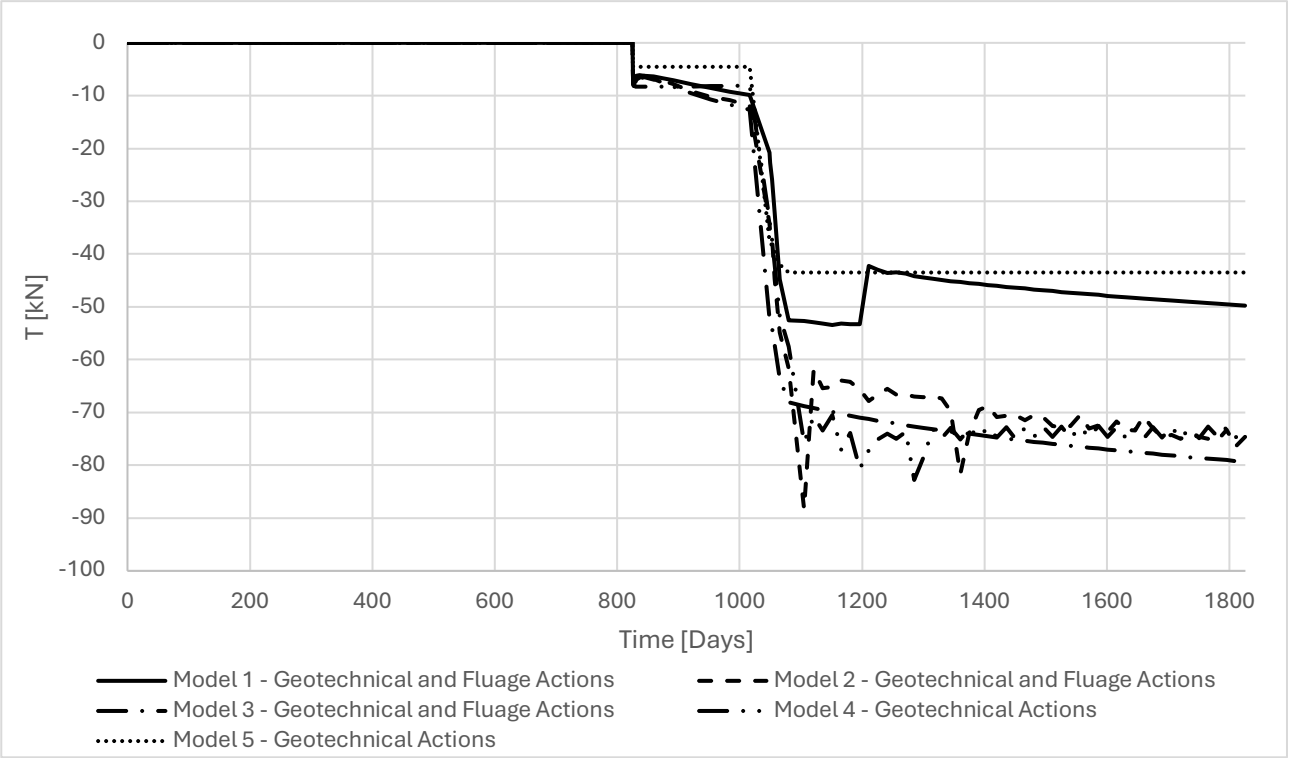


Figure 4-143 – Shear Force - Geotechnical and Creep Actions - Top Downhill Wall

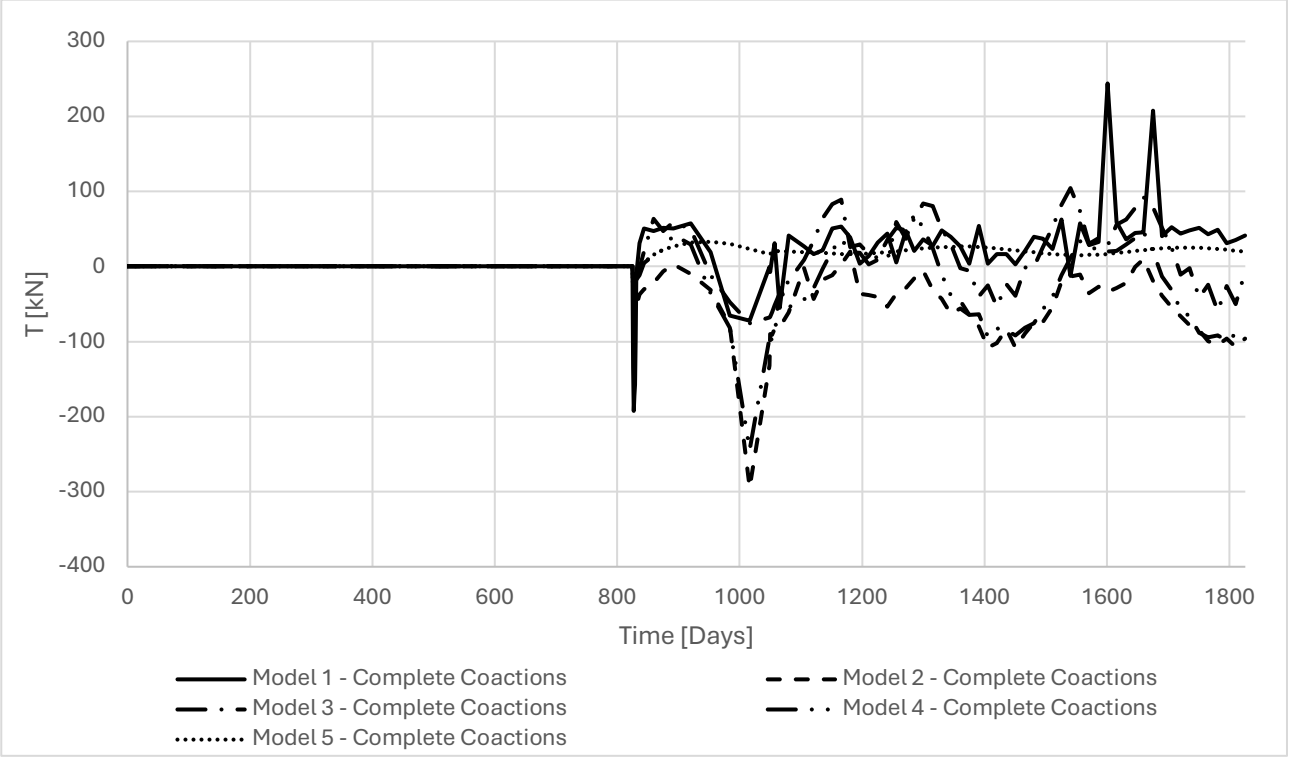


Figure 4-144 – Shear Force - Complete Coactions - Top Downhill Wall

4.7.2 Mid-height Section

Moment diagrams:

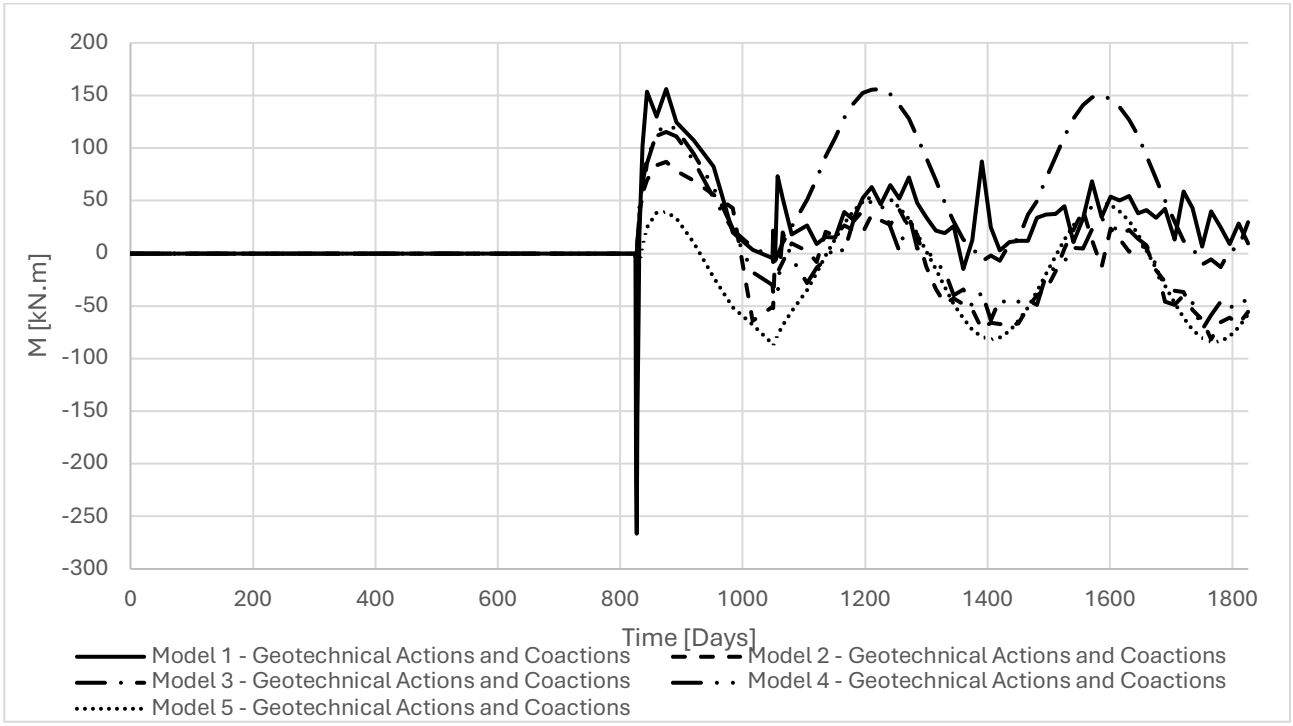


Figure 4-145 - Moment - Geotechnical Actions and Coactions – Mid-height Downhill Wall

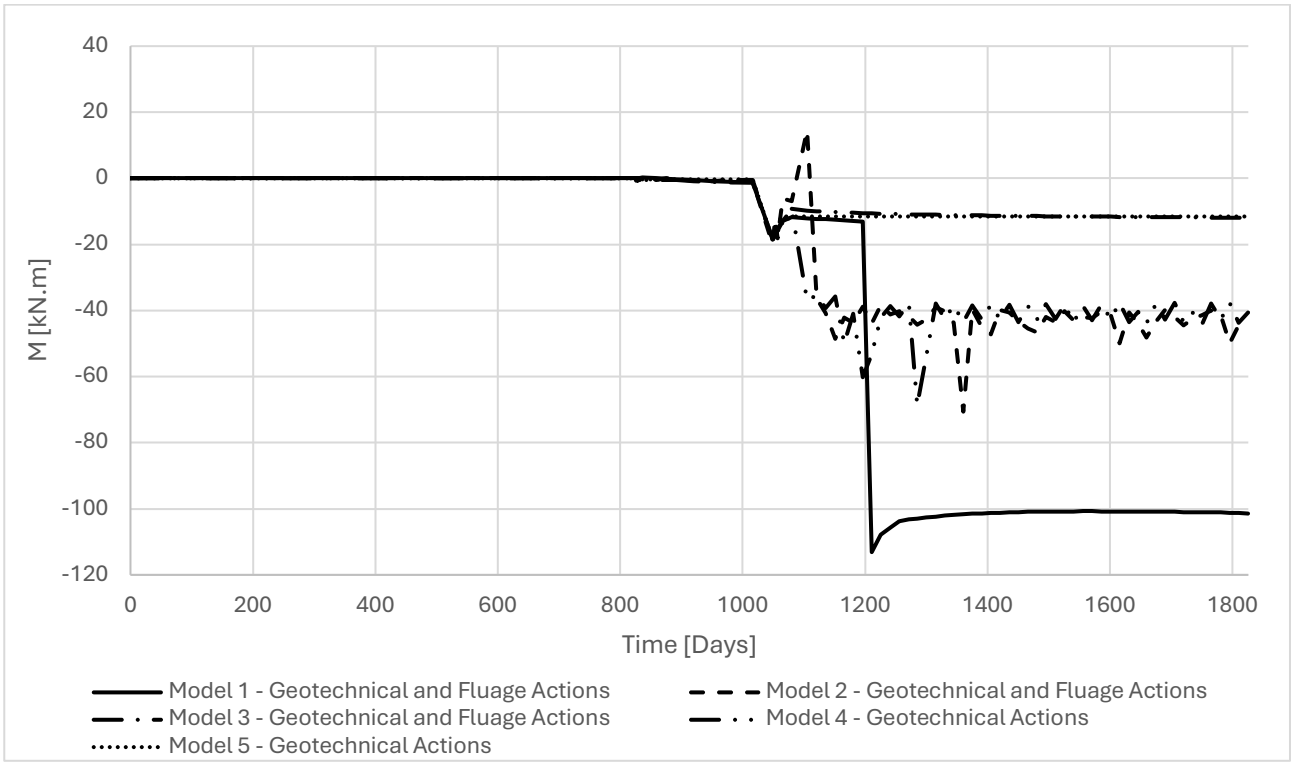


Figure 4-146 - Moment - Geotechnical and Creep Actions – Mid-height Downhill Wall

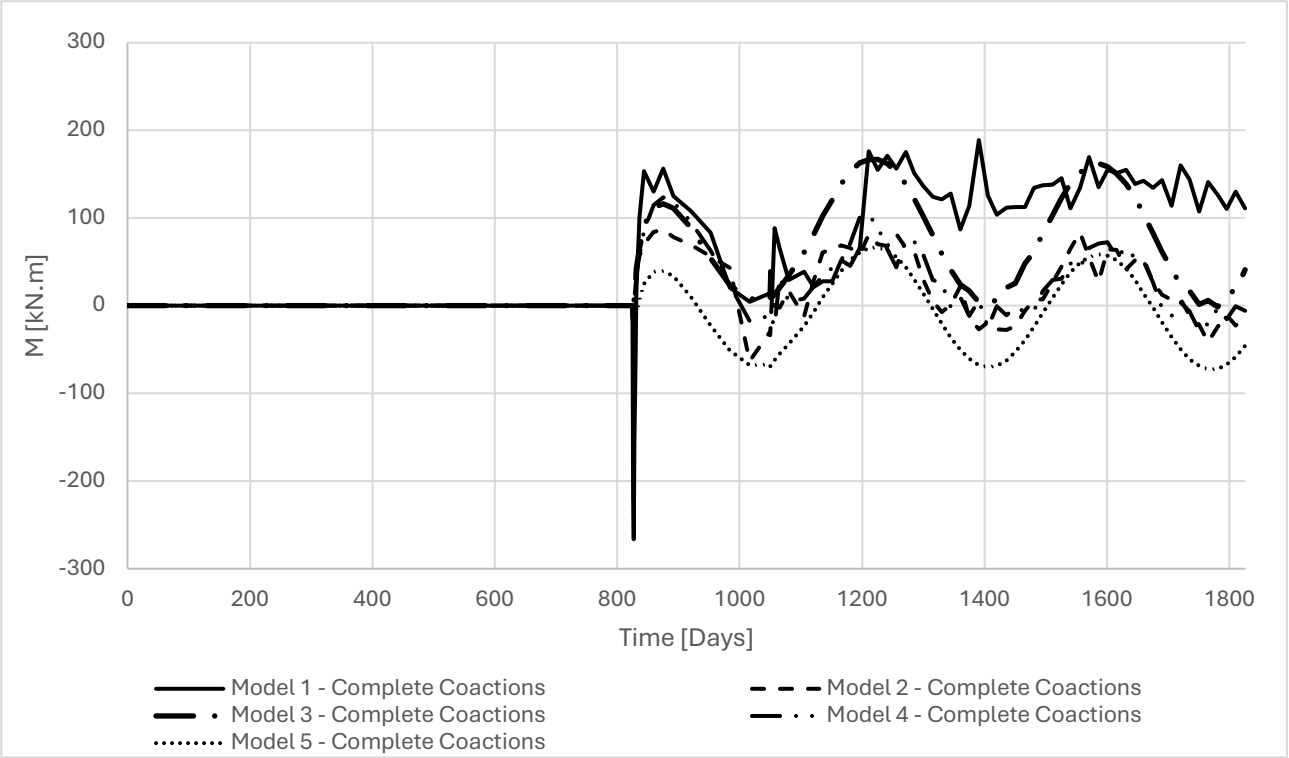


Figure 4-147 - Moment - Complete Coactions – Mid-height Downhill Wall

Axial force diagrams:

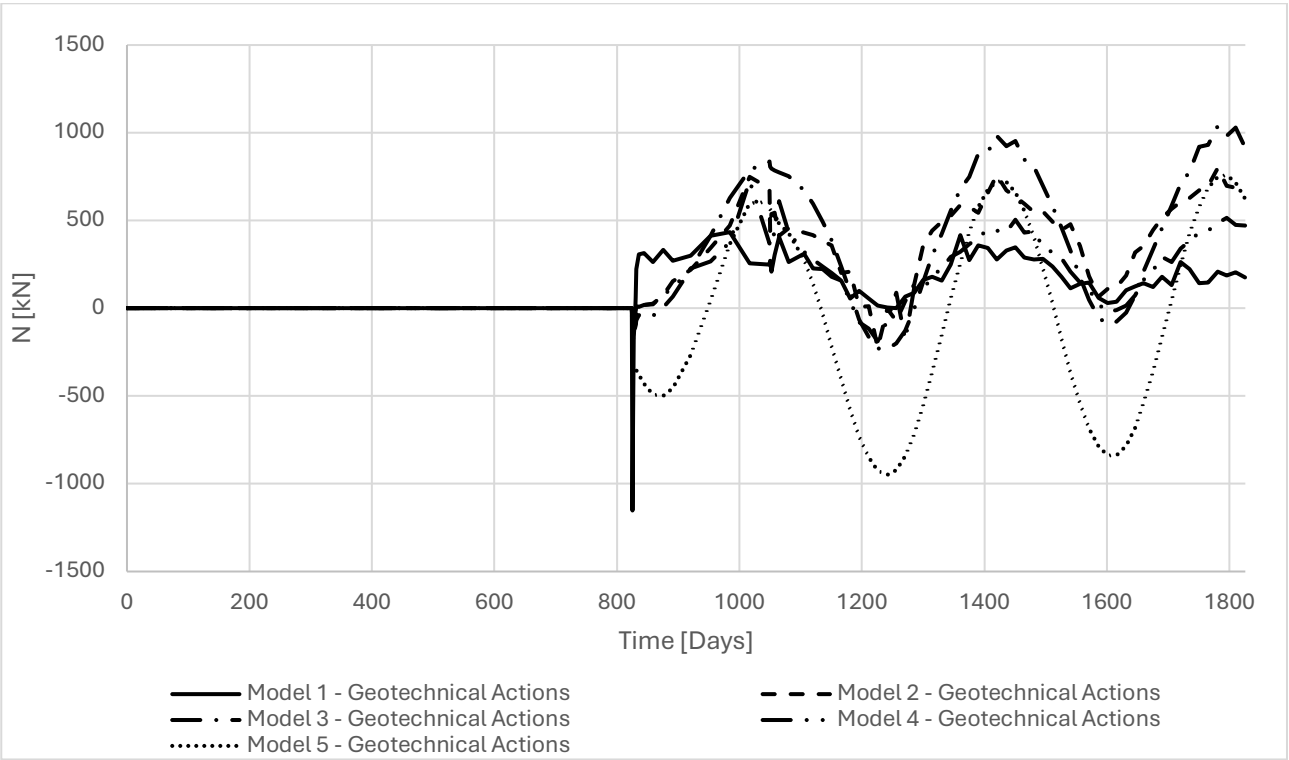


Figure 4-148 - Axial Force - Geotechnical Actions and Coactions – Mid-height Downhill Wall

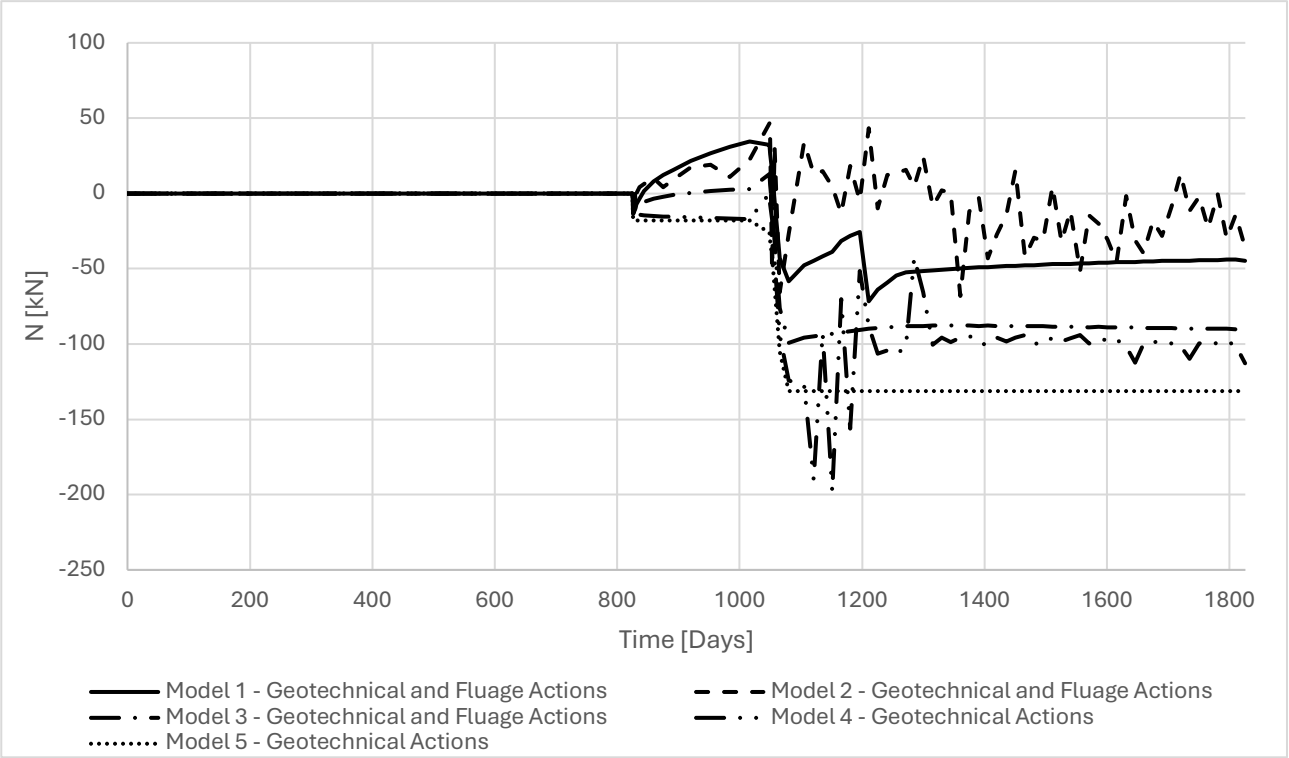


Figure 4-149 - Axial Force - Geotechnical and Fluage Actions – Mid-height Downhill Wall

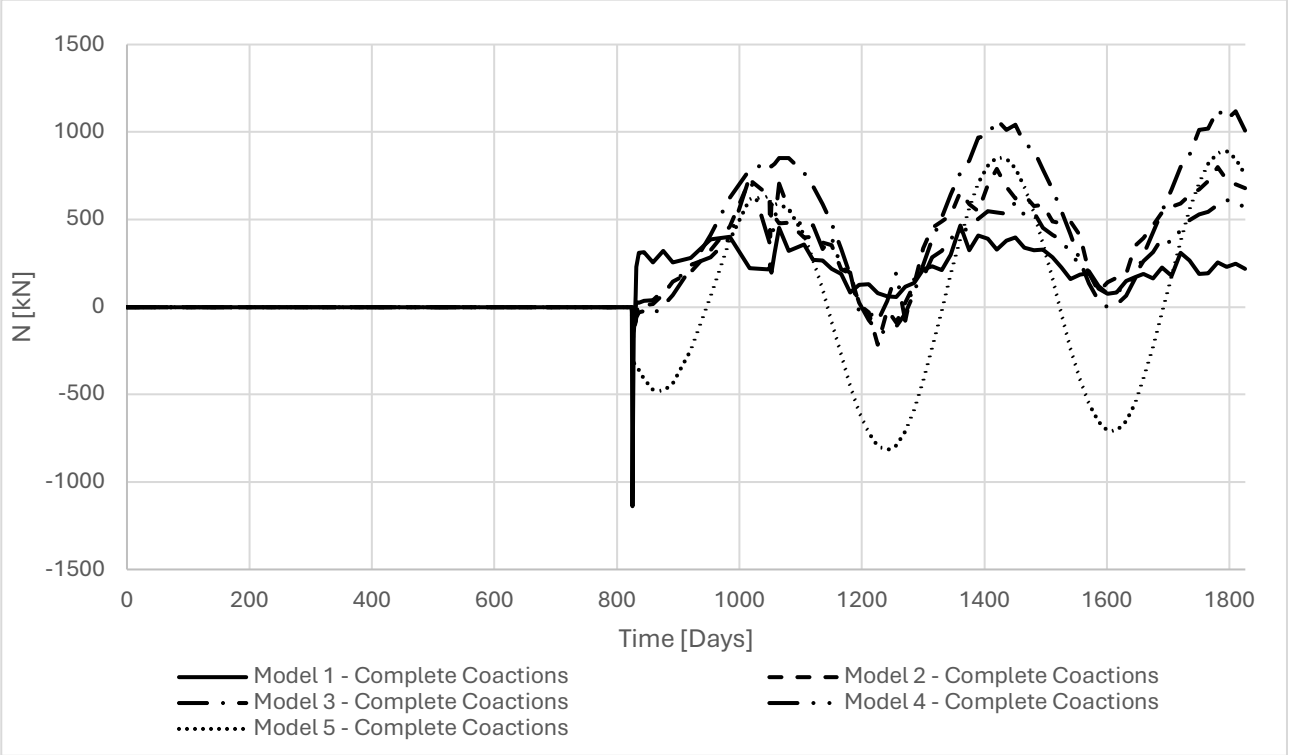


Figure 4-150 - Axial Force - Complete Coactions – Mid-height Downhill Wall

Shear force diagrams:

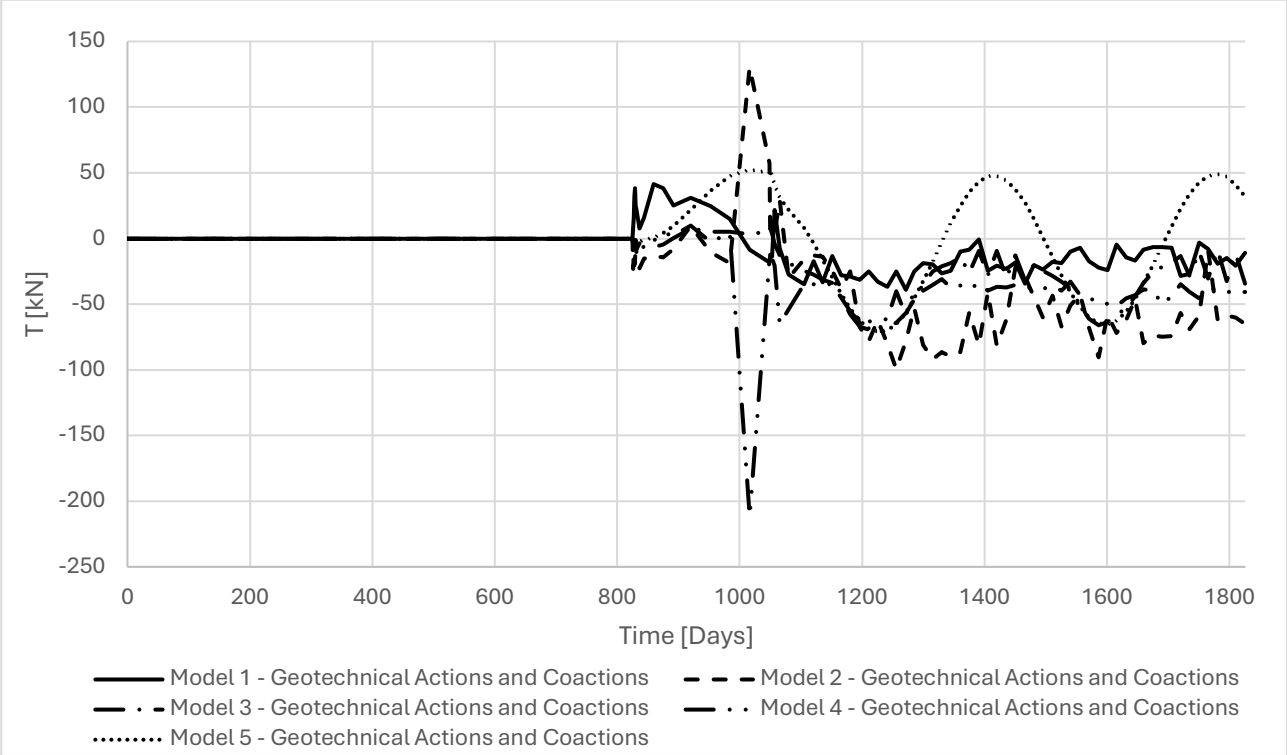


Figure 4-151 – Shear Force - Geotechnical Actions and Coactions – Mid-height Downhill Wall

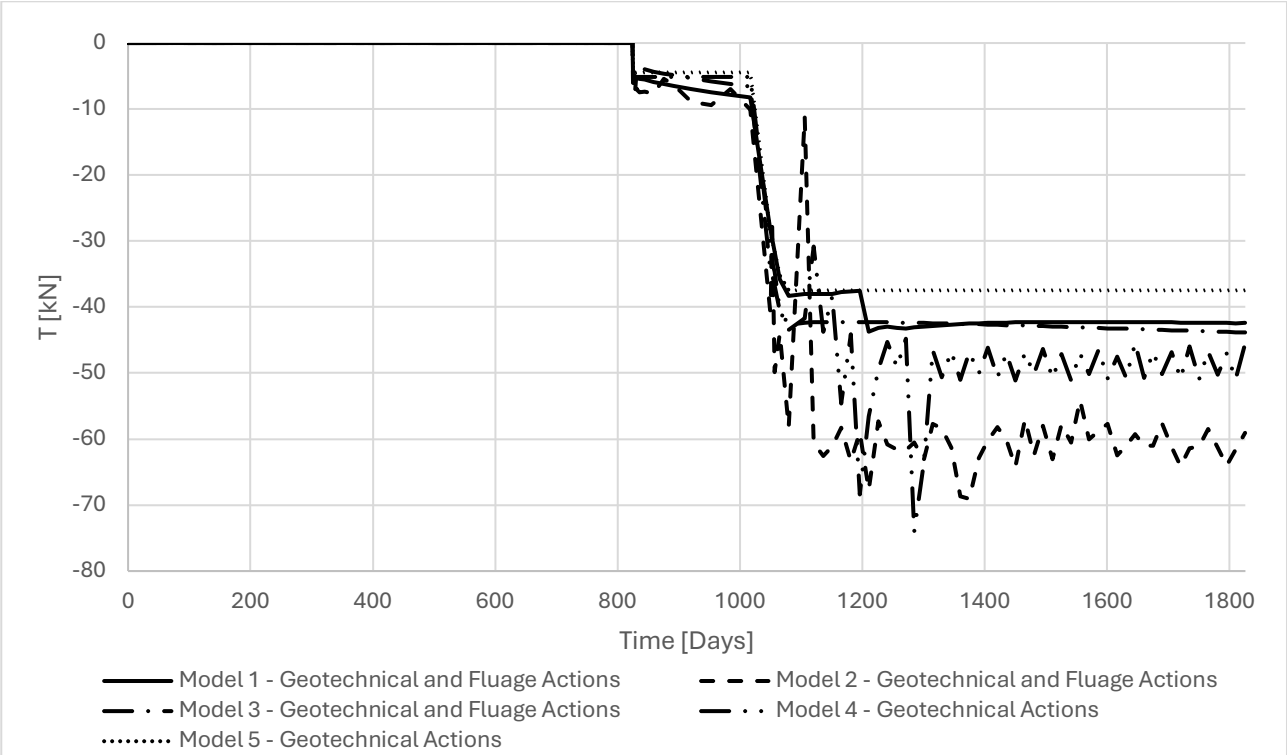


Figure 4-152 – Shear Force - Geotechnical and Creep Actions – Mid-height Downhill Wall

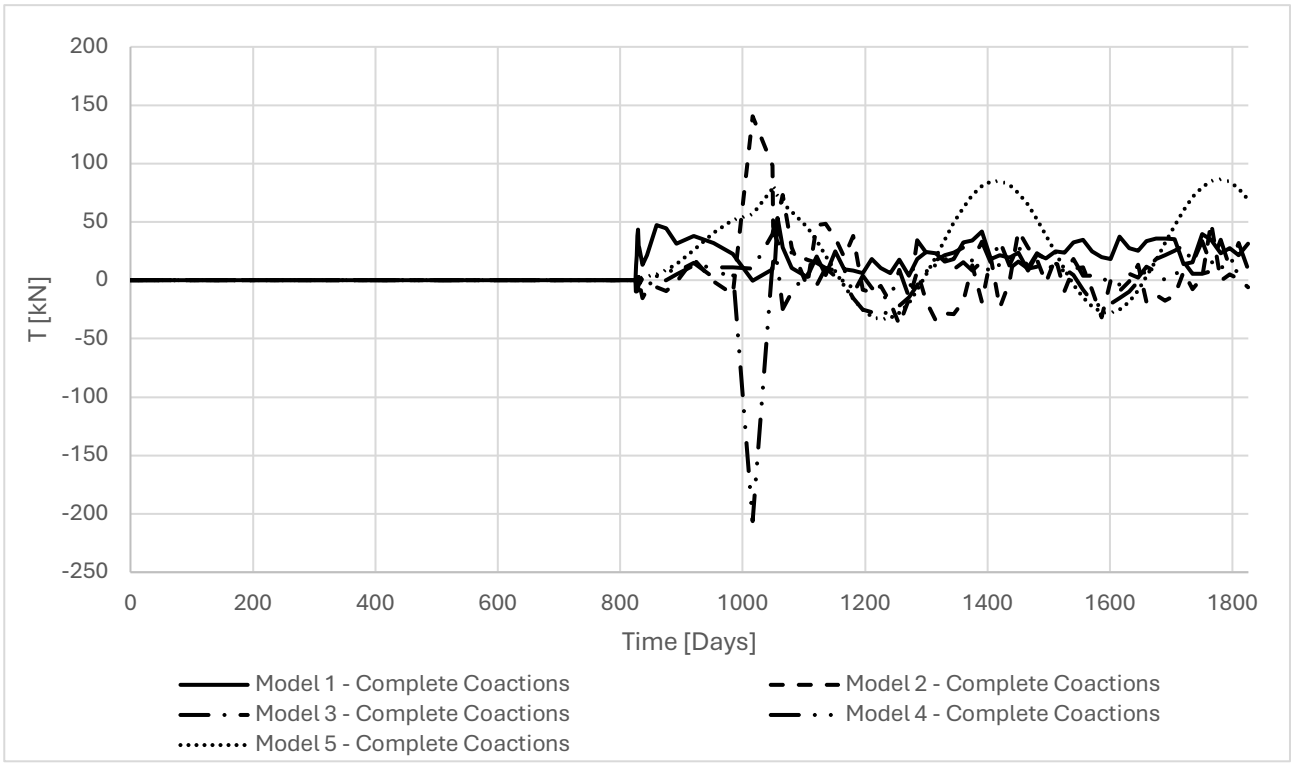


Figure 4-153 – Shear Force - Complete Coactions – Mid-height Downhill Wall

4.7.3 Bottom Section

Moment diagrams:

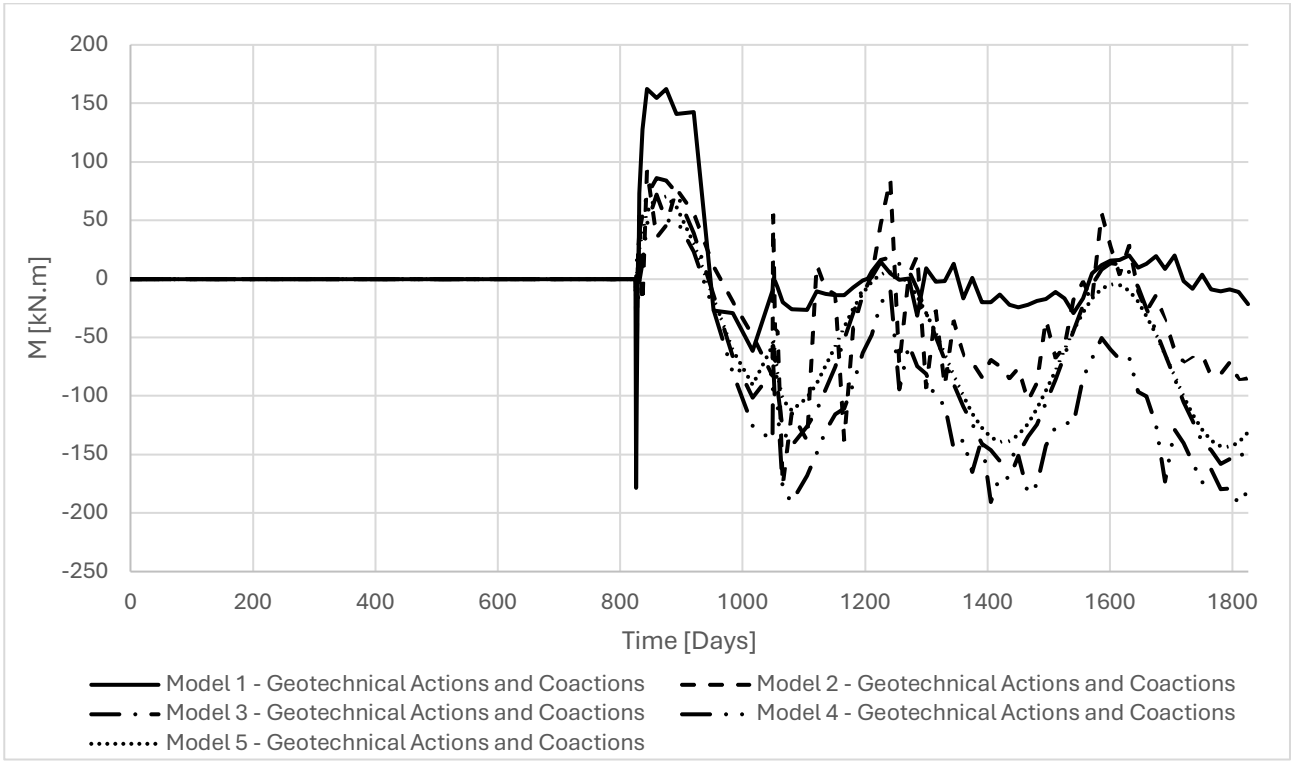


Figure 4-154 - Moment - Geotechnical Actions and Coactions - Bottom Downhill Wall

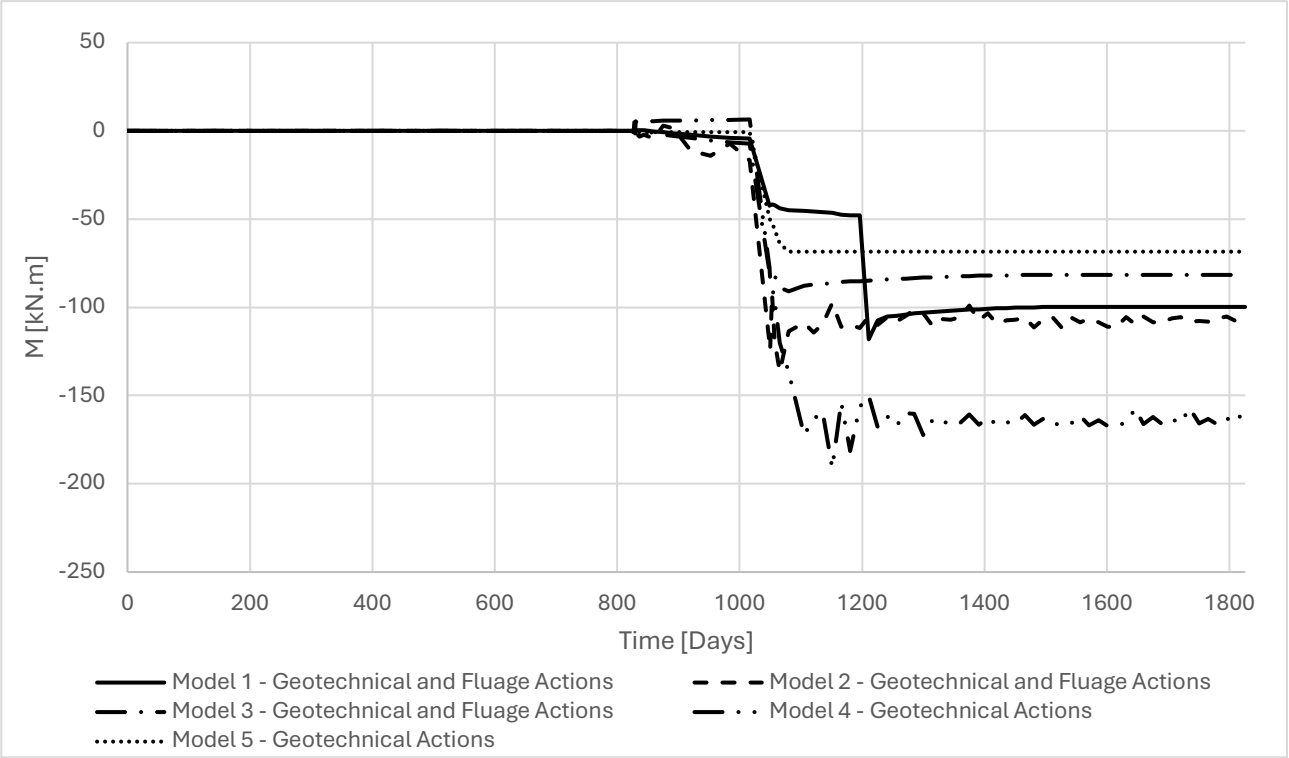


Figure 4-155 - Moment - Geotechnical and Creep Actions - Bottom Downhill Wall

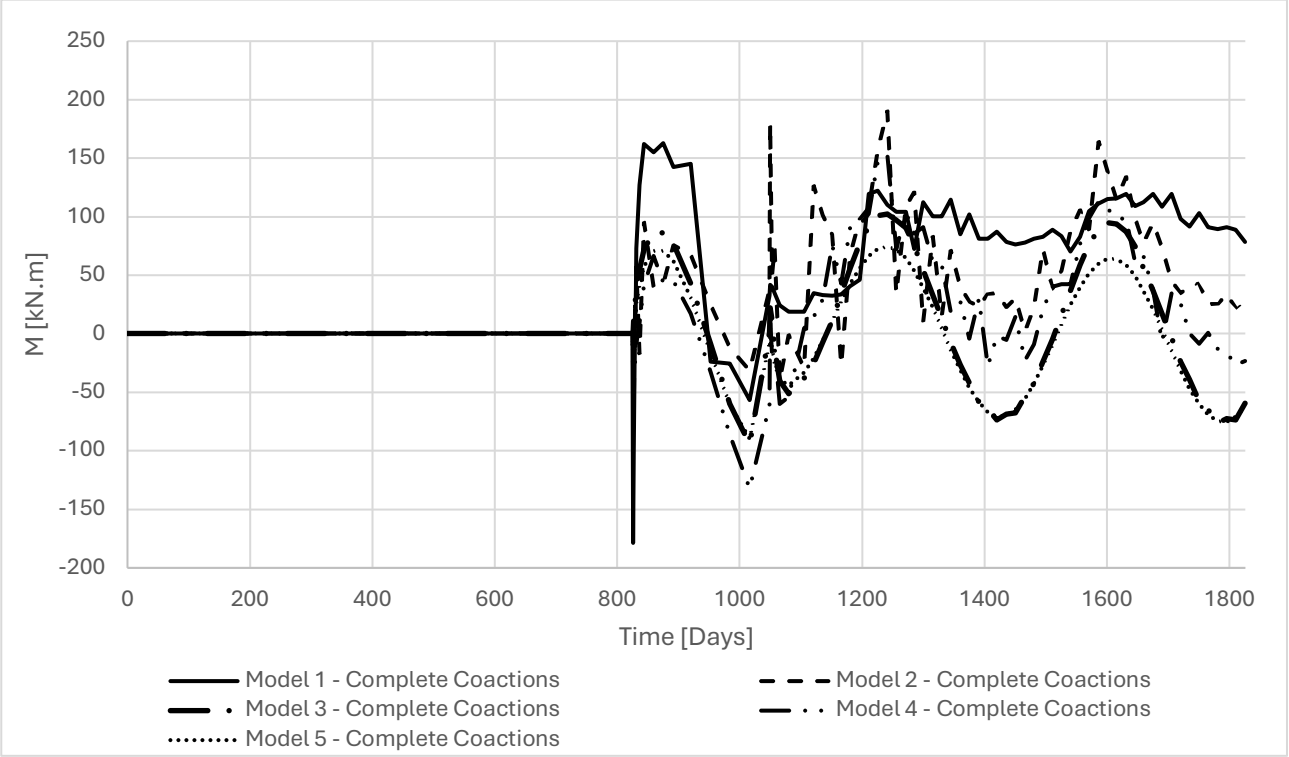


Figure 4-156 - Moment - Complete Coactions - Bottom Downhill Wall

Axial force diagrams:

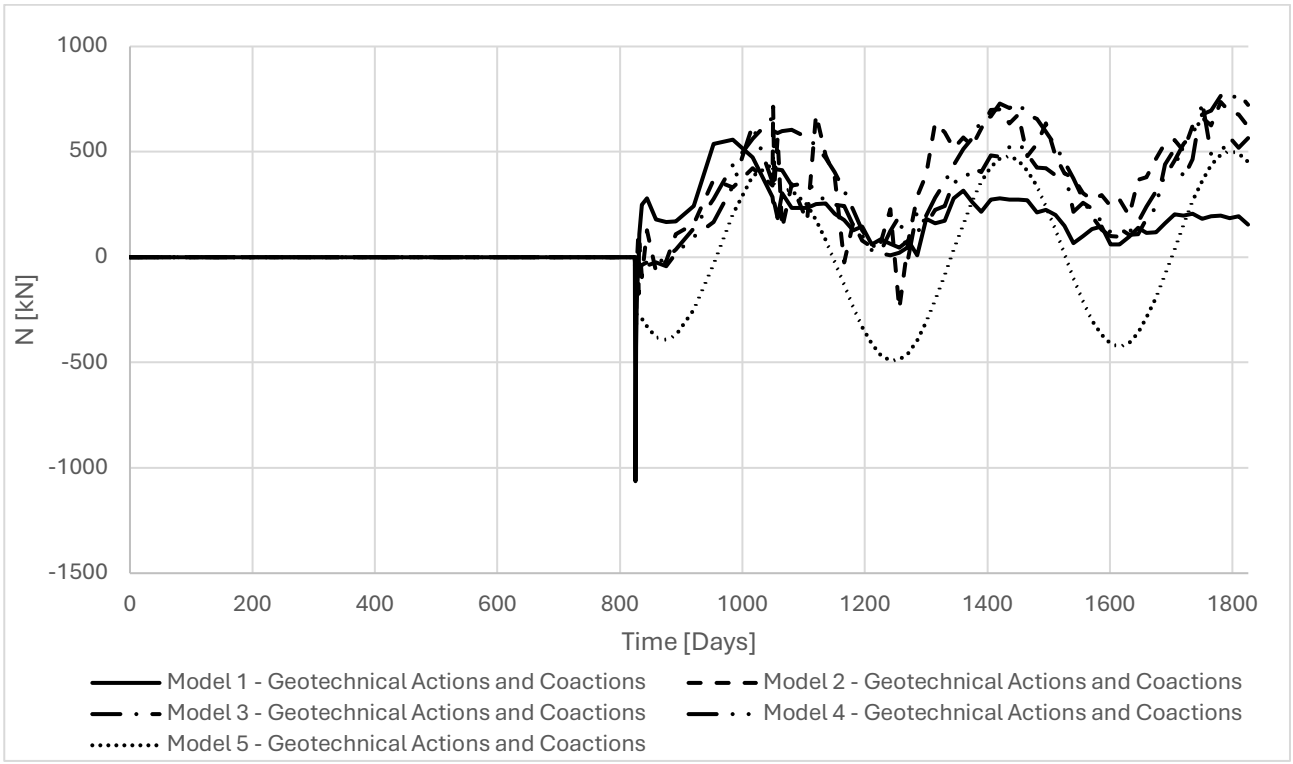


Figure 4-157 - Axial Force - Geotechnical Actions and Coactions- Bottom Downhill Wall

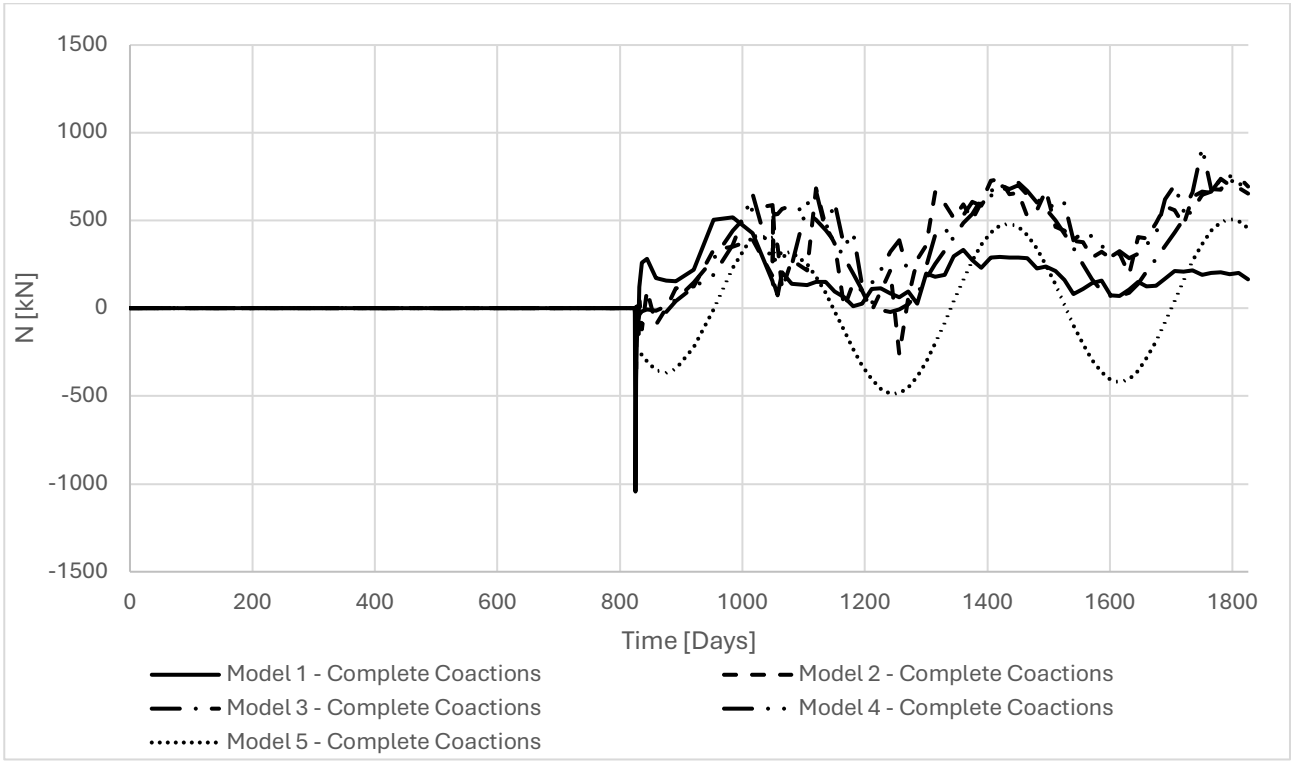


Figure 4-158 - Axial Force - Geotechnical and Creep Actions - Bottom Downhill Wall

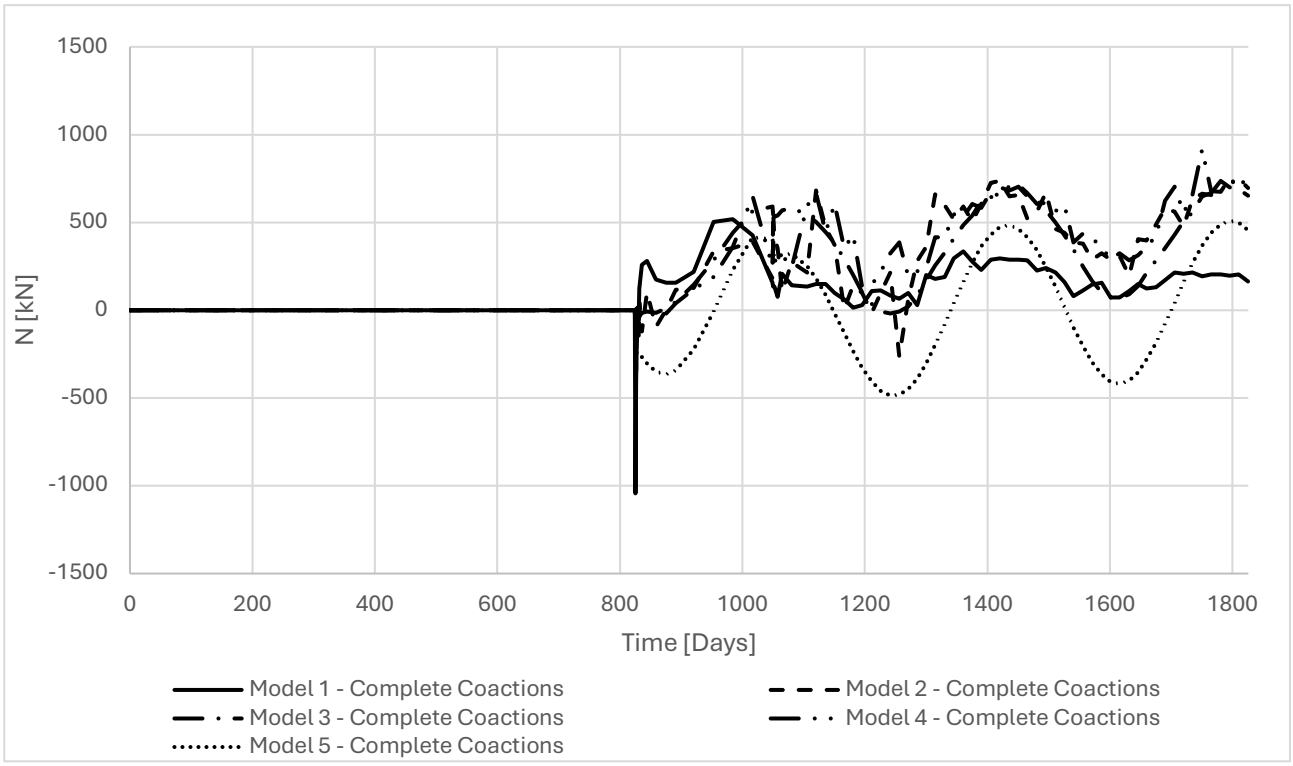


Figure 4-159 - Axial Force - Complete Coactions - Bottom Downhill Wall

Shear force diagrams:

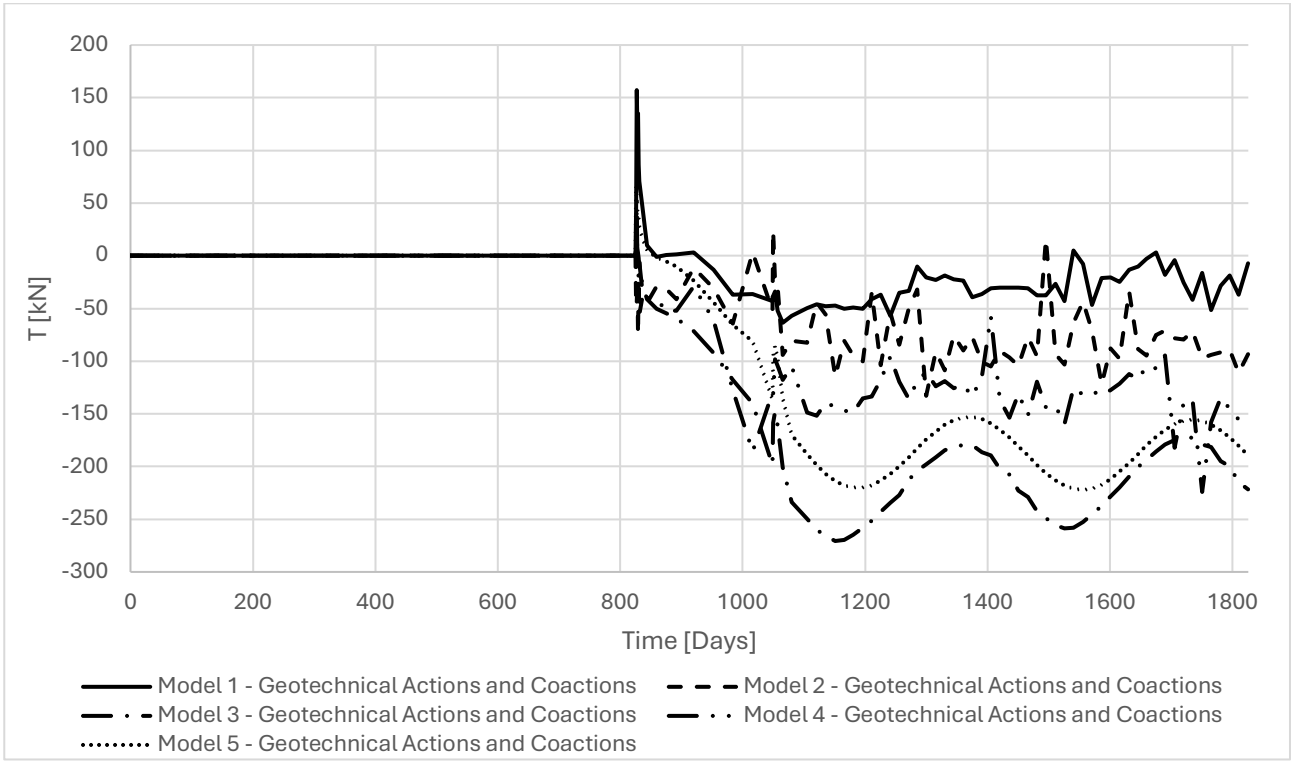


Figure 4-160 – Shear Force - Geotechnical Actions and Coactions - Bottom Downhill Wall

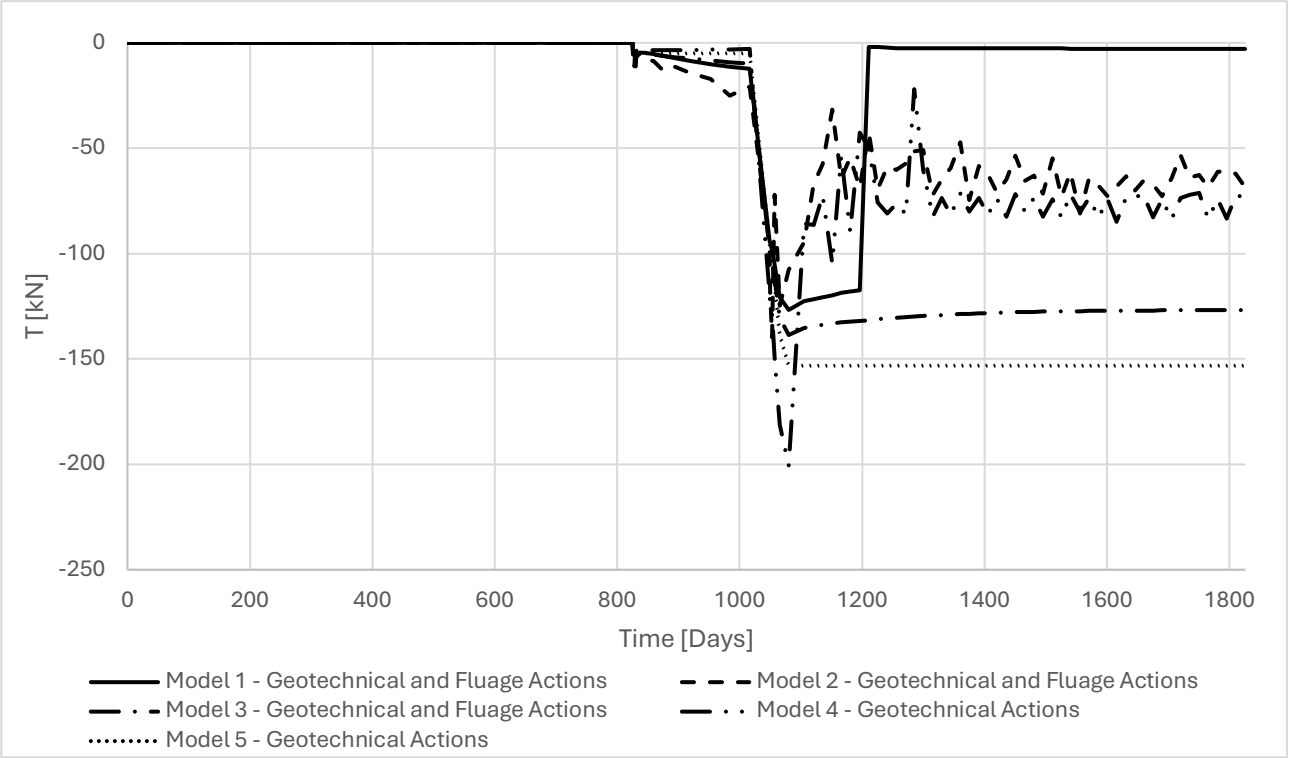


Figure 4-161 – Shear Force - Geotechnical and Creep Actions - Bottom Downhill Wall

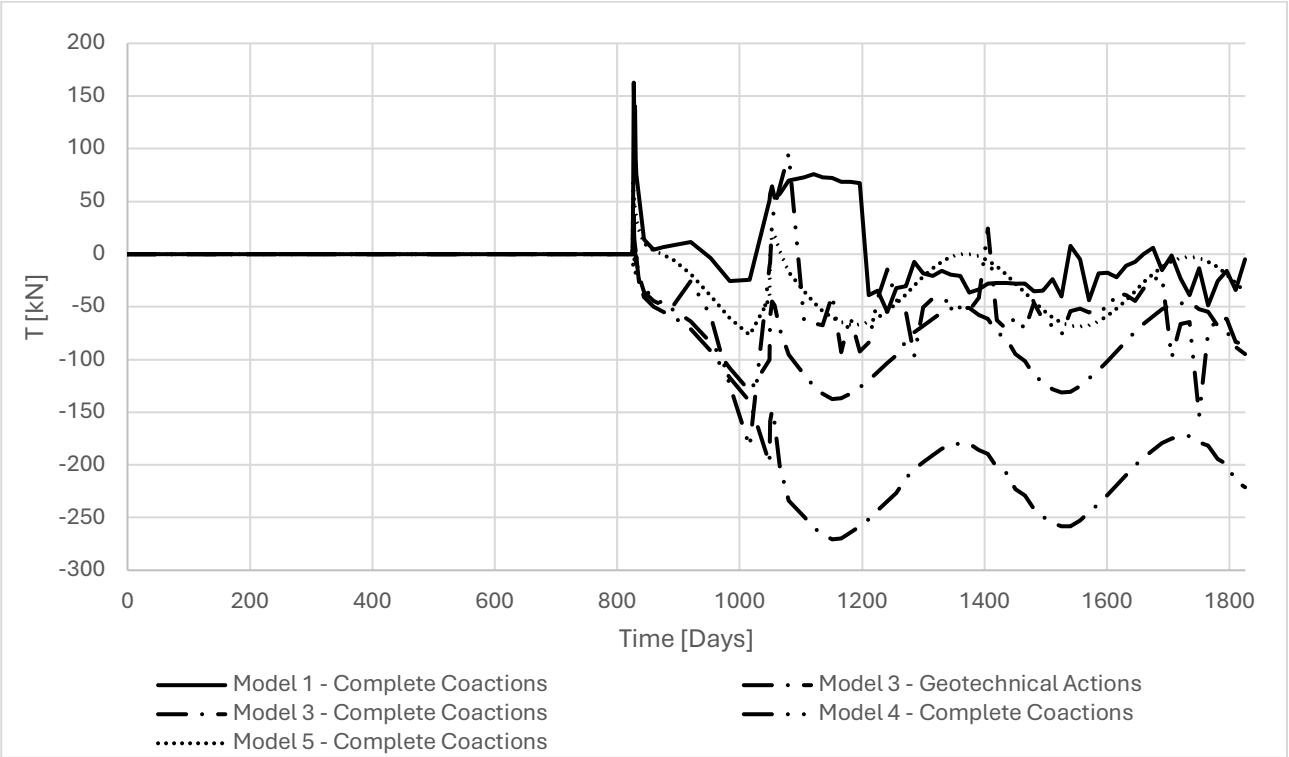


Figure 4-162 – Shear Force - Complete Coactions - Bottom Downhill Wall

4.7.4 Discrepancies between Models and Actions Combinations

Prior to phase 8 ($t = 841$ days), all internal actions across the downhill wall are identically zero ($M = 0, N = 0, T = 0$) because the corresponding continuum finite elements remain deactivated in the numerical staging throughout the preliminary excavation, kerb, cover slab, and foundation invert construction phases. Once activated upon casting at $t = 841$ days, the comparative evaluation across the top, mid-height, and bottom sections demonstrates how multi-field thermo-mechanical coupling, non-linear tensile softening, and viscoelastic creep govern the structural behaviour of the valley-side wall under asymmetric boundary restraints.

During early-age maturation, the degree-of-reaction thermo-mechanical kinetics modelled in model 1 capture severe transient coactions that are absent in standard formulations. The rapid exothermic expansion of the wall concrete, rigidly confined between the previously matured top cover slab and the foundation invert, generates an immediate longitudinal compressive surge along the entire wall height ($N \approx -900\ kN$ at the top in Figure 4-139 and Figure 4-141; $N \approx -1100\ kN$ at mid-height in Figure 4-148 and Figure 4-150; $N \approx -1050\ kN$ at the bottom in Figure 4-157 and Figure 4-159). Concurrently, steep through-thickness thermal gradients induce sharp early negative bending drops ($M \approx -145\ kN * m$ at the top in Figure 4-136 and Figure 4-138; $M \approx -265\ kN * m$ at mid-height in Figure 4-145 and Figure 4-147; $M \approx -180\ kN * m$ at the bottom in Figure 4-154 and Figure 4-156) accompanied by localized joint shear shocks ($T \approx -200\ kN$ at the top in Figure 4-142 and Figure 4-144; $T \approx +160\ kN$ at the bottom in Figure 4-160 and Figure 4-162). In contrast, models 2 through 5 omit hydration kinetics on subsequent pours, exhibiting smooth, monotonic baselines that fail to account for these early-age stress peaks.

Following the complete backfilling phase at $t = 1065$ days (phase 9), viscoelastic relaxation becomes the dominant mechanism governing long-term equilibrium. In the linear baseline (model 5), the placement of the overburden locks in elevated, unrelaxed compressive forces ($N = -295\ kN$ at the top and $N = -130$ kN at mid-height; Figure 4-140 and Figure 4-149) and high sustained shear forces ($T = -43\ kN$ at the top and $T = -150\ kN$ at the bottom; Figure 4-143 and Figure 4-161). In models 1 and 2, the creep enables the wall to shed vertical axial loads to the adjacent ground and foundation piles, relaxing sustained top compression to $N \approx -20$ to $-25\ kN$ (Figure 4-140) and mid-height compression to $N \approx -40$ to $-45\ kN$ (Figure 4-149), while reducing sustained bottom shear by 53% ($T \approx -75$ kN in Figure 4-161). Conversely, model 4 (cracking without creep) suffers $ stiffness loss without viscous relaxation,

locking in an excessive sustained negative bending moment at the base ($M \approx -160\ kN*m$, Figure 4-155).

In the long-term cyclic service regime ($t > 1122$ days), the linear elastic assumption in model 5 treats seasonal temperature fluctuations as rigid external loads, generating extreme cyclic axial swings ($\Delta N \approx 2150\ kN$ at the top in Figure 4-139; $\Delta N \approx 1850$ kN at mid-height in Figure 4-148; $\Delta N \approx 1000$ kN at the bottom in Figure 4-157). This produces artificial summer tensile excursions ($N \approx +900$ to $+950$ kN) that would drive spurious cross-sectional reinforcement additions in standard design checks. In models 1 and 2, localized cracking relieves tensile restraint stresses while viscoelastic creep absorbs compressive cycles, restricting cyclic axial variations to a narrow envelope: $\Delta N \approx 450$ to $650\ kN$, representing an over 70% reduction relative to model 5 and stabilizing cyclic bending moments within narrow bands ($M \approx -50$ to $+50\ kN*m$ at the top in Figure 4-136; $M \approx -20$ to $+20\ kN*m$ at the bottom in Figure 4-154). This shows that under the modelling assumptions the linear elastic evaluations overestimate force demands and mischaracterize the true stress state of underground walls by neglecting the natural stress-relieving mechanisms of concrete.

Chapter 5 Safety Evaluation

A safety format is simply a standardized mathematical rule used to build safety margins into our calculations, ensuring the structure can easily handle unexpected overloads or weaker-than-expected materials. The goal of this chapter and more globally of this work, is to compare different safety formats at 50 years to observe if the advanced non-linear model and therefore their safety format reveal hidden structural safety reserves that the traditional approach misses.

5.1 Traditional Design Approach

5.1.1 Theoretical Principles

The traditional safety format is structurally rooted in the semi-probabilistic partial safety factor method, which forms the regulatory baseline for modern structural design codes such as Eurocode 2 (EN 1992) and the Italian National Building Code (NTC 2018). The core theoretical philosophy of this format relies on the strict segregation of uncertainties. Instead of assessing the statistical reliability of a structure as a unified system, the method separates variables into two independent domains: the action side: loads and the resistance side: material strengths. A key capability of the finite element solver DIANA FEA and the model methodology is the possibility to isolate the different actions by repeating the analysis and changing the loads. Therefore, the structural response is discretized into four distinct, independent action components:

- Geotechnical actions (GEO): Internal forces generated by the static self-weight of the concrete frame, lateral earth pressures from the landslide and hydrostatic groundwater variations.
- Thermal hydration actions (TH): Restrained internal forces triggered exclusively by early-age exothermic cement hydration heat cycles and transient temperature fields.
- Shrinkage actions (SH): Internal volumetric contraction forces arising from the chemical maturation of the concrete matrix over time.
- Viscoelastic creep actions (CR): Time-dependent stress relaxation components that modify the long-term internal force distribution under sustained boundary constraints.

Rather than applying a single uniform safety multiplier to the entire model output, these individual raw action components are combined linearly. Distinct partial safety factors, γ_i are applied to each independent physical contributor to compute the ultimate global design actions (M_{Ed}, N_{Ed} and T_{Ed}).

The verifications will be carried out for the geotechnical actions alone, and for a combination of the 4 components listed above by using these specific partial safety coefficients:

Table 5-1- Safety Factor Combination

Combination Framework	γ_{GEO}	γ_{TH}	γ_{SH}	γ_{CR}
Version 1	1,3	1,5	1,0	1,0
Version 2	1,3	1,5	1,2	1,2

To compile the individual components extracted from DIANA FEA into the final ultimate limit state design actions, the linear superposition operator is applied using the following explicit system of formulas:

$$M_{Ed} = \gamma_{GEO} * M_{GEO} + \gamma_{TH} * M_{TH} + \gamma_{SH} * M_{SH} + \gamma_{CR} * M_{CR} \quad (59)$$

$$N_{Ed} = \gamma_{GEO} * N_{GEO} + \gamma_{TH} * N_{TH} + \gamma_{SH} * N_{SH} + \gamma_{CR} * N_{CR} \quad (60)$$

$$V_{Ed} = \gamma_{GEO} * V_{GEO} + \gamma_{TH} * V_{TH} + \gamma_{SH} * V_{SH} + \gamma_{CR} * V_{CR} \quad (61)$$

5.1.2 Component Breakdown of Internal Actions

Prior to applying the partial safety factors defined in Table 5-1, t is essential to examine the un-factored, time-dependent evolution of each individual physical action component. Disaggregating the raw FEA results into its isolated contributors provides clear insight into the governing drivers of structural demand across the operational lifespan of the portal frame. The following time-history figures plot the individual physical components of bending moment, axial force, and transverse shear thrust extracted at the governing critical section for each primary structural member over an extended timeline of up to 18,000 days, 50 years.

Cover slab

The critical section for the cover slab is the midspan and it reveals different insights on which physical action governs each internal force.

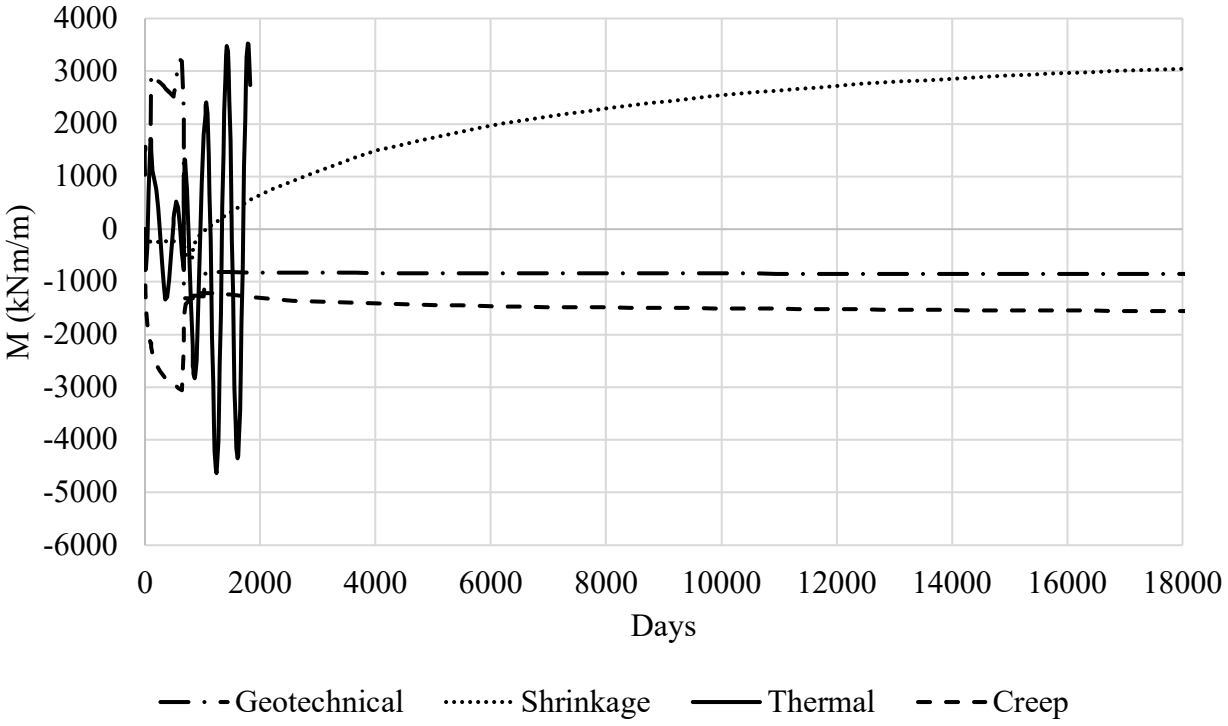


Figure 5-1 - Component Disaggregation of Bending Moment – Cover Slab Midspan

The bending moment in the cover slab is governed by the thermal actions, through a cyclic flexural demand following the season thermal oscillations between 3500 kNm/m and -5000 kNm/m and the concrete shrinkage in the long term, steadily accumulating to a permanent baseline of 3000 kNm/m over 50 years.

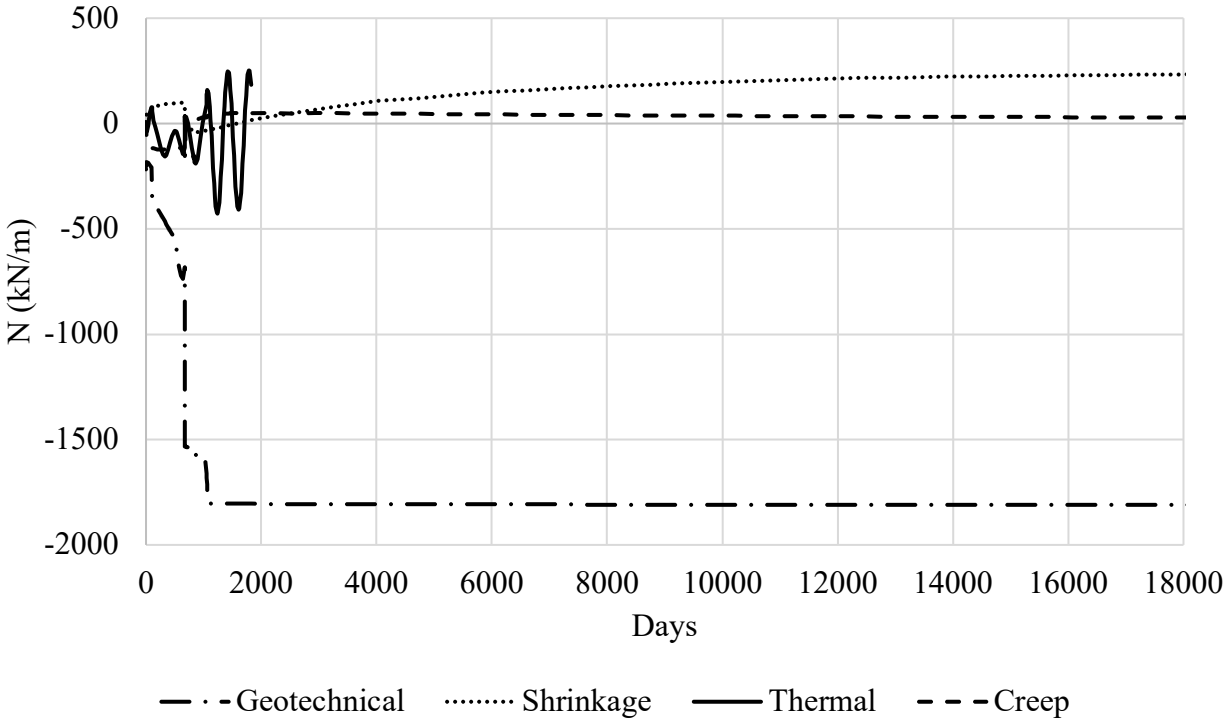


Figure 5-2 - Component Disaggregation of Axial Force – Cover Slab Midspan

The axial normal force (N) is governed by the geotechnical actions, triggering an immediate step-jump down to -1700 kN/m at day 673, corresponding to the core excavation.

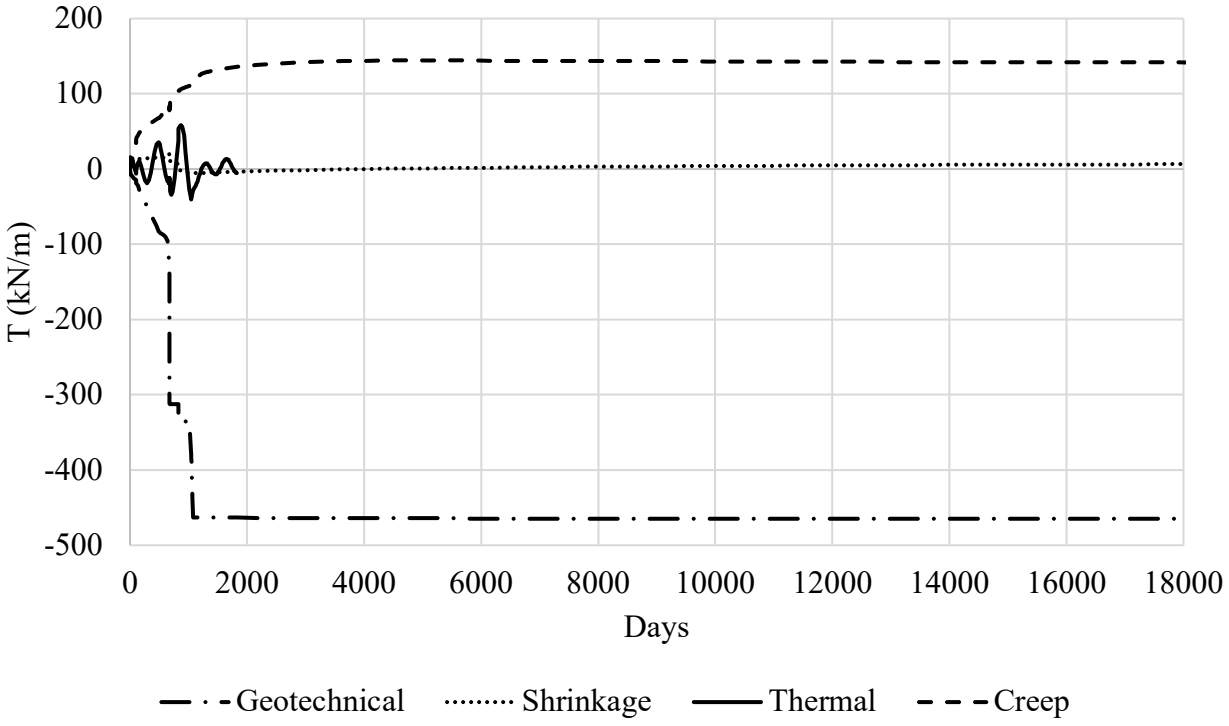


Figure 5-3 - Component Disaggregation of Shear Force – Cover Slab Midspan

The transverse shear thrust is governed by the geotechnical actions, demanding a permanent baseline of -450 kN/m that is partially offset by the long-term creep redistribution: 120 kN/m.

Uphill (Φ=1200 mm) pile

The most critical section of the uphill pile of 1200 mm diameter is the head of the pile.

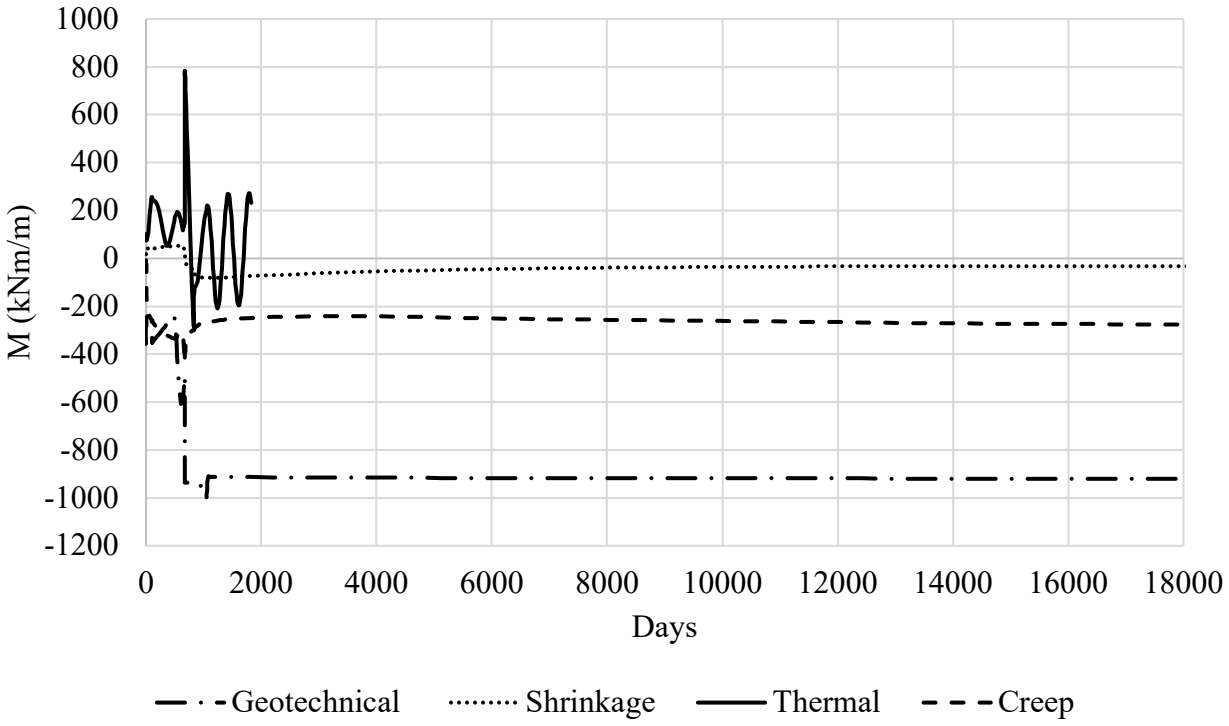


Figure 5-4 - Component Disaggregation of Bending Moment - Head of Pile 1200 Uphill

The thermal actions govern the bending moment, through seasonal flexural swings, oscillating between 700 kNm/m and -1000 kNm/m. Then from the day 673, the geotechnical and creep actions create a baseline of -1100 kNm/m and -250 kNm/m respectively.

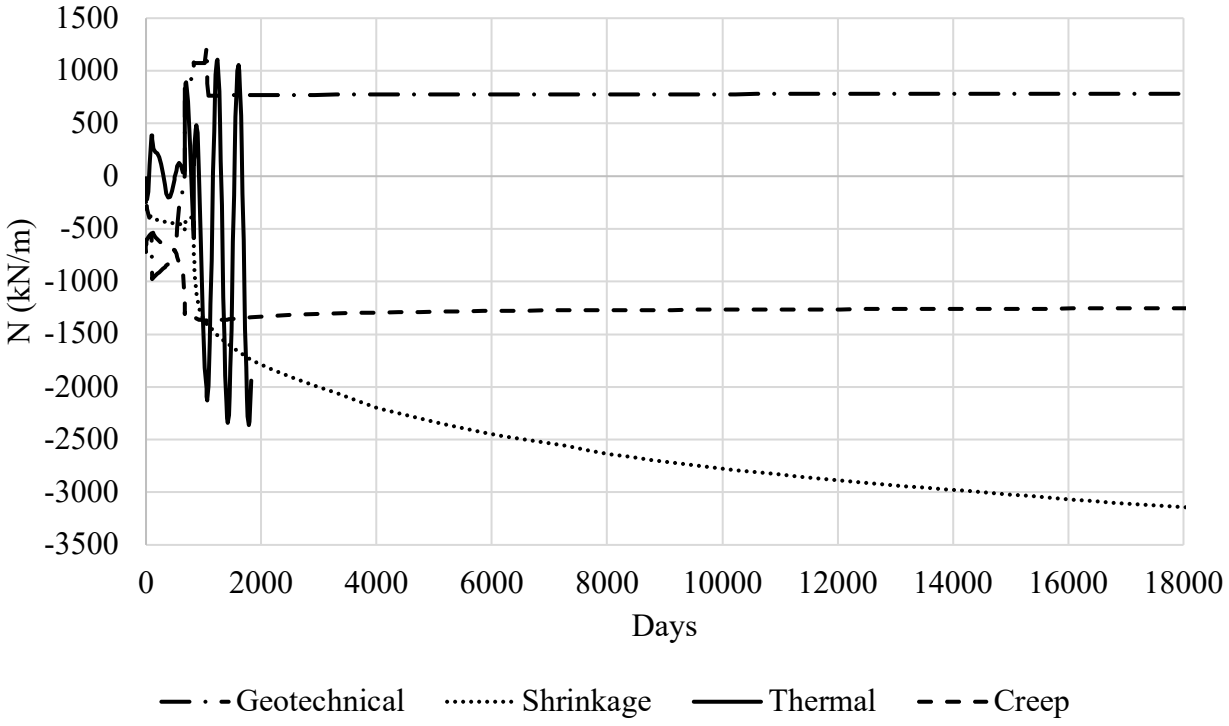


Figure 5-5 - Component Disaggregation of Axial Force - Head of Pile 1200 Uphill

The shrinkage and creep action dictate long term axial compression by reaching a plateau at the end of the analysis of -1900 kN/m and -3500 kN/m respectively. On the contrary, in the short term, the axial force is governed by the fluctuations of the thermal actions between -1000 and 1000 kN/m.

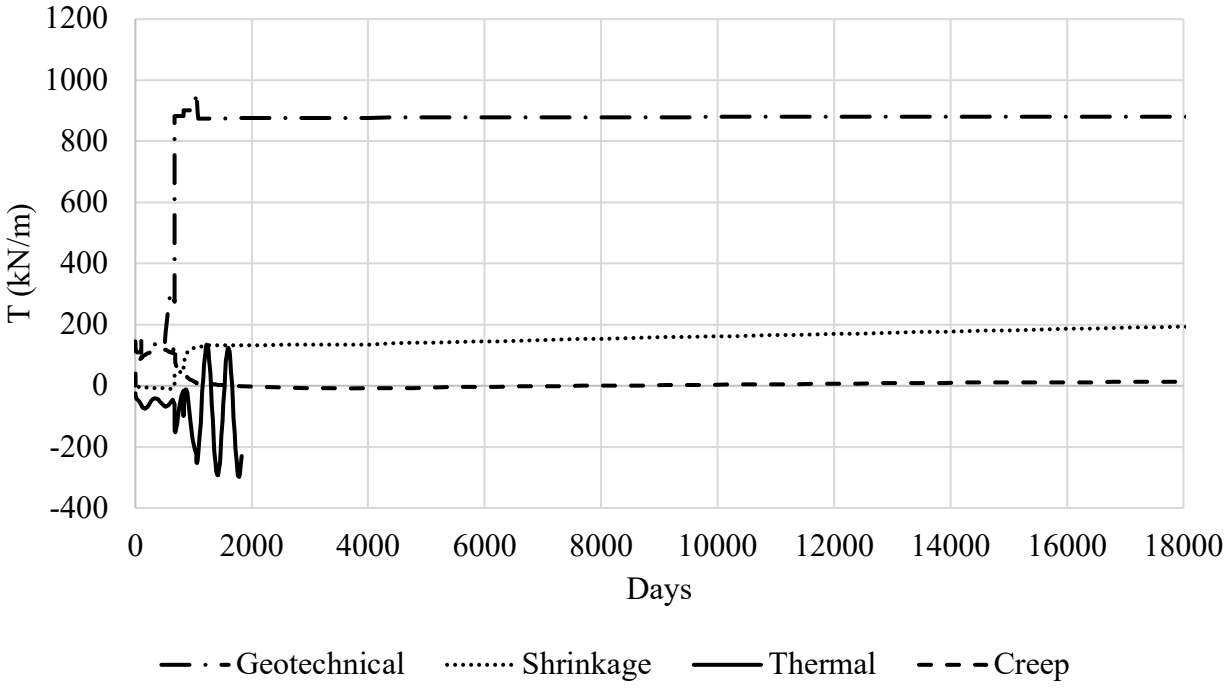


Figure 5-6 - Component Disaggregation of Shear Force - Head of Pile 1200 Uphill

The geotechnical actions govern permanent shear demand, jumping post-excavation at day 673 to a massive, sustained positive plateau of 900 kN/m. In this case creep and shrinkage play minor roles.

Uphill (Φ=2000 mm) pile

The most critical section of the uphill pile of 2000 mm diameter is the section at the level of the cover slab.

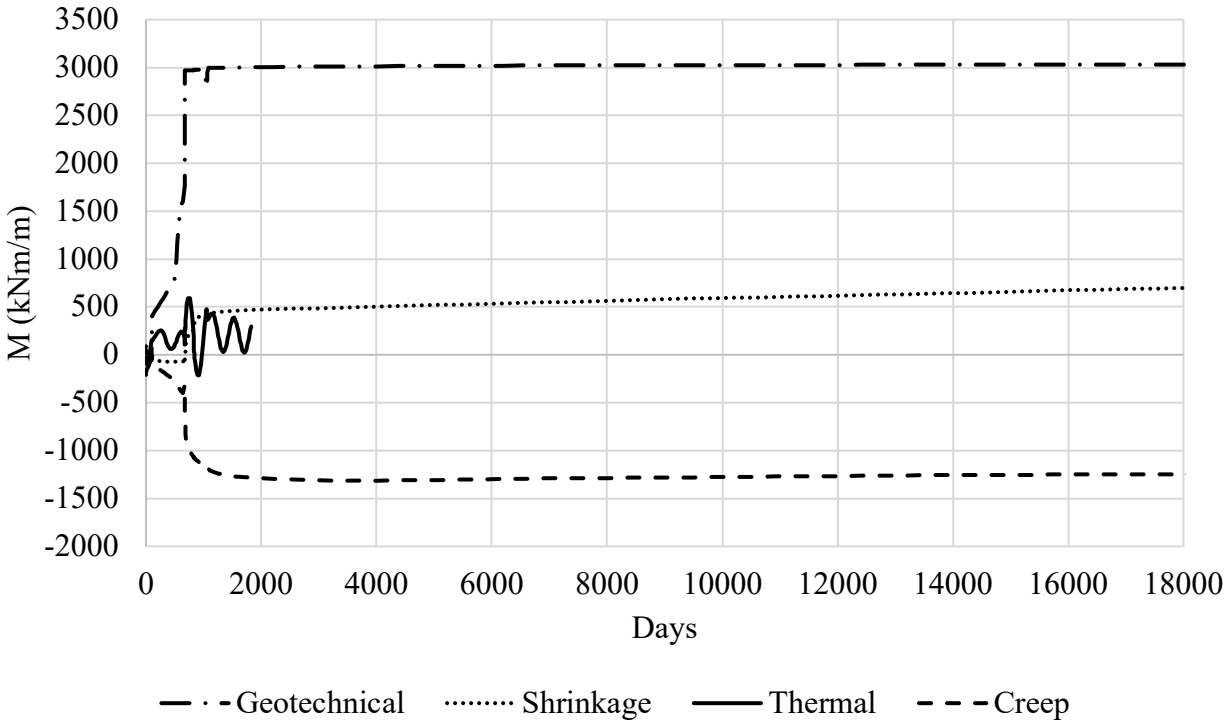


Figure 5-7 - Component Disaggregation of Bending Moment - Pile 2000 Uphill Cover Slab level

The geotechnical actions govern the bending moment by a baseline of 3000 kNm/m post day 673. This baseline is partly counterbalanced by the creep action providing a negative plateau of -1400 kNm/m. The shrinkage actions contribute to long term positive bending moment, accumulating up to 600 kNm/m.

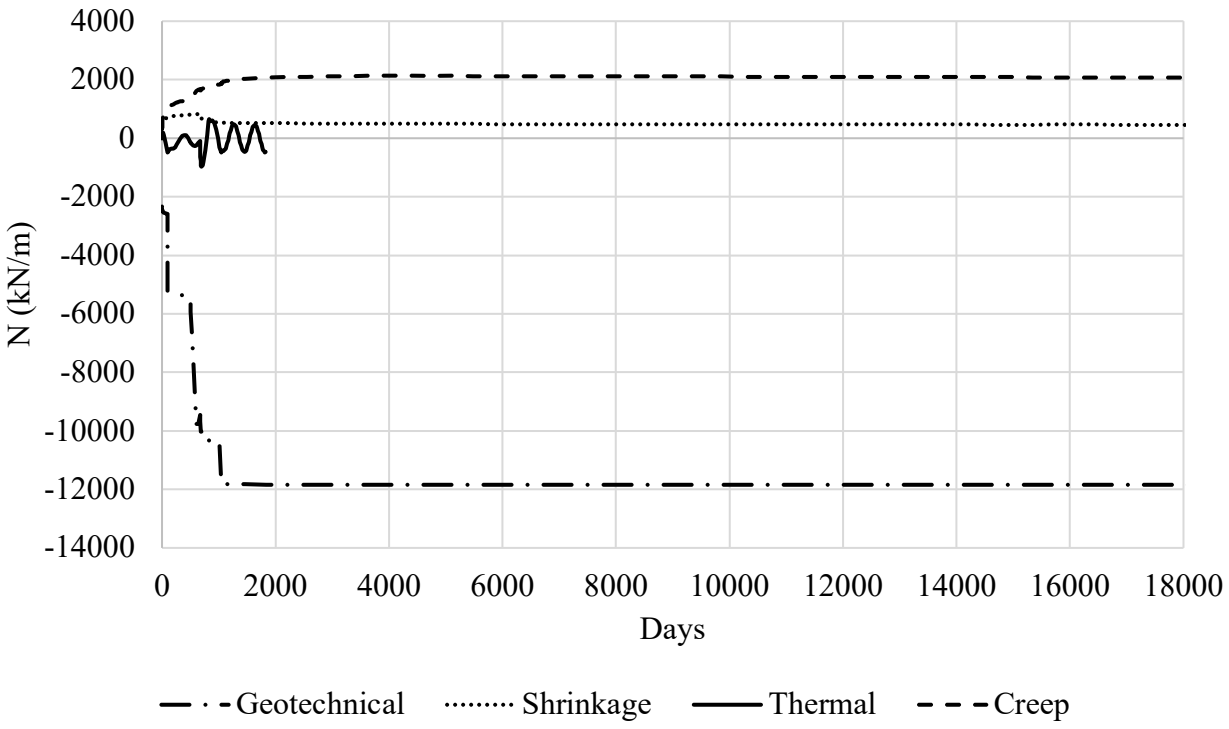


Figure 5-8 - Component Disaggregation of Axial Force - Pile 2000 Uphill Cover Slab level

The geotechnical completely dictates the axial load state, triggering an extreme compressive step-jump down to -12000 kN/m at day 678 core excavation. Creep actions act as a permanent positive stress relaxation contribution, stepping up ot 1500 kN/m.

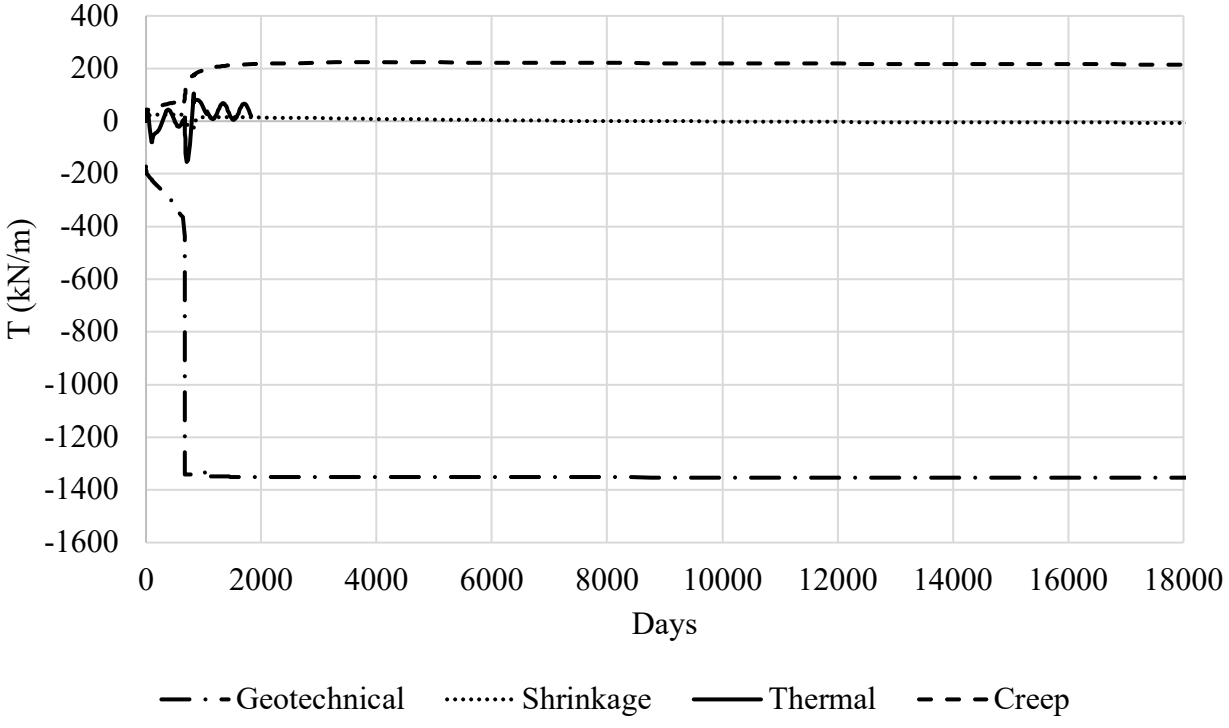


Figure 5-9 - Component Disaggregation of Shear Force - Pile 2000 Uphill Cover Slab level

In a similar way than the axial force, the shear force is overwhelmingly governed by the geotechnical action, experiencing a massive negative step-jump down to -1200 kN/m at day 678 to equilibrate lateral thrusts at the roof strut junction. Creep actions provide a long-term positive shear relaxation contribution stepping up to 200 kN/m.

Downhill (Φ=2000 mm) pile

The most critical section of the downhill pile of 2000 mm diameter is the head of the pile.

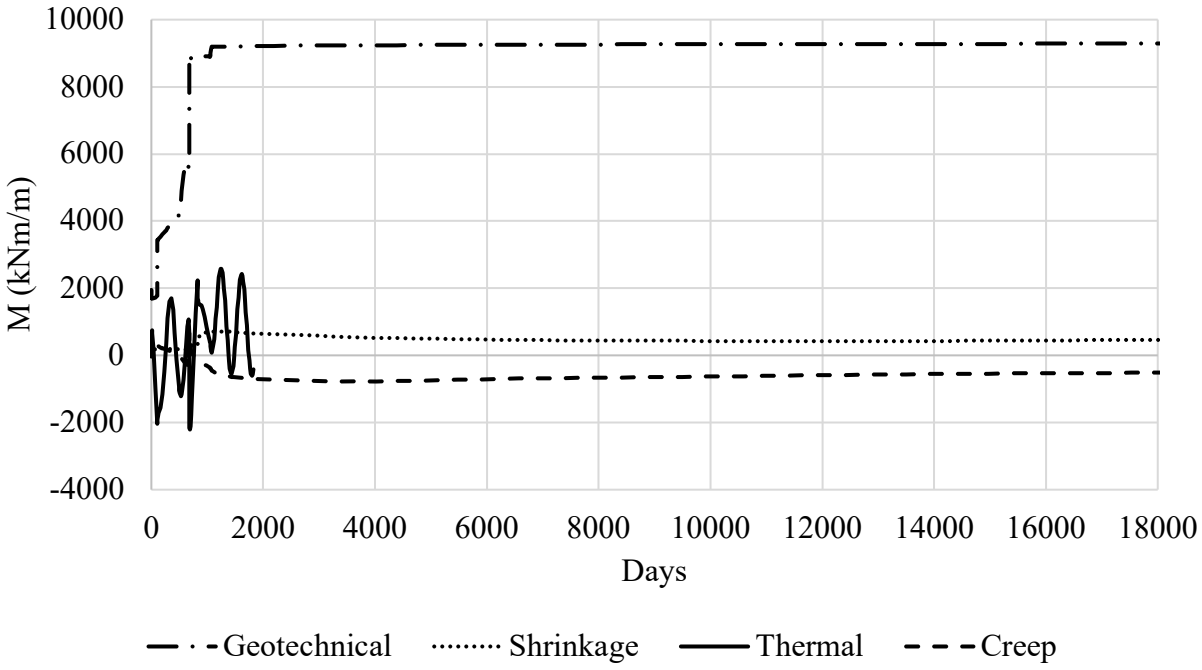


Figure 5-10 - Component Disaggregation of Bending Moment - Head of Pile 2000 Downhill

The bending moment is dictated by the geotechnical actions, that reach a plateau of 9000 kNm/m from the day 678. The thermal action governs in the short-term, by the seasonal flexural swings generating severe oscillations between 2500 kNm/m and -3000kNm/m.

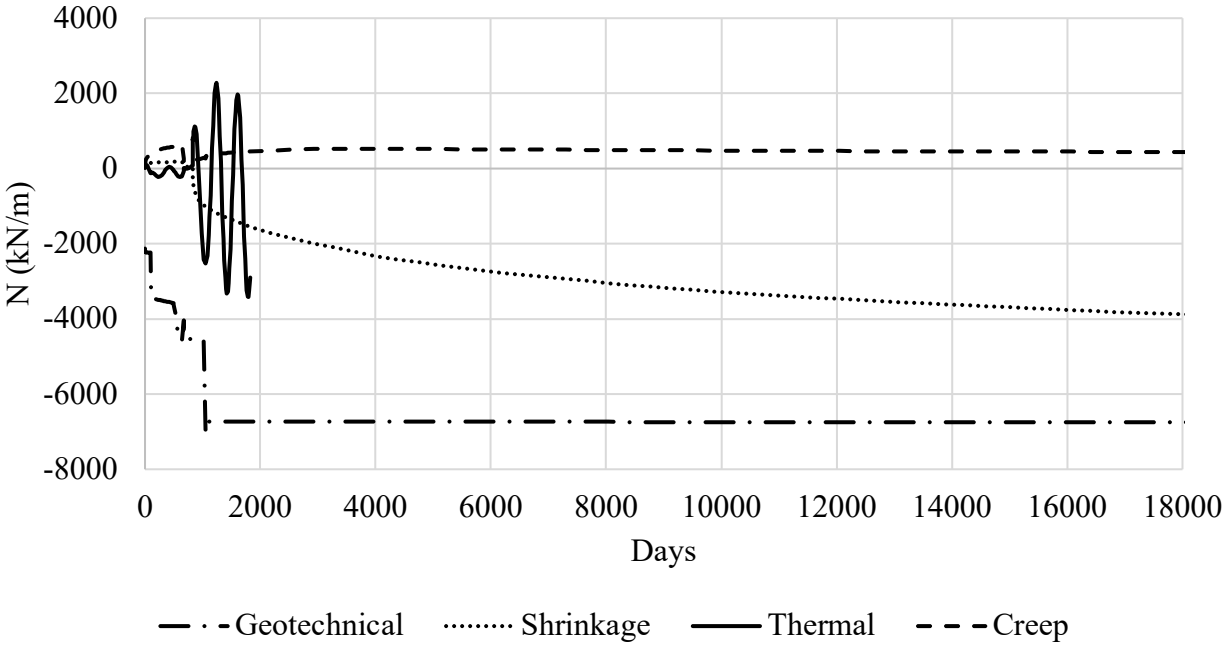


Figure 5-11 - Component Disaggregation of Axial Force - Head of Pile 2000 Downhill

Similarly to the pile uphill, the axial force is completely governed by the geotechnical actions, that reaches a plateau of -7000 kN/m from day of the core excavation. Thermal actions also play a big role and drive early seasonal axial force fluctuations across a wide range between 2000 kN/m tension and -4000 kN/m compression. Finally, the shrinkage actions also contribute vastly to the axial force by adding an extra compression of nearly -4000 kN/m at the end of the 18000 days.

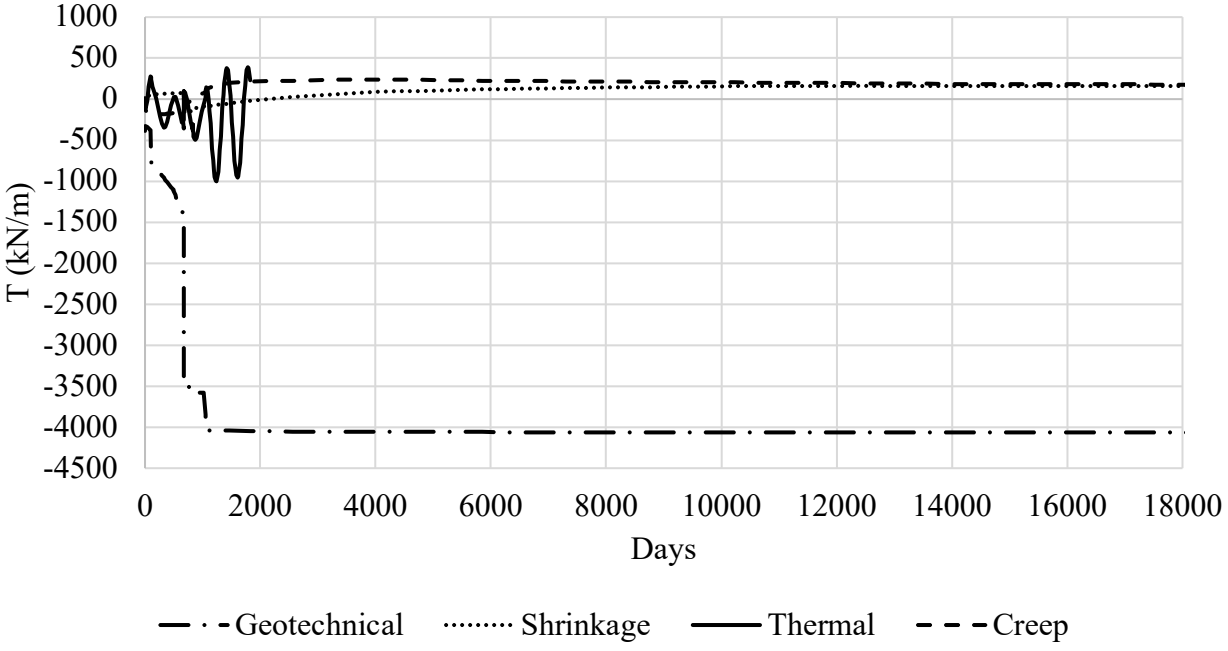


Figure 5-12 - Component Disaggregation of Shear Force - Head of Pile 2000 Downhill

The geotechnical actions govern permanent shear demand, experiencing a massive negative step-jump down to -3600 kN/m at day 678 excavation to equilibrate lateral ground thrusts.

Uphill wall

The most critical section of the uphill wall is the top section of the wall. It is worth noting that all internal remain strictly zero prior to day 800, reflecting the lining wall casting.

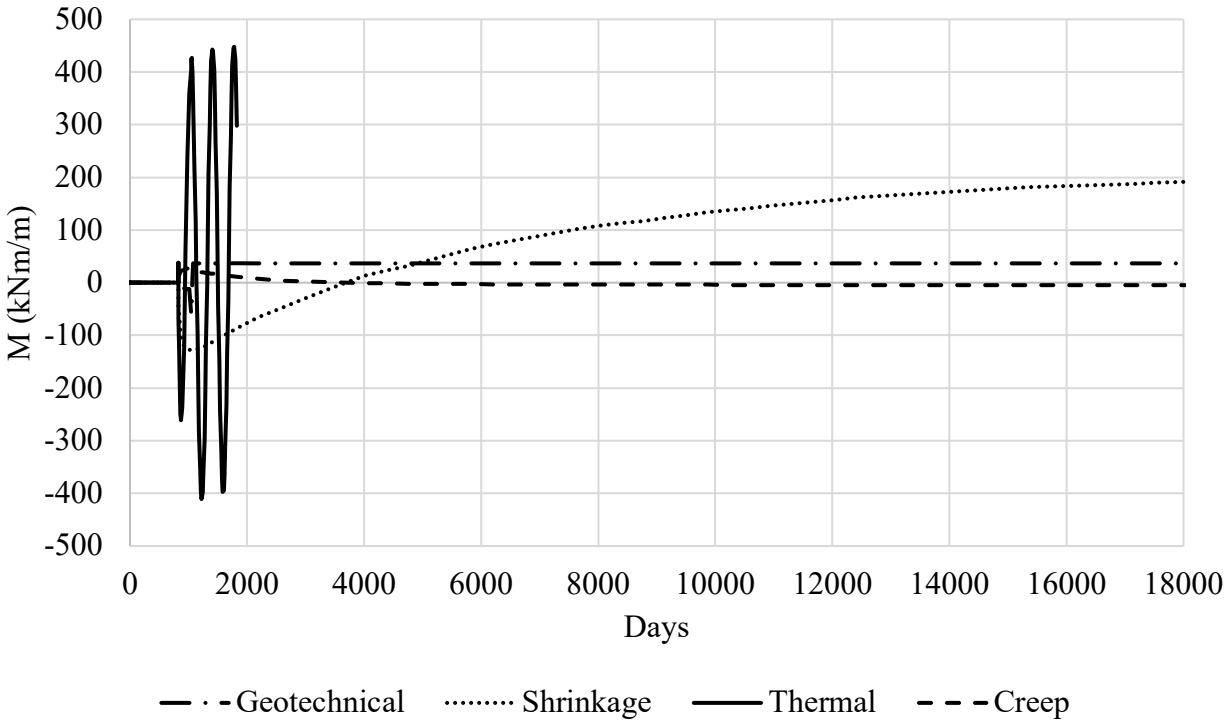


Figure 5-13 - Component Disaggregation of Bending Moment - Top Uphill Wall

The thermal action governs the bending moment at long and short term, oscillating between 450 kNm/m and -350 kNm/m. At long term shrinkage actions play a bigger role accumulating to nearly 200 kNm/m at the end of the time period of 18 000 days. Geotechnical and creep have baseline contributions nearly negligeable.

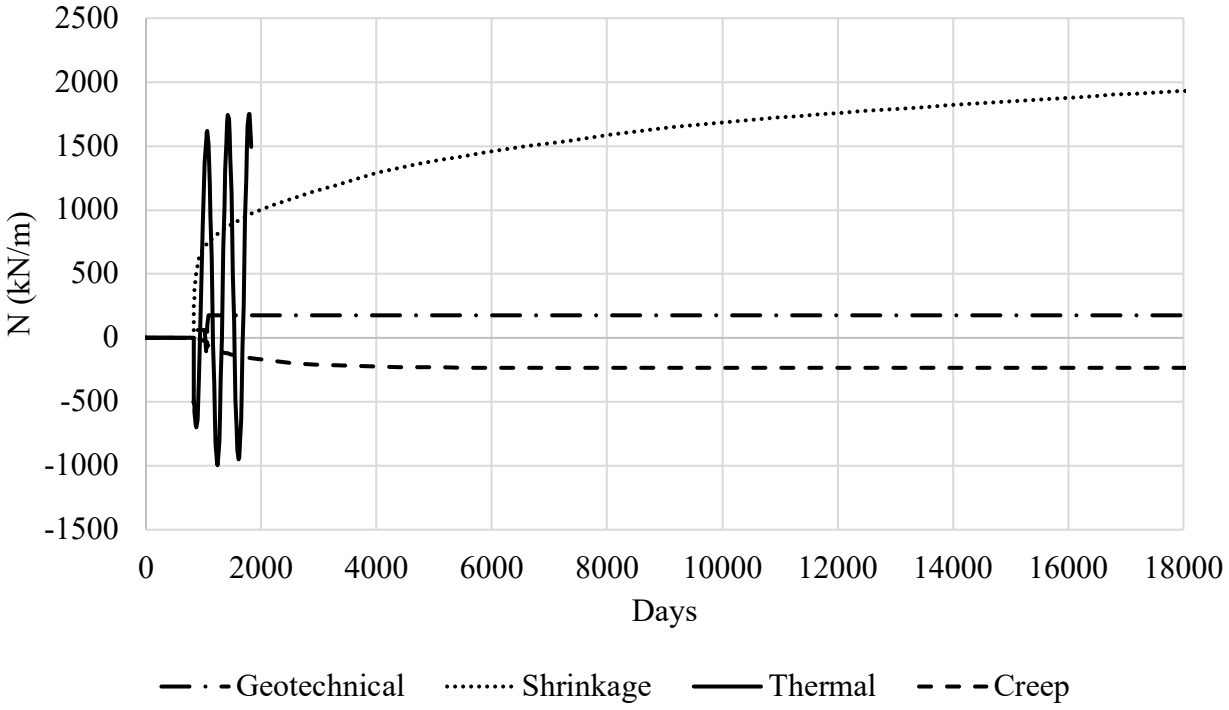


Figure 5-14 - Component Disaggregation of Axial Force - Top Uphill Wall

The axial normal force (N) is dominated in the short term by the oscillations of the thermal actions, fluctuating between 1700 kNm/m tension and -1000 kNm/m compression, but in the long term the shrinkage actions take over and accumulates to a massive 1800 kNm/m tensile restrain load over 50 years.

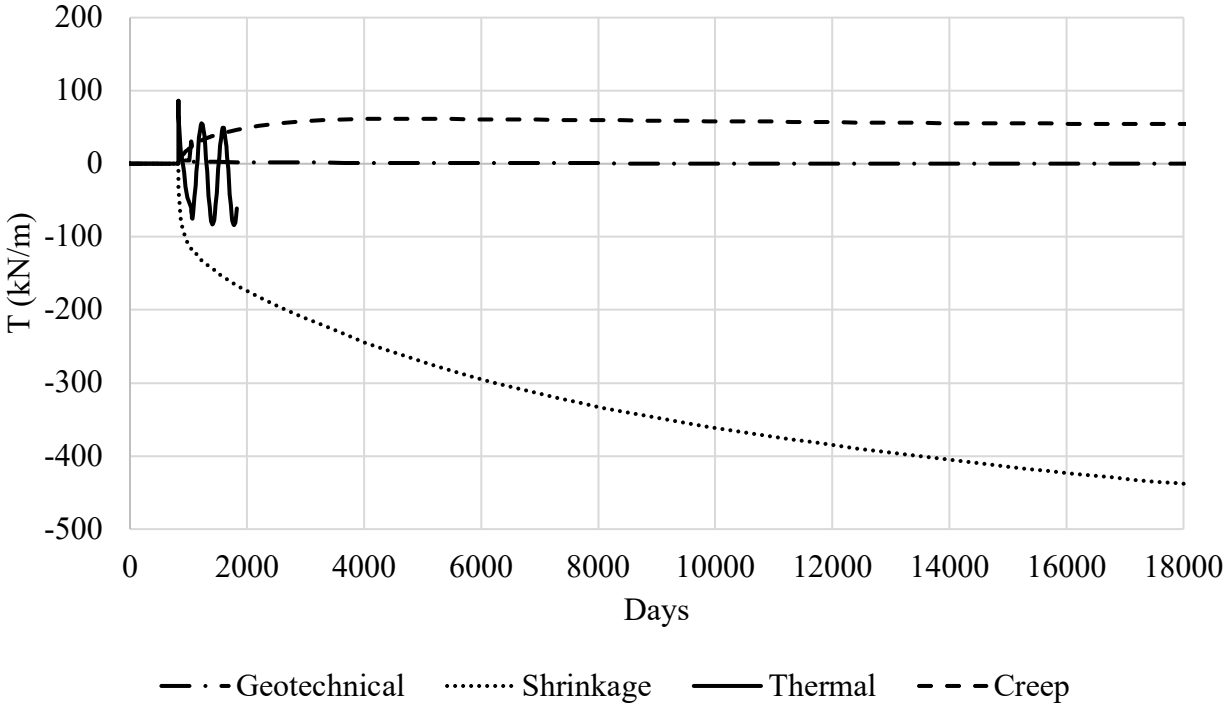


Figure 5-15 - Component Disaggregation of Shear Force - Top Uphill Wall

The shrinkage actions and the thermal actions oscillations govern short-term shear post day 800. The thermal actions oscillate between 100 kN/m and -100 kN/m whereas the shrinkage actions accumulate over time until reaching -450 kN/m at the end of the 18 000-day period. The geotechnical actions don't contribute at all, remaining near 0 kN/m, and creep actions reaches a plateau of 50 kN/m starting from the day 2000.

Downhill wall

The most critical section of the downhill wall is the top section of the wall. It is worth noting that all internal remain strictly zero prior to day 800, reflecting the lining wall casting.

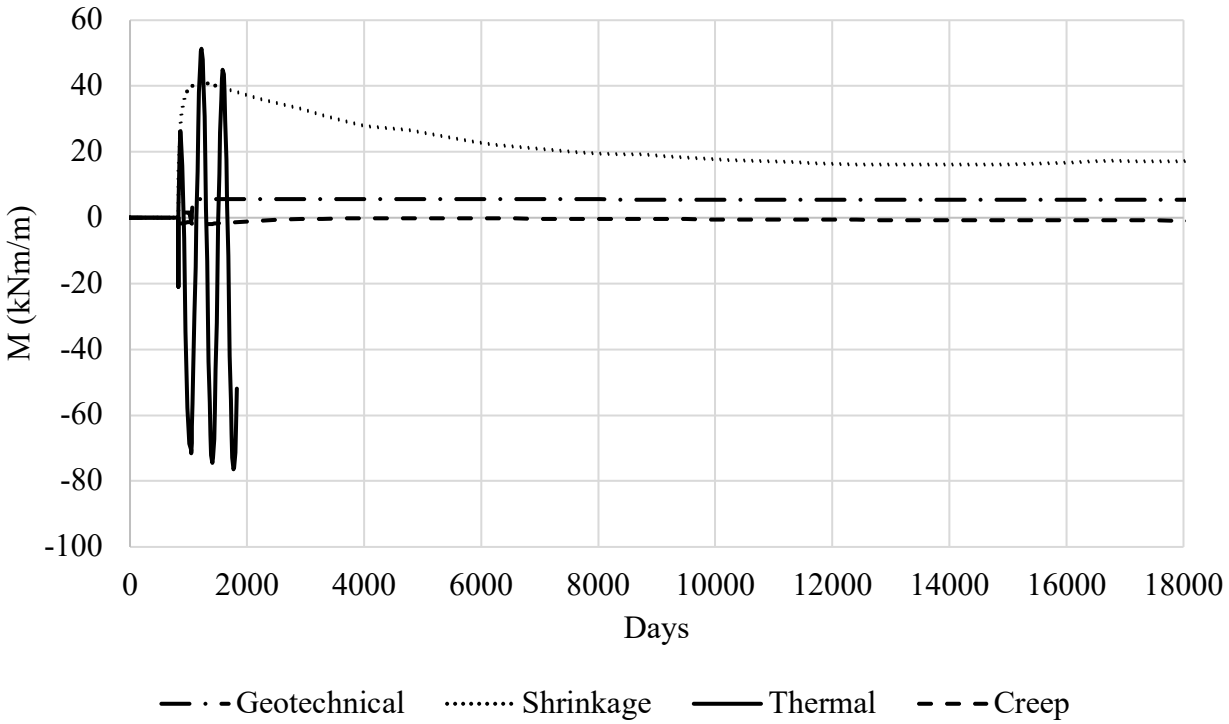


Figure 5-16 -Component Disaggregation of Bending Moment – Top Downhill Wall

Post day 800, the bending moment is almost entirely governed by the thermal actions, oscillating between 50 kNm/m and -100 kNm/m. At short-term the contribution of shrinkage actions is not negligeable, it reaches 40 kNm/m at day 800 but then gradually decreases until it reaches a plateau of around 15 kNm/m. Geotechnical and creep actions plays a minor and secondary role as they contribute to nearly 5 kNm/m and 0 kNm/m respectively.

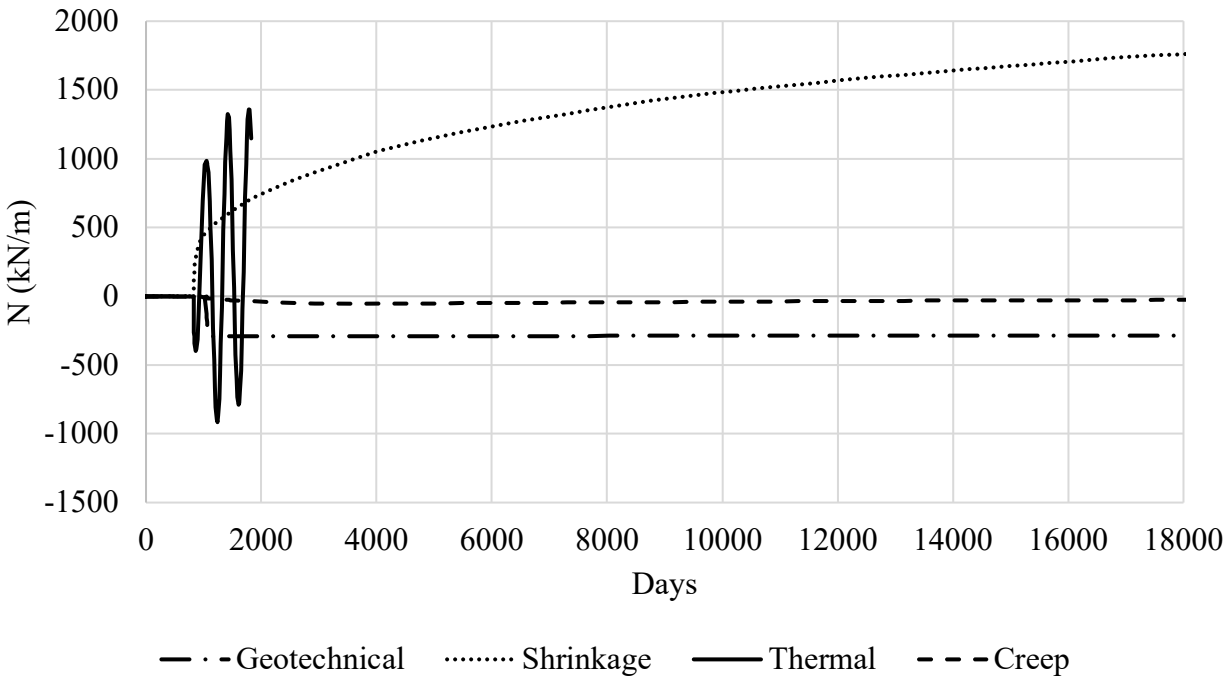


Figure 5-17 - Component Disaggregation of Axial Force - Top Downhill Wall

In the sort-term the axial force is driving the axial force through seasonal oscillations post day 800, swinging between 1300 kN/m and -700 kN/m. The shrinkage actions, at day 800 jumps to 400 kN/m and the increases steadily up to 1800 kN/m completely overpassing the thermal actions and dominating the axial force. The creep actions are not contributors and stays constant to -100 kN/m.

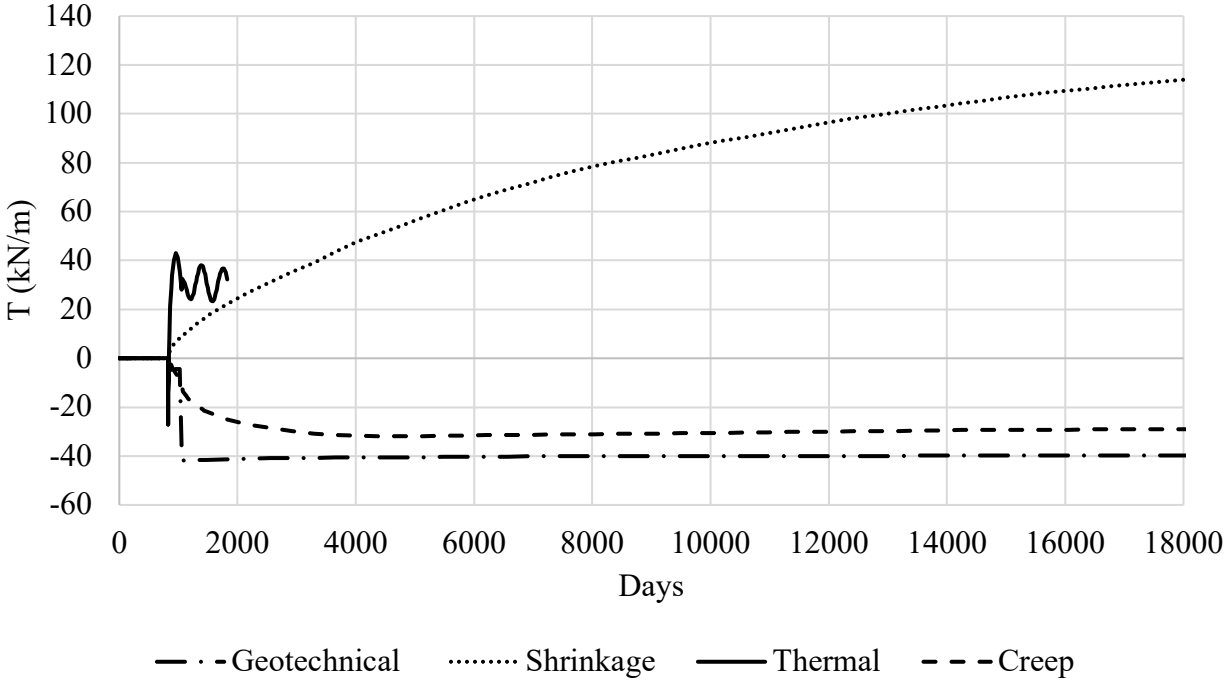


Figure 5-18 - Component Disaggregation of Shear Force - Top Downhill Wall

Post day 800, at short term, the shear force is governed by the thermal actions, oscillating between 40 kN/m and 50 kN/m, and the geotechnical actions providing a compensation of -40 kN/m. The shrinkage actions increase nearly linearly from 0 kN/m at day 800 to nearly 120 kN/m at day 18 000. Similarly to the other internal actions, the creep actions are not significant contributors in the downhill wall.

Foundation Slab

The most critical section of the foundation slab is the uphill section. All internal actions remain strictly zero prior to day 673, reflecting the field construction timeline where the foundation slab and strut elements are cast during phase 3 and 4 core excavation.

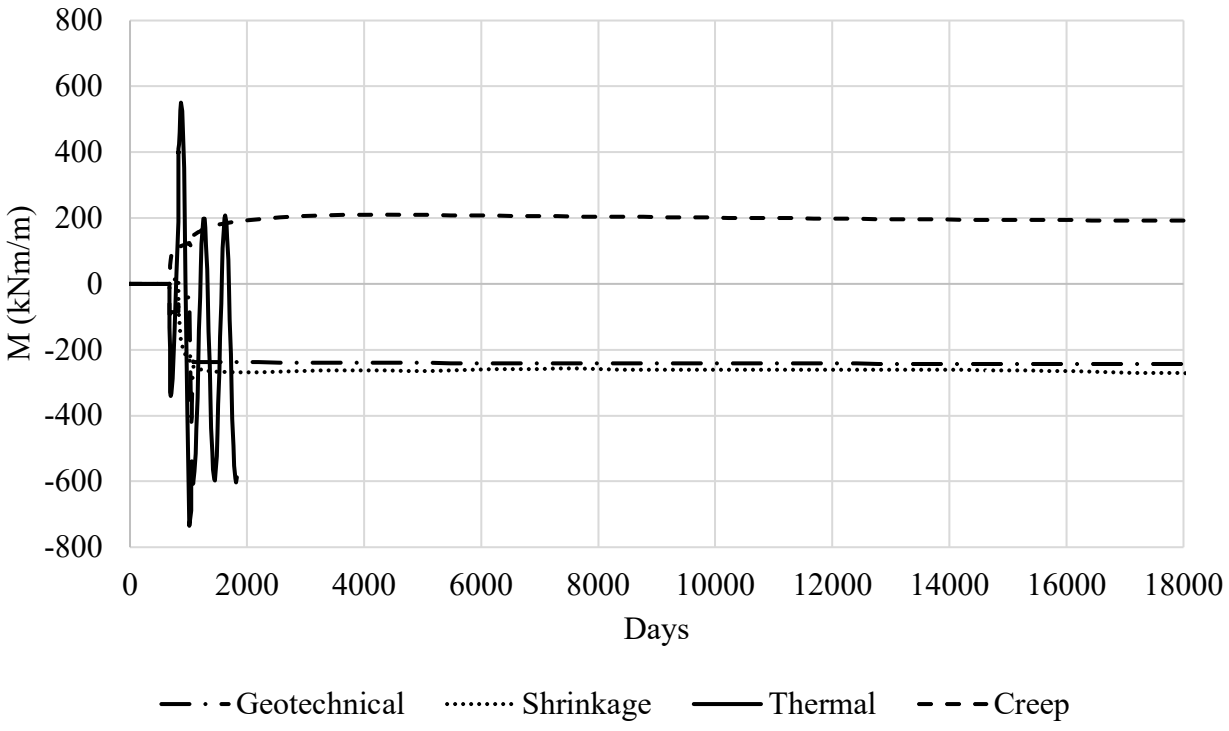


Figure 5-19 - Component Disaggregation of Bending Moment - Uphill Section Foundation Slab

The main contributor to the bending moment (M) is the thermal action affecting both the long-term and short-term final value of the bending moment, through oscillations swinging between 600 kNm/m and -700 kNm/m in the short term before dampening to oscillations between 200 kNm/m and -600 kNm/m. The remaining contributors are also contributing heavily: the shrinkage and geotechnical actions reach a plateau of -250 kNm/m and the creep actions step-up post excavation to a plateau of 200 kNm/m over 18 000 days.

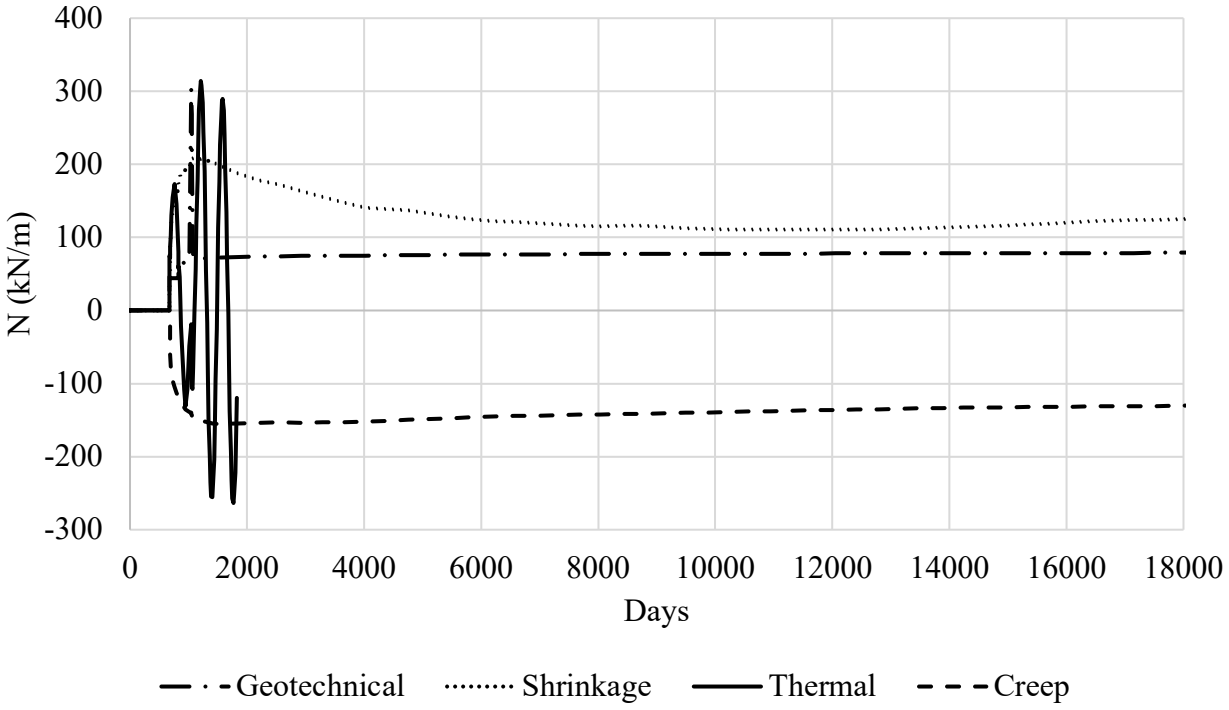


Figure 5-20 - Component Disaggregation of Axial Force - Uphill Section Foundation Slab

The thermal actions drive the axial force through seasonal variations post day 678 bounded between 300 kN/m tension and -300 kN/m compression. The shrinkage actions reach a peak of 200 kN/m and then provide a long-term baseline of around 120 kN/m. In opposition to the shrinkage baseline the creep actions steps down to a compressive baseline of -150 kN/m.

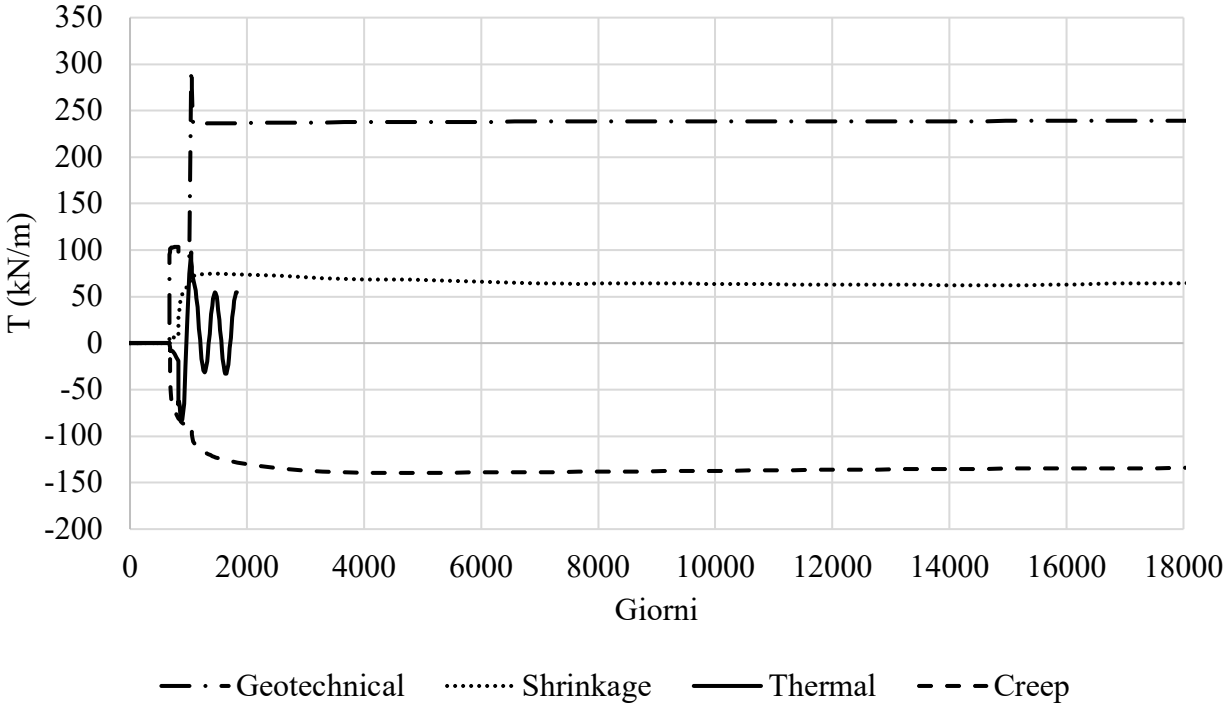


Figure 5-21 - Component Disaggregation of Shear Force - Uphill Section Foundation Slab

The shear force is governed by both the geotechnical actions and the creep actions. The geotechnical actions dictate positive shear demand by stepping up post day 678 to a permanent plateau of 240 kN/m. On the other side the creep actions step down post-excavation to a constant value of -160 kN/m to balance ground pressure. The thermal oscillations between 100 kN/m and -150 kN/m plays a minor role in total shear force value.

5.1.3 ULS for Bending and Axial Actions – Rectangular Section

The evaluation of the ultimate resisting moment (M_{Rd}) of a reinforced concrete cross-section under combined bending and axial load (N_{Ed}) relies on a semi-probabilistic limit state approach. The methodology evaluates the internal stress-strain state of the section at the onset of failure, governed by the following fundamental kinematic and constitutive hypotheses (EN 1992-1-1, §6.1):

- Conservation of plane sections: Strain distribution across the section remains strictly linear (Bernoulli-Navier hypothesis).
- Perfect bond: Strain in the reinforcing steel equals the strain in the adjacent concrete ($\varepsilon_s = \varepsilon_c$)
- Negligible tensile strength: The tensile strength of the concrete is entirely neglected in ULS resistance calculations.
- Strain limits: Ultimate failure is bounded by a maximum concrete compressive strain ($\varepsilon_{cu2} = 0{,}0035$) or maximum steel tensile strain ($\varepsilon_{ud} = 0{,}01$).

By assuming a linear strain profile across the depth y of the section can be defined, for any assumed neutral axis depth x, as so:

$$\varepsilon(y) = \varepsilon_c * \frac{y - x}{x} \tag{62}$$

Where ε_c is the compressive strain at the extreme top fibre. Consequently, the strain at any specific steel layer i located at depth y_i, is determined by geometric proportionality:

$$\varepsilon_{si}(x) = \varepsilon_c * \frac{y_i - x}{x} \tag{63}$$

The sign convention states that a positive strain is considered tension and negative strain is compression.

To transition from kinematics (strains) to statics (forces), the strains are mapped to stresses via material-specific constitutive laws. For concrete classes up to C50/60, a uniform compressive stress is assumed over an effective depth λx, where $\lambda = 0{,}8$:

$$\sigma_c(y) = f(x) = \begin{cases} \alpha_{cc} * f_{cd}, & 0 \leq y \leq 0{,}8x \\ 0 \quad , & y > 0{,}8x \end{cases} \tag{64}$$

For the steel reinforcement, considering a generic layer i, the stress in each steel layer σ_{si} depends on its strain $\varepsilon_{si}(x)$ evaluated against the elastic-perfectly plastic designed model of the steel ($E_s = 200\,000\ MPa$, yield strain $\varepsilon_{yd} = \frac{f_{yd}}{E_s}$):

$$\sigma_{si}(y) = f(x) = \begin{cases} f_{yd} * sgn(\ \varepsilon_{si}), & if\ |\ \varepsilon_{si}(x)| \geq\ \varepsilon_{yd}\ (Yielded) \\ E_s *\ \varepsilon_{si}(x) \quad , & if\ |\ \varepsilon_{si}(x)| \leq\ \varepsilon_{yd}\ (Elastic) \end{cases} \tag{65}$$

The true position of the neutral axis x is the unique depth that satisfies the translational equilibrium between the applied design axial force (N_{Ed}) and the sum of all internal resistive force. For a standard regular section with constant width, b:

$$F_C(x) = 0{,}8 * b * x * \alpha_{cc} * f_{cd} \tag{66}$$

The internal force contributed by the steel is the discrete summation of the force in every individual layer:

$$F_s(x) = \sum_{i=1}^{n} A_{si} * \sigma_{si}(x) \tag{67}$$

The global translational equilibrium equation is then:

$$N_{int}(x) = F_c(x) + F_s(x) = N_{Ed} \tag{68}$$

Because $\sigma_{si}(x)$ contains conditional (piecewise) elastic/plastic boundaries, $N_{int}(x)$ cannot be solved analytically via a closed-form algebraic equation. Instead, the solution requires an iterative numerical procedure to find the specific position of the neutral axis where:

$$N_{int}(x) - N_{Ed} = 0 \tag{69}$$

Once the iterative procedure converges on the exact, kinetically compatible depth of the neutral axis x, the stress state of every fiber and steel layer in the section is definitively known. The design resisting moment (M_{Rd}) is then calculated by enforcing rotational equilibrium. To directly compare the section's capacity against the applied design moment (M_{Ed}), the moments

of the internal forces must be calculated around the exact same reference axis used in the global structural analysis, defined as the geometric centroid of the gross concrete cross-section (y_G). For a strictly rectangular section, $y_G = \frac{h}{2}$ and the concrete resultant acts as 0,4x. The final capacity is the generic summation of all internal forces multiplied by their respective lever arms relative to y_G:

$$M_{Rd} = F_c(x) * \left(\frac{h}{2} - 0{,}4 * x\right) + \sum_{i=1}^{n} \left[A_{si} * \sigma_{si}(x) * \left(\frac{h}{2} - y_i\right)\right] \tag{70}$$

The cross-section is structurally verified for the given axial load N_{Ed}, if the derived capacity is greater than or equal to the applied action: $M_{Ed} \leq M_{Rd}$

Therefore, the safety format is computed as the ratio of the applied action over the capacity:

$$SF = \frac{M_{Rd}}{M_{Ed}} \geq 1 \tag{71}$$

5.1.4 ULS for Bending and Axial Actions – Circular Section

The fundamentals hypothesis remains the same, but in a rectangular section, the concrete compression zone was a simple rectangle, in a circular section, the compression zone is a circular segment. Furthermore, the steel is no longer distributed in simple horizontal layers but is distributed uniformly around a ring.

Considering a circular cross section of total radius R, the longitudinal reinforcement consists of n discrete bars, assumed for analytical simplicity to be uniformly distributed along an internal circumference of radius:

$$r_s = R - c - \phi_t - (\phi_l/2) \tag{72}$$

Where c is the concrete cover, ϕ_t is the stirrup diameter and ϕ_l is the longitudinal bar diameter. Let x represent the depth of the neutral axis measured from the extreme compressive fiber. According to Eurocode 2 (EN 1992-1-1), the parabolic-rectangular stress distribution can be simplified to an equivalent rectangular stress block of depth $y = \lambda x$ (where $\lambda = 0{,}8$ for $f_{ck} \leq$ 50 MPa). Unlike a rectangular where the compression area is simply $A_c = b * y$, the area of a circular segment is a non-linear trigonometric function.

By assuming the origin of the coordinate system is the geometric centre of the circular section, it is convenient to define the depth of the stress block using a central angle $2\theta_c$, which subtends

the compressed concrete chord. The relationship between the stress block depth y and the half-angle θ_c is:

$$y = R(1 - \cos\theta_c) \quad \Rightarrow \quad \theta_c = \arccos\left(1 - \frac{0.8x}{R}\right) \tag{73}$$

The area of this compressed concrete segment (A_{cc}) is:

$$A_{cc} = R^2(\theta_c - \sin\theta_c \cos\theta_c) \tag{74}$$

The effective design compressive stress acting uniformly over this area is:

$$\sigma_c = \alpha_{cc} f_{cd} \tag{75}$$

The ultimate limit state requires establishing a kinetically admissible strain profile that satisfies global translational and rotational equilibrium against the external design actions (N_{Ed}, M_{Ed}). The strain profile across the section varies linearly from the maximum compressive strain at the extreme concrete fibre (ε_c) to the tensile strain at the opposite face. For a discrete rebar i located at an angle α_i relative to the axis of bending, its vertical distance from the center is $y_i = r_s \cos\alpha_i$. Its distance from the extreme compressive fiber is $(R - y_i)$.

The strain in rebar i as a function of the neutral axis depth x is:

$$\varepsilon_{si}(x) = \varepsilon_c * \frac{R - r_s * cos(\alpha_i) - x}{x} \tag{76}$$

To find the true neutral axis position, the internal forces must balance the applied axial load N_{Ed}. First let's consider the concrete compressive forces:

$$F_c(x) = A_{cc} * \alpha_{cc} * f_{cd} = R^2(\theta_c - \sin(\theta_c) * \cos(\theta_c)) * \alpha_{cc} * f_{cd} \tag{77}$$

Then the steel forces:

$$F_s(x) = \sum_{i=1}^{n} A_{si} * \sigma_{si}(x) \tag{78}$$

The same way as the rectangular section, the equilibrium is written as follows:

$$N_{int}(x) = F_c(x) + F_s(x) = N_{Ed} \tag{79}$$

Because θ_c is a trigonometric function of x, and $\sigma_{si}(x)$ contains conditional elastic/plastic boundaries for each bar around the circumference, this equation is highly non-linear and transcendental. It is mathematically impossible to isolate x algebraically. The solution strictly demands numerical iteration (the Newton-Raphson method) to locate the root x where $N_{int}(x) - N_{Ed} = 0$.

Once the iterative procedure converges on the exact neutral axis depth x, the corresponding half-angle θ_c and the stress state of every individual reinforcing bar are definitively known. To evaluate the resisting moment M_{Rd}, the sum of moments of all internal forces must be calculated around the geometric centroid of the gross cross-section (which, for a circle, is simply its geometric centre, $y = 0$). First, to compute the moment of the concrete, M_c, the lever arm z_c is needed and it is the distance from the centre of the circle to the centroid of the circular segment:

$$z_c = \frac{2}{3} * R * \frac{\sin^3(\theta_c)}{\theta_c - \sin(\theta_c)\cos(\theta_c)} \tag{80}$$

Therefore, the resisting moment contributed by the concrete is:

$$M_c(x) = F_c \cdot z_c = [R^2(\theta_c - \sin(\theta_c)\cos(\theta_c) \cdot \alpha_{cc} f_{cd}] \cdot \left[\frac{2}{3} * R * \frac{\sin^3(\theta_c)}{\theta_c - \sin(\theta_c)\cos(\theta_c)}\right] \tag{81}$$

$$M_c(x) = \frac{2}{3} * \alpha_{cc} * f_{cd} * R^3 \sin^3(\theta_c) \tag{82}$$

To obtain the moment of the steel M_s, the lever arm for each discrete bar i relative to the centre is: $y_i = r_s \cos \alpha_i$.

$$M_s(x) = \sum_{i=1}^{n} [A_{si} \cdot \sigma_{si}(x) \cdot (r_s \cos(\alpha_i))] \tag{83}$$

Finally, the total design resisting moment is the superposition of the concrete and steel contributions:

$$M_{Rd} = M_c(x) + M_s(x) \tag{84}$$

And the cross section is verified if the safety factor is greater than 1:

$$SF = \frac{M_{Rd}}{M_{Ed}} \geq 1 \tag{85}$$

5.1.5 ULS for Shear Actions – Rectangular Section

Unlike flexure, the shear behaviour of a cracked reinforced concrete element deviates from Bernoulli-Navier continuum mechanics. Post-cracking shear resistance is evaluated using the Variable-Angle Truss Analogy, which conceptualizes the beam as a structural truss system (EN 1992-1-1, §6.2.3; NTC 2018, §4.1.2.2). The theoretical truss is comprised of four components:

- Top chord: The uncracked concrete compression zone
- Bottom chord: The longitudinal tensile reinforcement
- Transverse ties: the steel shear reinforcement (stirrups), resisting vertical tension
- Diagonal struts: the cracked concrete web, resisting diagonal compression at an inclination angle θ.

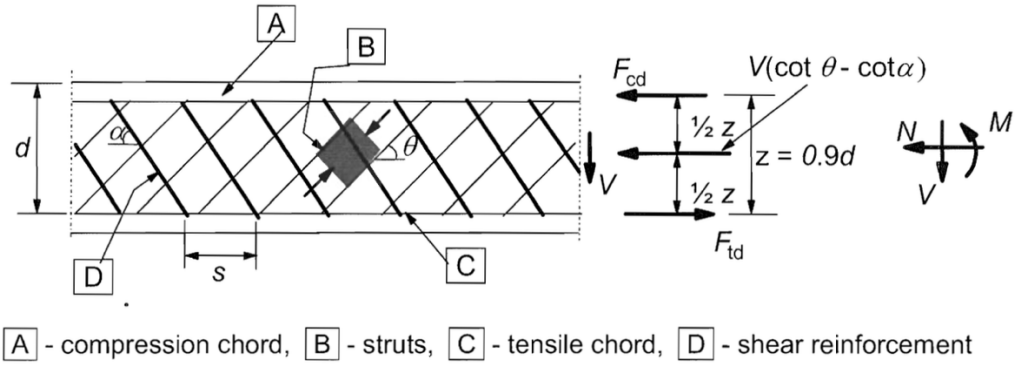


Figure 5-22 - Variable Angle Truss Model

The limit state theorem of plasticity permits the designer to select the strut inclination angle θ within defined kinematic limits, provided that the required transverse and longitudinal reinforcement is furnished. The standard limits are:

$$1{,}0 \leq \cot\theta \leq 2{,}5 \tag{86}$$

This equates to an allowable strut angle between 21.8° and 45°.

With reference to the transverse reinforcement, the design shear resistance is the smaller value of:

$$V_{Rd,s} = \frac{A_{sw}}{s} * z * f_{ywd} * \cot\theta \tag{87}$$

And:

$$V_{Rd,max} = \alpha_{cw} * b_w * z * \upsilon_1 * \frac{f_{cd}}{\cot\theta + tan\theta} \tag{88}$$

$$V_{Rd} = \min(V_{Rd,s}, V_{Rd,\max}) \tag{89}$$

Where $A_{sw}$is the cross-sectional area of the shea reinforcement, s is the spacing of the stirrups, f_{ywd} is the design yield strength of the shear reinforcement, $b_w$is the web width, $\upsilon_1$is a strength reduction factor for concrete cracked in shear and is computed like so:

$$\upsilon_1 = 0{,}6 * \left(1 - \frac{f_{ck}}{250}\right) \tag{90}$$

α_{cw} is a coefficient taking account of the state of stress in the compression chord:

- $\alpha_{cw} = 1$ for non-prestressed structures
- $\alpha_{cw} = 1 + \frac{\sigma_{cp}}{f_{cd}}$ for $0 < \sigma_{cp} < 0{,}25 * f_{cd}$
- $\alpha_{cw} = 1{,}25$ for $0{,}25 * f_{cd} < \sigma_{cp} < 0{,}5 * f_{cd}$
- $\alpha_{cw} = 2{,}5 * \left(1 - \frac{\sigma_{cp}}{f_{cd}}\right)$ for $0{,}5 * f_{cd} < \sigma_{cp} < 1{,}0 * f_{cd}$

The safety format is obtained in the same way that for the bending verification:

$$SF = \left|\frac{V_{Rd}}{V_{Ed}}\right| \geq 1 \tag{91}$$

Absolute signs have been used to allow the comparison of safety factors between the sections.

5.1.6 ULS for Shear Actions – Circular Section

While the Variable-Angle Truss Analogy (Figure 4-1) is natively formulated for rectangular sections, its application to circular cross-sections requires geometric adjustments to the standard Eurocode 2 variables. The primary challenge arises from the non-linear distribution of the cross-sectional width and the uniform, continuous distribution of the longitudinal reinforcement around the perimeter. To accurately evaluate the capacity of the diagonal concrete struts ($V_{Rd,max}$), the parameter representing the web width (b_w) must be modified. Unlike a rectangular section where b_w is constant, a circular section exhibits maximum width at the centroidal axis and decreases toward the extreme fibres. Therefore, the effective depth width is adjusted as a function of the total section diameter:

$$b_w = 0{,}9 * D \tag{92}$$

Similarly, the calculation of the shear reinforcement capacity ($V_{Rd,s}$) and the concrete strut capacity relies heavily on the internal lever arm (z). The radial distribution of reinforcement in a circular section necessitates a redefinition of the distance between the resultant compressive and tensile chords of the theoretical truss and is standardized as:

$$z = 0{,}8 * D \tag{93}$$

5.1.7 Bending Moment Verification Results

This section presents the Ultimate Limit State (ULS) flexural verification results computed using the traditional partial safety factor approach. Combined bending moment and axial force interaction (M – N) capacities are evaluated at the governing critical sections to determine the demand-to-capacity safety margins ($SF = E_d/R_d$) across the system. The verifications are detailed for the seven principal structural elements constituting the Galleria Piscinale portal frame and using the three safety factor combinations detailed in the Chapter 5.1.1:

- Cover slab,
- Foundation slab
- Uphill wall
- Downhill wall
- Uphill pile ϕ = 2000 mm
- Uphill pile ϕ = 1200 mm
- Downhill pile ϕ = 2000 mm

Table 5-2 - Bending Moment Cover Slab Linear Verification

		Cover Slab - C35/45					
		Uphill Section		*Midspan Section*		*Downhill Section*	
GEO	**N**	-2326	kN	-2352	kN	-2370	kN
	Med	-1378	kN.m	-1066	kN.m	-13454	kN.m
	Mrd	-20581	kN.m	-15819	kN.m	-20623	kN.m
	SF	14,935		14,840		1,533	
GEO + TH + SH + CR - V1	**N**	-2655	kN	-2704	kN	-2638	kN
	Med	-4910	kN.m	-6133	kN.m	-16654	kN.m
	Mrd	-20897	kN.m	-16131	kN.m	-20876	kN.m
	SF	4,256		2,630		1,254	
GEO + TH + SH + CR - V2	**N**	-2602	kN	-2651	kN	-2578	kN
	Med	-4814	kN.m	-5833	kN.m	-16049	kN.m
	Mrd	-20843	kN.m	-16085	kN.m	-20819	kN.m
	SF	4,330		2,758		1,297	

Table 5-3 - Bending Moment Foundation Slab Linear Verification

		Foundation Slab - C30/37					
		Uphill Section		*Midspan Section*		*Downhill Section*	
GEO	**N**	103	kN	38	kN	-195	kN
	Med	-316	kN.m	382	kN.m	-676	kN.m
	Mrd	-2266	kN.m	1371	kN.m	-2467	kN.m
	SF	7,173		3,587		3,649	
GEO + TH + SH + CR - V1	**N**	-168	kN	315	kN	-522	kN
	Med	-1300	kN.m	-58	kN.m	-1525	kN.m
	Mrd	-2449	kN.m	-790	kN.m	-2686	kN.m
	SF	1,883		13,551		1,761	
GEO + TH + SH + CR - V2	**N**	-169	kN	313	kN	-520	kN
	Med	-1316	kN.m	-149	kN.m	-1544	kN.m
	Mrd	-2449	kN.m	-791	kN.m	-2684	kN.m
	SF	1,860		5,327		1,739	

Table 5-4 - Bending Moment Uphill Wall Linear Verification

		Uphill Wall - C35/45					
		Top Section		*Mid-height Section*		*Bottom Section*	
GEO	**N**	233	kN	33	kN	31	kN
	Med	48	kN.m	66	kN.m	73	kN.m
	Mrd	3418	kN.m	3092	kN.m	3516	kN.m
	SF	71,060		46,637		48,297	
GEO + TH + SH + CR - V1	**N**	4561	kN	3426	kN	1960	kN
	Med	871	kN.m	373	kN.m	286	kN.m
	Mrd	1159	kN.m	1833	kN.m	2566	kN.m
	SF	1,331		4,914		8,963	
GEO + TH + SH + CR - V2	**N**	4770	kN	3752	kN	2165	kN
	Med	909	kN.m	307	kN.m	236	kN.m
	Mrd	1025	kN.m	1655	kN.m	-464	kN.m
	SF	1,128		5,391		10,427	

Table 5-5 - Bending Moment Downhill Wall Linear Verification

		Downhill Wall - C35/45					
		Top Section		*Mid-height Section*		*Bottom Section*	
GEO	**N**	-372	kN	-179	kN	-8	kN
	Med	7	kN.m	-12	kN.m	-113	kN.m
	Mrd	802	kN.m	-1589	kN.m	-1566	kN.m
	SF	123,385		135,812		13,846	
GEO + TH + SH + CR - V1	**N**	185	kN	3047	kN	2039	kN
	Med	90	kN.m	-20	kN.m	-178	kN.m
	Mrd	687	kN.m	-1084	kN.m	-1274	kN.m
	SF	7,633		55,025		7,153	
GEO + TH + SH + CR - V2	**N**	533	kN	3386	kN	2273	kN
	Med	93	kN.m	-4	kN.m	-165	kN.m
	Mrd	605	kN.m	-995	kN.m	-1239	kN.m
	SF	6,491		255,128		7,523	

Table 5-6 - Bending Moment Pile 2000 Uphill Linear Verification

		Piles 2000 Uphill - C30/37			
		Head Section		*Cover Slab Level Section*	
GEO	**N**	-10657	kN	-15459	kN
	Med	-2280	kN.m	3939	kN.m
	Mrd	-22259	kN.m	22997	kN.m
	SF	9,761		5,838	
GEO + TH + SH + CR - V1	**N**	-9173	kN	-13533	kN
	Med	-6907	kN.m	3987	kN.m
	Mrd	-21916	kN.m	22768	kN.m
	SF	3,173		5,711	
GEO + TH + SH + CR - V2	**N**	-8742	kN	-13015	kN
	Med	-7300	kN.m	3853	kN.m
	Mrd	-21812	kN.m	22691	kN.m
	SF	2,988		5,889	

Table 5-7 - Bending Moment Pile 1200 Uphill Linear Verification

		Pile 1200 Uphill - C30/37			
		Head Section		*Cover Slab Level Section*	
GEO	**N**	1040	kN	-609	kN
	Med	-1196	kN.m	-302	kN.m
	Mrd	-3956	kN.m	4400	kN.m
	SF	3,308		14,566	
GEO + TH + SH + CR - V1	**N**	-6934	kN	-2927	kN
	Med	-1799	kN.m	-4	kN.m
	Mrd	-5148	kN.m	4850	kN.m
	SF	2,862		1276,316	
GEO + TH + SH + CR - V2	**N**	-7815	kN	-3307	kN
	Med	-1860	kN.m	65	kN.m
	Mrd	-5127	kN.m	4904	kN.m
	SF	2,757		75,446	

Table 5-8 - Bending Moment Pile 2000 Downhill Linear Verification

		Pile 2000 Downhill - C30/37			
		Head Section		*Cover Slab Level Section*	
GEO	**N**	-8774	kN	-11792	kN
	Med	12068	kN.m	-3465	kN.m
	Mrd	21820	kN.m	-22482	kN.m
	SF	1,808		6,489	
GEO + TH + SH + CR - V1	**N**	-9618	kN	-10952	kN
	Med	15322	kN.m	-5860	kN.m
	Mrd	22022	kN.m	-22318	kN.m
	SF	1,437		3,809	
GEO + TH + SH + CR - V2	**N**	-10305	kN	-10762	kN
	Med	15312	kN.m	-6105	kN.m
	Mrd	22182	kN.m	-22280	kN.m
	SF	1,449		3,650	

Note: The safety factors from some of the sections: the cover slab level section of the uphill ϕ = 1200 pile or the mid-height section of the downhill wall, exhibits excessively large safety factors due to a M_{Ed} close to 0. Therefore, this safety factors cannot be considered reliable or meaningful and are not take into account in the analysis and conclusions.

The top section of the uphill wall under load combination version 2 represents the governing critical section for flexure across the entire tunnel structure, reaching a peak utilization ratio of $SF = 1{,}128$. This maximum flexural demand occurs because version 2 applies the highest partial safety multipliers to environmental coaction ($\gamma_{TH} = 1{,}5$, $\gamma_{SH} = \gamma_{CR} = 1{,}2$, $\gamma_{GEO} = 1{,}3$). At this rigid roof-wall knee joint, the stiff cover slab severely restrains thermal and shrinkage movements, concentrating a high design bending moment of $M_{ED} = 909\ kNm$ alongside a heavy compressive axial load of $N_{ED} = 4770\ kN$. This resulting ratio marks the highest flexural demand recorded anywhere in the critical sections of the structure. But other sections are highly demanded as the downhill section of the cover slab with a $SF = 1{,}254$ under load combination version 1 or the head section of the downhill pile of ϕ = 2000 mm that record safety factors of 1,437 and 1,449 under load combination version 1 and 2 respectively. This structure is highly demanded with various structural elements going below a safety factor of 1,4 for bending moment actions, explaining the need for a different safety format approach.

A critical finding in the linear elastic verification concerns the severe flexural demand concentrated at the uphill wall. In the preliminary cross-sectional assessment, the original longitudinal reinforcement layout failed the Ultimate Limit State bending verification, requiring a design modification through the addition of a supplementary layer of $5\phi14$ longitudinal bars. Crucially, even after incorporating this additional reinforcement, the top section of the uphill wall remained the most critically stressed zone of the entire tunnel, governing the global linear assessment with the highest structural safety factor of $SF = 1{,}128$. This outcome is of fundamental importance: it underscores the inherent limitations and severe conservatism of conventional linear elastic cross-sectional methods. Because linear models treat self-equilibrating kinematic restraints as rigid external coactions and cannot account for stress relief via concrete tensile micro-cracking or plastic moment redistribution, they generate extreme, artificial bending moment peaks at rigid knee joints. This forces unnecessary structural re-dimensioning and steel over-provisioning at frame corners

5.1.8 Shear Force Verification Results

This section presents the Ultimate Limit State (ULS) shear verification results across the critical governing sections of the portal frame and deep foundation elements (see Chapter 5.1.7). The design shear demand (V_{Ed}), compiled from the factored superposition of individual action components, is evaluated against the ultimate shear resistance (V_{Rd}) formulated in

Eurocode 2. Safety factors ($SF = V_{Rd}/V_{Ed}$) across all evaluated critical sections are synthesized below, confirming that transverse shear demand remains strictly within code-mandated safety boundaries ($SF \geq 1.0$) under the traditional partial factor format.

Table 5-9 – Shear Force Cover Slab Linear Verification

		Cover Slab - C35/45					
		Uphill Section		*Midspan Section*		*Downhill Section*	
GEO	**N**	-2326	kN	-2352	kN	-2370	kN
	Ved	868	kN	-605	kN	-2322	kN
	Vrd	15671	kN	15671	kN	12853	kN
	SF	18,046		25,924		5,536	
GEO + TH + SH + CR - V1	**N**	-2655	kN	-659	kN	-2638	kN
	Ved	889	kN	-518	kN	-2156	kN
	Vrd	15671	kN	15671	kN	12709	kN
	SF	17,620		30,282		5,895	
GEO + TH + SH + CR - V2	**N**	-2602	kN	-2651	kN	-2578	kN
	Ved	906	kN	-488	kN	-2111	kN
	Vrd	15671	kN	15671	kN	12903	kN
	SF	17,293		32,106		6,113	

Table 5-10 – Shear Force Foundation Slab Linear Verification

		Foundation Slab - C30/37					
		Uphill Section		*Midspan Section*		*Downhill Section*	
GEO	**N**	103	kN	38	kN	-195	kN
	Ved	311	kN	-36	kN	-312	kN
	Vrd	1553	kN	1553	kN	1553	kN
	SF	4,998		42,665		4,978	
GEO + TH + SH + CR - V1	**N**	-168	kN	315	kN	-522	kN
	Ved	191	kN	-12	kN	-338	kN
	Vrd	1553	kN	1553	kN	1553	kN
	SF	8,122		125,242		4,601	
GEO + TH + SH + CR - V2	**N**	-169	kN	313	kN	-520	kN
	Ved	177	kN	-11	kN	-332	kN
	Vrd	1553	kN	1553	kN	1553	kN
	SF	8,764		138,661		4,676	

Table 5-11 – Shear Force Uphill Wall Linear Verification

		Uphill Wall - C35/45					
		Top Section		*Mid-height Section*		*Bottom Section*	
GEO	**N**	233	kN	66	kN	31	kN
	Ved	1	kN	-35	kN	218	kN
	Vrd	1444	kN	1444	kN	1444	kN
	SF	1444,000		41,140		6,612	
GEO + TH + SH + CR - V1	**N**	4429	kN	3426	kN	1960	kN
	Ved	-302	kN	3	kN	457	kN
	Vrd	1444	kN	1444	kN	1444	kN
	SF	4,781		424,706		3,160	
GEO + TH + SH + CR - V2	**N**	4770	kN	3752	kN	2165	kN
	Ved	-379	kN	-27	kN	455	kN
	Vrd	1444	kN	1444	kN	1444	kN
	SF	3,808		53,481		3,177	

Table 5-12 – Shear Force Downhill Wall Linear Verification

		Downhill Wall - C35/45					
		Top Section		*Mid-height Section*		*Bottom Section*	
GEO	**N**	-372	kN	-179	kN	-8	kN
	Ved	-52	kN	-49	kN	-217	kN
	Vrd	1444	kN	1444	kN	1444	kN
	SF	27,769		29,231		6,651	
GEO + TH + SH + CR - V1	**N**	185	kN	3047	kN	2039	kN
	Ved	87	kN	-53	kN	-293	kN
	Vrd	1444	kN	1444	kN	1444	kN
	SF	16,694		27,297		4,935	
GEO + TH + SH + CR - V2	**N**	533	kN	3386	kN	2273	kN
	Ved	104	kN	-43	kN	-278	kN
	Vrd	1444	kN	1444	kN	1444	kN
	SF	13,925		33,503		5,194	

Table 5-13 – Shear Force Pile 2000 Uphill Linear Verification

		Piles 2000 Uphill - C30/37			
		Head Section		*Cover Slab Level Section*	
GEO	**N**	-10656	kN	-15458	kN
	Ved	2413	kN	-1758	kN
	Vrd	17017	kN	17487	kN
	SF	7,053		9,949	
GEO + TH + SH + CR - V1	**N**	-9173	kN	-13533	kN
	Ved	2951	kN	-1495	kN
	Vrd	16774	kN	17446	kN
	SF	5,685		11,666	
GEO + TH + SH + CR - V2	**N**	-8742	kN	-13015	kN
	Ved	2972	kN	-1453	kN
	Vrd	16774	kN	17369	kN
	SF	5,645		11,952	

Table 5-14 – Shear Force Pile 1200 Uphill Linear Verification

		Pile 1200 Uphill - C30/37			
		Head Section		*Cover Slab Level Section*	
GEO	**N**	1040	kN	-641	kN
	Ved	1148	kN	-169	kN
	Vrd	7421	kN	6498	kN
	SF	6,465		38,450	
GEO + TH + SH + CR - V1	**N**	-6934	kN	-2927	kN
	Ved	903,3	kN	-490	kN
	Vrd	7421	kN	6888	kN
	SF	8,215		14,072	
GEO + TH + SH + CR - V2	**N**	-7815	kN	-3307	kN
	Ved	944	kN	-533	kN
	Vrd	7505	kN	6952	kN
	SF	7,948		13,046	

Table 5-15 – Shear Force Pile 2000 Downhill Linear Verification

		Pile 2000 Downhill - C30/37			
		Head Section		*Cover Slab Level Section*	
GEO	**N**	-8778	kN	-11792	kN
	Ved	-5287	kN	-567	kN
	Vrd	16774	kN	17186	kN
	SF	3,173		0,033	
GEO + TH + SH + CR - V1	**N**	-9618	kN	-10952	kN
	Ved	-4346	kN	-253	kN
	Vrd	16774	kN	17061	kN
	SF	3,860		0,015	
GEO + TH + SH + CR - V2	**N**	-10305	kN	-10762	kN
	Ved	-4274	kN	-145	kN
	Vrd	16965	kN	17033	kN
	SF	3,969		0,008	

Note: The safety factors from some of the sections: the mid-span section of the cover slab or the mid-height section of the downhill and uphill wall, exhibits excessively large safety factors due to a V_{Ed} close to 0. Therefore, this safety factors cannot be considered reliable or meaningful and are not take into account in the analysis and conclusions.

The bottom section of the uphill wall under load combination version 1 and 2 represents the governing critical section for shear across the entire tunnel structure, reaching a peak utilization ratio of $SF = 3{,}160$ and $SF = 3{,}177$ respectively. Under full environmental coactions (GEO + TH + SH + CR), lateral earth pressures combined with restrained thermal and shrinkage shifts generate a peak design shear demand of $V_{Ed} = 457\ kN$ acting alongside an axial compression of $N_{Ed} = 1960\ kN$. The downhill pile is also highly demanded with a demand ratio of $SF = 3{,}173$ in the head section under geotechnical actions exclusively.

5.2 ECOV Global Safety Format Approach

5.2.1 Conceptual Framework

The implementation of Non-Linear Finite Element Analysis (NLFEA) to evaluate the safety margins of the Galleria Piscinale requires a fundamental shift away from local cross-sectional verification formats. The core philosophical principle of the ECOV (Estimate of Coefficient of Variation) format is to separate the numerical simulation of structural behaviour from the application of safety coefficients. The finite element solver is executed using unmodified material parameters to capture the true, un-distorted physical response of the infrastructure system up to its ultimate failure mechanism. Once the global resistance capacity is determined, a globally derived safety factor is applied to the overall system resistance. This global safety factor is calculated using a semi-probabilistic strategy that quantifies how variation in the underlying material properties propagates through the complex, non-linear structural system.

5.2.2 Load Evolution

To capture the realistic stress-strain history of the Galleria Piscinale tunnel, the numerical model applies actions a chronological, time-dependent framework. In DIANA FEA, each load case is defined by a base spatial load vector scaled over time by a dimensionless multiplier, $f(t)$. Across the structure's service life and subsequent Ultimate Limit State (ULS) pushover phase, following a general rule of multiplying the operational factors by 10 upon entering the ULS phase, ten distinct time-load functions govern the simulation:

- Time Load 1: Represents the primary landslide, it is activated at $t \approx 5.31 * 10^7$ s ($\approx$ 1,7 years) as slope movement initiates, scaling up to a baseline operational factor of 200 at $t = 1.189 * 10^8$ s to represent the sustained lateral earth thrust imposed on the uphill retaining system. When reaching the ULS at year 50 it jumps up to 2000.
- Time Load 2: Represents the self-weight and is held constant at 1,0 throughout the service life until the ULS phase when it increases to 10.
- Time Load 2: Simulates groundwater table lowering and in the same manner as self-weight loads it is held constant at 1,0 until the ULS phase where it increases at 10.
- Time Loads 4 to 9: Represent the excavation sequence. They are initially held constant at 0,6 until they jump to 6 during the ULS phase.

- Time Load 10: Represents the additional landslide, it is introduced at $t \approx 1.532 * 10^8$ s (≈ 4,8 years) with a factor of 25, during the ULS phase at year 50 it is multiplied by 10 to reach 250.

5.2.3 Dual Non-Linear Computational Strategy

The method assumes that the global resistance of a structural system follows a lognormal probabilistic distribution. By performing two specific simulations, you can estimate how much the structure's strength varies based on material uncertainties, while always considering material properties at 50 years.

The first non-linear calculation loop is executed using the mean values of the material: $f_{cm}, f_{ctm}, E_{cm}, f_{ym}$.

First, the estimation of the long-term compressive strength development is derived from the Eurocode 2 (EN 1992-1-1):

$$f_{cm}(t) = \beta_{cc}(t) * f_{cm} \tag{94}$$

With:

$$\beta_{cc}(t) = \exp\left[s\left(1 - \sqrt{\frac{28}{t}}\right)\right] \tag{95}$$

At 50 years, a conservative upper bound of $\beta_{cc} = 1{,}30$ is adopted, therefore:

$$f_{ck,50y} = 1{,}30 * f_{ck} \tag{96}$$

- For the class C35/45: $f_{ck,50y} = 1{,}30 * 35 = 45{,}5\ MPa$
- For the class C30/37: $f_{ck,50y} = 1{,}30 * 30 = 39\ MPa$

The mean compressive strength, $f_{cm,50y}$, represents the average crushing resistance of a concrete cylinder at 50 years, in accordance with EN 1992-1-1, it is computed by adding a fixed statistical offset of 8 MPa to the characteristic cylinder strength, $f_{ck,50y}$ at 50 years:

$$f_{cm,50y} = f_{ck,50\,y} + \Delta f = F_{ck} + 8\ [MPa] \tag{97}$$

- For the class C35/45: $f_{cm,50y} = 45{,}5 + 8 = 53{,}5\ MPa$.
- For the class C30/37: $f_{cm,50y} = 39 + 8 = 47\ MPa$.

For concrete strength classes less than or equal to C50/60, the development of microstructural matrix tensile capacity does not scale linearly with compression. Instead, it follows a non-linear power law based on the 2/3 exponent of the characteristic strength:

$$f_{ctm,50y} = 0{,}30 * \left(f_{ck,50y}\right)^{2/3} [MPa] \quad (98)$$

- For the class C35/45: $f_{ctm,50y} = 0{,}30 * (45{,}5)^{2/3} = 3{,}7\ MPa$
- For the class C30/37: $f_{ctm,50y} = 0{,}30 * (39)^{\frac{2}{3}} = 3{,}4\ MPa$.

The mean modulus of elasticity at 50 years controls the elastic deformations and deformation-induced restraint stresses within the finite element mesh. It is calculated as a function of the mean compressive strength at 50 years:

$$E_{cm,50y} = 22 * \left(\frac{f_{cm,50y}}{10}\right)^{0,3} [MPa] \quad (99)$$

- For the class C35/45

$$E_{cm,50y} = 22 * \left(\frac{53{,}5}{10}\right)^{0,3} = 36{,}4\ GPa \quad (100)$$

- For the class C30/37:

$$E_{cm,50y} = 22 * \left(\frac{47}{10}\right)^{0,3} = 35{,}0\ GPa \quad (101)$$

This run represents the most realistic rendering of the physical asset. It ensures that the early-age thermomechanical cooling constraints, stress relaxation paths, and microstructural micro-cracking develop under true physical conditions. The model is pushed beyond its operational design limits by monotonically scaling the structural actions until a global collapse mechanism is reached, yielding the Mean Structural Resistance at 50 years for both the geotechnical actions and the thermal ones ($R_{m,GEO}, R_{m,TH}$).

The second non-linear simulation loop is identical in its geometric definition, boundary non-linearities, and construction phasing sequence, but the material properties are downgraded to their characteristic thresholds at 50 years ($f_{ck}, f_{ctk}, E_k, f_{yk}$). By re-running the solver under these lower-bound properties, the system captures how a global reduction in material parameters affects the failure path and load-carrying capacity. This model is also loaded to collapse, yielding the Characteristic Structural Resistance for both the geotechnical actions and the thermal ones ($R_{k,GEO}, R_{k,TH}$).

5.2.4 Probabilistic Formulation

Once R_m and R_k are extracted from the finite element environment, the global structural resistance is assumed to follow a lognormal distribution. This statistical assumption ensures that resistance values remain strictly positive and accounts for the typical asymmetric scattering found in concrete structures. First, it is needed to compute the global coefficient of variation V_R, which represents the sensitivity of the entire structural system to material scatter, is derived directly from the ratio of the two non-linear load capacities:

$$V_R = \frac{1}{1{,}65} * \ln\left(\frac{R_m}{R_k}\right) \tag{102}$$

Where R_k is the structural resistance predicted by a non-linear analysis using the characteristic values of the material properties and R_m, is the structural performance predicted by a non-linear analysis using the mean values of the material properties. This formula is repeated for both the structural resistance related to the geotechnical effects and thermal effects, obtaining therefore: $V_{R,GEO}, V_{R,TH}$. The constant 1,65 represents the distance between the mean value and the 5% characteristic fractile on a standard normal distribution curve. By passing the log-ratio of the finite element failure loads through this operator, V_R filters out how local variation in concrete and steel properties interact, combine and propagate through the non-linear frame.

Using the calculated system variance (V_R), the global material safety factor is determined using the reliability format derived from Eurocode 0 (EN 1990) for the geotechnical and thermal effects ($\gamma_{R,GEO}, \gamma_{R,TH}$):

$$\gamma_R = \exp(\alpha_R * \beta_{tgt} * V_R) \tag{103}$$

Where β is the target value of the reliability index required for standard Ultimate Limit State (ULS) verification, set as $\beta = 4{,}3$ for a conventional 100-year design reference period and highest possible consequence class and α_R is the first-order reliability method (FORM) sensitivity equal to 0,8.

5.2.5 Model Uncertainty in Non-Linear Analyses

In nonlinear finite element analyses (NLFEA), the predicted resistance depends not only on material properties but also on modelling choices. Model uncertainty therefore represents the discrepancy between the actual physical response and the numerical prediction arising, for

example, from constitutive laws, discretisation, crack representation, boundary conditions and the solution procedure.

$$\theta_i = \frac{R_{exp,i}}{R_{NLFEA,i}} \tag{104}$$

Where R_{EXP} is the experimental resistance and R_{NLFEA} is the resistance predicted by the model. A value θ < 1 indicates that the model overestimates the resistance, whereas θ > 1 indicates a conservative prediction. The mean value μθ and the coefficient of variation Vθ are obtained from the set of θi values.

Two separate components are distinguished: a within-model component, representing the dispersion observed when applying the same numerical strategy to different benchmarks, and a between-model component, reflecting the variability among different numerical strategies. Unless a strategy has undergone extensive validation, both components must be incorporated into the factor. A "solution strategy" refers to a unified modelling setup that consistently combines element type and size, meshing, constitutive laws, cracking and softening formulations, fracture energy, reinforcement and bond modelling, boundary constraints, contact definitions, loading protocol, increment size, and convergence criteria.

- Numerical verification: Evaluating sensitivity to mesh size and load step increments, conducting equilibrium checks, and ensuring the robustness of the iterative procedure.
- Validation: Comparing numerical predictions against relevant experimental test data using the exact solution strategy intended for the real structure.
- Benchmark selection: Benchmarks must accurately mirror the structural typology, stress state, parameter range and the expected failure mode. For instance, validating a model exclusively against flexural failures is insufficient to justify its application for shear failure prediction.

$$\gamma_{Rd} = \frac{1}{\mu_\theta} * \exp(\alpha_R * \beta * V_\theta) \tag{105}$$

In this expression, α_R is the sensitivity factor associated with model uncertainty, β is the target reliability index, and μ_θ and V_θ describe the bias and dispersion of the numerical prediction. Engen et al. assume $\alpha_R = 0{,}4 * 0{,}8 = 0{,}32$.

The final Design Global Resistance (R_d) or the design Load Multipliers (LM_d) of the artificial tunnel system is evaluated as:

$$LM_d = \frac{R_m}{\gamma_R * \gamma_{Rd}} \tag{106}$$

Table 5-16 - Calculation of γ_{Rd} Depending on Various Cases

Case	Statistical Parameter	$\boldsymbol{\beta = 3,8}$	$\boldsymbol{\beta = 4,3}$
Within-model Component only	$\mu_\theta = 1{,}020; V_\theta = 0{,}13$	$\gamma_{Rd} \approx 1{,}15$	$\gamma_{Rd} \approx 1{,}17$
Between-model component only	$\mu_\theta = 1{,}000; V_\theta = 0{,}14$	$\gamma_{Rd} \approx 1{,}18$	$\gamma_{Rd} \approx 1{,}21$
Combined, without extensive validation	Product of the two components	$\gamma_{Rd} \approx 1{,}35$	$\gamma_{Rd} \approx 1{,}42$

To evaluate structural safety and account for numerical variability, the safety-format verifications for both model 1 and model 2 are conducted across two distinct model uncertainty scenarios: Low Model Uncertainty (LMU) and High Model Uncertainty (HMU).

In the LMU scenario, a partial factor of $\gamma_{Rd} = 1{,}17$ is adopted, calibrated based on a target reliability index of $\beta = 4{,}3$ by considering solely the within-model component. In contrast the HMU scenario incorporates a higher partial factor of $\gamma_{Rd} = 1{,}42$, which is determined by considering both the within-model component and the between-model component. Importantly, these LMU and HMU values must be interpreted as sensitivity assumptions rather than definitive, universally applicable safety factors. In accordance with fib Model Code 2010 guidelines and the framework established by Engen et al., applying a reduced factor such as $\gamma_{Rd} = 1{,}17$ is strictly permissible only when the specific non-linear solution strategy has been systematically validated against a relevant experimental benchmark suite of similar underground structural typologies. In the absence of comprehensive physical test validation for the specific box-tunnel kinematics, the HMU scenario ($\gamma_{Rd} = 1{,}42$) serves as the governing benchmark for regulatory compliance.

Furthermore, it must be emphasized that increasing numerical complexity does not automatically produce a more accurate or intrinsically safer resistance estimate, as it will be discussed with the Figure 5-23.

5.2.6 Design Global Resistance

The Design Global Resistance is computed both for the geotechnical and thermal effects, $LM_{d,GEO}, LM_{d,TH}$. These values represent the true, physically justified non-linear capacity thresholds allowed for the structure under regulatory safety criteria. The final verification check evaluates the ratio of the standard code demand to the computed non-linear design capacity, for both the geotechnical and thermal effect:

$$SF_{GEO} = \frac{LM_{d,GEO}}{Standard\ LM_{GEO}} > 1 \quad (107)$$

$$SF_{TH} = \frac{LM_{d,TH}}{Standard\ LM_{TH}} > 1 \quad (108)$$

Table 5-17 - Standard Load Multipliers

Standard LM_{GEO}	1,30
Standard LM_{TH}	1,50

A value over 1,0 states that the absolute worst-case loading demanded by regulatory design codes sits safely within the structure's ultimate non-linear capacity envelope. The limit state is not crossed, confirming the structure is fully compliant with safety codes.

This statistically superior resistance in model 2 is directly attributed to differences in the early-age thermo-mechanical loading history. In model 2, the heat of hydration associated with select concrete casting phases is not considered, meaning the concrete continuum is effectively subjected to one fewer action at an early age. By omitting the hydration thermal spikes and resulting self-equilibrating restraint stresses for these pours, model 2 avoids the early-age thermal micro-cracking and locked-in residual stress concentrations that develop in model 1. Spared from this initial thermal damage, the structure in model 2 retains a higher effective cross-sectional integrity and stiffness prior to the Ultimate Limit State pushover phase, which translates directly into a higher mean capacity and a significantly elevated 5th percentile global design resistance.

Furthermore, it must be emphasized that increasing numerical complexity does not automatically produce a more accurate or intrinsically safer resistance estimate, as it will be discussed with the Figure 5-23.The probability density functions (Figure 5-23) and cumulative distribution functions (Figure 5-24), compare the statistical distribution of the collapse load multiplier between the two numerical formulations, with the vertical lines denoting their

respective 5th percentile characteristic thresholds. Across both representations, model 2 demonstrates a statistically higher global resistance than model 1. This is evident from the rightward shift of the probability density peak and the corresponding displacement of the 5th percentile value from $\lambda_{5\%} = 2{,}8$ in model 1 to $\lambda_{5\%} = 3{,}3$ in model 2. Furthermore, model 2 exhibits a taller, narrower PDF curve and a steeper CDF slope, highlighting a lower variance and reduced statistical dispersion in its ultimate collapse capacity. This statistically superior resistance in model 2 is directly attributed to differences in the early-age thermo-mechanical loading history. In model 2, the heat of hydration associated with select concrete casting phases is not considered, meaning the concrete continuum is effectively subjected to one fewer action at an early age. By omitting the hydration thermal spikes and resulting self-equilibrating restraint stresses for these pours, model 2 avoids the early-age thermal micro-cracking and locked-in residual stress concentrations that develop in model 1. Spared from this initial thermal damage, the structure in model 2 retains a higher effective cross-sectional integrity and stiffness prior to the Ultimate Limit State pushover phase, which translates directly into a higher mean capacity and a significantly elevated 5th percentile global design resistance.

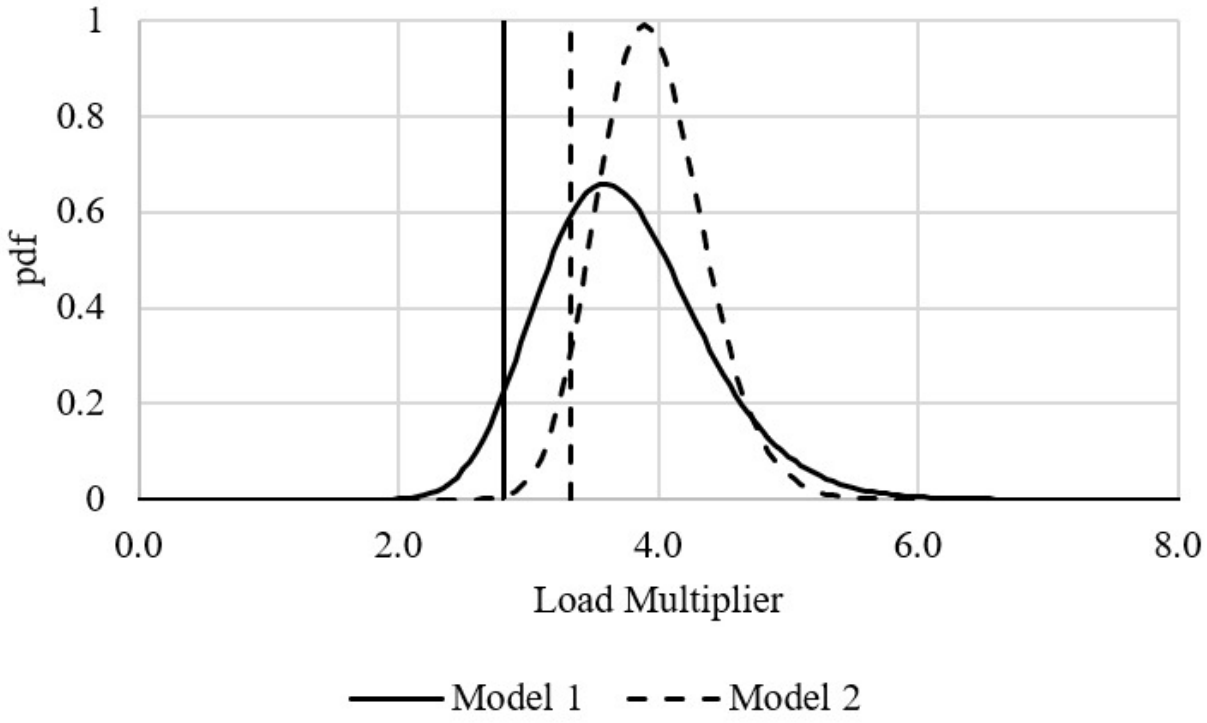


Figure 5-23 - Probability Density Function of Load Multipliers

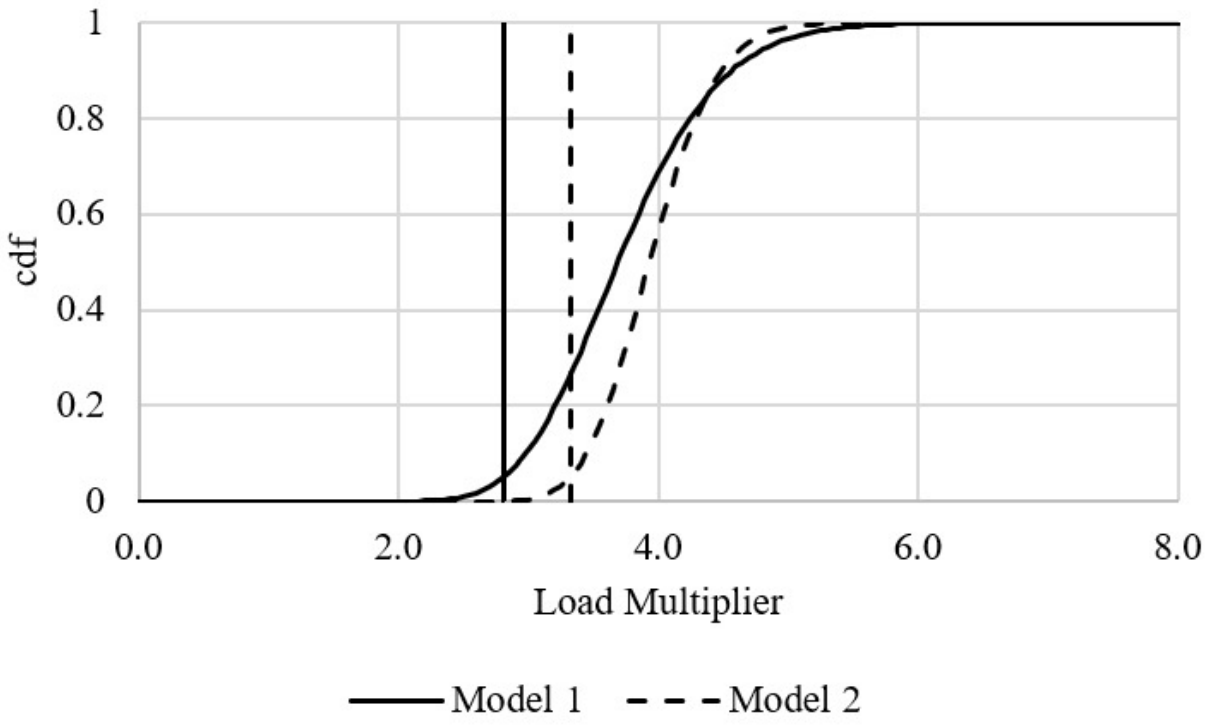


Figure 5-24 - Cumulative Density Function of Load Multipliers

5.2.7 Global Safety Evaluation via the ECOV Method

This section presents the global structural reliability assessment of the Galleria Piscinale using the Estimation of Coefficient of Variation (ECOV) format, detailed in the chapter above. To rigorously map the safety margins across operational and environmental variations, a comprehensive parametric matrix was analysed using the two highest-fidelity numerical formulations (model 1 and model 2). The safety evaluation encompasses three primary operational and modelling variables:

- Seasonal construction chronology: winter or summer start. The initial casting schedule dictates the early-age thermo-mechanical history, concrete maturity trajectory, and thermal restraint stresses. Consequently, both winter-start and summer-start timelines were simulated to capture the governing initial environmental state.
- Model uncertainty: To address uncertainties in numerical representation, material non-linearity, and soil-structure interaction, two distinct model uncertainty levels were applied:
    - Low Model Uncertainty (LMU): $\gamma_{Rd} = 1{,}17$
    - High Model Uncertainty (HMU): $\gamma_{Rd} = 1{,}42$

- Thermal operational extremes: For every model configuration, global resistance factors and collapse mechanisms were systematically verified under both Peak Maximum Temperatures (maximum volumetric expansion demand) and Peak Minimum Temperatures (maximum tensile contraction demand).

Table 5-18 - Model 1 Winter Start LMU

	Peak Maximum Temperatures		Peak Minimum Temperatures	
	Mean ULS Factor	Characteristic ULS Factor	Mean ULS Factor	Characteristic ULS Factor
R_GEO	3,770	3,608	3,380	3,218
R_TH	4,350	4,163	3,900	3,713
γ_{Rd}	1,17		1,17	
V_R GEO	0,027		0,030	
V_R THERMAL	0,027		0,030	
β	4,300		4,300	
α_R	0,800		0,800	
γ_R GEO	1,096		1,108	
γ_R THERMAL	1,096		1,108	
Design GEO LM_d	2,939		2,607	
Design THERMAL LM_d	3,391640384		3,007923978	
GEO LM_d	2,261		2,005	
THERMAL LM_d	2,261		2,005	
Type of collapse	Crushing of the concrete on the downhill side section of the cover slab		Shear at the top of uphill side wall	
CHECK	OK		OK	

Table 5-19 - Model 1 Winter Start HMU

	Peak Maximum Temperatures		Peak Minimum Temperatures	
	Mean ULS Factor	Characteristic ULS Factor	Mean ULS Factor	Characteristic ULS Factor
R_GEO	3,770	3,608	3,380	3,218
R_TH	4,350	4,163	3,900	3,713
γ_{Rd}	1,42		1,42	
V_R GEO	0,027		0,030	
V_R THERMAL	0,027		0,030	
β	4,300		4,300	
α_R	0,800		0,800	
γ_R GEO	1,096		1,108	
γ_R THERMAL	1,096		1,108	
Design GEO LM_d	2,422		2,148	
Design THERMAL LM_d	2,794520598		2,478359897	
GEO LM_d	1,863		1,652	
THERMAL LM_d	1,863		1,652	
Type of collapse	Crushing of the concrete on the downhill side section of the cover slab		Shear at the top of uphill side wall	
CHECK	OK		OK	

Table 5-20 - Model 1 Summer Start LMU

	Peak Maximum Temperatures		Peak Minimum Temperatures	
	Mean ULS Factor	Characteristic ULS Factor	Mean ULS Factor	Characteristic ULS Factor
R_GEO	3,153	2,990	4,615	4,420
R_TH	3,638	3,450	5,325	5,100
γ_{Rd}	1,17		1,17	
V_R GEO	0,032		0,026	
V_R THERMAL	0,032		0,026	
β	4,300		4,300	
α_R	0,800		0,800	
γ_R GEO	1,117		1,094	
γ_R THERMAL	1,117		1,094	
Design GEO LM_d	2,413		3,605	
Design THERMAL LM_d	2,784191971		4,159527665	
GEO LM_d	1,856		2,773	
THERMAL LM_d	1,856		2,773	
Type of collapse	Crushing of the concrete on the downhill side section of the cover slab		Flexural failure on the downhill side section of the cover slab	
CHECK	OK		OK	

Table 5-21 - Model 1 Summer Start HMU

	Peak Maximum Temperatures		Peak Minimum Temperatures	
	Mean ULS Factor	Characteristic ULS Factor	Mean ULS Factor	Characteristic ULS Factor
R_GEO	3,153	2,990	4,615	4,420
R_TH	3,638	3,450	5,325	5,100
γ_{Rd}	1,42		1,42	
V_R GEO	0,032		0,026	
V_R THERMAL	0,032		0,026	
β	4,300		4,300	
α_R	0,800		0,800	
γ_R GEO	1,117		1,094	
γ_R THERMAL	1,117		1,094	
Design GEO LM_d	1,988		2,970	
Design THERMAL LM_d	2,294017328		3,427216456	
GEO LM_d	1,529		2,285	
THERMAL LM_d	1,529		2,285	
Type of collapse	Crushing of the concrete on the downhill side section of the cover slab		Flexural failure on the downhill side section of the cover slab	
CHECK	OK		OK	

Table 5-22 - Model 2 Winter Start LMU

	Peak Maximum Temperatures		Peak Minimum Temperatures	
	Mean ULS Factor	Characteristic ULS Factor	Mean ULS Factor	Characteristic ULS Factor
R_GEO	4,225	3,868	4,030	3,673
R_TH	4,875	4,463	4,650	4,238
γ_{Rd}	1,17		1,17	
V_R GEO	0,054		0,056	
V_R THERMAL	0,054		0,056	
β	4,300		4,300	
α_R	0,800		0,800	
γ_R GEO	1,202		1,214	
γ_R THERMAL	1,202		1,214	
Design GEO LM_d	3,003		2,838	
Design THERMAL LM_d	3,465278155		3,274594627	
GEO LM_d	2,310		2,183	
THERMAL LM_d	2,310		2,183	
Type of collapse	Shear at the base of downhill side wall		Shear at the base of downhill side wall	
CHECK	OK		OK	

Table 5-23 - Model 2 Winter Start HMU

	Peak Maximum Temperatures		Peak Minimum Temperatures	
	Mean ULS Factor	Characteristic ULS Factor	Mean ULS Factor	Characteristic ULS Factor
R_GEO	4,225	3,868	4,030	3,673
R_TH	4,875	4,463	4,650	4,238
γ_{Rd}	1,42		1,42	
V_R GEO	0,054		0,056	
V_R THERMAL	0,054		0,056	
β	4,300		4,300	
α_R	0,800		0,800	
γ_R GEO	1,202		1,214	
γ_R THERMAL	1,202		1,214	
Design GEO LM_d	2,475		2,338	
Design THERMAL LM_d	2,855193973		2,698081488	
GEO LM_d	1,903		1,799	
THERMAL LM_d	1,903		1,799	
Type of collapse	Shear at the base of downhill side wall		Shear at the base of downhill side wall	
CHECK	OK		OK	

Table 5-24 - Model 2 Summer Start LMU

	Peak Maximum Temperatures		Peak Minimum Temperatures	
	Mean ULS Factor	Characteristic ULS Factor	Mean ULS Factor	Characteristic ULS Factor
R_GEO	3,380	3,185	4,160	3,250
R_TH	3,900	3,675	4,800	3,750
γ_{Rd}	1,17		1,17	
V_R GEO	0,036		0,150	
V_R THERMAL	0,036		0,150	
β	4,300		4,300	
α_R	0,800		0,800	
γ_R GEO	1,132		1,673	
γ_R THERMAL	1,132		1,673	
Design GEO LM_d	2,552		2,125	
Design THERMAL LM_d	2,944926844		2,452103701	
GEO LM_d	1,963		1,635	
THERMAL LM_d	1,963		1,635	
Type of collapse	Crushing of the concrete on the downhill side section of the cover slab		Shear at the top of uphill side wall	
CHECK	OK		OK	

Table 5-25 - Model 2 Summer Start HMU

	Peak Maximum Temperatures		Peak Minimum Temperatures	
	Mean ULS Factor	Characteristic ULS Factor	Mean ULS Factor	Characteristic ULS Factor
R_GEO	3,380	3,185	4,160	3,250
R_TH	3,900	3,675	4,800	3,750
γ_{Rd}	1,42		1,42	
V_R GEO	0,036		0,150	
V_R THERMAL	0,036		0,150	
β	4,300		4,300	
α_R	0,800		0,800	
γ_R GEO	1,132		1,673	
γ_R THERMAL	1,132		1,673	
Design GEO LM_d	2,103		1,751	
Design THERMAL LM_d	2,426453808		2,020395303	
GEO LM_d	1,618		1,347	
THERMAL LM_d	1,618		1,347	
Type of collapse	Crushing of the concrete on the downhill side section of the cover slab		Shear at the top of uphill side wall	
CHECK	OK		OK	

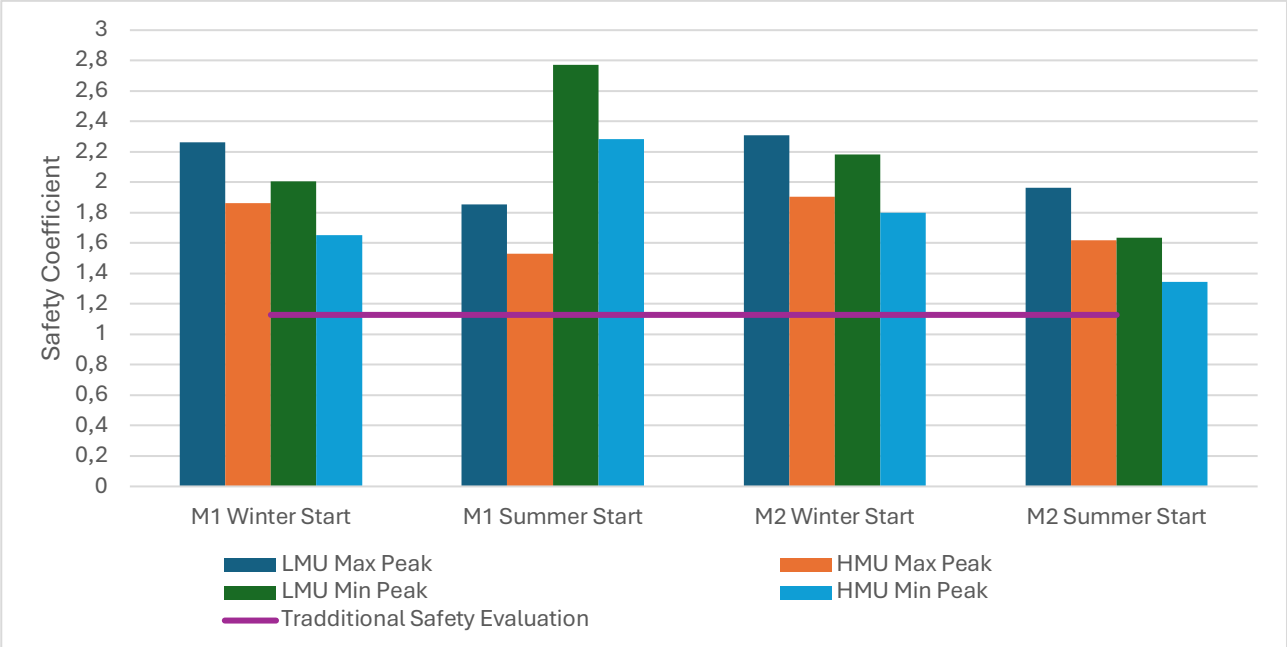


Figure 5-25 - Safety Coefficients Comparison

A comparative assessment of the global safety results obtained via the Estimation of Coefficient of Variation (ECOV) format reveals clear trends regarding the influence of modelling uncertainties, construction seasonality, and non-linear stress redistribution across the tunnel structure.

Regarding the internal sensitivity of the ECOV framework, transitioning from Low Model Uncertainty ($\gamma_{Rd} = 1{,}17$) to High Model Uncertainty ($\gamma_{Rd} = 1{,}42$) introduces a systematic 21% increase on the global design capacity multiplier, driving the load multiplier, LM_d, downward across all scenarios.

Construction chronology also strongly influences the governing collapse state. For model 1, a summer start induces its critical utilization during peak maximum temperatures ($LM_d = 1{,}529$ under HMU) due to early-age thermal locking combined with seasonal expansion, whereas a winter start is governed by peak minimum winter contraction ($LM_d = 1{,}652$ under HMU). Across these configurations, the identified collapse mechanisms shift from cover slab concrete crushing and ductile flexural failure under thermal expansion to shear failure at the base or top of the vertical side walls under winter contraction.

When compared against the traditional deterministic linear elastic approach of model 5, the ECOV global safety format demonstrates a substantial and systematic reduction in structural utilization. In Model 5, the cross-sectional linear verification at the uphill wall top section was governed by a maximum safety factor of $SF_{max} = 1{,}128$, indicating an apparent remaining safety margin of only 12,8%. Under the advanced ECOV formulation, the global utilization factors drop markedly, spanning from $LM_d = 2{,}773$ referring to model 1 under summer construction and low model uncertainty, to $LM_d = 1{,}347$ under the most penalizing combination of high model uncertainty, summer casting, and peak minimum temperatures. This results in an increase of safety between 19,41% and 145,83%.

This pronounced reduction in structural utilization is directly attributable to the capacity of Non-Linear Finite Element Analysis (NLFEA) to capture realistic physical stress-relief mechanisms. While standard linear elastic checks excessively penalize self-equilibrating thermal and shrinkage coactions, the non-linear continuum inherently accounts for concrete tensile cracking and compressive plasticity. These non-linear phenomena naturally dissipate localized stress concentrations, enabling an efficient redistribution of internal forces throughout the integrated box-pile foundation system. Consequently, coupling refined numerical formulations (models 1 and 2) with the ECOV global safety format eliminates the

artificial conservatism of traditional cross-sectional methods, demonstrating that the structure retains substantial unexploited capacity reserves and validating its full Ultimate Limit State compliance.

Chapter 6 Non-Linear Failure Mechanisms and Collapse Analysis

Building upon the global safety factors and reliability metrics derived through the ECOV method in Chapter 5, this chapter investigates the physical kinematics, strain localization patterns, and internal stress redistributions that govern the ultimate collapse of the Galleria Piscinale structure.

6.1 Methodological Framework

To systematically identify the governing collapse mechanism, non-linear failure envelopes are extracted for eight distinct parametric configurations combining model complexity, construction seasonality, and operational thermal extremes:

- Model 1 configurations: Winter and Summer construction starts, evaluated at both Peak Maximum and Peak Minimum operational temperatures: 4 cases
- Model 2 configurations: Winter and Summer construction starts, evaluated at both Peak Maximum and Peak Minimum operational temperatures: 4 cases

In each scenario, structural collapse is reached by monotonically scaling the governing action multipliers until convergence cannot be restored, signalling physical instability or cross-sectional failure. At this ultimate load increment, the internal mechanical state of the continuum is characterized through five complementary response fields:

- Crack normal strain (ε_{kn}): measures the localized opening strain perpendicular to the crack plane within DIANA FEA's smeared fixed crack framework. This field identifies the exact kinematic path of discrete fracture zones, distinguishing between broad diffuse flexural micro-cracking and discrete, highly localized macro-cracks that drive diagonal shear bands or hinge mechanisms.
- Major principal Cauchy stress (S_1): represents the maximum principal tensile stress in the concrete continuum. In uncracked regions, it maps elastic tensile stress trajectories, while in damaged zones, it illustrates the residual tensile traction transferred across the crack interface.
- Minor principal Cauchy stress (S_2): maps the minimum principal (maximum compressive) Cauchy stress trajectories throughout the concrete members. This contour is essential for visualizing the development and inclination of compressive arches, frame corner thrust vectors, and internal concrete struts, directly revealing whether structural collapse involves compressive concrete crushing where S_2 reaches the ultimate plastic compressive strength (f_{cd}).
- Horizontal reinforcement Cauchy stress (S_{xx}): Quantifies the normal true stress developed within steel reinforcement aligned along the global horizontal X-axis. This tracks the structural activation of top and bottom flexural reinforcement in the cover slab and foundation invert slab, as well as horizontal distribution steel within the vertical walls. Comparing S_{xx} against the steel design yield strength (f_{yd}) indicates whether plastic rebar yielding precedes collapse or whether the member fails in a brittle manner while steel remains elastic.
- Vertical reinforcement Cauchy stress (S_{yy}): Captures the normal true stress in steel bars oriented along the global vertical Y-axis. This component maps the flexural engagement of the primary vertical reinforcement in the uphill and downhill lining walls, the longitudinal bars in the deep foundation piles, and the tensile mobilization of vertical shear stirrup legs.

6.2 Collapse Dynamics of Model 1

6.2.1 Winter Casting: Peak Maximum and Peak Minimum Temperature

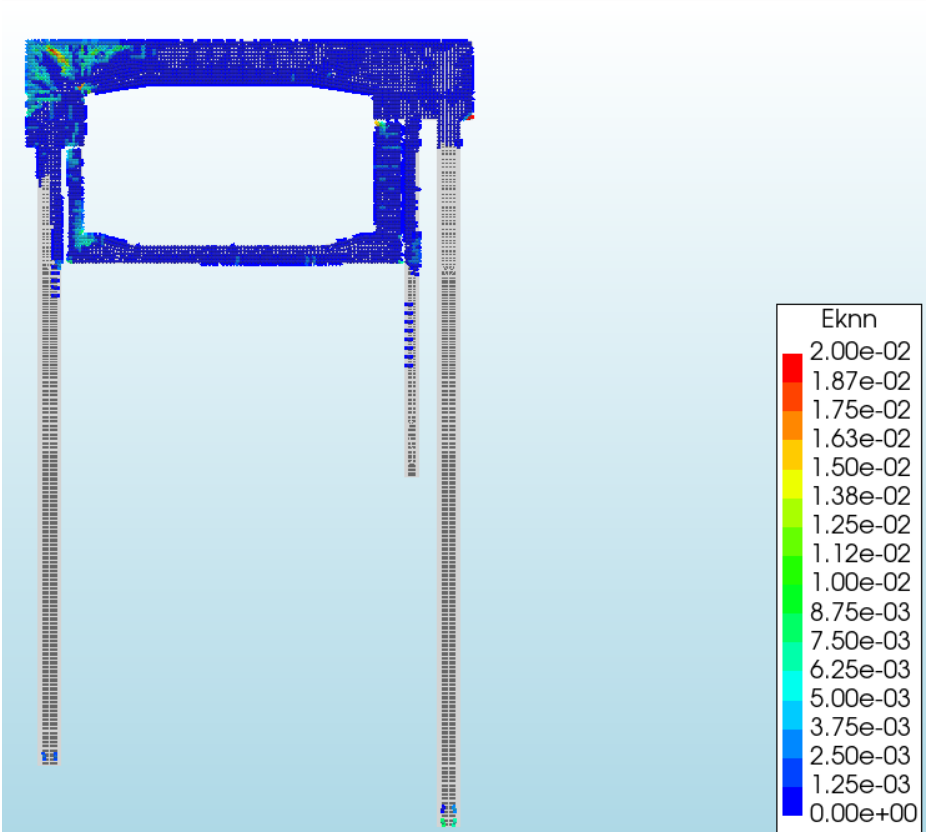


Figure 6-1 - Model 1: Winter Casting Max Temperatures - ε_{kn}

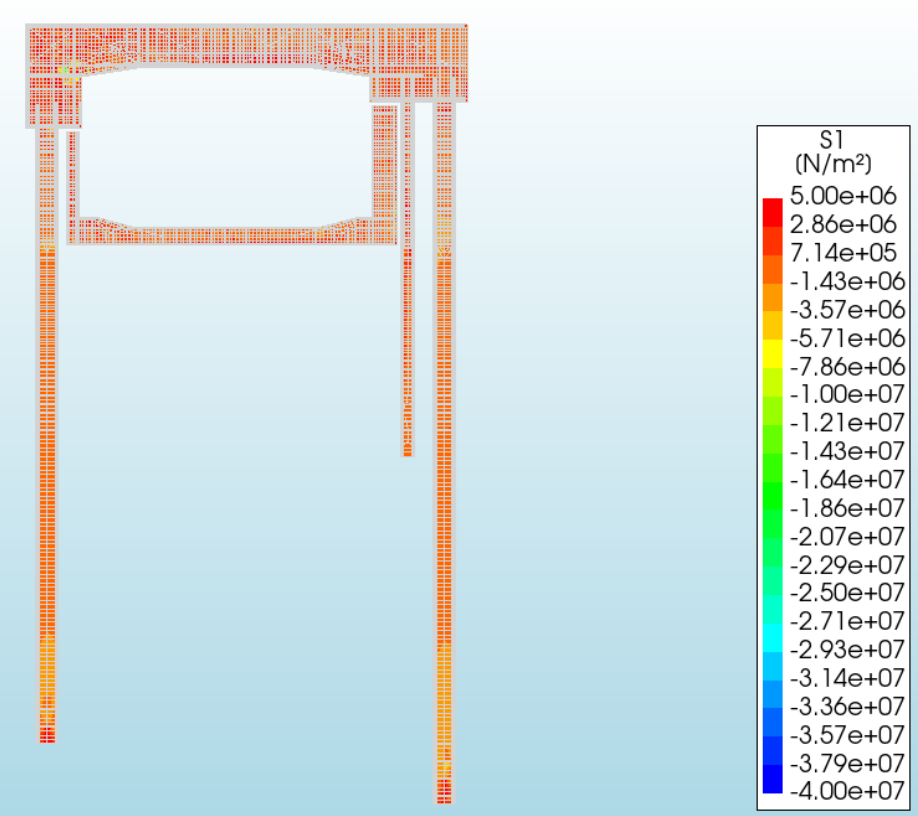


Figure 6-2 - Model 1: Winter Casting Max Temperatures - S_1

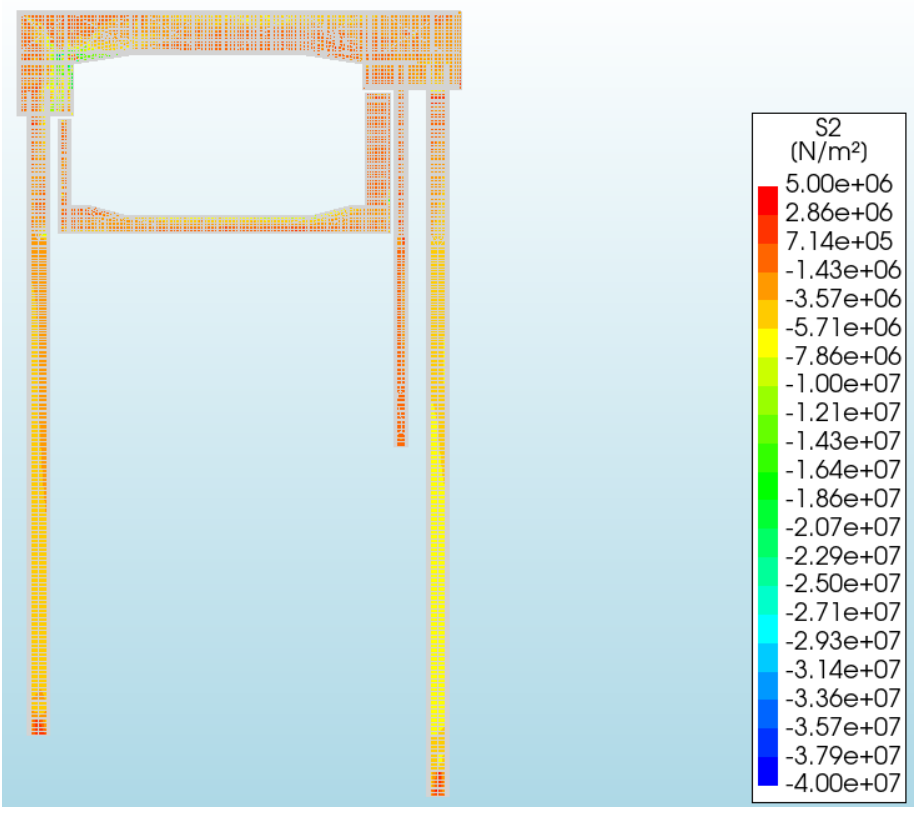


Figure 6-3 - Model 1: Winter Casting Max Temperatures - S_2

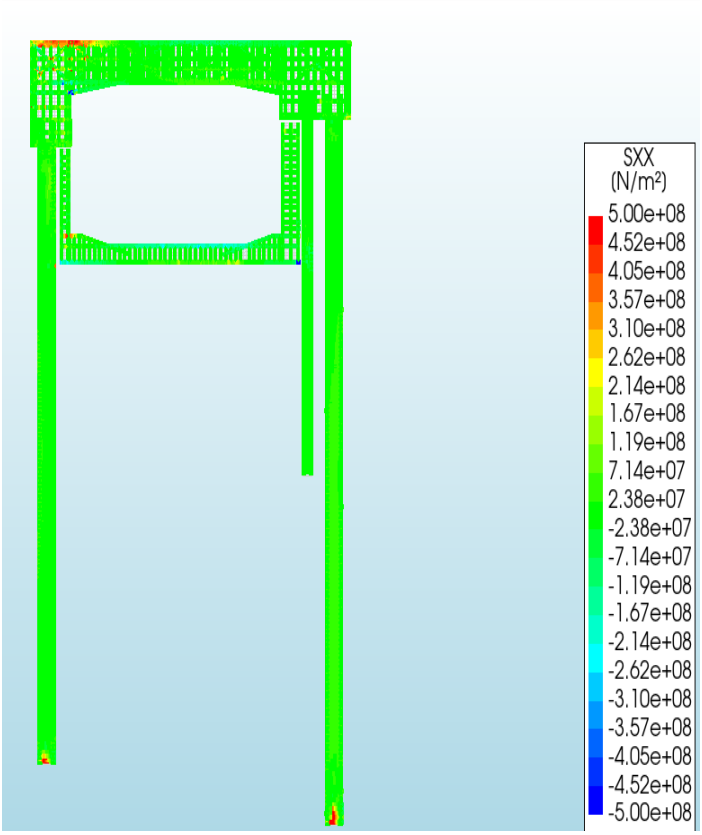


Figure 6-4 - Model 1: Winter Casting Max Temperatures - S_{xx}

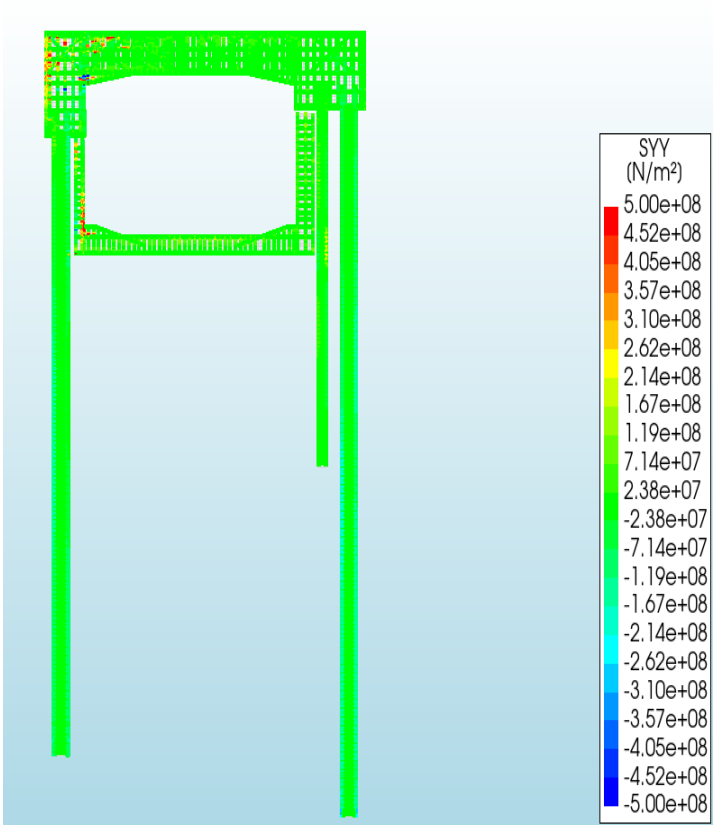


Figure 6-5 - Figure 6 2 - Model 1: Winter Casting Max Temperatures - S_{yy}

Under the model 1 winter casting scenario subjected to operational peak maximum temperatures, structural collapse is governed by concrete crushing on the downhill side section of the cover slab. During peak summer operational heating, the massive cover slab undergoes global volumetric thermal expansion. As the roof expands outward against the lateral earth pressure and boundary restraints, intense compressive arching thrusts channel directly into the downhill knee joint. This severe compressive stress concentration drives the minor principal stress to $S_2 = -79{,}1$ MPa, surpassing the ultimate concrete compressive capacity and triggering local plastic crushing at the top-left corner of the frame. Simultaneously, the extreme localized rotations activate extensive plastic yielding in both the horizontal ($S_{xx} = \pm 901$ MPa) and vertical ($S_{yy} = \pm 901$ MPa) reinforcement across the downhill part of the section: in the top of the cover slab and the downhill wall, respectively. This combined plastic flow and crushing zone is marked by localized crack opening strains reaching $\varepsilon_{kn} = 2{,}03 * 10^{-2}$, precipitating global loss of equilibrium through compressive degradation of the roof slab rather than web shear failure.

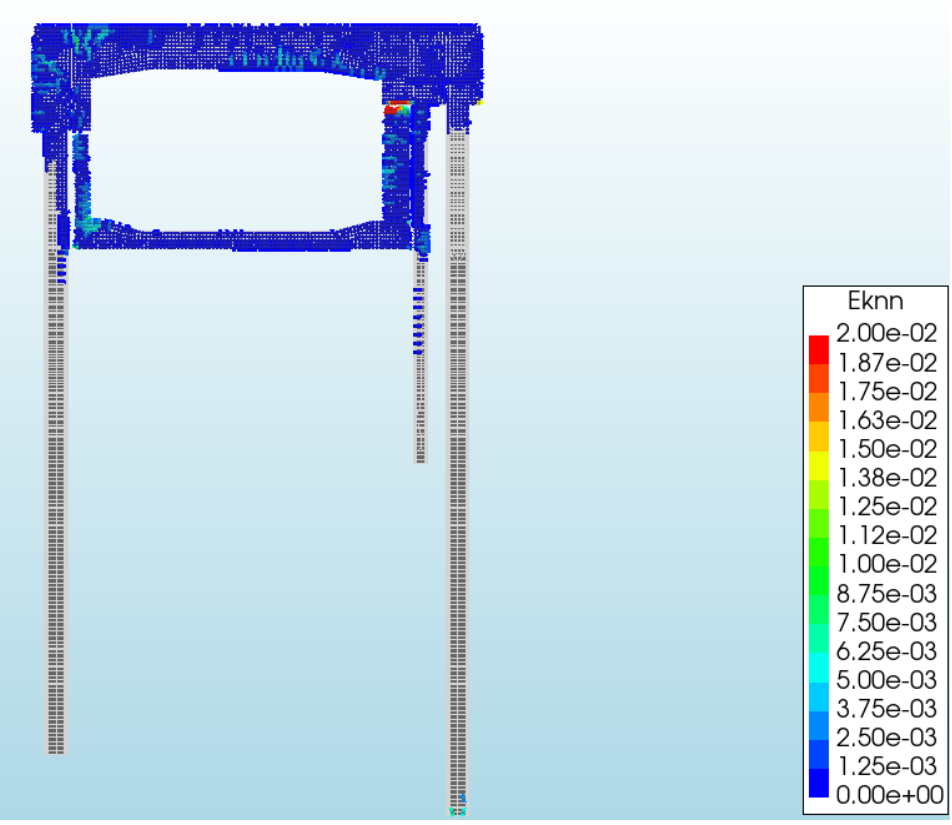


Figure 6-6 - Model 1: Winter Casting Min Temperatures - ε_{kn}

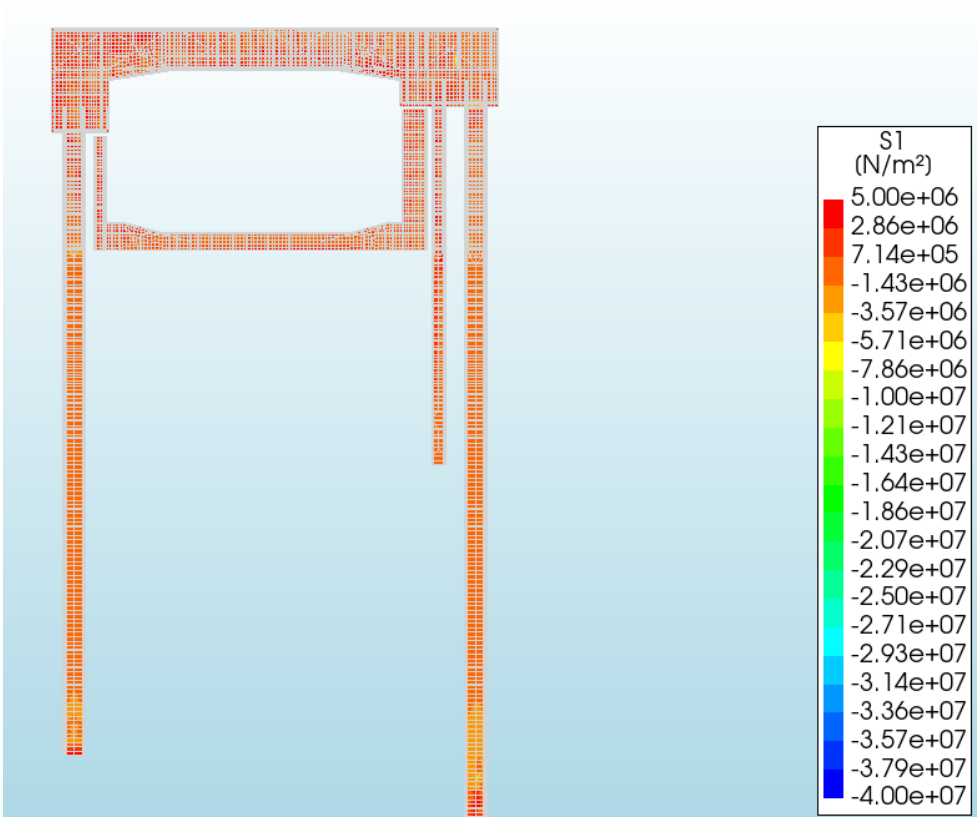


Figure 6-7 - Model 1: Winter Casting Min Temperatures - S_1

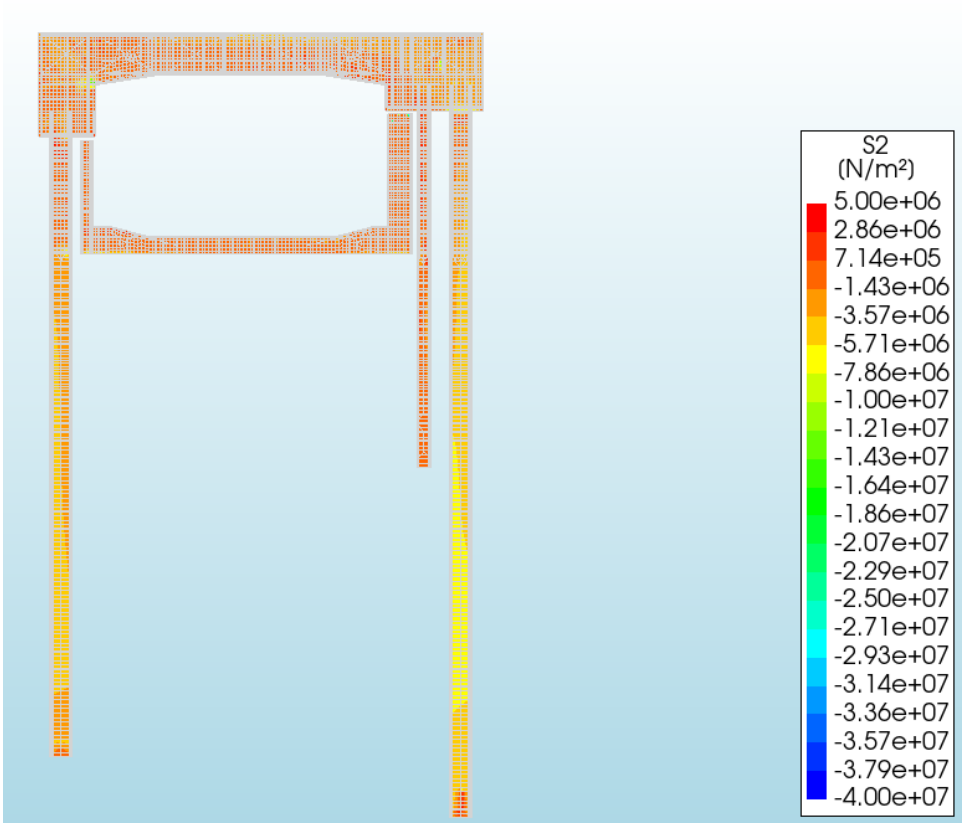


Figure 6-8 - Model 1: Winter Casting Min Temperatures - S_2

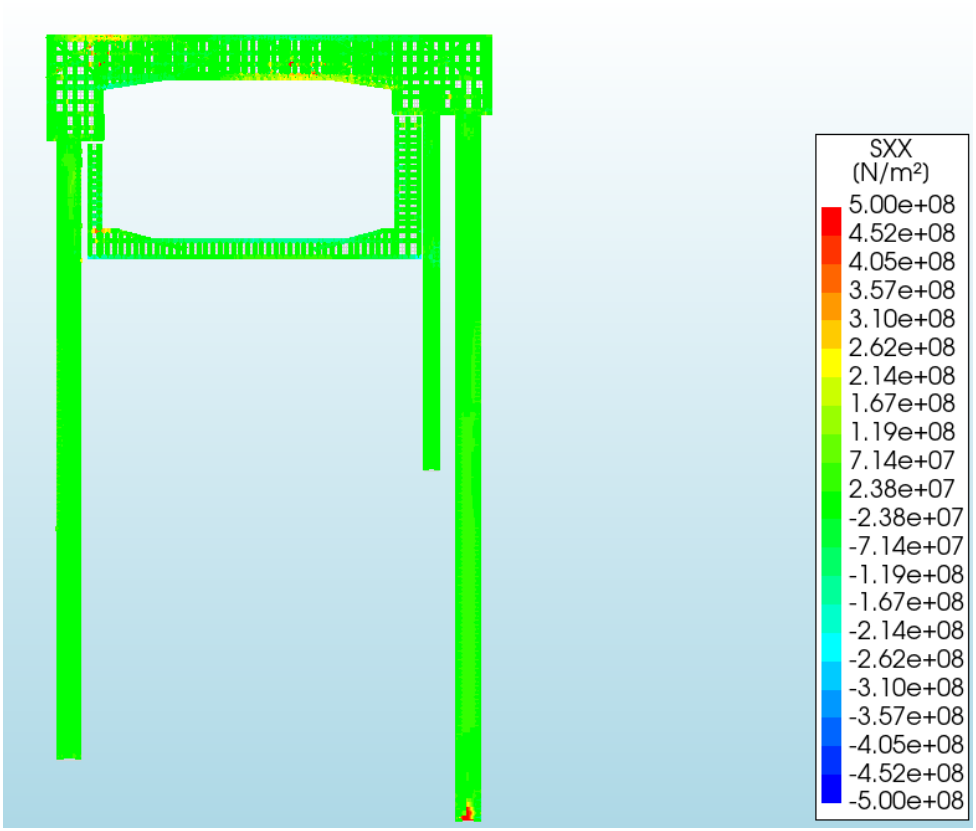


Figure 6-9 - Model 1: Winter Casting Min Temperatures - S_{xx}

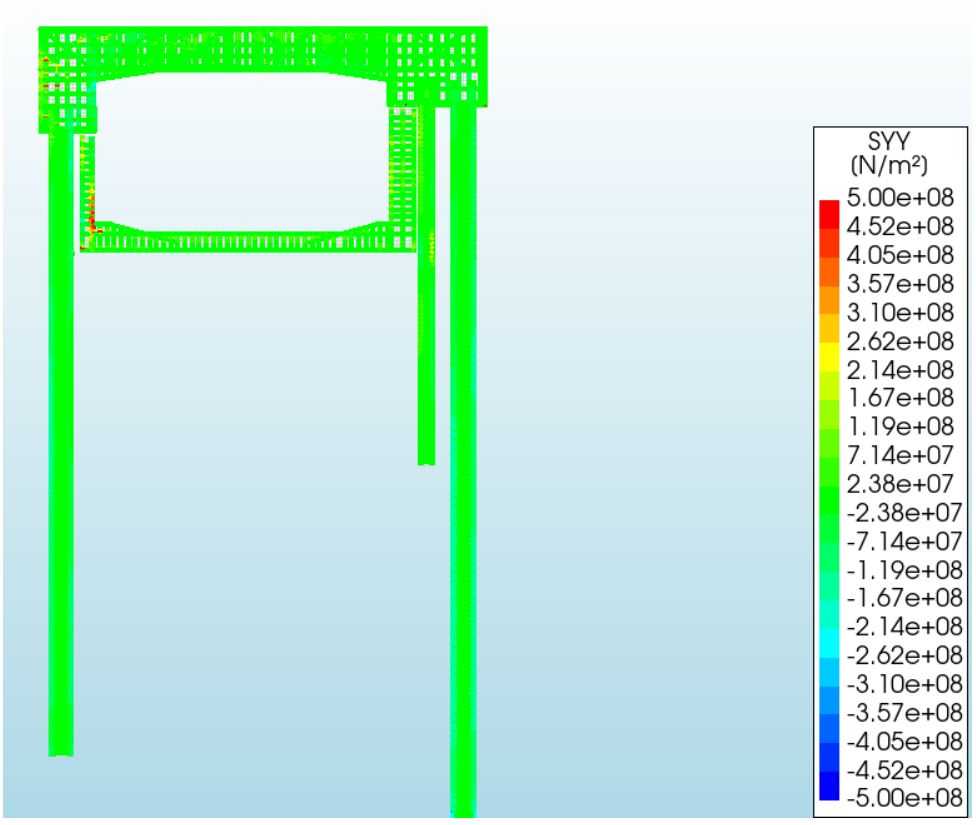


Figure 6-10 - Model 1: Winter Casting Min Temperatures - S_{yy}

Under the model 1 winter casting scenario at peak minimum operational temperatures, structural collapse is governed by a brittle shear failure at the top of the uphill vertical wall. Severe winter thermal contraction causes the massive cover slab to shorten horizontally, but this inward movement is heavily restrained by the stiff uphill pile foundations ($D = 2000$ mm and $D = 1200$ mm). This kinematic restraint concentrates massive shear thrust and bending tension at the foundation slab and downhill wall connection, driving the vertical wall reinforcement into full plastic yielding ($S_{yy} = 733$ MPa). Once the steel yields and concrete tensile softening occur (S_1), a critical diagonal shear crack band rapidly localizes across the top of the uphill wall ($\varepsilon_{kn} = 1{,}08 * 10^{-1}$), degrading the internal compressive strut (S_2) and triggering a sudden loss of static equilibrium prior to any compressive concrete crushing in the cover slab.

For model 1 with winter casting, switching between operational thermal extremes completely reverses the structural kinematics and governing failure mode. Under peak minimum temperatures, winter contraction, inward cover slab shortening is heavily restrained by the stiff uphill piles, concentrating severe tensile and shear demand at the top of the uphill wall. This triggers a brittle shear collapse governed by vertical rebar yielding ($S_{yy} = 733$ MPa) and diagonal crack localization ($\varepsilon_{kn} = 0{,}108$).

Conversely, under peak maximum temperatures, summer expansion, outward roof expansion channels heavy compressive thrust toward the downhill corner, shifting the failure mechanism to concrete crushing within the downhill cover slab ($S_2 = -79{,}1$ MPa).

6.2.2 Summer Casting: Peak Maximum and Peak Minimum Temperature

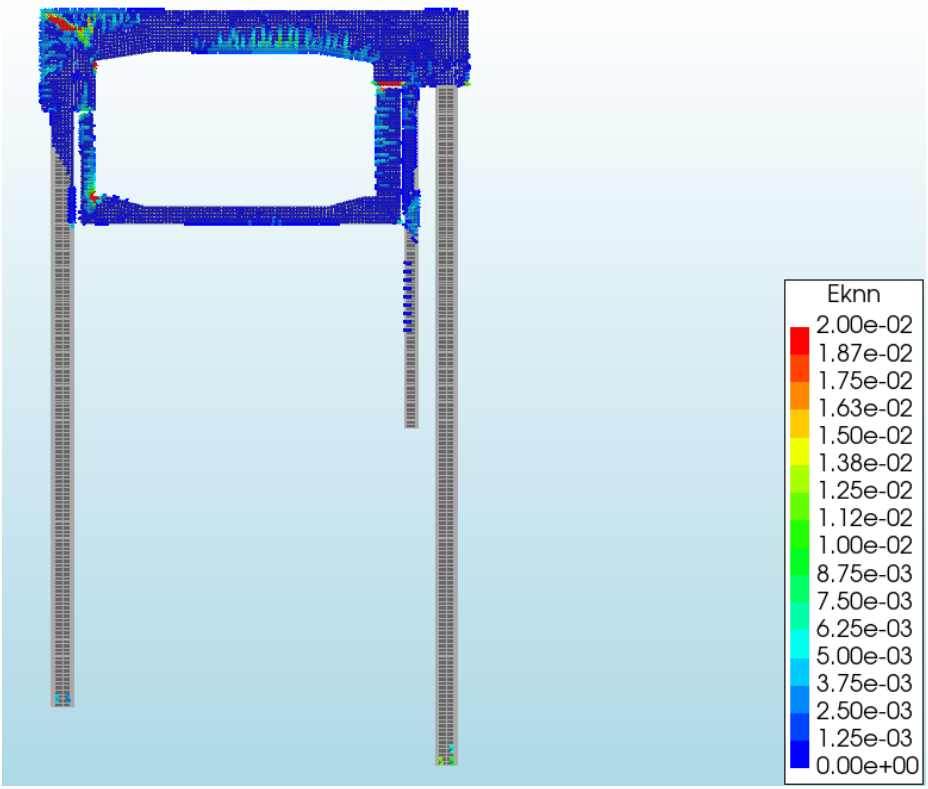


Figure 6-11 - Model 1: Summer Casting Max Temperatures - ε_{kn}

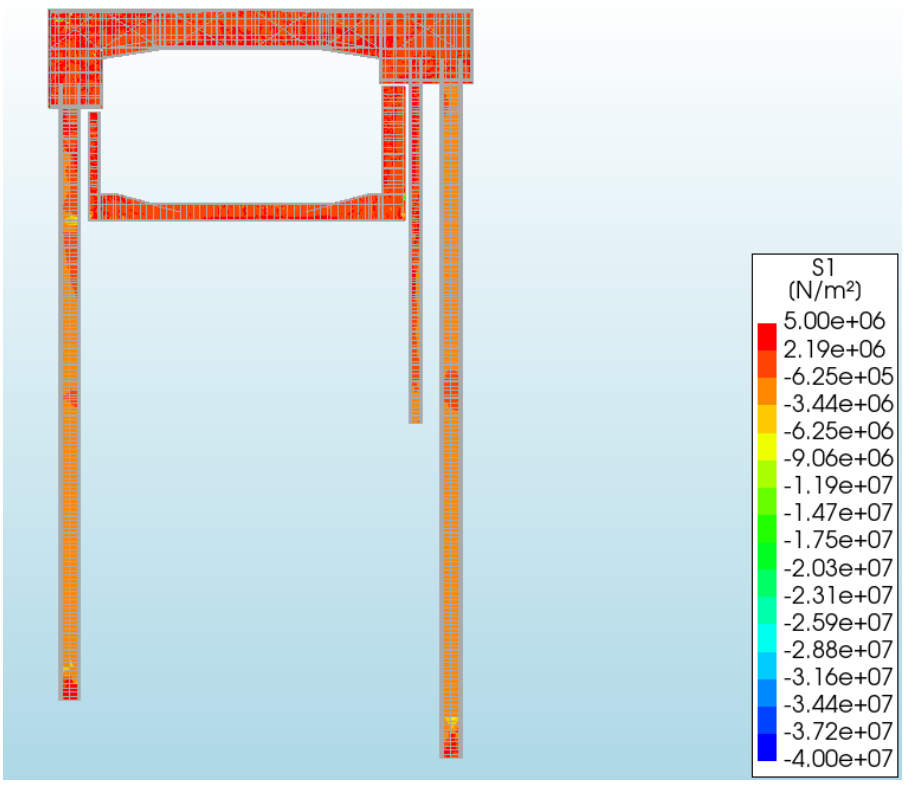


Figure 6-12 - Model 1: Summer Casting Max Temperatures - S_1

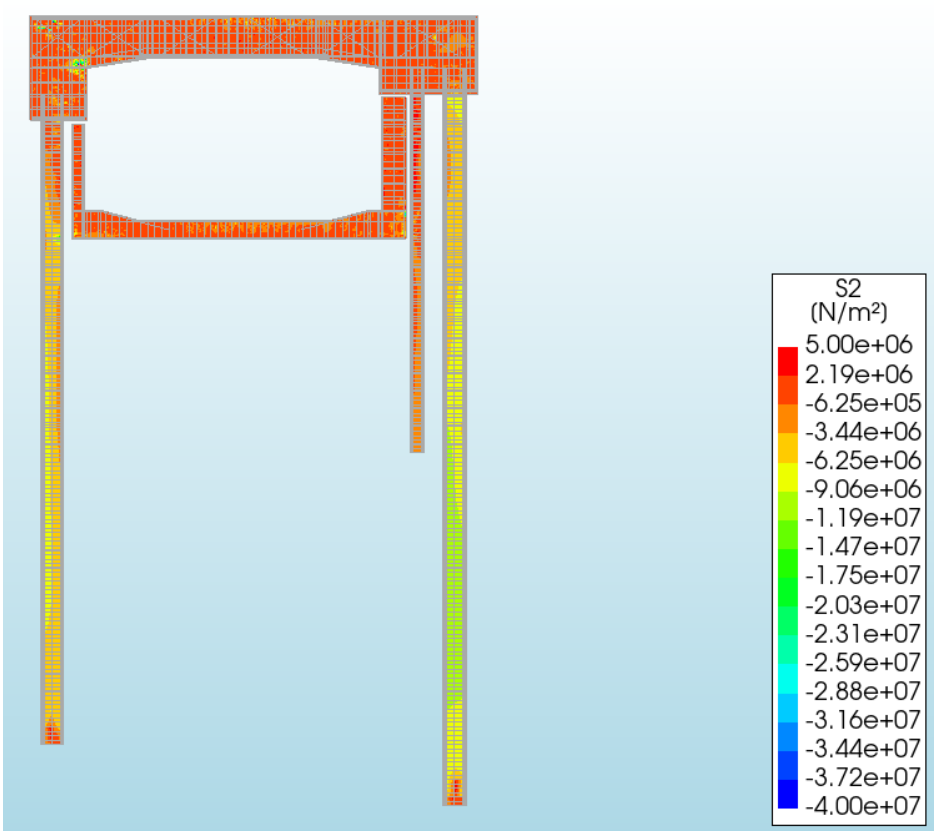


Figure 6-13 - Model 1: Summer Casting Max Temperatures - S_2

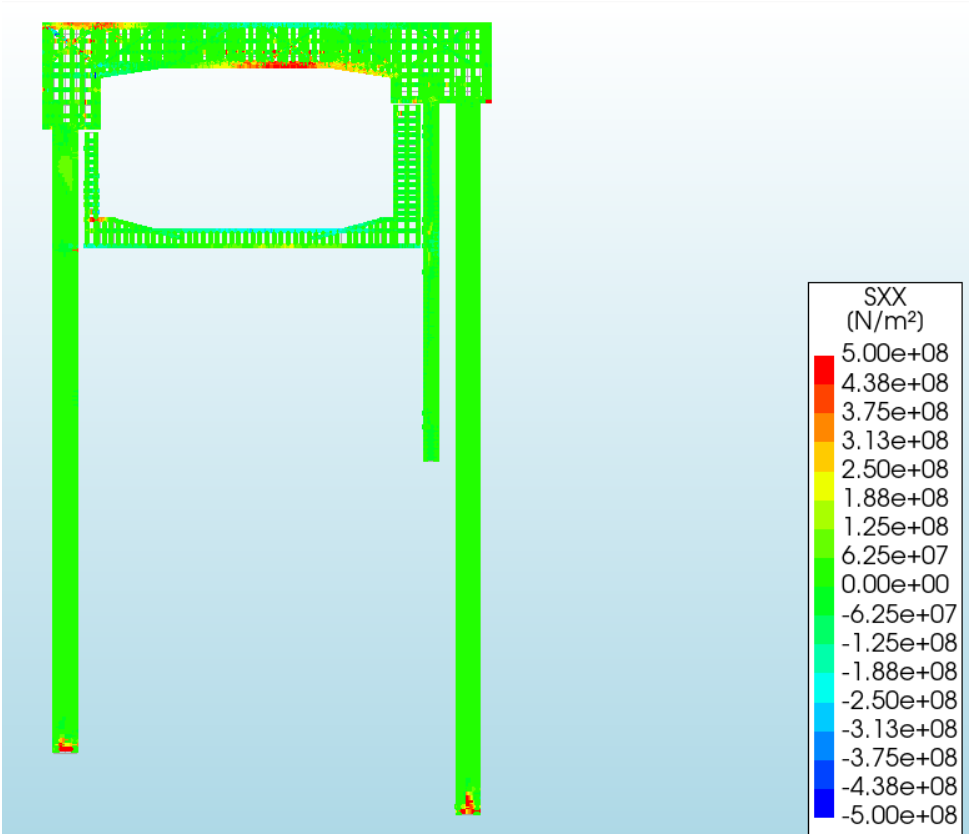


Figure 6-14 - Model 1: Summer Casting Max Temperatures – S_{XX}

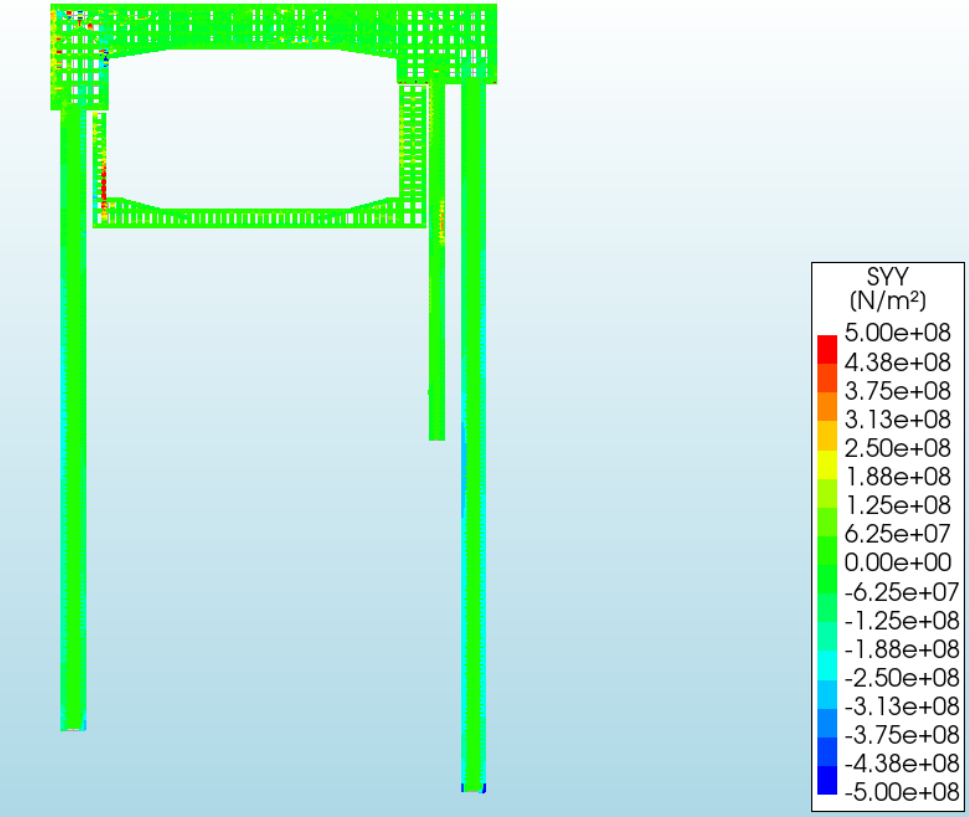


Figure 6-15 - Model 1: Summer Casting Max Temperatures - S_{yy}

Under the model 1 summer casting scenario at peak maximum operational temperatures, structural collapse is governed by concrete crushing on the downhill side section of the cover sla. Because the tunnel is cast in summer and subjected to peak operational heating, early-age hydration thermal locking combines with extreme seasonal expansion. As the massive cover slab expands outward against the lateral soil and pile restraints, heavy compressive arching thrust is driven directly into the downhill corner connection. This concentration forces the minor principal stress to $S_2 = -76{,}3$ MPa, exceeding the concrete compressive strength and initiating localized plastic crushing in the upper left corner of the roof slab.

This severe compressive concentration is accompanied by extensive plastic yielding in both the horizontal reinforcement ($S_{xx} = 684$ MPa) in the top part of the cover slab and vertical reinforcement ($S_{yy} = +04$ MPa) in the connection between the downhill wall and the foundation slab. Crack normal strains reach $\varepsilon_{kn} = 1.64 * 10^{-2}$ around the compressive zone, leading to concrete tension softening (S_1) and triggering structural collapse via compressive crushing and plastic hinge degradation at the downhill roof connection rather than wall shear failure.

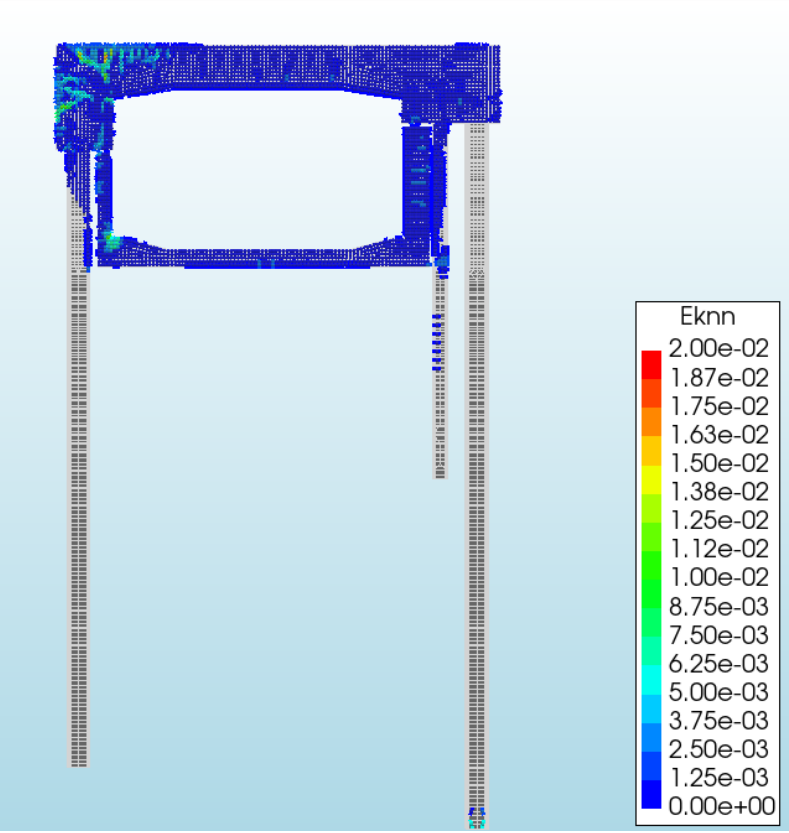


Figure 6-16 - Model 1: Summer Casting Min Temperatures - ε_{kn}

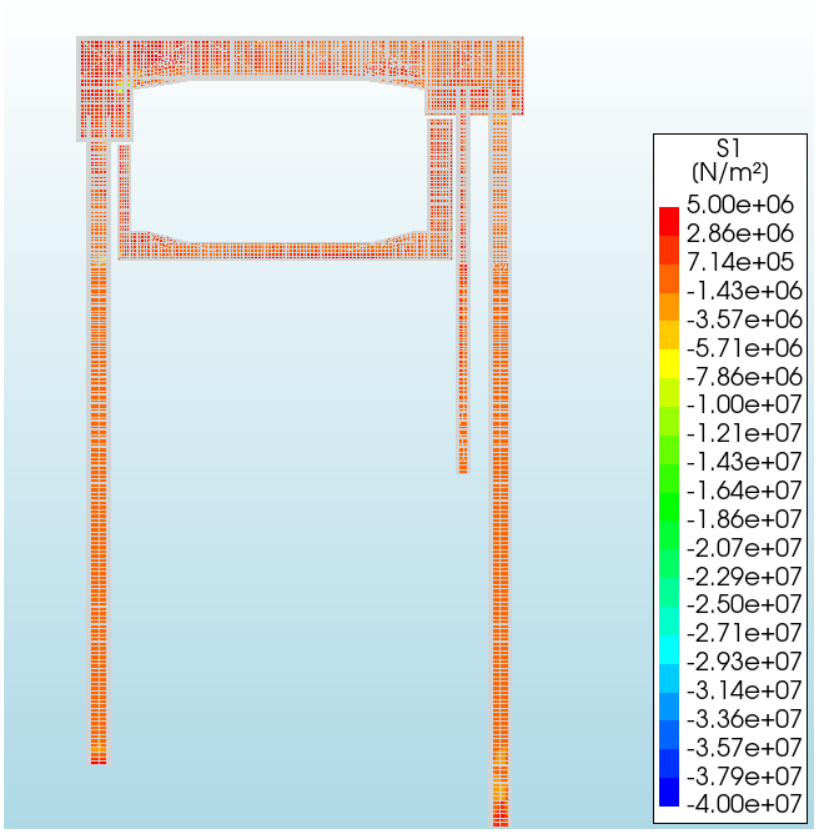


Figure 6-17 - Model 1: Summer Casting Min Temperatures - S_1

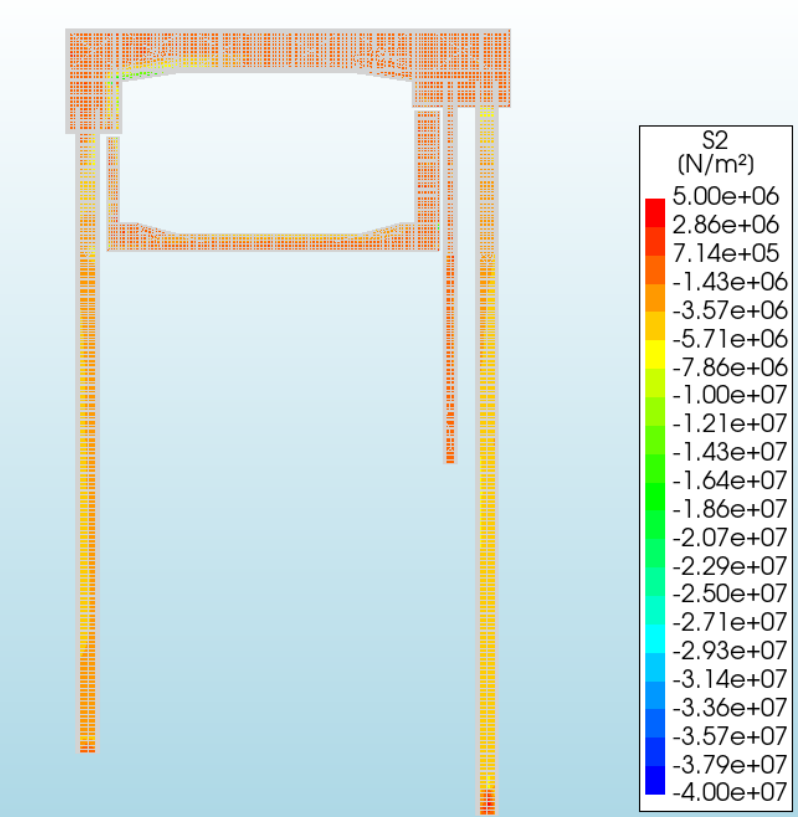


Figure 6-18- Model 1: Summer Casting Min Temperatures - S_2

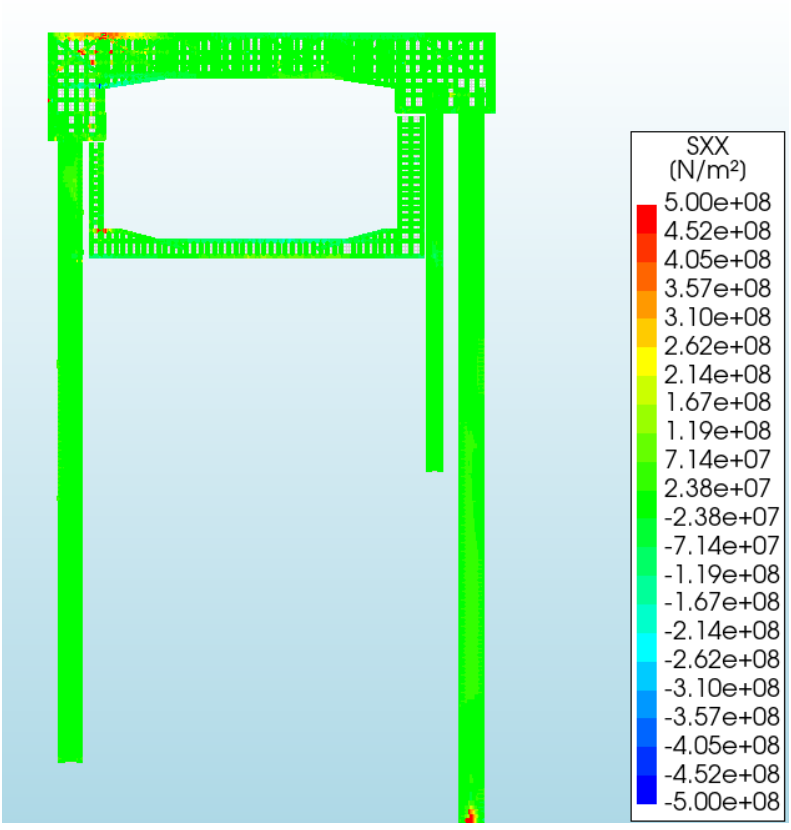


Figure 6-19- Model 1: Summer Casting Min Temperatures - S_{xx}

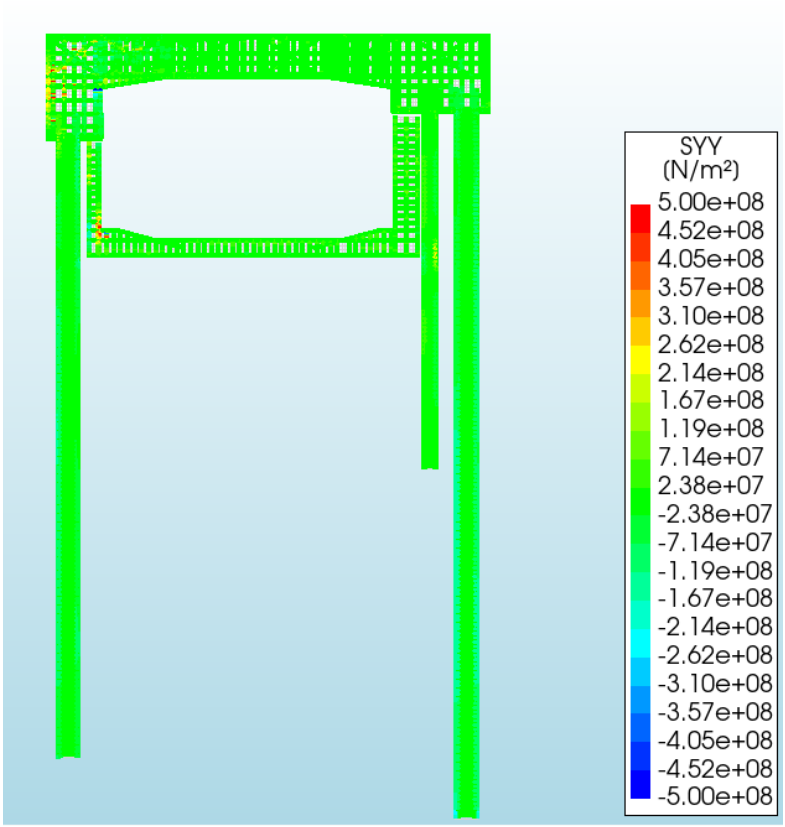


Figure 6-20 - Model 1: Summer Casting Min Temperatures - S_{yy}

When cast in summer and subjected to peak operational freezing, the model 1 structure fails via ductile flexural yielding on the downhill side of the cover slab. The failure begins with thermal contraction. As the massive roof slab cools during winter, it pulls inward, driving heavy sagging moments across the span and sharp hogging moments at the top-left rigid knee joint. These bending forces extensive horizontal yielding through the slab's tensile reinforcement ($S_{xx} = +717$ MPa), alongside vertical rebar yielding at the corner wall interface ($S_{yy} = \pm 901$ MPa). Kinematic rotation then takes over. It opens widespread flexural cracks along the bottom fibres of the roof and concentrates a dense tensile crack band at the valley-side connection, where peak strain reaches $\varepsilon_{kn} = 7.88 \times 10^{-2}$. Because collapse develops through steel yield lines rather than abrupt concrete web shearing, the structure sustains substantial plastic deformation before finally losing global equilibrium.

For model 1 with summer casting, comparing operational thermal extremes demonstrates a fundamental shift in the failure mechanism at the valley-side corner connection alongside a clear divergence in safety margins. Under peak maximum temperatures, thermal expansion drives heavy compressive arching thrust against the downhill boundary, resulting in brittle concrete crushing within the valley-side cover slab ($S_2 = -76.3$ MPa, $\varepsilon_{kn} = 1{,}64 \times 10^{-2}$) and representing the governing operational case with higher utilization ($\mathrm{LM}_d = 0.539$ LMU /

0.654 HMU). In contrast, peak minimum temperatures reverse the kinematics into thermal contraction, shifting the collapse into a ductile flexural yield mechanism characterized by wide tensile crack opening ($\varepsilon_{kn} = 7.88 \times 10^{-2}$) and extensive steel yielding ($S_{xx} = +717$ MPa). Consequently, summer-cast structures retain their largest global safety reserve during winter cooling, operating at a significantly lower utilization factor.

6.3 Collapse Dynamics of Model 2

6.3.1 Winter Casting: Peak Maximum and Peak Minimum Temperatures

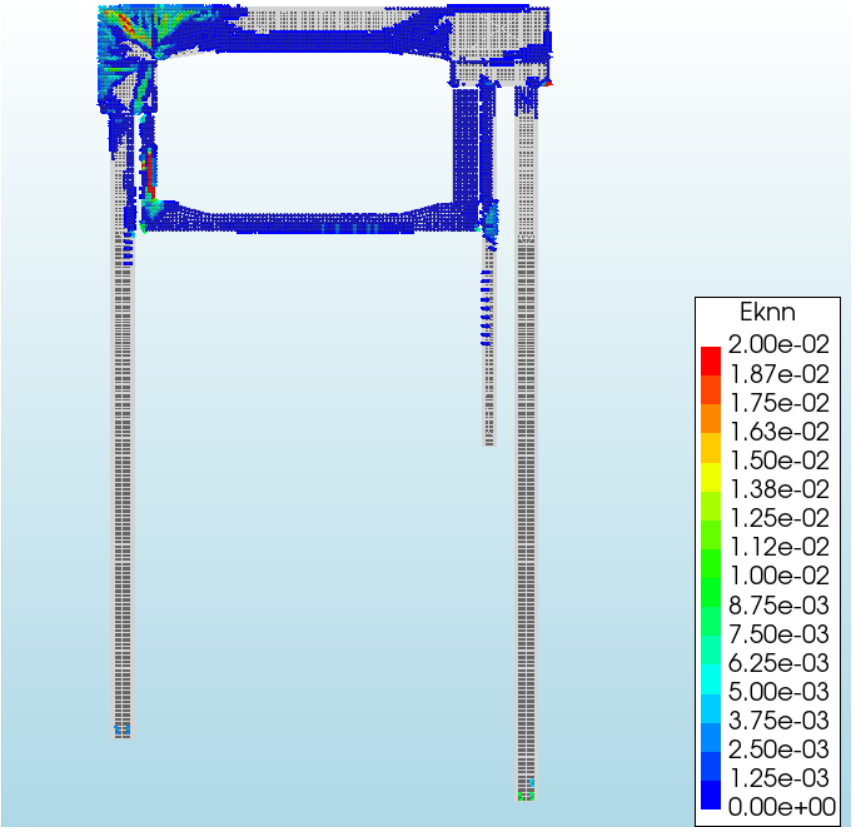


Figure 6-21 - Model 2: Winter Casting Max Temperatures - ε_{kn}

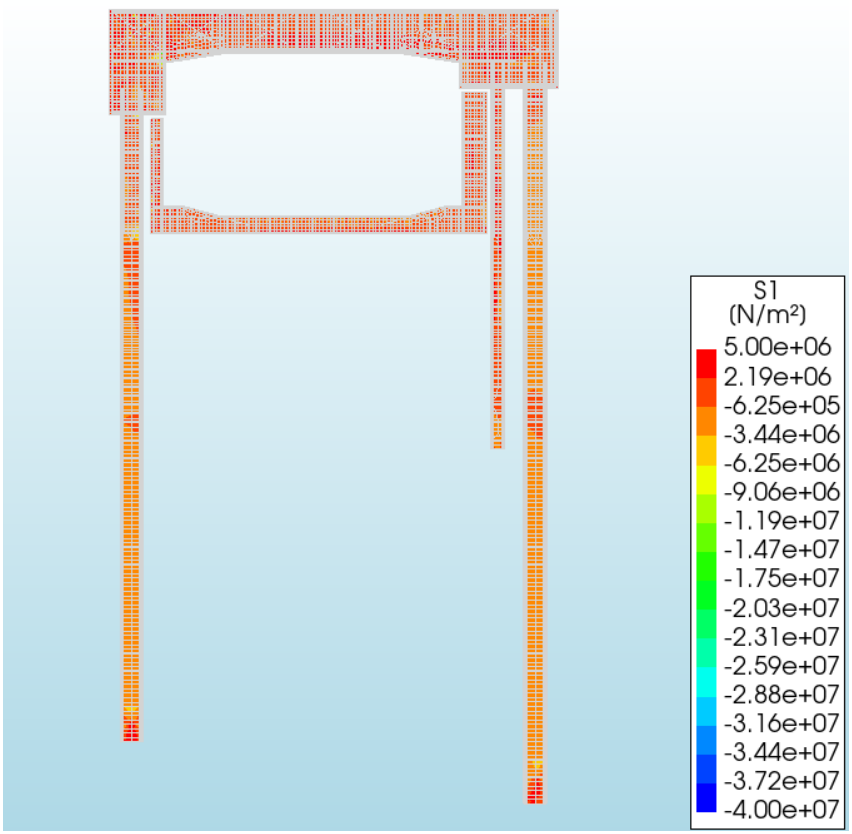


Figure 6-22- Model 2: Winter Casting Max Temperatures -S_1

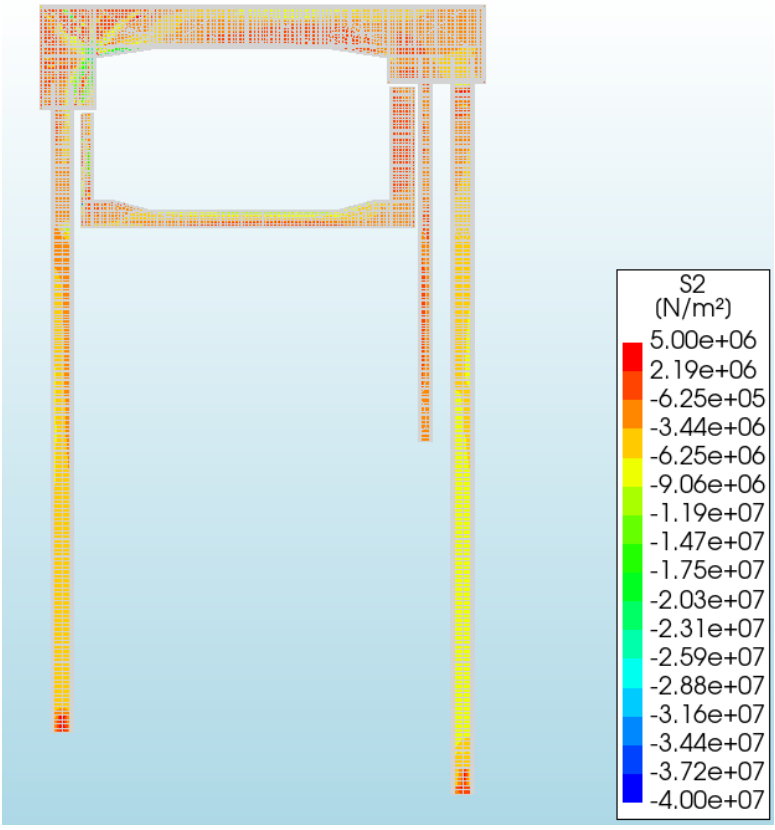


Figure 6-23- Model 2: Winter Casting Max Temperatures - S_2

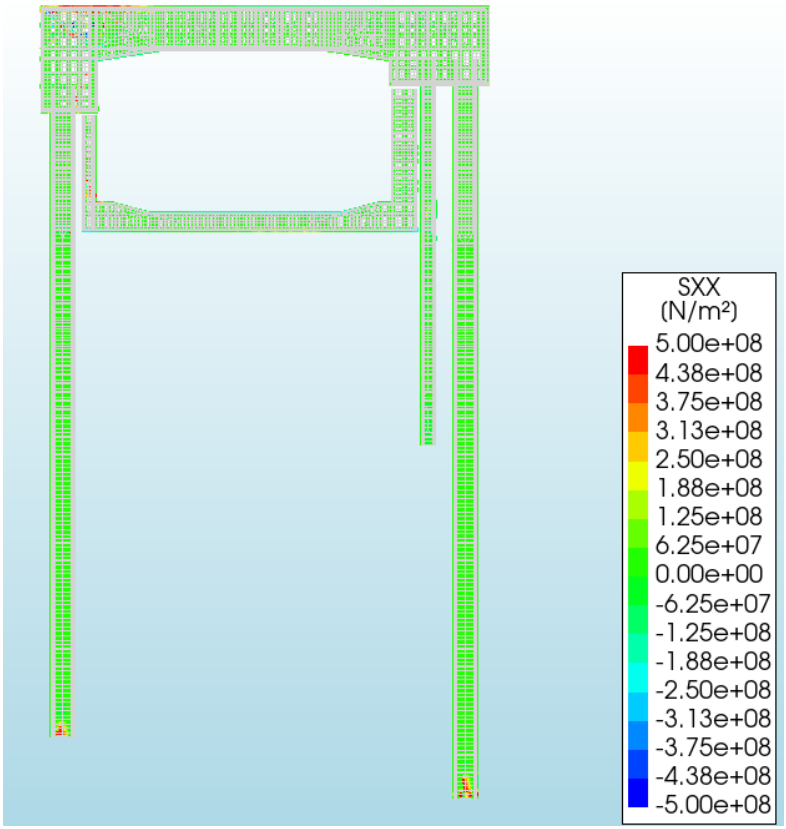


Figure 6-24 - Model 2: Winter Casting Max Temperatures -S_{xx}

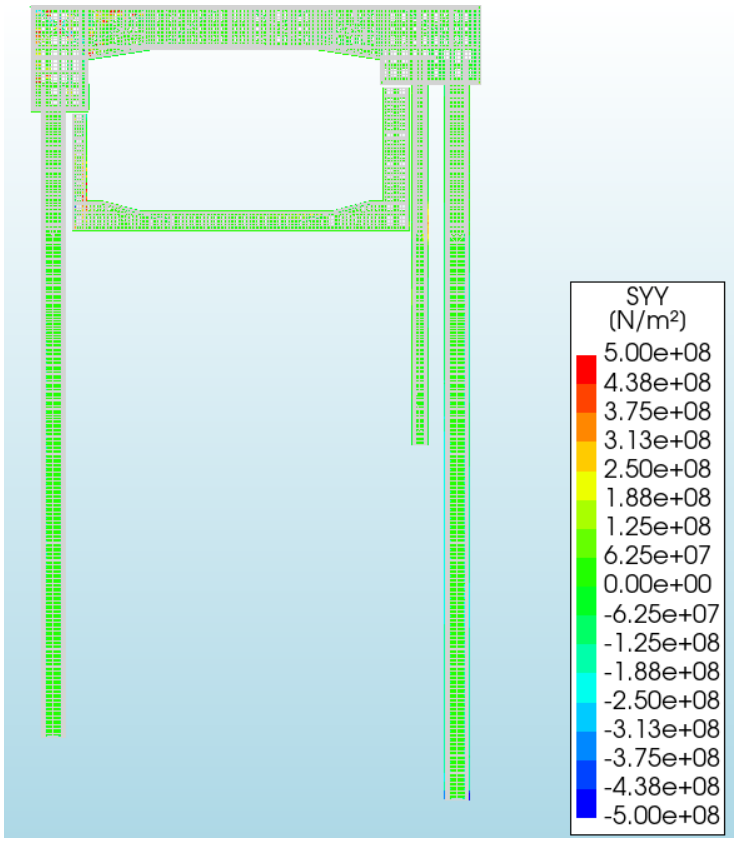


Figure 6-25 - Model 2: Winter Casting Max Temperatures - S_{yy}

Cast in winter and exposed to peak summer heat, model 2 collapses through shear failure along its downhill wall. Thermal expansion drives the entire process. As the massive cover slab heats up and expands, it exerts severe outward thrust against the downhill retaining system. In model 2's staged formulation, this outward shove mobilizes a steep diagonal compressive strut across the downhill corner joint ($S_2 = -77{,}1$ MPa dumping intense lateral shear straight into the valley-side vertical lining wall. Both horizontal ($S_{xx} = 866$ MPa) and vertical ($S_{yy} = 758$ MPa) reinforcement yield under the load. As the concrete softens in tension (S_1), heavy shear cracks localize across the downhill frame corner and propagate down the vertical wall stem toward the base. Peak crack strain reaches $\varepsilon_{kn} = 7{,}84 * 10^{-2}$, steadily degrading the shear capacity until the structure loses static equilibrium entirely.

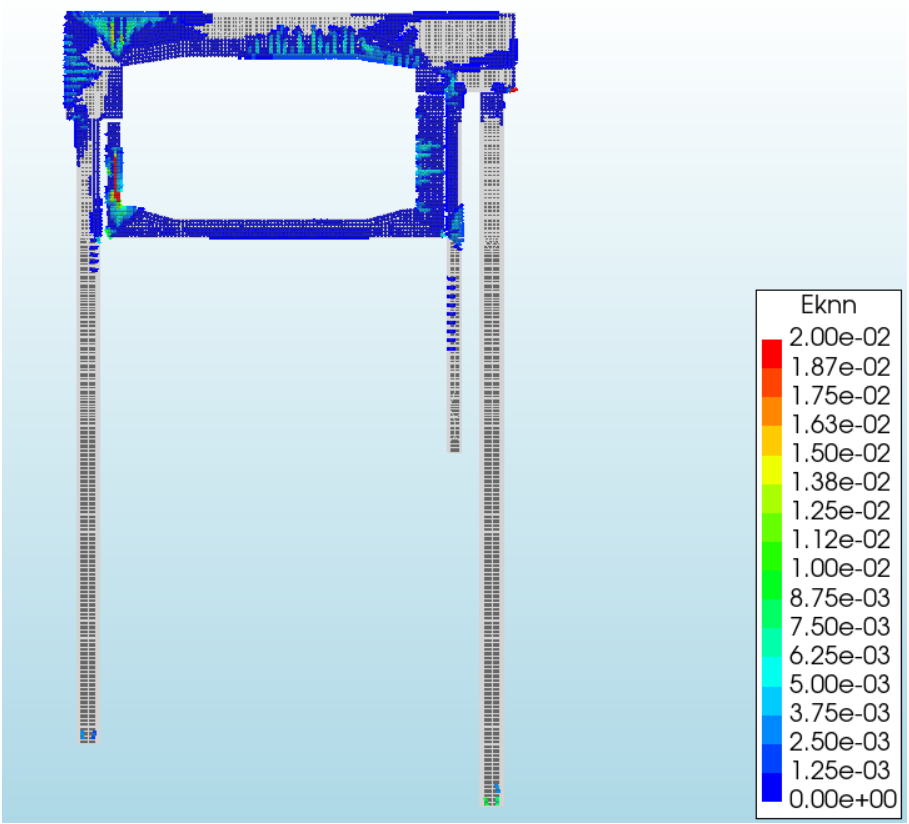


Figure 6-26 - Model 2: Winter Casting Min Temperatures - ε_{kn}

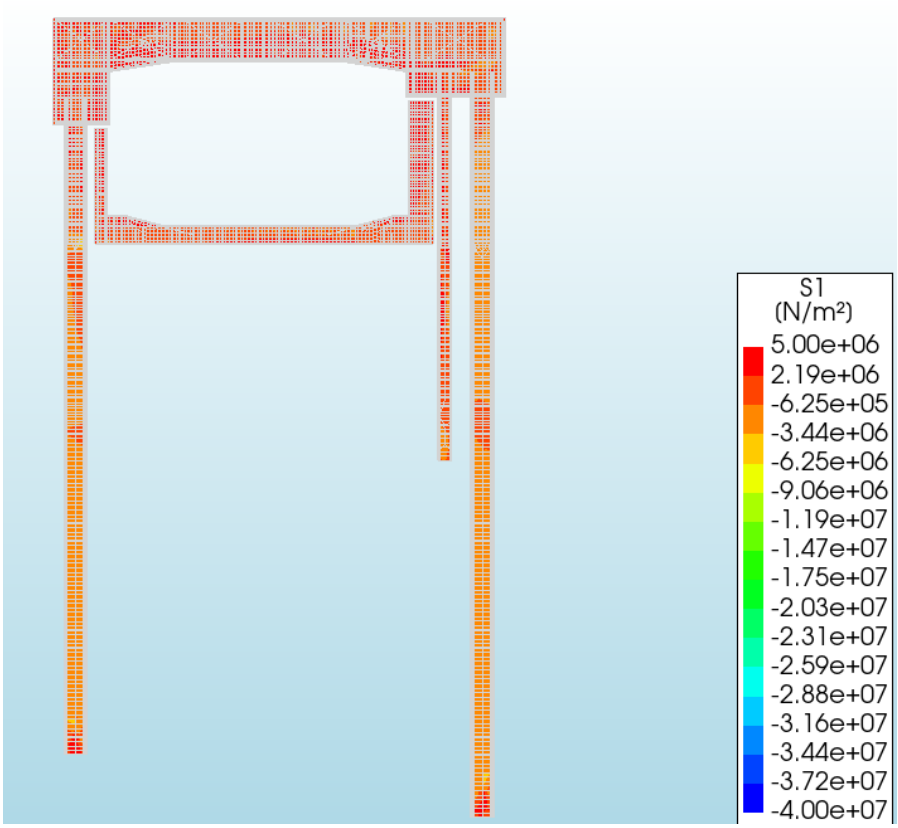


Figure 6-27- Model 2: Winter Casting Min Temperatures - S_1

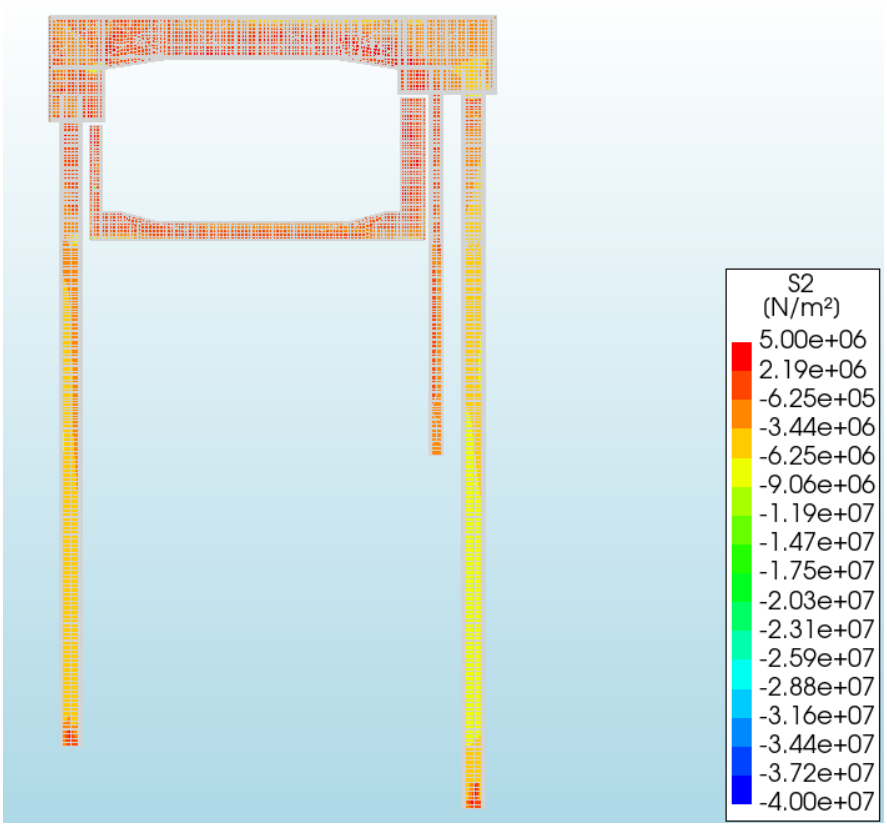


Figure 6-28- Model 2: Winter Casting Min Temperatures - S_2

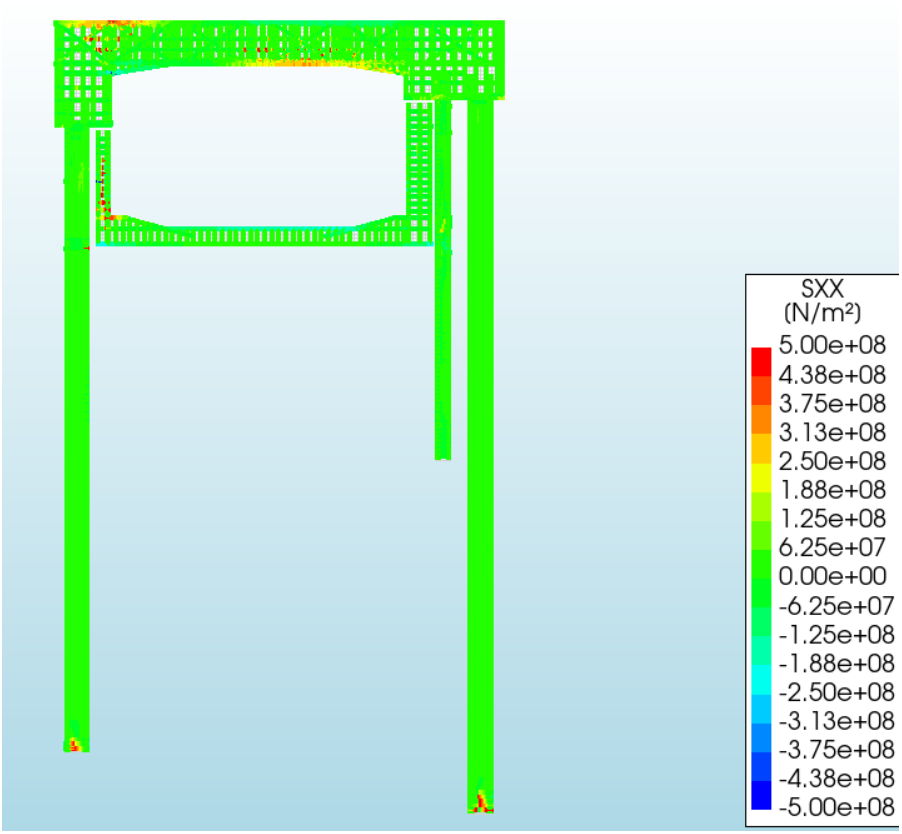


Figure 6-29- Model 2: Winter Casting Min Temperatures - S_{xx}

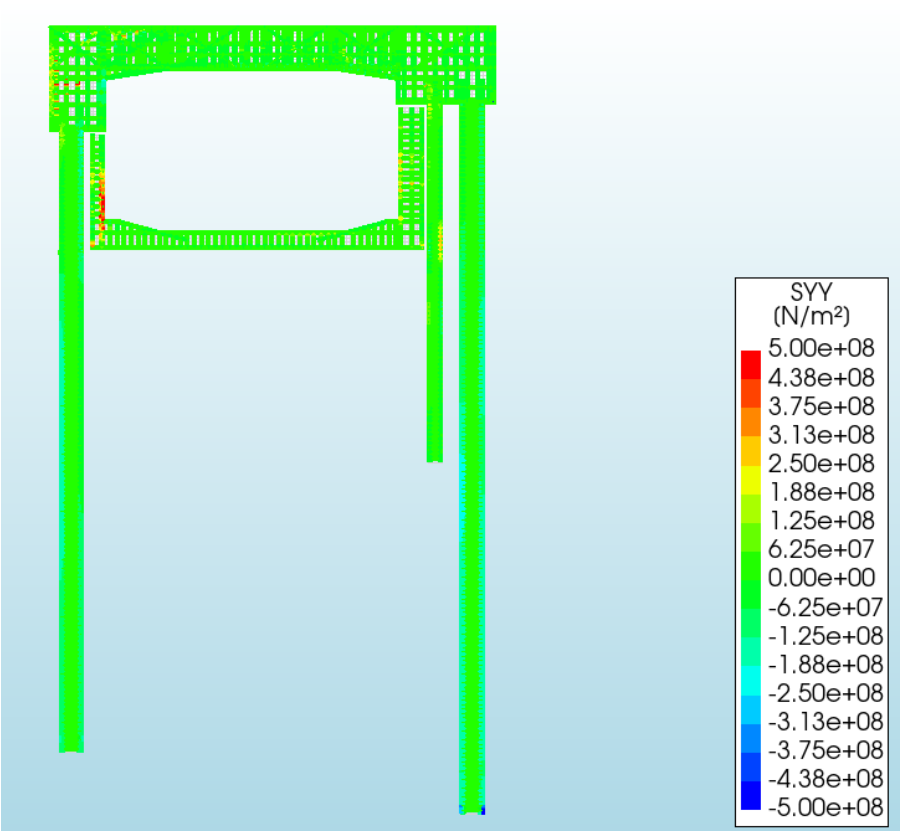


Figure 6-30- Model 2: Winter Casting Min Temperatures - S_{yy}

Under the model 2 winter casting scenario subjected to operational peak minimum temperatures, structural collapse is governed by a shear failure at the base of the downhill side wall.

During winter cooling, thermal contraction causes the upper box structure to pull inward against the stiff foundation constraints, while asymmetric lateral earth thrust continues to push the frame towards the downhill side. In model 2's refined staged formulation, this combined action concentrates severe transverse shear and bending at the base of the downhill vertical wall near its connection with the invert slab and pile head. This concentrated shear force drives the vertical wall reinforcement into full plastic yielding ($S_{yy} = 772$ MPa) and mobilizes significant horizontal rebar yielding ($S_{xx} = 723$ MPa). As concrete tensile softening takes place (S_1), a critical diagonal shear crack rapidly localizes across the lower stem of the valley wall, reaching an extreme strain of $\varepsilon_{kn} = 1{,}13 * 10^{-1}$. This widespread crack opening degrades the internal compressive strut ($S_2 = 69{,}0$ MPa), triggering a brittle shear loss of static equilibrium at the base of the valley-side wall.

For a winter-cast Model 2, the collapse mechanism stays the same across both temperature extremes: shear failure at the base of the valley-side wall. What changes is the damage intensity.

Under peak heat, outward roof thrust bears against the downhill retaining wall, concentrating shear across the corner and wall stem at a crack strain of $\varepsilon_{kn} = 7{,}84 * 10^{-2}$. Peak cold proves more punishing. As the cover slab contracts inward, its pull combines with lateral earth pressures to spike the base shear restraint at the downhill foundation node. This opens a substantially wider crack ($\varepsilon_{kn} = 1{,}13 * 10^{-1}$) and drives the utilization factor slightly higher.

Consequently, while both thermal extremes trigger shear collapse along the same structural member, peak minimum temperatures represent the governing critical condition for the winter-cast model 2 structure due to the heightened shear crack dilation and lower remaining capacity reserves.

6.3.2 Summer Casting: Peak Maximum Temperatures and Peak Minimum Temperatures

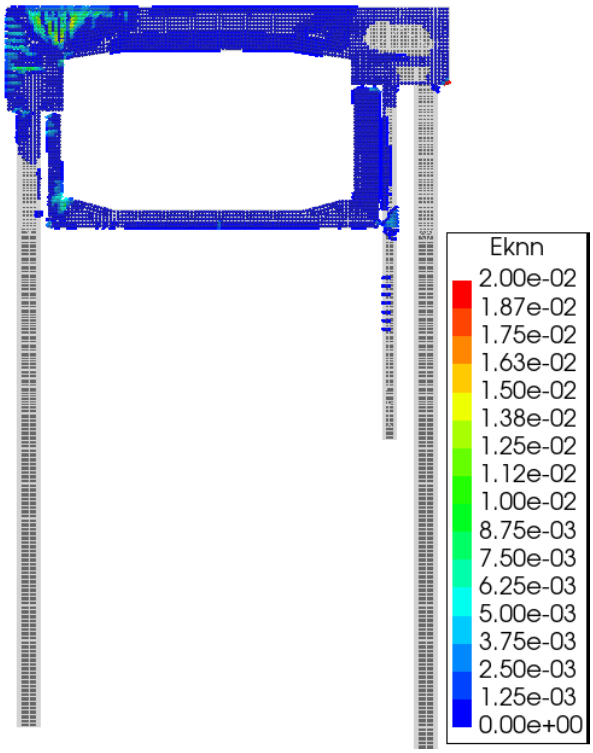


Figure 6-31- Model 2: Summer Casting Max Temperatures - ε_{kn}

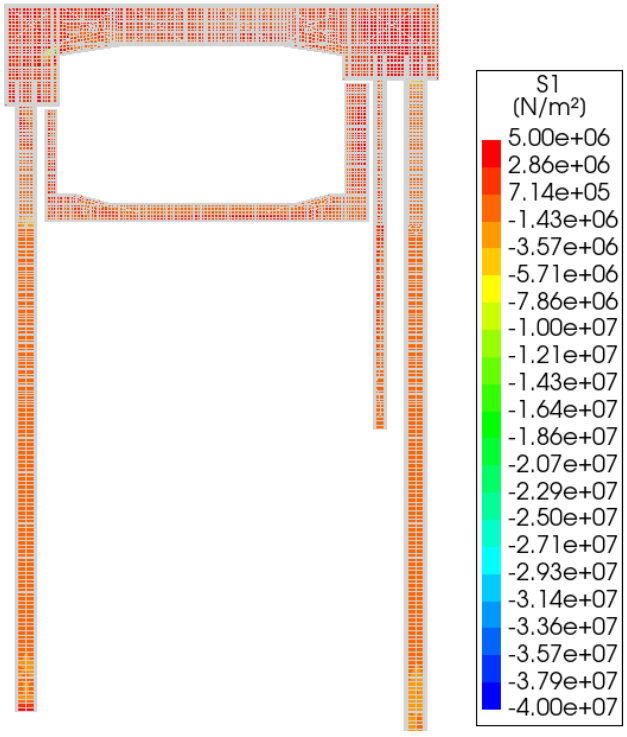


Figure 6-32- Model 2: Summer Casting Max Temperatures - S_1

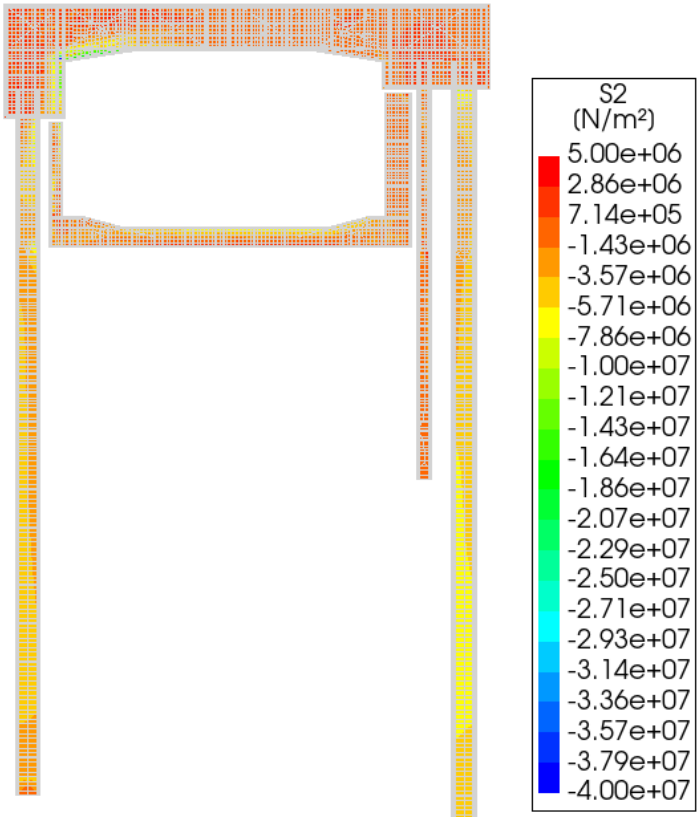


Figure 6-33- Model 2: Summer Casting Max Temperatures - S_2

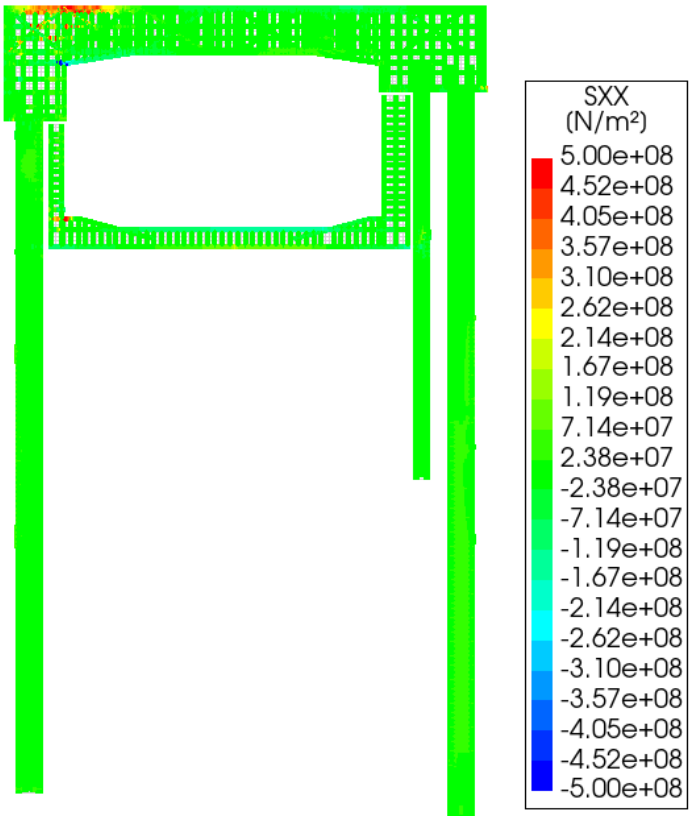


Figure 6-34- Model 2: Summer Casting Max Temperatures - S_{xx}

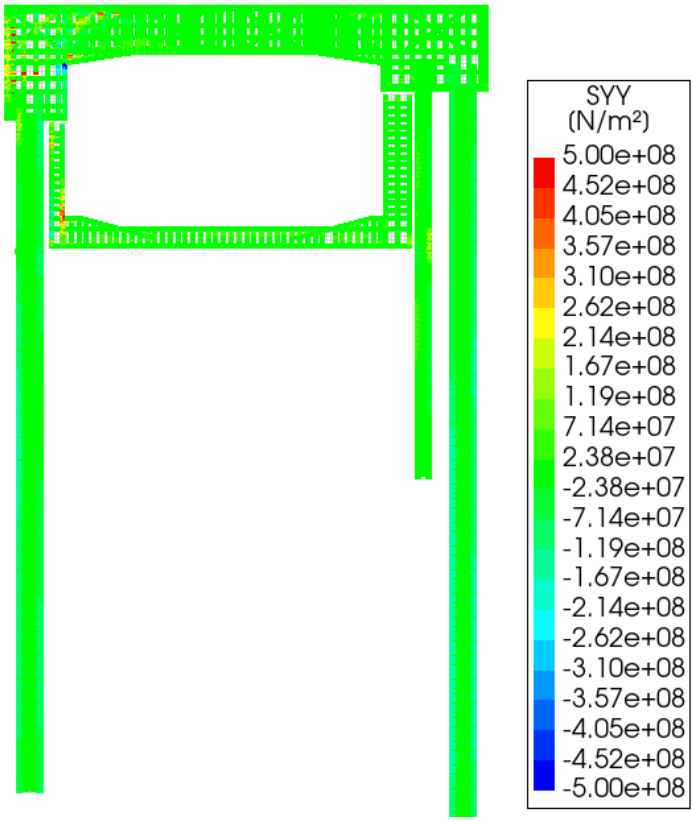


Figure 6-35- Model 2: Summer Casting Max Temperatures – S_{yy}

Under the model 2 summer casting scenario subjected to operational peak maximum temperatures, structural collapse is governed by concrete crushing on the downhill side section of the cover slab, top-left knee joint. During peak summer heating, the combination of early-age thermal locking from summer casting and extreme seasonal temperature rise drives intense outward thermal expansion of the cover slab against the downhill soil and pile boundary. In model 2's staged continuum, this outward thrust generates a massive diagonal compressive arching stress concentrated directly at the top-left corner of the frame. The minor principal compressive stress reaches $S_2 = -75{,}2$ MPa, surpassing the concrete compressive capacity and initiating localized plastic crushing within the valley-side cover slab. This intense compressive concentration induces extensive plastic yielding in both the horizontal $S_{xx} = 711$ MPa and vertical $S_{yy} = 736$ MPa reinforcement across the corner node. Accompanied by localized crack normal strains reaching $\varepsilon_{kn} = 2{,}33 * 10^{-2}$ and concrete tension softening (S_1), the structural failure is dictated by compressive degradation and plastic hinge formation at the roof-wall connection rather than web shear failure.

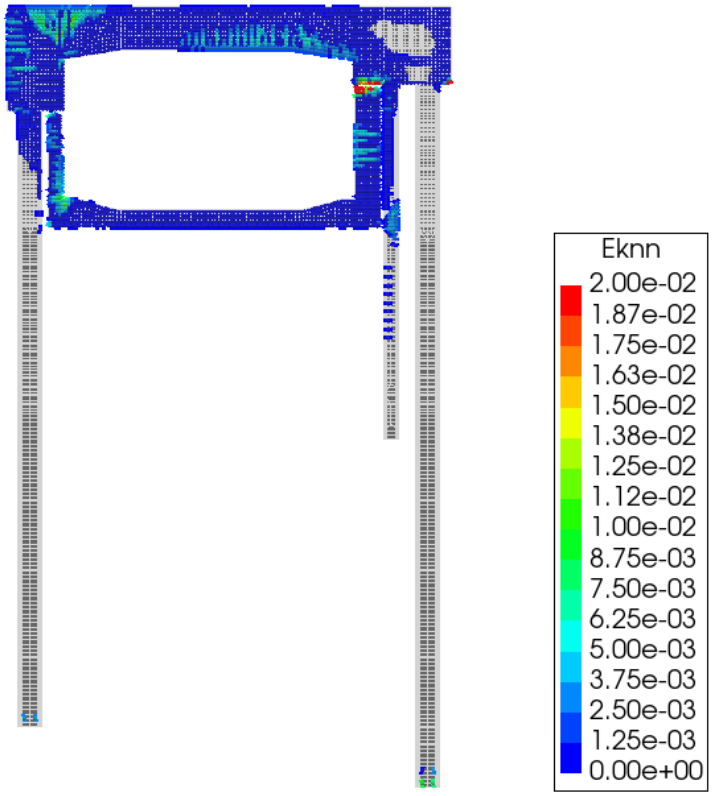


Figure 6-36 - Model 2: Summer Casting Min Temperatures - ε_{kn}

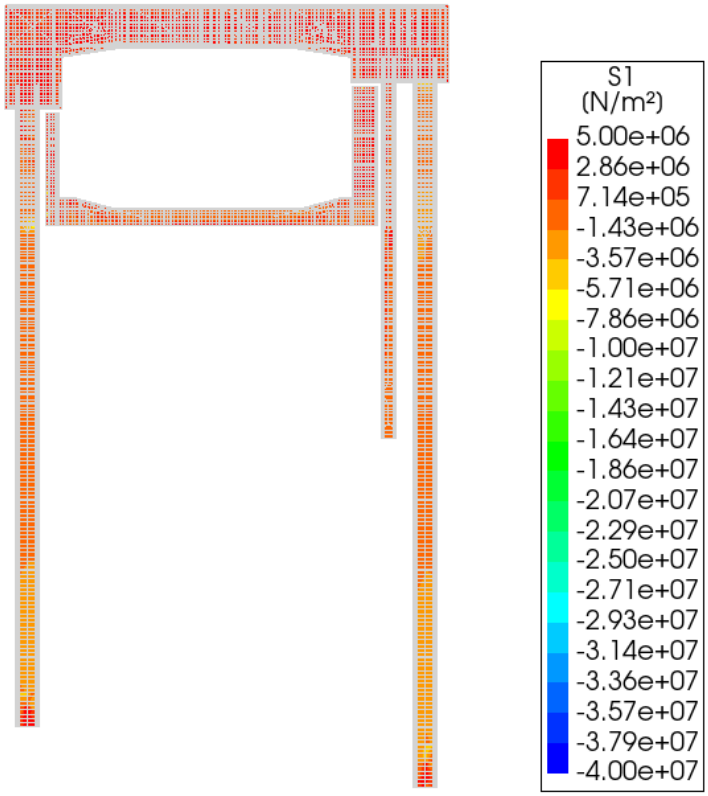


Figure 6-37- Model 2: Summer Casting Min Temperatures - S_1

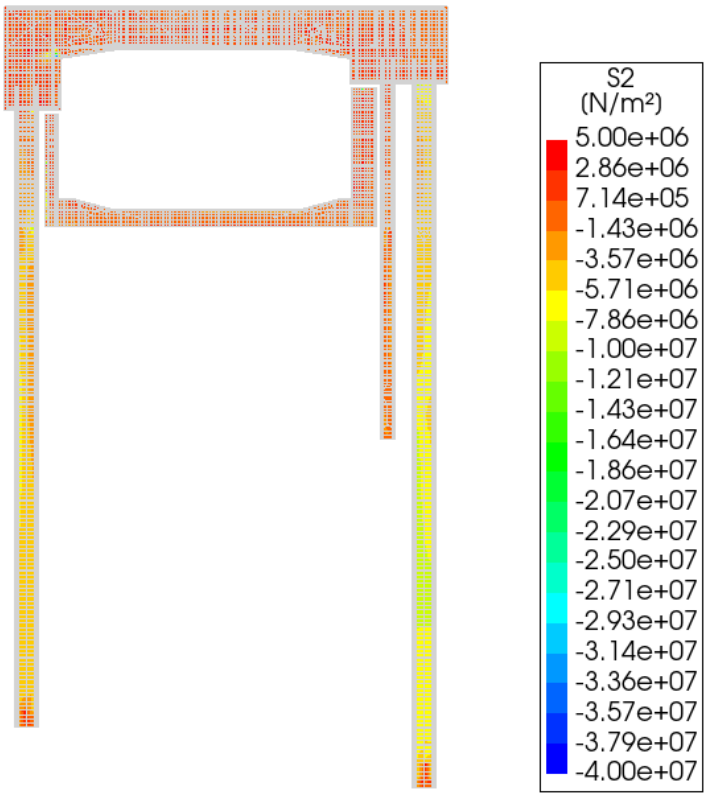


Figure 6-38- Model 2: Summer Casting Min Temperatures -S_2

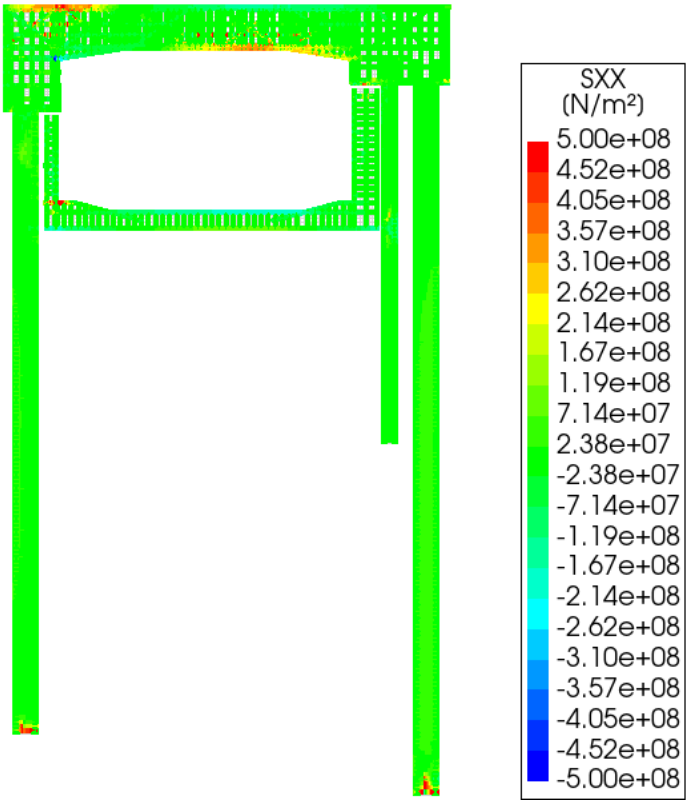


Figure 6-39- Model 2: Summer Casting Min Temperatures - S_{xx}

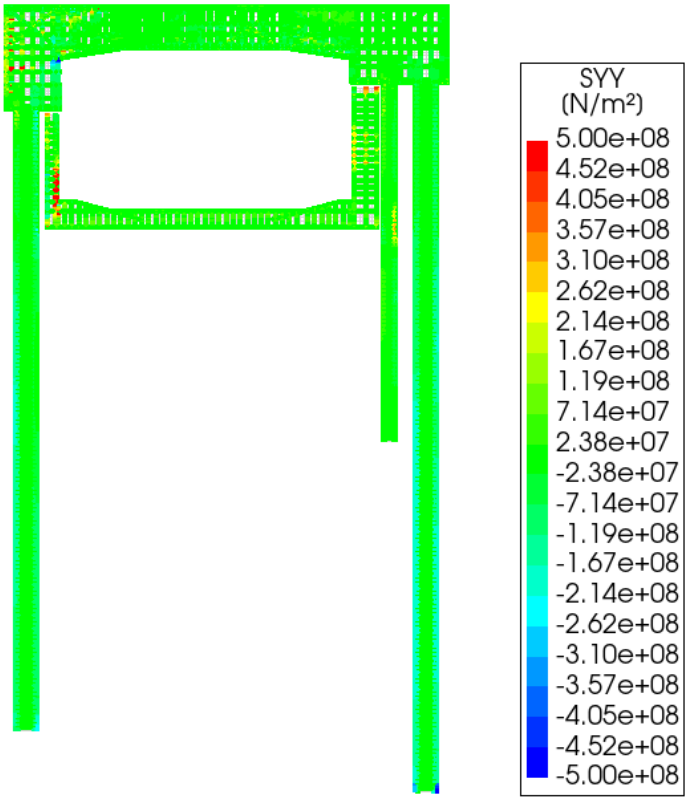


Figure 6-40- Model 2: Summer Casting Min Temperatures - S_{yy}

Under the model 2 summer casting scenario subjected to operational peak minimum temperatures, structural collapse is governed by a shear failure at the top of the uphill side wall.

During winter operational cooling following a summer construction start, the massive cover slab undergoes global thermal contraction, pulling inward against the highly rigid uphill deep foundation piles ($D = 2000$ mm and $D = 1200$ mm). This kinematic restraint concentrates intense shear thrust and hogging bending directly at the upper connection of the uphill vertical wall. The resulting localized demand drives the vertical wall reinforcement into extensive plastic yielding ($S_{yy} = 731$ MPa) alongside high horizontal tensile steel yielding in the cover slab ($S_{xx} = 719$ MPa). As concrete tension softening develops (S_1), a critical diagonal shear crack band rapidly localizes across the top section of the uphill wall, reaching a peak strain of $\varepsilon_{kn} = 3{,}28 * 10^{-2}$. This localized fracture degrades the internal compressive strut ($S_2 = -84{,}1$ MPa), triggering a sudden loss of static equilibrium through brittle web shear failure at the uphill wall head.

Cast in summer, model 2 undergoes a complete flip in its governing failure mechanism between temperature extremes, with winter cooling driving structural demand sharply upward. Under

peak heat, outward thermal expansion against the downhill boundary sets up compressive arching at the roof corner. This trigger localized concrete crushing in the downhill-side cover slab ($S_2 = -75{,}2$ Mpa, $\varepsilon_{kn} = 2{,}33 * 10^{-2}$) at a moderate utilization factor of $LM_d = 0{,}509\ LMU/0{,}618\ HMU$. Peak cold reverses the mechanism entirely. The outward thrust turns into an intense inward pull against the stiff uphill foundation piles, shifting the collapse mode to brittle shear failure at the top of the uphill wall ($\varepsilon_{kn} = 3{,}28 * 10^{-2}, S_{yy} = 731$MPa. This winter contraction scenario is the most critical operational case across the entire model 2 parametric study. Because the structure heavily restrains thermal shrinkage following summer placement, it yields the highest global utilization factor of $LM_d = 0{,}612\ LMU/0{,}618\ HMU$.

6.4 Comparative Synthesis: Model 1 vs Model 2 Collapse Behaviour

A comparative evaluation of the collapse kinematics between model 1 (fully coupled multi-field formulation) and model 2 (staged non-linear formulation) reveals key mechanical commonalities alongside critical differences driven by construction sequence effects. Across both models, operational thermal expansion under summer casting produces identical failure mechanics: outward thrust of the cover slab concentrates massive compressive arching into the top-left downhill knee joint, triggering localized concrete compressive crushing ($S_2 \approx -75$ to -79 MPa) accompanied by extensive yield-line formation in both horizontal (S_{xx}) and vertical (S_{yy}) reinforcement. Furthermore, both models demonstrate the rigid anchoring role of the uphill deep foundation piles ($D = 2000$ mm and $D = 1200$ mm), which prevent free thermal contraction and focus high shear and bending demands at the uphill frame corners. In all evaluated cases, both numerical continuum formulations activate significant plastic stress redistribution prior to collapse, systematically reducing global load multipliers ($LM_d = 1{,}347 - 2{,}773$) well above the conservative linear elastic benchmark of $SF_{\max} = 1{,}128$.

Despite these fundamental similarities, the two models diverge significantly in how they redistribute thermal contraction stresses. Under winter casting, model 1 exhibits a sharp bifurcation between thermal extremes, transitioning from a brittle shear failure at the top of the uphill wall under winter cooling ($\varepsilon_{kn} = 0{,}108$) to cover slab crushing under summer heating ($\varepsilon_{kn} = 0{,}020$). Conversely, model 2 maintains a consistent failure mode governed by localized shear along the base of the valley-side wall across both thermal limits ($\varepsilon_{kn} = 0.078 - 0.113$).

Furthermore, the governing operational extreme for summer casting is inverted between the two formulations: while model 1 is governed by peak summer heating ($LM_d = 1{,}529\ HMU$) and retains large ductile reserves during winter cooling ($LM_d = 2{,}285\ HMU$), model 2 is governed by peak winter cooling, which drives the load multiplier to $LM_d = 1{,}347$ through brittle shear at the top of the uphill wall.

Ultimately, model 2 yields higher and more localized peak utilization factors than model 1. By explicitly simulating the chronological construction stages, groundwater drawdown, and sequential backfilling, model 2 preserves localized residual stress concentrations at the frame and foundation nodes that are partially smoothed out in model 1's coupled framework. This demonstrates that capturing both non-linear material damage and the full geotechnical staging history is vital for accurately identifying the controlling shear collapse mechanisms in massive underground cut-and-cover structures.

Chapter 7 Final Conclusions

This thesis investigated the structural response, non-linear behaviour, and simulated collapse mechanisms of massive cut-and-cover underground infrastructure, using the top-down reinforced concrete Galleria Piscinale tunnel as a case study. The methodological framework transitioned from conventional deterministic linear elastic cross-sectional checks (model 5) to advanced non-linear finite element continuum formulations (models 1 and 2) evaluated through the Estimation of Coefficient of Variation (ECOV) global safety format. Across these numerical configurations, a parametric matrix was analysed to evaluate the interacting effects of construction seasonality, operational thermal extremes, viscoelastic creep, and epistemic model uncertainty.

Under the adopted linear elastic modelling assumptions, the conventional cross-sectional approach indicated high structural demand driven by self-equilibrating thermal and shrinkage coactions. Because a linear continuum formulation enforces uncracked elastic stiffness across the entire service life, it cannot simulate the natural stress-relaxing mechanisms of concrete, such as tensile micro-cracking, fracture softening, or long-term viscoelastic creep. Consequently, imposed kinematic displacements: stemming from concrete drying and autogenous shrinkage, early-age thermal cooling, and seasonal temperature cycling are converted directly into extreme, artificial internal restraint forces. At rigid monolithic nodes, particularly where the cover slab frames into the uphill retaining system, this unyielding elastic stiffness generates localized bending moment and shear spikes that dominate the cross-sectional checks. This mechanism was evident at the top critical section of the uphill wall. Under preliminary linear elastic Ultimate Limit State (ULS) combinations, the combined axial-bending demand exceeded the design resistance of the baseline cross-section $\frac{M_{Rd}}{M_{Ed}} < 1.0$, signaling

structural inadequacy under conventional verification rules. To satisfy the regulatory sectional checks, the longitudinal reinforcement layout had to be modified through the addition of a supplementary layer of $5\Phi14$ rebars in the uphill wall. Crucially, even with this added reinforcement, the structural element still exhibited the highest demand across the entire structure, yielding a critical utilization factor of $SF = 1{,}128$ in model 5. These findings show that, within the scope of this specific underground tunnel example, standard linear elastic sectional checks tend to treat displacement-controlled coactions with constant stiffness assumptions, resulting in localized demand peaks that govern the structural verification.

In contrast, the non-linear continuum assessments yielded higher global resistance estimates across all analysed operational configurations, with load multipliers reaching $\mathrm{LM}_d = 1{,}347 - 2{,}773$. Within this non-linear continuum framework, incorporating tensile micro-cracking through fracture energy softening, compressive plasticity, and long-term viscoelastic relaxation allows the simulated lining to undergo progressive stress redistribution. As tensile stresses reach the concrete tensile strength at rigid frame corners, localized cracking and compliance naturally attenuate the self-equilibrating restraint forces induced by cyclic temperature fields and drying shrinkage, rather than allowing them to accumulate linearly. Under these modelling assumptions, the integrated frame-pile system mobilizes ductile redistribution across the structure and into the surrounding geotechnical domain, engaging structural reserves that are not captured by localized, elastic cross-sectional checks.

Furthermore, within the comparative framework of this research, the results between model 1 and model 2 illustrate how global reliability estimates remain sensitive to the specific modelling assumptions adopted for the early-age stages. In model 2, where the heat of hydration was omitted, the continuum was subjected to one fewer thermal coaction during its initial curing period. Under the adopted constitutive formulations, omitting these thermal spikes resulted in less accumulated early-age tensile micro-cracking and lower locked-in residual stress concentrations prior to the service and pushover phases. Within the ECOV evaluation, this preserved cross-sectional integrity translated into reduced numerical scatter and a higher 5th-percentile global capacity estimate ($\lambda_{5\%} \approx 3{,}3$) compared to the fully coupled thermo-hydration formulation of model 1 ($\lambda_{5\%} \approx 2{,}8$). These comparative findings indicate that, within the scope and numerical assumptions of this case study, evaluated safety margins are dependent not only on long-term operational actions, but also on the chronological history of early-age thermal actions and the initial damage state incorporated into the numerical continuum.

The numerical pushover simulations further suggest that the prevailing failure kinematics are strongly dependent on the coupling between casting chronology and operational thermal extremes. Under summer casting and peak operational heating, outward expansion of the cover slab generates compressive arching thrust that leads to localized concrete crushing at the downhill knee joint. Conversely, under winter conditions, inward thermal contraction is restrained by the rigid uphill pile group, shifting the governing mechanism toward localized shear demands along the vertical wall sections. Additionally, the explicit simulation of sequential excavation, groundwater lowering, and staged backfilling in model 2 captured localized pre-stress fields that influenced the critical design state.

In conclusion, the findings suggest that evaluating massive underground structures through staged non-linear finite element analysis combined with the ECOV global safety format provides a viable alternative framework to conventional linear sectional checks. By accounting for material softening, creep compliance, and systemic load redistribution under complex soil-structure boundary conditions, this approach allows structural safety margins to be assessed on a global kinematic basis rather than relying exclusively on localized elastic stress peaks.

Although under the specific assumptions and numerical framework adopted in this study, the non-linear finite element analysis of the Galleria Piscinale highlighted encouraging results, indicating potential strength reserves and more favourable safety margins than those obtained through conventional linear checks, within the scope of current practice and governing design codes, the non-linear safety approach is not yet considered sufficiently standardized for routine structural verification. A primary reason for this caution is the high sensitivity of non-linear simulations to initial modelling choices. Assumptions regarding tensile fracture energy, post-peak softening behaviour, mesh regularization, and bond mechanisms can substantially influence the computed global response. Furthermore, solver convergence difficulties and potential numerical instabilities make it challenging for independent checkers to clearly distinguish between genuine physical failure mechanisms and purely algorithmic artifacts. Consequently, the standard linear-elastic method paired with cross-sectional partial safety factors remains the prevailing benchmark, offering a straightforward, easily verifiable, and consistently conservative approach to structural safety. Nevertheless, the positive trends observed when refining the model: particularly by accounting for time-dependent phenomena such as creep, autogenous and drying shrinkage suggest that incorporating a higher level of detail helps capture realistic stress redistributions and long-term strain histories. While these findings remain specific to the models and hypotheses investigated in this thesis, multiplying

this type of comparative numerical research provides valuable benchmark data. Continued exploration along these lines could serve as a useful contribution toward the gradual calibration and possible evolution of future code provisions.

Bibliography

- ACI Committee 207 (2007) ACI 207.1R-07: Guide to Mass Concrete. Farmington Hills, MI: American Concrete Institute.
- Bamforth, P.B. (2007) Early-age thermal crack control in concrete (CIRIA Report C660). London: CIRIA.
- Bertagnoli, G. Mancini, G. and Tondolo, F. (2009) 'Numerical modelling if early age concrete hardening', Magazine of Concrete Research, 61(4), pp. 299-307
- Bertagnoli, G. Mancini, G. and Tondolo, F. (2011) 'Early Age cracking of massive concrete piers', Magazine of Concrete Research, 63(10), pp. 723-736.
- CEN (2005) EN 1994-2: Eurocode 4 — Design of composite steel and concrete structures — Part 2: General rules and rules for bridges. Brussels: European Committee for Standardization (CEN)
- Engen, M., Hendriks, M.A.N., Monti, G., Allaix, D.L. (2021). 'Treatment of modelling uncertainty of NLFEA' in fib Model Code 2020. Structural Concrete, 22(6), 3202–3212. DOI: 10.1002/suco.202100420.
- fib (2013) fib Model Code for Concrete Structures 2010. Berlin: Ernst & Sohn / Wiley.
- Hendy, C.R. and Johnson, R.P. (2006) Designers' Guide to EN 1994-2: Eurocode 4: Design of composite steel and concrete structures. Part 2: General rules and rules for bridges. London: Thomas Telford Publishing.
- Klemczak, B. and Knoppik-Wróbel, A. (2015) 'Reinforcement requirements for early-age thermal and shrinkage effects in massive concrete structures', Engineering Structures, 102, pp. 119-130.
- Mehta, P.K. and Monteiro, P.J.M. (2006) Concrete: Microstructure, Properties, and Materials. 3rd edn. New York: McGraw-Hill.
- Mihashi, H. and Leite, J.P.B. (2004) 'State-of-the-art report on control of cracking in early age concrete', Journal of Advanced Concrete Technology, 2(2), pp. 141–154.
- Neville, A.M (2011) Properties of Concrete. 5th edn. Harlow: Pearson Education.
- Safiuddin, M., Kaish, A.B.M.A., Woon, C.O. and Raman, S.N. (2018) 'Early-age cracking in concrete: Causes, consequences, remedial measures, and recommendations', Applied Sciences, 8(10), p. 1730.
- SETRA (2010) Eurocodes 3 and 4: Application to steel-concrete composite road bridges — Guidance book. Bagneux: Service d'Études sur les Transports, les Routes et leurs Aménagements.

- Tuutti, K. (1982) Corrosion of steel in concrete. Swedish Cement and Concrete Research Institute Report No. 4.82. Stockholm: CBI.